Constraining the Cooling Rates of Chondrules

Thesis

Constraining the cooling rates of chondrules

Thesis submitted for the degree of Doctor of Philosophy

School of Physical Sciences

The Open University

Shannon Charles Stockdale (MGeol)

August 2020

Supervised by Dr Ian Franchi, Dr Mahesh Anand and Professor Monica Grady

External collaborator - Dr Dan Morgan, School of Earth and Environment, University of Leeds

Abstract

The evolution of the protoplanetary disk is inferred in large part from chondritic meteorites which contain the oldest Solar System material. A major component of these meteorites are chondrules, small, ~mm, silicate melt droplets. These formed as a result of transient, widespread heating of dust in the protoplanetary disk. The processes that created chondrules remain poorly understood, with many different competing mechanisms proposed. These range from shockwaves in the solar nebula, impacts between planetesimals and interactions with the early Sun. The cooling rates chondrules experienced during their formation are key constraints on chondrule formation mechanisms and can distinguish between models that are consistent with these constraints and those which are not.

Many type II, FeO-rich porphyritic chondrules contain features called forsteritic-olivine relict grains which originated in the chondrule precursor assemblage and survived the melting event. These grains were able to exchange with the chondrule melt during cooling creating a diffuse boundary. Twelve type II porphyritic chondrules containing forsteritic-olivine grains have been identified and characterised in samples of ALHA 77307 (CO3.00), NWA 8276 (L3.00) and NWA 4910 (L3.1). Fe-Mg compositional profiles have been measured across the grain boundary using calibrated BSE greyscales. These profiles are compared to model diffusion profiles generated using a 1-D explicit finite difference forward modelling program to determine chondrule cooling rates.

Determined chondrule cooling rates for chondrules range from 5 to 8000 Kh^{-1}, with one chondrule in ALHA 77307 showing evidence for extremely rapid cooling at 50000 Kh^{-1}. Chondrules also often show complex, non-linear cooling histories which are most consistent with formation in planetary embryo bow shocks with shock speeds of 6 to 7 kms^{-1}. This places chondrule formation after the formation of large planetary embryos, suggesting that chondrules are a by-product of planet formation rather than representing an important stage in the planet-building process.

Acknowledgements

I am incredibly grateful that I have had the opportunity to complete this PhD at The Open University which was funded by a studentship grant from the Science and Technology Facilities Council.

I would like to thank my supervisors, Ian Franchi, Mahesh Anand, and Monica Grady, as well as Dan Morgan at the University of Leeds. Without their support, guidance, and expertise, this work would not have been possible. In addition, I would like to thank my examiners who provided lots of useful feedback which has considerably improved the thesis.

I would also like to thank a list of people who provided invaluable technical support. This includes Giulia Degli-Alessandrini, Sam Hammond, and Diane Johnson for their training and support on the scanning electron microscope and the electron microprobe, Gordon Imlach for his help with EBSD analyses, Xuchao Zhao for his help conducting NanoSIMS analyses, and Pete Landsberg for helping me prepare my samples for analysis.

Many friends have also helped me during my PhD, particularly my officemates Hannah and Hannah, and my flatmate Rachel. Without their support and friendship this would have been an incredibly difficult and lonely experience. I am also grateful to my parents who have always pushed me to do my best and succeed, while also giving me the independence to pursue my own career and interests. They also provided a wonderful seaside cottage in the north of Scotland with our Border Collie, Rafe, to escape to whenever I needed it. And lastly, I also need to thank my partner, Peter, who supported me throughout the PhD and gave me a kick up the backside when it was necessary.

Nomenclature

Chondrite groups

LL	Ordinary chondrite with the lowest Fe and lowest Fe/SiO_2 ratio
L	Ordinary chondrite with low Fe and low Fe/SiO_2 ratio
H	Ordinary chondrite with high Fe and high Fe/SiO_2 ratio
CI	Ivuna-like carbonaceous chondrite
CO	Ornans-like carbonaceous chondrite
CV	Vigarano-like carbonaceous chondrite
CR	Renazzo-like carbonaceous chondrite
CM	Mighei-like carbonaceous chondrite
CB	Bencubbin-like carbonaceous chondrite

Chondrule terminology

Type I	FeO-poor (<10%) chondrule (MgO-rich)
Type II	FeO-rich (>10%) chondrule (MgO-poor)
R	Chondrule displaying a radial texture
B	Chondrule displaying a barred texture
P	Chondrule displaying a porphyritic texture
A	Chondrule silicates are dominated by olivine (>90%)
B	Chondrule silicates are dominated by pyroxene (>90%)
AB	Chondrule silicates contain more equal amounts of olivine and pyroxene

Analytical instruments and techniques

SEM	Scanning Electron Microscope or Scanning Electron Microscopy
BSE	Backscattered Electron
SE	Secondary Electron
CL	Cathodoluminescence
EDS	Energy-dispersive X-ray Spectroscopy
WDS	Wavelength-dispersive X-ray Spectroscopy
EBSD	Electron Backscatter Diffraction

EBSP	Electron Backscatter Pattern or Kikuchi pattern
EPMA	Electron Probe Microanalysis or Electron Microprobe analyses
NanoSIMS	Nano Secondary Ion Mass Spectrometry
FIB-SEM	Focussed Ion Beam Scanning Electron Microscope
FEG-SEM	Field Emission Gun Scanning Electron Microscope

Diffusion mechanisms

ID	Intrinsic Domain
TaMED	Transition Metal Extrinsic Domain
PED	Purely Extrinsic Domain

Others

CAI	Calcium and Aluminium Rich Inclusion
AOA	Amoeboid Olivine Aggregate
IW	Iron-wüstite buffer

Contents

List of Figures

List of Tables

Chapter 1

Introduction to chondrites, chondrules and chondrule formation

This chapter introduces chondrites, chondrules and chondrule formation which are the focus of this thesis. Chondrites are some of the oldest materials in the Solar System and therefore, can tell us about processes occurring at the beginning of the Solar System. Chondrules are one of the major constituents of these chondrites and are often the most abundant feature. They are small, usually sub-mm, roughly spherical melt droplets formed by widespread but transient heating events in the protoplanetary disk. Despite decades of study, the origin of chondrules is still unknown, and many different potential chondrule formation mechanisms have been proposed, for example, impacts between planetesimals, shockwaves in the protoplanetary disk and interactions with the early Sun. Chondrule cooling rates are one of the important constraints on these potential formation mechanisms and can discriminate between mechanisms which meet these constraints and those which do not. Dynamic crystallisation experiments, aimed at reproducing chondrule textures experimentally, remain the most widely cited method of determining chondrule cooling rates. However, these are an indirect measure of chondrule cooling rate which needs to be validated by using more direct measurements, of which there are relatively few. Forsteritic-olivine relict grains present in type II, FeO-rich chondrules provide an opportunity to study chondrule cooling rates more directly. By measuring and modelling the shape of Fe-Mg diffusion profiles in these relict grains, chondrule cooling rates and thermal histories can be obtained and used to evaluate the currently proposed chondrule formation mechanisms.

1.1 The early Solar System and the protoplanetary disk

Newly forming stars are present in dense molecular clouds, which appear opaque to relatively short wavelengths such as visible light. However, observations using relatively long wavelengths such as far infrared, ~1 mm, can probe deep within these dense molecular clouds. These observations have led to the widely accepted theory that stars, such as the Sun, form as a result of the gravitational self-collapse of a dense region within one of these molecular clouds (Boss and Goswami, 2006). This collapse forms a protostar, which rapidly accretes mass from the surrounding gas and dust while simultaneously ejecting material from its poles by bipolar jets. Throughout this stage, the protostar is shrinking, and therefore increasing in density. This causes infalling material to rotate around the star more rapidly to conserve angular momentum. Any slow-moving material ends up accreted into the protostar, but some material will be moving rapidly

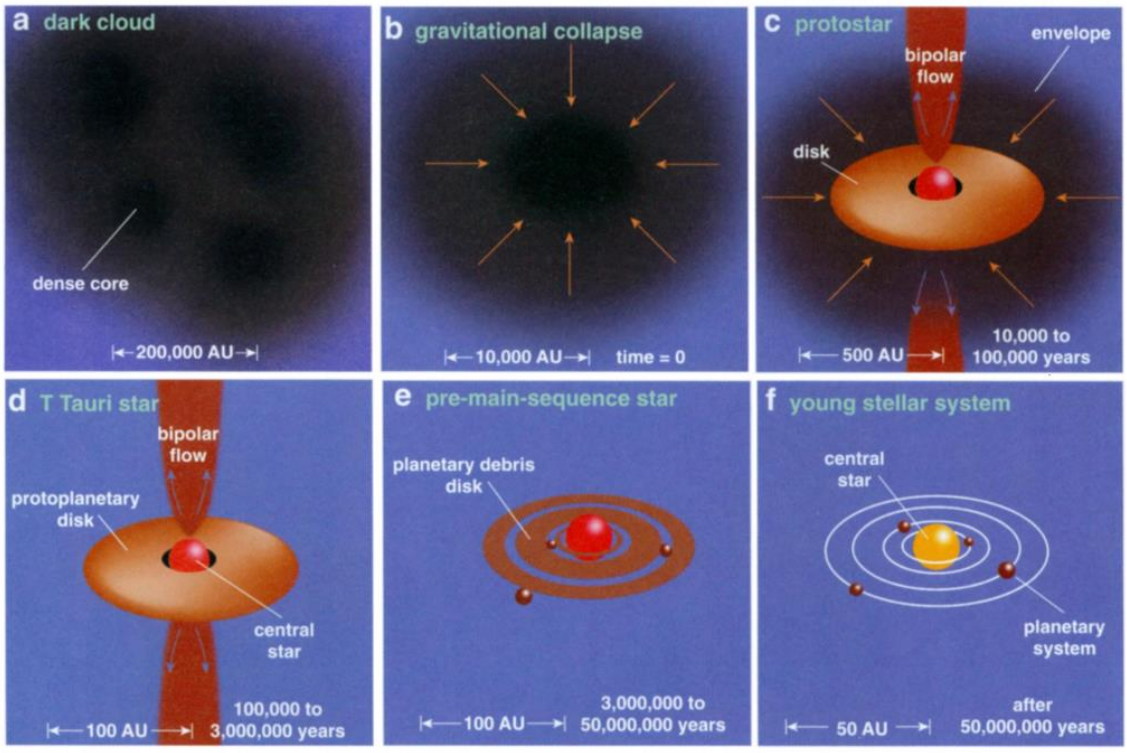

Figure 1.1 – Diagram outlining the formation of a sun-like star: a) star formation begins in a dense region of a molecular cloud; b) the dense region begins to collapse under gravitational forces to form a protostar; c) the protostar rapidly accretes material from the surrounding gas and dust, material is also ejected from the star in the form of bipolar flows; d) surrounding dust dissipates leaving a pre-main sequence star surrounded by a protoplanetary disk; e) most of the protoplanetary disk material is dissipated, leaving a bare pre-main sequence star, however, it is possible that a debris disk containing newly formed planets can remain around the star; f) the continuing gravitational collapse of the star allows the star to reach core temperatures hot enough for nuclear fusion to take place, becoming a main sequence star (Greene 2001).

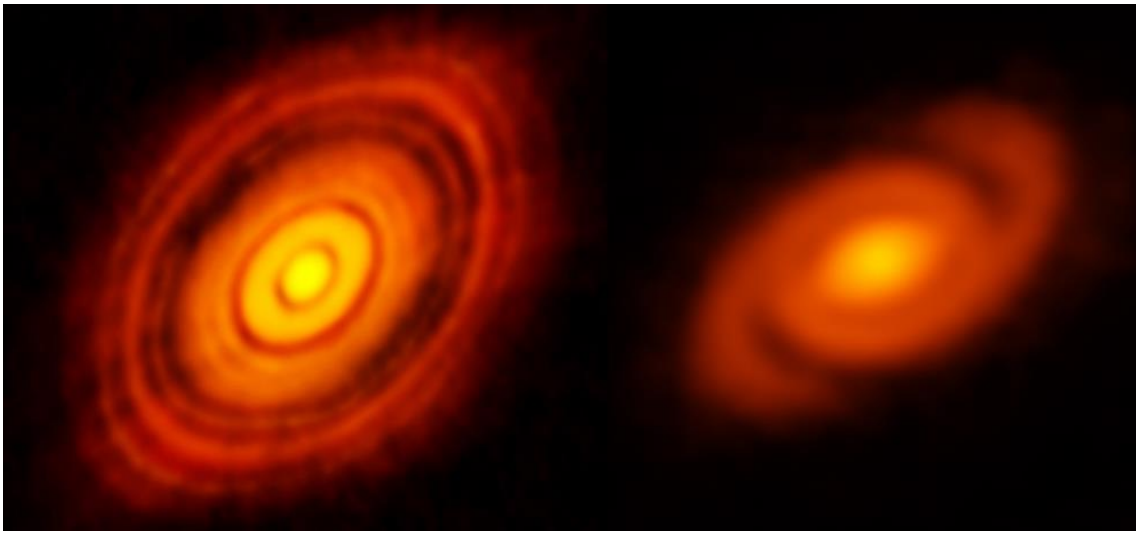

Figure 1.2 – Images of protoplanetary disks around stars. Left: protoplanetary disk around star HL Tauri showing evidence of forming planets. Credit: ALMA (ESO/NAOJ/NRAO) (https://www.almaobservatory.org/en/press-release/revolutionary-alma-image-reveals-planetary-genesis, last visited 29/01/2019. Right: protoplanetary disk around star Elias 2-27 showing spiral arms. Credit: B. Saxton (NRAO/AUI/NSF); ALMA (ESO/NAOJ/NRAO) (https://phys.org/news/2016-09-spiral-arms-embrace-young-star.html, last visited 29/01/2019).

enough to travel in orbit forming a circumstellar disk. When the material surrounding the star has dissipated, the accretion process stops, resulting in a pre-main sequence star surrounded by a protoplanetary disk. Eventually, most of the material in this disk is lost leaving a bare star which may be surrounded by several large bodies which are remnants of the protoplanetary disk. For our Solar System, asteroids, comets and planets are this remnant (Greene, 2001). The process of star and protoplanetary disk formation is summarised in Figure 1.1. These protoplanetary disks have been observed around many stars such as HL Tauri (Kwon et al., 2011) and Elias 2-27 (Pérez et al., 2016) (See Figure 1.2).

The bulk of the material in protoplanetary disks is gas, however, the solid component, composed of dust grains, is significant as it is these dust grains that are the building blocks for the formation of planetesimals and ultimately planets (Natta et al., 2006). Most of this material was either lost to the star or has been geologically processed in planets. However, a small amount does remain largely preserved in the form of primitive chondritic meteorites originating from the asteroid belt despite some possible processing by aqueous alteration and thermal metamorphism. Cosmochemical studies of this material provide us with detailed information about the formation and evolution of the early Solar System and protoplanetary disk.

1.2 Overview of planet formation

Planet formation occurs as a result of accretion of dust over several incremental growth stages (Ward, 1996; Chambers, 2004; Cuzzi and Weidenschilling, 2006; Weidenschilling and Cuzzi, 2006; Raymond, 2007). According to dynamical simulations, the formation of Earth-like terrestrial planets takes ~10 to 100 Myrs (e.g. Agnor et al. 1999; Chambers 2001).

In the first stage sub-µm to µm sized dust grains begin to settle towards the mid plane of the protoplanetary disk, creating a solid rich layer. In a non-turbulent nebula, a dust grain will settle in 10^4 years, however, given the solar nebula was turbulent (Desch and Cuzzi, 2000; Cuzzi et al., 2001), it would likely take longer. The degree of turbulence governs the thickness of this layer, and therefore the density, or solid to gas ratio in this layer. A more turbulent nebula will result in a thicker less dense layer, whereas a less turbulent nebula results in a thinner, denser layer (Cuzzi et al., 1993). As they settle, they may collide and coagulate into pebbles and boulders up to 1 m in diameter by non-gravitational forces (Ward, 1996; Chambers, 2004; Cuzzi and Weidenschilling, 2006; Raymond, 2007). These may include van der Waals, electrostatic and electromagnetic forces (Ward, 1996; Chambers, 2004; Cuzzi and Weidenschilling, 2006). Above this size, growth is supressed by more rapid collisions which break up the pebbles and boulders, erosional headwinds and infalling as a result of loss of angular momentum (Chambers, 2004; Raymond, 2007).

The second stage of planet formation requires these boulders to accrete to form larger planetesimals. This could be achieved by the formation of dense regions with higher solid to gas ratios in the solar nebula, producing gravitational instabilities. These gravitational instabilities require concentration of these pebbles and boulders (Chambers, 2004; Raymond, 2007). This might be achieved in several ways, for example, turbulent eddies and vortices (Tanga et al., 1996; Desch and Cuzzi, 2000; Cuzzi et al., 2001), streaming instabilities (Johansen et al., 2007), concentration by drag induced infalling (Youdin and Chiang, 2004) or by photoevaporation of nebular gas (Throop and Bally, 2005). The self-collapse under gravity of this denser region may form kilometre sizes planetesimals (Chambers, 2004; Raymond, 2007). If no gravitational instability is possible, then planetesimals must be formed gradually by low velocity collisions between pebbles and boulders (Chambers, 2004).

Once planetesimals have formed, the third stage of accretion begins. These planetesimals are now large enough to gravitationally perturb each other when they approach each other. Larger planetesimals sweep up smaller planetesimals by gravitational focussing and inelastic collisions in a process called runaway accretion (Chambers, 2004; Raymond, 2007). When several of the larger planetesimals become much larger than their surrounding planetesimals (~100 times larger), runaway growth ends, and oligarchic growth begins. In this phase, accretion is dominated by the large planetesimals which accrete material from their own region of the protoplanetary disk, but do not otherwise interact. Accretion rate in this period is much slower than in runaway growth. This phase persists for ~1 Myr until several large protoplanets or planetary embryos (moon to Mars sized objects) have formed (Chambers, 2004; Raymond, 2007).

Once their surrounding planetesimals are depleted, the final stage of accretion begins. In this stage, neighbouring planetary embryos can begin to interact with each other. During this phase accretion may occur by accreting any remaining planetesimals or by giant impacts between these planetary embryos to form larger planets. However, these impacts may not be accretionary and may result in the breakup of the planetary embryo (Chambers, 2004; Raymond, 2007).

There are challenges to this model, including the *bouncing barrier* and the *metre-size barrier* (e.g. Morbidelli and Raymond, 2016). When silicate grains grow to a size of ~1 mm, upon collision, they bounce away rather than accreting making it difficult to create aggregates of dust particles larger than this size resulting in the *bouncing barrier*. In addition, gas drag causes these particles to rapidly migrate towards the star at the centre of the protoplanetary disk. This rapid migration towards the star also means that material would be lost so rapidly to the star that further opportunities for collisions would be limited. The rapid migration also causes large relative velocities between particles, resulting in disruptive rather than accretionary collisions when they do occur. Together these issues are the *metre-size barrier*. It may be possible to overcome these barriers by turbulent concentration (Tanga et al., 1996; Desch and Cuzzi, 2000; Cuzzi et al., 2001), streaming instabilities (Youdin and Goodman, 2005; Johansen et al., 2007), and collisional coagulation (Kataoka et al., 2013). However, it remains uncertain if the solar nebula was turbulent enough to concentrate particles, and particles may need to be as large as ~20 cm in order to clump together in turbulent eddies and vortices (Johansen et al., 2007). It is

unclear how particles could grow to this size (Morbidelli and Raymond, 2016). Streaming instabilities can only be formed at solid/gas ratios which are higher than in a canonical solar nebula, and it is unclear whether this can be realistically achieved (Morbidelli and Raymond, 2016). Further accretion may be achievable in collisional coagulation; however, this may only be achievable for icy particles beyond the snowline in the protoplanetary disk. Collisions between these icy particles tend to form fluffy aggregates with very high porosity. These aggregates have slow radial drift and are resistant to disruption during collisions (Kataoka et al., 2013). On the other hand, silicate particles have different sticking properties and cannot coagulate by this mechanism (Morbidelli and Raymond, 2016).

These challenges to the planet building model show that there are problems at a size roughly equivalent to chondrules (Morbidelli and Raymond, 2016). Studying chondrules to gain a greater understanding of chondrule formation may contribute to our knowledge of the planet building process.

1.3 Chondrites

1.3.1 Introduction to chondrites

Chondrites are the most common meteorite type to fall to Earth and account for ~70% of observed falls (Hutchison, 2004). They are also the oldest known rocks in the Solar System with an age of ~4.567 Ga, based on the ages of Calcium and Aluminium-rich Inclusions (CAIs) (Connelly et al., 2017). The abundances of non-volatile elements in these chondritic meteorites, especially the CI chondrites, are similar to those found in the solar photosphere (e.g. Lodders 2019). They are primarily composed of a mix of chondrules (small silicate melt droplets that have solidified) and fine-grained matrix with a minor component of CAIs (calcium and aluminium-rich inclusions). These components were formed at different locations and/or times before being combined into one rock. Because of this, chondrites offer us the opportunity to study processes and environments in the early Solar System and the protoplanetary disk.

1.3.2 Chondrite classification

Chondrites are generally divided into 3 classes and 15 groups: ordinary chondrites (H, L and LL), carbonaceous chondrites (CO, CI, CM, CR, CV, CH, CB and CK) and enstatite chondrites (EH and EL). K and R chondrites do not fit into the 3 main classes, however, they each

constitute a group. Some chondritic meteorites do not fit in these groups and are therefore ungrouped.

The divisions between chondrite groups are mainly based upon differences in bulk chemical composition, mineralogical properties and oxygen isotope composition which vary widely between the different chondrite groups (see Table 1.1). Specifically, classification is usually based upon refractory lithophile compositions and oxygen isotope compositions (Clayton et al., 1991; Clayton and Mayeda, 1999; Scott, 2007). In addition, the properties and proportion of chondrules, refractory inclusions (such as CAIs), matrix and metal vary significantly between the different chondrite groups, for example, mean chondrule size and the volume percentage of different chondrite components (see Table 1.1).

Table 1.1 – Summary of chondrite groups and some of their properties. Values are from Scott and Krot (2003)

Chondrite group	Volume of CAIs and AOAs (vol %)	Mean chondrule diameter (mm)	Volume of chondrules (vol %)[a]	Volume of metal (vol %)	Volume of matrix (vol %)[b]	Refractory lithophile/Mg ratio relative to CI[c]
Ordinary chondrites						
H	0.01-0.02	0.3	60-80	8	10-15	0.93
L	<0.1	0.5	60-80	3	10-15	0.94
LL	<0.1	0.6	60-80	1.6	10-15	0.90
Carbonaceous chondrites						
CO	13	0.15	40	1-5	30-50	1.13
CI	<0.01	-	<5	<0.01	95	1.00
CM	5	0.3	20	0.1	70	1.15
CR	0.5	0.7	50-60	5-8	30-50	1.03
CV	10	1.0	45	0-5	40	1.35
CH	0.1	0.02-0.09	~70	20	5	1.00
CB_a	<0.1	~5	40	60	<5	1.0
CB_b	<0.1	~0.5	30	70	<5	1.4
CK	4	0.8	15	<0.01	75	1.21
Enstatite chondrites						
EL	<0.1	0.6	60-80	15	<0.1-10	0.83
EH	<0.1	0.2	60-80	8	<0.1-10	0.87
Other chondrites						
K	<0.1	0.6	20-30	6-9	70	0.9
R	<0.1	0.4	>40	<0.1	35	0.95

[a]Includes chondrule fragments and silicates inferred to be fragments of chondrules
[b]Includes matrix-rich clasts which account for all matrix in CH and CB_b chondrites
[c]Mean ratio of refractory lithophiles relative to magnesium, normalised to CI chondrites

Table 1.2 – Petrologic types of meteorites in different chondrite groups.

Chondrite Group	1 Most aqueously altered	2	3 Most pristine	4	5	6 Most thermally metamorphosed
	Aqueous alteration ←					→ Thermal metamorphism
H						
L						
LL						
CO						
CI						
CM						
CR						
CV						
CH						
CB						
CK						
EL						
EH						
K						
R						

1.3.3 Chondrite petrologic types

Chondrites are also classified into petrologic types 1 to 6, see Table 1.2. These types relate to the amount of parent body processing that has taken place. Petrologic type 3 is the least aqueously altered and least thermally metamorphosed, showing sharply defined chondrules containing clear isotropic glass, and the matrix is clastic, fine-grained and opaque in transmitted light. Moving towards petrologic type 6 reflects increasing metamorphic grade. By petrologic type 6, chondrules are poorly defined with a crystalline mesostasis, the matrix has increased in transparency and grain-size has coarsened. Moving towards petrologic type 1 reflects an increasing degree of aqueous alteration experienced on the parent body. Chondrites in petrologic type 1 do not contain chondrules and are composed of minerals that formed during aqueous alteration (Hutchison, 2004). When studying processes in the protoplanetary disk which occurred before the accretion of the

chondrite parent body, it is necessary to study meteorites which have experienced the least thermal metamorphism and aqueous alteration on the parent body, petrologic type 3.0.

1.3.4 Chondrite components

1.3.4.1 Chondrules

Chondrules are usually one of the major components of chondritic meteorites and are often the most abundant, constituting up to 80% of the rock (see Table 1.1). They are small, usually sub-mm, but can be up to several millimetres in diameter, roughly spherical solidified droplets composed of ferromagnesian silicates, metal, sulfides and glass. They are some of the earliest objects in the Solar System and formed in the first 4 Myrs of the Solar System (Bollard et al., 2017; Pape et al., 2019). They formed as a result of widespread heating and melting of dust particles in the protoplanetary disk, forming droplets which subsequently cooled and solidified. However, the nature of the heating event is poorly understood. This is the focus of this thesis, and further background to chondrules and chondrule formation is provided in section 1.4 onward.

1.3.4.2 CAIs

All chondrite groups contain calcium and aluminium-rich inclusions (CAIs), although these are very rare in CI chondrites. The name CAI covers a range of objects defined by being enriched in refractory elements e.g. Ca and Al. They are primarily composed of Ca-Al-Ti minerals, such as, corundum, hibonite, grossite, perovskite, spinel, melilite, Al-diopside and anorthite. They are the oldest objects that formed in the solar nebula, with ages of 4.567 Ga according to Pb-Pb dating, contemporaneously with the oldest chondrules (Connelly et al., 2012; Connelly et al., 2017). They formed in a ^{16}O-rich and highly reducing environment. Some are thought to be condensates based upon their irregular shapes, fluffy textures and mineralogy that is consistent with condensation from a solar nebula gas. Some CAIs have large isotopic anomalies which suggests that they underwent evaporation. Some are spherical with coarse grains and igneous textures which suggests that they formed by melting and crystallisation over timescales of days (Yoneda and Grossman, 1995; Grossman et al., 2000; Davis et al., 2005; Scott, 2007).

1.3.4.3 Matrix

The other major component of chondritic meteorites in the matrix. This is a fine-grained (<5 μm) material that surrounds the other chondrite components and fills the spaces

between them. The fine-grained nature of chondrite matrix makes it prone to alteration. The most primitive matrices found in carbonaceous chondrites such as ALHA 77307 (CO3.00) and Acfer 094 (C-ungrouped 3.0) are composed of crystalline Mg-rich silicates, amorphous silicates, Fe,Ni metal, sulphides, refractory oxides, carbonaceous material, organics and some presolar grains (Brearley, 1993; Greshake, 1997; Scott, 2007). The Mg-rich silicates have high concentrations of MnO, comparable to refractory Amoeboid Olivine Aggregates (AOAs), which formed by condensation in the solar nebula. This suggests these Mg-rich silicates also formed by condensation from solar nebula gas (Scott, 2007). The amorphous silicates are also nebular condensates (Greshake, 1997; Scott, 2007). Alteration of this material results in the formation of phyllosilicates (e.g. serpentine), carbonates, magnetite, and Fe-rich olivine. Chondrite matrix may also contain chondrule fragments in the form of olivine or pyroxene grains with similar compositions to chondrules. Chondrite matrix represents a complex mix of material including presolar grains, nebula condensates and chondrule fragments which experienced varying degrees of alteration in the chondrite parent body (Brearley, 1993; Greshake, 1997; Hutchison, 2004; Huss et al., 2005; Bland et al., 2007; Scott, 2007; Hezel et al., 2018).

1.4 Chondrules

As chondrules are the focus of this thesis, they are discussed in more detail in the following section.

1.4.1 Chondrule textures

One of the most striking features of chondrules is their textural diversity. There are three main chondrule textures: porphyritic, barred, and radial. Porphyritic chondrules show crystals of olivine and/or pyroxene with more equant shapes than barred or radial textures (e.g. Figure 1.3a). A chondrule displaying barred texture has crystals, usually olivine, which occur in sets of parallel plates or bars (e.g. Figure 1.3b). Chondrules with a radial texture show acicular crystals, usually of pyroxene, radiating from points within, or on the edge of the chondrule (Figure 1.3c). In all three textural types, crystals are surrounded by glassy to cryptocrystalline mesostasis (Gooding and Keil, 1981; Lofgren, 1996; Hewins, 1997; Desch and Connolly, 2002; Jones et al., 2005; Desch et al., 2012; Jones et al., 2018).

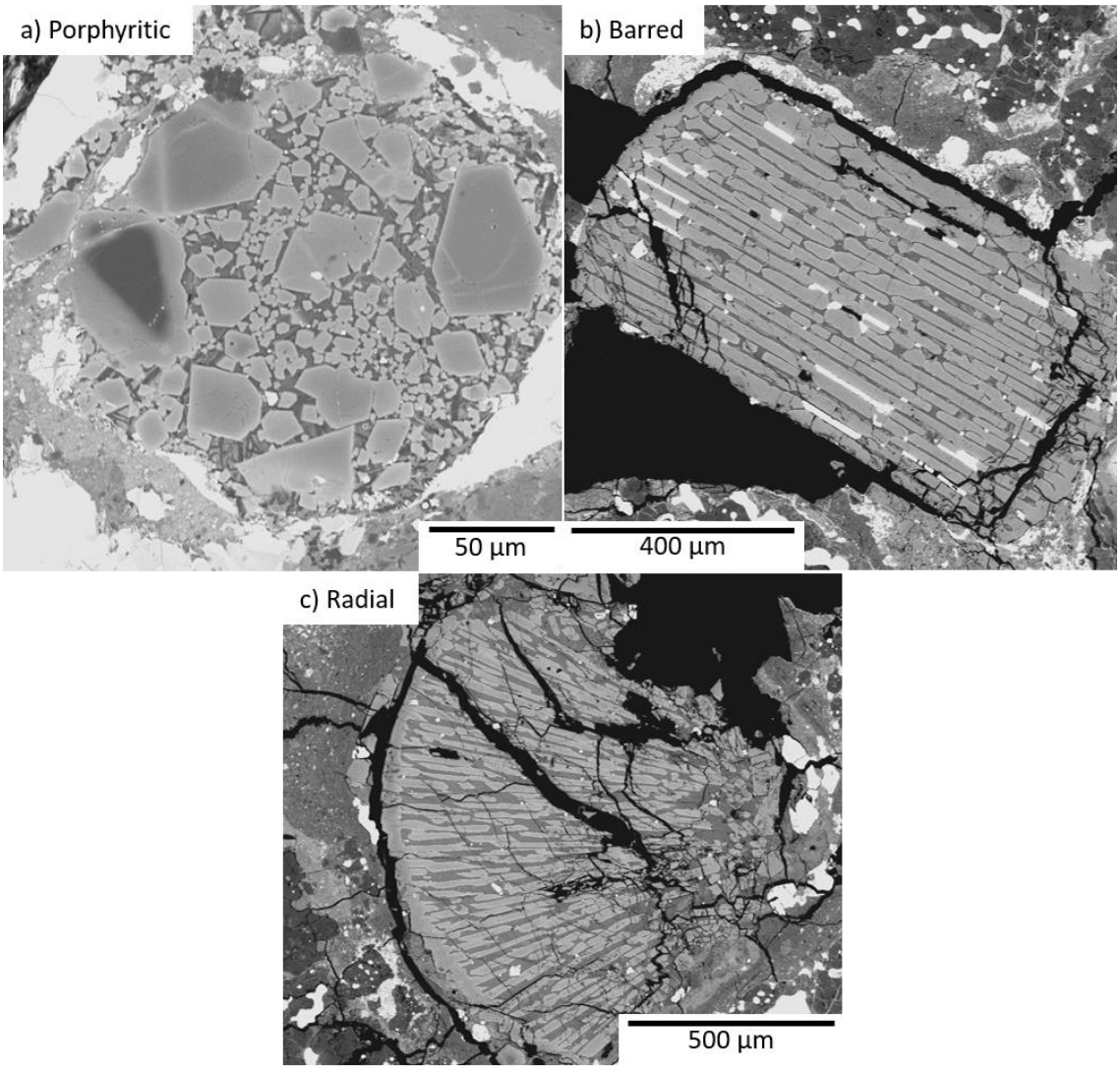

Figure 1.3 – Variety of chondrules textures shown in backscattered electron images: a) porphyritic texture in a chondrule from NWA 4910; b) barred texture in a chondrule fragment from EET 87847; c) radial texture in a chondrule fragment from EET 87847. Images from this study.

Dynamic crystallisation experiments have reproduced chondrule textures, in an effort to understand chondrule formation conditions (Hewins et al., 1981; Lofgren and Russell, 1986; Lofgren, 1989; Lofgren and Lanier, 1990; Radomsky and Hewins, 1990; Connolly and Hewins, 1991; Jones and Lofgren, 1993; Kennedy et al., 1993; Connolly and Hewins, 1995; Dehart and Lofgren, 1996; Connolly et al., 1998; Tsuchiyama et al., 2004; Wick and Jones, 2012). These experiments have shown that chondrule texture is mainly controlled by the availability of nucleation sites for crystal growth during chondrule cooling by the process of heterogeneous nucleation. This requires solid material from the chondrule precursor which has been incompletely melted. The availability of these crystalline nuclei is a function of several factors, for example, grain size of chondrule precursor, peak temperature relative

to the chondrule liquidus and heating time. Porphyritic textures are generally produced from heating below the chondrule liquidus temperature which preserves numerous nucleation sites for crystal growth. Barred textures are produced from heating to temperatures slightly above the chondrule liquidus which destroys most, but not all, nucleation sites. Radial textures are produced by heating to temperatures above the chondrule liquidus which preserves very few or no nucleation sites. This is summarised in Figure 1.4 (Lofgren and Russell, 1986; Radomsky and Hewins, 1990; Lofgren, 1996; Jones et al., 2018).

The strong relationship between availability of crystal nucleation sites and chondrule texture means that chondrule cooling rates play a secondary role in determining the chondrule texture. For example, porphyritic chondrules generally require slower cooling

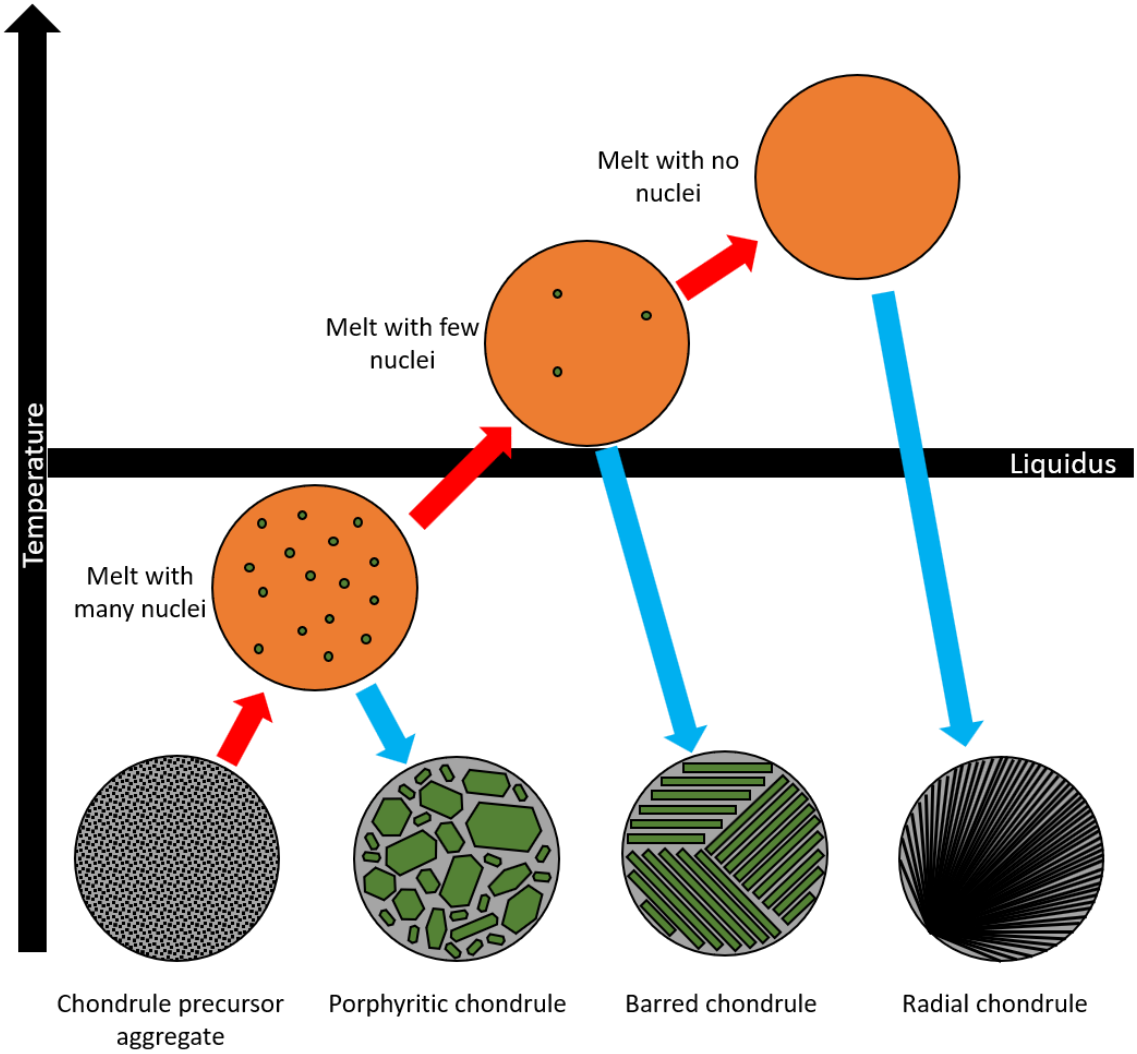

Figure 1.4 – Diagram showing the peak temperature compared to the chondrule liquidus for porphyritic, barred and radial chondrule textures (adapted from Jones et al. 2018).

rates than barred and radial textures. (Lofgren and Russell, 1986; Radomsky and Hewins, 1990; Lofgren, 1996; Hewins et al., 2005; Desch et al., 2012; Jones et al., 2018). A more thorough discussion on the effect of cooling rate on chondrule texture can be found in section 1.6.

1.4.2 Chondrule chemical groups

Chondrules are divided into two chemical groups, type I, and type II. Type I chondrules are low in FeO, contain MgO-rich silicates and are relatively rich in Fe,Ni metal (e.g. Figure 1.5a). Type II chondrules are relatively high in FeO, with more FeO-rich silicates (e.g. Figure 1.5b). A simple way to distinguish between the two types is the atomic ratio of Mg to Fe, or Mg#, of silicates in the chondrule. In type I chondrules, this value is >90%, whereas in type II chondrules this is <90%. Type I chondrules record crystallisation under relatively reducing conditions, several log units beneath the iron-wüstite buffer, whereas type II chondrules crystallised under relatively oxidising conditions, closer to the iron-wüstite buffer (Scott and Taylor, 1983; Jones et al., 2005; Jacquet et al., 2015).

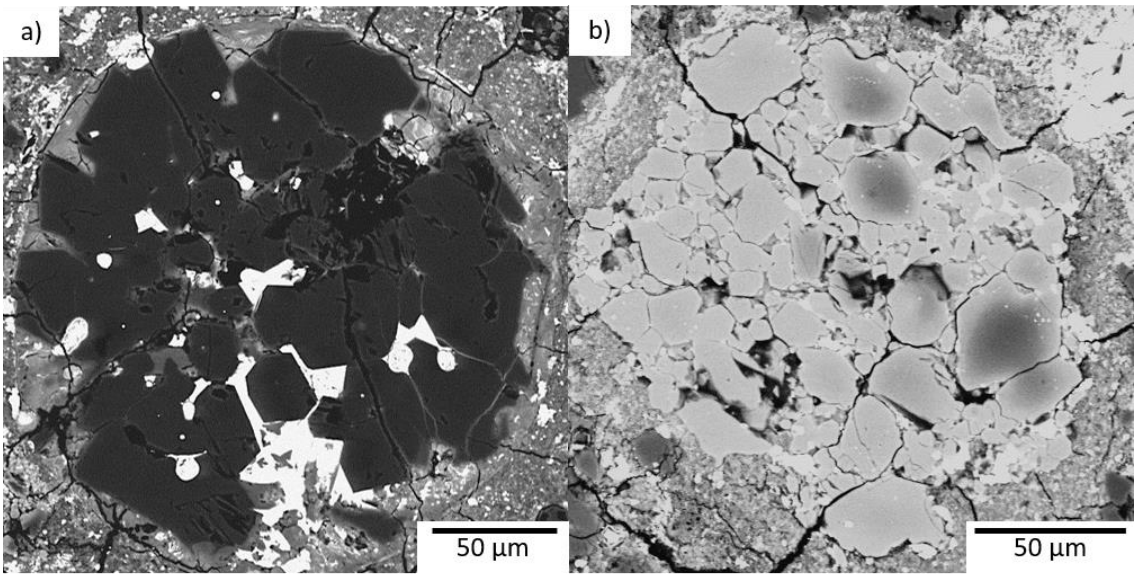

Figure 1.5 – a) BSE image of a type I porphyritic olivine in ALHA 77307 chondrule containing MgO-rich olivine, which appears relatively dark, and Fe,Ni metal which appears white; b) BSE image of a type II porphyritic olivine chondrule in ALHA 77307 containing more FeO-rich olivine which appears light grey.

1.4.3 Chondrule classification

Chondrules are classified by their texture, chemistry, and mineralogy. The prefix P, B or R refers to porphyritic, barred, or radial textures, respectively. As noted in section 1.4.2, type I refers to FeO-poor chondrules whereas type II chondrules are relatively FeO-rich. The

ratio of olivine to pyroxene is also used for classification. In type A chondrules, olivine is the dominant mineral (90% or more), whereas, in type B chondrules, pyroxene is the dominant mineral. Where the value is intermediate, with more equal amounts of olivine and pyroxene, the chondrule is type AB. The suffix O, P or OP also shows which minerals dominate within the chondrule. Chondrules where olivine is the dominant mineral use the suffix O; chondrules where pyroxene is the dominant mineral use the suffix P, and where they are more equal, the suffix is OP. These classifications make it easy to quickly describe chondrules, for example, a type IIA BO chondrule refers to an FeO-rich, barred olivine chondrule, whereas type IAB POP refers to an FeO-poor, porphyritic olivine and pyroxene chondrule (Hewins et al., 2005; Jones et al., 2005).

1.5 Relict grains in chondrules

Many chondrules contain features called relict grains. These are grains that are considerably different from their host chondrule. They are thought to originate from the solid chondrule precursor assemblage and survived the melting event without completely melting. They are surrounded by overgrowths which are similar in composition to their host chondrule. There are two major groups of these grains, forsteritic-olivine and dusty olivine (see Figure 1.6), as well as several other types (Jones, 2012).

1.5.1 Forsteritic-olivine relict grains

Forsteritic-olivine relict grains are commonly found in type IIA chondrules in many chondrite groups: LL (Jones, 1990; Ruzicka et al., 2008; Berlin et al., 2011), CO (Jones, 1992; Wasson and Rubin, 2003; Berlin et al., 2011), CR (Leshin et al., 1998; Connolly and Huss, 2010), CV (Hertwig et al., 2018), and CM (Hanowski and Brearley, 2001; Hewins et al., 2014), however they are most common in CO chondrites. Approximately 90% of type IIA chondrules in CO chondrites contain forsteritic-olivine relict grains (Wasson and Rubin, 2003), whereas, only ~30% of type IIA chondrules in LL chondrites contain forsteritic-olivine relict grains (Jones, 1990). They generally appear as highly forsteritic olivine (>Fo_{98}) surrounded by more FeO-rich overgrowth. As well as being compositionally distinct from the surrounding chondrule, they may also be isotopically distinct and richer in ^{16}O compared to the host chondrule olivines. Forsteritic-olivine relict grains that show similar O-isotope values to melt grown olivines in the host chondrule likely formed in type I chondrules in the same region and are recycled chondrule fragments. Grains which are

richer in ^{16}O may originate from a refractory source, for example AOAs or CAIs (Jones et al., 2000; Ruzicka et al., 2007; Kita et al., 2008; Connolly and Huss, 2010; Tenner et al., 2018).

1.5.2 Dusty olivine relict grains

Dusty olivine relict grains are found in type I chondrules in both ordinary and carbonaceous chondrites, however they are more common in ordinary chondrites where they occur in ~10% of type I chondrules. They appear as forsteritic-olivine speckled with exsolved iron metal grains and they form as a result of the reduction of FeO-rich relict grains during the formation of the host chondrule (Rambaldi, 1981; Rambaldi and Wasson, 1981; Kracher et al., 1984; Jones and Danielson, 1997; Leroux et al., 2003; Jones, 2012).

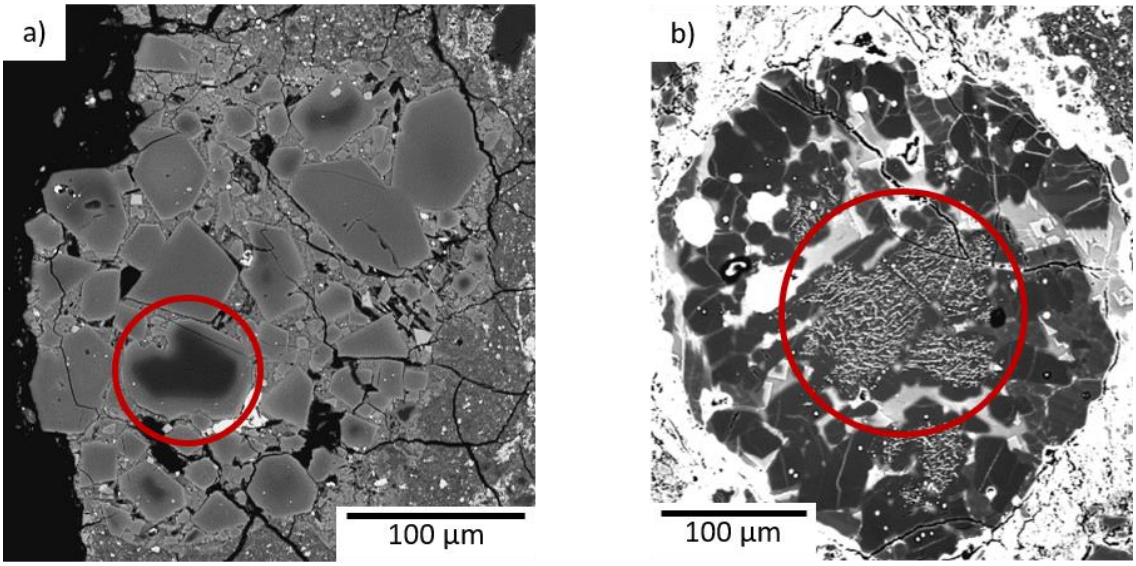

Figure 1.6 – a) BSE image of a type II porphyritic olivine chondrule in ALHA 77307 containing a forsteritic-olivine relict grain (circled in red) from this study. b) BSE image of a type I porphyritic olivine chondrule in Semarkona containing dusty olivine relict grains (circled in red) (Leroux et al. 2003).

1.5.3 Other examples of relict grains

Other examples of relict grains include: forsteritic-olivine relict grains in type I chondrules, identified by their cathodoluminescence properties (Steele et al., 1985; Steele, 1986; Klerner et al., 2000; Jones and Carey, 2006; Kita et al., 2010); FeO-rich relict grains found in type II chondrules identified by Mn/Fe compositions (Berlin et al., 2011); olivine crystals that are isotopically distinct from their host chondrules (Kita et al., 2010); and relict pyroxene grains (Kracher et al., 1984; Jones, 1996; Hewins, 1999).

1.5.4 Significance of relict grains

Most relict grains are generally considered to be derived from previous generations of chondrules. For example, forsteritic-olivine relict grains in type II chondrules are compositionally similar to olivine grains in type I chondrules (Jones and Scott, 1989; Jones, 1990; Jones, 1992). This means that the chondrule formation event occurred multiple times, including time for the breakup of an earlier generation of chondrules into new precursor assemblages. As they are a common feature across many chondrite groups, chondrule recycling must have been a common process in the chondrule formation region. Any potential chondrule formation mechanism must, therefore, be widespread and repeatable (Jones, 2012).

Forsteritic-olivine relict grains are most common in carbonaceous chondrites, and dusty olivine relict grains are more common in ordinary chondrites. This adds to the observation that type I chondrules were more common than type II chondrules in the carbonaceous chondrite formation region, leading to the higher prevalence of forsteritic-olivine relict grains in type II chondrules. Conversely, type II chondrules were more common than type I chondrules in the ordinary chondrite formation region leading to a higher proportion of dusty olivine grains in type I chondrules. This means that there were likely at least two separate reservoirs in which chondrule formation occurred; one for carbonaceous chondrites and another for ordinary chondrites (Jones, 2012). These reservoirs could be separated in space or time, however, the age of chondrules in carbonaceous and ordinary chondrites indicates that they were forming at the same time (Connelly et al., 2012; Bollard et al., 2017). This means that they were likely separated in space (Jones, 2012).

1.5.5 Chondrule precursors

Relict grains in chondrules also provide information on the nature of chondrule precursors. These precursors were of isotopically diverse and the aggregates may have contained material from a variety of sources, including CAIs (e.g. Wakaki et al., 2013; Krot et al., 2017), AOAs (e.g. Nagashima et al., 2015), fragments of previously formed chondrules (e.g. Jones, 1990; Jones, 1992), as well as fine-grained matrix like material (Krot et al., 2018).

1.6 Constraints on chondrule formation from chondrule cooling rates

The cooling rates of chondrules are perhaps the most important constraints on chondrule formation, as they are a direct measure of (part of) the heat pulse that is fundamental to chondrule formation and has the potential to be determined in several different ways. Cooling rates therefore perhaps offer the best approach to distinguish between competing chondrule formation models (see section 1.8).

1.6.1 Dynamic crystallisation experiments

The most widely cited method of determining chondrule cooling rates is dynamic crystallisation experiments (Hewins et al., 1981; Lofgren and Russell, 1986; Lofgren, 1989; Lofgren and Lanier, 1990; Radomsky and Hewins, 1990; Connolly and Hewins, 1991; Jones and Lofgren, 1993; Kennedy et al., 1993; Connolly and Hewins, 1995; Dehart and Lofgren, 1996; Connolly et al., 1998; Weinbruch et al., 1998; Tsuchiyama et al., 2004; Wick and Jones, 2012; Perez, 2018). These experiments attempted to produce chondrule-like objects

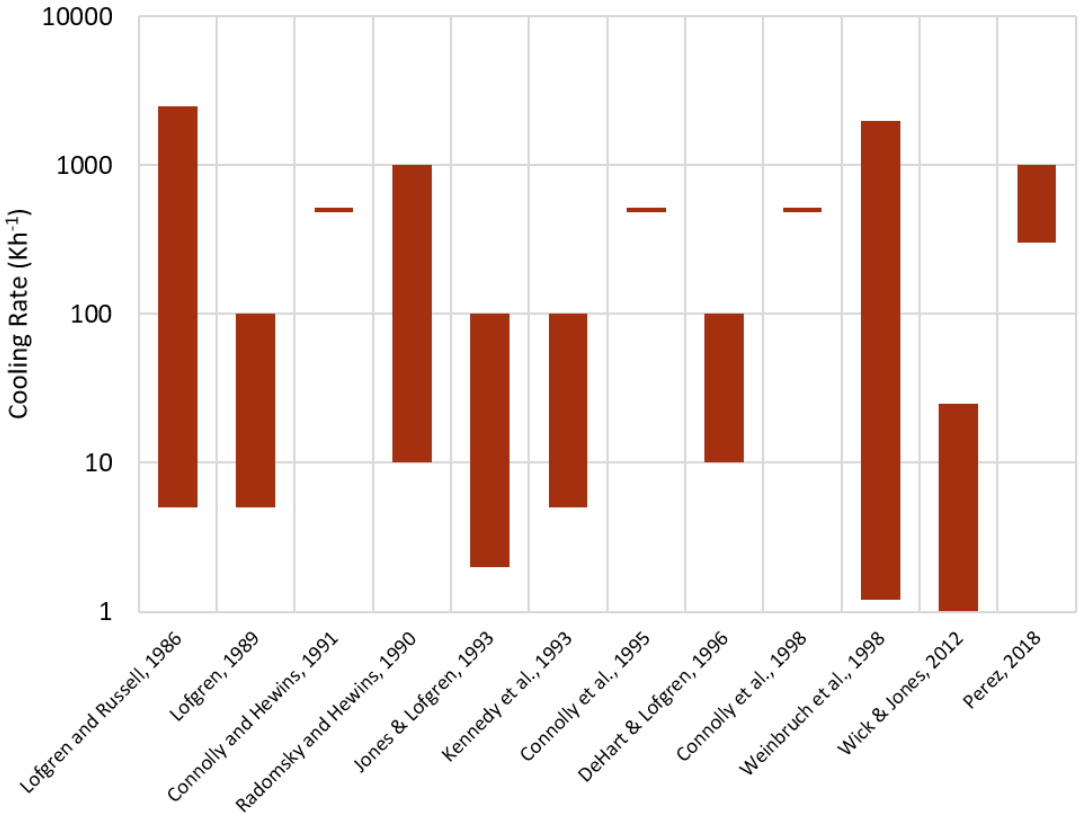

Figure 1.7 – Summary of the cooling rates at which porphyritic textures were produced in dynamic crystallisation experiments. Porphyritic textures were produced at cooling rates from 1.2 to 2500 Kh^{-1}. These results are also shown in Table 1.3.

Table 1.3 – Table summarising the cooling rates at which porphyritic textures were produced in dynamic crystallisation experiments. Porphyritic textures were produced at cooling rates of 1.2 to 2500 Kh^{-1}. These results are also shown in Figure 1.7.

Reference	Starting material composition	Heating duration	Melting temperature	Cooling rate (Kh^{-1})	Texture produced
Lofgren and Russell (1986)	RP and PP	17 h	Subliquidus to just above liquidus	5 to 2500	PO and PP
Lofgren (1989)	IA	120 mins	Liquidus and superliquidus	5 to 100	PO
Connolly and Hewins (1991)	IA and II	12 mins and 30 mins	Subliquidus, liquidus and superliquidus	500	PO
Radomsky and Hewins (1990)	II	30 mins	Subliqudius and liquidus	10 to 1000	PO and POP
Jones and Lofgren (1993)	II	120 to 180 mins	Subliquidus	2 to 100	PO
Kennedy et al. (1993)	II	Varying	Subliqudus	5 to 100	PO and PP
Connolly and Hewins (1995)[1]	IIA and IIAB	30 mins[1]	Superliquidus[1]	500	PO, BO/POP and POP
Dehart and Lofgren (1996)	IA and IB	30 mins	Subliquidus and superliquidus	10 to 100	PO
Connolly et al. (1998)	II – very FeO rich	Flash	Superliquidus	500	PO
Weinbruch et al. (1998)[2]	IIAB	110 mins[2]	Subliquidus	1.2 to 2000	PO, POP and PP
Wick and Jones (2012)	I AB	30 s	Subliquidus	1 to 25	POP
Perez (2018)	I	1, 5 and 10 mins	Subliquidus, liquidus and superliquidus	300 to 1000	P, B and R

[1]Connolly and Hewins (1995) seeded complete melts with dust grains to examine the effect of dust collisions with chondrule melts. The experimental charges were heated for 30 mins at superliquidus temperatures before being bombarded with dust at different temperatures during cooling.

[2]Weinbruch and Müller (1995) heated experimental charges at 20 Kmin-1 until 1723 K, then 5 Kmin^{-1} until 1773 K where they were held at a constant temperature for 30 mins. The total heating time from 293 K is 110 mins.

in a laboratory with known conditions, e.g. peak temperature, cooling rate, pressure, composition, and grain size. By comparing the texture of the analogue chondrules formed in such experiments to natural chondrules, aspects of the heating event and the subsequent cooling rates of the chondrules can be inferred. The conditions of these experiments, such as the starting composition, heating time, melting temperature and cooling rate are shown in Table 1.3 and Table 1.4.

Textures resembling natural chondrules have been produced over a very wide range of cooling rates from 1.2 Kh^{-1} to 5000 Kh^{-1} (see Figure 1.7 and Figure 1.8). However, the relationship between chondrule texture and cooling rate is weak. Porphyritic, barred and

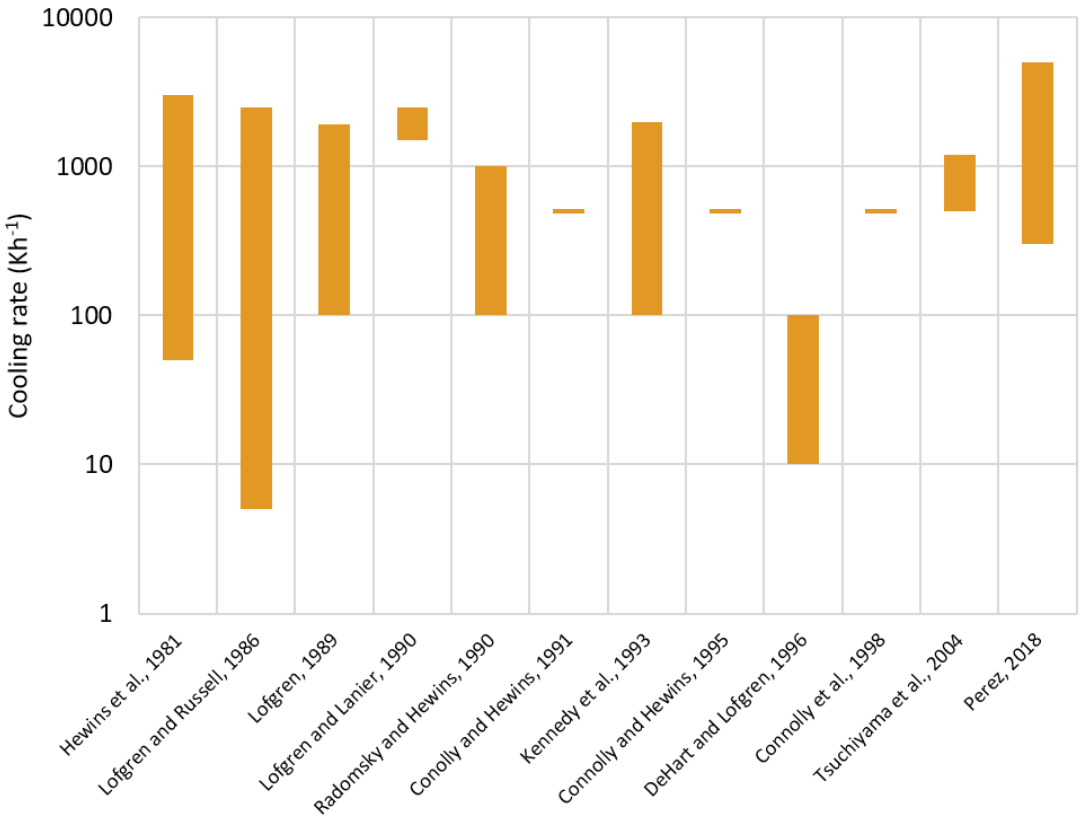

Figure 1.8 – Summary of the cooling rates at which barred and radial textures were produced in dynamic crystallisation experiments. Barred textures were produced at cooling rates of 5 to 2500 Kh^{-1} and radial textures were produced at cooling rates of 50 to 3000 Kh^{-1}. Results are also shown in Table 1.4.

radial textures can be produced at the same cooling rates by varying other conditions such as peak temperature, heating duration, composition and precursor grain size (e.g. Connolly et al., 1998). These conditions alter the potential availability of crystal nucleation sites. Higher peak temperatures compared to the liquidus destroy more nucleation sites, resulting in more barred and radial textures. Longer heating duration will also destroy more nucleation sites, resulting in more barred and radial textures. More magnesian compositions have higher liquidus temperatures which require higher peak temperatures to melt. This means that nucleation sites are more likely to be preserved resulting in porphyritic textures. A larger precursor grain size requires longer heating durations, or more vigorous heating to destroy nucleation sites resulting in more porphyritic textures. As an example of this, Connolly et al., (1998) produced both porphyritic, barred and glassy chondrules at cooling rates of 500 Kh^{-1} by varying the precursor grain size. Because of the ambiguous relationship between cooling rate and texture, this wide range of cooling rates (1.2 to 5000 Kh^{-1}) needs to be validated or constrained by using more direct methods to determine the cooling rate.

Table 1.4 – Table summarising the cooling rates at which barred and radial textures were produced in dynamic crystallisation experiments. Barred textures were produced at cooling rates of 5 to 2500 Kh^{-1} and radial textures were produced at cooling rates of 50-3000 Kh^{-1}. These results are also shown in Figure 1.8.

Reference	Starting material composition	Heating duration	Melting temperature	Cooling rate (Kh^{-1})	Textures produced
Hewins et al. (1981)	RP	120 mins	Subliquidus	50 to 3000	RP
Lofgren and Russell (1986)	PP and RP	17 h	Superliquidus	5 to 2500	BO and RP
Lofgren (1989)	IA	120 mins	Superliquidus	100 to 1900	BO
Lofgren and Lanier (1990)	I and II	15 and 30 mins	Liquidus and superliquidus	1500 to 2500	BO
Radomsky and Hewins (1990)	II	30 mins	Subliquidus and liquidus	100 to 1000	BO
Connolly and Hewins (1991)	IA and II	12 and 30 mins	Subliquidus, liquidus and superliquidus	500	BO
Kennedy et al. (1993)	II	Varying	Superliquidus	100 to 2000	BO
Connolly and Hewins (1995)[1]	IIA and IIAB	30 mins	Superliquidus[1]	500[1]	BO/POP, BO, RP, RPO and RPO/POP
Dehart and Lofgren (1996)	IA and IB	30 mins	Superliquidus	10 to 100	BO
Connolly et al. (1998)	II – very FeO-rich	Flash	Superliquidus	500	BO
Tsuchiyama et al. (2004)	II – very FeO-rich	0 to 120 mins	Superliquidus	500 to 1200	BO
Perez (2018)	I	1, 5 and 10 mins	Subliquidus, liquidus and superliquidus	300 to 5000	P, B and R

[1]Connolly and Hewins (1995) seeded complete melts with dust grains to examine the effect of dust collisions with chondrule melts. The experimental charges were heated for 30 mins at superliquidus temperatures before being bombarded with dust at different temperatures during cooling.

1.6.2 Other methods of determining chondrule cooling rates

To assess whether the results from the dynamic crystallisation experiments provide an accurate determination of the cooling rates chondrules experienced during their formation, several attempts have been made to determine chondrule cooling rates using a range of methods. These approaches are generally more direct than the dynamic crystallisation experiment comparisons and include the study of structures and zoning present in chondrule phenocrysts (Jones and Lofgren, 1993; Weinbruch and Müller, 1995; Weinbruch et al., 2001; Wasson and Rubin, 2003; Wasson, 2004; Miyamoto et al., 2009; Cuvillier et al., 2018), diffusion modelling in chondrule olivines (Greeney and Ruzicka, 2004;

Béjina et al., 2009; Hewins et al., 2009; Miyamoto et al., 2009), diffusion modelling in metals associated with chondrules (Humayun, 2012; Chaumard et al., 2018) and olivine dissolution experiments (Soulié et al., 2017). These cooling rates are summarised in Figure 1.9 and Table 1.5.

1.6.2.1 The microstructure of plagioclase and clinopyroxene

Weinbruch and Müller (1995) and Weinbruch et al. (2001) examined the microstructure of clinopyroxene and plagioclase crystals in type I porphyritic olivine and pyroxene chondrules. Modelling of pyroxene lamellae growth during cooling provided cooling rates of 7 to 25 Kh^{-1}. Similarly, low cooling rates of 3 to 30 Kh^{-1} were suggested from plagioclase microstructure (Weinbruch and Müller, 1995). Further work on clinopyroxene microstructures found cooling rates of 0.1 to 50 Kh^{-1} (Weinbruch et al., 2001) and 10 to 1000 Kh^{-1} (Cuvillier et al., 2018). These cooling rates are relevant to the latest stages of chondrule crystallisation, close to the solidus.

The ratio of clinoenstatite to orthoenstatite in chondrules is dependent on cooling rate (Smyth, 1974; Brearley and Jones, 1993). Clinoenstatite can be abundant in chondrules and the ratio of clinoenstatite to orthoenstatite is >70% but may approach 100%. These proportions suggest that cooling rates were high, up to 10000 Kh^{-1} at ~1270 K (Jones et al., 2018). These cooling rates are much higher than those suggested by dynamic crystallisation experiments.

1.6.2.2 Overgrowth width on forsteritic-olivine relict grains

Wasson and Rubin (2003) and Wasson (2004) examined narrow overgrowths found around forsteritic-olivine relict grains in chondrules from CO and ordinary chondrites. It is argued that these could only have formed from very fast cooling rates, up to 3.6×10^6 Kh^{-1} (Wasson, 2004). It was also argued that these narrow overgrowths represent the amount of material able to crystallise from the last melting event, and any olivine phenocrysts with radii wider than this must also contain relict cores which grew over repeated melting events (Wasson and Rubin, 2003). However, zoning profiles across these olivine phenocrysts show normal zoning that can be modelled by closed-system fractional crystallisation in a single cooling event (Jones, 1990), suggesting that they do not represent multiple growth stages (Jones et al., 2005). The narrow width of the overgrowth may suggest later growth around the grain during the final stages of olivine crystallisation (Connolly and Jones, 2005). Similar textures are observed in experimental results from a single heating event (Lofgren and Le,

2000; Hewins and Fox, 2004). Connolly and Jones (2005) also argue that these incredibly high cooling rates are much higher than blackbody radiation for a molten chondrule and therefore impossible.

1.6.2.3 Olivine zoning profiles

Chondrule phenocryst zoning patterns have also been used to infer cooling rates. Zoning profiles for major and minor elements in phenocrysts in Semarkona chondrules matched those of experimentally produced crystals at cooling rates of 2, 5 and 100 Kh^{-1} (Jones and Lofgren, 1993). Zoning profiles in phenocrysts present in Semarkona chondrules have also been compared to modelled zoning profiles. These have suggested cooling rates of 0.7 to 2400 Kh^{-1}, spanning the entire range of cooling rates suggested by dynamic crystallisation experiments. Zoning profiles from different phenocrysts within the same chondrule generally produce similar values, for example, one chondrule showed cooling rates of 7.3 to 23 Kh^{-1} with an average value of 16 Kh^{-1} (Miyamoto et al., 2009). This approach was also applied to the experimental phenocrysts produced by Jones and Lofgren (1993). Overall, they were in good agreement, with only relatively minor overestimations of ~1.2 times the actual value. For experimentally produced phenocrysts cooled at 2, 5 and 100 Kh^{-1}, model profiles provided values of 2.5, 6.2 and 124 Kh^{-1} respectively (Miyamoto et al., 2009).

1.6.2.4 Diffusion modelling in olivine

Modelling of diffusion between forsteritic-olivine relict grains and the surrounding overgrowth crystal has been used to determine chondrule cooling rates. Greeney and Ruzicka (2004) modelled diffusion of Fe, Mg, Mn, and Ca at a range of temperatures and oxygen fugacity conditions and compared these to diffusion profiles present in forsteritic-olivine relict grains measured using EPMA. Using this technique, they found cooling rates of ~200 to 6000 Kh^{-1} which are broadly similar to those inferred for chondrules based on dynamic crystallisation experiments. However, the meteorites examined (Sahara-97210 LL3.2, Wells LL3.3 and Chainpur LL3.4) have experienced some degree of thermal metamorphism and the diffusion profiles may have been altered by this secondary process. Béjina et al. (2009) found cooling rates of 700 to 3600 Kh^{-1} for chondrules from the same meteorites. Hewins et al. (2009) measured profiles of Mg, Fe and Cr composition across the interface between a forsteritic-olivine relict grain and the overgrowth crystal in a chondrule from Semarkona (LL3.00) using EPMA. Model profiles suggested an initial cooling rate of

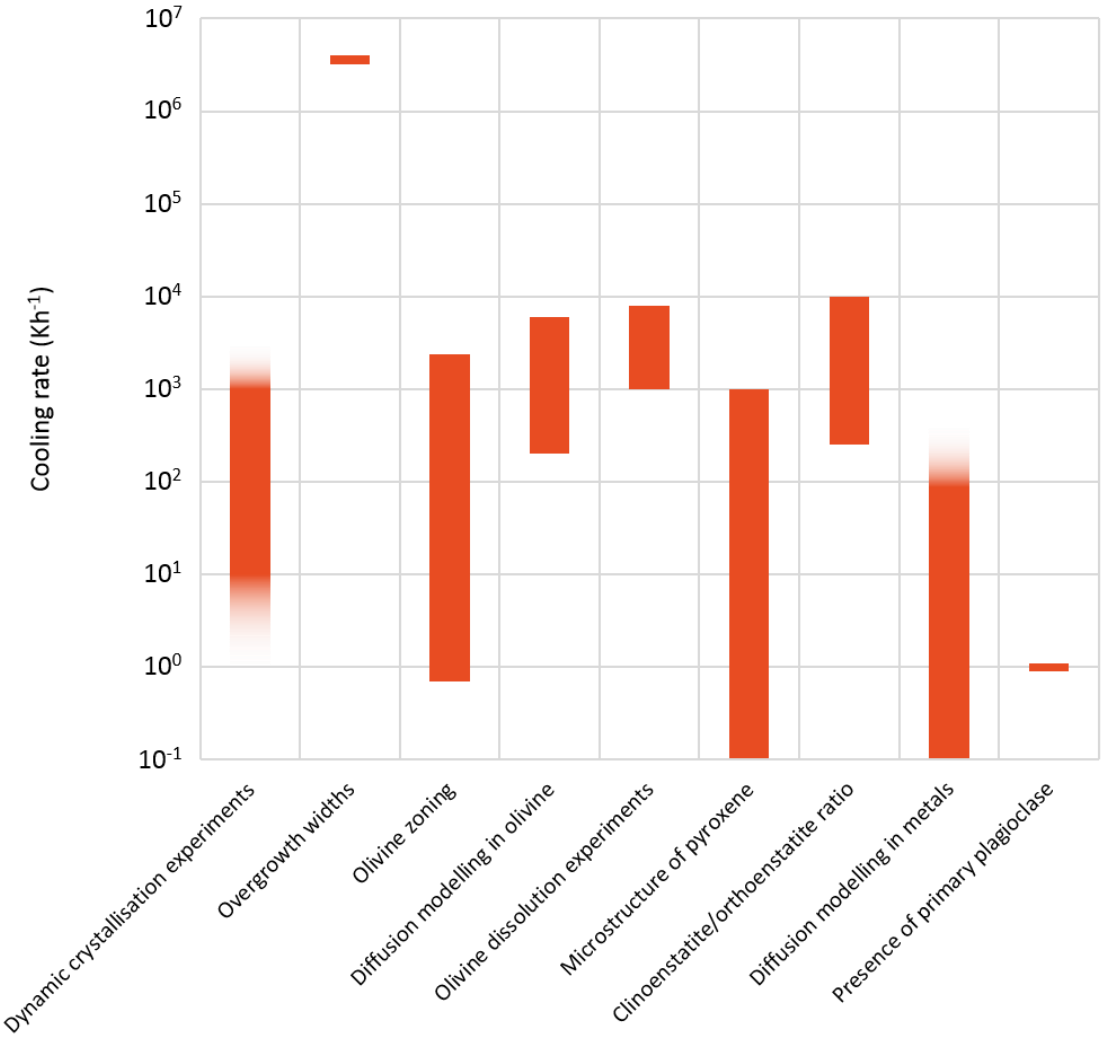

Figure 1.9 - Results of previously determined chondrule cooling rates: dynamic crystallisation experiments (Connolly and Hewins 1991, 1995; Connolly et al. 1998; Dehart and Lofgren 1996; Hewins et al. 1981; Jones and Lofgren 1993; Kennedy et al. 1993; Lofgren 1989; Lofgren and Lanier 1990; Lofgren and Russell 1986; Radomsky and Hewins 1990; Tsuchiyama et al. 2004; Weinbruch et al. 1998; Wick et al. 2010); Overgrowth widths (Wasson 2004); Olivine zoning (Jones and Lofgren 1993; Miyamoto et al. 2009); Diffusion modelling in olivine (Béjina et al. 2009; Greeney and Ruzicka 2004; Hewins et al. 2009); Olivine dissolution experiments (Soulié et al. 2017); Microstructure of pyroxene (Cuvillier et al. 2018; Weinbruch and Müller 1995; Weinbruch et al. 2001); clinoenstatite/orthoenstatite ratio (Jones et al. 2018); Diffusion modelling in metals (Chaumard et al. 2018; Humayun 2012); Presence of primary plagioclase (Jones 1997; Lewis and Jones 2019; Wick and Jones 2012).

400 Kh^{-1} from the Fe-Mg diffusion profile and an initial cooling rate of 300 Kh^{-1} from the Cr diffusion profile.

1.6.2.5 Diffusion in metals associated with chondrules

Humayun (2012) and Chaumard et al. (2018) measured Cu and Ga diffusion profiles in metal lumps in type I chondrules in CR2 meteorites. By modelling these diffusion profiles, cooling rates of 0.1 to 50 Kh^{-1} at ~1470 K were calculated for chondrules in Acfer 097, with maximum cooling rates of 400 Kh^{-1} at higher temperatures (Humayun, 2012). Similar results

Table 1.5 – Results of previously determined chondrule cooling rates.

Reference(s)	Cooling rate (Kh^{-1})	High temperature or low temperature	Method	Chondrules measured
Dynamic crystallization experiments (see Table 1.3 and Table 1.4)	1.2 to 5000	High	**Dynamic crystallization experiments**	Type I and II chondrules with porphyritic, barred and radial textures
Wasson (2004)	3.6×10^6	High	**Overgrowth width:** presence of narrow overgrowths on forsteritic-olivine relict grains	Type II PO chondrules from CO and ordinary chondrites
Jones and Lofgren (1993) and Miyamoto (2009)	0.7 to 2400	High	**Olivine zoning:** comparison of zoning profiles in olivine phenocrysts in chondrules to olivine phenocrysts from dynamic crystallization experiments (Jones and Lofgren 1993) and model zoning profiles (Miyamoto et al. 2009)	Type II chondrules from ordinary chondrites
Greeney and Ruzicka (2004); Béjina et al. (2009) and Hewins et al. (2009)	200 to 6000	High	**Diffusion modelling in olivine:** modelling major and trace element diffusion profiles between forsteritic-olivine relict grains and overgrowths	Type II chondrules from ordinary chondrites
Soulié et al. (2017)	1000 to 8000	High	**Olivine dissolution experiments**	Type IA chondrules
Weinbruch and Müller (1995); Weinbruch et al. (2001) and Cuvillier et al. (2018)	0.1 to 1000	Low	**Microstructure of pyroxene**	Type I chondrules in CM, CR and CV chondrites
Brearley and Jones (1993) and Jones et al. (2018)	250 to 10000	Low	**Clinoenstatite/orthoenstatite ratio**	Porphyritic chondrules
Humayun (2012) and Chaumard et al. (2018)	0.5 to 400	Low	**Diffusion modelling in metal lumps** in chondrules	Type I chondrules in CR chondrites
Jones (1997); Wick and Jones (2012) and Lewis and Jones (2019)	1	Low	**Presence of primary plagioclase** which requires very low cooling rates in order to crystallise	Type I and II chondrules

of 1.2 to 86 Kh^{-1} at 1570 to 1670 K were obtained for type I chondrules in the Renazzo meteorite (Chaumard et al., 2018).

1.6.2.6 Olivine dissolution experiments

Soulié et al. (2017) performed olivine dissolution experiments and found that forsterite dissolution in type IA chondrule melts is very rapid, 5 to 22 µm/min. To preserve forsterite in these chondrules, cooling rates need to be in the range of 1000 to 8000 Kh^{-1}.

1.6.2.7 Presence of primary plagioclase

Type I and II chondrules in ordinary and carbonaceous chondrite groups may contain primary plagioclase (Jones, 1997; Lewis and Jones, 2019). In order to crystallise the plagioclase crystals, cooling rates may need to be as low as 1 Kh^{-1} at low temperatures (Wick and Jones, 2012).

1.7 Non-thermal constraints on chondrule formation

1.7.1 Chondrule chronology

Three different isotope systems have been used to assess the chronology of chondrule formation: the Al-Mg isotope system, the Hf-W isotope system and the U-Pb isotope system.

1.7.1.1 Al-Mg isotopes

^{26}Al decays to ^{26}Mg with a half-life of 0.71 Myrs (Norris et al., 1983) and because of this relatively short half-life, ^{26}Al is now extinct. Excesses of ^{26}Mg over Solar System average in early Solar System objects show that they formed while ^{26}Al was decaying (Lee et al., 1976). Correlation of excess ^{26}Mg with the Al/Mg ratio of minerals within a single object, e.g. a CAI, suggests that ^{26}Mg decay occurred within that mineral. Initial $^{26}Al/^{27}Al$ ratios can be calculated for when the minerals in this object crystallised. By comparing the initial $^{26}Al/^{27}Al$ ratios between different objects, relative ages between the objects can be calculated, because this ratio decreases with time in accordance with the half-life of ^{26}Al. In order to calculate their age, the ratio present in different Solar System objects is usually compared to the ratio present in CAIs as these are the earliest formed objects in the Solar System (Bizzarro et al., 2004; Jacobsen et al., 2008; Larsen et al., 2011). This, however, depends upon the assumption that ^{26}Al was distributed homogeneously throughout the Solar System, with an initial $^{26}Al/^{27}Al$ ratio equivalent to the value obtained for CAIs. This

assumption has been supported (Villeneuve et al., 2009; Gregory et al., 2020) and challenged (Larsen et al., 2011; Luu et al., 2016; Olsen et al., 2016; Van Kooten et al., 2016; Bollard et al., 2019) and the assumption remains controversial (Nagashima et al., 2018). Al-Mg dating of the least altered chondrites (by aqueous alteration or thermal metamorphism) suggest that chondrule formation began ~1.5 Myrs after the formation of CAIs and continued for a few Myrs (Nagashima et al., 2018; Pape et al., 2019).

1.7.1.2 Hf-W isotopes

The Hf-W isotope system is another extinct system where ^{182}Hf decays to ^{182}W with a half-life of 8.9 Myrs. Hf is lithophile whereas W is siderophile, therefore, this isotope system can be used to date the metal-silicate fractionation that occurred during chondrule formation (Kleine et al., 2018). Unlike the Al-Mg system or Pb-Pb system, Hf-W dating cannot be applied to single chondrules as the concentrations of W in a single chondrule are too low for precise analysis. Instead, studies have used separates of 100s to 1000s of chondrules. Using Hf-W dating, two chondrite groups have been dated. Chondrules and matrix from Allende (CV) define an isochron corresponding to an age of 2.2 ± 0.8 Myrs after CAIs (Budde et al., 2016b). Chondrules from four CR chondrites define an isochron corresponding to an age of 3.6 ± 0.6 Myrs after CAIs (Budde et al., 2018).

1.7.1.3 U-Pb and Pb-Pb dating

^{238}U decays to ^{206}Pb with a half-life of ~4 Gyrs and ^{235}U decays to ^{207}Pb with a half-life of 0.5 Gyrs. The long half-lives and dual decay of these isotopes makes this system one of the best to determine precise absolute (rather than relative) ages of early Solar System objects. By exploiting the dual decay of both U isotopes, ^{207}Pb/^{206}Pb ratios can be determined which are unique for different ages (Connelly and Bizzarro, 2018). Unlike Hf-W, Pb-Pb dating can be applied to single chondrules. So far, 22 individual chondrules from ordinary, CV and CR chondrites have been dated using this system (Connelly et al., 2012; Bollard et al., 2017). The ages of these chondrules show that chondrules began forming at the same time as CAIs, with chondrule formation continuing for ~4 Myrs. Chondrules from individual chondrites span a wide age range, for example, chondrules from NWA 5697 show an age range of ~4 Myrs (Connelly et al., 2012; Bollard et al., 2017; Connelly and Bizzarro, 2018).

1.7.1.4 Summary and implications

Both Al-Mg and Hf-W ages of chondrules suggest chondrule formation began ~1.5 Myrs after the formation of CAIs and continued for several Myrs (Budde et al., 2016b; Budde et

al., 2018; Kleine et al., 2018; Nagashima et al., 2018; Pape et al., 2019). However, Pb-Pb ages of chondrules show chondrule formation beginning at the same time as the formation of CAIs and continuing for ~4 Myrs (Connelly et al., 2012; Bollard et al., 2017; Connelly and Bizzarro, 2018). Al-Mg and Hf-W ages of chondrules are generally consistent within a chondrite, suggesting chondrules in that chondrite formed at the same time and were lithified into a chondrite before mixing between different reservoirs of chondrules took place (Budde et al., 2016b; Budde et al., 2018; Kleine et al., 2018; Nagashima et al., 2018). However, Pb-Pb ages of chondrules within a chondrite span a wide range of ages and suggest that different reservoirs of chondrules with different ages did mix together, or chondrules were forming in separate regions over a protracted period and these regions were kept isolated until chondrite formation took place (Connelly and Bizzarro, 2018). Chondrules in different chondrite groups display characteristic properties, for example, abundance of different textural types, size, isotopic composition, bulk composition and petrographic properties of chondrules, which suggest that chondrules in different chondrite groups formed in distinct reservoirs (Jones, 2012). The Pb-Pb ages of chondrules within a chondrite therefore imply chondrule formation in isolated regions over a long period of time.

1.7.2 Volatile elements and open system behaviour

Experimental simulations of chondrule textures suggest that chondrule formation events formed chondrules over a period of several hours to days (e.g. Lofgren, 1996; Hewins et al., 2005; Desch et al., 2012; Jones et al., 2018). Over these timescales, there should be interactions between nebular gas and molten chondrules. During free evaporation, with no back reaction to the chondrule melt, elemental fractionation would be accompanied by isotopic fractionation. The chondrule melt will become more enriched in the heavy isotope of an element relative to the light isotope as the concentration of the element decreases according to Rayleigh fractionation laws. If chondrules formed under canonical nebular conditions, with low pressure and low solid to gas ratios, they should show characteristic fractionations in many elements (Ebel et al., 2018). However, there is very little evidence for the presence of these isotope fractionations. Alexander and Grossman (2005) found no evidence for K isotope fractionations in chondrules from Semarkona. Other compelling evidence that very little or no evaporation was taking place is the presence of significant quantities of Na in olivine phenocrysts in chondrules from Semarkona, with Na zoning

profiles approximating closed-system fractional crystallisation (Alexander et al., 2008). Na must have been present in these chondrules in roughly the observed amounts during chondrule crystallisation with little to no evaporation of Na. These measurements are confirmed by several other studies (Borisov et al., 2008; Kropf and Pack, 2008; Kropf et al., 2009; Hewins and Zanda, 2012; Florentin et al., 2017). In addition, there are only very minor systematic Fe isotope fractionations in chondrule phenocrysts with wide-ranging FeO compositions (Alexander and Wang, 2001; Zhu et al., 2001; Kehm et al., 2003; Mullane et al., 2005; Needham et al., 2009; Hezel et al., 2010), however, these minor fractionations are much less than what is expected from free evaporation (Ebel et al., 2018). Similarly small fractionations exist for Mg isotopes (Deng et al., 2017) and Si isotopes (Clayton et al., 1991; Hezel et al., 2010) again suggesting very little evaporation occurred during chondrule formation.

It is suggested that it is possible to prevent this evaporation by rapid heating and cooling (Desch et al., 2012), however evidence from micrometeorites and cosmic spherules argue that this is not the case. These micrometeorites and cosmic spherules were heated and cooled on very short timescales, a matter of seconds, and they show extensive elemental and isotope fractionations for K, Fe, O, Si and Mg which are consistent with evaporation (Alexander et al., 2002; Taylor et al., 2005). The most likely solution for the absence of systematic isotope fractionations in chondrules is that chondrules were almost stable melts in equilibrium with the surrounding gas (Ebel et al., 2018). To generate gas with the necessary composition, there must have been significant evaporation from the surrounding materials, e.g. dust, and from chondrules themselves. The amount of evaporation required to generate this vapour depends upon the solid to gas ratio in the region. The lower the solid to gas ratio, the more evaporation required from chondrules and dust to generate this vapour and therefore the greater the amount of isotope fractionation present in the chondrules (Ebel et al., 2018). In order to prevent evaporation of Na as required by Alexander et al. (2008) and prevent significant Fe evaporation, enrichments of CI-like dust by orders of magnitude (>1000) above canonical nebula conditions are required. Type II chondrules require less solid enrichments by 2 orders of magnitude than type I chondrules and are therefore more likely to act as stable melts (Fedkin and Grossman, 2013).

Despite the lack of evidence of open system behaviour in isotope fractionations and the volatile contents of chondrules, there is growing evidence that type I chondrules

experienced exchange with surrounding gas during chondrule formation. An example of this is the presence of mineralogically zoned chondrules which contain a core of olivine crystals surrounded by a low-Ca pyroxene mantle. These are expected to be formed by recondensation of SiO gas into chondrules during cooling. This creates a Si enrichment at the chondrule margins resulting in the crystallisation of low-Ca pyroxene rather than olivine (Tissandeer et al., 2002; Krot et al., 2004; Libourel et al., 2006; Friend et al., 2016). This is contrary to the observations on Na and Fe above, as it suggests that Si, which is relatively refractory, underwent evaporation, while significantly more volatile elements, Na and Fe, did not (Ebel et al., 2018). Another example is gas-assisted growth of olivine in type I chondrules in a nebular gas with high partial pressures of Mg and SiO, which has been revealed in high-resolution SEM-CL images (Libourel and Portail, 2018). There is also evidence that type II chondrules may have exchanged with an O-rich vapour allowing Fe,Ni grains in the precursor assemblage to oxidise during chondrule formation (Villeneuve et al., 2015). These constraints pose challenges to chondrule formation mechanisms and imply that chondrules formed in regions of high solid density, which would suppress evaporation, and did not form under canonical nebular conditions.

1.7.3 Chondrule-matrix complementarity

Another potential constraint on chondrule formation mechanisms is the concept of chondrule-matrix complementarity. For many chondrites, particularly carbonaceous chondrites, the bulk composition is close to solar, or CI compositions, for several element and isotope ratios. Chondrules and matrix, however, show non-chondritic compositions of these elements and isotopes. Examples of this include Mg and Si ratios (Hezel and Palme, 2010), Fe and Mg (Palme et al., 2015) and W and Hf (Becker et al., 2015; Budde et al., 2016b). In these examples, chondrule values are either sub or superchondritic while the matrix shows the opposite. When these two components are added together to form a bulk chondrite, the composition is CI like. Evidence from W and Mo isotopes also argues for complementarity between chondrules and matrix. In the CV chondrite Allende, chondrules and matrix show complementarity while bulk chondrite shows the same ratio as other chondrite meteorites (Becker et al., 2015; Budde et al., 2016b; Budde et al., 2016a). To randomly mix these components to create a bulk chondrite with CI compositions of these element and isotope ratios is unlikely, and points to the formation of chondrules and matrix from a single reservoir of material with CI composition for a single chondrite

parent body. It also implies that chondrite formation occurred soon after chondrule formation to prevent mixing of the different chondrite components between different reservoirs which would remove evidence of this complementarity (Hezel et al., 2018; Hubbard and Ebel, 2018). However, the observation of chondrule-matrix complementarity is still controversial and is not universally accepted. Zanda et al. (2018) suggest that these observations can be explained by mixing average chondrule compositions with CI-like matrix and Fe,Ni metal and then exposing this assemblage to parent body processing. Zanda et al. (2018) also argue that the isotopic differences between chondrules and matrix are caused by nucleosynthetic isotope differences in the reservoirs of these different chondrite components rather than forming them from a single nebular reservoir.

1.8 Chondrule formation models

Despite the high abundance of chondrules in chondritic meteorites, their origins are still unknown. Many models have been proposed that attempt to describe chondrule formation, drawing upon different energy sources and in different settings. The main types of model include large-scale nebular shockwaves with energy sources such as gravitational instabilities (Ciesla and Hood, 2002; Desch and Connolly, 2002; Morris and Desch, 2010; Morris et al., 2016; Morris and Boley, 2018); planetesimal and planetary embryo bow shocks (Ciesla et al., 2004; Morris et al., 2012; Boley et al., 2013; Mann et al., 2016; Morris and Boley, 2018); impact jetting during collisions between solid objects (Hasegawa et al., 2015; Johnson et al., 2015; Wakita et al., 2017; Johnson et al., 2018; Oshino et al., 2019); collisions between molten planetesimals (Asphaug et al., 2011; Sanders and Scott, 2012); nebular lightning (Desch and Cuzzi, 2000; Johansen and Okuzumi, 2017; Johansen and Okuzumi, 2018) and heating in X-winds close to the Sun (Shu et al., 1996; Shu et al., 1997; Shu et al., 2001; Desch et al., 2010). In order for a chondrule formation mechanism to be valid, it must satisfy several thermal constraints, as described in Desch et al. (2012):

- The presence of primary sulfides in chondrules places limits upon the initial temperature of chondrule precursors, which must be below 650 K in order to condense troilite in the original chondrule precursor (Rubin et al., 1999; Desch et al., 2012).
- In order to preserve the level of volatile elements and prevent evaporation, e.g. Na and S, it has been suggested that heating must have been rapid, lasting less than

several minutes (Yu and Hewins, 1998; Desch et al., 2012). However, as noted in section 1.7.2, this may not be valid as high partial pressures of volatiles can suppress evaporation, and rapid heating and cooling do not prevent evaporation and fractionation of volatile elements in micrometeorites and cosmic spherules (Alexander et al., 2002; Taylor et al., 2005; Ebel et al., 2018).

- Suitable peak temperatures need to be reached to achieve a wide range of chondrule textures. Texture is strongly related to liquidus temperature, which for most chondrules ranges from ~1600 to 1900 K (Radomsky and Hewins, 1990; Berlin et al., 2011; Hewins et al., 2012; Jones et al., 2018). Peak temperatures for porphyritic textures should be close to, but not exceed, the liquidus. For barred and radial textures, peak temperatures should be superliquidus (e.g. Jones et al., 2018). As a result, this constraint is not specific, but a range of ~1750 to 2100 K would be appropriate for most chondrules (Desch et al., 2012; Jones et al., 2018).
- Cooling rate from peak to sub-liquidus temperatures needs to be rapid, 10^3 to 10^4 Kh^{-1}, to retain volatile elements (Desch et al., 2012). Again, this may not be valid as high partial pressures of these volatile elements will prevent evaporation, and fast cooling does not preserve levels of volatile elements in micrometeorites and cosmic spherules (Alexander et al., 2002; Taylor et al., 2005; Ebel et al., 2018).
- Cooling rates of ~1 to 3000 Kh^{-1} based upon crystallisation experiments and petrographic studies (see section 1.6)

1.8.1 Large-scale nebular shockwaves

During the evolution of the protoplanetary disk, it was gravitationally unstable (Boss and Durisen, 2005). This gravitational instability may have created density perturbations, which led to the formation of spiral arms and clumps in the solar nebula. Spiral arms have been observed in forming star systems, for example, Elias 2-27 (Pérez et al., 2016) (See Figure 1.2). These spiral arms and clumps would drive shock fronts into the inner protoplanetary disk (Boss and Durisen, 2005). As these shock fronts move through the solar nebula, they interact with nebula gas and dust, see Figure 1.10. As the shock front approaches, the first interaction is that chondrule precursors begin to absorb infrared radiation from heated particles behind the approaching shock front. This is transferred to the surrounding gas by thermal collisions increasing gas temperature and pressure. This phenomenon is known as a Marshack wave and allows precursors to be heated to temperatures of ~1740 K, before

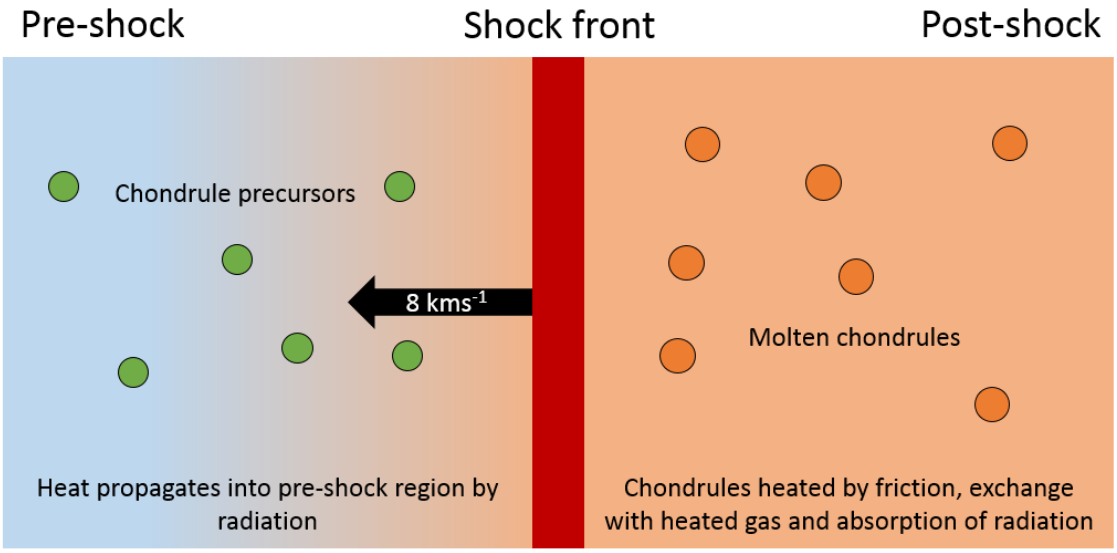

Figure 1.10 – Schematic diagram of a large-scale nebular shock wave. In the pre-shock region chondrule precursors experience preheating due to radiation from behind the shock front. As these precursors pass through the shock front, they are heated by gas drag frictional heating, exchange with hot gas and radiation from the surrounding chondrules (Desch and Connolly 2002; Morris and Desch 2010; Morris et al. 2016).

encountering the shock front (Desch and Connolly, 2002; Morris and Desch, 2010). Incorporating a population of microchondrules (Morris and Desch, 2011) and including multiple particle sizes (Morris et al., 2016) in models reduces the effect of this preheating. When the shock front hits, gas temperature increases to ~3120 K. At these high temperatures, hydrogen dissociation occurs causing temperatures to decrease rapidly at rates of ~5 x 10^4 Kh^{-1}. Chondrule precursors passing through the shock are heated by gas-drag frictional heating and thermal exchange with hot nebular gas. This rapid temperature decrease persists until temperatures of ~1700 K are reached. At this point cooling rate slows to 35 to 50 Kh^{-1}. Shock conditions play a strong role in chondrule thermal history. Increasing shock speed increases peak temperatures, while lowering gas density reduces the effect of frictional heating and thermal exchange with gas, reducing peak temperatures. Increasing the concentration of chondrule precursors may allow peak temperatures to rise (Desch and Connolly, 2002), however, this was not seen in the modelling of Morris and Desch (2010).

In large-scale nebula shock waves, chondrule cooling rates are primarily controlled by the concentration of chondrules and the opacity of the solar nebula in the formation region. The heated zone is composed of chondrules and hot gas. The hot gas is unable to radiate the stored heat away and must transfer the heat to chondrules, which are then able to

radiate this heat away, allowing the heated zone to cool. By increasing the concentration of chondrules, the surface area available for thermal exchange with gas and radiation of heat also increases, allowing the area to cool more quickly (Ciesla and Hood, 2002; Desch and Connolly, 2002; Morris and Desch, 2010; Morris et al., 2016). However, Stammler and Dullemond (2014) predict that in large-scale nebular shocks, cooling in the plane of the disk is insufficient to cool chondrules at cooling rates consistent with dynamic crystallisation experiments, and that significant cooling only begins after reaching long distances away from the shock front, distances equivalent to the scale-height of the protoplanetary disk.

1.8.2 Planetesimal and planetary embryo bow shocks

Planetesimals and planetary embryos moving in eccentric or inclined orbits can move supersonically with respect to nebular gas. This means that they can drive a strong bow shock in front of them, capable of processing solid material in a similar way to gravitational instability driven nebular shockwaves, but on a smaller scale (see Figure 1.11). Bow shocks from planetesimals are generally inconsistent with thermal constraints on chondrule formation. A 10 km planetesimal with a shock speed of 6 kms^{-1} produces peak temperatures of 1440 K with chondrules cooling rapidly at $>10^5$ Kh^{-1}. For a planetesimal with a diameter of 100 km and 6 kms^{-1}, peak temperatures are 1580 K with cooling rates of $>10^4$ Kh^{-1}. Larger planetesimals with a diameter of 1000 km generate peak temperatures

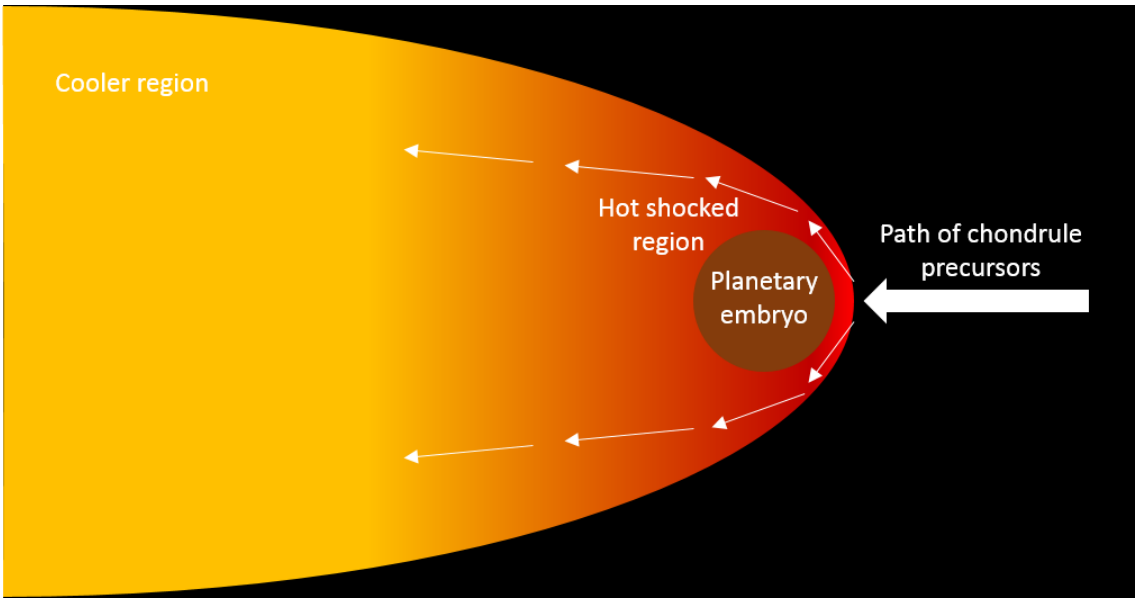

Figure 1.11 – Schematic diagram of a planetary embryo bow shock. Chondrule precursors are heated as they pass through the bow shock and enter the hot shocked region shown in red. They are then swept around behind the planetary embryo to cooler regions where they undergo adiabatic expansion and can cool rapidly (Boley et al. 2013; Mann et al. 2016).

that are slightly higher ~1600 K and with slower cooling rates of ~1000 Kh^{-1}. This is more consistent with the thermal constraints on chondrule formation (Ciesla et al., 2004).

The larger size of planetary embryos (6000 km diameter) makes them a better candidate for chondrule formation and the Hf-W age of shergottite-nahklite-chassignite (SNC) meteorites from Mars, suggests that Mars-sized bodies existed at the same time as chondrules were forming (Dauphas and Pourmand, 2011), although this may not be consistent with the Pb-Pb ages of the earliest formed chondrules (Connelly et al., 2012; Connelly et al., 2017). Unlike gravitational instability-driven nebular shockwaves, which can be approximated in one dimension, bow shocks around planetary embryos are complex three-dimensional structures which can produce varied thermal histories depending upon chondrule precursor trajectory. Initially, particles passing through the bow shock are heated by gas-drag frictional heating and thermal exchange with hot gas to peak temperatures causing melting and droplet production. After passing through the bow shock, these droplets are either accreted onto or swept around the planetary embryo. As the chondrules are swept around the planetary embryo, they are kept in contact with hot gas and cool relatively slowly ~1000 Kh^{-1}. Behind the planetary embryo, adiabatic expansion of hot gas allows for rapid cooling rates ~5000 Kh^{-1}. Including radiative effects increases cooling rates towards 10^4 Kh^{-1}, possibly as high as 2 x 10^4 Kh^{-1}. Behind the embryo, they may also experience minor tail shocks which may cause secondary heating events (Morris et al., 2012; Boley et al., 2013). Planetary atmospheres composed of nebular gas mixed with volatiles from a degassing magma ocean may also affect chondrule cooling rates. Inclusion of high-mass atmospheres could keep cooling rates lower, closer to 1000 Kh^{-1}, and possibly as low as 200 Kh^{-1} for a 6 kms^{-1} bow shock (Mann et al., 2016).

1.8.3 Impacts between planetesimals

Collisions between planetesimals also need to be considered as a potential mechanism for chondrule formation. Asphaug et al. (2011) and Sanders and Scott (2012) invoke low-velocity (10 to 100 ms^{-1}) impacts between molten planetesimals, whereas Hasegawa et al. (2015); Johnson et al. (2015); Wakita et al. (2017); Johnson et al. (2018) and Oshino et al. (2019) suggest the possibility of chondrule formation via high-velocity (>2.5 kms^{-1}) impacts between solid planetesimals.

1.8.3.1 Collisions between molten planetesimals

Molten planetesimals may be a source of chondrules. Evidence from iron meteorites suggests they came from planetesimals that accreted and differentiated very early, between 0.1 and 0.3 Myrs after CAI formation (Burkhardt et al., 2008; Kruijer et al., 2012; Kruijer et al., 2014). At this time, ^{26}Al is a readily available heat source sufficient to melt the interior of planetary bodies if they accreted early enough (Sanders and Scott, 2012). With coeval accretion of a planetesimal with CAIs, the decay of ^{26}Al leads to rapid heating to a liquidus temperature of ~1850 K within 0.3 Myrs. If accretion is delayed by 0.75 Myrs, heating is slower, but total internal melting may be achieved in 1.5 Myrs. Accretion at 1.5 Myrs results in a planetesimal that just reaches liquidus temperatures taking ~5 Myrs to melt. Any delay in accretion beyond 5 Myrs results in a planetesimal that is not able to melt as the remaining ^{26}Al is insufficient to raise temperatures above the solidus (Sanders and Scott, 2012).

Asphaug et al. (2011) modelled collisions between these molten planetesimals with diameters of 30 to 100 km, at low velocities of ~10 to 100 ms^{-1}. During an impact, a sheet of droplets is produced that rains upon the impacted planetesimal over a period of several days. Energetic droplets may escape the impacted planetesimal and form their own discrete body. Cooling over this period is generally consistent with experimental constraints on chondrule cooling rates, however, the models make no detailed predictions (Asphaug et al., 2011; Desch et al., 2012; Sanders and Scott, 2012).

1.8.3.2 Impact jetting

Shock heating during impacts between solid planetesimals with diameters of 10 to 1000 km has the potential to melt chondrule precursor material (Hasegawa et al., 2015; Johnson et al., 2015; Hasegawa et al., 2016; Wakita et al., 2017; Johnson et al., 2018; Oshino et al., 2019). Upon impact, a small amount of material is heated to high temperatures and is ejected from the impacted region (see Figure 1.12). For impacts with velocities lower than 2.5 kms^{-1}, no material is ejected above escape velocity. If the target body is undifferentiated, or partially differentiated with undifferentiated outer shells (Weiss and Elkins-Tanton, 2013; Fu and Elkins-Tanton, 2014), then melts with primitive compositions would be produced. Ejected chondrules and dust are decelerated by nebular gas then accreted onto the planetesimal (Johnson et al., 2015). Predictions of chondrule cooling rates in these impact plumes are consistent with thermal constraints from dynamic

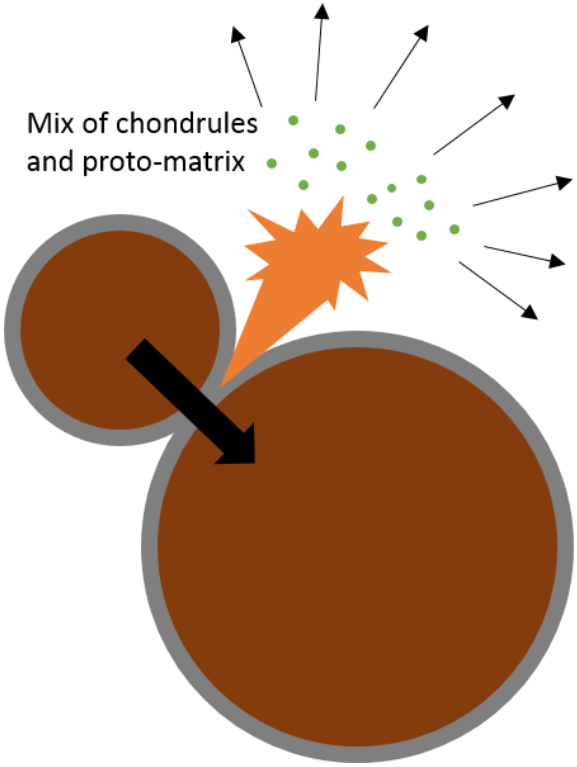

Figure 1.12 – Schematic diagram of chondrule formation by the impact jetting model (Johnson et al. 2015, 2017, 2018).

crystallisation experiments. For an impactor with a diameter of 100 km, chondrule cooling rates are expected to be ~1000 to 2000 Kh^{-1}. For larger impactors, 1000 km diameter, cooling rates range from ~100 to 200 Kh^{-1} (Johnson et al., 2015).

1.8.3.3 Thermal history of droplets formed in impact plumes

Dullemond et al. (2014) created models describing the thermal history of droplets within an expanding impact cloud with initial diameters of 0.02 to 20 km which is relevant to chondrules forming in an impact scenario (e.g. Asphaug et al., 2011; Sanders and Scott, 2012; Johnson et al., 2015). The main factors governing the cooling rates of droplets in these impact clouds are the mass of the cloud, the initial temperature of the cloud and the expansion rate of the cloud. A slowly expanding cloud will remain optically thick for longer, hindering radiation and keeping cooling rates low. Higher mass clouds will also cool more slowly as they contain more droplets which will radiate heat to each other, reducing the cooling rate. Reported cooling rates are very wide-ranging, from 0.1 Kh^{-1} for very high mass but slowly expanding impact clouds, to >10^5 Kh^{-1} for low mass, rapidly expanding impact clouds. Initially, droplets are held at peak temperature within the cloud, before experiencing exponentially decreasing cooling rates (Dullemond et al., 2014).

1.8.4 Nebular lightning

Solar nebula lightning is another possible chondrule formation mechanism. For this to occur, particles in the solar nebula must become charged. This could happen in two ways: turbulent charge separation (Desch and Cuzzi, 2000) or charging caused by the decay of ^{26}Al (Johansen and Okuzumi, 2017; Johansen and Okuzumi, 2018). These charged particles must be separated by charge rapidly enough to allow electric fields to be generated without leakage of charge by nebular gas. If these criteria are satisfied, electric fields can grow to breakdown point and electric discharge may occur.

In the turbulent charge separation model (Desch and Cuzzi, 2000), charging occurs due to triboelectric charging. This is charging because of differences in contact potential between two materials. Chondrule precursor grains are primarily made from silicates which have low contact potential; metal grains in the solar nebula have high contact potential. If these two types of grains touch, electrons are transferred from the chondrule precursor leaving them positively charged, while metal grains become negatively charged. In charging by the decay of ^{26}Al, particles in dense pebble structures in the protoplanetary disk become charged when positrons (β^+) are released during the decay of ^{26}Al atoms (Johansen and Okuzumi, 2017; Johansen and Okuzumi, 2018).

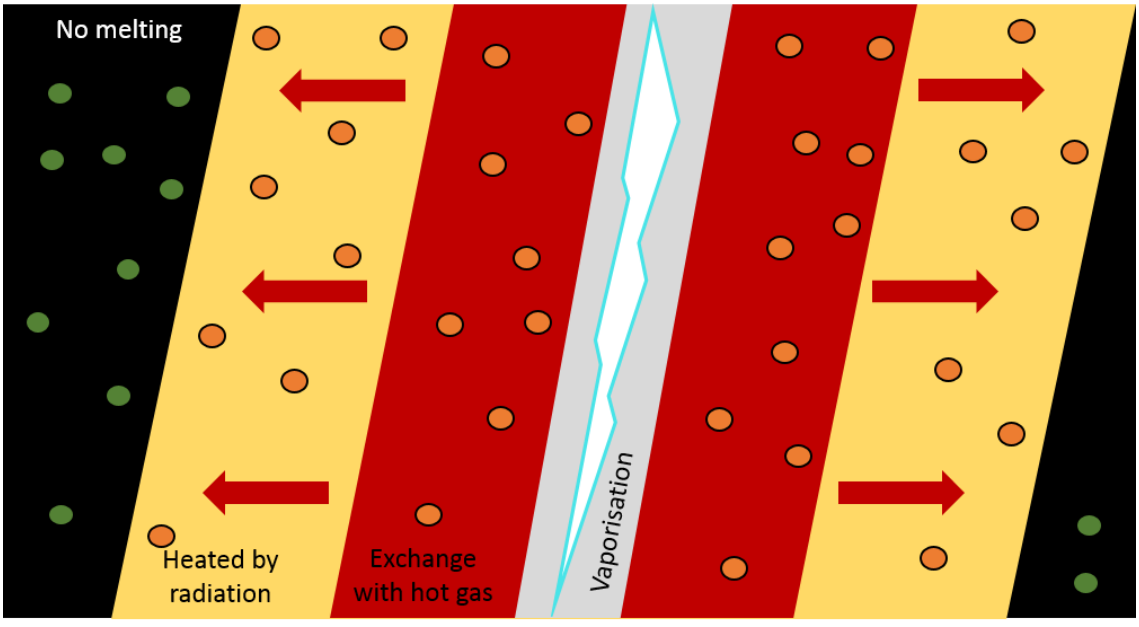

Figure 1.13 – Schematic diagram of the nebular lightning model. The channel where lightning occurs (in grey) is completely vaporised. This increase in gas pressure causes expansion of the channel where chondrule precursors exchange heat with hot gas. Around this zone, chondrule precursors are heated by radiation (Desch et al. 2012).

The Reynolds number, or ratio of inertial to viscous forces, is used to determine whether a fluid undergoes laminar or turbulent flow. The Reynolds number of the solar nebula exceeds that of the onset of turbulence by several orders of magnitude, indicating the solar nebula was turbulent. Turbulence causes eddies which may concentrate particles well above background density. If a sufficient number of positively charged chondrule precursors are concentrated, electric fields may reach breakdown, generating lightning (Desch and Cuzzi, 2000).

Lightning is the movement of charge through a thin channel. In the solar nebula, this is likely to be ~1 to 10 m wide and possibly 100s km long. As electrons move through this channel, ohmic heating occurs, raising the temperature by 1000s K almost instantaneously. These high temperatures completely vaporise any chondrule precursors within the channel. The sudden increase in pressure causes the channel to expand until pressure equilibrium is reached, increasing channel width. Chondrule precursors next to the channel are initially heated by radiation from the channel after the lightning, however, most of the heating occurs when exchanging with hot gas as the channel expands (see Figure 1.13). Cooling of the heated zone is likely to be rapid, at least 10^4 Kh^{-1}, generally much faster than determined by dynamic crystallisation experiments (Desch et al., 2012). Johansen and Okuzumi (2018), however, report cooling rates of several 10^3 Kh^{-1} which decrease to 100s Kh^{-1} close to the solidus, which is still generally higher than predictions from dynamic crystallisation experiments but may be consistent with chondrule formation.

1.8.5 X-wind

Another proposed chondrule formation mechanism is the X-wind model (Shu et al., 1996; Shu et al., 1997; Shu et al., 2001). The interaction between the early Sun's magnetic field and the protoplanetary disk creates an X shaped geometry. At the inner edge of the protoplanetary disk, there is a strong magnetocentrifugal wind, which may loft chondrule precursors above the protoplanetary disk into direct sunlight, where they are heated to peak temperatures up to 1700 K over a period of several hours (see Figure 1.14). As chondrules move away from the sun, they receive less sunlight and therefore begin to cool at rates of 6 to 10 Kh^{-1}. This is potentially consistent with the production of porphyritic chondrules, but cooling rates are too low to produce barred and radial textures (Desch et al., 2010; Desch et al., 2012).

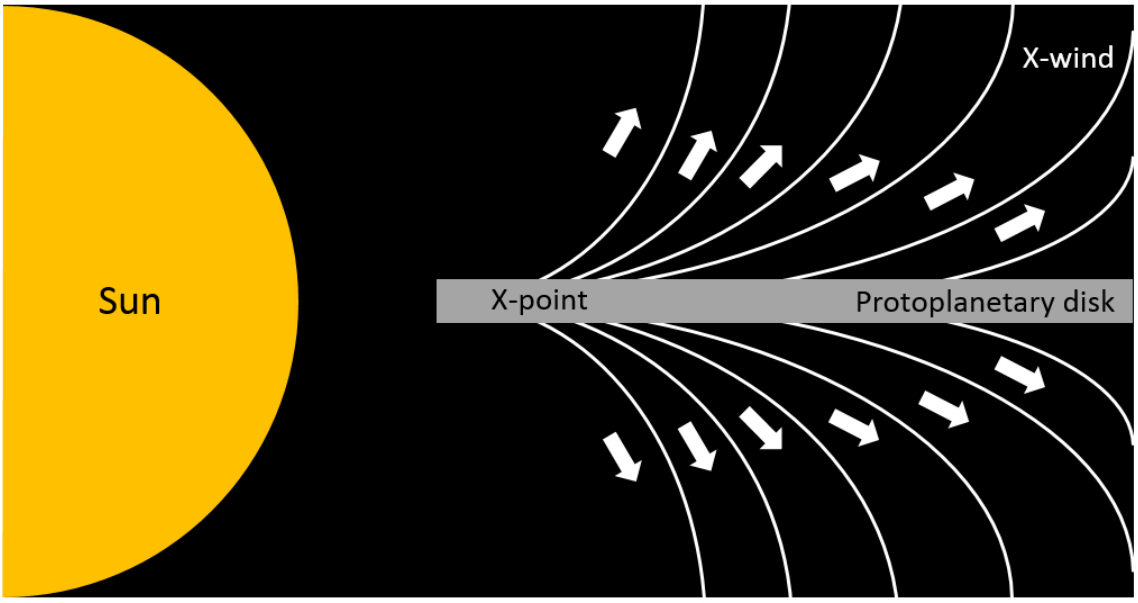

Figure 1.14 – Schematic diagram of the X-wind model for chondrule formation. Chondrule precursors are lofted from the protoplanetary disk by magnetocentrifugal outflows into direct sunlight where they are heated. Over time they move away from the sun where they can cool (Desch et al. 2010, 2012; Shu et al. 1996, 1997, 2001).

1.8.6 Radiative heating from molten planetesimals

Radiative heating from lava oceans at the surface of molten planetesimals is another potential chondrule formation mechanism (Herbst and Greenwood, 2016; Herbst and Greenwood, 2019). In this model, chondrules and chondrites are formed when pre-existing dust clumps or small primitive planetesimals (1 to 1000 m in diameter) pass within several km to larger planetesimals (>100 km in diameter) with exposed lava on their surface (see Figure 1.15). The dust clump or small planetesimal is heated by radiation from the exposed lava driving chondrule and chondrite formation. The factors which affect peak temperatures and cooling rate are the size of the large planetesimal, the temperature at the surface of the large planetesimal, the extent of melting within the large planetesimal, the closest approach of the small planetesimal or dust clump, and the depth within the small planetesimal. Unlike many other mechanisms which invoke flash heating (e.g. large-scale nebular shockwaves), radiative heating predicts generally symmetrical heating and cooling curves. Predicted heating and cooling rates range from 100s to 1000s Kh^{-1}, which are mostly consistent with the cooling rates predicted in dynamic crystallisation experiments.

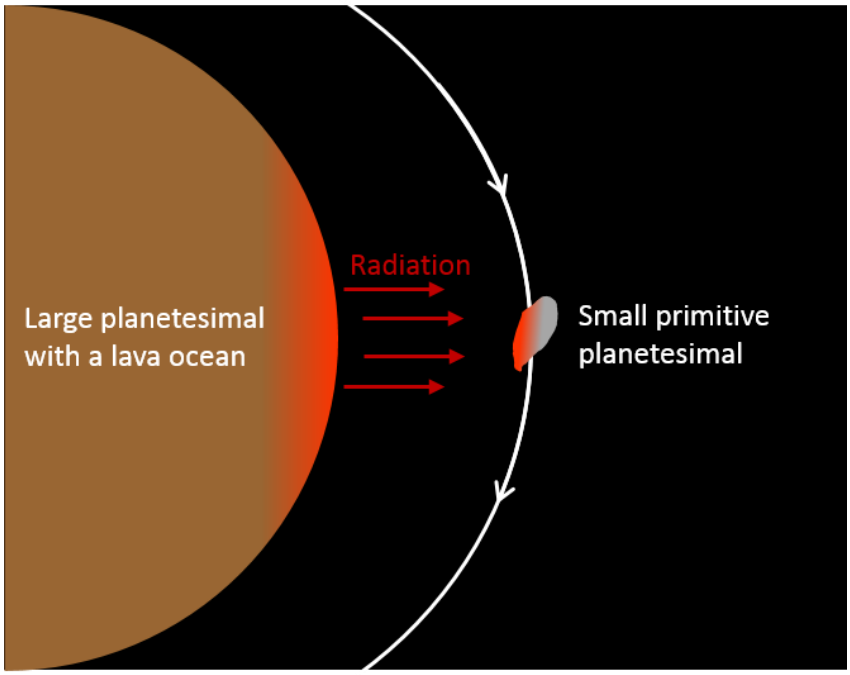

Figure 1.15 – Schematic diagram of the radiative heating model (Herbst and Greenwood 2019). The small primitive planetesimal is heated by radiation when passing larger planetesimals with a lava ocean at the surface.

1.8.7 Other potential chondrule formation mechanisms

Although six potential chondrule formation mechanisms have been discussed in some detail (Large-scale nebular shockwaves (Ciesla and Hood, 2002; Desch and Connolly, 2002; Morris and Desch, 2010; Morris et al., 2016; Morris and Boley, 2018), planetesimal and planetary embryo bow shocks (Ciesla et al., 2004; Morris et al., 2012; Boley et al., 2013; Mann et al., 2016; Morris and Boley, 2018), impacts between planetesimals (Asphaug et al., 2011; Sanders and Scott, 2012; Hasegawa et al., 2015; Johnson et al., 2015; Wakita et al., 2017; Johnson et al., 2018; Oshino et al., 2019), nebular lightning (Desch and Cuzzi, 2000; Desch et al., 2012; Johansen and Okuzumi, 2018) the X-wind (Shu et al., 1996; Shu et al., 1997; Shu et al., 2001; Desch et al., 2010) and radiative heating from molten planetesimals (Herbst and Greenwood, 2016; Herbst and Greenwood, 2019), many others exist. These include current sheets close to the sun (McNally et al., 2013); ablation in bipolar outflows from the sun (Liffman, 2009); magnetic flares (Levy and Araki, 1989) and X-ray flares (Nakamoto et al., 2005). These models may be able to match some of the constraints on chondrule formation; however, they make limited predictions on chondrule thermal histories, which makes them difficult to evaluate as candidate mechanisms for chondrule formation.

1.8.8 Summary

Figure 1.16 summarises the expected cooling rates of chondrules formed by the six discussed chondrule formation mechanisms. Figure 1.17 shows example thermal histories of chondrules in each of the discussed formation mechanisms. Currently, none of the discussed chondrule formation mechanisms can account for the thermal constraints on chondrule formation. The X-wind fails to fit most of the thermal constraints: the starting temperature is too high to account for the presence of primary sulfides; the heating duration is too long and expected peak temperatures may be too low to form chondrules. One constraint the model may achieve is the appropriate cooling rate during crystallisation (6 to 10 Kh^{-1}) to account for the formation of porphyritic textures, although this is too low to account for the formation of barred and radial textures (Shu et al., 1996; Shu et al., 1997; Shu et al., 2001; Desch et al., 2010; Desch et al., 2012). Nebular lightning also fails to meet many of the thermal constraints on chondrule formation. Starting temperature, heating time and cooling rates post peak temperature can account for the presence of volatile

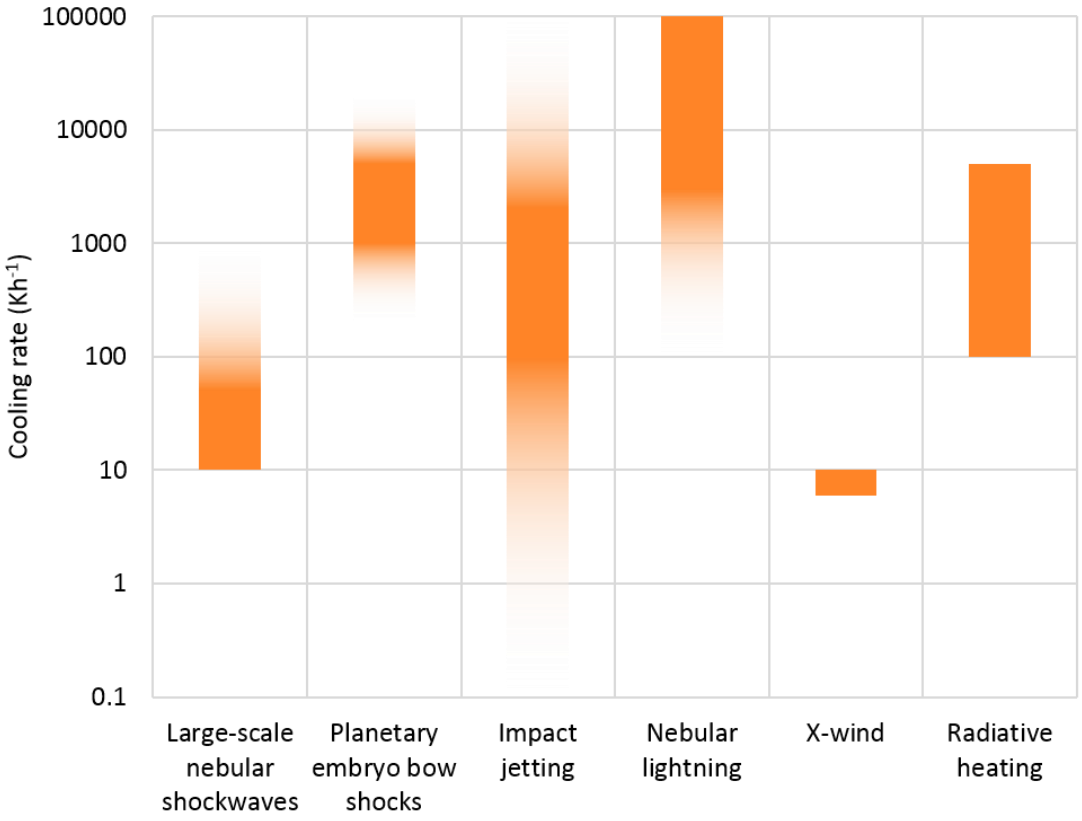

Figure 1.16 – Expected cooling rates from the six discussed chondrule formation mechanisms: large-scale nebular shockwaves (Desch et al. 2012; Morris and Desch 2010; Morris et al. 2016); planetary embryo bow shocks (Boley et al. 2013; Mann et al. 2016); impact jetting (Dullemond et al. 2014; Johnson et al. 2015); nebular lightning (Desch et al. 2012); X-wind (Desch et al. 2012; Shu et al. 1996, 1997, (Desch et al. 2012; Shu et al. 1996, 1997, 2001); radiative heating (Herbst and Greenwood 2016, 2019).

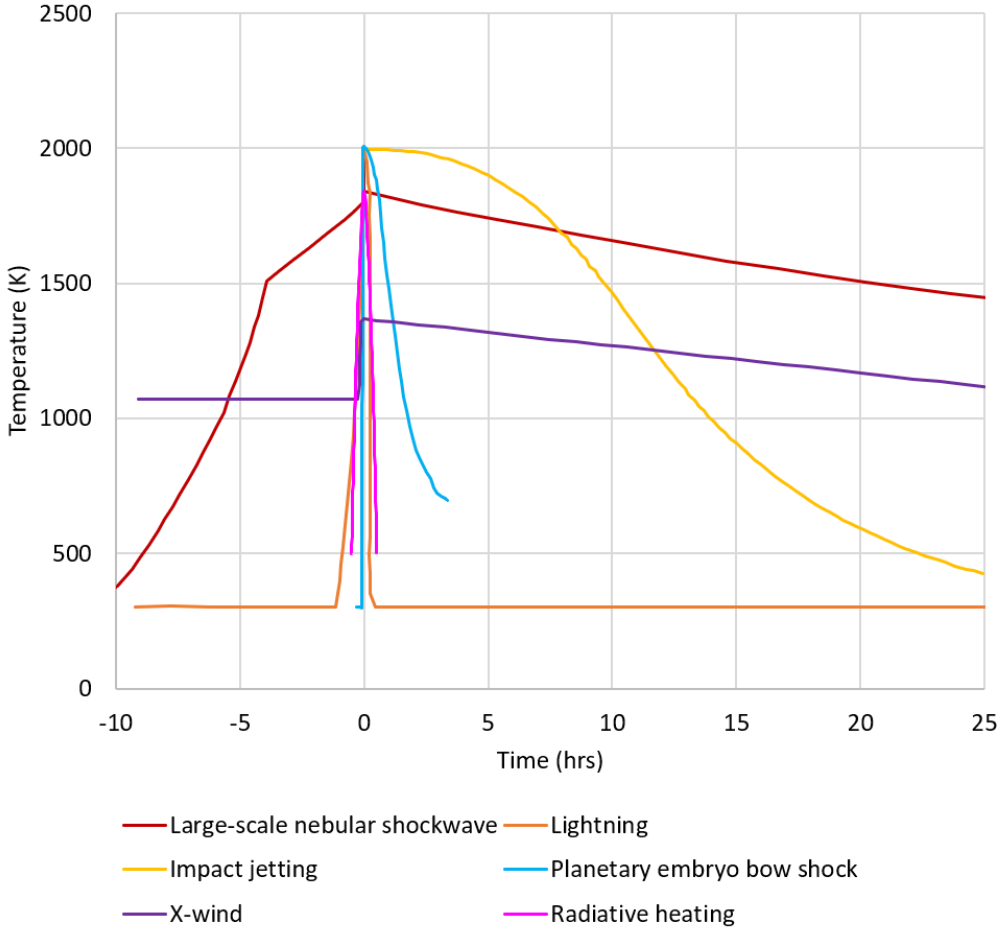

Figure 1.17 – Thermal history of chondrules formed in different chondrule formation mechanisms: large-scale nebular shockwave with shock speed of 8 kms^{-1} (Morris and Desch 2010); lightning (Desch et al. 2012); impact jetting from an impactor with a diameter of 1000 km (Johnson et al. 2015); planetary embryo bow shock around a planetary embryo with a radius of 3000 km, a high mass atmosphere and shock speed of 7 kms^{-1} (Mann et al. 2016); X-wind (Desch et al. 2010); radiative heating with a closest approach of 2 km (Herbst and Greenwood 2016). Peak temperatures have been set to occur at 0 hours.

elements, however cooling rates remain high, 10^3 to 10^4 Kh^{-1} which is generally inconsistent with experimental constraints (Desch et al., 2012; Johansen and Okuzumi, 2018). It may be that the near-instantaneous heating time and high peak temperatures associated with nebular lightning are incompatible with chondrule formation. Güttler et al. (2008) performed experiments where siliciclastic dust particles were heated by electrical discharge. The sudden heating caused the particles to explode and only a small amount of material was thermally processed. This material formed porous spherical structures that did not resemble chondrules. Models invoking collisions between molten planetesimals (Asphaug et al., 2011; Sanders and Scott, 2012) make no detailed predictions of chondrule cooling rate other than overall timescale, which could be consistent. However, it is inconsistent with all other thermal constraints. Impact jetting fits the thermal constraints more than collisions between molten planetesimals. Heating is rapid and appropriate peak

temperatures are achievable. Expected cooling rates of 100 to 2000 Kh^{-1} are within the range predicted by dynamic crystallisation experiments (Johnson et al., 2015). Radiative heating from molten planetesimals also fits many of the thermal constraints, including peak temperatures and cooling rates through the chondrule crystallisation period. The model also predicts symmetrical heating and cooling curves, which may mean that the heating period is too long, however, this may not be valid if there are high partial pressures of volatiles in the formation region (Herbst and Greenwood, 2016; Herbst and Greenwood, 2019). Overall, the best fit for the current thermal constraints are shocks in the protoplanetary disk. Planetary embryo bow shocks have heating times and peak temperatures consistent with crystallisation experiments, but cooling rates are relatively high, and it is still uncertain whether they are consistent with chondrule formation (Morris et al., 2012; Boley et al., 2013; Mann et al., 2016). The best fit for the thermal constraints comes from large-scale nebular shock waves. The models have peak temperatures and cooling rates that are consistent with experimental constraints (Ciesla and Hood, 2002; Desch and Connolly, 2002; Morris and Desch, 2010; Morris et al., 2016; Morris and Boley, 2018). The only constraint the model fails to meet is the desired heating duration, which is too long. This heating could be reduced by a population of dust or microchondrules with a diameter of 10 µm or less. This increases the opacity of the solar nebula and reduces the propagation of the Marshack wave in front of the shock (Morris and Desch, 2011). Including multiple particle sizes also reduces the duration of preheating (Morris et al., 2016).

1.9 Research questions and thesis outline

Chemical analyses of primitive chondritic meteorites provide detailed records of processes in the protoplanetary disk. Chondrules are one of the most common components of these meteorites and formed as a result of brief heating events in the protoplanetary disk and they crystallised from the resulting melt droplets. They are therefore evidence of common and/or widespread transient high-temperature events occurring in the protoplanetary disk. However, the actual process is still unknown, and many different mechanisms have been proposed and modelled. Chondrule cooling rates and thermal histories are key constraints on chondrule formation mechanisms and can help identify the environment and mechanism of chondrule formation while eliminating mechanisms that do not meet these constraints. Dynamic crystallisation experiments provide the most widely cited constraints

on chondrule cooling rate. However, cooling rate is one of multiple factors that affect chondrule texture making the relationship between cooling rate and texture somewhat ambiguous. The results of these experiments should be validated or constrained by more direct measurements, of which there remain relatively few. This leads to several important questions:

- What are the cooling rates of chondrules measured using a direct method?
- Are the thermal histories of chondrules from carbonaceous chondrites and ordinary chondrites the same?
- Which chondrule formation mechanism(s) do the cooling rates and thermal histories of chondrules support?
- What are the implications of the supported chondrule formation mechanism(s)?

To answer these questions, type II chondrules containing forsteritic-olivine relict grains from both ordinary and carbonaceous chondrites have been examined. These relict grains are important features which provide an opportunity to study cooling rates. During cooling, partial equilibration occurs between the relict grain and the surrounding melt and any subsequent crystal growth. By modelling this diffusional exchange, chondrule cooling rates can be calculated. This has been explored previously (Greeney and Ruzicka, 2004; Béjina et al., 2009; Hewins et al., 2009), however, the results were limited. Béjina et al. (2009) and Greeney and Ruzicka (2004) studied forsteritic-olivine relict grains in metamorphosed ordinary chondrites, which may have affected the observed diffusion profiles, while Hewins et al. (2009) presented results from a single chondrule.

By focussing on chondrites that have experienced the least thermal metamorphism on their parent bodies, diffusion that occurred during chondrule formation is observed. Here, a new approach is explored using calibrated backscattered electron images to measure Fe-Mg diffusion profiles and a new explicit finite-difference Fe-Mg diffusion model to create model diffusion profiles and calculate cooling rates. These cooling rates are then compared to the predictions from different chondrule formation mechanisms to evaluate which match these constraints and those which do not. The implications of the supported chondrule formation mechanisms on the evolution of the early Solar System and protoplanetary disk are discussed.

Chapter 2
Samples and analytical methods

This chapter introduces the samples used in this work, ALHA 77307, NWA 8276 and NWA 4910. These meteorites, particularly ALHA 77307 and NWA 8276, represent some of the most pristine material in the meteorite collection. This makes them ideal for studying protoplanetary disk processes such as chondrule formation. This chapter also details the analytical methods employed in this thesis, including electron microscopy techniques and NanoSIMS. In addition, this chapter also outlines the analyses and calculations which lead up to diffusion modelling, and the diffusion modelling approach itself.

2.1 Samples

To focus on diffusion that occurred during chondrule formation, the most primitive and least thermally altered meteorite samples have been studied. The three studied samples range in petrologic type from 3.00 to 3.1 and represent some of the most pristine material in the meteorite collection. This makes them ideal to study protoplanetary disk processes like chondrule formation.

2.1.1 ALHA 77307

ALHA 77307 is a meteorite in the CO chondrite group, which is defined by the Ornans meteorite. ALHA 77307 consist of numerous small chondrules, up to 0.5 mm in diameter, chondrule fragments and CAIs set in a dark matrix. The approximate chondrule to matrix ratio is 0.5 (McSween, 1977). All known CO chondrites are described as petrologic type 3, but they do still show a range of metamorphic textures. Scott and Jones (1990) created a classification scheme for this series of metamorphic textures, ranging from 3.0 to 3.7, based on chondrule petrography. A similar scheme ranging from 3.0 to 3.8 based on the composition of Amoeboid Olivine Aggregates (AOAs) was created by Chizmadia et al. (2002). Grossman and Brearley (2005) also proposed a scheme for CO chondrites up to petrologic type 3.2 based upon the distribution of Cr_2O_3 in FeO-rich olivine in chondrules.

ALHA 77307 is one of the most primitive samples in the CO chondrite group. Scott and Jones (1990) and Chizmadia et al. (2002) both proposed a classification of CO3.0. Grossman and Brearley (2005) went a step further and proposed a classification of CO3.00. Other evidence for minimal metamorphism includes the presence of presolar grains (Huss et al., 2003) and the structural ordering of organic matter in the meteorite (Bonal et al., 2007). Huss et al. (2006) suggest a maximum metamorphic temperature for ALHA 77307 of ~470 K.

Type II chondrules in ALHA 77307 contain large numbers of the forsteritic-olivine relict grains which are necessary for this work. Wasson and Rubin (2003) noted that ~90% of type II chondrules in ALHA 77307 contain forsteritic-olivine relict grains, whereas the percentage in ordinary chondrites is ~30% (Jones, 1990). Of the 51 type II chondrules observed in this thin section six containing forsteritic-olivine relict grains were chosen for further study. These are described in Chapter 3. This is thin section number 84 of ALHA 77307 on loan from the Meteorite Working Group, NASA.

2.1.2 NWA 8276 and NWA 4910

NWA 8276 and NWA 4910 are ordinary chondrites. Ordinary chondrites are split into 3 groups depending upon their total iron content: H, L and LL (e.g. Urey and Craig 1953). The H group meteorites have the highest total Fe content. Meteorites in the L group have low total Fe content, while meteorites in the LL group have low metallic Fe relative to total Fe content, in addition to low Fe content (Greshake and Fritz, 2018). Ordinary chondrites show wide-ranging textures from sharply defined chondrules set in a dark, fine-grained matrix, through to chondrites with very poorly defined chondrules and a hypidiomorphic texture, containing subhedral to anhedral crystals (Dodd, 1969). This represents changing petrologic types from 3 to 6 as the degree of thermal metamorphism increases (Van Schmus and Wood, 1967). Sears et al. (1980) further refined this scheme by using thermoluminescence sensitivity of the chondrite to subdivide petrologic type for petrologic type 3 chondrites into 10 subdivisions, 3.0 to 3.9. Grossman and Brearley (2005) also used their scheme based upon Cr_2O_3 distributions in olivine to further sub-divide meteorites into finer petrologic types between 3.0 and 3.2.

NWA 8276 is classified as L3.00 based on the distribution of Cr_2O_3 in FeO-rich olivine in chondrules (Grossman and Brearley, 2005) and presence of a sulfur-rich matrix (Ruzicka et al., 2017). Alexander et al. (1989) suggest an upper limit of ~530 K as the maximum metamorphic temperature for Semarkona (LL3.00) based upon the presence of smectite and maghemite in the meteorite matrix. However, this also indicates that the matrix of Semarkona has been aqueously altered. As NWA 8276 is the same petrologic type, it likely experienced a similar metamorphic temperature. This makes NWA 8276 one of the most pristine unequilibrated ordinary chondrites. NWA 4910 is classified as LL3.1 (Weisberg et al., 2009). The Bishunpur meteorite (LL3.15) experienced metamorphic temperatures of 570 to 620 K based upon the Ni content of metal in the meteorite matrix (Rambaldi and Wasson, 1981). As NWA 4910 is a similar petrologic type to Bishunpur, it likely experienced similar metamorphic temperatures.

Of seven type II chondrules examined in a polished block of NWA 8276, three containing forsteritic-olivine relict grains were chosen for further study. Of 14 type II chondrules examined in a thin section of NWA 4910, three containing forsteritic-olivine relict grains were chosen for further study. The sample ID for NWA 8276 is P20998, while the sample ID for NWA 4910 is P17374, on loan from the Natural History Museum, London.

2.2 Analytical techniques

2.2.1 Scanning electron microscopy (SEM)

The first stage in this project was to identify and characterise type II chondrules containing forsteritic-olivine relict grains; this is best achieved using Scanning Electron Microscopy (SEM). The scanning electron microscope accelerates a beam of electrons towards the sample and the electrons interact with the sample in several different ways to produce a variety of signals.

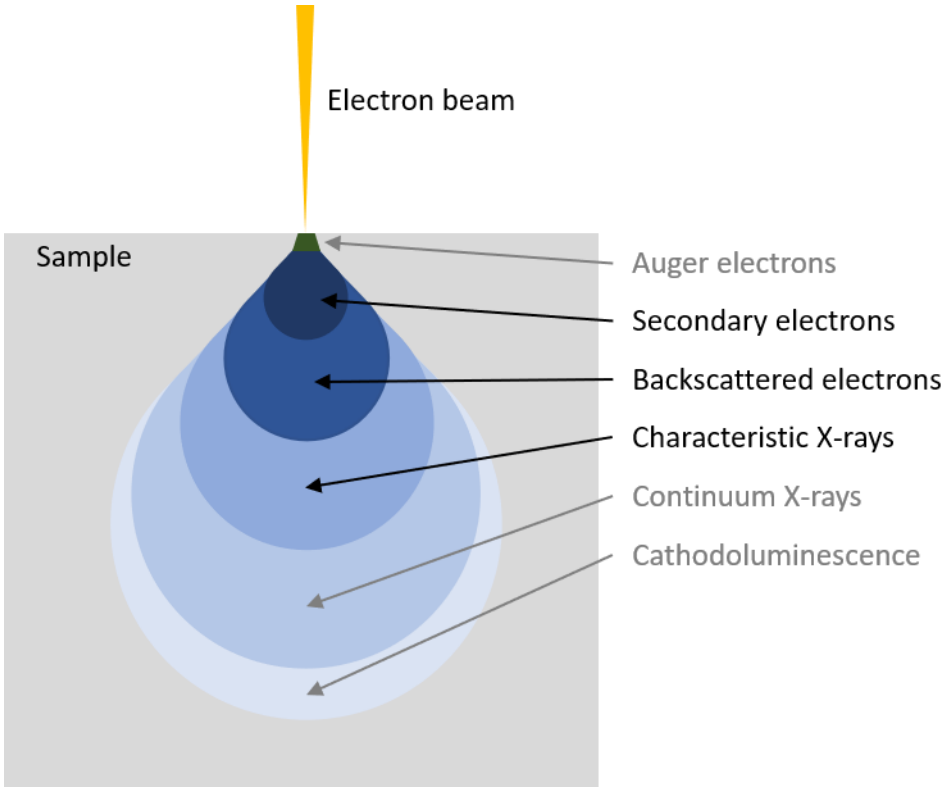

Figure 2.1 – Diagram of the interaction between the electron beam and the sample showing the locations where the major signals are produced. Signals not used in this thesis have been labelled in grey. Secondary electrons detected in secondary electron (SE) imaging originate from close to the sample surface. Backscattered electrons detected in backscattered electron (BSE) imaging originate from deeper within the sample. Characteristic X-rays measured in energy dispersive X-ray spectroscopy (EDS) originate from even deeper regions of the sample. The size of the interaction depends upon the accelerating voltage of the electron beam and the density of the sample; however, the depth is generally between 1 and 5 µm.

2.2.1.1 Sample preparation

When a beam of electrons interacts with a non-conductive sample, for example, a meteorite sample, it causes a build-up of negative charge in the sample which can disrupt the electron beam and the signals produced by the beam. To counter these effects, non-conductive samples must be coated in a conductive layer to conduct the charge away.

Samples were therefore coated in a thin layer of carbon, ~15-30 nm, using an Emitech K950 carbon coater. This carbon coat allows charge to be conducted away from the sample and ensures good signal production.

2.2.1.2 Electron imaging

When the electron beam interacts with atoms in the sample, electrons from the primary electron beam are scattered and create a roughly ball-shaped interaction volume (see Figure 2.1). If electrons are scattered at high angles, they can leave the sample and create the Backscattered Electron (BSE) signal. Atoms with higher atomic numbers (e.g. Fe) generally cause higher scattering angles than atoms with lower atomic numbers (e.g. Mg) and will create a more intense signal (Dijkstra, 2016). In BSE images, contrast is related to the average atomic number of the atoms within the mineral. For example, iron sulfides

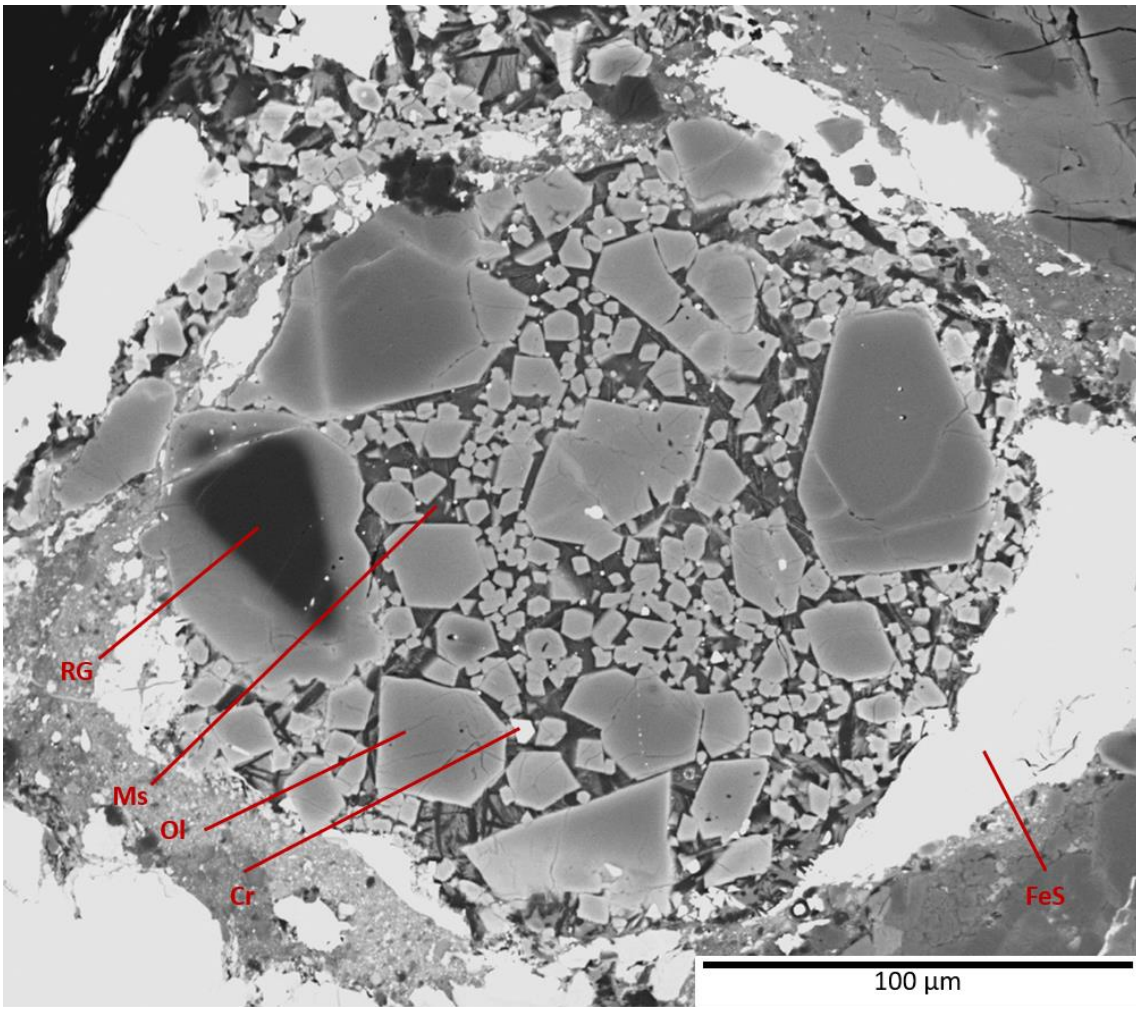

Figure 2.2 – BSE image of a type II porphyritic olivine chondrule, chondrule N4-2, in NWA 4910 showing different mineral phases in the chondrule in different shades of grey: RG = forsteritic-olivine relict grain; Ol = olivine; Ms = mesostasis; Cr = chromite; FeS = iron sulfides.

(FeS) appears white, whereas forsteritic-olivine (Mg_2SiO_4) appears dark grey, as shown in Figure 2.2.

Electrons from the primary electron beam can also collide with electrons in the sample, knocking them out of their orbits. This creates free-travelling electrons, or secondary electrons, which have low energies. As they have such low energy, they cannot easily escape the sample. This means that secondary electrons detected by the secondary electron detector must originate from close to the surface of the sample. This means that the secondary electron (SE) image is sensitive to surface roughness and can provide a good image of surface texture (Dijkstra, 2016), e.g. Figure 2.3. Therefore, SE imaging is used to ensure that analyses take place on flat and well-polished areas of the sample.

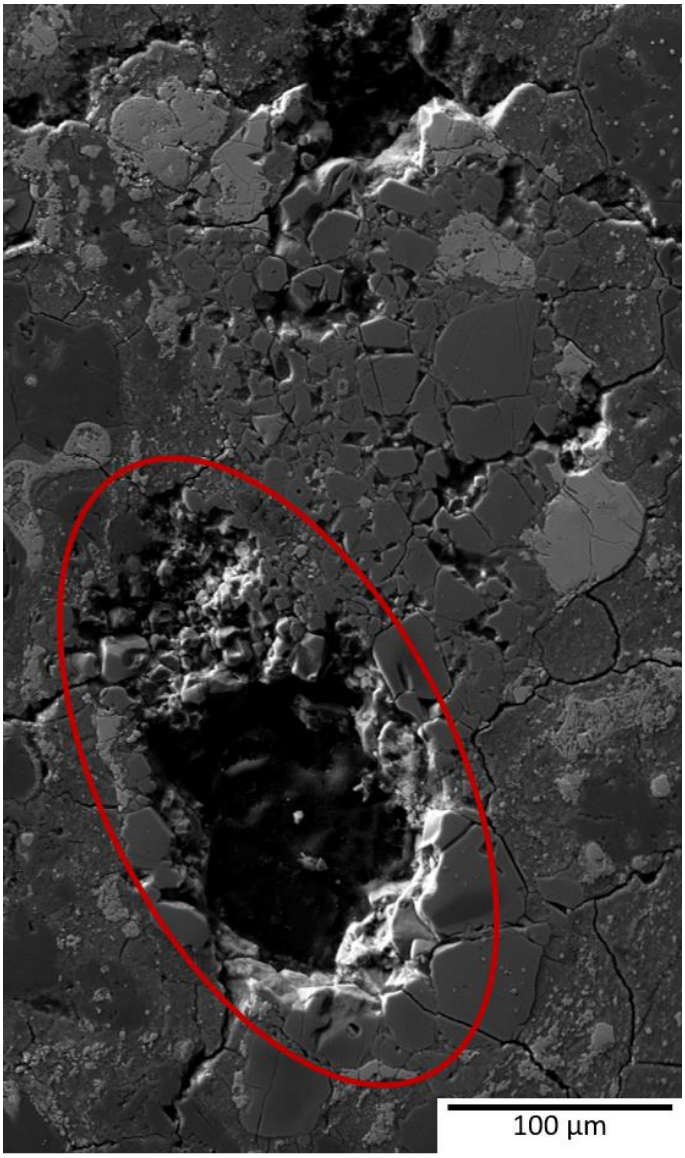

Figure 2.3 – SE image of chondrule Al-4 in ALHA 77307 which has been damaged by plucking during polishing, creating the hole and rough topography shown in the red ellipse.

2.2.1.3 Identifying type II chondrules containing forsteritic-olivine relict grains

BSE and SE images were acquired using the FEI Quanta 200 3D FIB-SEM with a tungsten filament at The Open University. Type II chondrules are FeO-rich, therefore, they generally appear light grey in BSE images when compared with type I chondrules, which are much more MgO-rich, and appear dark grey (see Figure 1.5 in chapter 1). Forsteritic-olivine relict grains present within type II chondrules contain much less FeO (<10 mol %) than surrounding crystals, therefore they appear as dark patches within lighter olivine crystals in BSE images, e.g. Figure 2.2.

Type II chondrules were initially identified based upon their light grey colouration in comparison to darker type I chondrules. High-resolution BSE images of type II chondrules containing relict grains and the relict grains themselves were acquired using an accelerating voltage of 20 kV, beam current of 0.6 nA and counting time of 100 ms/pixel. Images of whole chondrules were used to construct phase maps of chondrules and images of the relict grains were used to obtain Fe-Mg diffusion profiles.

2.2.1.4 Energy-dispersive X-ray spectroscopy (EDS)

When the primary electron beam interacts with the sample, X-rays are also produced. When a secondary electron is emitted from an atom, it creates a vacancy in an electron shell. When this is filled by an electron descending from a higher energy shell, the excess energy is emitted in the form of an X-ray. The energy and wavelength of this X-ray are characteristic of the atom. In EDS, X-rays are characterised by their energies (Dijkstra, 2016). X-rays were detected using the Oxford Instruments X-Max 80 mm^2 silicon drift detector mounted upon the FEI Quanta 200 3D FIB-SEM at The Open University.

EDS mapping was used to produce element maps of chondrules to assess the mineralogy and help construct phase maps of each chondrule. By creating composite element maps, where elements appear in different colours, different phases can be highlighted and distinguished more easily than using BSE images where they may have similar contrasts. A good example of this is the colour scheme where Mg, Fe and Si assigned red, green, and blue respectively, e.g. Figure 2.4. Olivine crystals appear pink in colour, whereas pyroxene appears purple because of its higher Si content. In this colour scheme, mesostasis appears blue. As a result of lower Fe and higher Mg contents, forsteritic-olivine relict grains may appear darker pink, but this is not always obvious. This means that BSE images are the clearest way of identifying these grains (e.g. Figure 2.2). This scheme and other useful

Table 2.1 – Different EDS element map colour schemes used to distinguish and highlight chondrule phases.

Colour scheme	Red	Green	Blue	Useful for identifying:
1	Mg	Fe	Si	Olivine – pink Pyroxene – purple Mesostasis - blue
2	Mg	Ca	Al	Mesostasis – appears green or blue depending on the composition Pyroxene – can appear green if Ca-rich
3	Mg	Cr	Al	Chromite – green Mesostasis - blue
4	Ni	S	Fe	FeNi metal – red Sulfides – green Fe metal and oxides – blue

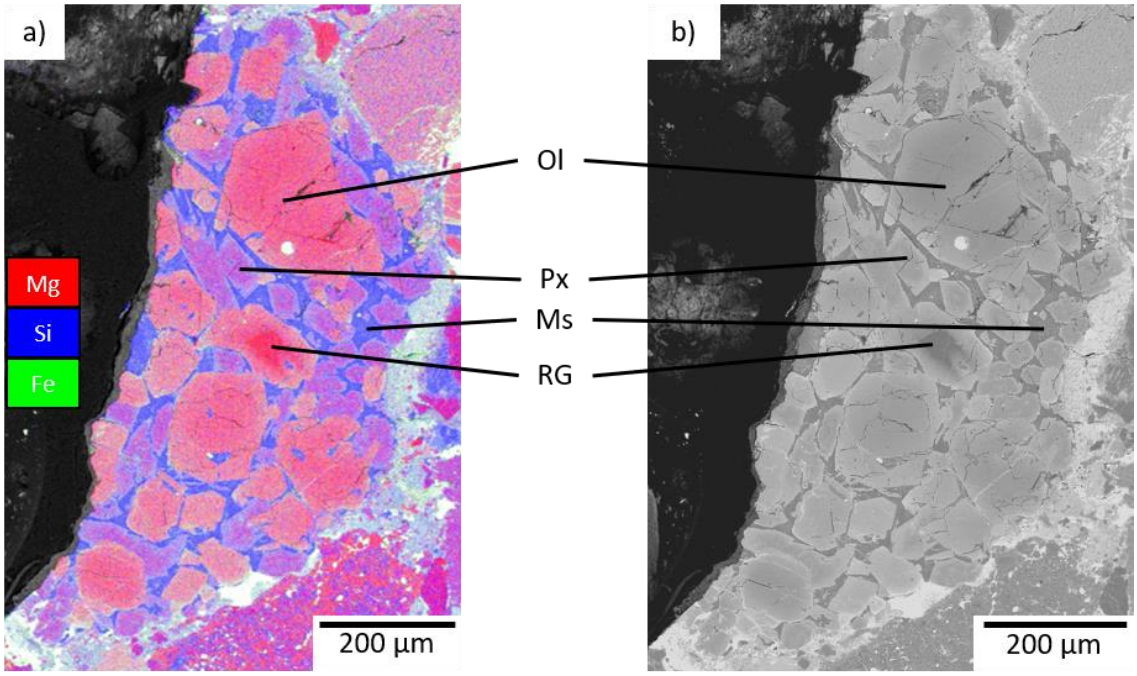

Figure 2.4 – a) EDS element map of a type II chondrule fragment in NWA 4910 highlighting different mineral phases. Mg is coloured red; Fe is green; and Si is blue. Olivine (Ol) crystals appear pink in colour. Pyroxene (Px) appears purple due to higher Si content compared to olivine. Forsteritic-olivine relict grains (RG) appear a darker pink/red colour due to the high Mg content and lack of Fe. Mesostasis (Ms) appears blue as a result of the very high Si content. b) BSE image of the same type II chondrule fragment in NWA 4910.

schemes are shown in Table 2.1. Maps of chondrules were produced with an accelerating voltage of 20 kV, a beam current of 0.60 nA and a beam dwell time of 100 ms/pixel.

EDS point analyses can be used to further characterise chondrules and confirm the presence of forsteritic-olivine relict grains. These grains should be highly forsteritic, with the Mg#, or atomic ratio of Mg to Fe, of the olivine (see Equation 2.1), of 90 or higher (Jones et al., 2005). Analyses were conducted with an accelerating voltage of 20 kV, a beam

current of 0.60 nA with a counting time of 60 s. These analyses are only semi-quantitative; fully quantitative analyses of chondrule phases were obtained using electron microprobe analyses and wavelength dispersive X-ray spectroscopy.

$$Mg\# = \frac{Mg}{(Mg + Fe)} \times 100$$

Equation 2.1 – Equation used to calculate Mg#, or ratio of Mg to Fe, in olivine in atomic %.

2.2.1.5 Electron backscatter diffraction (EBSD)

Diffusion in olivine crystals is highly anisotropic (e.g. Dohmen and Chakraborty 2007). This means that to undertake accurate diffusion modelling in olivine, the orientation of the grains with respect to the measured diffusion profile must be accounted for. The orientation of the crystallographic axes can be obtained using Electron Backscatter Diffraction (EBSD).

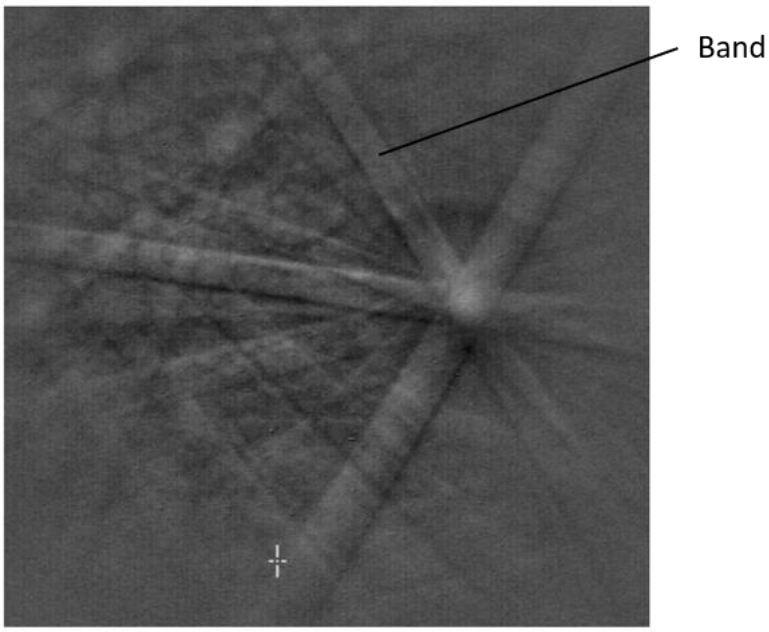

Figure 2.5 – EBSP or Kikuchi pattern for olivine showing a set of bands which are related to the geometry of the lattice planes within the crystal (Faul and Gerald 1999).

If the primary electron beam hits the sample at an angle (usually 70°), backscattered electrons will be scattered in a distribution related to the crystal structure and orientation at the location of the beam impact. This distribution can be imaged on a phosphor screen where the backscattered electrons create a set of bands in an Electron Backscatter Diffraction Pattern (EBSP) (see Figure 2.5) which is then captured by a camera. The patterns are then indexed using software which compares the imaged bands to a database of

selected phases and presents a solution. Once indexing is complete, the crystal and its orientation with regards to the whole sample can be visualised (Brisett, 2016). An example pole figure showing the orientation of the crystallographic axes in an olivine crystal is shown in Figure 2.6.

Analysis by EBSD requires the sample to be highly polished, beyond ordinary mechanical polishing, and requires a pristine crystal lattice at the sample surface (Mariani et al., 2008). This is achieved by adding an extra polishing step using colloidal silica.

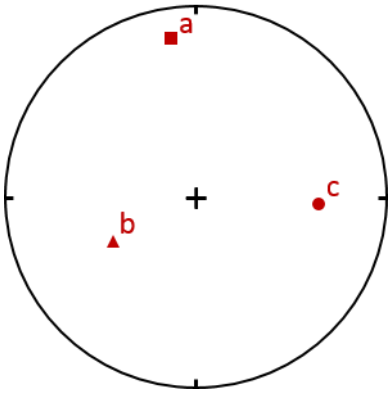

Figure 2.6 – Example pole figure showing the orientation of the different crystallographic axes in an olivine crystal.

EBSD maps of forsteritic-olivine relict grains were produced using the Zeiss SUPRA^{TM} 55VP FEG-SEM equipped with an Aztec HKL EBSD system and HKL Nordlys Nano high-sensitivity camera at The Open University. The beam operated in high current mode, with an accelerating voltage of 20 kV and a mapping step size of 1 µm.

2.2.2 Electron probe microanalysis (EPMA) and wavelength-dispersive X-ray spectroscopy (WDS)

Once chondrules and forsteritic-olivine relict grains are suitably characterised by SEM and EBSD, further analysis is required to gain more precise and fully quantitative chemical analyses of chondrule phases and forsteritic-olivine relict grains. These are also used to calculate the chondrule bulk composition and to determine the chemical composition of the relict grains and surrounding overgrowth. This is achieved using Wavelength Dispersive X-ray Spectroscopy (WDS). Unlike EDS, WDS characterises the emitted X-rays by their wavelength (Matthews, 2016), however, each spectrometer can only analyse one element at a time.

Analyses were conducted using the Cameca SX100 electron microprobe at The Open University. Five spectrometers with a set of diffracting crystals are present on this system allowing for the measurement of five elements simultaneously. As more than five elements were analysed, the position of the diffracting crystals were changed during the analyses to allow for the measurement of other elements. The electron beam used in these analyses had an accelerating voltage of 20 kV, a beam current of 10 nA, and was focussed to a 1 µm spot size. Peak counting times were 15 to 30 s depending upon the analysed element, with background counting times of 15 s. The calibration standards and elements analysed are shown in Table 2.2, while typical detection limits are shown in Table 2.3.

Table 2.2 – Elements analysed and calibration standards for EPMA analyses.

Standard	Elements
Alkali feldspar	Na, Al, Si, K
Forsterite	Mg
Haematite	Fe
Bustamite	Ca, Mn
Chromite	Cr
Apatite	P
Rutile	Ti
Nickel alloy	Ni

Table 2.3 – Typical detection limits for EPMA analyses.

Oxide	Detection limit (wt %)
Na_2O	0.05
MgO	0.07
Al_2O_3	0.05
SiO_2	0.07
P_2O_5	0.09
K_2O	0.02
CaO	0.02
TiO_2	0.04
Cr_2O_3	0.04
MnO	0.03
FeO	0.03
NiO	0.06

Analyses where the total calculated oxide abundance fell outside the range of 98 to 102 wt % were excluded in most circumstances. Results with obvious contamination from surrounding phases, as indicated by poor stoichiometry compared to expected, have also been excluded. Chondrule mesostasis analyses were challenging because of the presence of microcrystallites, small areas of roughness, holes, and alteration products. As a result of this, results with totals down to ~90 wt % have been accepted in some cases for mesostasis

analyses. Matrix corrections were applied according to the Pouchou and Pilchoir procedure (PAP model, Pouchou and Pichoir, 1987), or the X-Phi model (Merlet, 1994).

2.2.3 Chondrule bulk composition and liquidus temperature

Chondrule bulk compositions can be determined in two ways, defocussed beam analyses and by modal recombination analysis. Of the two, it has been shown that modal recombination analyses are more reliable than defocused beam analyses (Berlin et al., 2008), therefore chondrule bulk compositions have been calculated using a modal recombination analysis. This technique combines the proportion, average composition, and density of each phase within the chondrule into a single bulk composition using Equation 2.2 for each element (Berlin et al., 2008). Only phases which contributed to the silicate melt were included in the bulk compositions. This means that metal and sulfides were not included in the calculation. In addition, forsteritic-olivine relict grains were not part of the most recent melt so have also not been included in the bulk composition calculation.

$$Bulk\ Mg = conc^{Mg}_{phase\ 1} \times \left[\frac{vol\ \%_{phase\ 1} \times \rho_{phase\ 1}}{\sum(vol\ \%_{phases} \times \rho_{phases})}\right] + conc^{Mg}_{phase\ 2} \times \left[\frac{vol\ \%_{phase\ 2} \times \rho_{phase\ 2}}{\sum(vol\ \%_{phases} \times \rho_{phases})}\right] + \cdots + conc^{Mg}_{phase\ n} \times \left[\frac{vol\ \%_{phase\ n} \times \rho_{phase\ n}}{\sum(vol\ \%_{phases} \times \rho_{phases})}\right]$$

Equation 2.2 – Equation used to calculate the bulk composition of an element within a chondrule (Berlin et al., 2008).

To calculate the bulk composition, the average composition for each phase must be known. For this, electron microprobe measurements have been used (see section 2.2.2). Olivine and pyroxene phenocrysts within the chondrules may be heavily compositionally zoned. To determine an average value for these phases, many analyses covering a wide range of phenocrysts were undertaken. These include analyses covering a range of positions within phenocrysts and a range of phenocryst sizes. For the density of mineral phases, values from www.webmineral.com (last accessed 24/09/2019) have been used. As a result of the compositional zoning within phenocrysts, an average value for these phenocrysts is used in the calculation. The website uses values for olivine and forsterite from Dana et al. (1915) and values for chromite and enstatite from Roberts et al. (1990). For chondrule mesostasis, the value for basaltic glass has been taken from Sparks et al. (1980). The values for density are shown in Table 2.4.

Table 2.4 – Density of phases used in the calculation of chondrule bulk composition. Values for olivine, forsterite, enstatite and chromite are taken from www.webmineral.com (last accessed 24/09/2019). The values on the website for olivine and forsterite are from Dana et al. (1915) and the values for enstatite and chromite are from Roberts et al. (1990). The value for basaltic glass is taken from Sparks et al. (1980).

Phase	Density (gcm^{-3})
Olivine	3.32
Forsterite (relict grains)	3.27
Enstatite (pyroxene crystals)	3.2
Chromite	4.79
Basaltic glass (mesostasis)	2.75

To calculate the relative proportion of each phase present in the chondrule, phase maps were drawn using open-source software Inkscape. A combination of high-resolution BSE images and element maps were used to distinguish between each phase. An example phase map is shown in Figure 2.7.

The proportion of each phase present within the chondrule by area was extracted using

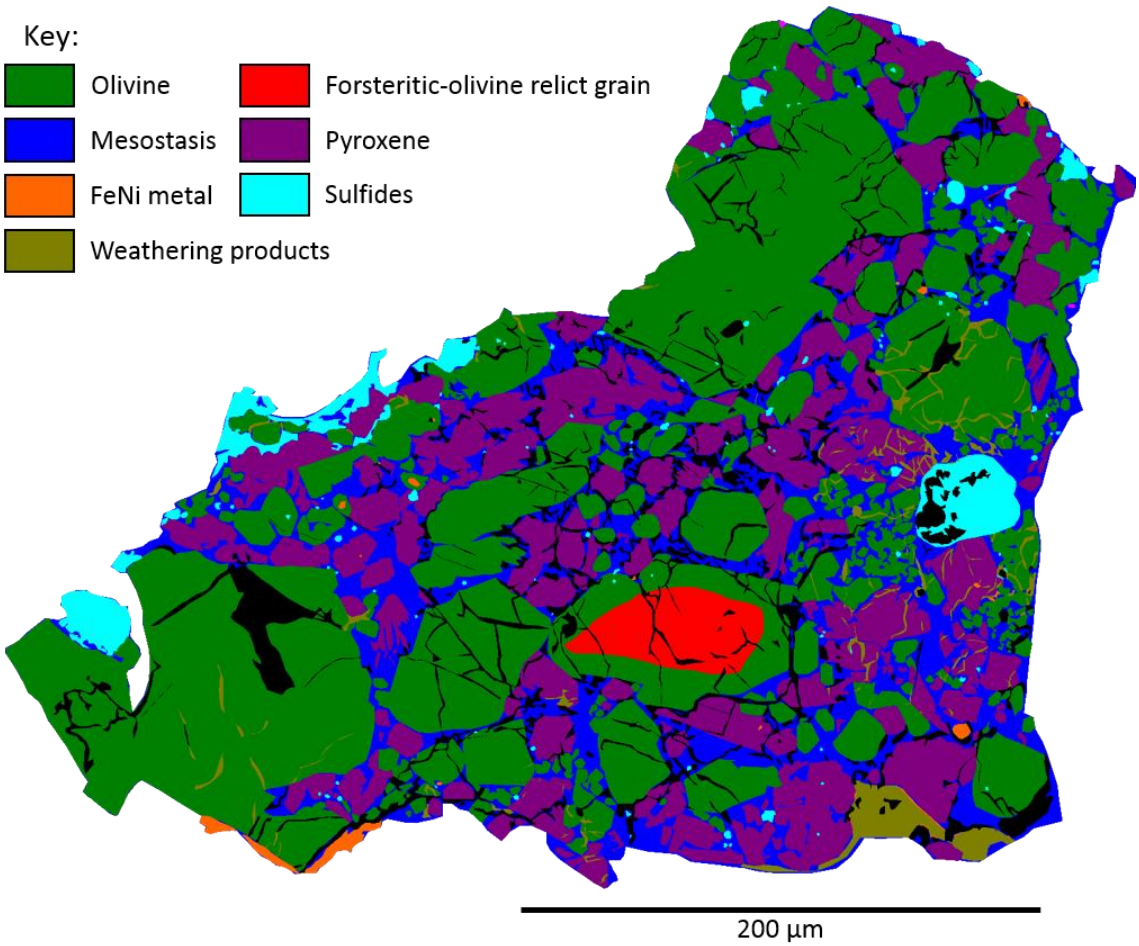

Figure 2.7 – Example phase map of chondrule N4-3 from NWA 4910. This phase map was drawn using open source software Inkscape. Black areas indicate fractures and holes.

colour thresholds and particle analyses in open source software ImageJ (Schneider et al., 2012). Once the composition, proportion and density of the phases are known, Equation 2.2 can be used for each element to calculate the overall bulk composition.

The bulk compositions were then entered into geochemical modelling software Petrolog3 (Danyushevsky and Plechov, 2011) in order to calculate chondrule liquidus temperatures and obtain olivine-saturated liquidus curves showing how the melt composition changes during chondrule cooling and crystallisation. Calculations were performed at a pressure of 0.001 kbar and fO_2 of IW-1 using the mineral-melt models of Danyushevsky (2001), Bolikhovskaya et al. (1995) and Nielsen (1985) for olivine, pyroxene and chromite respectively. A value of IW-1 was used for the oxygen fugacity as most of the analysed chondrules contain small amounts of Fe,Ni metal and crystallisation experiments have reproduced type II chondrule features at oxygen fugacities from IW-1 to IW-0.5 (Lofgren and Russell, 1986; Lofgren, 1989; Radomsky and Hewins, 1990; Connolly and Hewins, 1991; Jones and Lofgren, 1993; Kennedy et al., 1993; Connolly and Hewins, 1995; Dehart and Lofgren, 1996; Connolly et al., 1998; Weinbruch et al., 1998).

2.2.4 Fe-Mg diffusion profiles

2.2.4.1 Calibrated BSE greyscales

Fe-Mg diffusion profiles have been measured using calibrated BSE greyscales using an approach similar to Hartley et al. (2016) and Martin et al. (2008). The BSE greyscale responds linearly to Fe-Mg compositions in olivine crystals (Reed, 2005). High-resolution BSE images of forsteritic-olivine relict grains were calibrated to electron microprobe measurements using the calibrate function in ImageJ (Schneider et al., 2012).

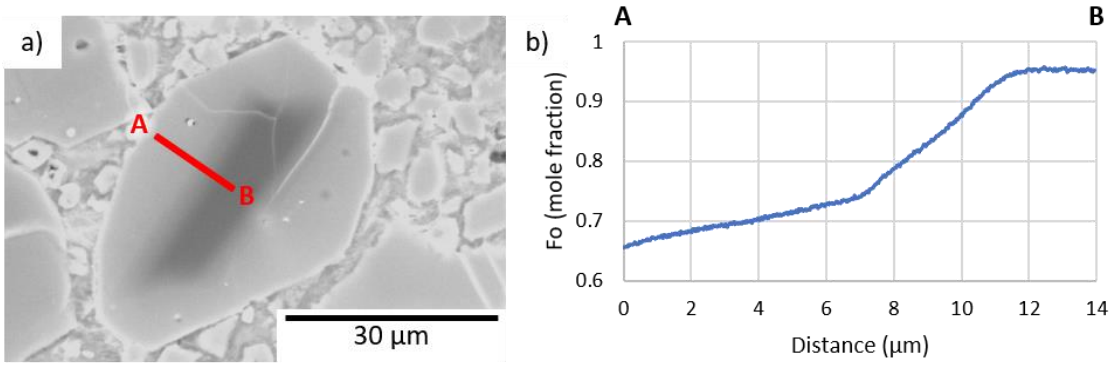

Figure 2.8 – a) forsteritic-olivine relict grain in chondrule N8-3 in NWA 8276 showing the location of profile AB. b) profile AB, an example of a calibrated BSE Fe-Mg compositional profile.

Compositional profiles were extracted from these calibrated BSE images using the line function in ImageJ. The extracted lines were 50 or 100 pixels wide (typically ~0.5 to 3 µm in width), which reduces noise in the measured compositional profiles by averaging the profile across this width. An example compositional profile diffusion profile is shown in Figure 2.8.

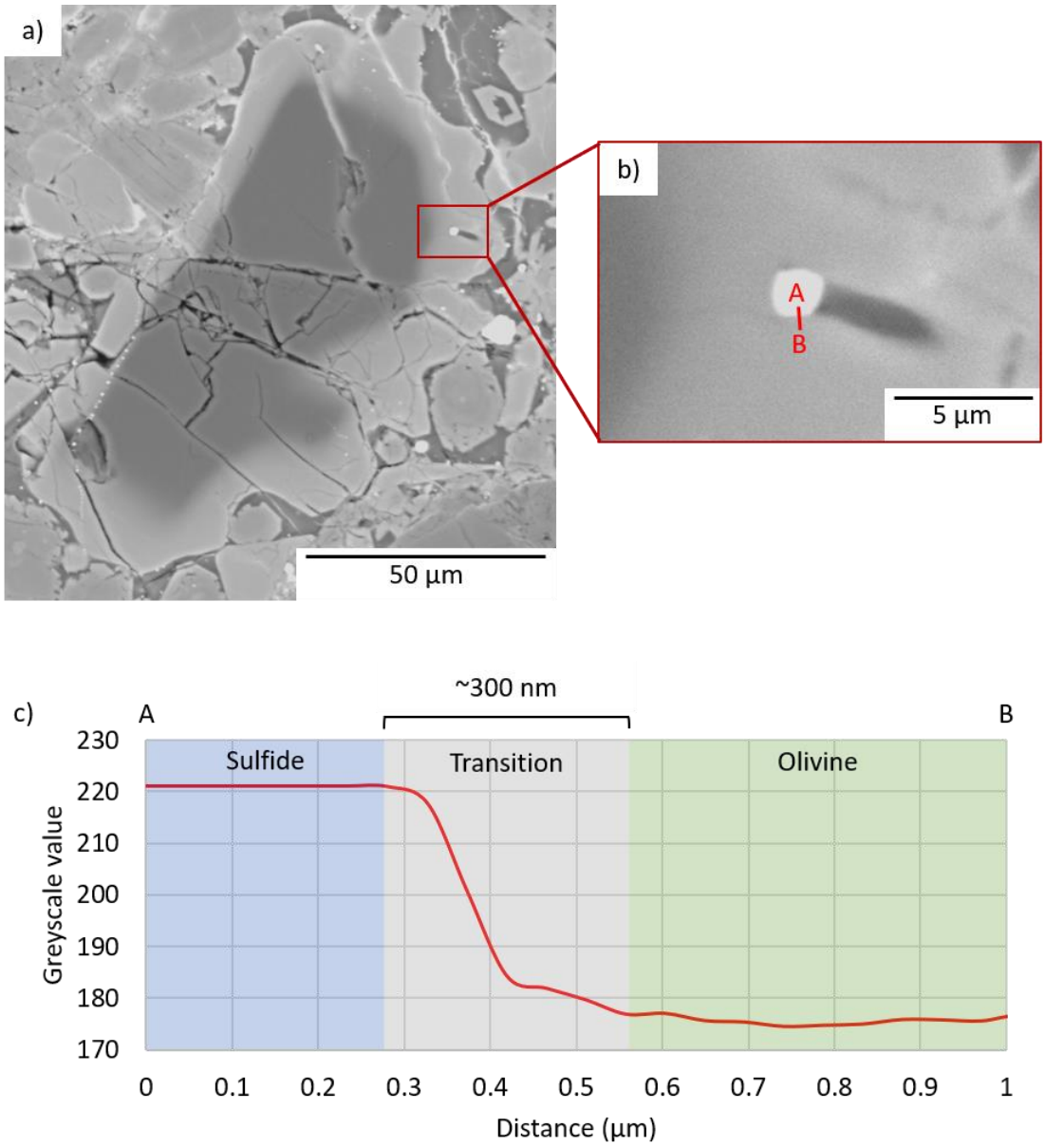

Figure 2.9 – a) BSE image of forsteritic-olivine relict grain N4-1 RG1 in chondrule N4-1 in NWA 4910; b) BSE image of a small sulfide inclusion showing the location of profile AB; c) Profile AB which shows the blurred transition between sulfide on the left to olivine on the right. Using this, the spatial resolution of the BSE image can be conservatively estimated to be ~300 nm.

2.2.4.2 Resolution of BSE images

The spatial resolution of the BSE images is limited by the electron beam spot size and interaction volume of the beam. To test the resolution of BSE images, profiles were taken across instantaneous boundaries with significant contrast differences, for example, the boundary between olivine and chromite or sulfide inclusions within the crystal. As a result of the beam spot size and interaction volume, this boundary will not appear instantaneous in the BSE images and the blurred region between the two phases represents the spatial resolution of the BSE images. By undertaking this analysis, the spatial resolution of the BSE images can be assessed (see Figure 2.9). Conservative estimates of the spatial resolution of the BSE images of the forsteritic-olivine relict grains ranges from approximately 200 to 400 nm.

2.2.4.3 Selection of grain boundaries for diffusional analysis

As Fe-Mg diffusion in olivine is highly anisotropic (e.g. Dohmen and Chakraborty 2007). A correction can be applied in order to correct for varying diffusion rates along the different crystallographic axes (Costa et al., 2008). However, there are no quantitative corrections for problems associated with crystal sectioning and morphological effects (see Figure 2.10), and therefore, only the best possible profiles would be used for diffusion modelling.

Figure 2.10 shows some of the potential sectioning and morphological effects. Figure 2.10a shows a regularly shaped grain which is sectioned parallel to the c-axis. This allows for measurement of compositional profiles measured perpendicular to the grain boundary, which show the true diffusion width. This allows the most accurate diffusion timescales and cooling rates to be calculated. In addition, the compositional profiles measured on opposite crystal faces will be symmetrical. Figure 2.10b shows the same regularly shaped grain sectioned off-axis. This still results in symmetrical compositional profiles on opposite crystal faces; however, the apparent width of the compositional profile is now wider than the real width as a result of the more shallowly dipping grain boundary. This will result in overestimations of diffusion timescales and cooling rate underestimates. Figure 2.10c shows an irregularly shaped grain. This has resulted in highly asymmetric compositional profiles, one of which shows a much wider width over the actual width of the diffuse boundary.

Many of the forsteritic-olivine relict grains show irregular shapes (e.g. Figure 2.9a), and are unlikely to be sectioned in an idea manner (e.g. Figure 2.10a). The sections are likely to

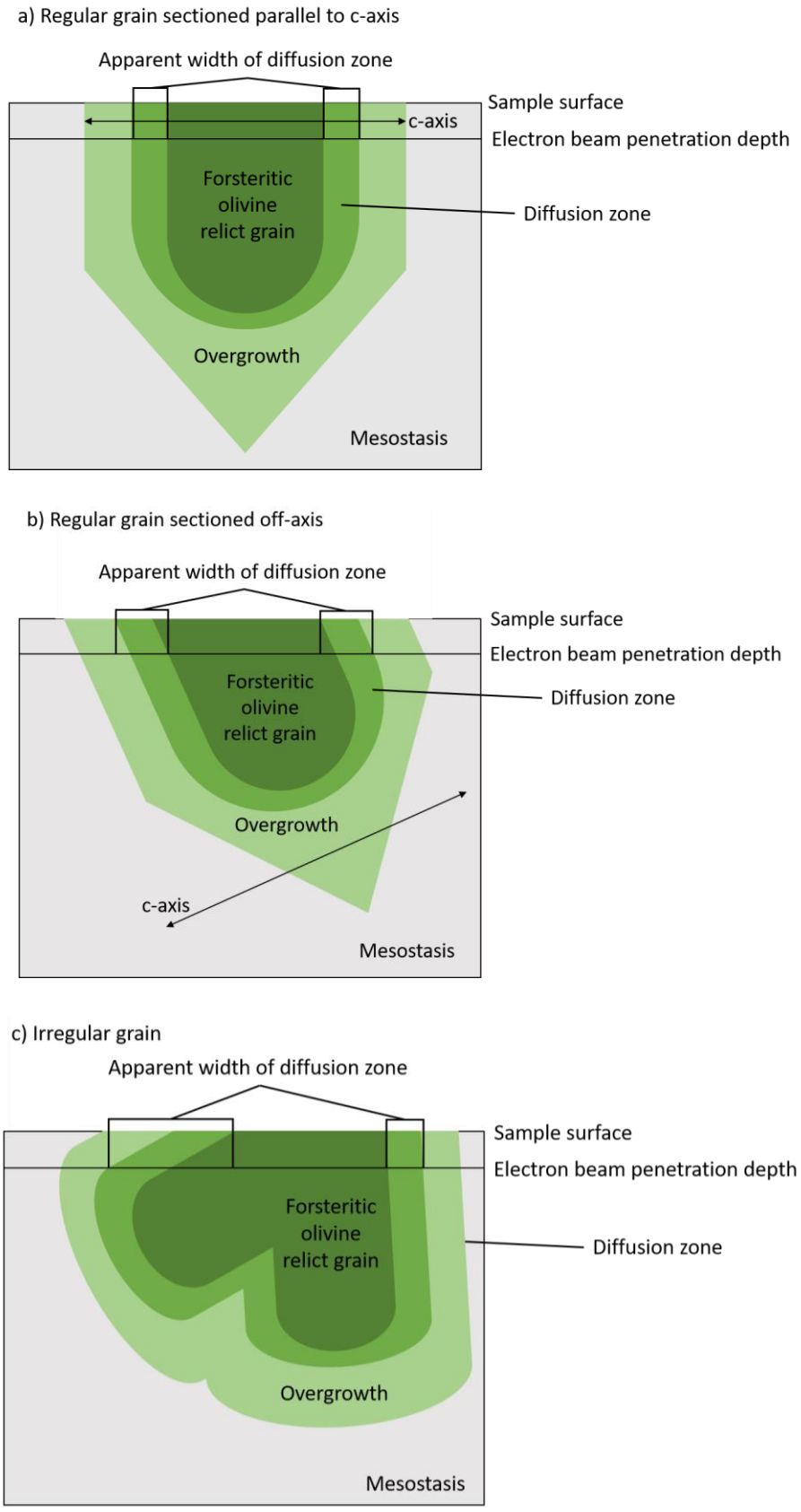

Figure 2.10 – Diagrams showing how sectioning and morphological effects affect the apparent width of the diffuse boundary between forsteritic-olivine relict grains and the overgrowth: a) regular grain sectioned parallel to crystallographic axes; b) regular grain sectioned off-axis; c) irregular grain.

show randomly oriented sections through these irregularly shaped grains. Diffusion profiles measured perpendicular to the forsteritic-olivine relict grain boundary visible in the section are likely not measured perpendicular to the grain boundary in the third dimension (e.g. Figure 2.10). This artificially extends the measured diffusion profiles, leading to underestimated cooling rates. To illustrate the effect of sectioning effects Shea et al. (2015) reported that modelling compositional profiles from off-centre, randomly oriented sections through olivine grains resulted in significant time overestimates and underestimates of the true diffusion time ranging from 50 to 590% within a single crystal. To choose the best boundaries, a checklist of criteria was created:

- In a chondrule containing multiple relict grains, choose the largest grain(s). These are most likely to be cut through the centre of the relict grain and are most likely to show the true grain composition. Apparently small grains could be very off-centre transects through large grains.
- Choose grains showing a clear concentration plateau within the forsteritic-olivine relict grain. Grains which show a dipping plateau, or a compositional change from one end to the other, suggest an off-centre section which clips the edge of the forsteritic-olivine relict grain. This means this grain may not show the true grain composition.
- Choose grains that display symmetry between opposite crystal faces. Grains which show significant asymmetry suggest irregular grain shapes or off-centre transects which may result in diffusion profiles which overestimate the diffusion time and underestimate cooling rates.
- Obtain diffusion profiles away from merging diffusion fronts caused by diffusion from corners and rounded edges. Modelling compositional profiles measured close to these merging diffusion fronts will result in inaccurate timescales and cooling rates.
- Choose grains allowing for the measurement of more than one compositional profile. Measuring compositional profiles across multiple boundaries tests the variability of timescales and cooling rates obtained from a single grain.

Shea et al. (2015) also suggest that for most natural systems, >20 transects are required to obtain accurate diffusion timescales and cooling rates. However, each chondrule has a

unique thermal history and therefore given the size of typical chondrules (<1 mm) and the rarity of relict grains, it is impossible to even approach this requirement.

By following these criteria as closely as possible, while also avoiding grains which are heavily fractured or contain a high density of inclusions, twelve chondrules have been analysed. All twelve chondrules have one suitable forsteritic-olivine relict grain, except Al-5, which contains two. This means that each chondrule has 1 to 4 modelled compositional profiles.

2.2.5 NanoSIMS

Secondary Ion Mass Spectrometry (SIMS) is a technique used to determine the abundances of studied species *in-situ*. The sample is bombarded by a beam of primary ions causing atoms and small molecules to be ejected from the sample in a process called sputtering. A tiny fraction of these particles are ionised and referred to as secondary ions. As they are charged, they can be accelerated into a mass spectrometer where they are separated by a magnetic field and their relative abundances measured.

The Cameca NanoSIMS 50L can use a very narrow primary beam (down to 50 nm for the Cs^+ primary beam) and geometry which ensures high transmission of secondary ions with good mass resolution. This approach combines high sensitivity with high spatial resolution. Secondary ions are separated in a magnetic field and collected in up to 7 detectors where they are counted (Hoppe et al., 2013).

NanoSIMS analyses are useful to measure trace element concentrations down to ppm detection limits at a very high (sub-µm) spatial resolution. This means that trace element compositional profiles for very narrow boundaries can be constructed. These are potentially useful for trace element diffusion modelling or, in the case of very slow diffusing elements, for example, phosphorus (Watson et al., 2015), to trace the original relict grain boundary.

2.2.5.1 NanoSIMS sample preparation

Relief on the sample can make NanoSIMS analysis challenging. Topographic features on samples can enhance or hinder secondary ion production resulting in images which are dominated by these topographic features rather than reflecting the composition of the sample (Li et al., 2020). Samples must, therefore, be flat and polished before analysis. ALHA 77307 and NWA 4910 are polished sections and NWA 8276 is a polished block. Using the

secondary electron detector on the SEM, any relief present on the sample surface is observed and can, therefore, be avoided. To help with charge conduction and avoid charging effects, samples were coated in ~30 nm carbon.

2.2.5.2 Analysis setup and species analysed

Trace-element maps and compositional profiles were produced for elements and molecules of $^{56}Fe^{16}O$, $^{24}Mg^{16}O$ and ^{31}P. A relatively high beam current (~100 pA) Cs^+ primary probe was used to presputter areas of 20 x 20 µm or 25 x 25 µm for ~2 minutes prior to analyses, removing the carbon coating and any possible contamination until sputter equilibrium is achieved. Measurements were undertaken in raster imaging mode by scanning a focussed Cs^+ primary ion beam with a current of 2 pA (~200 nm diameter) over 15 x 15 µm or 20 x 20 µm with a resolution of 256 x 256 pixels. Secondary ion counts of the studied species were collected on electron multipliers. The electron flood gun was used to assist with charge compensation. Analyses typically comprised 300 frames with each frame taking ~32 s to complete leading to a typical analysis time of just under 3 hours. Standards of San Carlos Olivine were used to set up detectors for $^{56}Fe^{16}O$ and $^{24}Mg^{16}O$, and apatite for ^{31}P. However, the results were not calibrated as the only information required was the shape of the diffusion profile. The results were processed in L'Image software (courtesy L. Nittler, DTM, Carnegie Institute, Washington DC). Data were correct for detector dead time (44 ns) and image drift (usually only a few pixels).

2.2.6 Diffusion modelling

Two different approaches were used in this project using two different diffusion models. The first approach combines AutoDIFF which is a diffusion model that has been used in terrestrial systems (e.g. Hartley et al. 2016) with a secondary worksheet to calculate chondrule cooling rates. The second approach uses an explicit finite difference forward modelling program. The two approaches are outlined below but are discussed in significantly more detail in Chapter 5 – Diffusion modelling.

2.2.6.1 Approach 1: AutoDIFF and secondary worksheet

AutoDIFF is a fixed temperature diffusion model for Fe-Mg interdiffusion in olivine. It works by utilising a database of model diffusion profiles which obey composition-dependent diffusion in a one-dimensional geometry, calculated using a finite difference method. As diffusion in olivine is highly composition dependent (Dohmen and Chakraborty, 2007), the

more compositional variation displayed between the olivine crystal edge and the core region, the more a diffused profile will change from a symmetrical sigmoid to an asymmetric sigmoid. For a given set of boundary conditions (temperature, oxygen fugacity, anisotropy, and composition), diffusion profiles are self-similar in time. After 4 time-units, the observed diffusion profile is twice as wide as the profile after 1 time-unit, however, it is identical in other geometrical respects. A stretch factor can be applied to the length of the model profile to try and match the observed diffusion profile if they have the same diffusional behaviour. If boundary conditions are known, then the curve with the correct shape can be selected from the database of model diffusion profiles and scaled using the stretch factor. A stretch factor scaling law can then be applied to estimate diffusion time and the Dt product (a measure of how much material has moved). The Dt product is then transferred to a secondary worksheet which fits the Dt product from AutoDIFF to a linear cooling curve using the goal seek function in Microsoft Excel. The initial conditions in the worksheet are the same as the conditions in AutoDIFF.

AutoDIFF is available on request from Dr Dan Morgan, School of Earth and Environment, University of Leeds. The secondary worksheet was developed independently for this work and is available in the supplementary materials.

2.2.6.2 Approach 2: Explicit finite difference forward modelling

A second approach uses an explicit finite difference forward modelling program coded into Microsoft Excel using macros. Diffusion coefficients are calculated according to Dohmen and Chakraborty (2007). Unlike AutoDIFF, which uses fixed boundary conditions, this model is capable of modelling diffusion with shifting boundary conditions, making it a powerful tool to model diffusion in forsteritic-olivine relict grains. Model diffusion profiles created at different cooling rates can be compared to measured diffusion profiles to determine chondrule cooling rates.

The explicit finite difference forward modelling program was developed in conjunction with Dr Dan Morgan, School of Earth and Environment, University of Leeds. Dan Morgan provided the main code after discussing the needs of the project. Modification to the code to include customisable relict grain compositions and diffusion anisotropy were completed independently. The explicit finite difference forward modelling program is available in the supplementary materials.

2.2.6.3 Required inputs

To model diffusion profiles using either method, several different parameters must be identified. These include magmatic temperature, pressure, oxygen fugacity, the orientation of the grain relative to the measured diffusion profile to account for diffusion anisotropy, olivine composition, the olivine saturated liquidus curve for each chondrule, and crystal growth rate.

2.3 Summary

Type II chondrules containing forsteritic-olivine relict grains in thin sections of ALHA 77307 and NWA 4910 and a polished block of NWA 8276 have been identified using BSE imaging. They were further characterised using EDS mapping and point analyses. The compositions of chondrule phases were determined by EPMA. Compositional profiles across the forsteritic-olivine relict grain boundary were measured by extracting compositional information from BSE greyscale images of the grains, calibrated to EPMA measurements of the grains, using open-source software ImageJ. The orientations of the forsteritic-olivine relict grains were determined by EBSD. The data were used to calculate the angle between the crystallographic axes and the measured compositional profiles, allowing for the correction of diffusion rate because of diffusion anisotropy. Chondrule bulk compositions were calculated using a modal recombination analysis combining the proportion, density, and composition of each phase. To calculate the proportion of each phase in a chondrule, phase maps of each chondrule were drawn using open-source software Inkscape. Chondrule phases were distinguished using high-resolution BSE images and EDS element maps. Open-source software ImageJ (Schneider et al., 2012) was used to determine the relative proportion of each phase. Chondrule bulk compositions were modelled using Petrolog3 (Danyushevsky and Plechov, 2011) in order to determine chondrule liquidus temperatures and the olivine saturated liquidus curve, showing how the chondrule melt evolves during cooling and crystallisation. NanoSIMS analyses were undertaken to identify the forsteritic-olivine relict grain boundary using the behaviour of P, which is a slow diffusing element. These analyses and calculations are necessary as they are important parameters in the diffusion models.

Chapter 3
Chondrule petrography

This chapter describes the petrography of twelve chondrules from three different meteorites. Six chondrules are from ALHA 77307, three are from NWA 8276 and the final three are from NWA 4910. Ten of the twelve chondrules are type IIA porphyritic olivine chondrules, while two are type IIAB porphyritic olivine and pyroxene chondrules. Olivine is the most abundant phase in these chondrules and all twelve contain at least one forsteritic-olivine relict grain. Observed trends in olivine compositions and Fe-Mn systematics suggest the chondrules underwent closed-system fractional crystallisation and they show little evidence of open system behaviour.

3.1 Overview of chondrule petrography

3.1.1 ALHA 77307

The six studied chondrules in the CO chondrite ALHA 77307 are type II porphyritic olivine chondrules, however, chondrule Al-5 appears to be a chondrule fragment. They generally show rounded shapes, but most are not circular (e.g. Al-4, see Figure 3.2b). The chondrules range in maximum diameter from 110 to 490 µm. The chondrules are composed of euhedral or fragmented olivine phenocrysts (Wasson and Rubin, 2003) which range in length from several micrometres to 100 µm. These phenocrysts are set in a mesostasis composed of glass, microcrystallites and alteration products such as phyllosilicates. The chondrules also contain minor amounts of chromite, sulfides and metal. Chondrule Al-1 also contains a minor amount of pyroxene. Figure 3.1 shows BSE images and phase maps of chondrules Al-1 to Al-3 and Figure 3.2 shows BSE images and phase maps of chondrules Al-4 to Al-6. Table 3.1 shows a summary of key chondrule properties, andTable 3.2 shows the proportion of phases present in each of the studied chondrules determined from chondrule phase maps.

Table 3.1 – Summary of chondrule properties.

Chondrule	Texture	Max diameter (µm)	Mean Fo (mole %)	Mean molar Fe/Mn	Number of forsteritic-olivine relict grains	Full chondrule classification
Al-1	PO	280	65.6	99	2	Type IIA PO
Al-2	PO	320	69.3	93	2	Type IIA PO
Al-3	PO	130	54.1	117	1	Type IIA PO
Al-4	PO	490	66.4	112	2	Type IIA PO
Al-5	PO	110	59.0	101	3	Type IIA PO
Al-6	PO	190	69.0	99	2	Type IIA PO
N8-1	PO	340	74.6	58	2	Type IIA PO
N8-2	PO	480	72.7	54	2	Type IIA PO
N8-3	PO	270	71.2	64	3	Type IIA PO
N4-1	POP	320	80.5	33	1	Type IIAB POP
N4-2	PO	230	70.0	59	1	Type IIA PO
N4-3	POP	450	89.0	26	1	Type IIAB POP

3.1.2 NWA 8276

The three studied chondrules in the L chondrite NWA 8276 are type II porphyritic olivine chondrules. Like those in ALHA 77307, they show rounded shapes but are not circular. The chondrules range in maximum diameter from 270 to 480 µm. The chondrules are

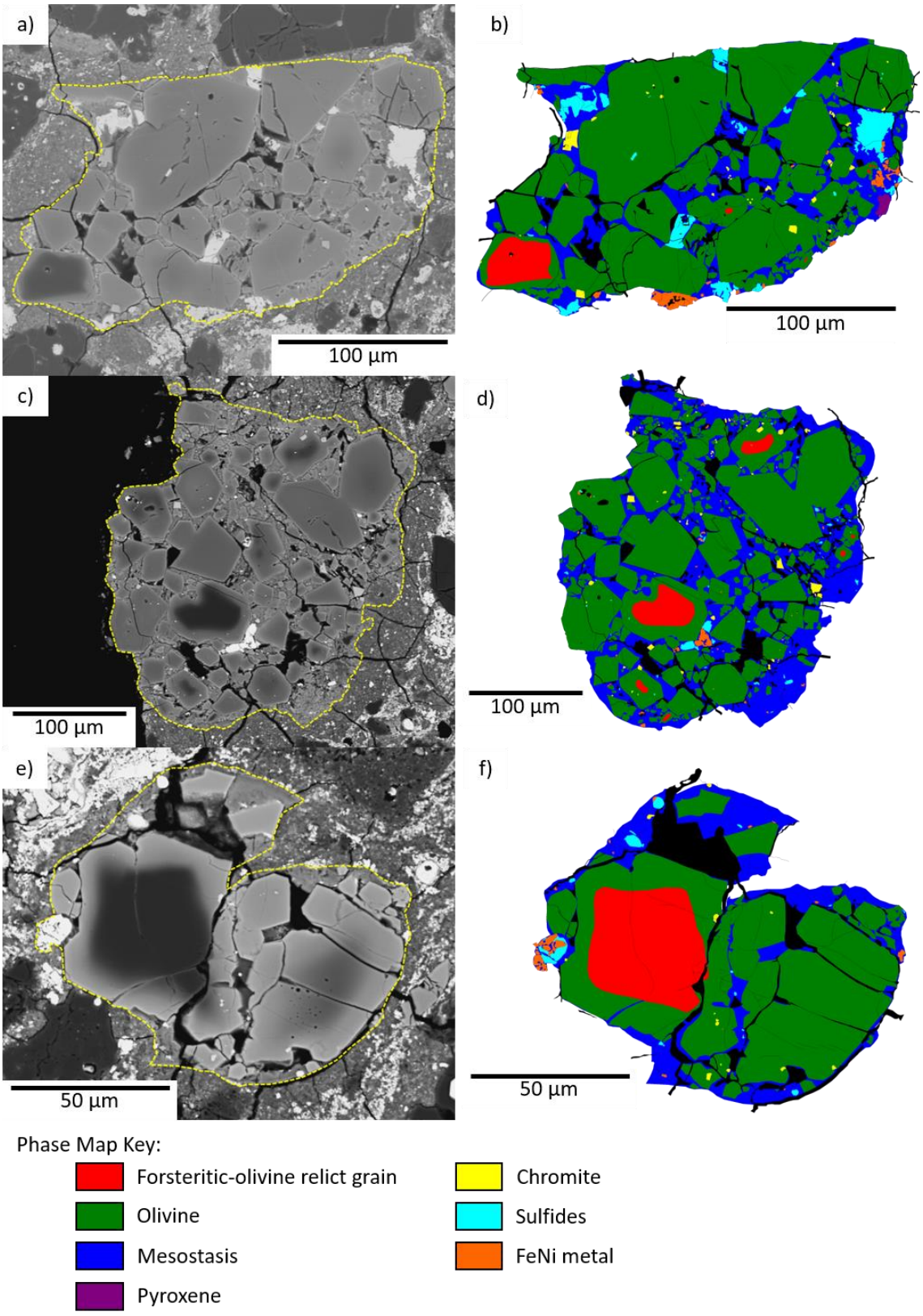

Figure 3.1 – a) BSE image of chondrule Al-1; b) phase map of chondrule Al-1; c) BSE image of chondrule Al-2; d) phase map of chondrule Al-2; e) BSE image of chondrule Al-3; f) phase map of chondrule Al-3. In phase maps, black areas represent cracks and holes.

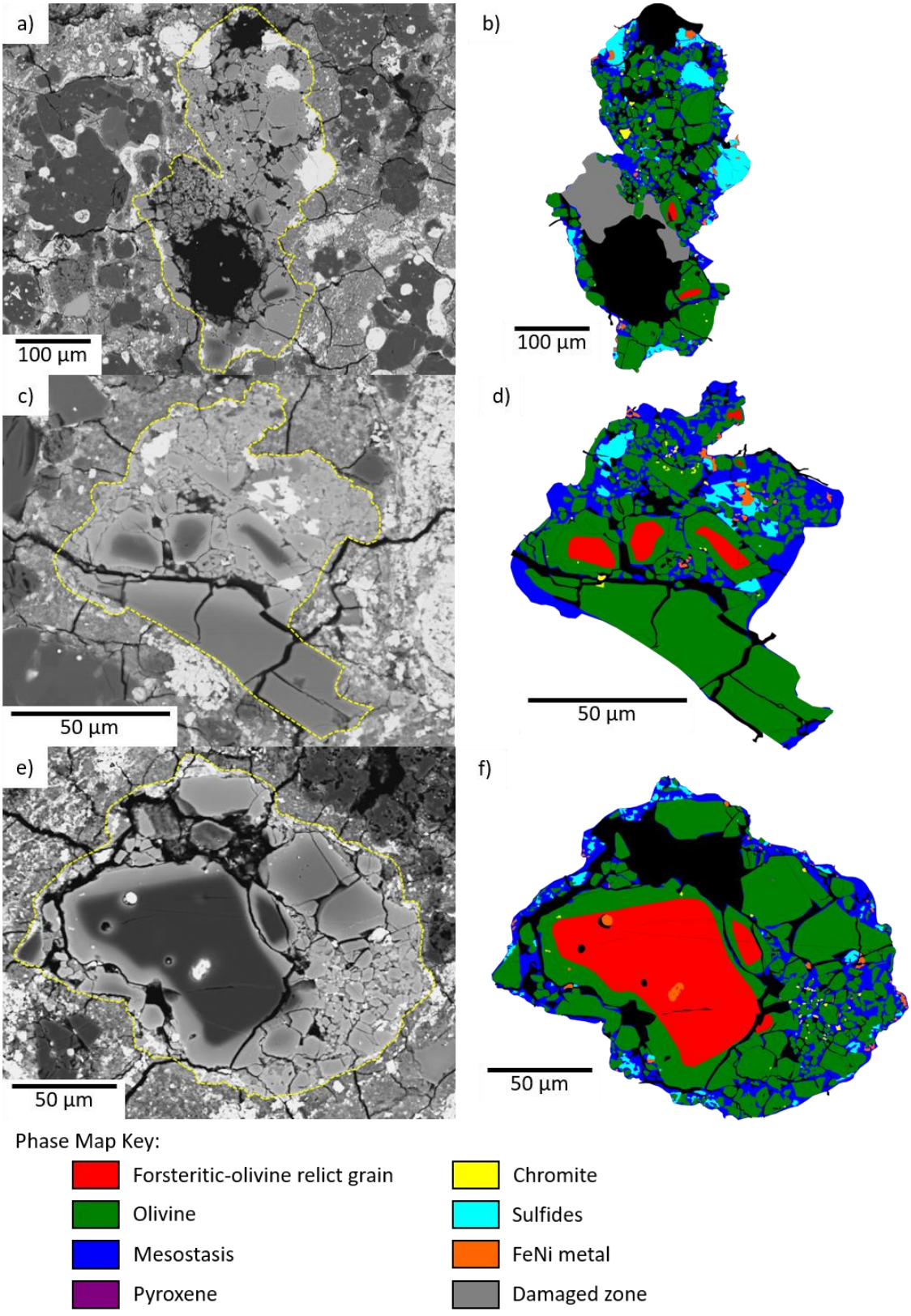

Figure 3.2 – a) BSE image of chondrule Al-4; b) phase map of chondrule Al-4; c) BSE image of chondrule Al-5; d) phase map of chondrule Al-5; e) BSE image of chondrule Al-6; f) phase map of chondrule Al-6. Black areas represent cracks and holes. The damaged zone represents an area that has been damaged by plucking during polishing.

Table 3.2 – Proportion of phases in the studied chondrules extracted from chondrule phase maps. Cracks, holes, and other pore spaces were ignored in the calculation. The main source of error is the accuracy of the chondrule phase maps. Other sources of error include the resolution of BSE images and element maps. Values for normal olivine do not include forsteritic-olivine

Chondrule	Normal Olivine	Pyroxene	Mesostasis	Chromite	Sulfides	Metal	Forsteritic-olivine	Weathering products
Al-1	73.4	0.3	17.3	0.7	4.1	1.1	3.1	0.0
Al-2	64.4	0.0	30.8	0.7	0.5	0.5	3.1	0.0
Al-3	60.9	0.0	19.8	0.2	1.0	0.8	17.3	0.0
Al-4	61.3	0.0	23.4	0.9	12.0	1.4	1.0	0.0
Al-5	64.6	0.0	24.9	0.4	3.8	1.0	5.3	0.0
Al-6	52.9	0.0	16.8	0.3	2.1	0.6	27.3	0.0
N8-1	66.0	0.0	30.1	0.3	0.0	0.0	3.6	0.0
N8-2	67.8	0.0	26.6	0.5	0.2	0.0	4.9	0.0
N8-3	51.3	0.0	36.4	0.9	0.0	0.0	3.7	7.7
N4-1	54.5	21.9	12.7	0.2	1.0	0.2	7.7	1.8
N4-2	64.9	1.9	27.0	0.8	2.3	0.0	3.1	0.0
N4-3	52.1	23.8	15.9	0.0	3.5	0.4	2.1	2.2

composed of euhedral olivine phenocrysts set in a glassy mesostasis. All three chondrules also contain a minor amount of chromite. Chondrule N8-2 contains a small amount of sulfide, while chondrule N8-3 contains weathering products in the form of veins running through mesostasis and olivine phenocrysts. Fe,Ni metal is not found in any of these chondrules. Figure 3.3 shows BSE images and phase maps of the studied chondrules. Table 3.1 shows a summary of key chondrule properties, and Table 3.2 gives the proportion of phases present in each of the studied chondrules determined from chondrule phase maps.

3.1.3 NWA 4910

Of the three studied chondrules in the LL chondrites NWA 4910, two are porphyritic olivine and pyroxene chondrules and one is a porphyritic olivine chondrule. Chondrules N4-1 and N4-3 are rounded but show irregular shapes while chondrule N4-2 is very round. The chondrules range in max diameter from 230 to 450 µm. The chondrules are composed of phenocrysts of olivine, or olivine and pyroxene set in glassy mesostasis containing crystallites. The chondrules may also contain minor amounts of chromite, sulfides, metal and weathering products. Figure 3.4 shows BSE images and phase maps of the studied chondrules. Table 3.1 contains a summary of key chondrule properties, and Table 3.2 gives the proportion of phases present in each of the studied chondrules determined from chondrule phase maps.

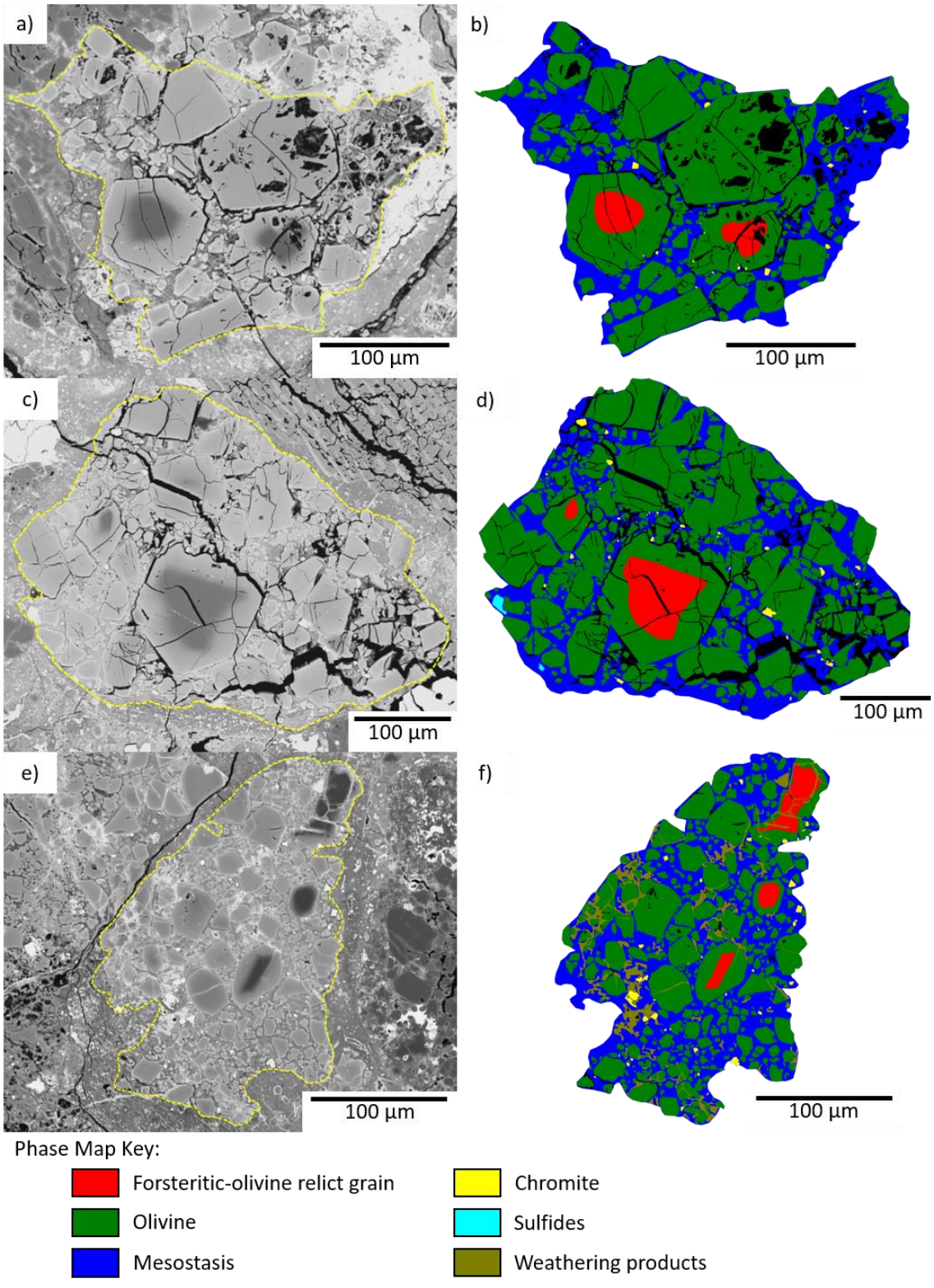

Figure 3.3 – a) BSE image of chondrule N8-1; b) phase map of chondrule N8-1; c) BSE image of chondrule N8-2; d) phase map of chondrule N8-2; e) BSE image of chondrule N8-3; f) phase map of chondrule N8-3. Black areas represent cracks and holes.

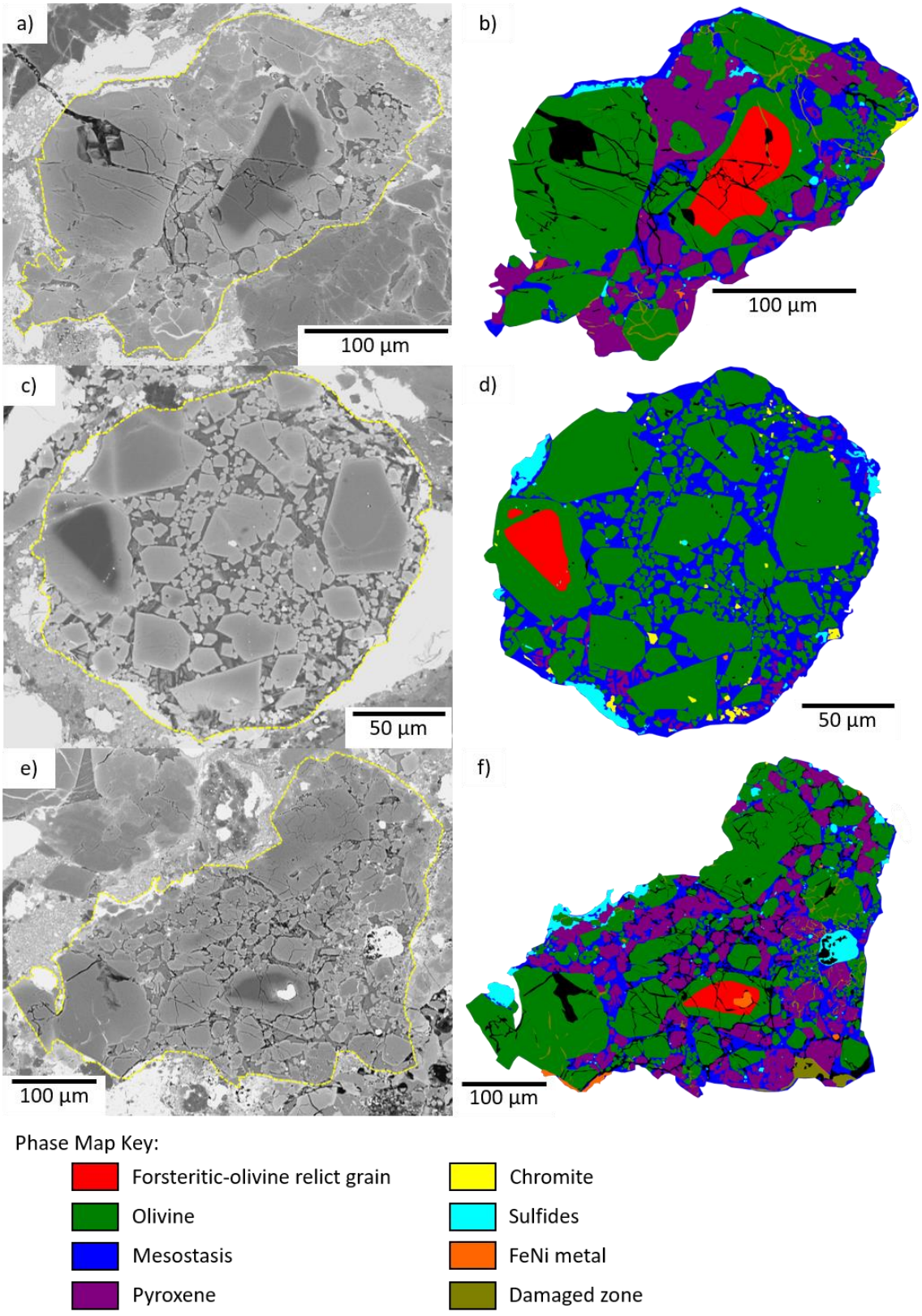

Figure 3.4 – a) BSE image of chondrule N4-1; b) phase map of chondrule N4-1; c) BSE image of chondrule N4-2; d) phase map of chondrule N4-2; e) BSE image of chondrule N4-3; f) phase map of chondrule N4-3. Black areas represent cracks and holes.

3.2 Olivine

Olivine appears in all the studied chondrules and is the most abundant phase. In this section, olivine refers to relatively FeO-rich olivine and does not include the forsteritic-olivine relict grains. Table 3.3 summarises the olivine analyses, and the full results are available in Appendix B.

In the chondrules in ALHA 77307, olivine grains generally appear euhedral, however, some are clearly fragmented (e.g. chondrules Al-3 and Al-6, Figure 3.1c and Figure 3.2c). Olivine phenocrysts range in length from several micrometres to 100 µm. Many of the olivine phenocrysts display normal igneous zoning which can be seen clearly in BSE images (e.g. Figure 3.5a). In the BSE images, these crystals appear darker in the centre and lighten towards the rims, indicating a progression to more FeO-rich compositions towards the crystal edge. Overall, olivine crystals are very FeO-rich with mean compositions between 27 and 38 wt % FeO and range in forsterite composition from Fo_{53} to Fo_{85}. These analyses are not from a single crystal but include analyses covering a range of positions within phenocrysts and a range of phenocryst sizes. The range in composition suggests zoning is pronounced. Smaller olivine crystals appear to have more FeO-rich cores than larger crystals. This could be caused by off-centre sectioning of larger olivine crystals, or later nucleation of these smaller crystals (Jones, 1990). Olivine phenocrysts in the chondrules within ALHA 77307 commonly show inclusions of chromite, Fe,Ni metal, and sulfides.

The olivine phenocrysts within all the studied chondrules in ALHA 77307 show wide-ranging compositions. All six chondrules show increasing CaO and MnO with increasing FeO in their olivine phenocrysts (see Figure 3.6 to Figure 3.11, compiled in Figure 3.18). There is little correlation between Cr_2O_3 and FeO, but if present, there is a slight decrease in Cr_2O_3 abundance with increasing FeO (see Figure 3.6 to Figure 3.11, compiled in Figure 3.18). Chondrules Al-1, Al-2, Al-4, and Al-6 show similar ranges in olivine compositions with mean compositions of Fo_{59} to Fo_{69}. Al-3 has the most FeO-rich olivine compositions, with values up to 46 wt % FeO (Fo_{42} to Fo_{78}; mean Fo_{54}). Chondrule Al-5 is the smallest chondrule with a maximum diameter of 110 µm. Many of the phenocrysts within this chondrule are very small, several µm, and it was difficult to obtain analyses with acceptable totals and/or stochiometry. As a result of this, only four analyses were considered suitable for reporting. Olivine compositions are shown in Table 3.3.

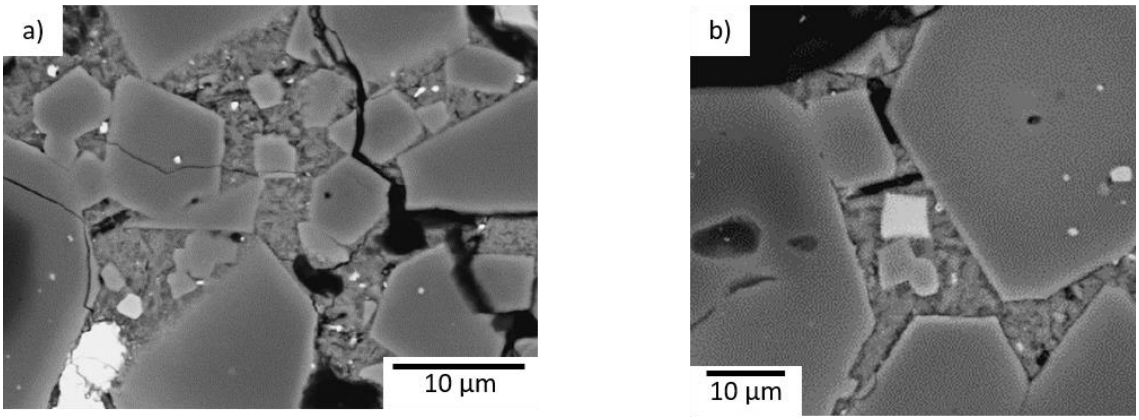

Figure 3.5 – BSE images of representative chondrule textures in ALHA 77307. Both images are from Al-2: a) normally zoned olivine crystals set in mesostasis; b) a square chromite crystal in the centre surrounded by mesostasis and normally zoned olivine crystals.

In the chondrules in NWA 8276, olivine phenocrysts range in length from several micrometres to 120 µm, a similar range to the phenocrysts in the studied chondrules in ALHA 77307, and they are generally euhedral or fragmented. Phenocrysts appear normally zoned with darker centres and lighter rims in BSE images. The composition of olivine phenocrysts is generally FeO-rich with mean FeO values ranging from 19 to 28 wt % FeO and Fo values ranging from Fo_{68} to Fo_{80}. These values are less FeO-rich than the studied chondrules in ALHA 77307. Olivine phenocrysts may contain inclusion of chromite; however, they are not as abundant as in olivine phenocrysts in the studied chondrules in ALHA 77307.

Olivine compositions within a chondrule vary significantly (see Figure 3.12 to Figure 3.14, compiled in Figure 3.19), however, the distribution of values is reasonably consistent between chondrules and they plot in similar areas on the graphs in Figure 3.19. Like the olivine in chondrules in ALHA 77307, the olivine in chondrules in NWA 8276 show CaO and MnO values increasing with FeO. Also visible in the olivine in chondrules from NWA 8276 is a significant decrease in Cr_2O_3 with increasing FeO values, which is less obvious in the olivine in chondrules in ALHA 77307. Olivine compositions are shown in Table 3.3.

For chondrules in NWA 4910, olivine remains the most dominant phase in all the studied chondrules, even with the two porphyritic olivine pyroxene chondrules (N4-1 and N4-3). In chondrules N4-1 and N4-3, olivine phenocrysts are present as subhedral to euhedral crystals which are often fractured. In chondrule N4-2, olivine phenocrysts appear much more euhedral. Olivine phenocrysts range in length from several micrometres to 140 µm, similar to the ranges reported for chondrules in ALHA 77307 and NWA 8276. Olivine

Table 3.3 – Mean, minimum and maximum olivine compositions from the 12 analysed chondrules in ALHA 77307, NWA 8276 and NWA 4910. Major and minor elements in wt %, Fo in mol %, N is number of analyses. For each oxide, the mean value is derived from the oxide content from all olivine analyses in that chondrule. Mean total refers to the sum of the mean of the oxides. Min and Max refer to the minimum and maximum values obtained across the analyses for the chondrule, however, the maximum and minimum values across different oxides are not necessarily from the same analyses. Min and Max totals refer to the analysis with the minimum or maximum value. These values do not include forsteritic-olivine relict grains.

Chondrule	Na_2O	MgO	Al_2O_3	SiO_2	P_2O_5	K_2O	CaO	TiO_2	Cr_2O_3	MnO	FeO	NiO	Total	Fo	N
Al-1															
Mean	<0.05	32.4	0.08	37.1	<0.09	<0.02	0.41	<0.04	0.31	0.30	30.3	0.08	101.1	65.6	19
Min	<0.05	28.8	<0.05	36.1	<0.09	<0.02	0.22	<0.04	0.17	0.25	22.2	<0.06	100.5	60.8	
Max	0.33	39.2	0.76	38.9	0.26	<0.02	0.65	0.04	0.91	0.36	33.6	0.28	101.8	75.9	
Al-2															
Mean	<0.05	34.7	<0.05	37.3	0.10	<0.02	0.34	<0.04	0.41	0.29	27.3	0.09	100.6	69.3	24
Min	<0.05	31.2	<0.05	36.6	<0.09	<0.02	0.25	<0.04	0.29	0.23	23.5	<0.06	98.8	63.0	
Max	<0.05	37.3	0.10	38.2	0.25	<0.02	0.47	0.07	0.67	0.35	32.6	0.36	101.8	73.8	
Al-3															
Mean	<0.05	26.0	<0.05	34.3	<0.09	<0.02	0.28	<0.04	0.31	0.33	38.0	0.15	99.5	54.1	18
Min	<0.05	18.8	<0.05	31.8	<0.09	<0.02	0.18	<0.04	0.18	0.16	20.5	0.07	98.4	41.9	
Max	0.05	41.1	<0.05	38.2	0.30	<0.02	0.51	0.04	0.45	0.47	46.4	0.44	100.8	78.1	
Al-4															
Mean	<0.05	32.9	<0.05	37.3	<0.09	<0.02	0.39	<0.04	0.28	0.26	29.5	0.08	100.8	66.4	15
Min	<0.05	30.0	<0.05	36.6	<0.09	<0.02	0.18	<0.04	0.18	0.12	14.7	<0.06	99.6	62.1	
Max	0.05	45.7	0.18	40.5	0.14	<0.02	0.52	0.05	0.69	0.29	33.2	0.20	102.0	84.8	
Al-5															
Mean	0.11	28.3	0.45	35.5	0.29	<0.02	0.83	0.04	0.13	0.34	34.5	0.22	100.8	59.0	4
Min	<0.05	24.3	<0.05	34.2	<0.09	<0.02	0.21	<0.04	0.05	0.24	23.0	0.06	100.4	52.7	
Max	0.17	38.3	0.87	38.4	0.45	<0.02	1.26	0.09	0.20	0.39	38.9	0.31	101.0	74.8	
Al-6															
Mean	<0.05	34.5	0.05	37.7	0.10	<0.02	0.38	<0.04	0.44	0.27	27.4	0.06	100.9	69.0	9
Min	<0.05	28.0	<0.05	36.4	<0.09	<0.02	0.24	<0.04	<0.04	0.20	19.6	<0.06	100.3	59.0	
Max	<0.05	40.9	0.17	39.0	0.18	<0.02	0.61	0.06	0.91	0.36	34.7	0.16	101.5	78.8	
N8-1															
Mean	<0.05	38.0	<0.05	36.8	0.10	<0.02	0.24	<0.04	0.54	0.39	23.0	0.06	99.1	74.6	12
Min	<0.05	35.6	<0.05	35.0	<0.09	<0.02	0.18	<0.04	0.44	0.35	19.8	<0.06	98.1	71.6	
Max	0.07	40.7	<0.05	38.9	0.24	<0.02	0.30	<0.04	0.60	0.43	25.3	0.30	101.1	78.6	
N8-2															
Mean	<0.05	36.7	<0.05	37.5	0.12	<0.02	0.21	<0.04	0.45	0.45	24.6	<0.06	100.1	72.7	19
Min	<0.05	34.5	<0.05	36.1	<0.09	<0.02	0.13	<0.04	0.26	0.33	18.6	<0.06	98.9	68.9	
Max	0.07	41.2	<0.05	38.7	0.38	<0.02	0.28	<0.04	0.59	0.51	27.8	0.09	101.3	79.8	
N8-3															
Mean	<0.05	35.7	<0.05	37.4	0.13	<0.02	0.28	<0.04	0.41	0.39	25.7	<0.06	100.2	71.2	19
Min	<0.05	33.3	<0.05	36.8	<0.09	<0.02	0.19	<0.04	0.23	0.33	21.0	<0.06	98.9	67.8	
Max	0.05	40.2	0.11	38.5	0.29	<0.02	0.40	0.04	0.79	0.45	28.4	0.11	100.9	77.3	
N4-1															
Mean	<0.05	41.7	0.06	39.2	<0.09	<0.02	0.23	<0.04	0.51	0.53	17.7	0.16	100.2	80.5	21
Min	<0.05	38.1	<0.05	38.4	<0.09	<0.02	0.09	<0.04	0.34	0.29	9.66	<0.06	99.3	76.5	
Max	0.13	49.1	0.32	41.1	0.17	0.04	0.40	0.06	0.67	0.70	20.8	0.85	101.1	90.0	
N4-2															
Mean	<0.05	35.0	0.05	37.8	0.15	<0.02	0.29	<0.04	0.40	0.44	25.9	0.20	100.3	70.0	38
Min	<0.05	26.3	<0.05	35.4	<0.09	<0.02	0.15	<0.04	0.23	0.29	16.7	<0.06	98.2	56.0	
Max	0.14	42.3	0.53	40.0	0.41	<0.02	0.48	0.05	0.51	0.64	36.9	0.92	101.7	81.9	
N4-3															
Mean	<0.05	48.6	<0.05	40.3	<0.09	<0.02	0.16	<0.04	0.52	0.41	10.7	0.07	100.9	89.0	16
Min	<0.05	46.4	<0.05	39.6	<0.09	<0.02	0.10	<0.04	0.28	0.28	8.08	<0.06	100.0	86.6	
Max	<0.05	50.9	0.17	41.1	<0.09	<0.02	0.28	0.09	0.64	0.49	13.0	0.27	101.6	91.8	

phenocrysts appear normally zoned, showing darker cores and lighter rims. Average olivine compositions across the three chondrules are quite different, ranging from 10 to 25 wt % FeO. Olivine phenocrysts from chondrules N4-1 and N4-3 have significantly lower FeO contents than olivine phenocrysts from chondrules in NWA 8276 and ALHA 77307, whereas the values from chondrule N4-2 are much more similar to those in chondrules from NWA

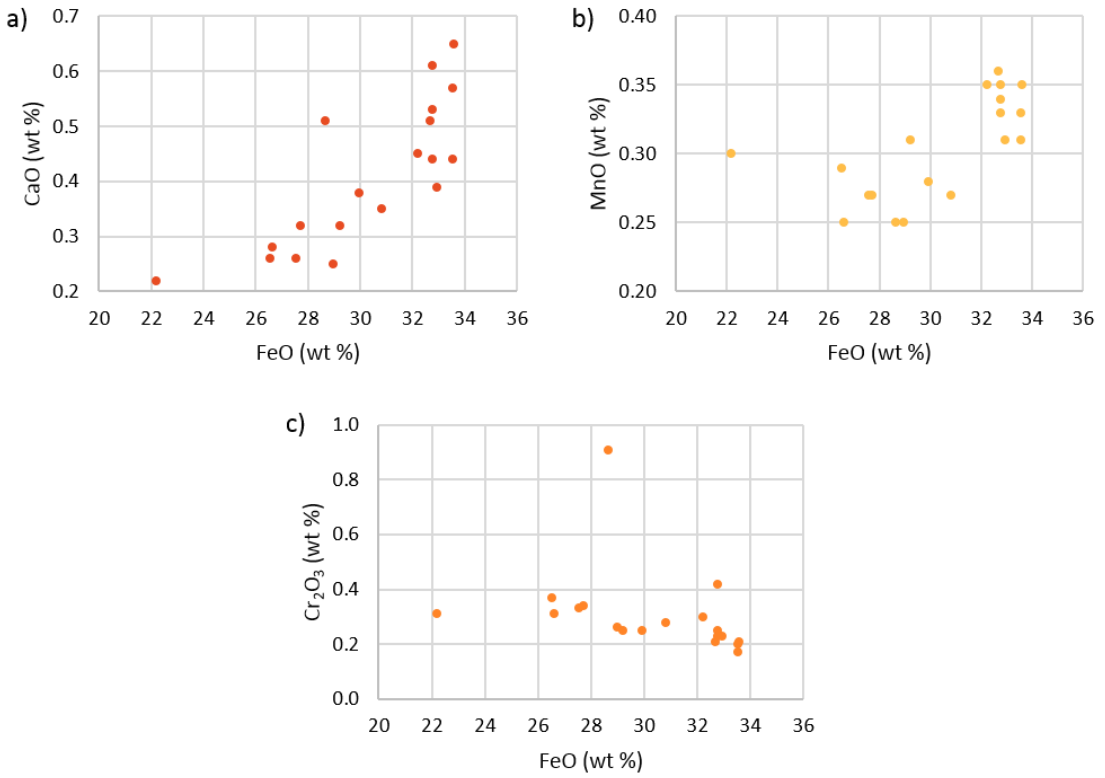

Figure 3.6 – Oxides vs FeO for olivine phenocrysts in chondrule Al-1: a) CaO vs FeO; b) MnO vs FeO; c) Cr_2O_3 vs FeO. Points represent individual EPMA analyses.

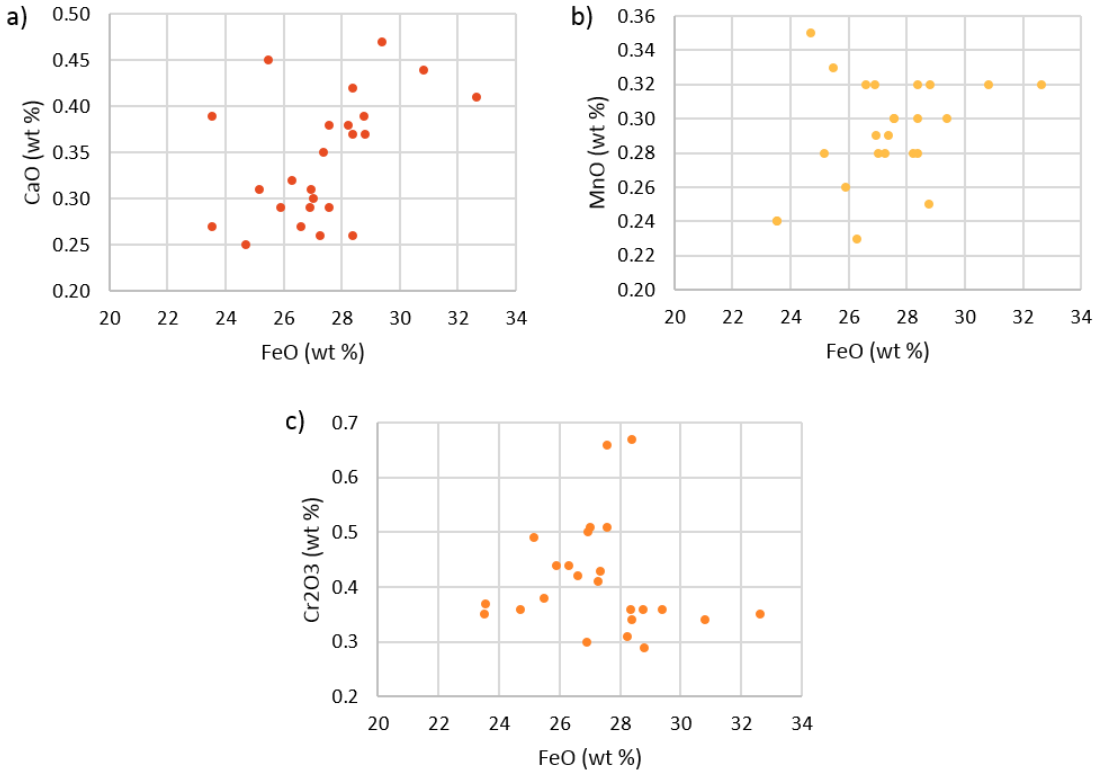

Figure 3.7 – Oxides vs FeO for olivine phenocrysts in chondrule Al-2: a) CaO vs FeO; b) MnO vs FeO; c) Cr_2O_3 vs FeO. Points represent individual EPMA analyses.

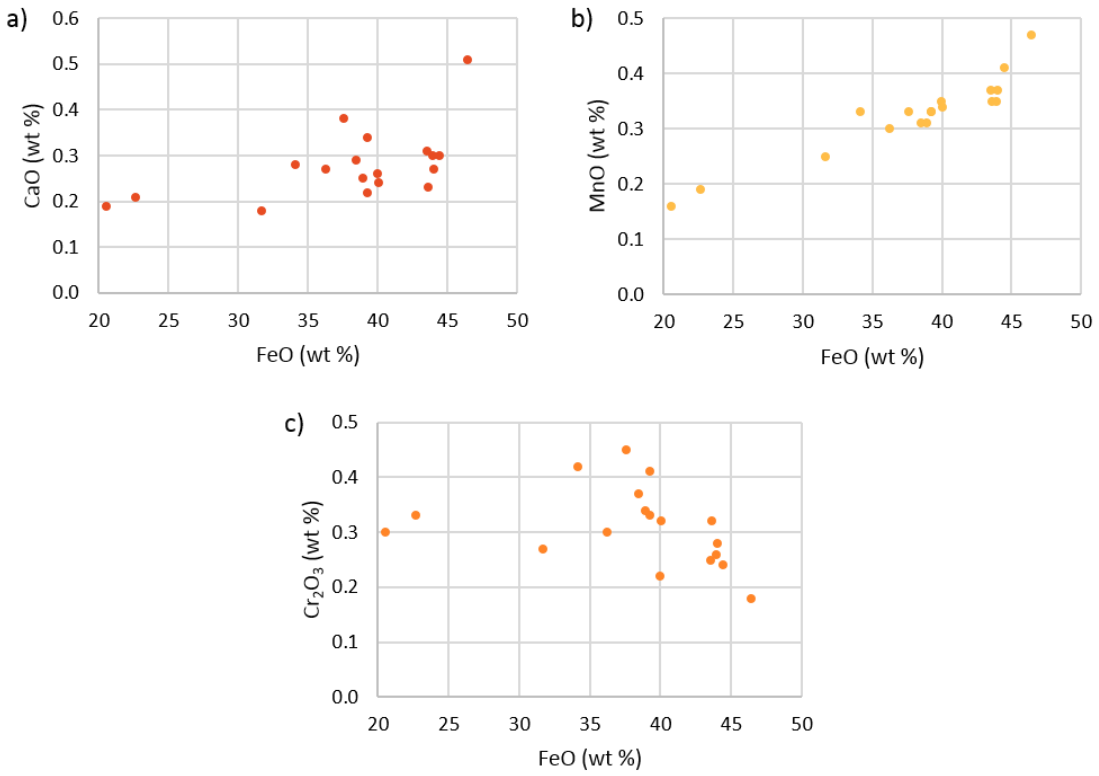

Figure 3.8 – Oxides vs FeO for olivine phenocrysts in chondrule Al-3: a) CaO vs FeO; b) MnO vs FeO; c) Cr_2O_3 vs FeO. Points represent individual EPMA analyses.

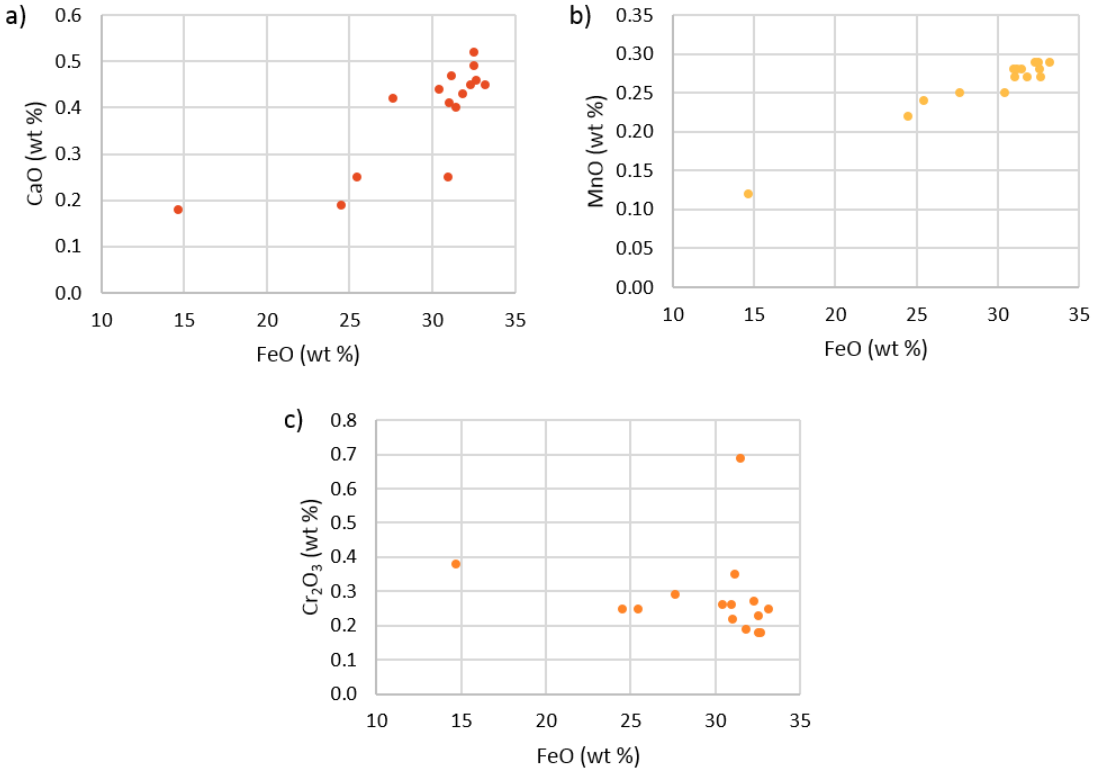

Figure 3.9 – Oxides vs FeO for olivine phenocrysts in chondrule Al-4: a) CaO vs FeO; b) MnO vs FeO; c) Cr_2O_3 vs FeO. Points represent individual EPMA analyses.

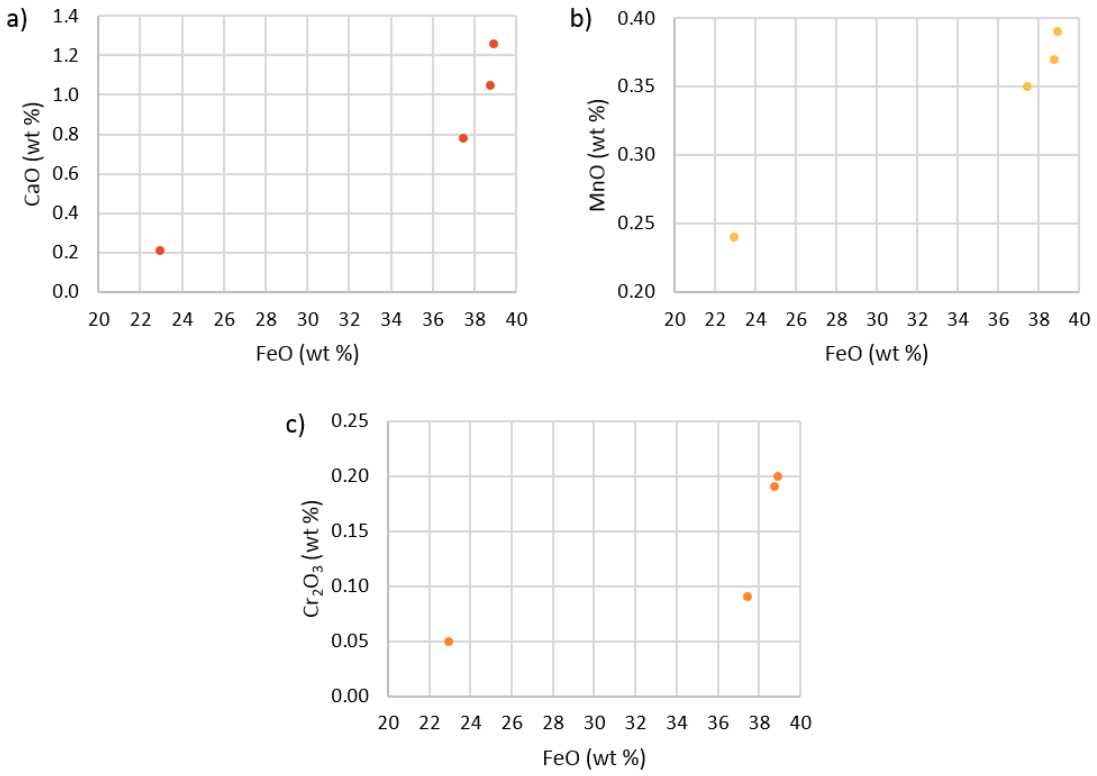

Figure 3.10 – Oxides vs FeO for olivine phenocrysts in chondrule Al-5: a) CaO vs FeO; b) MnO vs FeO; c) Cr_2O_3 vs FeO. Points represent individual EPMA analyses.

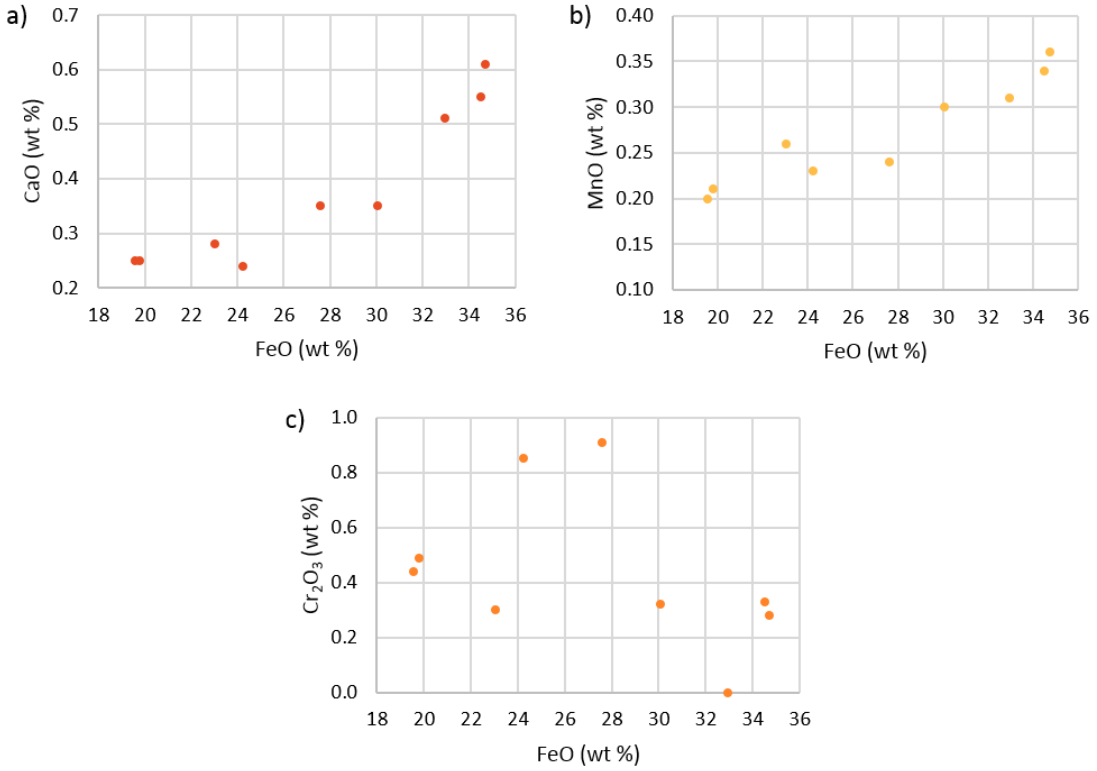

Figure 3.11 – Oxides vs FeO for olivine phenocrysts in chondrule Al-6: a) CaO vs FeO; b) MnO vs FeO; c) Cr_2O_3 vs FeO. Points represent individual EPMA analyses.

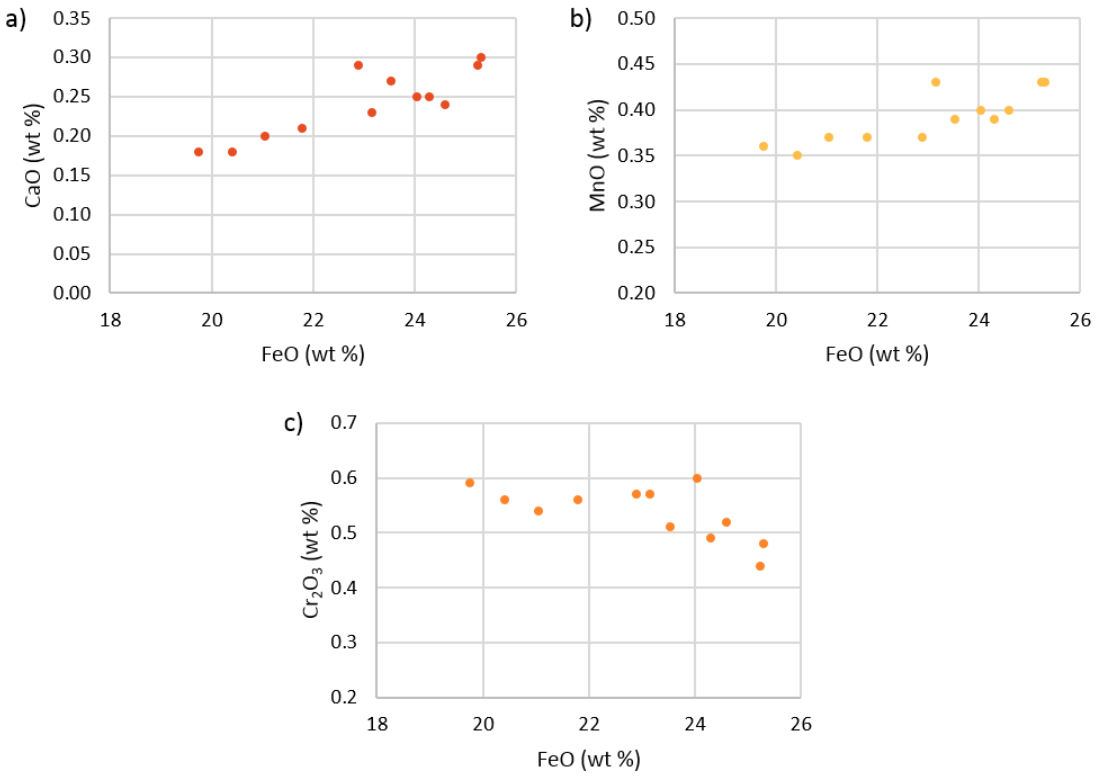

Figure 3.12 – Oxides vs FeO for olivine phenocrysts in chondrule N8-1: a) CaO vs FeO; b) MnO vs FeO; c) Cr_2O_3 vs FeO. Points represent individual EPMA analyses.

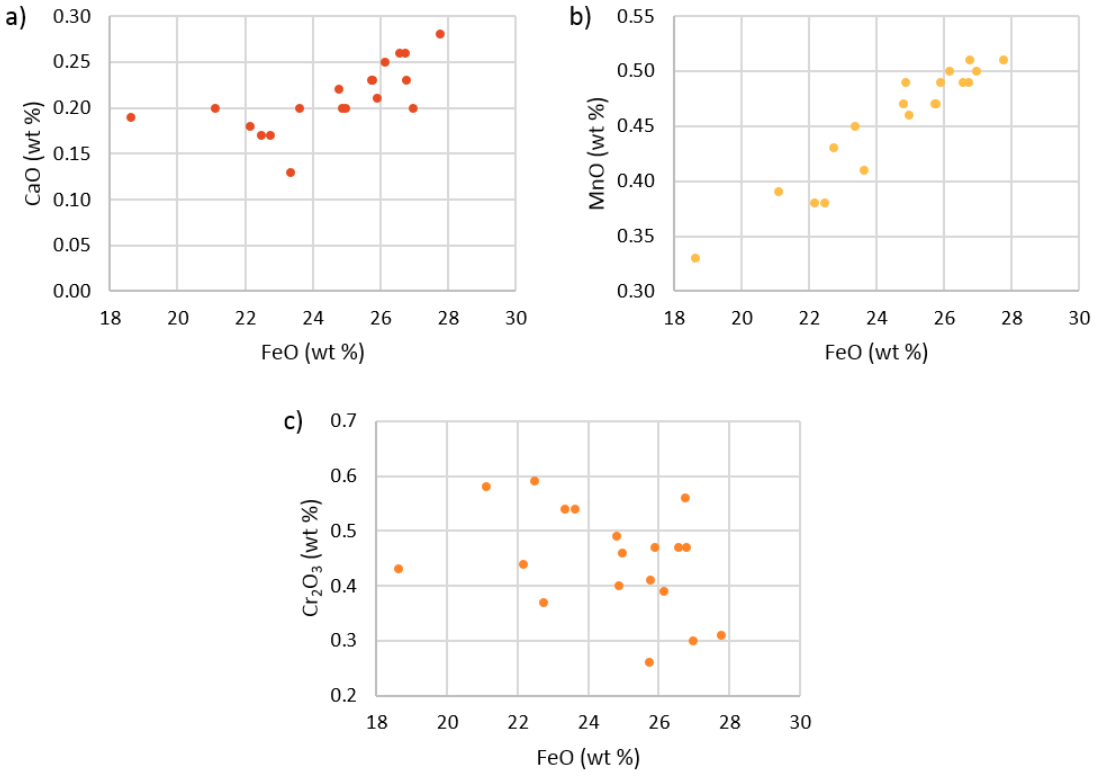

Figure 3.13 – Oxides vs FeO for olivine phenocrysts in chondrule N8-2: a) CaO vs FeO; b) MnO vs FeO; c) Cr_2O_3 vs FeO. Points represent individual EPMA analyses.

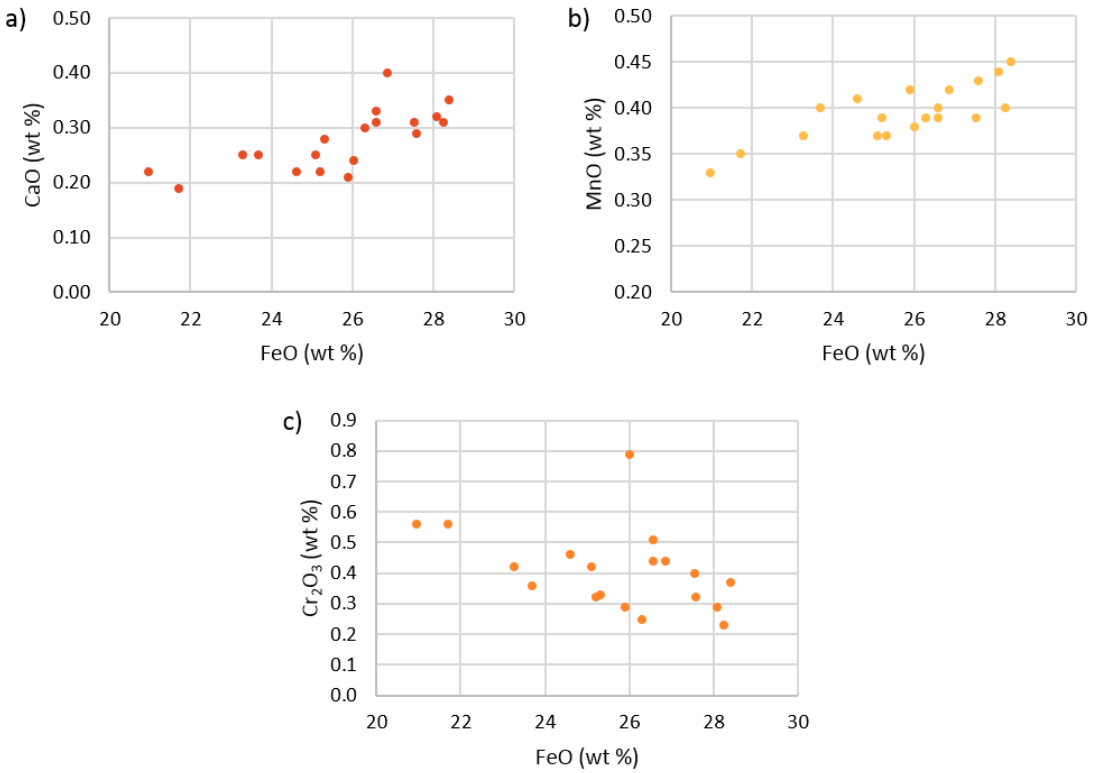

Figure 3.14 – Oxides vs FeO for olivine phenocrysts in chondrule N8-3: a) CaO vs FeO; b) MnO vs FeO; c) Cr_2O_3 vs FeO. Points represent individual EPMA analyses.

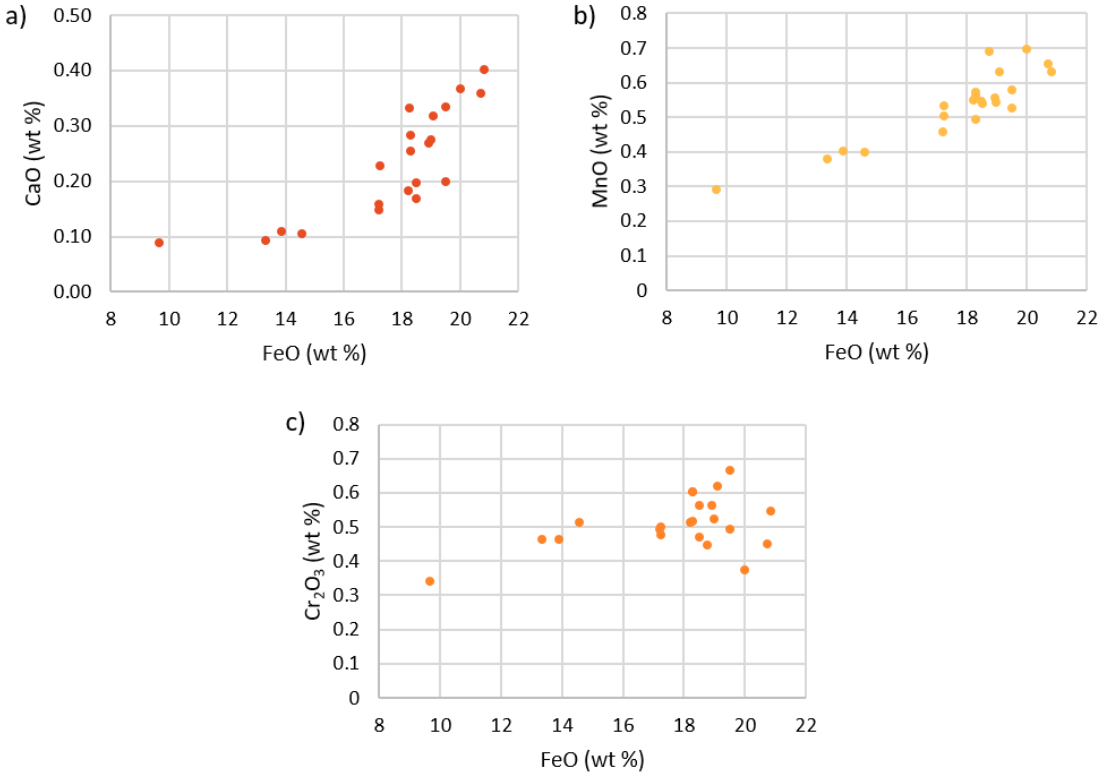

Figure 3.15 – Oxides vs FeO for olivine phenocrysts in chondrule N4-1: a) CaO vs FeO; b) MnO vs FeO; c) Cr_2O_3 vs FeO. Points represent individual EPMA analyses.

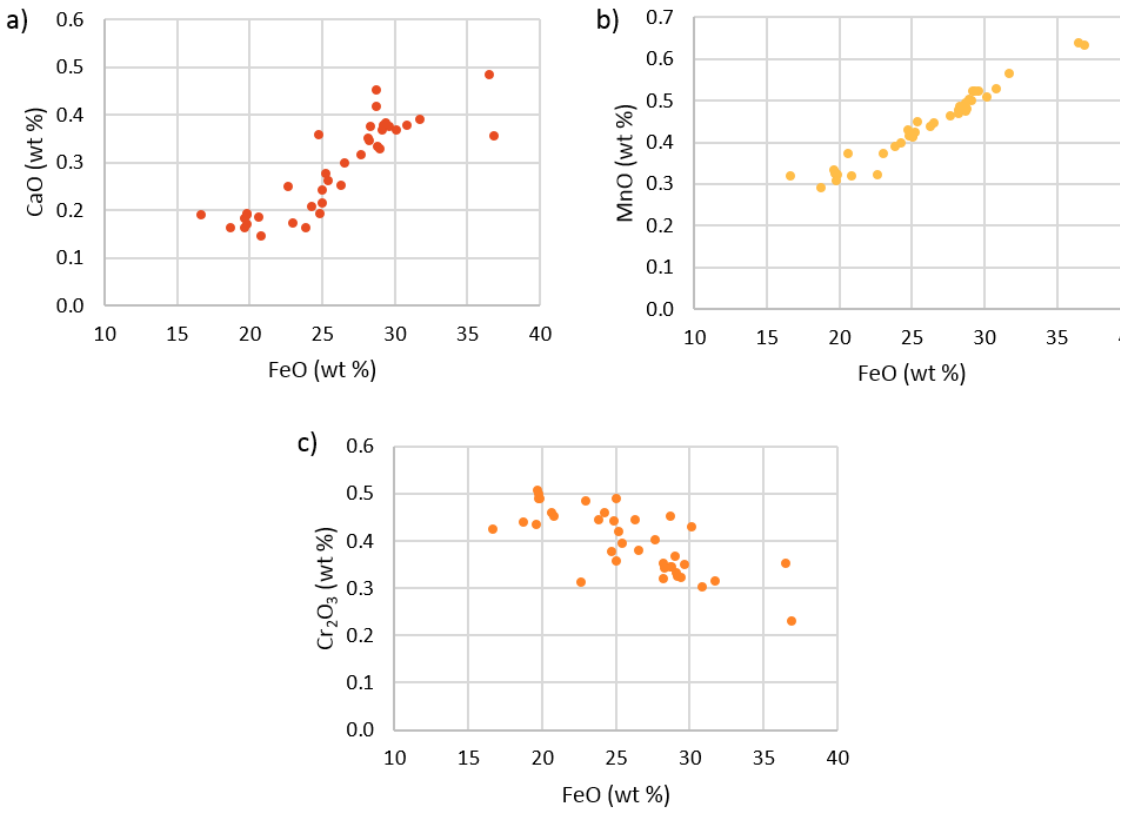

Figure 3.16 – Oxides vs FeO for olivine phenocrysts in chondrule N4-2: a) CaO vs FeO; b) MnO vs FeO; c) Cr_2O_3 vs FeO. Points represent individual EPMA analyses.

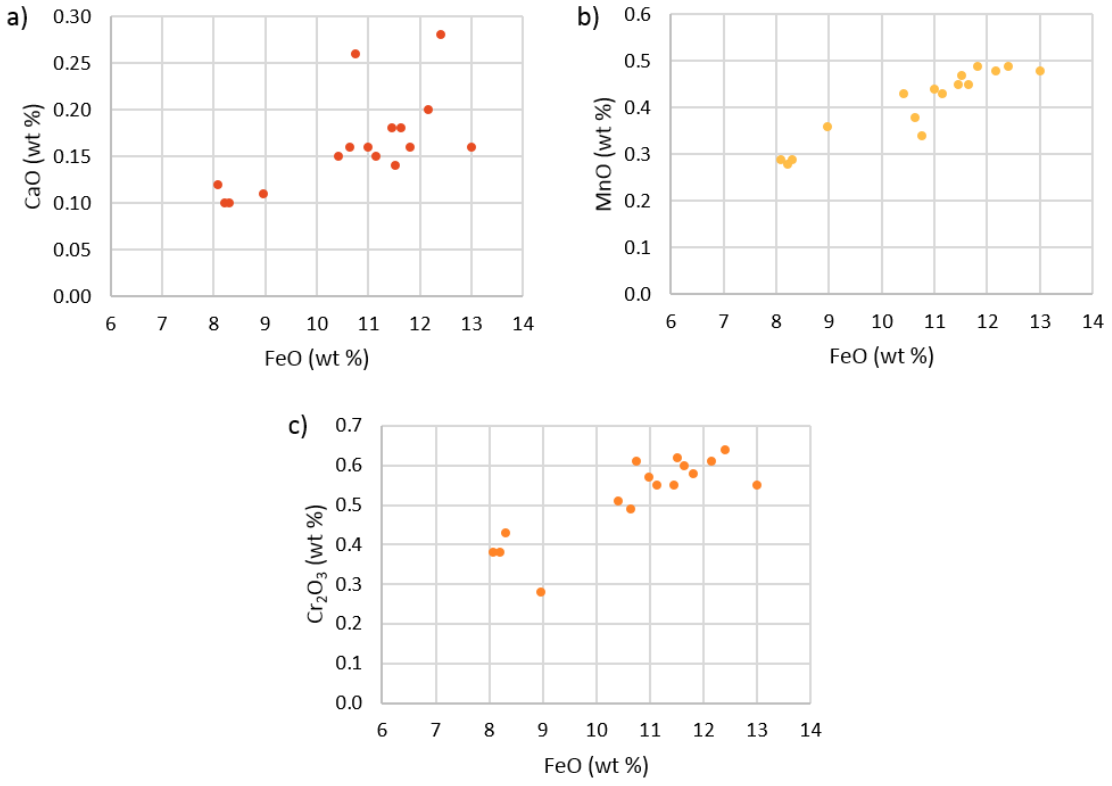

Figure 3.17 – Oxides vs FeO for olivine phenocrysts in chondrule N4-3: a) CaO vs FeO; b) MnO vs FeO; c) Cr_2O_3 vs FeO. Points represent individual EPMA analyses.

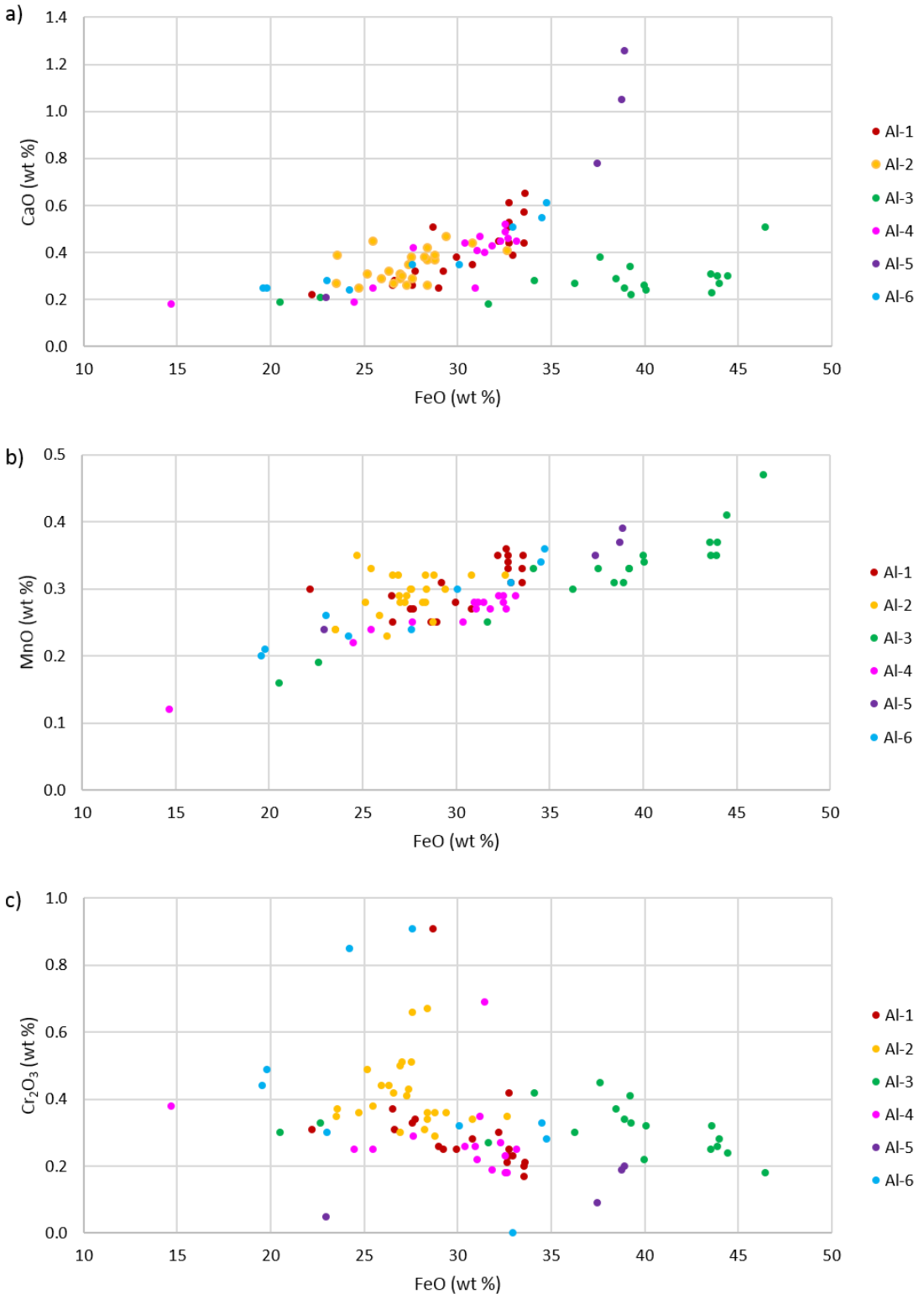

Figure 3.18 – Oxides vs FeO for olivine phenocrysts in all chondrules in ALHA 77307: a) CaO vs FeO; b) MnO vs FeO; c) Cr_2O_3 vs FeO. Points represent individual EPMA analyses.

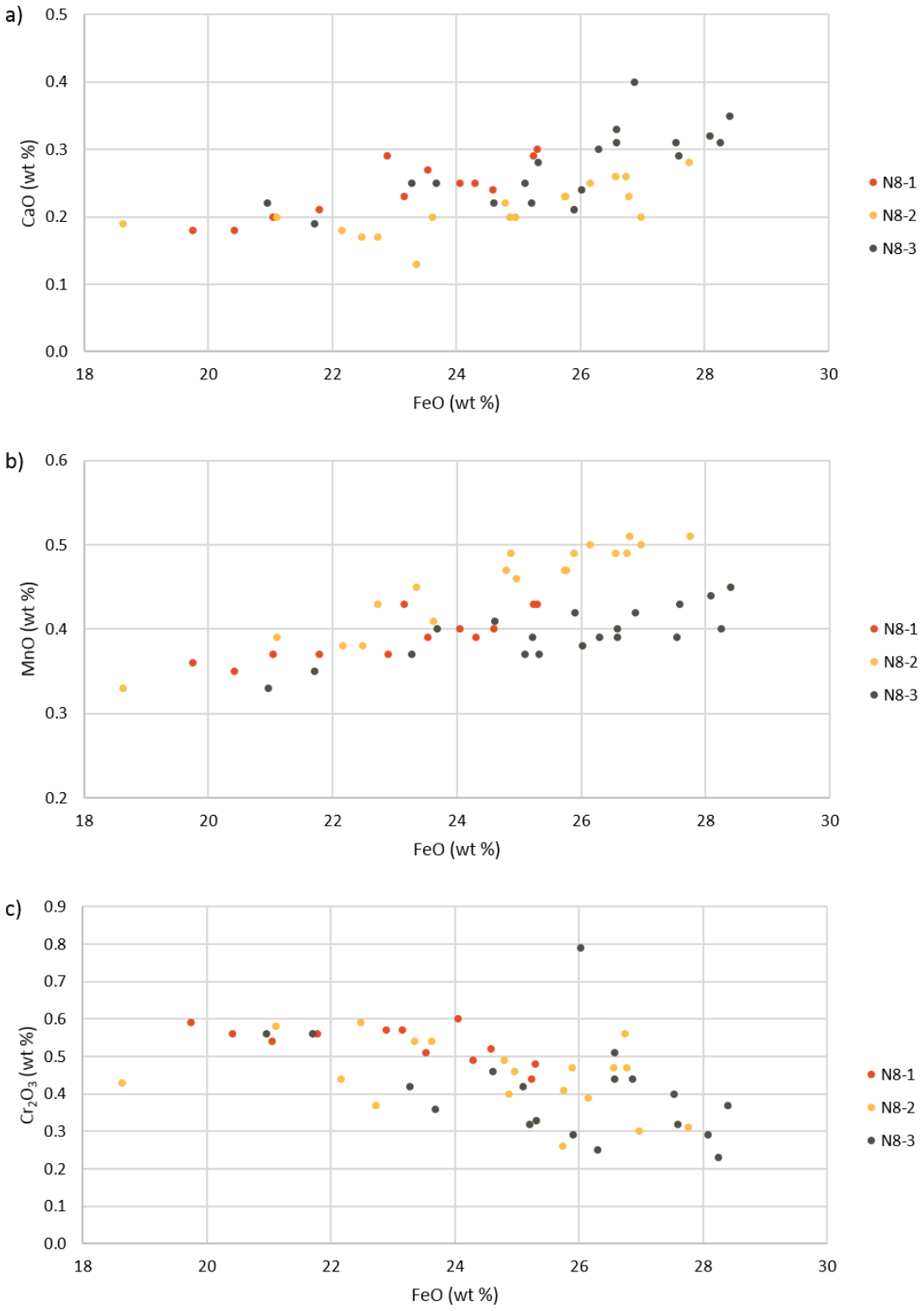

Figure 3.19 – Oxides vs FeO for olivine phenocrysts in all chondrules in NWA 8276: a) CaO vs FeO; b) MnO vs FeO; c) Cr_2O_3 vs FeO. Points represent individual EPMA analyses.

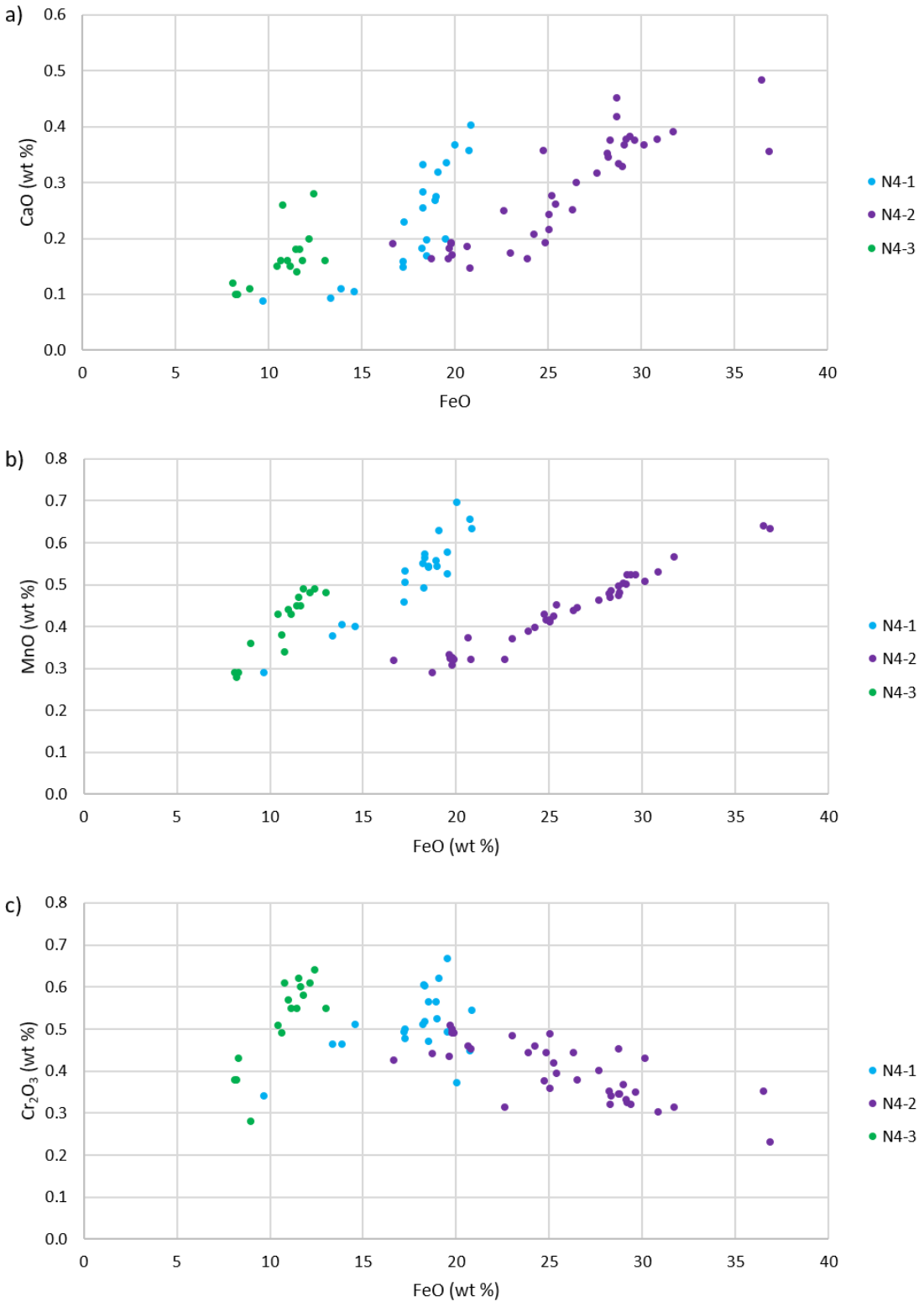

Figure 3.20 – Oxides vs FeO for olivine phenocrysts in all chondrules in NWA 4910: a) CaO vs FeO; b) MnO vs FeO; c) Cr_2O_3 vs FeO. Points represent individual EPMA analyses.

8276 and ALHA 77307. Across the three chondrules, forsterite content ranges from Fo_{56} to Fo_{92} with the most MgO-rich compositions from chondrules N4-1 and N4-3. Olivine phenocrysts occasionally contain inclusions of chromite, sulfides and metal. Olivine compositions in these chondrules are summarised in Table 3.3.

The chondrules studied in NWA 4910 show olivine with diverse compositions (see Figure 3.15 to Figure 3.17, compiled in Figure 3.20). Each chondrule shows wide-ranging compositions within the chondrule. Compositions between chondrules are also significantly different with little overlap between them. Overall, trends are similar to those observed in chondrules in ALHA 77307 and NWA 8276. CaO and MnO increase with increasing FeO, however, two chondrules, N4-1 and N4-3, show increasing Cr_2O_3 with increasing FeO. Chondrule N4-2 shows a distinct downward trend for Cr_2O_3 with increasing FeO.

3.3 Pyroxene

Pyroxene is only present in significant quantities on chondrules N4-1 and N4-3. It is absent from all other chondrules except chondrule Al-1, which contains a single small crystal, and chondrule N4-2 in which it is confined to small crystals in mesostasis.

In chondrules N4-1 and N4-3, pyroxene is the second most abundant phase. Crystal shapes vary from subhedral to euhedral with many showing skeletal features and irregular edges (see Figure 3.21). Like olivine crystals, pyroxene phenocrysts appear to be zoned, with many displaying darker cores and lighter rims. Element maps show that the rims are Ca-rich, indicating that the zoning is a combination of Fe-Mg and Ca zoning. In chondrules N4-1 and N4-3, pyroxene crystals range in size from several micrometres to 45 µm in length. In chondrule N4-2, they are much more restricted in size, up to 15 µm in length. Compositions for pyroxene in chondrules N4-1 and N4-3 generally plot towards

Table 3.4 – Mean, minimum and maximum oxide compositions of pyroxene crystals in chondrules N4-1 and N4-3 in wt % determined by EPMA. N is the number of analyses.

Chondrule	Na_2O	MgO	Al_2O_3	SiO_2	P_2O_5	K_2O	CaO	TiO_2	Cr_2O_3	MnO	FeO	NiO	Total	N
N4-1														
Mean	0.16	27.6	0.51	55.1	<0.09	<0.02	2.85	0.09	1.08	0.57	11.8	0.22	100.0	10
Min	0.05	23.6	0.25	52.6	<0.09	<0.02	1.20	0.00	0.98	0.51	10.9	<0.06	98.8	
Max	0.38	29.9	1.40	56.8	<0.09	0.08	6.17	0.30	1.19	0.62	12.8	0.57	101.1	
N4-3														
Mean	0.08	32.5	0.35	56.4	<0.09	<0.02	1.76	0.06	0.91	0.47	7.71	0.09	100.3	8
Min	<0.05	28.2	0.16	54.5	<0.09	<0.02	0.97	0.02	0.85	0.43	7.02	<0.06	98.1	
Max	0.26	34.4	0.95	58.3	<0.09	0.05	4.72	0.11	1.00	0.52	8.22	0.26	101.9	

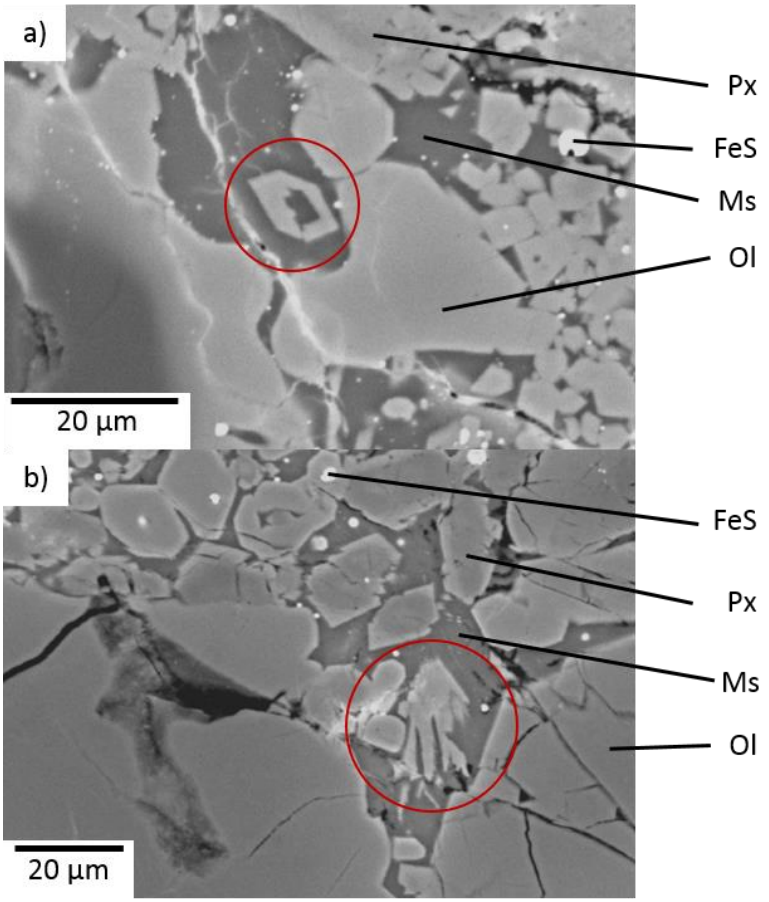

Figure 3.21 – BSE images of textures in chondrules from a) N4-1 and b) N4-3. Circled in red are examples of skeletal and irregular pyroxene crystals. Ol is olivine, Px is pyroxene, Ms is mesostasis and FeS is sulfide.

enstatite (see Figure 3.22). As a result of the small crystal size of pyroxene in chondrule N4-2, only one analysis was successful. This analysis suggests that these pyroxenes may be augites (Figure 3.22). Compositions of pyroxenes in chondrules N4-1 and N4-3 are shown in Table 3.4.

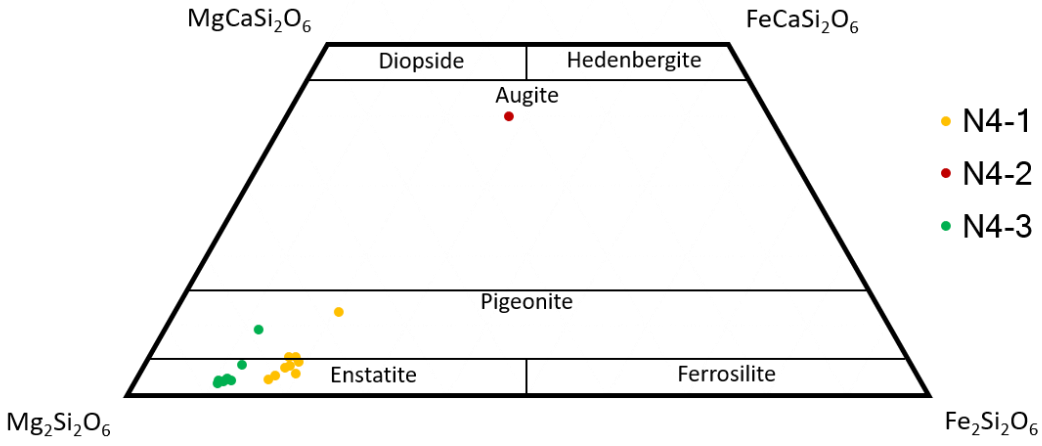

Figure 3.22 – Ternary plot of Ca, Mg and Fe in atomic % for pyroxenes in chondrules in NWA 4910.

3.4 Mesostasis

In the studied chondrules, olivine and pyroxene phenocrysts are set in a mesostasis containing glassy material, microcrystallites and possibly alteration products.

In ALHA 77307, analyses of chondrule mesostases show that SiO_2 and FeO are the most abundant oxides, with values of 25 to 35, and 27 to 36 wt %, respectively. Mesostasis is also rich in MgO, Al_2O_3 and CaO. Although SiO_2 is abundant in these chondrule mesostases, it is present in much lower quantities than in other CO chondrites. Berlin et al. (2011) report average SiO_2 values of 50 to 59 wt % for type II chondrule mesostases in Kainsaz CO3.2. Ikeda (1983) show that many of the mesostases of chondrules in ALHA 77307 have been altered to phyllosilicates. The composition of mesostasis in the studied chondrules is similar to values obtained for other chondrule mesostases in ALHA 77307 by Ikeda (1983)

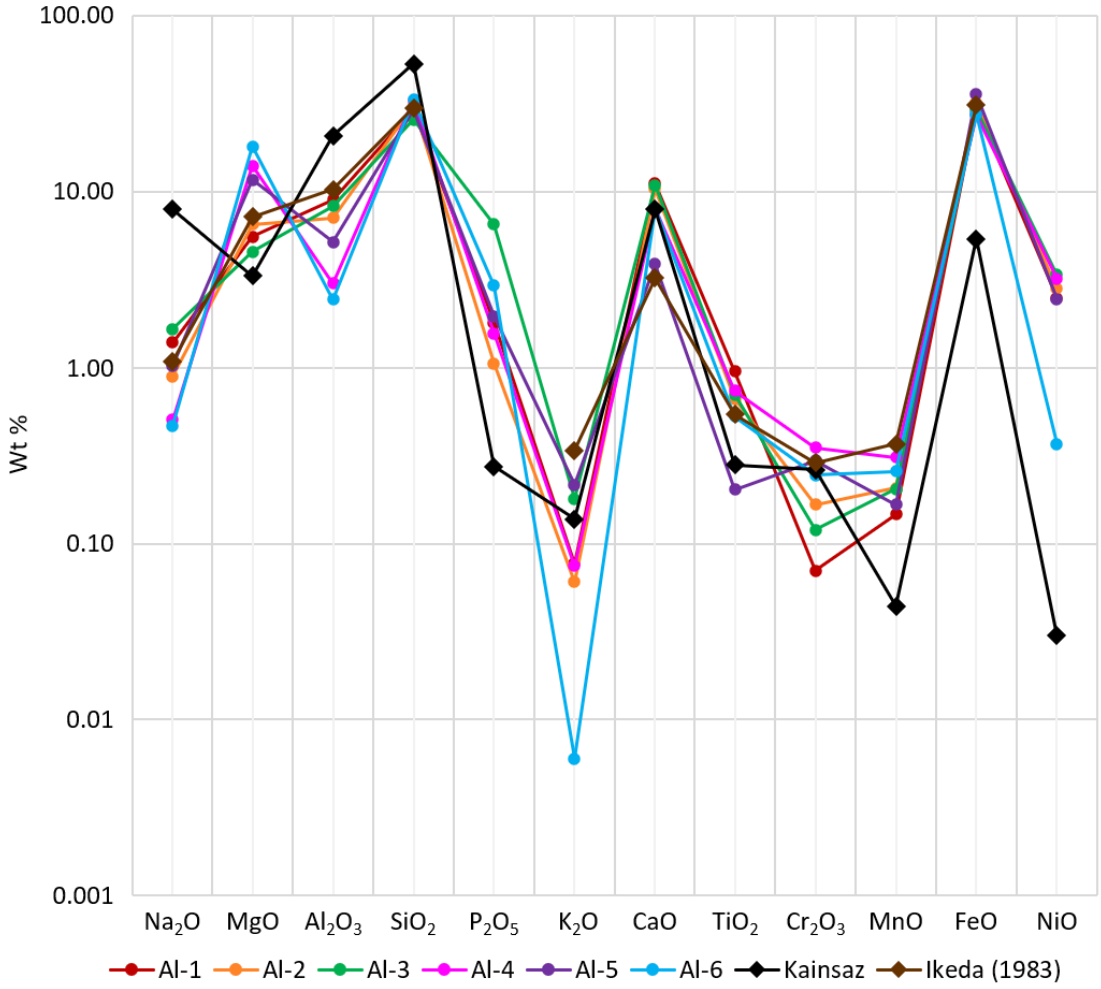

Figure 3.23 – Average composition of mesostasis in chondrules in ALHA 77307. Kainsaz shows the average composition of the mesostases of five type II chondrules in Kainsaz CO3.2 (Berlin et al., 2011). Ikeda (1983) shows the average composition of altered mesostases in chondrules in ALHA 77307 and they show similar compositions to the chondrules studied here.

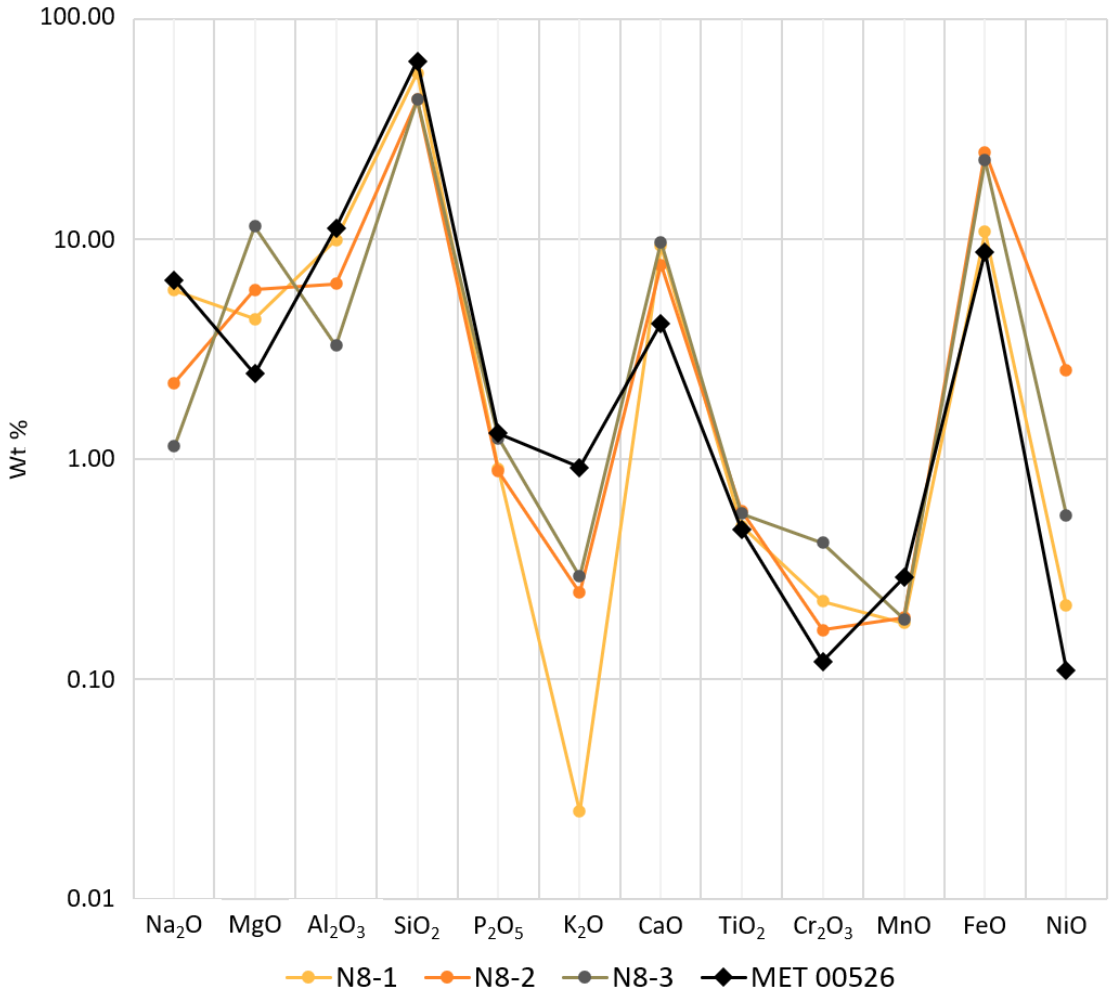

Figure 3.24 – Average composition of mesostasis in chondrules in NWA 8276 . MET 00526 shows the average composition of the mesostases of three type II chondrules in MET 00526 L3.05 (Berlin et al., 2011).

(See Figure 3.23). They are also similar in composition to phyllosilicate assemblages in altered chondrule mesostases in both Renazzo (CR2) and Murchison (CM2) (Richardson, 1981). Despite this alteration, olivine compositions appear to remain pristine (Ikeda, 1983). Average mesostasis compositions for these chondrules are shown in Table 3.5.

The mesostasis of the studied chondrules in NWA 8276 show a much glassier texture. The most abundant oxide in the mesostasis is SiO_2; the abundance is generally much higher than in the chondrules in ALHA 77307. Mesostasis is also abundant in CaO, Al_2O_3 and FeO. Abundance of Na_2O is higher than in chondrules in ALHA 77307. The higher SiO_2 and Na_2O values and glassier texture suggest that these mesostases may be less altered than those in chondrules in ALHA 77307. In general, mesostasis composition shows some variation between the three chondrules, particularly in their Na_2O, MgO, Al_2O_3 and FeO compositions. Average mesostasis compositions for these chondrules are shown in Table 3.5 and Figure 3.24.

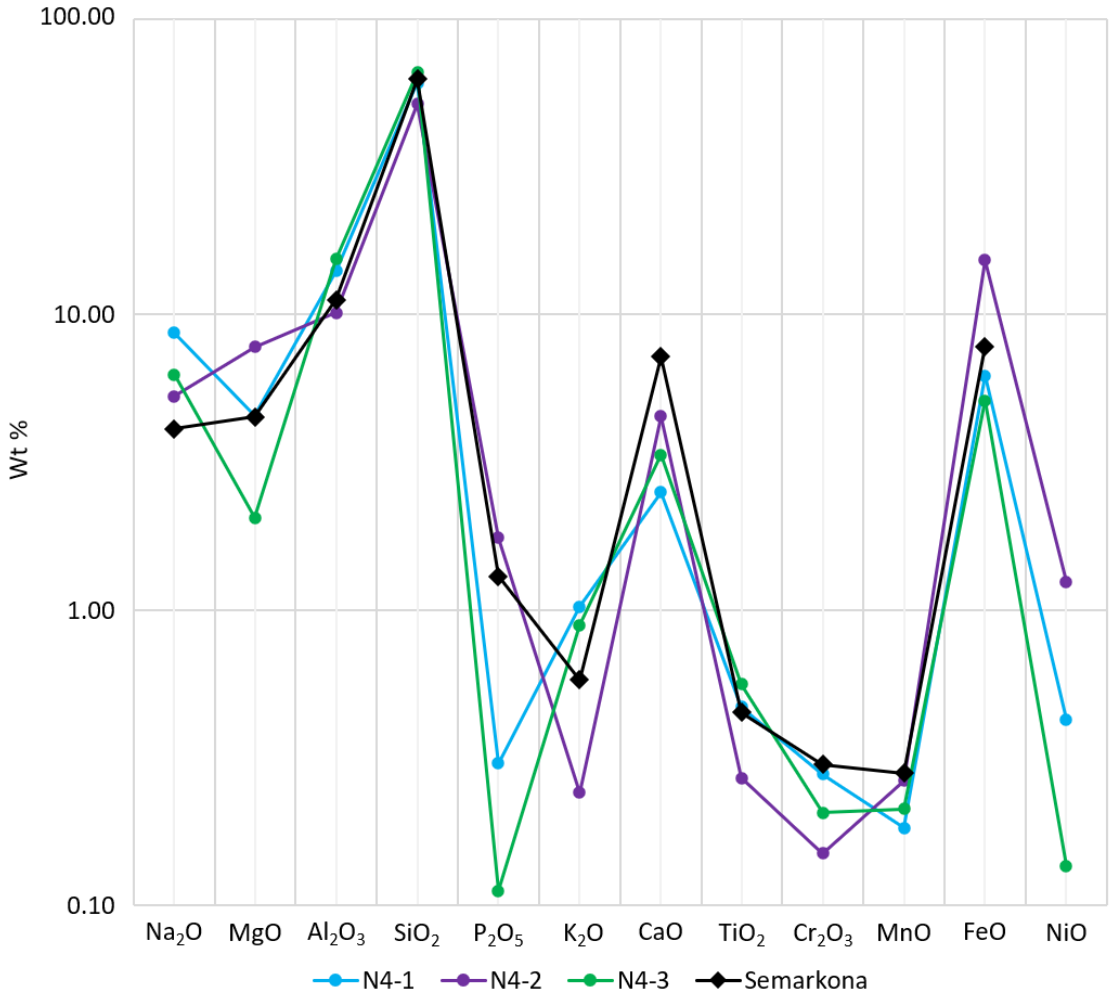

Figure 3.25 – Average composition of mesostasis in chondrules in NWA 4910. Semarkona shows the average composition of the mesostases type II chondrules in Semarkona (LL3.00) (Jones, 1990).

The mesostasis of the studied chondrules in NWA 4910 is glassy and contains crystallites. These three chondrules show the most pristine mesostasis, evident in EPMA analyses which show totals close to 100% and high SiO_2 content. SiO_2 accounts for over 50% of the mesostasis. The mesostasis is also rich in Al_2O_3, FeO, MgO and Na_2O. Overall, there is some variation in mesostasis between chondrules, however, N4-1 and N4-3 show broadly similar compositions with higher SiO_2 and lower FeO. Chondrule N4-2 shows lower SiO_2 and higher FeO. Average mesostasis compositions for these chondrules are shown in Table 3.5 and Figure 3.25.

Table 3.5 – Average mesostasis compositions for chondrules in ALHA 77307, NWA 8276 and NWA 4910 in wt %. N is number of analyses for the average.

Chondrule	Na_2O	MgO	Al_2O_3	SiO_2	P_2O_5	K_2O	CaO	TiO_2	Cr_2O_3	MnO	FeO	NiO	Total	N
Al-1	1.39	5.58	9.06	29.4	1.81	0.08	11.2	0.95	0.07	0.15	30.3	2.49	92.4	3
Al-2	0.89	6.55	7.14	31.2	1.06	0.06	10.4	0.67	0.17	0.21	32.2	2.81	93.4	6
Al-3	1.66	4.58	8.30	25.9	6.57	0.18	10.9	0.71	0.12	0.21	29.2	3.39	91.7	2
Al-4	0.51	14.1	3.02	33.2	1.57	0.08	8.03	0.74	0.35	0.31	27.5	3.22	92.6	4
Al-5	1.03	11.8	5.19	29.6	1.97	0.22	3.88	0.20	0.30	0.17	35.9	2.47	92.6	3
Al-6	0.47	18.1	2.45	33.6	2.93	0.01	8.07	0.53	0.25	0.26	27.7	0.37	94.7	5
N8-1	5.83	4.32	9.90	56.8	0.90	0.03	9.29	0.50	0.23	0.18	10.8	0.22	99.0	2
N8-2	2.22	5.87	6.24	43.1	0.88	0.25	7.62	0.58	0.17	0.19	24.8	2.54	94.5	3
N8-3	1.14	11.4	3.28	43.1	1.24	0.29	9.65	0.56	0.42	0.19	22.8	0.56	94.6	3
N4-1	8.66	4.53	14.0	60.7	0.30	1.02	2.50	0.47	0.28	0.18	6.20	0.43	99.3	5
N4-2	5.29	7.76	10.1	51.6	1.75	0.24	4.51	0.27	0.15	0.26	15.3	1.25	98.5	3
N4-3	6.26	2.05	15.4	65.7	0.11	0.89	3.35	0.56	0.21	0.21	5.11	0.14	100.0	5

3.5 Chromite

Chromite is present as a minor component of all the chondrules (<1%), however, only single grains of chromite are present in chondrules N4-1 and N4-3. Chromite generally appears as small, up to several µm, euhedral grains. They are found encased in mesostasis (e.g. Figure 3.5b) or as inclusions in olivine phenocrysts (e.g. Figure 3.26). The largest grain occurs in chondrule Al-4 and has a maximum length of 17 µm.

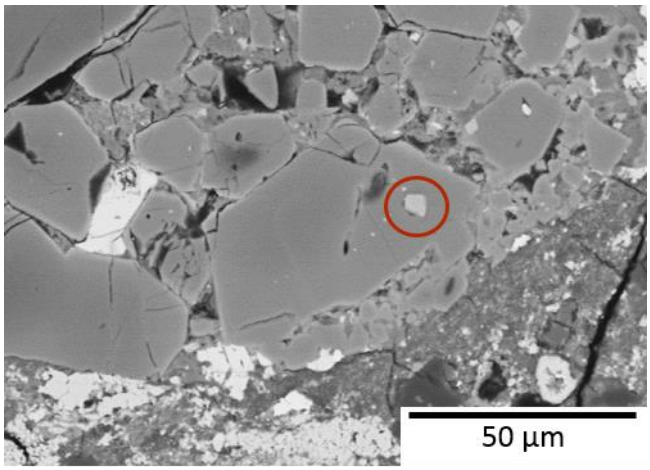

Figure 3.26 – Olivine phenocryst showing a chromite inclusion (circled) from Al-1

Compositional analyses of chromite grains were obtained for chondrules Al-1, Al-2, Al-4, N8-2, and N8-3 and are shown in Table 3.1. In other chondrules, chromite grains were too small to analyse and returned values with very low totals or obvious contamination from the surrounding phases. Analysis totals are generally several wt % lower than 100. This could be a result of uncertain Fe^{2+}/Fe^{3+} ratios in the chromite grains. In these analyses, all Fe is assumed to be FeO (Fe^{2+}). Recalculating analyses to 100% Fe_2O_3 (Fe^{3+}) results in totals

Table 3.6 – Individual analyses showing the composition of chromite grains.

Grain	Na_2O	MgO	Al_2O_3	SiO_2	P_2O_5	K_2O	CaO	TiO_2	Cr_2O_3	MnO	FeO	NiO	Total
Al-1 Cr 1	0.08	6.83	17.7	1.02	<0.09	<0.02	0.18	0.86	42.3	0.24	26.6	0.17	96.1
Al-1 Cr 2	<0.05	6.09	16.2	1.26	<0.09	<0.02	0.08	1.47	42.5	0.28	29.1	0.09	97.1
Al-2 Cr 1	<0.05	7.29	13.9	0.34	<0.09	<0.02	0.19	1.50	46.6	0.31	26.2	0.07	96.4
Al-2 Cr 2	<0.05	7.89	15.2	0.31	<0.09	<0.02	0.18	0.93	46.1	0.25	24.8	<0.06	95.6
Al-4 Cr 1	<0.05	7.27	20.6	0.93	<0.09	<0.02	0.19	1.11	40.3	0.34	27.5	0.40	98.7
N8-2 Cr 1	<0.05	6.55	8.76	0.49	<0.09	<0.02	0.21	1.44	53.7	0.48	25.2	0.09	96.9
N8-3 Cr 3	<0.05	5.24	5.37	0.53	<0.09	<0.02	0.08	2.08	54.0	0.44	28.6	0.13	96.4

above 98 wt %. Cr_2O_3 is the most abundant component of chromite grains, followed by FeO. In the chondrules in ALHA 77307, the Al_2O_3 composition is high, up to 20 wt %. In the chondrules in NWA 8276, Al_2O_3 composition is lower, <9 wt %.

3.6 Metal and sulfides

Troilite is present in most of the studied chondrules, except chondrules N8-1 and N8-3, and is only present in very small quantities (<0.2%) in chondrule N8-2. Troilite grains generally appear as rounded to irregularly shaped lumps in the mesostasis, at chondrule rims, or as inclusions in olivine or pyroxene phenocrysts. Troilite abundance is up to 12% in chondrule Al-4 but is <4% in the other studied chondrules. Fe,Ni metal grains are present in chondrules in ALHA 77307 and NWA 4910, but are absent in those from NWA 8276. Abundance of these metal grains is generally less than the abundance of troilite, up to 1.4%. They appear as rounded to irregularly shaped grains that can be found isolated in

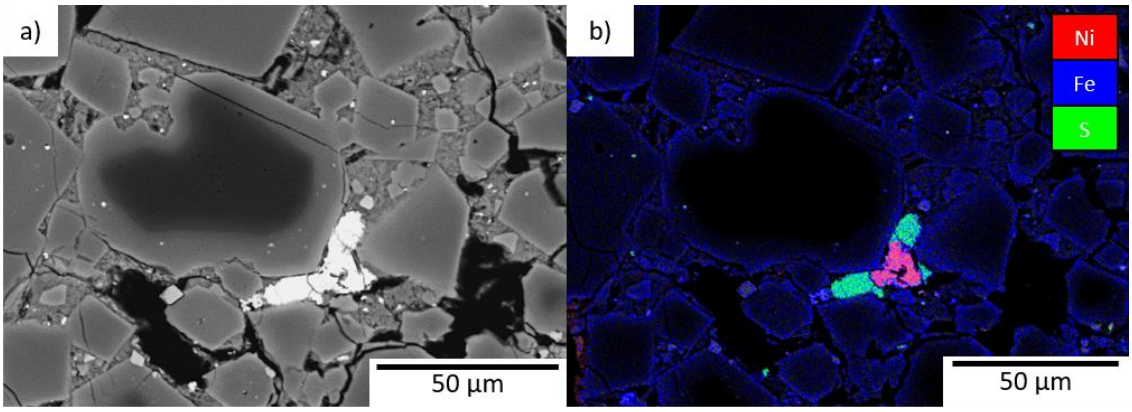

Figure 3.27 – a) BSE image of troilite and Fe,Ni metal grains (both appear white) occurring in association. b) element map showing Ni, Fe and S as red, blue, and green respectively. This highlights the central part of white section as Fe,Ni metal (appears red) and troilite to the sides (appears green).

mesostasis, as inclusions in olivine or pyroxene crystals or as inclusions in forsteritic-olivine grains. Some grains contain significant quantities of Ni; however, others are mainly Fe. Metal grains often occur in association with troilite, e.g. Figure 3.27.

3.7 Forsteritic-olivine

All the studied chondrules contain at least one forsteritic-olivine relict grain which are visible in BSE images as dark patches within lighter olivine phenocrysts (see Figure 3.1 to Figure 3.4). These are discussed in more detail in Chapter 4 – Petrography of forsteritic-olivine relict grains.

3.8 Weathering and alteration products

Many of the studied chondrules show evidence of secondary processing after their formation, such as aqueous alteration and terrestrial weathering. For example, the mesostases of chondrules in ALHA 77307 appear to have been partially altered to phyllosilicate assemblages, based upon their FeO-rich, SiO_2 poor compositions (Richardson, 1981; Ikeda, 1983). Ikeda (1983) also shows that despite mesostais alteration, olivine compositions remain pristine and unaltered. Fe-rich sulfide veins present in chondrules N8-3, N4-1 and N4-3 suggest that these chondrules have been altered and compositional profiles should be measured in locations that have not been influenced by these sulfide veins.

3.9 Discussion

3.9.1 Chondrule texture

All chondrules reported in this study are porphyritic olivine or porphyritic olivine and pyroxene chondrules which consist mainly of zoned olivine phenocrysts set in a mesostasis. Although chondrules N4-1 and N4-3 contain abundant pyroxene, olivine is still the dominant mineral. This texture is consistent with an igneous origin for these chondrules (Jones, 1990). Chondrule textures are similar across the studied chondrite classes and groups (L, LL, and CO), suggesting strong similarities across different chondrule forming regions. This is supported throughout the wider chondrule population where multiple textural types are found in the different chondrite groups (Jones, 2012). Despite this, there are often notable textural differences in a particular textural type between the different chondrite groups. The best example of this is type IAB chondrules, which are present in

many different chondrite groups, but exhibit differences in chondrule shape and structure across different chondrite groups (Rubin, 1984; Jones and Scott, 1989; Krot et al., 2004; Rubin and Wasson, 2005). This suggests that chondrules sample different reservoirs with similar over-arching processes, but with some differences in processing between chondrite groups (Jones, 2012).

3.9.2 Chondrule cooling rates

The compositional zoning observed in olivine phenocrysts in the studied chondrules shows that equilibrium was not achieved during crystallisation. This alone is evidence for rapid cooling (Jones, 1990). Porphyritic textures similar to those observed in the studied chondrules have been reproduced experimentally at cooling rates from 1 to 2500 Kh^{-1}, however, the textures were best reproduced at cooling rates of 10 to 1000 Kh^{-1} (Lofgren and Russell, 1986; Radomsky and Hewins, 1990; Connolly and Hewins, 1991; Jones and Lofgren, 1993; Kennedy et al., 1993; Connolly and Hewins, 1995; Connolly et al., 1998; Weinbruch et al., 1998). Miyamoto et al. (2009) found cooling rates of 0.7 to 2400 Kh^{-1} for type IIA chondrules in Semarkona (LL3.00) by modelling the formation of zoning profiles present in olivine phenocrysts.

3.9.3 Chondrule sizes

The twelve studied chondrules range in diameter from 70 to 490 µm and chondrules from different chondrite groups show a similar overall size range, suggesting similarly sized chondrules in each chondrite group. However, it has been observed that mean chondrule size varies between chondrite groups. Mean chondrule diameters in L and LL chondrites are 500 µm and 600 µm, respectively. In CO chondrites, mean chondrule diameter is 150 µm which is considerably smaller than in L and LL chondrites (Scott and Krot, 2003; Scott and Krot, 2005; Jones, 2012). Although the size ranges of the studied chondrules are similar, the smallest chondrules are found in ALHA 77307, a CO chondrite, which is consistent with the reported lower average chondrule diameter. The observed differences in chondrule size between different chondrite groups suggest that some size sorting likely occurred in the solar nebula, possibly caused by turbulence (Cuzzi et al., 2001). However, Rubin (2010) argues that the apparent size sorting between chondrite groups is a result of differences in the abundance of dust and the number of chondrule melting events that occurred in the different chondrule forming regions and that size sorting only occurred during chondrite accretion.

3.9.4 Olivine composition

Olivine phenocryst compositions in chondrules, particularly type IIA chondrules, are often diagnostic of their host chondrite group and show particular trends which vary between different chondrite groups. Average forsterite composition of olivine phenocrysts present in chondrules is one indicator of chondrite group. Berlin et al. (2011) report average olivine compositions, excluding forsteritic-olivine, for type IIA chondrules in the CO3.2 chondrite Kainsaz of Fo_{66}. Mean values obtained here for chondrules in the CO chondrite ALHA 77307 range from Fo_{54} to Fo_{69}. Four of the six chondrules have values close to this mean value of Fo_{66}. The other two show much lower values (see Figure 3.28). Values for average olivine composition, not including forsteritic-olivine, in type IIA chondrules in the L3.05 chondrites MET 00526 and QUE 97005 are ~Fo_{80} (Berlin et al., 2011). Average values obtained here for the L chondrite NWA 8276 are all considerably lower than this with values of Fo_{75}, Fo_{73} and Fo_{71} for chondrules N8-1, N8-2 and N8-3 respectively (see Figure 3.28). Jones (1990)

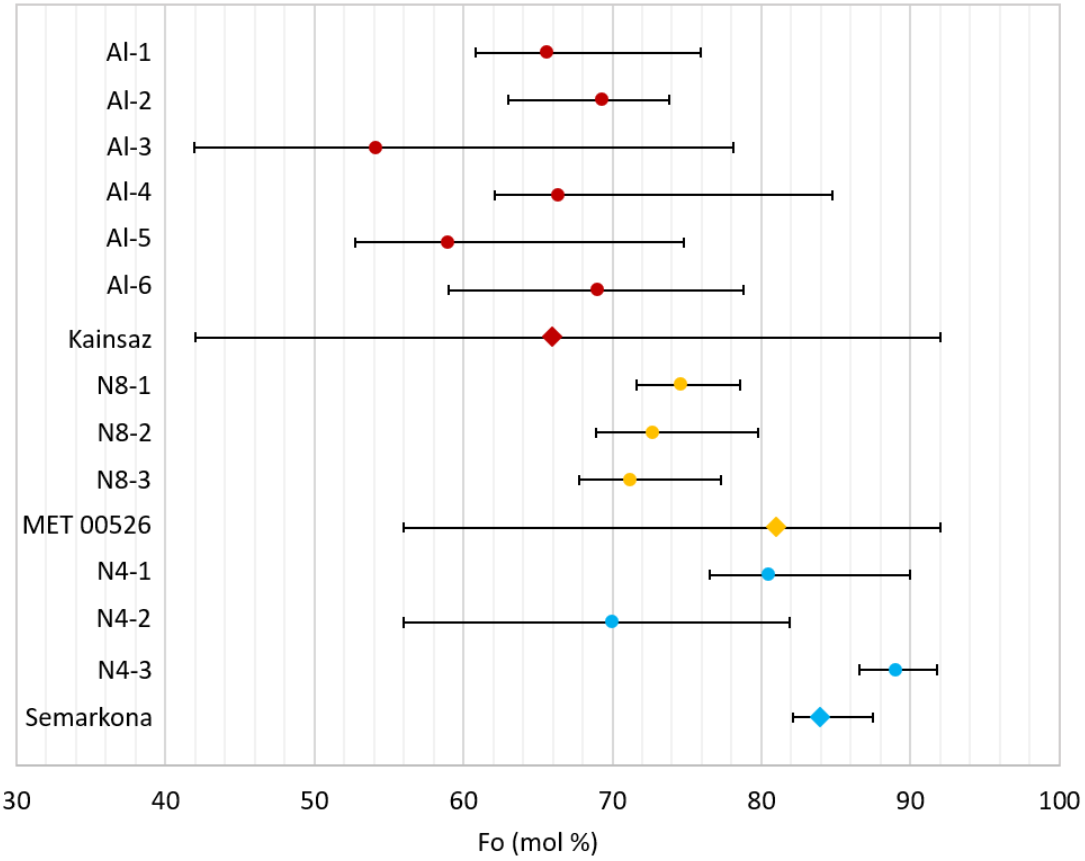

Figure 3.28 – Mean and range of forsterite composition for studied chondrules. Points show the mean of the analyses, whereas the black lines show the overall range in forsterite composition. Kainsaz represents the mean and range of analyses of 5 type II chondrules (Berlin et al., 2011). MET 00526 represents the mean and range of analyses of 3 type II chondrules (Berlin et al., 2011). Semarkona shows the mean of mean values for 10 chondrules, while the line shows the range of those mean values.

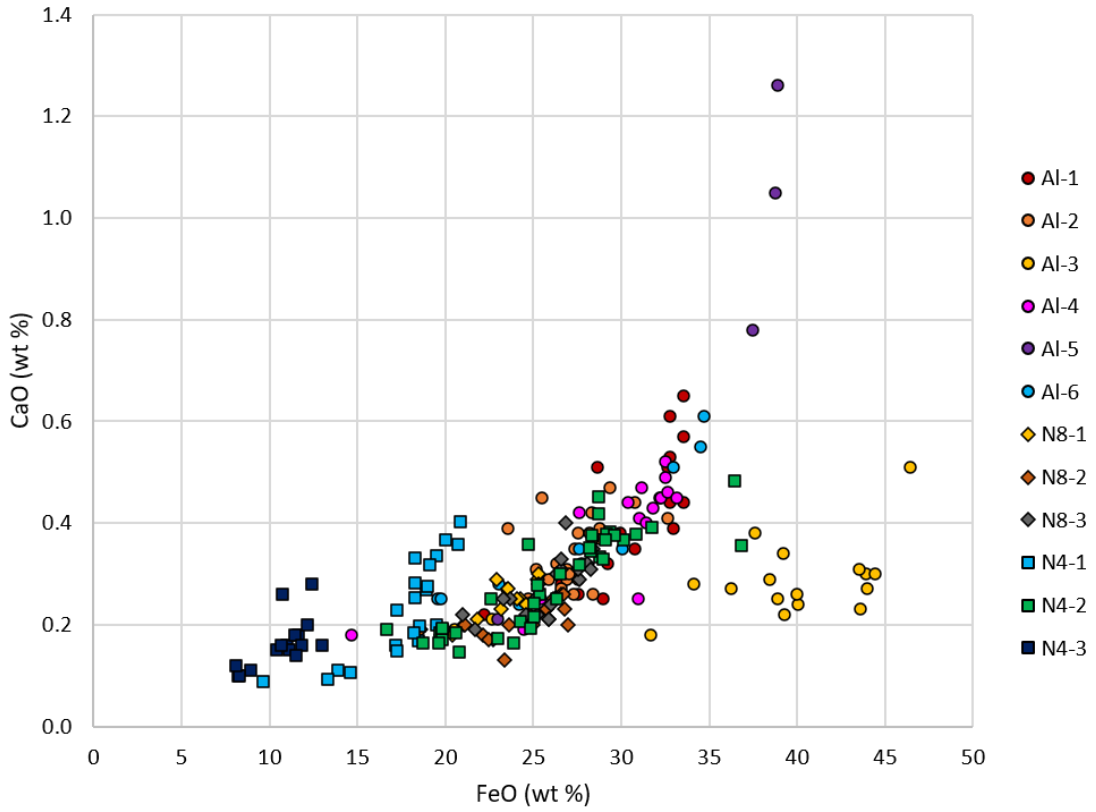

Figure 3.29 – FeO vs CaO for olivine phenocrysts in all chondrules.

reported an average olivine composition for type IIA chondrules in Semarkona LL3.00 that is even more MgO-rich with a value of ~Fo_{84}. Type II chondrules from the LL chondrite 3.1 analysed here have average forsterite compositions of $Fo_{81,}$ Fo_{70} and Fo_{89} for chondrules N4-1, N4-2, and N4-3, respectively. While the type IIAB chondrules N4-1 and N4-3 are relatively consistent with the more MgO-rich average from Jones (1990), the type IIA chondrule analysed from this chondrite (N4-2) has an average Fo value of Fo_{70}, considerably lower. This is closer to the values reported by Berlin et al. (2011) for type IIA chondrules in CO chondrites, and similar to values obtained for L chondrites here (see Figure 3.28). Overall, average olivine composition divides chondrules, firstly, between carbonaceous and ordinary chondrite classes. Mean forsterite content of olivine phenocrysts is lowest in the chondrules from the carbonaceous chondrite ALHA 77307 and is higher in the ordinary chondrites. Average olivine composition also appears to divide the type IIAB chondrules present in the ordinary chondrites from the type IIA chondrules. Chondrule N4-2 has average olivine compositions which are similar to the composition of olivine in the chondrules in NWA 8276, while the two type IIAB chondrules, N4-1 and N4-3 have much higher forsterite contents.

The observed trends in the FeO vs oxide plots shown in Figure 3.29 to Figure 3.31 are generally consistent with the closed system fractional crystallisation trends observed in Jones (1990). For FeO vs CaO shown in Figure 3.29, all chondrules show increasing CaO with increasing FeO. As Ca is incompatible in olivine, this is consistent with fractional crystallisation (Jones, 1990). A similar trend is observed in Figure 3.31 for Mn vs Fe, which shows increasing Mn with Fe. These trends have also been observed in type II chondrules by Jones (1990) and Berlin et al. (2011), and in the results of dynamic crystallisation experiments with bulk compositions similar to chondrules (Lofgren, 1989; Jones and Lofgren, 1993), consistent with fractional crystallisation. FeO vs Cr_2O_3, shown in Figure 3.30, shows two different trends. All chondrules in ALHA 77307 and NWA 8276, as well as chondrule N4-2 from NWA 4910, show Cr_2O_3 decreases with FeO, whereas chondrules N4-1 and N4-3 show Cr_2O_3 increases with FeO. This appears to be related to the amount of chromite present in each chondrule. Chondrules N4-1 and N4-3 both show very little or no chromite present, whereas all other chondrules show chromite in larger quantities. It is therefore likely that the observed trends in Cr_2O_3 are related to crystallisation of chromite removing Cr from the melt as olivine crystallised, which creates the negative gradients

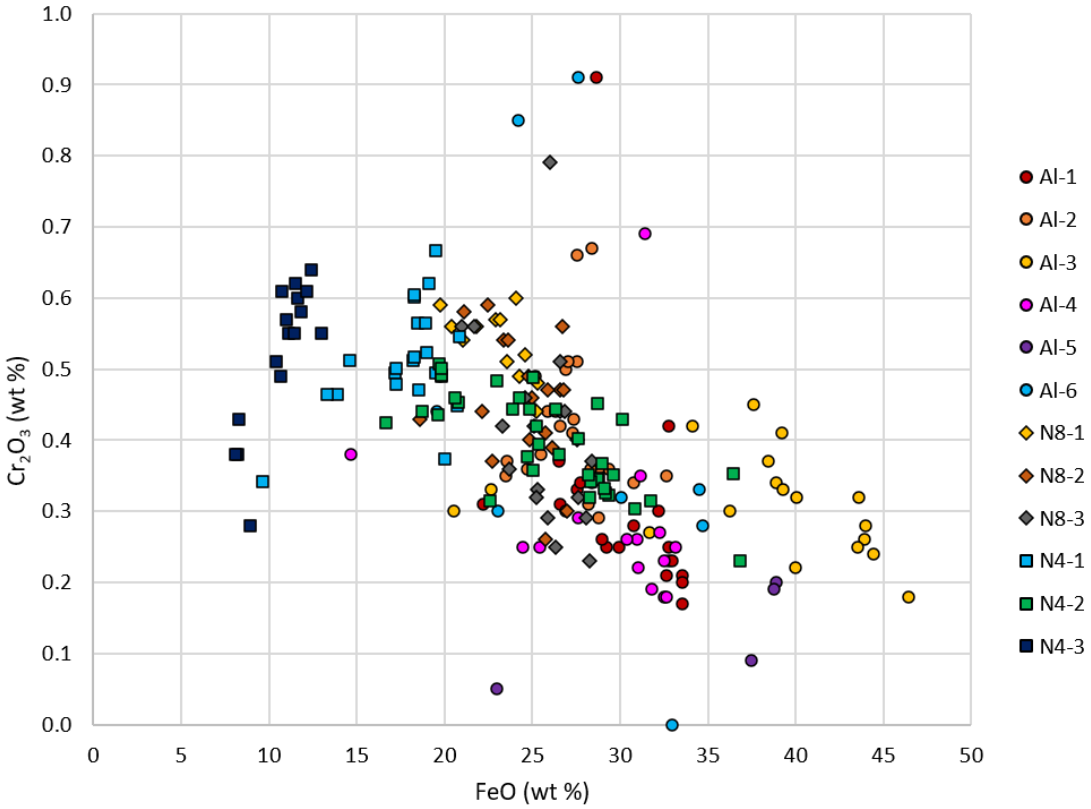

Figure 3.30 – Cr_2O_3 vs FeO for olivine phenocrysts from all chondrules.

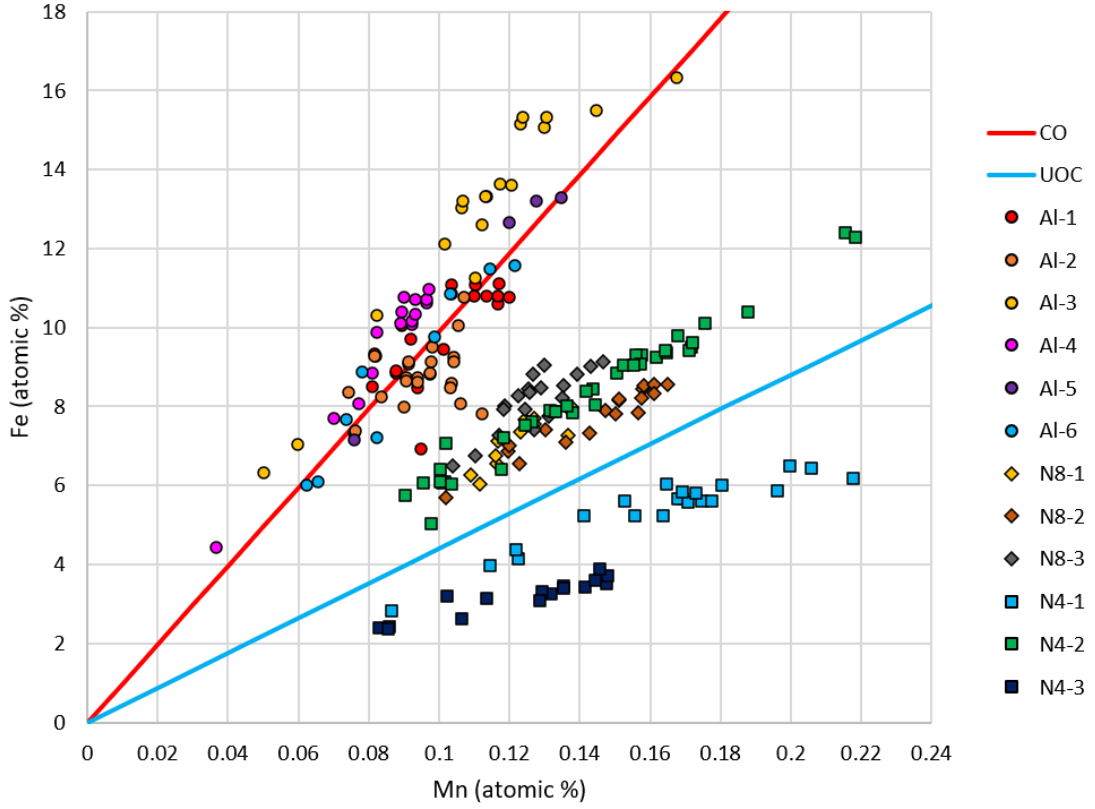

Figure 3.31 – Fe vs Mn for all chondrules. The red line shows the average Fe/Mn ratio for chondrules in the CO chondrites ALHA 77307 (Jones, 1992) and Kainsaz (Berlin et al., 2011). The blue line shows the average Fe/Mn ratio in the unequilibrated ordinary chondrites Semarkona (LL3.00) (Jones, 1990), MET 00526 (L3.05), and QUE 97008 (L3.05) (Berlin et al., 2011).

observed in chondrules from ALHA 77307, NWA 8276, and chondrule N4-2. In chondrules N4-1 and N4-3, no or very little chromite crystallised resulting in a normal igneous trend related to fractional crystallisation of olivine and pyroxene. However, Jones (1990) discussed that the partition coefficients for Cr in olivine could be more than 1, which could indicate that Cr is compatible in these olivine phenocrysts, suggesting that the observed negative trends in Figure 3.30 are not related to chromite content. The results of dynamic crystallisation experiments with chondrule bulk compositions show that Cr_2O_3 does increase with FeO (Lofgren, 1989; Jones and Lofgren, 1993), suggesting Cr is incompatible in these olivine phenocrysts and that increasing Cr_2O_3 with FeO is the normal zoning trend (Jones, 1990).

Distinct Fe/Mn ratios are observed in the olivine phenocrysts within all chondrules (see Figure 3.31). Three distinct trends are observed: Chondrules from the CO chondrite ALHA 77307 show average Fe/Mn ratios of 103; type IIA chondrules from ordinary chondrites NWA 8276 and NWA 4910 (chondrules N8-1, N8-2, N8-3 and N4-2) show average Fe/Mn of

59; type IIAB chondrules from NWA 4910, chondrules N4-1 and N4-3 show Fe/Mn ratios of 33 and 26 respectively. Like mean forsterite content, this divides chondrules, firstly by class. Chondrules from the carbonaceous chondrite ALHA 77307 show much higher Fe/Mn ratios than the ordinary chondrites NWA 8276 and NWA 4910. The second division occurs between the type IIA and type IIAB chondrules in the ordinary chondrites, with higher Fe/Mn ratios in the type IIA chondrules than the type IIAB. The same trends were observed by Berlin et al. (2011) for type IIA chondrules in CO, L and LL chondrites which show significantly higher Fe/Mn ratios for chondrules in CO chondrites than chondrules in L and LL chondrites. However, type IIA chondrules in the studied L and LL chondrites have average Fe/Mn ratios that are higher than the value off 44 reported by Berlin et al. (2011), but they do form a parallel trend. As observed in NWA 4910 and NWA 8276, the Fe/Mn ratios of olivine in type IIA chondrules in L and LL chondrites are indistinguishable (Berlin et al., 2011).

Differences in Fe/Mn ratios of type IIA chondrules from ordinary and carbonaceous chondrites could be the result of the properties of the chondrule precursors in closed system behaviour as well as open system behaviour that may have occurred during chondrule formation. One possibility is that chondrule precursors had different depletions of moderately volatile elements. Berlin et al. (2011) rule this out as bulk Fe composition of CO chondrules are higher than ordinary chondrites but differences in Mn composition are small. Another explanation is differences in the abundance of silicates, metals, and sulfides in the chondrule precursor assemblages (Berlin et al., 2011). Precursors with a higher proportion of sulfides and/or metal would result in the higher Fe/Mn ratios observed in CO chondrules. The reverse, a lower proportion of sulfides or metal would result in chondrules with lower Fe/Mn ratios, observed in chondrules from ordinary chondrites. Metal and sulfide proportions in type II chondrules from both CO chondrites and ordinary chondrites are generally low; accounting for <5% of the chondrules studied here (except Al-4). If more metal were present in the precursors of type II chondrules in CO chondrites it must have been oxidised before or during chondrule formation. This would result in the olivine in these chondrules showing higher NiO values, which is not observed. If CO chondrule precursors were richer in sulfides, S could be lost because of evaporation during chondrule formation, leaving extra Fe, however no increase in NiO would be observed (Berlin et al., 2011). Another potential explanation is the reduction of the precursor assemblage, which

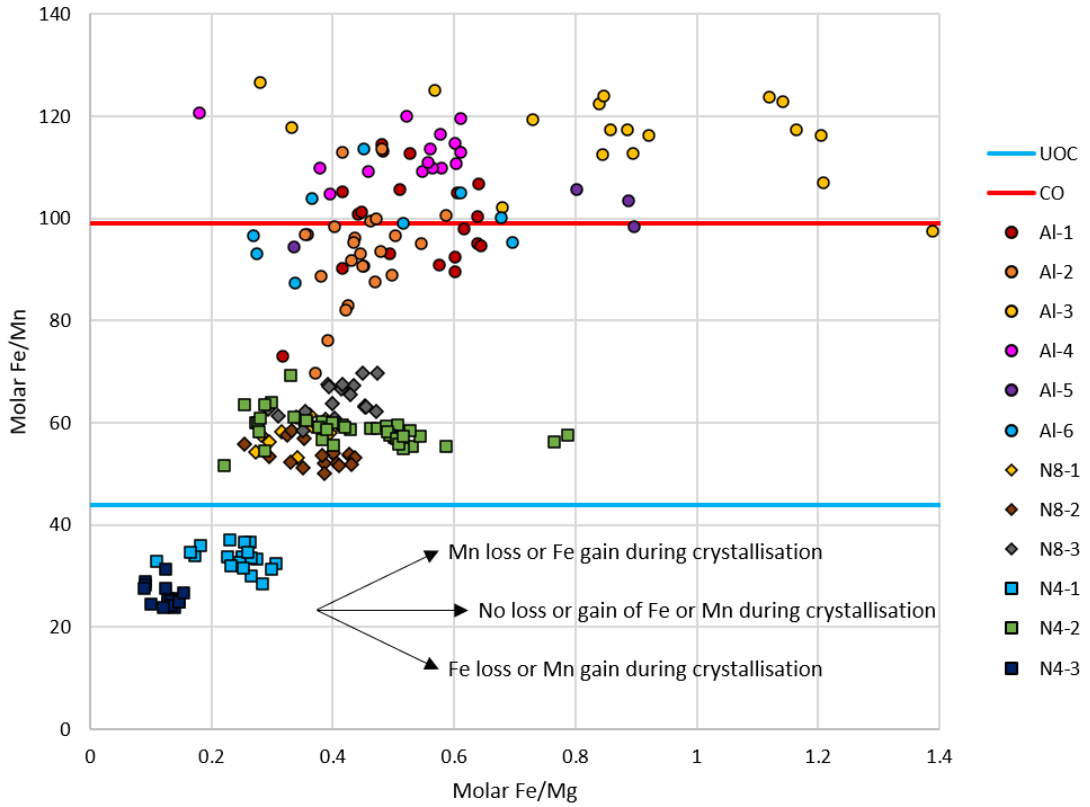

Figure 3.32 – Molar Fe/Mn vs Fe/Mg for olivine phenocrysts in all studied chondrules. The red line shows the average Fe/Mn ratio for chondrules in the CO chondrites ALHA 77307 (Jones, 1992) and Kainsaz (Berlin et al., 2011). The blue line shows the average Fe/Mn ratio in the unequilibrated ordinary chondrites Semarkona (LL3.00) (Jones, 1990), MET 00526 (L3.05), and QUE 97008 (L3.05) (Berlin et al., 2011).

would create Fe metal, which is then lost. Lower Fe/Mn ratios found in olivine phenocrysts in ordinary chondrites could be caused by the reduction of the chondrule precursor by carbon (Connolly et al., 1994) or a reducing nebular gas. Sutton et al. (1996) show that Cr^{2+} to Cr^{3+} ratio in olivine in chondrules in Semarkona (LL3.00) is higher than in chondrules in ALHA 77307 (CO3.0), suggesting that chondrules from CO chondrites might have formed in more oxidising conditions. This is consistent with the Fe/Mn ratios found in the type IIA chondrules studied here and an in the type IIA chondrules in Berlin et al. (2011).

Open system behaviour during chondrule formation, for example, evaporation or condensation of Mn during crystallisation, may cause differences in the Fe/Mn ratio between different chondrite groups. Comparing how the Fe/Mn ratio changes with the Fe/Mg ratio may indicate what processes occurred to cause the observed differing Fe/Mn ratios. Fe/Mn ratios that remain constant as Fe/Mg ratios increase suggests that crystallisation occurred without the addition or removal of Fe or Mn. Increasing Fe/Mn ratios with increasing Fe/Mg suggests loss of Mn by evaporation or addition of Fe by

oxidation of sulfides or metal during chondrule formation. Fe/Mn ratios that decrease with increasing Fe/Mg suggest the addition of Mn by condensation or loss of Fe by reduction and removal during olivine crystallisation (Berlin et al., 2011). Figure 3.32 shows a plot of the Fe/Mn ratio against the Fe/Mg ratio. Individual chondrules from all chondrites show roughly constant Fe/Mn values, suggesting minimal addition or loss of Mn or Fe occurred during chondrule formation. Similar to trends were observed in CO, L and LL chondrites by Berlin et al. (2011).

The variation of Fe/Mn ratios between different chondrite groups suggests that CO chondrites and ordinary chondrites sample spatially separate reservoirs of type II chondrules with distinct chemical properties (Berlin et al., 2011; Jones, 2012).

3.9.5 Bulk compositions and liquidus temperatures

Chondrule bulk compositions were calculated using a modal recombination analysis, which combines the proportion, average composition and density of each phase into a single bulk composition (Berlin et al., 2008). Only the silicate portions of the chondrules were included, therefore metal and sulfides were excluded. Easily resolvable weathering and alteration products have also been excluded, for example, secondary sulfide veins observed in chondrule N8-3, N4-1, and N4-3. Forsteritic-olivine grains have also been excluded as they are not part of the most recent chondrule melt. Phases that have been included in the bulk composition calculation include olivine, pyroxene, mesostasis and chromite.

The bulk composition of the studied chondrules are shown in Table 3.7. The most abundant oxides in the studied chondrules are SiO_2, FeO and MgO, which together account for >90% of the chondrules. Chondrule bulk compositions also show a spread in these major

Table 3.7 – Bulk composition of chondrules in ALHA 77307, NWA 8276 and NWA 4910 in wt %, determined by modal recombination analysis. Liquidus temperature is calculated using geochemical modelling software Petrolog3.

Chondrule	Na_2O	M_gO	Al_2O_3	SiO_2	P_2O_5	K_2O	CaO	TiO_2	Cr_2O_3	MnO	FeO	NiO	Total	Liquidus temperature (°C)
Al-1	0.26	27.52	1.78	35.39	0.36	0.01	2.21	0.19	0.83	0.28	30.36	0.48	99.66	1634
Al-2	0.26	26.50	2.18	35.19	0.37	0.02	3.17	0.21	0.83	0.27	28.67	0.85	98.52	1622
Al-3	0.35	21.34	1.75	32.44	1.43	0.04	2.52	0.15	0.27	0.30	36.00	0.83	97.43	1556
Al-4	0.13	27.98	1.08	35.73	0.42	0.02	2.22	0.20	0.95	0.27	28.97	0.84	98.81	1637
Al-5	0.33	24.17	1.59	33.86	0.69	0.05	1.56	0.08	0.17	0.29	34.64	0.76	98.19	1595
Al-6	0.11	30.91	0.55	36.59	0.69	0.00	1.97	0.13	0.39	0.27	27.28	0.13	99.00	1670
N8-1	1.62	28.62	2.73	42.16	0.32	0.01	2.72	0.15	0.63	0.33	19.68	0.10	99.08	1607
N8-2	0.56	28.99	1.58	38.58	0.30	0.06	2.01	0.16	0.77	0.39	24.65	0.65	98.71	1627
N8-3	0.43	26.40	1.32	38.87	0.53	0.11	3.68	0.23	1.26	0.32	24.66	0.22	98.03	1588
N4-1	1.10	33.34	1.86	45.78	0.07	0.12	1.21	0.09	0.62	0.50	14.85	0.20	99.76	1634
N4-2	1.42	27.40	2.76	41.17	0.57	0.06	1.60	0.09	0.77	0.39	23.00	0.51	99.75	1586
N4-3	0.96	37.45	2.39	48.28	0.02	0.13	1.05	0.10	0.58	0.40	9.10	0.08	100.53	1663

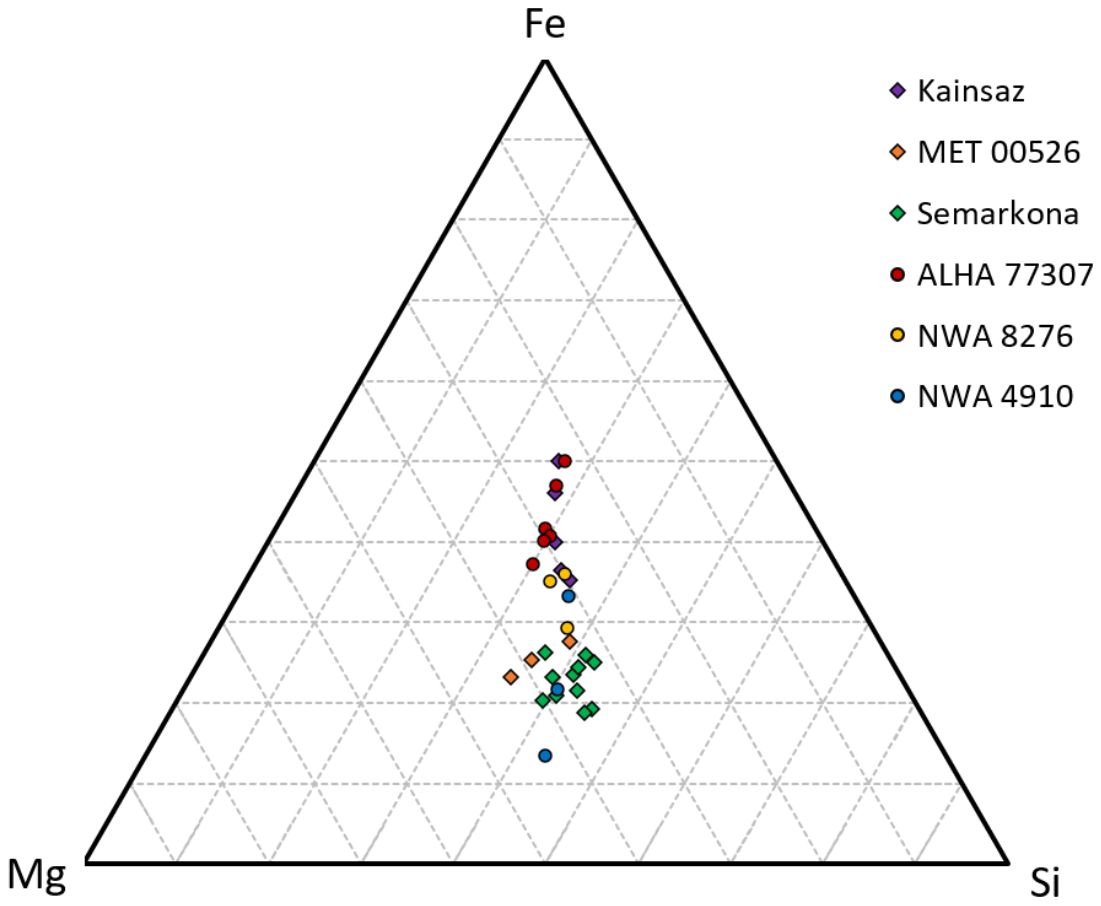

Figure 3.33 – Ternary plot for bulk element wt % Mg, Fe and Si for chondrules. Circles represent chondrules in this study from ALHA 77307, NWA 8276 and NWA 4910. Kainsaz shows the bulk compositions of five type II chondrules in Kainsaz CO3.2 from Berlin et al. (2011). MET 00526 shows the bulk composition of three type II chondrules in MET 00526 L3.05 from Berlin et al. (2011). Semarkona shows the bulk composition of 11 type II chondrules from Semarkona from Jones (1990).

elements with the chondrules in ALHA 77307 showing the most FeO-rich and SiO_2 poor bulk compositions. Totals are generally less than 100% because of low totals in mesostasis analyses, particularly in the chondrules in ALHA 77307. There is a wide range in volatile element compositions, e.g. Na_2O, with chondrules in ALHA 77307 showing much lower Na_2O contents than chondrules in NWA 8276 and NWA 4910. The high FeO and low SiO_2 content of the chondrules from ALHA 77307 is a combination of higher FeO contents in olivine in comparison to chondrules in NWA 8276 and NWA 4910, and the apparent secondary alteration of chondrule mesostasis to FeO-rich phyllosilicates. The addition of FeO to the chondrule mesostasis would result in bulk compositions with higher FeO and lower SiO_2 compositions. However, the magnitude of this effect must be limited as the bulk compositions of chondrules from ALHA 77307 are indistinguishable from relatively pristine chondrules in Kainsaz CO3.2 (see Figure 3.33) (Berlin et al., 2011).

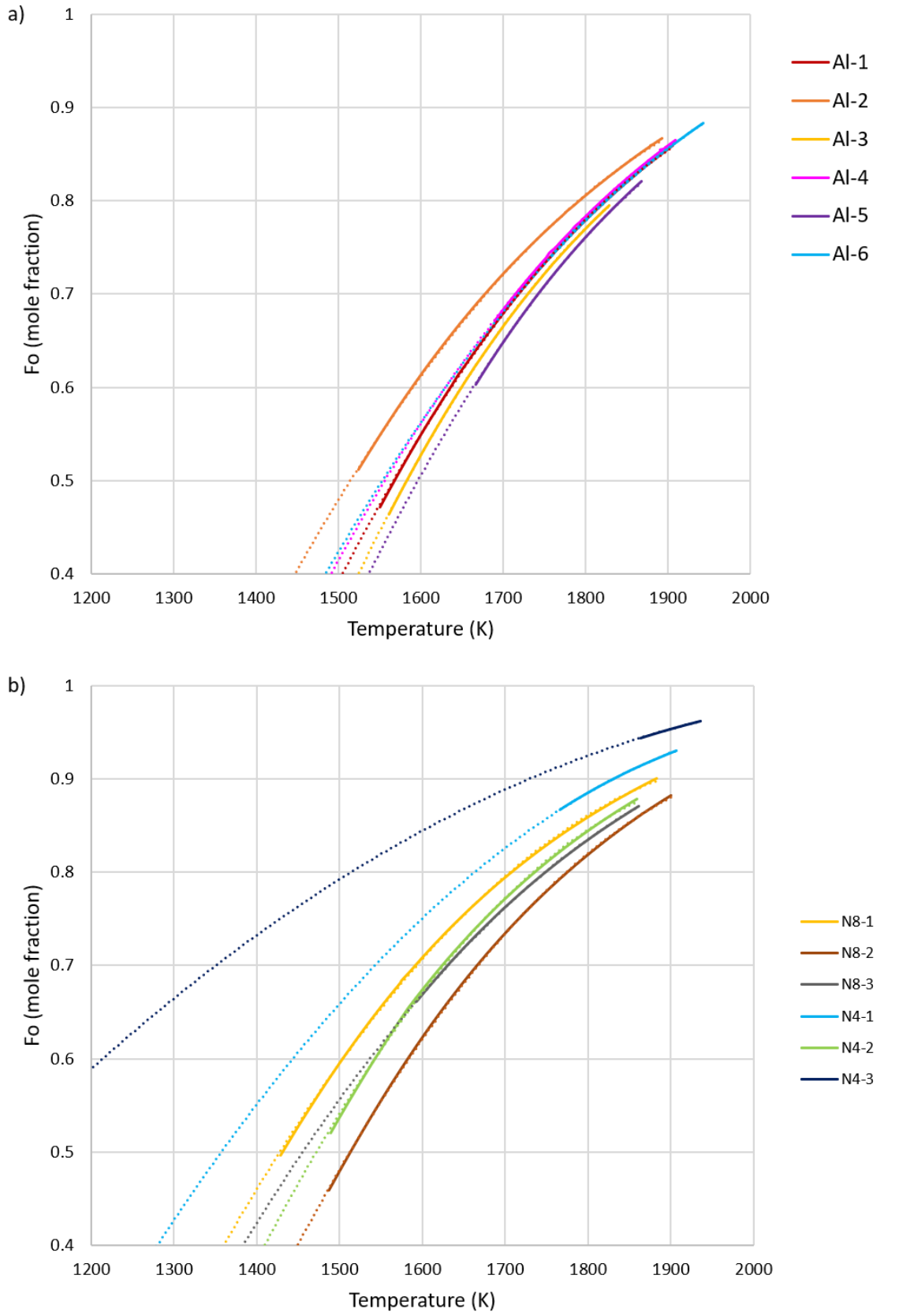

Figure 3.34 – Olivine liquidus curves calculated by modelling chondrule bulk compositions using Petrolog3 (Danyushevsky and Plechov, 2011): a) chondrules in ALHA 77307; b) chondrules in NWA 8276 and NWA 4910.

Chondrule liquidus temperatures have been calculated by modelling chondrule bulk compositions using Petrolog3 (Danyushevsky and Plechov, 2011). Chondrule bulk compositions and liquidus temperatures are shown in Table 3.7. Chondrule liquidus temperatures range from 1556 to 1670 °C. These are similar to liquidus temperatures of other type II chondrules determined in Berlin et al. (2011), who calculated liquidus temperatures of 1585 to 1770°C using MELTS (Ghiorso and Sack, 1995; Asimow and Ghiorso, 1998), and Hewins et al. (2012), who calculated liquidus temperatures of 1500 to 1718 °C using Petrolog3 (Danyushevsky and Plechov, 2011). Jones (1990) estimated chondrule liquidus temperatures to be ~1600 °C for type IIA chondrules in Semarkona by comparing chondrule bulk compositions to a ternary phase diagram of SiO_2-MgO-FeO (Bowen and Schairer, 1935). Olivine liquidus curves calculated using Petrolog3 (Danyushevsky and Plechov, 2011) are shown in Figure 3.34.

The main source of error in these calculations are whether the determined compositions of chondrule phases accurately represent the composition of the chondrule. Particularly the average olivine and mesostasis compositions. As discussed, zoning in olivine phenocrysts in the studied chondrules is pronounced and it may be that the determined average olivine composition does not accurately reflect this. In addition, mesostasis in the chondrules in ALHA 77307 is altered, therefore the determined composition may not reflect the original composition of mesostasis. Other sources of error include the accuracy of chondrule phase maps and the density of chondrule phases used in bulk composition calculations.

To test the potential effect of the alteration of chondrule mesostasis on chondrule bulk composition, liquidus temperature and olivine liquidus curves, additional calculations have been performed which substitute the altered mesostasis compositions in the ALHA 77307 chondrules with more pristine mesostasis compositions from type II chondrules in Kainsaz CO3.2 (Berlin et al., 2011). The major effect of this recalculation is to decrease the amount of FeO and increase the amount of SiO_2 in chondrule bulk compositions. This is visible as a shift towards Si in the ternary plot (see Figure 3.35) and a considerable increase in Na_2O and Al_2O_3 content. The change in bulk composition also results in a reduction in calculated liquidus temperatures of between 37 and 70 °C (see Table 3.8). This also changes the shape

Table 3.8 – Comparison of liquidus temperatures calculated using original mesostasis composition and liquidus temperatures calculated with substituted mesostasis composition.

Chondrule	Original liquidus temperature (°C)	Recalculated liquidus temperature (°C)	Difference in liquidus temperature (°C)
Al-1	1634	1597	37
Al-2	1622	1569	53
Al-3	1556	1519	37
Al-4	1637	1567	70
Al-5	1595	1527	68
Al-6	1670	1602	68

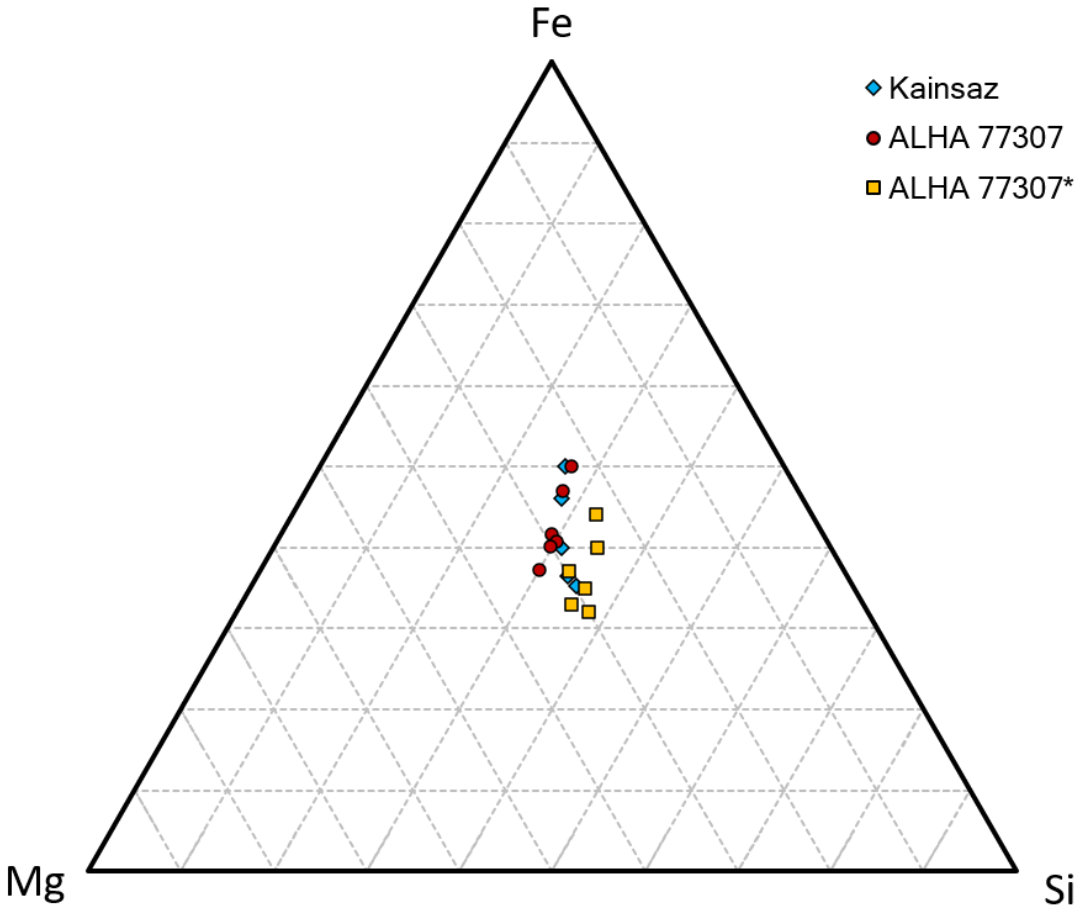

Figure 3.35 – Ternary plot for bulk element wt % Mg, Fe and Si for chondrules in ALHA 77307. Red circles represent the bulk composition of chondrules in this study. Blue diamonds represent the bulk composition of chondrules in type II chondrules in Kainsaz CO3.2 from Berlin et al. (2011). Yellow squares represent the bulk composition of chondrules from ALHA 77307 where chondrule mesostasis compositions have been substituted for mesostasis compositions of type II chondrules in Kainsaz (Berlin et al., 2011). There is a shift towards more Si-rich compositions between the original compositions (red circles) and substituted compositions (yellow squares). Both share similarities to the bulk composition of chondrules in Kainsaz.

of olivine liquidus curves for these chondrules (see Figure 3.36) and causes equivalent forsterite compositions to occur at lower temperatures in the curves where mesostasis compositions have been substituted. This suggests that chondrule liquidus temperatures may have been overestimated and the effects of this need to be considered when discussing the results of diffusion modelling.

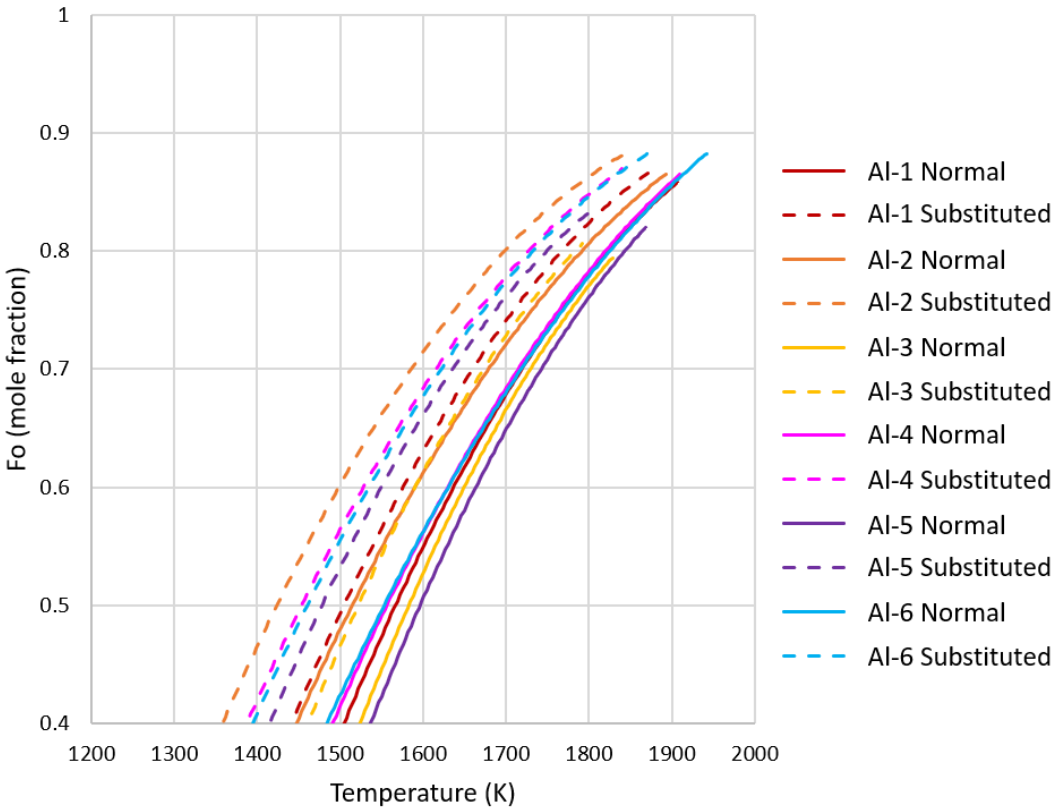

Figure 3.36 – Olivine liquidus curves calculated by modelling chondrule bulk compositions using Petrolog3 (Danyushevsky and Plechov, 2011) for chondrules in ALHA 77307. Full lines show the curves from the unmodified bulk compositions. Dashed lines show curves from compositions where mesostasis compositions have been substituted for mesostasis compositions from type II chondrules in Kainsaz CO3.2 (Berlin et al. 2011).

3.10 Summary and conclusions

The petrography of twelve chondrules in three chondrites, ALHA 77307 (CO3.00), NWA 8276 (L3.00) and NWA 4910 (LL3.1) has been studied. All the studied chondrules are type II, FeO-rich chondrules with porphyritic textures. Most chondrules are dominated by olivine phenocrysts and are therefore type IIA porphyritic olivine chondrules. However, two chondrules in NWA 4910, N4-1 and N4-3, contain significant quantities of pyroxene and are therefore type IIAB porphyritic olivine and pyroxene chondrules. Similar textures have been reproduced at cooling rates of 10 to 1000 Kh^{-1} in dynamic crystallisation experiments (Lofgren and Russell, 1986; Radomsky and Hewins, 1990; Connolly and Hewins, 1991; Jones and Lofgren, 1993; Kennedy et al., 1993; Connolly and Hewins, 1995; Connolly et al., 1998; Weinbruch et al., 1998).

The observed trends in olivine composition of the studied chondrules are generally consistent with closed-system fractional crystallisation (e.g. Jones 1990). Fe-Mn

systematics show that there is little evidence of significant open system behaviour in these chondrules, with no or only minimal evidence of evaporation or condensation of Mn, a moderately volatile element, during olivine crystallisation. Fe-Mn systematics also show that there is a significant difference in the Fe/Mn ratio between type IIA chondrules in CO chondrite ALHA 77307 and the ordinary chondrites NWA 8276 and NWA 4910. The average Fe/Mn ratio for chondrules in ALHA 77307 is 104, whereas for type IIA chondrules in the ordinary chondrites NWA 8276 and NWA 4910, the average Fe/Mn ratio is 59. For the type IIAB chondrules, Fe/Mn is even less, ~30. These trends observed in the type IIA chondrules are similar to trends in observed by Berlin et al. (2011) for type IIA chondrules in CO, L and LL chondrites. As there is little evidence for open system addition or removal of Mn from these chondrules, these differences must be caused by differences in the chondrule precursors; perhaps the precursors of type IIA chondrules in CO chondrites had a higher proportion of sulfides in comparison to ordinary chondrites (Berlin et al., 2011). The presence of similar textures across different chondrite groups, which display differences in olivine compositions and Fe-Mn systematics suggests that the different chondrite classes and groups sample different chondrule precursor reservoirs which experienced similar chondrule formation processes (Jones, 2012).

Chondrule bulk compositions vary between the three studied chondrite groups. ALHA 77307 shows the most FeO-rich and SiO_2-poor chondrules. This likely reflects the alteration of mesostases in these chondrules. Despite this, calculated liquidus temperatures for these chondrules span a similar range to the ordinary chondrites, which show more pristine mesostases. These temperatures are also similar to liquidus temperatures determined in Berlin et al. (2011), Hewins et al. (2012) and Jones (1990). In addition, these bulk compositions are similar to those obtained for type II chondrules in Kainsaz CO3.2 by Berlin et al. (2011). However, substituting the altered mesostasis compositions in the studied chondrules in ALHA 77307 for unaltered mesostasis compositions from type II chondrules in Kainsaz CO3.2 from Berlin et al. (2011) altered chondrule bulk compositions. This results in higher SiO_2 and lower FeO contents in the studied chondrules, which also reduces chondrule liquidus temperature. The possibility that chondrule liquidus temperatures have been overestimated will need to be considered going forwards.

Chapter 4
Petrography of forsteritic-olivine relict grains

This chapter describes the petrography of the forsteritic-olivine relict grains found in the twelve chondrules selected from ALHA 77307, NWA 8276 and NWA 4910. These forsteritic-olivine relict grains are evidence that chondrule recycling was a prevalent process in the protoplanetary disk. Type II porphyritic chondrules containing forsteritic-olivine relict grains must have formed from a minimum of two melting events. An initial melting event under reducing conditions formed a type I chondrule containing MgO-rich olivine followed by possible break up of this chondrule. A second melting event, under more oxidising conditions, incompletely melted MgO-rich material from this type I chondrule, to produce a type II chondrule containing unmelted forsteritic-olivine relict grains and relatively FeO-rich olivine. Compositional profiles measured in the forsteritic-olivine relict grains indicate that they were equilibrating with the chondrule melt during chondrule cooling, which provides an opportunity to study chondrule cooling rates.

4.1 Petrography and composition of forsteritic-olivine relict grains

Each of the studied chondrules in ALHA 77307, NWA 8276, and NWA 4910 contain at least one forsteritic-olivine relict grain. These are identified in BSE images as dark patches within lighter grey olivine phenocrysts (see Figure 4.1). These grains are generally anhedral, showing rounded edges, indicating they experienced resorption during the formation of the host chondrule (Jones, 1990). They are surrounded by more FeO-rich, normally zoned olivine, similar in composition to olivine phenocrysts present in the host chondrule. The interface between the forsteritic-olivine relict grain and the surrounding overgrowth is diffuse, which has been taken to indicate that exchange took place between the two zones (Wasson and Rubin, 2003). The studied relict grains range in diameter from 17 to 118 µm, with those in chondrules in ALHA 77307 showing the greatest size variation. Three of the grains (Al-1 RG1, Al-6 RG1, and N4-3 RG1) contain inclusions of Fe,Ni metal.

Individual EPMA analyses of these grains, shown in Table 4.1, confirm that they are very MgO-rich, with forsterite contents above Fo_{90} with many approaching Fo_{100}. Minor element concentrations of these grains vary and have CaO and Cr_2O_3 compositions ranging from 0.06 to 1.02 wt % for CaO and 0.07 to 0.55 wt % for Cr_2O_3. Forsteritic-olivine relict grains in NWA 4910 show high CaO contents, generally higher than olivine crystals in the host chondrule, while Cr_2O_3 is generally low in these grains (see Figure 4.2 and

Table 4.1 – Single EPMA point analyses showing the composition of forsteritic-olivine relict grains determined by EPMA. Major and minor elements in wt %, Forsterite content in mol %, calculated from EPMA measurements.

Forsteritic-olivine relict grain	Na_2O	MgO	Al_2O_3	SiO_2	P_2O_5	K_2O	CaO	TiO_2	Cr_2O_3	MnO	FeO	NiO	Total	Fo
Al-1 RG1	<0.05	56.4	<0.05	42.4	<0.09	<0.02	0.16	<0.04	0.55	0.18	1.75	0.06	101.5	98.3
Al-2 RG1	<0.05	55.9	<0.05	42.8	<0.09	<0.02	0.25	<0.04	0.54	0.13	1.98	<0.06	101.5	98.0
Al-3 RG1	<0.05	56.7	0.11	41.0	<0.09	<0.02	0.46	0.08	0.34	0.06	1.24	<0.06	100.1	98.8
Al-4 RG1	<0.05	56.3	0.30	42.4	<0.09	<0.02	0.62	0.12	0.07	<0.03	1.67	<0.06	101.6	98.4
Al-5 RG1	<0.05	52.4	<0.05	41.2	<0.09	<0.02	0.18	<0.04	0.30	0.26	5.67	<0.06	100.0	94.3
Al-5 RG2	<0.05	49.3	0.17	40.0	<0.09	<0.02	0.33	0.09	0.27	0.13	9.30	0.10	99.8	90.5
Al-6 RG1	<0.05	56.5	0.24	42.8	<0.09	<0.02	0.41	0.20	0.35	0.05	1.22	<0.06	101.8	98.8
N8-1 RG1	<0.05	55.4	0.05	40.4	<0.09	<0.02	0.46	<0.04	0.30	<0.03	2.15	<0.06	98.8	97.9
N8-2 RG1	<0.05	53.2	0.71	41.7	<0.09	<0.02	0.58	0.07	0.48	0.06	3.43	0.10	100.4	96.5
N8-3 RG1	<0.05	52.9	<0.05	40.9	<0.09	<0.02	0.06	<0.04	0.22	0.10	5.34	<0.06	99.5	94.6
N4-1 RG1	<0.05	54.9	0.29	42.5	<0.09	<0.02	0.71	0.05	0.22	<0.03	1.97	0.13	100.8	98.0
N4-2 RG1	<0.05	55.0	0.05	42.9	<0.09	<0.02	1.02	<0.04	0.10	<0.03	1.08	<0.06	100.2	98.9
N4-3 RG1	<0.05	55.0	0.97	42.2	<0.09	<0.02	0.85	0.09	0.07	0.04	0.83	0.17	100.3	99.2

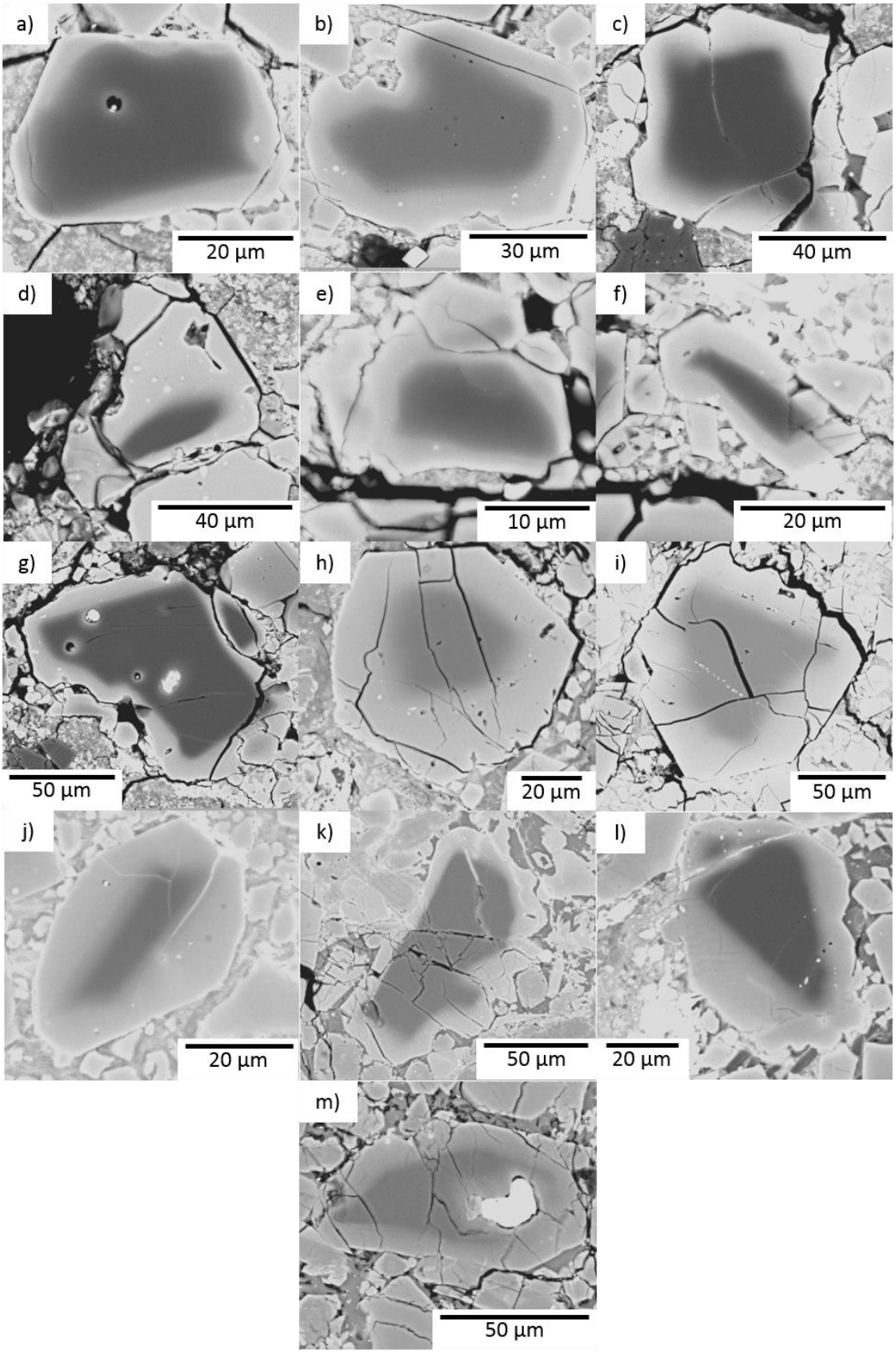

Figure 4.1 – BSE images of 13 forsteritic olivine relict grains present in type II chondrules in ALHA 77307, NWA 8276 and NWA 4910: a) Al-1 RG1; b) Al-2 RH1; c) Al-3 RG 1; d) Al-4 RG1; e) Al-5 RG1; f) Al-5 RG2; g) Al-6 RG1; h) N8-1 RG1; i) N8-2 RG1; j) N8-3 RG1; k) N4-1 RG1; l) N4-2 RG1; m) N4-3 RG1. Contrast settings are different between each BSE image therefore contrast is not an indicator of relative composition between grains.

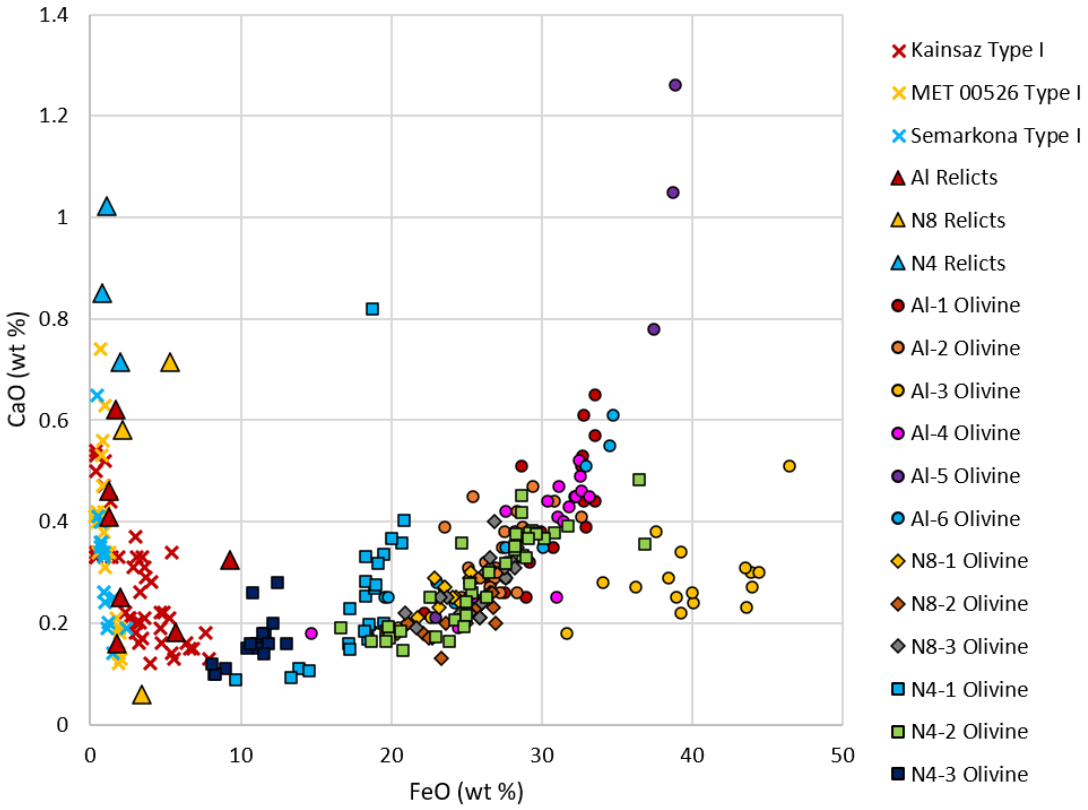

Figure 4.2 – CaO vs FeO for forsteritic-olivine relict grains and olivine phenocrysts in all studied chondrules compared to compositions of olivine in type I chondrules in Kainsaz CO3.2, MET 00526 L3.05 (Berlin, 2010), and Semarkona LL3.00 (Jones and Scott, 1989). Large triangles represent individual EPMA analyses of forsteritic-olivine relict grains in the studied chondrules; circles represent analyses of olivine phenocrysts in type II chondrules in ALHA 77307; diamonds represent analyses of olivine phenocrysts in type II chondrules in NWA 8276; squares represent analyses of olivine phenocrysts in type II chondrules in NWA 4910; and crosses represent analyses of olivine phenocrysts in type I chondrules in Kainsaz, MET 00526, and Semarkona.

Figure 4.3). Overall, MnO compositions are low, generally lower than olivine phenocrysts in host chondrules. There may be a weak relationship between Mn and Fe; grains with higher Fe compositions tend to have higher Mn compositions (see Figure 4.4).

There are several lines of evidence to indicate that these forsteritic grains did not crystallise *in situ* but are relict grains of chondrule precursor material that survived the melting event associated with chondrule formation. Firstly they have very high forsterite compositions which could not have crystallised from the chondrule melt according to fractional crystallisation modelling of the chondrule bulk compositions in Chapter 3 – Chondrule petrography using Petrolog3 (Danyushevsky and Plechov, 2011). This is supported by fractional crystallisation calculations in Jones (1990) for type IIA chondrules containing forsteritic-olivine relict grains in Semarkona. The forsteritic-olivine relict grains in Semarkona chondrules, as well as the chondrules studied here, have rounded, anhedral

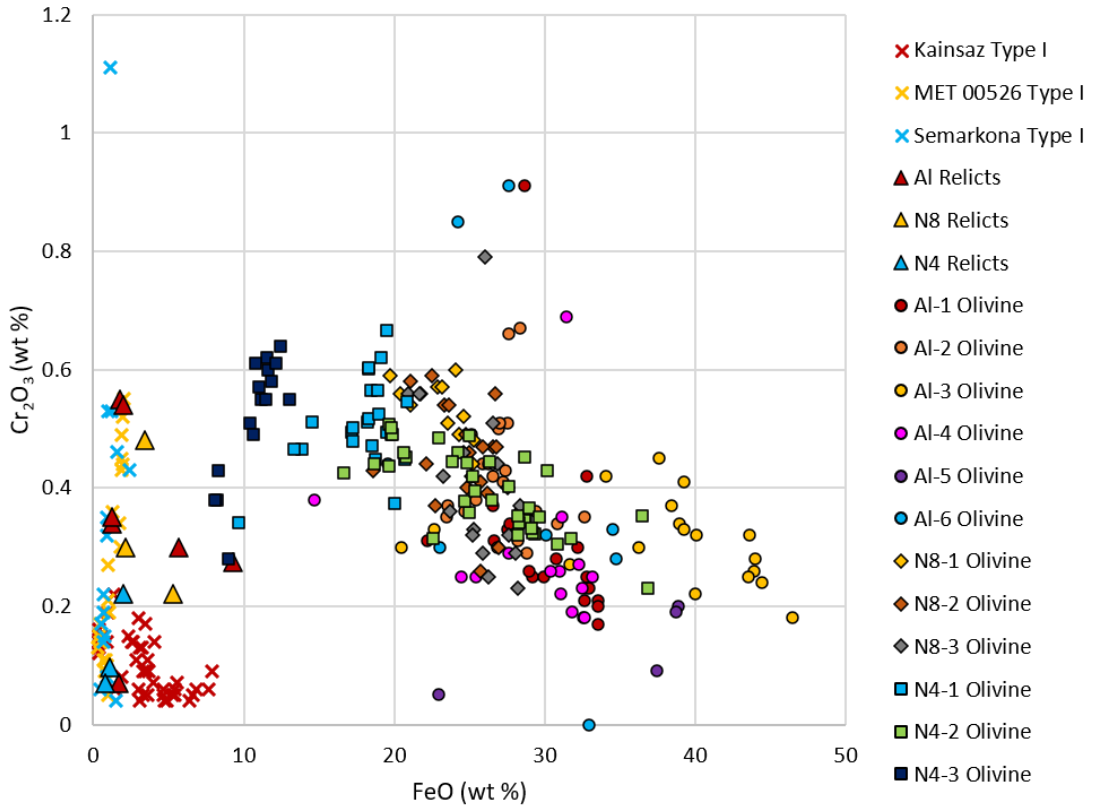

Figure 4.3 – Cr_2O_3 vs FeO for forsteritic-olivine relict grains and olivine phenocrysts in all studied chondrules compared to compositions of olivine in type I chondrules in Kainsaz CO3.2, MET 00526 L3.05 (Berlin, 2010), and Semarkona LL3.00 (Jones and Scott, 1989). Large triangles represent individual EPMA analyses of forsteritic-olivine relict grains in the studied chondrules; circles represent analyses of olivine phenocrysts in type II chondrules in ALHA 77307; diamonds represent analyses of olivine phenocrysts in type II chondrules in NWA 8276; squares represent analyses of olivine phenocrysts in type II chondrules in NWA 4910; and crosses represent analyses of olivine phenocrysts in type I chondrules in Kainsaz, MET 00526, and Semarkona.

morphologies indicating that they experienced resorption into the chondrule melt during chondrule crystallisation. Together, these observations imply that the relict grains must have been present in the chondrule precursor assemblage. Forsteritic-olivine relict grains have similar compositions to forsterite grains present in type IA chondrules (Jones and Scott, 1989; Jones, 1990; Jones, 1992) (see Figure 4.2 to Figure 4.5), suggesting that the relict olivine grains originate from type I chondrules. Another link between the forsteritic-olivine relict grains and type I chondrules is the presence of Fe,Ni metal inclusions in the relict grains. These are generally absent in olivine phenocrysts in type II chondrules, where troilite and chromite inclusions are more common. However, Fe,Ni metal inclusions are common in type IA chondrules, adding to the suggestion that forsteritic-olivine relict grains originate mainly from type I chondrules (Jones, 1990). Forsteritic-olivine relict grains have oxygen isotope compositions which are in isotopic disequilibrium, i.e. distinct $\Delta^{17}O$, with

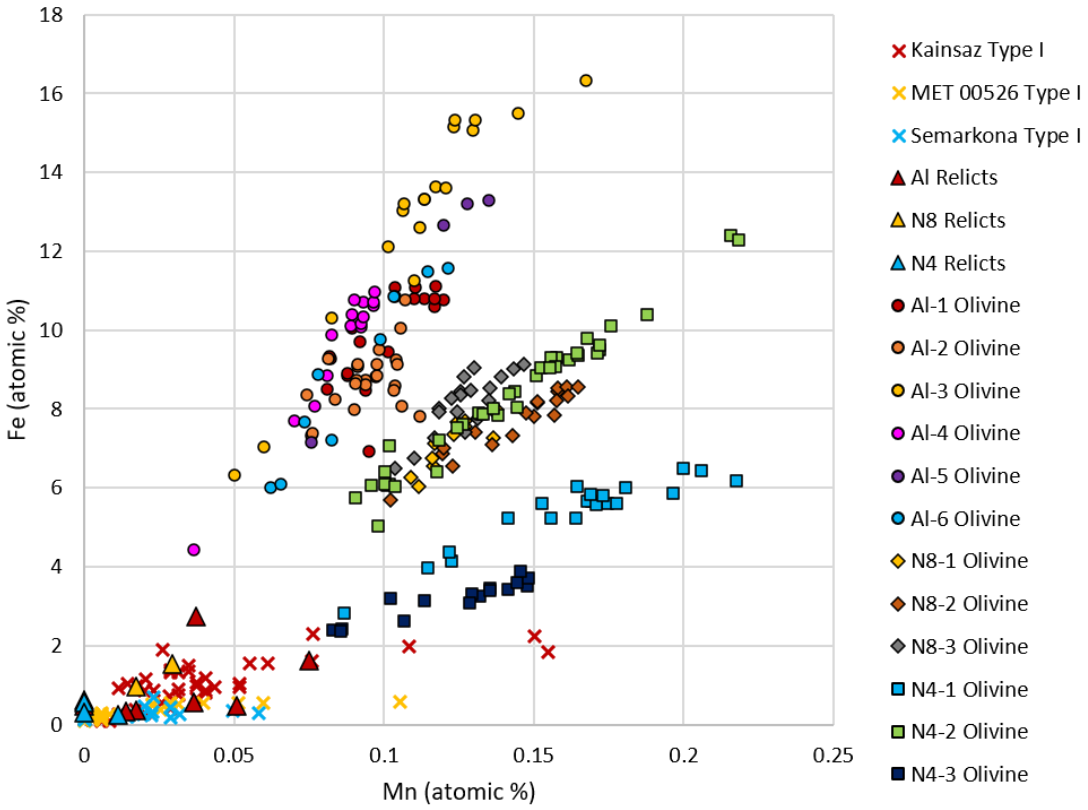

Figure 4.4 – Fe vs Mn for forsteritic-olivine relict grains and olivine phenocrysts in all studied chondrules compared to compositions of olivine in type I chondrules in Kainsaz CO3.2, MET 00526 L3.05 (Berlin, 2010), and Semarkona LL3.00 (Jones and Scott, 1989). Large triangles represent individual EPMA analyses of forsteritic-olivine relict grains in the studied chondrules; circles represent analyses of olivine phenocrysts in type II chondrules in ALHA 77307; diamonds represent analyses of olivine phenocrysts in type II chondrules in NWA 8276; squares represent analyses of olivine phenocrysts in type II chondrules in NWA 4910; and crosses represent analyses of olivine phenocrysts in type I chondrules in Kainsaz, MET 00526, and Semarkona.

the host chondrule. This also confirms that these grains are relict and did not crystallise from the chondrule melt. A complementary relationship is often observed between the oxygen isotopic compositions of type I chondrule olivine phenocrysts and forsteritic-olivine relict grains in type II chondrules (Ruzicka et al., 2007; Ushikubo et al., 2012; Tenner et al., 2018), again suggesting forsteritic-olivine relict grains originate from type I chondrules .

4.1.1 Vapour fractionation

As well as igneous fractionation, olivine compositions in chondrules may also have been established by interactions with surrounding gases, for example, through vaporisation and condensation of volatile elements. Plots of refractory elements (e.g. Ca, Al and Ti) vs volatile elements (e.g. Mn) can be used to recognise whether vapour fractionation is occurring in

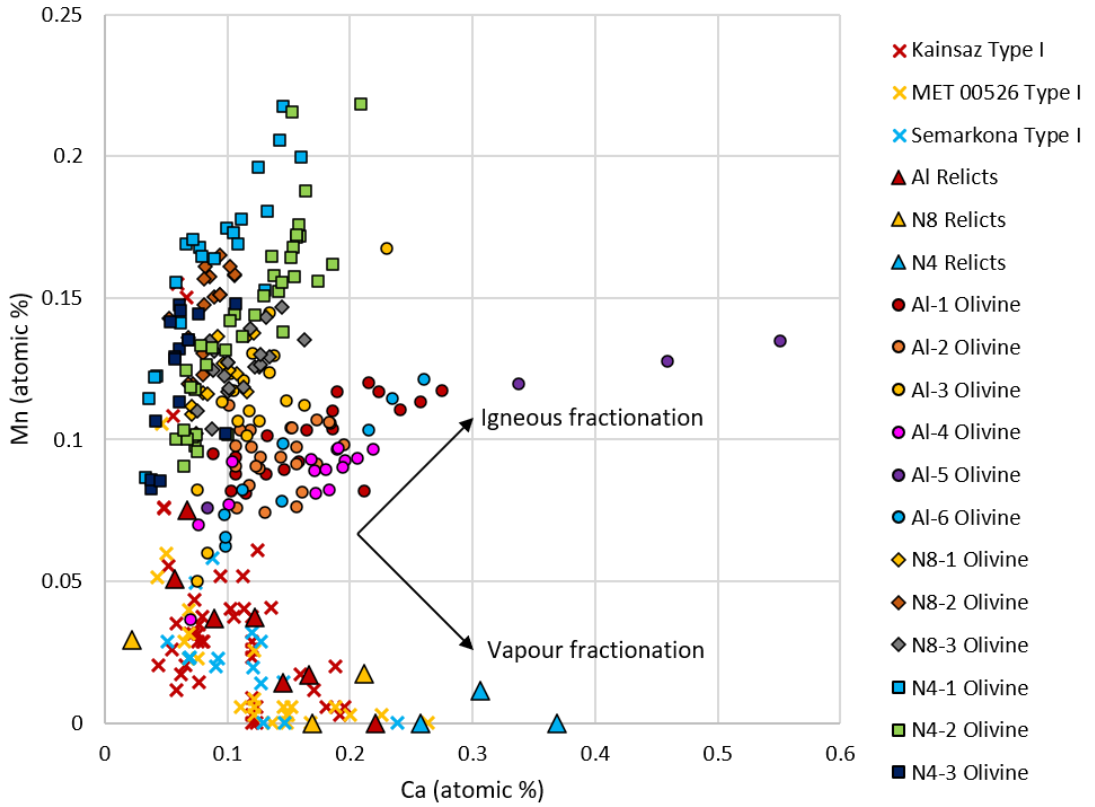

Figure 4.5 – Mn vs Ca for forsteritic-olivine relict grains and olivine phenocrysts in all studied chondrules compared to compositions of olivine in type I chondrules in Kainsaz CO3.2, MET 00526 L3.05 (Berlin, 2010), and Semarkona LL3.00 (Jones and Scott, 1989). Large triangles represent individual EPMA analyses of forsteritic-olivine relict grains in the studied chondrules; circles represent analyses of olivine phenocrysts in type II chondrules in ALHA 77307; diamonds represent analyses of olivine phenocrysts in type II chondrules in NWA 8276; squares represent analyses of olivine phenocrysts in type II chondrules in NWA 4910; and crosses represent analyses of olivine phenocrysts in type I chondrules in Kainsaz, MET 00526, and Semarkona.

chondrules. Figure 4.5 shows the variation of Ca (refractory) with Mn (volatile) for relict and normal olivine grains in the studied chondrules. As Ca and Mn are both incompatible in these olivine grains, normal igneous fractionation because of fractional crystallisation results in increasing Mn with increasing Ca. If vapour fractionation is occurring, Mn evaporates as crystallisation progresses creating the opposite trend, decreasing Mn with increasing Ca. FeO-rich olivine grains in all studied chondrules show a normal igneous fractionation trend, suggesting that fractional crystallisation is the dominant process in these chondrules. Olivine in the chondrules from the ordinary chondrites NWA 8276 and NWA 4910 are much more enriched in moderately volatile Mn and show a much steeper positive trend than chondrules from the CO chondrite ALHA 77307. This suggests that vapour fractionation may have been a more important process in the formation of chondrules from ALHA 77307. However, the Fe-Mn systematics of the studied chondrules

shown in chapter 3, Figure 3.32 suggest that no open system addition or removal of Mn was taking place. The observed differences must, therefore, represent differences in the precursor assemblages.

The forsteritic-olivine relict grains in the chondrules studied here show decreasing Mn with increasing Ca, which is the opposite trend to fractional crystallisation. This may suggest that vapour fractionation was taking place in the precursor chondrules for the forsteritic-olivine relict grains. However, the observed trend in the forsteritic-olivine relict grains is between different chondrules and therefore the relationship is not fully clear. This trend could indicate that the precursor chondrules experienced different degrees of a common process from a relatively homogeneous starting material. The same trend is found in olivine phenocrysts in type I chondrules in Semarkona L3.00 (Jones and Scott, 1989), MET 00526 L3.05 and Kanisaz CO3.2 (Berlin, 2010) (see Figure 4.5) as well as for forsteritic-olivine relict grains in type II chondrules and olivine phenocrysts in type I chondrules in five other LL chondrites (Ruzicka et al., 2008). This further strengthens the link between the forsteritic-olivine relict grains and type I chondrules. It also suggests that these type I chondrules and type I chondrules which were precursors of forsteritic-olivine relict grains in type II chondrules experienced significant vapour fractionation leaving them depleted in volatile elements (Ruzicka et al., 2008).

4.2 Compositional profiles

4.2.1 Fe-Mg compositional profiles

Compositional profiles across the boundary between the forsteritic-olivine relict grain and the surrounding overgrowth were determined from calibrated BSE greyscale images, an approach that has been used in other studies to measure compositional profiles in olivine crystals (e.g. Hartley et al. 2016; Martin et al. 2008). High-resolution BSE images of forsteritic-olivine relict grains were calibrated to Fo values from EPMA measurements of the forsteritic-olivine relict grains and overgrowths using the calibrate function in open source software ImageJ (Schneider et al., 2012), producing linear calibration curves. As the electron microprobe integrates signal from across the beam interaction volume in the sample, analyses were calibrated to average greyscale values within a circle with a diameter of several micrometres located at the same spot as the analysis. Images of the grains were generated with different brightness and contrast settings; therefore, each image requires

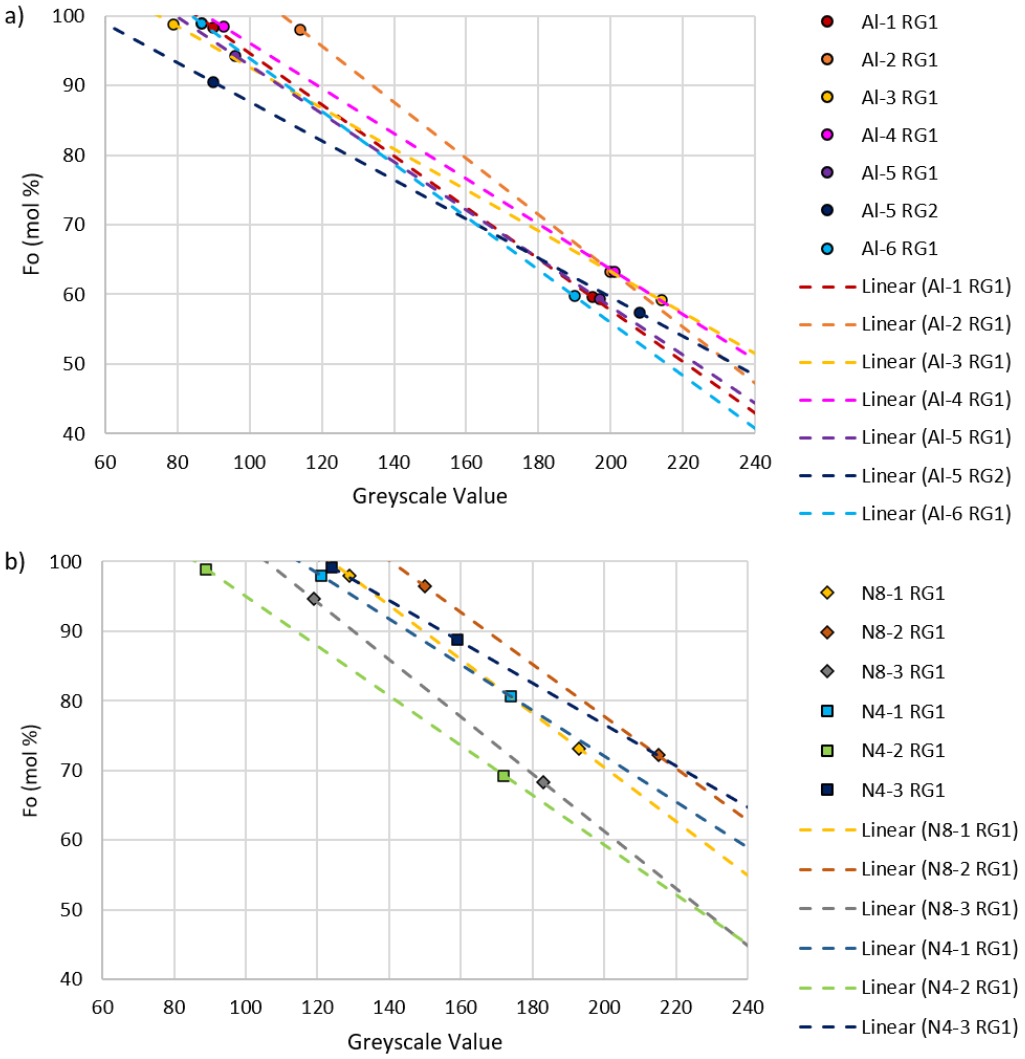

Figure 4.6 – Calibration curves for a) relict grains in type II chondrules in ALHA 77307 and b) relict grains in type II chondrules in NWA 8276 and NWA 4910.

Table 4.2 – BSE greyscale calibration to forsterite composition (mole %) taken from EPMA measurements.

Forsteritic-olivine relict grain	Forsterite composition of grain (%)	Greyscale value of grain	Forsterite composition of overgrowth (%)	Greyscale value of overgrowth	Equation x = greyscale value Fo= forsterite composition
Al-1 RG1	98.3	90	59.6	195	Fo = -0.369x + 131
Al-2 RG1	98.0	114	63.3	200	Fo = -0.404x + 144
Al-3 RG1	98.8	79	59.1	214	Fo = -0.294x + 122
Al-4 RG1	98.4	93	63.3	201	Fo = -0.325x + 129
Al-5 RG1	94.3	96	59.3	197	Fo = -0.347x + 128
Al-5 RG2	90.5	90	57.4	208	Fo = -0.281x + 116
Al-6 RG1	98.8	87	59.7	190	Fo = -0.380x + 132
N8-1 RG1	97.9	129	73.1	193	Fo = -0.388x + 148
N8-2 RG1	96.5	150	72.2	215	Fo = -0.374x + 153
N8-3 RG1	94.6	119	68.3	183	Fo = -0.411x + 144
N4-1 RG1	98.0	121	80.6	174	Fo = -0.335x + 138
N4-2 RG1	98.9	89	69.3	172	Fo = -0.357x + 131
N4-3 RG1	99.2	124	88.8	159	Fo = -0.297x + 136

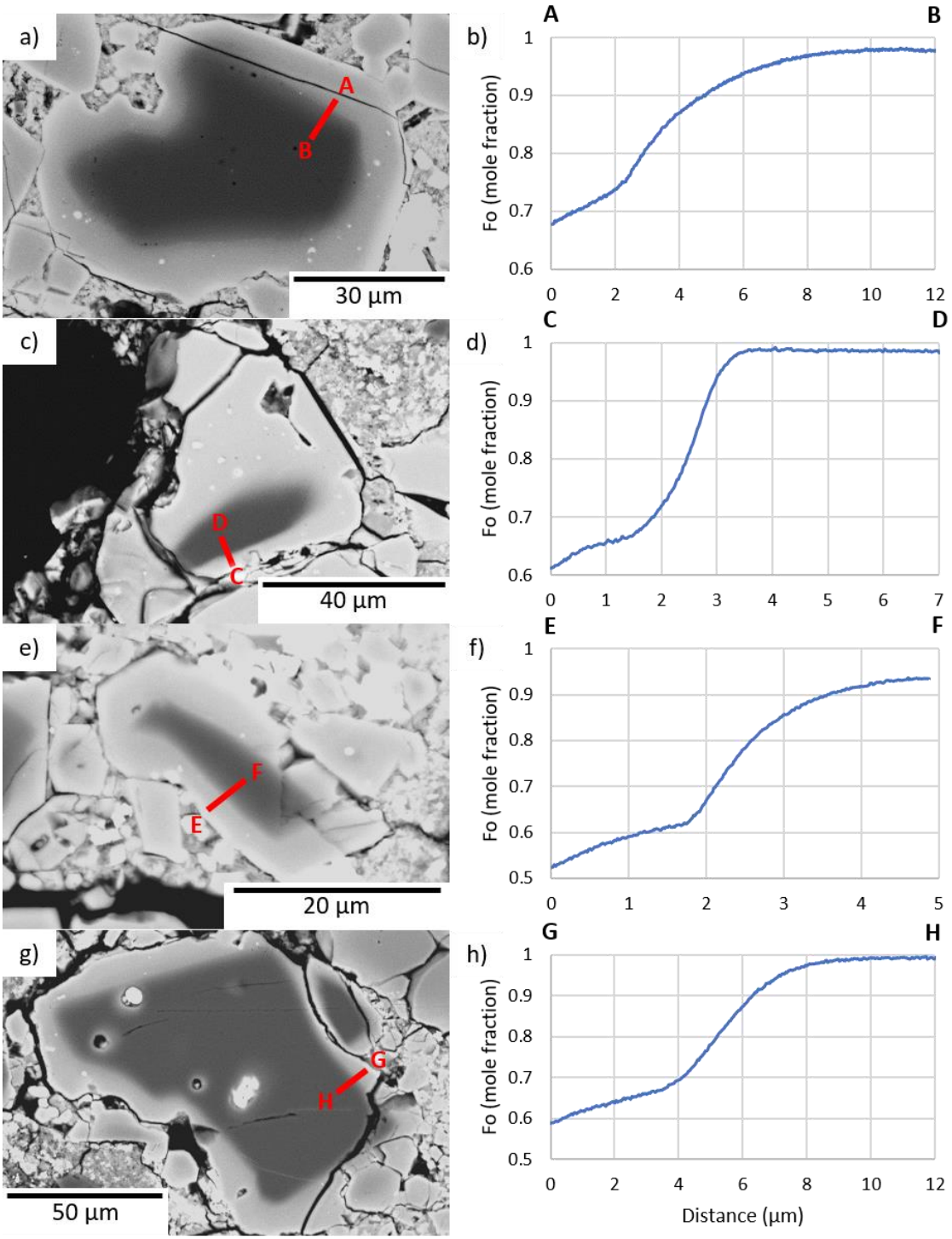

Figure 4.7 – BSE images of forsteritic-olivine relict grains in ALHA 77307 and compositional profiles measured using calibrated BSE greyscales: a) BSE image of Al-2 RG1 showing the location of profile AB; b) profile AB; c) BSE image of Al-4 RG1 showing the location of profile CD; d) profile CD; e) BSE image of Al-5 RG2 showing location of profile EF; f) profile EF; g) BSE image of Al-6 RG1 showing the location of profile GH; h) profile GH.

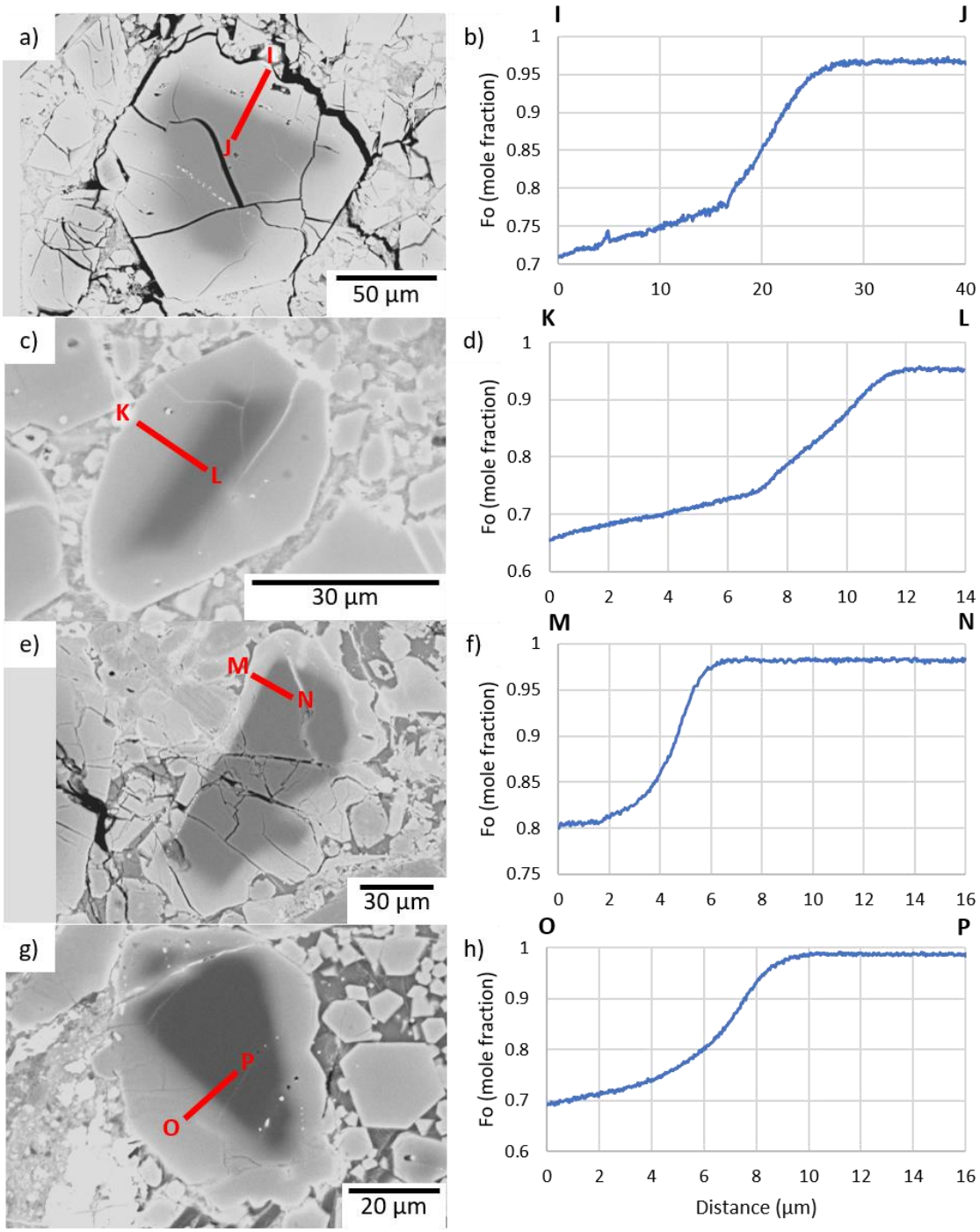

Figure 4.8 – BSE images of forsteritic-olivine relict grains in the ordinary chondrites, NWA 8276 and NWA 4910, and compositional profiles measured using calibrated BSE greyscales: a) BSE image of N8-2 RG1 showing the location of profile IJ; b) profile IJ; c) BSE image of N8-3 RG1 showing the location of profile KL; d) profile KL; e) BSE image of N4-1 RG1 showing the location of profile MN; f) profile MN; g) BSE image of N4-2 RG1 showing the location of profile OP; h) profile OP.

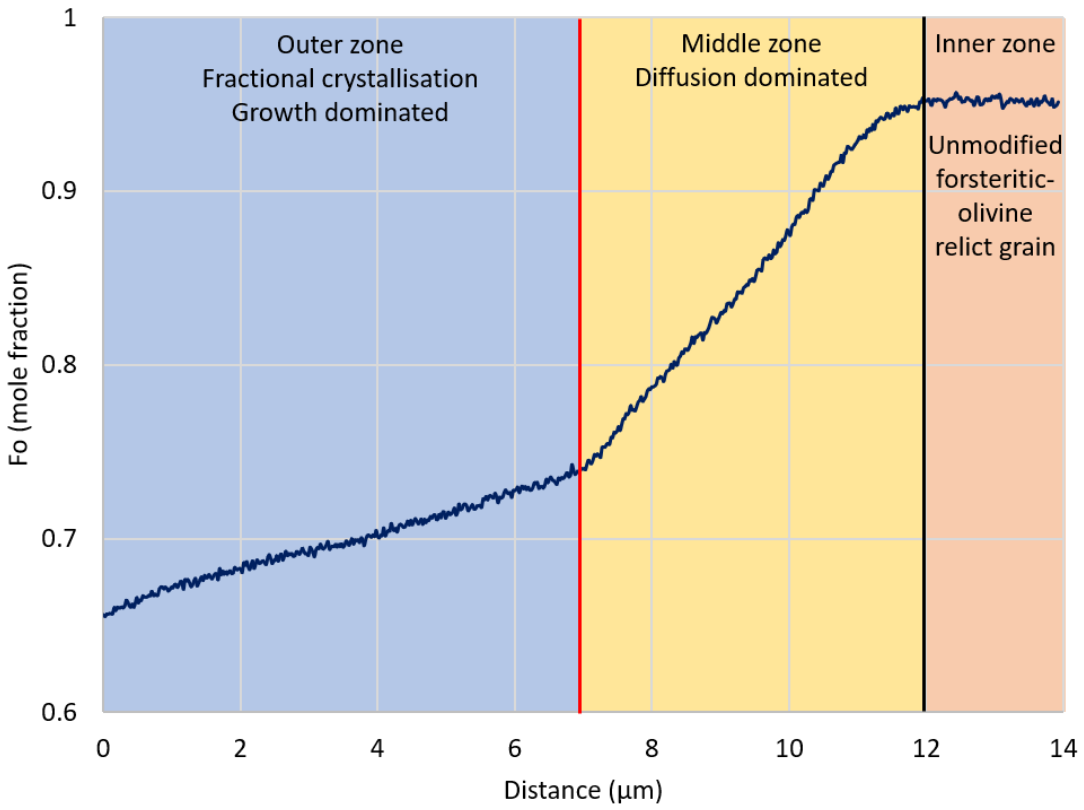

Figure 4.9 – Profile KL from forsteritic-olivine relict grain N8-3 RG1 annotated to show the different zones within the grain. The blue zone to the left shows a growth dominated, normally zoned fractional crystallisation trend. The orange zone on the right shows unmodified forsteritic-olivine in the forsteritic-olivine relict grain. The yellow zone is forsteritic-olivine that has been modified by diffusion from the chondrule melt during chondrule cooling. The red vertical line shows the boundary between the forsteritic-olivine relict grain and the overgrowth and the black vertical line shows the approximate location of the boundary between modified and unmodified forsteritic-olivine relict grain.

its own calibration. These calibration curves are shown in Figure 4.6. Compositional profiles were extracted from the BSE images using the line function in ImageJ; a line width of 50 or 100 pixels, typically ~0.5 to 3 µm wide, was used to reduce noise in the measured profiles. Spatial resolution of the BSE images ranges from 200 to 400 nm as discussed in Chapter 2 - Samples and analytical methods.

Representative calibrated BSE compositional profiles from forsteritic-olivine relict grains in chondrules in ALHA 77307 are shown in Figure 4.7 and profiles for grains in NWA 8276 and NWA 4910 are shown in Figure 4.8. The compositional profiles do not show a simple normal zoning trend but rather display 2 to 3 distinct zones, shown in Figure 4.9. The innermost of these zones is a highly forsteritic plateau representing unmodified forsteritic-olivine relict material (orange zone on right in Figure 4.9). This section is not zoned as the olivine phenocrysts in the precursor type I chondrules may have been able to maintain equilibrium

with the chondrule melt as they crystallised (Jacquet et al., 2015). This zone is present in most grains, however is less obvious or absent in some, for example profile EF in Al-5 RG2 (see Figure 4.7f), where diffusional modification has progressed into the centre of the grain. The outermost zone shows a normal zoning trend, formed by crystal growth during fractional crystallisation as the chondrule melt cooled (blue zone on left in Figure 4.9). Between these two zones is a third zone (yellow in middle in Figure 4.9) comprising a steep compositional gradient, curving down from the highly forsteritic core of the relict grain to compositions similar to the overgrowth. This is caused by exchange between the forsteritic-olivine relict grain and its surroundings as the chondrule cooled. The boundary between the outer fractional crystallisation trend and the inner diffusion dominated zone is often sharp (see red vertical line in Figure 4.9 and Figure 4.7b and f for examples). There are several lines of evidence that suggest that the diffusional exchange in the forsteritic-olivine relict grain occurred primarily between the grain and the chondrule melt, prior to crystal growth.

The first piece of evidence comes from the widths of the overgrowths present around forsteritic-olivine relict grains. The widths are often less than the radius of olivine phenocrysts present in the type II chondrules. Wasson and Rubin (2003) use this to argue that the width of overgrowth represents the amount of material able to crystallise from the last melting event, and therefore, any phenocrysts with radii wider than the overgrowths on forsteritic-olivine relict grains must also contain relict cores which grew over many melting events. However, zoning profiles across these large olivine grains show normal zoning which can be modelled by closed-system fractional crystallisation in a single cooling event (Jones, 1990), suggesting that they do not represent multiple growth stages (Jones et al., 2005). Connolly and Jones (2005) argue that no growth occurred on the forsteritic-olivine relict grains until late into the crystallisation process after cooling had significantly progressed. Therefore, the narrow width of the overgrowth around forsteritic-olivine relict grains is a result of later crystallisation during the final stages of growth in the chondrules. Similar textures where thin overgrowths on relict grains coexist with large olivine phenocrysts can be found in experimental results from a single crystallisation event (Lofgren and Le, 2000; Hewins and Fox, 2004). This delayed growth on forsteritic-olivine relict grains leaves them open to diffusional exchange with the chondrule melt as the chondrule crystallised.

Delayed nucleation is also supported by the composition of the overgrowth at the boundary between the outer and middle zones (red vertical line in Figure 4.9). This location records the composition of the first stages of overgrowth upon the forsteritic-olivine relict grains. The composition of the overgrowth at this location is always more fayalitic than the first crystals expected to crystallise from the chondrule melt, according to crystallisation modelling of chondrule bulk compositions (see Chapter 3 – Chondrule petrography), by 4 to 24 mol %. In addition, the composition of the overgrowth at the boundary between the outer and middle zones is also often more fayalitic than the centre of larger normal olivine phenocrysts which are most likely to record the initial melt grown olivine composition.

The second piece of evidence is the shape of the observed compositional profiles. In many of the observed profiles, the boundary between the outer zone dominated by crystal growth and the diffusion dominated middle zone is sharp. Diffusion between the two crystallised zones would result in a blurred transition which is observed in very few profiles (e.g. Figure 4.8h). Therefore, much of the diffusional exchange experienced by the forsteritic-olivine relict grains must have occurred prior to crystal growth.

The preservation of a sharp boundary in many grains also provides constraints on the subsequent thermal history of the chondrules. To achieve this, cooling rates during and following crystal growth must have been rapid to prevent significant exchange between the outer zone, dominated by crystal growth, and the middle zone, dominated by diffusion, which preserves the sharp transition between the two. If cooling rates were low, there would have been opportunity for significant exchange between the two zones, which would blur the boundary which is observed in very few profiles.

Considering the evidence above, it is suggested that the Mg-rich forsteritic-olivine relict grains interacted with relatively Fe-rich chondrule melts by ionic-exchange because of interdiffusion in the crystal lattice. The boundary condition in this case is the equilibrium composition of olivine, which is related to the composition of the chondrule melt as it undergoes fractional crystallisation. As cooling occurs, fractional crystallisation of olivine takes place. This preferentially removes Mg from the chondrule melt, leaving it progressively more enriched in Fe as cooling takes place. This causes the boundary composition, the equilibrium composition of olivine, to become more Fe-rich. This allows more Fe to diffuse into (and Mg out of) the forsteritic-olivine relict grain as cooling progresses. Late on into the fractional crystallisation process, the forsteritic-olivine relict

grain begins to grow. Cooling and crystal growth rates must have been high to preserve the sharp transition between the forsteritic-olivine relict grain and the overgrowth. Low cooling rates during this period would allow diffusion between the two zones, blurring the boundary between the two.

This scenario assumes a mostly static system with no, or very little crystal growth, occurring on forsteritic-olivine relict grains as the chondrule cooled, up until the formation of the overgrowth. It may be that the forsteritic-olivine relict grains were still resorbing into the chondrule melt, which complicates the scenario. As well as reducing the size of the forsteritic-olivine relict grain as cooling progresses, it may create a boundary layer which is enriched in Mg, around the forsteritic-olivine relict grain, which would have an effect on the shape of the compositional profile.

Villeneuve et al. (2015) suggest an alternative mechanism for the formation of type IIA porphyritic olivine chondrules containing forsteritic-olivine relict grains. In this mechanism, type I chondrules containing Fe,Ni metal are heated under oxidising conditions. The Fe,Ni metal present in the chondrule is oxidised to FeO, resulting in a melt enriched in FeO. This disequilibrium leads to the rapid dissolution of the MgO-rich olivine and once ferroan olivine saturation is reached, FeO-rich olivine begins to grow as isolated crystals in the mesostasis or as overgrowths on any remaining MgO-rich olivine. This mechanism is contradictory to evidence which suggests that zoning profiles in normal olivine phenocrysts in type IIA chondrules can be explained by closed-system fractional crystallisation (Jones, 1990), although the authors suggest that zoning trends in the grown olivine may mimic fractional crystallisation, depending upon thin-section cut. In this mechanism, chondrule cooling histories are expected to be non-linear with chondrules experiencing initially slow cooling allowing olivine dissolution and growth to occur, followed by rapid cooling. This rapid cooling prevents significant elemental diffusion, preserving evidence of this disequilibrium. In this scenario, the boundary composition, or the equilibrium olivine composition, is not modified by fractional crystallisation during chondrule cooling as is suggested here. Instead, the boundary composition evolves because of disequilibrium effects such as rapid oxidation of Fe,Ni metal followed by dissolution of Mg-rich olivine and FeO-rich olivine crystallisation. Melt composition evolves independently from temperature, which means that the boundary composition is not dependent upon the temperature.

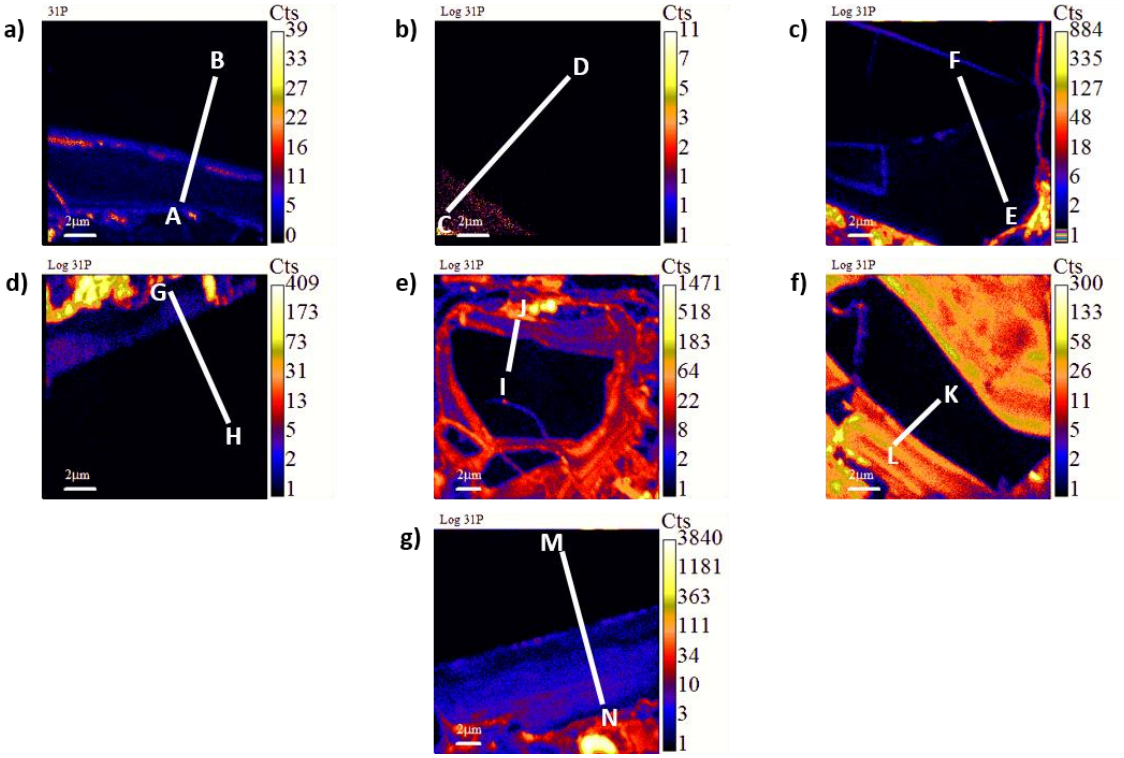

Figure 4.10 – ^{31}P NanoSIMS maps of forsteritic-olivine relict grains in ALHA 77307 highlighting the boundary between the forsteritic-olivine relict grain and overgrowth. All except a) show P counts on a log scale to better highlight the boundary. The relict grains themselves show very low or no P counts. In all gains there is a distinct P anomaly at the grain boundary: a) Al-1 RG1; b) Al-2 RG1; c) Al-3 RG1; d) Al4-RG4; e) Al-5 RG1; f) Al-5 RG2; Al-6 RG1.

4.2.2 NanoSIMS maps and compositional profiles

Trace-element maps and compositional profiles were produced for elements and molecules of $^{56}Fe^{16}O$, $^{24}Mg^{16}O$ and ^{31}P using NanoSIMS (See Chapter 2 – Samples and analytical methods). Phosphorus maps of the forsteritic-olivine relict grains and overgrowth for the forsteritic-olivine relict grains in chondrules in ALHA 77307 are shown in Figure 4.10. Figure 4.11 shows FeO/Si and P/Si compositional profiles. In all but one case there is a significant P spike in the region between the forsteritic-olivine relict grain and the overgrowth crystal (e.g. Figure 4.11a and b), while in the remaining case there is a significant change in P composition (Figure 4.11d). A break in slope in the FeO/Si profile also occurs at the same point as, or very close to, the P spike or change in P composition in the compositional profiles. This break in slope is also visible in the Fe-Mg profiles shown in Figure 4.7.

Solute trapping, or growth entrapment, is suggested as the process for features similar to those observed in Figure 4.10 and Figure 4.11, such as P oscillatory zoning often seen in olivine crystals (McCanta et al., 2008; Milman-Barris et al., 2008; McCanta et al., 2016). In

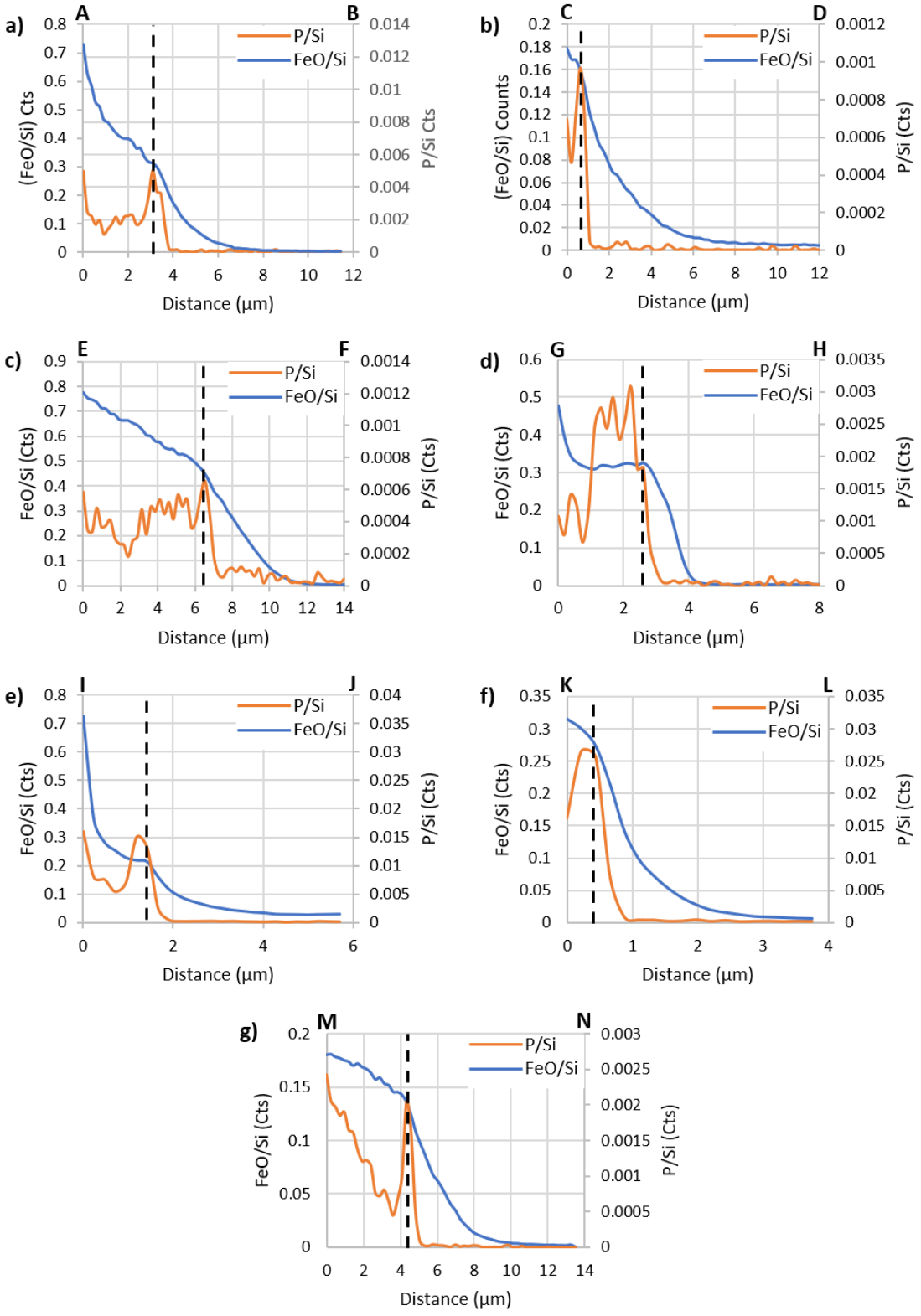

Figure 4.11 – FeO/Si and P/Si NanoSIMS profiles used to confirm the location of the boundary between the forsteritic-olivine relict grain and overgrowth. The dashed black vertical lines show the inferred location of the grain boundary. A significant P spike, or change in composition, occurs at the break in slope visible on the FeO profile in all observed grains. This break in the FeO diffusion profile is also visible in the calibrated BSE compositional profiles shown in figure Figure 4.7 and Figure 4.8. The location of these profiles are shown in Figure 4.10: Al-1 RG1; b) Al-2 RG1; c) Al-3 RG1; d) Al-4 RG1; e) Al-5 RG1; f) Al-5 RG 2; g) Al-6 RG1.

the growth entrapment model (Watson and Liang, 1995; Watson, 2004; Watson et al., 2015), impurities (e.g. P) near the boundary between the crystal and melt become incorporated or adsorbed into the crystal lattice, possibly at values exceeding equilibrium composition. When crystal growth begins, if this crystal growth rate is high or the diffusion rate of the impurity is low, the impurities cannot diffuse away from the original crystal boundary as crystal growth occurs. This buries a zone enriched in the impurity marking the original crystal boundary.

P is a slow diffusing element in olivine crystals with a diffusivity of ~2×10^{-18} m^2s^{-1} at 1570 K (Watson et al., 2015). This is three orders of magnitude lower than Fe-Mg diffusivity under the same conditions, which typically has values of ~8×10^{-15} m^2s^{-1} (Dohmen and Chakraborty, 2007). Crystal growth rates in porphyritic olivine chondrules are thought to be rapid, up to ~1.4×10^{-8} ms^{-1} (Hewins and Fox, 2004).

The coupling of low diffusivity of P and rapid growth rates in porphyritic olivine chondrules makes forsteritic-olivine relict grains good candidates for the growth entrapment process, and the observations displayed in Figure 4.10 and Figure 4.11 are consistent with growth entrapment. The P spike, or change in P composition, occurs at or near the break in slope in the FeO profile and, therefore, marks the boundary between the forsteritic-olivine relict grain and overgrowth, and allows accurate correlation of the NanoSIMS and SEM data sets.

4.3 Implications of forsteritic-olivine relict grains

Forsteritic-olivine relict grains are a common feature found in type IIA porphyritic olivine chondrules. They have been found in many chondrite groups, for example, LL chondrites (Jones, 1990; Ruzicka et al., 2008; Berlin et al., 2011), CO chondrites (Jones, 1992; Wasson and Rubin, 2003; Berlin et al., 2011), CR chondrites (Leshin et al., 1998; Connolly and Huss, 2010) and CM chondrites (Hanowski and Brearley, 2001; Hewins et al., 2014). They are most common in CO chondrites, where they are present in >90% of type IIA porphyritic olivine chondrules (Wasson and Rubin, 2003). They are less common in ordinary chondrites, for example, only 3 of 11 type IIA porphyritic olivine chondrules in Semarkona contained forsteritic-olivine relict grains (Jones, 1990). A similar dichotomy was noted in this study. Forsteritic-olivine relict grains were found in 38 of 51 type II chondrules, or 75% of the examined type II chondrules in the CO chondrite ALHA 77307. Finding forsteritic-olivine relict grains in type II chondrules in the ordinary chondrites NWA 8276 and NWA

4910 was a relatively rare occurrence. A survey of type II chondrules in the L/LL3.10 chondrite Adrar 003 found that 7 of 25 type II chondrules contained forsteritic-olivine relict grains, however, none were suitable for diffusional analysis.

Relict grains did not crystallise from the most recent chondrule melt and were present in the precursor assemblage. This means that the heating and duration of the last chondrule forming event was insufficient to melt these grains (Jones, 1996; Wasson and Rubin, 2003; Jones et al., 2005; Jones et al., 2018; Krot et al., 2018). These forsteritic-olivine relict grains are compositionally and isotopically similar to olivine crystals found in type IA chondrules within the same chondrite, suggesting that they originate from that population of chondrules (Jones and Scott, 1989; Jones, 1990; Jones, 1992; Ruzicka et al., 2007; Ushikubo et al., 2012; Tenner et al., 2018). The presence of these relict grains suggests that chondrule recycling was a common process in chondrule forming regions (Jones, 1996; Jones et al., 2005; Ruzicka et al., 2008; Jones, 2012). The disparity in abundance of chondrules containing forsteritic-olivine relict grains between carbonaceous and ordinary chondrites may be because of the differences in the number of type I and type II chondrules in the different chondrule forming regions. Type I chondrules are more common than type II chondrules in carbonaceous chondrites. This means that there is a large amount of type I material available for recycling in the carbonaceous chondrite chondrule formation region. Because of the high availability of type I material, there is a higher prevalence of forsteritic-olivine relict grains in the relatively few type II chondrules. In the ordinary chondrites, type II chondrules are more common than type I chondrules. This means that there is less type I material in the ordinary chondrite chondrule formation region to reprocess into the relatively common type II chondrules. This results in fewer forsteritic-olivine relict grains in the type II chondrules in ordinary chondrites (Jones, 2012). Chondrule recycling places constraints on the chondrule formation mechanism; the mechanism must be transient and be able to process the same material in multiple heating events (Jones, 2012).

4.3.1 Chondrule recycling model

The presence of relict grains in chondrules argues strongly that chondrules underwent multiple episodes of heating in a chondrule recycling process. Ruzicka et al. (2008) present a chondrule recycling model which summarises the events which must have occurred in order to produce chondrules containing relict grains; this is summarised in Figure 4.12.

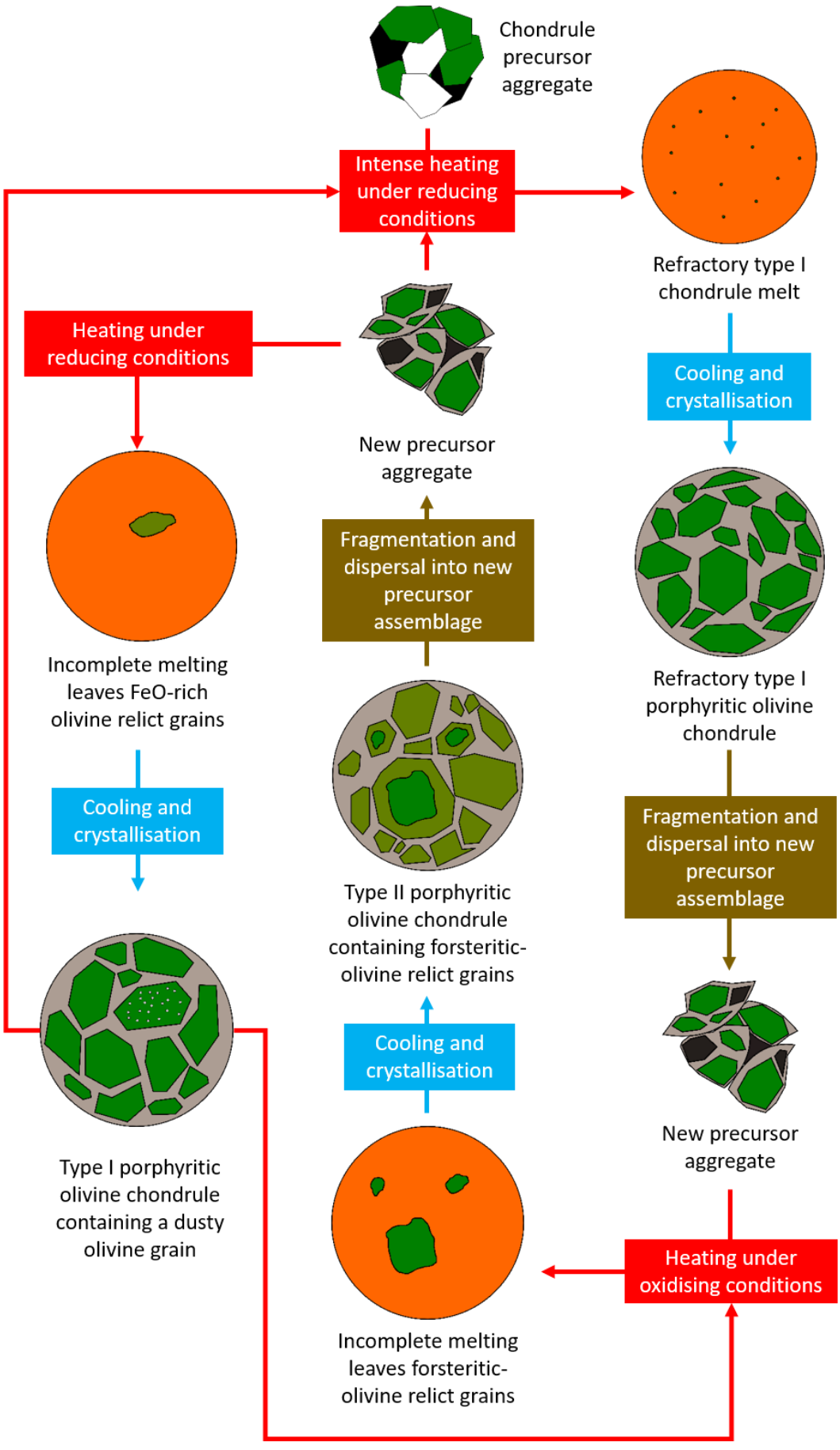

Figure 4.12 – The chondrule recycling model modified from Ruzicka et al. (2008).

In the recycling model, initial chondrule precursors are intensely heated under reducing conditions to produce refractory melts. These melts will crystallise into refractory type I porphyritic olivine chondrules. Olivine phenocrysts in these chondrules will contain high levels of refractory elements, e.g. Ti, Ca, and Al, with low abundances of more volatile elements, e.g. Mn, as observed in olivine in type I chondrules. These chondrules must have experienced intense thermal processing and vapour fractionation (Ruzicka et al., 2008). These early refractory type I chondrules may then be fragmented by collisions and dispersed. These fragments are incorporated into new chondrule precursor assemblages or preserved as isolated grains which are often observed in chondrites (Jones, 1992).

If type I chondrules, or precursors containing fragments of type I chondrules, are heated under more oxidising conditions, type II porphyritic olivine chondrules containing more ferroan olivine crystals are produced. The increased oxygen fugacity may be the result of a greater enrichment of CI-dust, or H_2O ice within the chondrule precursor of type II chondrules (Tenner et al., 2018). Incomplete melting may allow refractory forsteritic-olivine relict grains to be preserved because of the high melting temperature of forsteritic-olivine combined with a short heating event and rapid cooling. Soulié et al. (2017) show that rapid cooling rates of up to 8000 Kh^{-1} are required to preserve forsteritic-olivine relict grains in chondrule-like melts. These forsteritic-olivine relict grains then act as nucleation sites for more ferroan overgrowth from the surrounding melt during part of the crystallisation process. This creates the overgrowth surrounding the forsteritic-olivine relict grains. These chondrules are more volatile-rich than the initial refractory type I chondrules. In order to account for this, there must have been some combination of diffusion of volatile elements into the chondrule and diffusion of refractory elements out of the chondrules during crystallisation or unfractionated dust was added to the precursor assemblage (Ruzicka et al., 2008). The addition of unfractionated dust may have the additional effect of increasing the oxygen fugacity of the precursor assemblage (Tenner et al., 2018).

Some type I chondrules contain forsteritic olivine crystals studded with Fe-metal grains. These grains attest to further recycling and melting of type II chondrule material under reducing conditions. If precursors containing ferroan olivine from type II chondrules are incompletely melted under reducing conditions, metal exsolution in the unmelted grain occurs creating this dusty texture (Rambaldi, 1981; Rambaldi and Wasson, 1981; Kracher et al., 1984; Jones and Danielson, 1997; Leroux et al., 2003; Ruzicka et al., 2008). These

grains are not studied in this work as the resulting textures are not amenable to diffusion modelling.

4.4 Summary and conclusions

Thirteen forsteritic-olivine relict grains have been identified and characterised in twelve type II chondrules in ALHA 77307, NWA 8276 and NWA 4910. The rounded morphology of the grains suggests they were resorbing in the chondrule melt. This suggests that they were present in the precursor assemblage (Jones, 1990). They have highly forsteritic compositions which could not have crystallised from the host chondrule melt (Jones, 1990; Jones, 1992). The compositions of the grains are similar to olivine crystals in type IA chondrules which suggests that they originate from a previous generation of type I chondrules (Jones and Scott, 1989; Jones, 1990). This suggests that chondrule recycling was taking place and was a common process in the protoplanetary disk (Jones, 1996; Jones et al., 2005; Ruzicka et al., 2008; Jones, 2012). This places constraints on the chondrule formation mechanism, which must be transient, repeatable and able to process material in the same region multiple times (Jones, 2012).

Compositional profiles across the boundary between the forsteritic-olivine relict grain and surrounding overgrowth show that the relict grains were able to exchange with the chondrule melt during cooling. During this time, the chondrule was undergoing fractional crystallisation, however, the forsteritic-olivine relict grains did not begin to grow until late on in the crystallisation process, resulting in relatively narrow overgrowths (Jones, 1990; Wasson and Rubin, 2003; Connolly and Jones, 2005; Jones et al., 2005).

4.4.1 Formation of type II chondrules containing forsteritic-olivine relict grains

Type II porphyritic olivine chondrules can be formed in a minimum of two melting events. In the first melting event, a chondrule precursor aggregate is heated under reducing conditions to form a refractory melt which has undergone significant vapour fractionation. This melt cools and crystallises into a type I porphyritic olivine chondrule. The forsteritic-olivine relict grains studied here show evidence of vapour fractionation (see Figure 4.5), therefore were likely formed in a similar event. These type I chondrules may be fragmented and dispersed into new precursors. If these new precursors are heated under oxidising conditions and incompletely melted, a type II chondrule melt containing partially resorbed

forsteritic-olivine relict grains is formed. These grains are then able to exchange Fe and Mg with the chondrule melt during cooling, creating the observed compositional profiles. This melt crystallises into a type II porphyritic chondrule containing forsteritic-olivine relict grains. Clear diffusion profiles are observed in many of the grains shown in Figure 4.1, which makes them good candidates for investigation of their thermal history by Fe-Mg diffusion modelling.

Chapter 5

Cooling rates of chondrules from modelling Fe-Mg diffusion in forsteritic-olivine relict grains

This chapter describes how chondrule cooling rates and their thermal histories were determined by modelling Fe-Mg diffusion profiles in forsteritic-olivine relict grains present in chondrules in ALHA 77307 (CO3.00), NWA 8276 (L3.00) and NWA 4910 (LL3.1). Section 5.1 introduces some of the important concepts when modelling diffusion in olivine. Section 5.2 describes two separate approaches to modelling the Fe-Mg diffusion profiles. The results of Fe-Mg diffusion modelling are presented in section 5.3. The results are discussed in section 5.4, which also includes a discussion on possible sectioning effects which can influence the observed compositional profiles.

5.1 Diffusion theory

5.1.1 Fick's first and second laws

Diffusion is the process of matter transportation from one location in a system to another as a result of random molecular motions. Almost all diffusion behaviour is governed by two equations, known as Fick's first and second laws, shown in Equation 5.1 and Equation 5.2, below where *F* is the rate of transfer per unit area of section, *C* is the concentration of the diffusing substance, *x* is the space coordinate measured normal to the section, *t* is time and *D* is the diffusion coefficient (Crank, 1976). Fick's first law states that *the instantaneous flux of material across a region because of diffusion, F, is equal to the amount of change in abundance of material, ∂C, across the region, ∂x, multiplied by a constant, D.* The negative in the equation indicates that the direction of movement of material is opposite to the direction of the concentration gradient. Fick's second law is more complicated and states that *the amount of change of abundance of material, ∂C, per unit time, ∂t, caused by the action of diffusion, is equal to a constant, D, multiplied by the rate of change of the gradient of material, $\partial^2 C$, across the region, ∂x^2.*

$$F = -D\frac{\partial C}{\partial x}$$

Equation 5.1 – Fick's first law (Crank, 1976).

$$\frac{\partial C}{\partial t} = D\frac{\partial^2 C}{\partial x^2}$$

Equation 5.2 – Fick's second law (Crank, 1976).

5.1.2 Diffusion in olivine

Diffusion in olivine and other similar silicate minerals is mediated by point defects, such as vacancies, and the concentration of these defects affects how quickly diffusion occurs within that crystal. Higher concentrations of these defects, which are generated in greater numbers at higher temperatures, result in generally faster diffusion rates, or higher diffusion coefficients. Diffusion in olivine may occur by 3 different mechanisms. 1) A purely intrinsic domain, which occurs at high temperatures and requires high crystal purity. Vacancies are produced as a function of pressure and temperature only, with the highest concentration of vacancies produced at the highest temperatures with a high activation energy. 2) A purely extrinsic domain (PED) which occurs at lower temperatures and/or low oxygen fugacity condtions. In this domain, concentration of vacancies is a function of

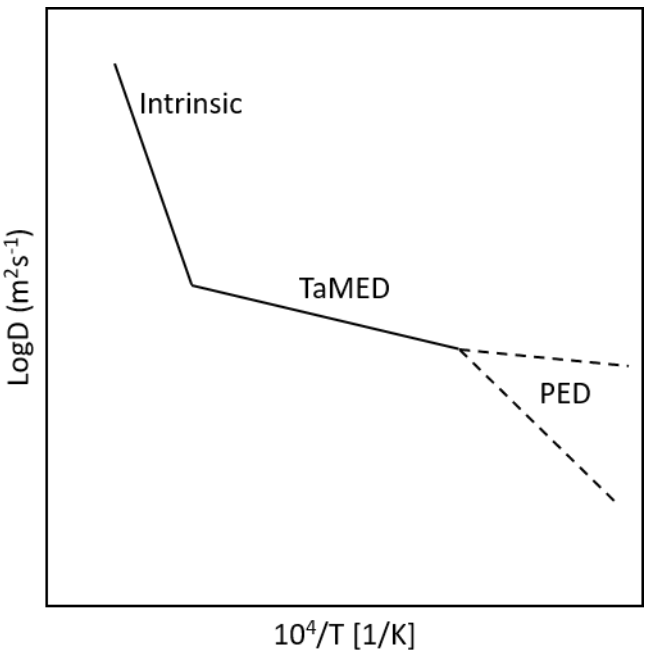

Figure 5.1 – Schematic Arrhenius plot showing the transition between the three different mechanisms of diffusion in silicates: Intrinsic, transition metal extrinsic (TaMED) and purely extrinsic (PED). Diffusion in the intrinsic domain occurs at high temperatures and has the strongest temperature dependence. The transition from intrinsic to TaMED is shown by the significant reduction in gradient, reflecting a large reduction in activation energy. Diffusion in the TaMED domain occurs at intermediate temperatures. The transition from TaMED to PED is marked by a smaller change in gradient, however, the transition could be to gentler or steeper gradients depending upon conditions (Chakraborty 2010).

pressure, temperature, and the chemical potential of heterovalent trace elements, e.g. Al. In this mechanism, activation energy is much lower than for the purely intrinsic domain. 3) A transition metal extrinsic domain (TaMED) at intermediate temperatures and oxygen fugacity conditions. In this mechanism, the concentration of vacancies is dependent upon pressure, temperature, and oxygen fugacity conditions. In this domain, activation energy is lower than in the intrinsic domain, but could by higher or lower than in the purely extrinsic domain. Vacancy generation in the TaMED domain dominates in most natural olivine crystals. The change in diffusion mechanism can be visualised on an Arrhenius plot, which plots the log of diffusivity or the diffusion coefficient against inverse temperature, e.g. Figure 5.1. The change in gradient between the different diffusion domains reflects the changes in activation energy; activation energy in the intrinsic domain is much higher than in the TaMED and PED domains (Chakraborty, 1997; Dohmen and Chakraborty, 2007; Chakraborty, 2010).

5.1.2.1 Fe-Mg interdiffusion coefficient

The Fe-Mg interdiffusion coefficient in olivine crystals is calculated using Equation 5.3 or Equation 5.4 below where P is pressure in Pa, R is the gas constant in $Jmol^{-1}K^{-1}$, T is the temperature in K, fO_2 is the oxygen fugacity in Pa and X_{Fe} is the mole fraction of fayalite. Using these equations, Dohmen and Chakraborty (2007) successfully reproduced all of their experimental measurements, 113 data points, to within half an order of magnitude. When oxygen fugacity is above 10^{-10} Pa, Equation 5.3 should be used, which incorporates oxygen fugacity conditions. At oxygen fugacities lower than 10^{-10} Pa, Equation 5.4 should be used. As the oxygen fugacities used in modelling diffusion in the forsteritic-olivine relict grains were higher than 10^{-10} Pa, only Equation 5.3 was used to calculate diffusion coefficients.

$$\log_{10}\left[D_{FeMg}(m^2s^{-1})\right] = -9.21 - \frac{201000 + (P - 10^5) \times 7 \times 10^{-6}}{2.303RT} + \frac{1}{6}\log_{10}\left(\frac{fO_2}{10^{-7}}\right) + 3X_{Fe}$$

Equation 5.3 –The equation used to calculate the Fe-Mg interdiffusion coefficient in olivine at oxygen fugacity above 10^{-10} Pa (Dohmen and Chakraborty, 2007).

$$\log_{10}\left[D_{FeMg}(m^2s^{-1})\right] = -8.91 - \frac{220000 + (P - 10^5) \times 7 \times 10^{-6}}{2.303RT} + 3X_{Fe}$$

Equation 5.4 – The equation used to calculate the Fe-Mg interdiffusion coefficient in olivine at oxygen fugacity below 10^{-10} Pa (Dohmen and Chakraborty, 2007).

The change from Equation 5.3 to Equation 5.4 represents the change from TaMED, where diffusivity depends upon oxygen fugacity, to PED. The equations also show the parameters which need to be taken into account when calculating Fe-Mg diffusion coefficients for diffusion modelling in olivine crystals, for example, temperature, pressure, fO_2 conditions, and olivine composition (Dohmen and Chakraborty, 2007).

Another complication is that diffusion in olivine is highly anisotropic. Equation 5.3 and Equation 5.4 are valid along the c-axis, where diffusion is fastest. Diffusion along the c-axis is ~6 times faster than along the a- or b-axes. This is because, along the c-axis, or the [001] direction, there are chains of interlinked octahedral sites allowing for faster diffusion. Along the other axes, the octahedra are less well-connected resulting in slower diffusion. In order to calculate diffusion coefficients for diffusion along the a- or b-axes, the diffusion coefficient for the c-axis should be divided by 6 (Chakraborty, 2010).

Tachibana et al. (2013) argue that at the high temperatures associated with chondrule formation, ~1800 K, may be sufficient to change to an intrinsic domain for diffusion in olivine. Diffusion experiments were performed to determine the Fe-Mg diffusion

coefficient at higher temperatures (1670 to 1870 K). The experimental results suggest that there is an increase in activation energy, equivalent to an increase in the gradient of an Arrhenius plot. This would correspond with a change from the TaMED domain to an intrinsic domain. The experiments were fixed at oxygen fugacity of $10^{-2.0}$ Pa to $10^{-3.5}$ Pa, and little oxygen fugacity dependence was observed. No compositional dependence was reported in the experiments. However, this could be because only a narrow, highly forsteritic, compositional range (Fo_{93-97}) was studied. Using the higher diffusion coefficients calculated for diffusion in the intrinsic domain (Tachibana et al., 2013) rather than the TaMED domain would result in faster diffusion, leading to estimated cooling rates which are much higher than estimations made using calculations set only in the TaMED domain (e.g. Dohmen and Chakraborty, 2007). Tachibana et al. (2013) calculated that the 400 Kh^{-1} cooling rate determined in Hewins et al. (2009) for a type II chondrule in Semarkona could be three times higher when using the higher diffusion coefficients.

5.2 Diffusion modelling

Two different approaches were used in this project, using two different diffusion models. The first approach combines a fixed temperature diffusion model named AutoDIFF, which has been used to model Fe-Mg diffusion in terrestrial igneous systems (e.g. Hartley et al., 2016), with a secondary worksheet, which is used to convert the timescale results from AutoDIFF into cooling rates. The second approach uses a new explicit finite difference forward modelling program.

5.2.1 AutoDIFF

AutoDIFF utilises a database of simulated diffusion profiles obeying composition-dependent diffusion in one-dimension calculated using finite difference software. As well as being highly anisotropic, Fe-Mg diffusion in olivine is highly composition dependent (Dohmen and Chakraborty, 2007). This means that the more compositional variation between the diffusion couple, in this case, the edge of the forsteritic-olivine relict grain and the core region, the more a diffused profile changes from a symmetrical diffusion sigmoid, to an increasingly asymmetric sigmoid. Under composition-dependent diffusion, for a given set of boundary conditions (e.g. temperature, oxygen fugacity, composition, and anisotropy), diffusion profiles are self-similar in time. This means that after four time units, the observed diffusion profile is twice as wide but is identical in other geometrical aspects

to the diffusion profile after one time unit. A stretch factor can be applied to the length of the observed profile compared to the model profile to bring them into congruency, provided they have the same diffusional behaviour. If the boundary conditions are known, then the curve with the correct shape, and therefore, diffusional behaviour can be selected from the database of modelled profiles. This model curve is then scaled to the observed profile using the stretch factor, and a stretch factor scaling law can be used to estimate diffusion time, *t*, and the *Dt* product (Hartley et al., 2016). *Dt* is the product of the diffusion coefficient, *D*, in m^2s^{-1}, and diffusion time, *t*, in s, and provides an estimate of how much material has moved in m^2. To turn this *Dt* product into a cooling rate, the product can be fitted to a cooling curve in the secondary worksheet to estimate the chondrule cooling rate.

5.2.1.1 Inputs

The model inputs are listed in Table 5.1 below. The liquidus temperature of the host chondrule was calculated from host chondrule bulk composition using Petrolog3 (Danyushevsky and Plechov, 2011). Porphyritic olivine chondrules must have been heated to temperatures close to, but not exceeding liquidus in order to preserve crystalline nuclei (e.g. Hewins et al., 2005), therefore the assumption that the liquidus temperature is the peak temperature is reasonable. Calculations were performed at a pressure of 10^5 Pa and oxygen fugacity of 1 log unit beneath the iron-wüstite buffer using the mineral-melt model of Danyushevsky (2001) for olivine. Diffusion modelling was also undertaken at this oxygen fugacity as most of the analysed chondrules contain small quantities of Fe,Ni metal and crystallisation experiments have reproduced type II chondrule textures at oxygen fugacities from IW-1 to IW-0.5 (Lofgren and Russell, 1986; Lofgren, 1989; Radomsky and Hewins,

Table 5.1 – AutoDIFF inputs

Input	Source of input
Magmatic temperature	The liquidus temperature of the host chondrule in K.
Pressure	100000 Pa
Oxygen fugacity	IW-1
Measured Fe-Mg diffusion profile	Compositional profiles were measured using calibrated BSE greyscales (see chapter 4)
Composition of olivine crystal edge	Values at the forsteritic-olivine relict grain and overgrowth interface taken from compositional profiles
Composition of core region of olivine crystal	Values in the core region of the olivine crystals taken from compositional profiles
Orientation of the crystal c-axis	EBSD measurements
Orientation of the measured diffusion profile	Measured from the BSE image of the forsteritic-olivine relict grain

1990; Connolly and Hewins, 1991; Jones and Lofgren, 1993; Kennedy et al., 1993; Connolly and Hewins, 1995; Dehart and Lofgren, 1996; Connolly et al., 1998; Weinbruch et al., 1998) as discussed in Chapter 2. The orientation of the c-axis was determined by EBSD measurements.

5.2.1.2 Outputs

The four major outputs from the model are diffusion timescale in seconds, Fe-Mg interdiffusion coefficients, the fraction of c-axis speed diffusion because of anisotropy, and the shape of the model diffusion profile compared to the observed diffusion profile.

By multiplying the diffusion timescale with the Fe-Mg interdiffusion coefficient, the *Dt* product is calculated which can be transferred to the secondary worksheet to calculate cooling rates. The shape of the model diffusion profile compared to the observed diffusion profile can be used to evaluate the fit. Ideally, model diffusion profiles should show the same shape as the measured compositional profiles. Differences in the shape indicate that AutoDIFF cannot replicate the shape of the compositional profile using the conditions set in the program. The fraction of c-axis diffusion speed because of anisotropy (on a scale of 1 to 1/6) is useful as it can be transferred to the explicit finite difference forward modelling program. The anisotropy is calculated in AutoDIFF according to Costa et al. (2008).

5.2.1.3 Calculation of cooling rates using the secondary worksheet

The secondary worksheet fits the *Dt* product calculated using the results from AutoDIFF to the *Dt* product for a linear cooling curve using the goal seek function in Microsoft Excel. The inputs for this worksheet are shown in Table 5.2.

In the secondary worksheet, the pressure and oxygen fugacities remain the same as in AutoDIFF, at 100000 Pa and IW-1. The values for these oxygen fugacity conditions at different temperatures were calculated using Equation 5.5. Initially, models were run with

Table 5.2 – Secondary worksheet inputs

Input	Source of input
Start temperature	Chondrule liquidus temperature in K
Pressure	100000 Pa
Composition of olivine crystal edge	Values at the forsteritic-olivine relict grain and overgrowth interface taken from compositional profiles
Oxygen fugacity	IW-1
Time-step	10 or 60 s
Dt product	Input from results of AutoDIFF

a time-step of 60 s. For those with faster cooling rates where there were few time steps of 60 s, models were rerun with a time-step of 10 s to provide a greater resolution.

$$IW \log fO_2 = \frac{-26834.7}{T} + 6.471$$

Equation 5.5 – Oxygen fugacity-temperature relationship for the iron-wüstite buffer according to Myers and Eugster (1983).

5.2.1.4 Results

Unfortunately, the results from this technique were mixed at best. The model fits produced from AutoDIFF were often poor. This means that AutoDIFF was not able to replicate the diffusion behaviour shown in the compositional profiles from forsteritic-olivine relict grains in the studied chondrules, for example, Figure 5.2, which shows a typical model fit. This may mean that the assumptions of fixed boundary conditions used in AutoDIFF are not valid for the diffusion occurring in these forsteritic-olivine relict grains, and diffusion may be happening under shifting boundary conditions. In this case, a different diffusion model is required to calculate chondrule cooling rates.

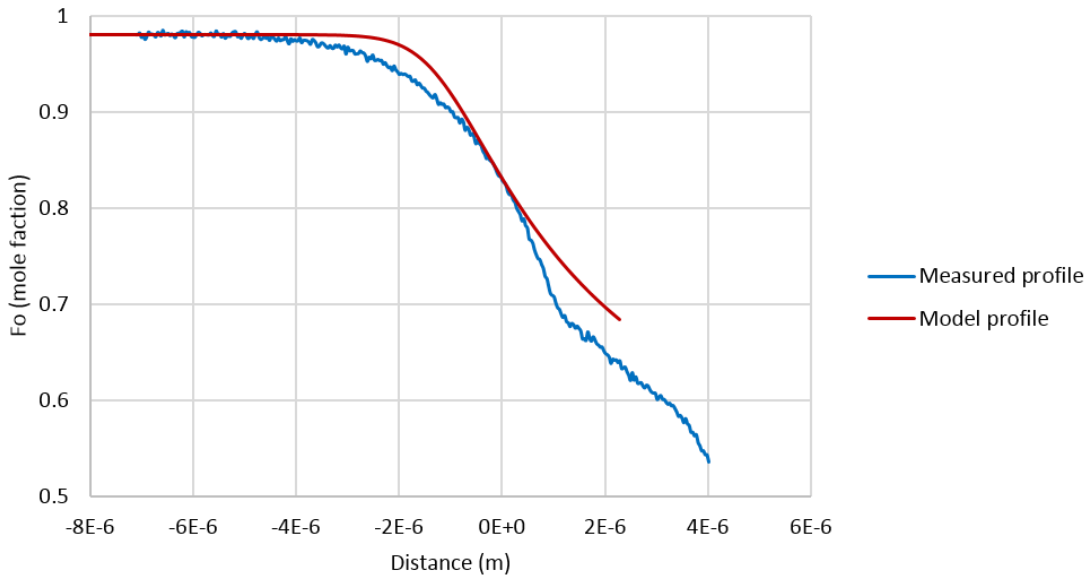

Figure 5.2 – Example model fit using AutoDIFF for Al-1 RG1 Profile A. The diffusion couple in this case was the composition of the forsteritic-olivine relict grain on the left and the composition of olivine at the boundary between the forsteritic-olivine relict grain and the overgrowth on the right. At this boundary there is a distinct kink in the Fe-Mg compositional profile.

5.2.2 Explicit finite difference forward-modelling program

The second approach uses a one-dimensional, macro-automated, explicit finite difference, forward-modelling program coded into Microsoft Excel. The model uses an explicit finite difference method which relies upon relatively simple approximations to diffusion behaviour that are extrapolated over large datasets. The forward-modelling aspect indicates that the end result from an initial set of parameters is unknown, therefore, a certain amount of trial and error is required to produce model profiles which match the observed compositional profiles. The model uses the composition-dependent formulation of Dohmen and Chakraborty (2007) for Fe-Mg interdiffusion coefficients. Unlike AutoDIFF, this model is capable of modelling diffusion under shifting boundary conditions, for example, temperature, oxygen fugacity conditions, and the equilibrium olivine composition, which all evolve with time during the formation of the chondrule. Temperature decreases over time because of chondrule cooling. The decreasing temperature also results in decreasing oxygen fugacity as the value of the iron-wüstite buffer decreases with temperature. Fractional crystallisation of olivine during cooling preferentially removes Mg from the melt leaving it richer in Fe over time, altering the equilibrium olivine composition. The model can also account for the effects of crystal growth and supplied diffusion anisotropy. The boundary conditions are dynamically controlled using the olivine-saturated liquidus curve for the chondrule as a function of temperature. Figure 5.3 shows the initial conditions that must be set, and the steps involved in each time step of the model.

5.2.2.1 Inputs

The inputs to the explicit one-dimensional finite difference forward modelling program are shown in Table 5.3 below. For the start temperature, the liquidus temperature of the host chondrule is used. For oxygen fugacity conditions, which are temperature dependent, a value of 1 log unit beneath the iron-wüstite buffer was used and is calculated using the formulation in Myers and Eugster (1983) (see Equation 5.5). Anisotropy is determined in AutoDIFF where it is calculated according to Costa et al. (2008) on a scale of 1 to $\frac{1}{6}$, and the value is transferred to this model. No growth was included in the models, as the overgrowths did not begin to grow on forsteritic- olivine relict grains until late into the crystallisation process. This assumption is based on the narrow width of these overgrowths, which is often less than the radius of olivine phenocrysts in the same chondrule (Connolly

Table 5.3 – Inputs to the explicit finite difference forward modelling program

Input	Source of input
Start temperature	Liquidus temperature in K
Cooling rate	Kh^{-1}
Pressure	10^5 Pa
Oxygen fugacity	IW-1
Anisotropy	Calculated according to Costa et al. (2008)
Growth rate	0 ms^{-1}
Forsteritic-olivine relict grain composition	Values of the core region of calibrated BSE images
Olivine saturated liquidus curve	Geochemical modelling using Petrolog3
Length-scale	Length of the observed compositional profile

and Jones, 2005; Jones et al., 2005), the shape of the observed compositional profiles andthe location of P spikes in P compositional profiles (see Chapter 4 – Petrography of forsteritic-olivine relict grains). Forsteritic-olivine relict grain composition was determined from EPMA measurements. The olivine-saturated liquidus curve was determined from the host chondrule bulk composition, not including the relict grains as these were not part of the most recent melt, using Petrolog3 (Danyushevsky and Plechov, 2011) using mineral-melt models for the phases present in each chondrule. For chondrules containing olivine, the mineral-melt model of Danyushevsky (2001) was used; for chondrules containing chromite, the mineral-melt model of Nielsen (1985) was used; for chondrules containing pyroxene, the mineral-melt model of Bolikhovskaya et al. (1995) was used. Inclusion of all the relevant phases is required as the crystallisation of different phases affects the evolution of the chondrule melt. The olivine-saturated liquidus curve was extracted from the results and fitted to a quadratic equation which is inputted into the model. This provides the equilibrium olivine composition at the edge of the forsteritic-olivine relict grain. The model length scale was set to be similar to the length of the observed compositional profile.

5.2.2.2 Running time steps

Within each time step, there are several stages. One of the first stages is to calculate the time step length, shown in stage 1 in Figure 5.3. As this is an explicit finite difference model, it relies upon relatively simple approximations to diffusion behaviour extrapolated over large datasets. This is only valid when the flux of material is low. This means that during a time step, the change in abundance has minimal or no effect upon the right side of Fick's second law (see Equation 5.2). To achieve this condition, the time step length must be very

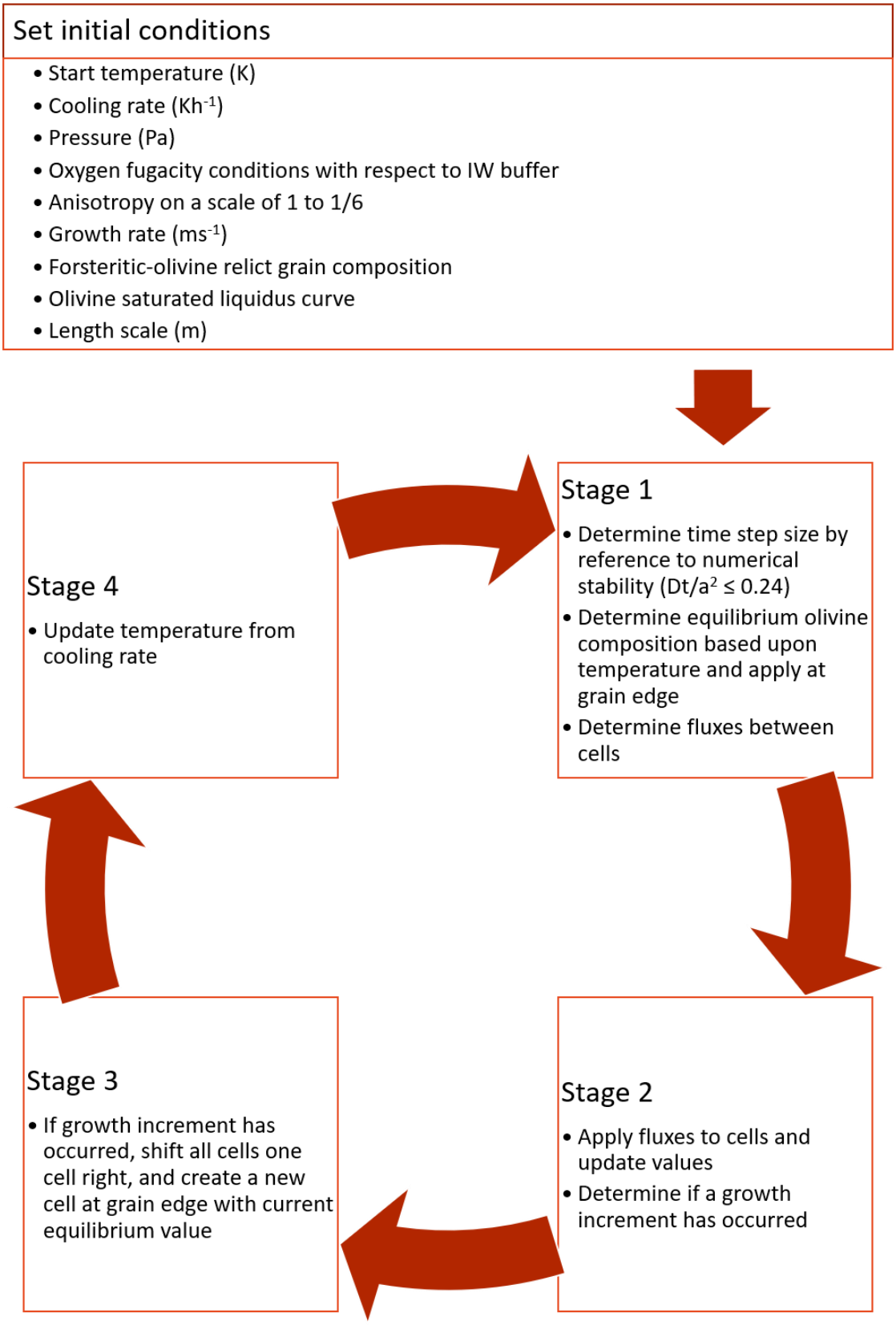

Figure 5.3 – Flow chart showing the stages involved in each time step of the explicit finite difference forward modelling program.

small. If the time step is too large, the simple approximations to diffusion behaviour are invalid and the model becomes unstable.

In the model, time step length is related to a stability factor (see Equation 5.6). To ensure the model remains numerically stable, this stability factor must be ≤0.24. This value prevents too much material moving out of a cell which could set up an inversion in the gradient, leading to numerical instability. In the most extreme example, for a cell containing 100% forsterite, surrounded by two cells containing 0% forsterite, a value of 0.24 or 24% means that 24% of this material will be transferred to each of the surrounding cells. After the time step is complete, the central cell will contain 52% forsterite and the surrounding cells will contain 24% forsterite. Using this value means that the central box did not lose more than half its material and no inversions were set up leading to instability. The time step length is calculated using Equation 5.7.

$$Stability\ Factor = \frac{Dt}{a^2}$$

Equation 5.6 – Equation to calculate the stability factor. To keep the model numerically stable, the stability factor must be ≤0.24. D is the diffusion coefficient in m^2s^{-1}, t is the time step length in s and a is the length scale of diffusion for a single cell in m.

$$time\ step\ length = \frac{stability\ factor \times x^2}{D}$$

Equation 5.7 – Equation showing how the time step length in s is calculated. Stability factor must be ≤0.24, x is the length scale of diffusion for a single cell in m and D is the maximum diffusion coefficient in the current time step in m^2s^{-1}.

$$\frac{\partial C_t}{\partial t} = -D\frac{\partial C_x}{\partial x}$$

Equation 5.8 – Small variation of Fick's first law, where ∂C_t is the change in abundance of material with respect to time in forsterite mole fraction, ∂t is time step length in s, D is the diffusion coefficient in m^2s^{-1}, ∂C_x is the difference in composition between the two cells in forsterite mole fraction, and ∂x is the distance between the two cells in m.

Another one of the initial stages is to calculate equilibrium olivine composition and apply this on the left, at the forsteritic-olivine relict grain edge, as a boundary condition, also shown in stage 1 of Figure 5.3. This is calculated from the quadratic equation for the olivine saturated liquidus curve for the temperature during the time step. With the time step length and equilibrium olivine composition calculated, the final part of stage 1 in Figure 5.3 is to calculate fluxes between the cells. This is achieved by using a small variation of Fick's

first law. Equation 5.8 calculates the flux of material in a time step and can be rearranged to calculate the abundance of material that moves in that time step.

The next stage in the time step, stage 2 in Figure 5.3, is to apply the fluxes and change the value of the cells because of the flux. Another consideration at this stage is whether enough time has passed to add a growth increment. This is determined from the growth rate supplied in the initial conditions as shown in Equation 5.9. The time passed in the model can then be compared to this value to determine if a new cell is required.

$$time\ for\ growth\ of\ a\ cell = \frac{length\ scale\ of\ a\ cell}{growth\ rate}$$

Equation 5.9 – Equation used to calculate the time required to grow 1 new cell.

Stage 3 in Figure 5.3 is to add this growth increment if required. This is achieved by moving all cells one cell to the right, towards the core region of the forsteritic-olivine relict grain, and creating a new cell on the left, at the edge of the forsteritic-olivine relict grain, with the current equilibrium olivine composition to simulate the growth of the crystal. As the forsteritic-olivine relict grains were equilibrating with the melt without crystal growth, no growth was included, therefore these stages do not happen. The final stage in the time step, stage 4, is to change the temperature as a result of cooling during that time step.

5.2.2.3 Outputs

The major outputs from this calculation are model diffusion profiles which are saved in the worksheet after each time step, along with the temperature, oxygen fugacity conditions, edge buffer composition, minimum and maximum diffusion coefficient, and length of that time step. These model diffusion profiles can be compared to observed diffusion profiles in forsteritic-olivine relict grains to determine how similar they are in terms of shape and overall diffusion profile width.

5.2.2.4 Example model diffusion profiles

This section examines the effect of the different initial conditions on the shape of the model diffusion profile. Schematic diffusion profiles illustrating the initial and final diffusion couples is shown in Figure 5.4. The example model diffusion profile in Figure 5.5 was created using the initial conditions in Table 5.4 and is shown. In the example model diffusion profiles, only the region inside the forsteritic-olivine relict grain is shown (green area in Figure 5.4). This means that the edge of the forsteritic-olivine relict grain is at 0.

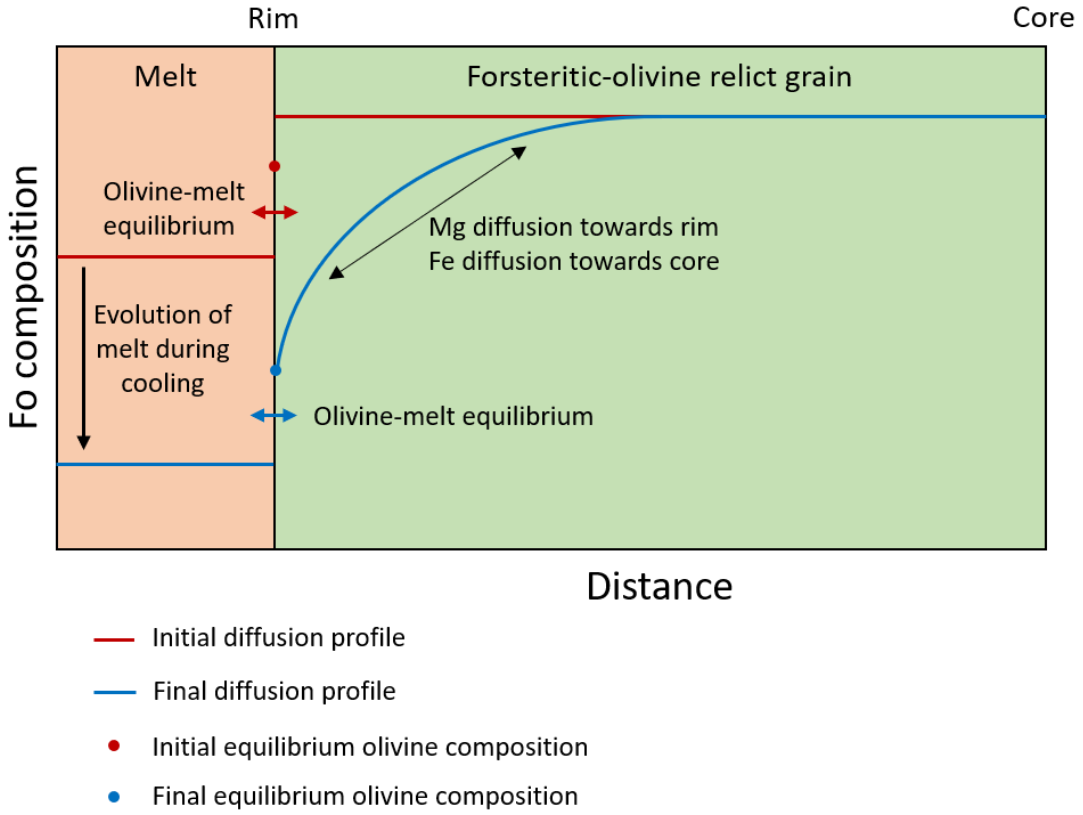

Figure 5.4 – Schematic diffusion profile showing the initial and final compositions of the diffusion couple. The initial couple shows a forsteritic-olivine relict grain with a homogenous composition which is beginning to equilibrate with the chondrule melt which acts as an infinite source with the equilibrium olivine composition at that temperature. Diffusion causes Mg to diffuse out of, and Fe to diffuse into the forsteritic-olivine relict grain. As the chondrule cools, fractional crystallisation of the chondrule melt preferentially removes Mg from the melt leaving it progressively more enriched in Fe. This causes the equilibrium olivine composition to shift to more Fe-rich compositions with time, allowing progressively more Fe to diffuse into, and Mg out of, the forsteritic-olivine relict grain.

Table 5.4 – Initial conditions set for the example model diffusion profile shown in Figure 5.5.

Initial condition	Value
Initial temperature (K)	1873
Cooling rate (Kh^{-1})	1000
Pressure (Pa)	100000
Oxygen fugacity relative to IW buffer (log units)	-1
Anisotropy	1 (c-axis)
Growth rate (ms^{-1})	0
Forsteritic-olivine relict grain composition (Fo mole fraction)	0.98
Olivine-saturated liquidus curve quadratic equation to determine equilibrium olivine composition	$Fo = -1.39 \times 10^{-6}T^2 + 5.86 \times 10^{-3}T - 5.29$

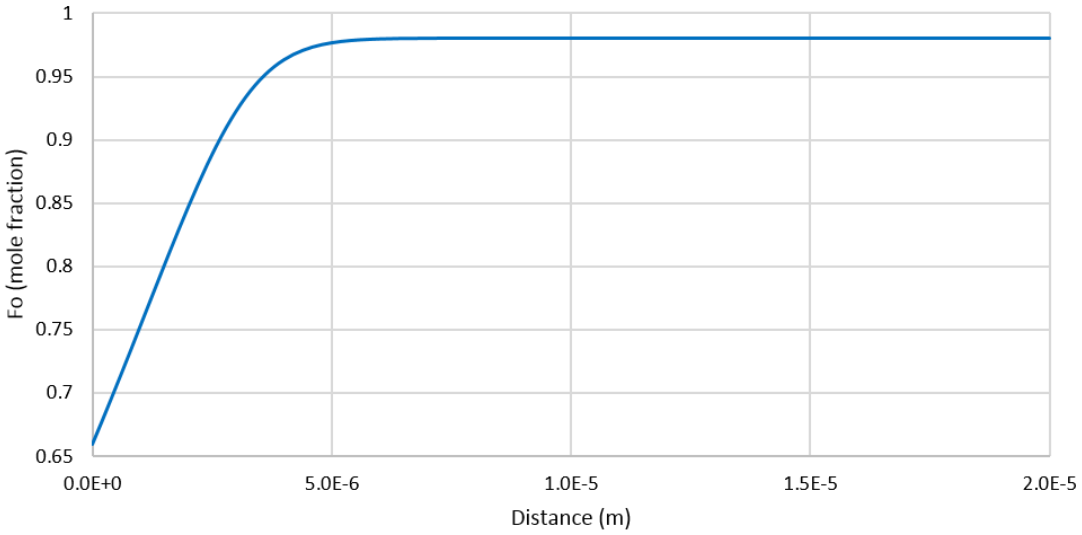

Figure 5.5 – Example model diffusion profile created using the initial conditions shown in Table 5.4.

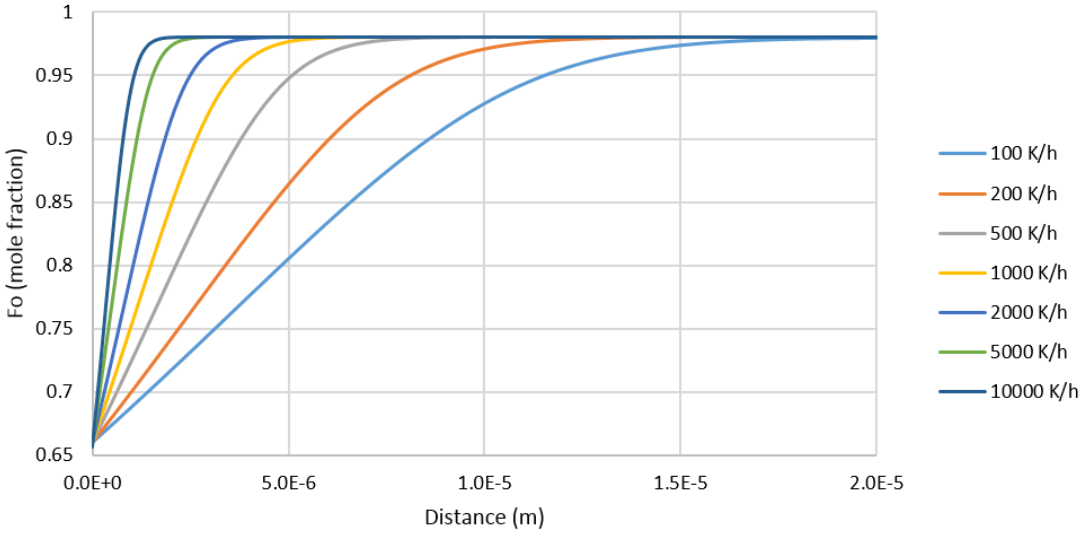

Figure 5.6 – Example model diffusion profiles showing the effect of cooling rate on model diffusion profile shape. Apart from cooling rate, initial conditions are the same as shown in Table 5.4.

Figure 5.6 shows the effect of cooling rate on the shape of the model diffusion profile. At a slower cooling rate, the forsteritic-olivine relict grain remains at high temperatures for a longer time, thereby allowing the grain to equilibrate with the chondrule melt for a longer time allowing diffusion to progress further into the relict grain. At a faster cooling rate, there is less time for diffusion, therefore, diffusion does not progress as far into the relict grain.

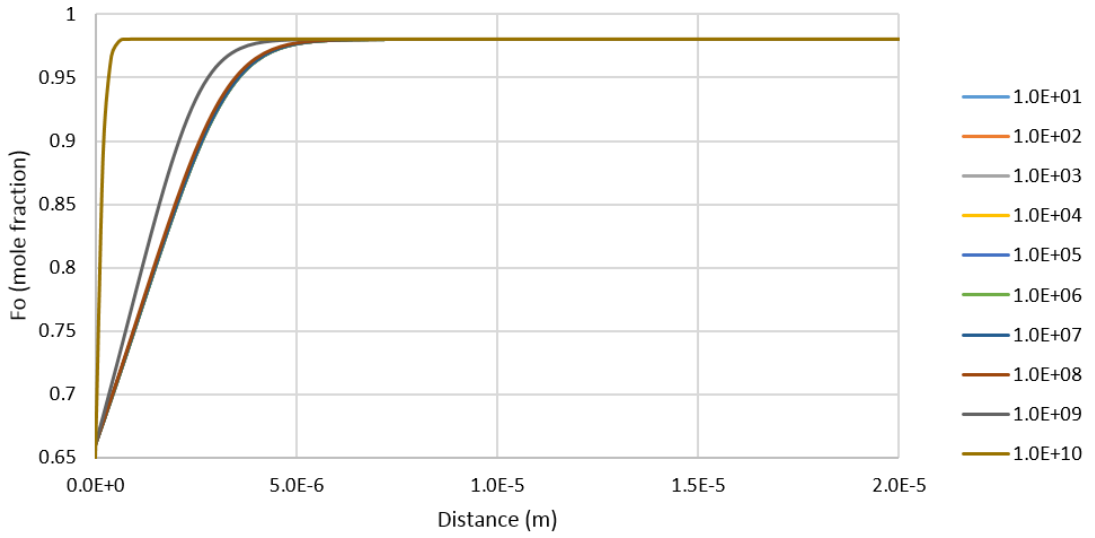

Figure 5.7 – Example model diffusion profiles showing the effects of pressure on model diffusion profile shape. Apart from pressure, initial conditions ae the same as shown in Table 5.4. Legend is pressure in Pa.

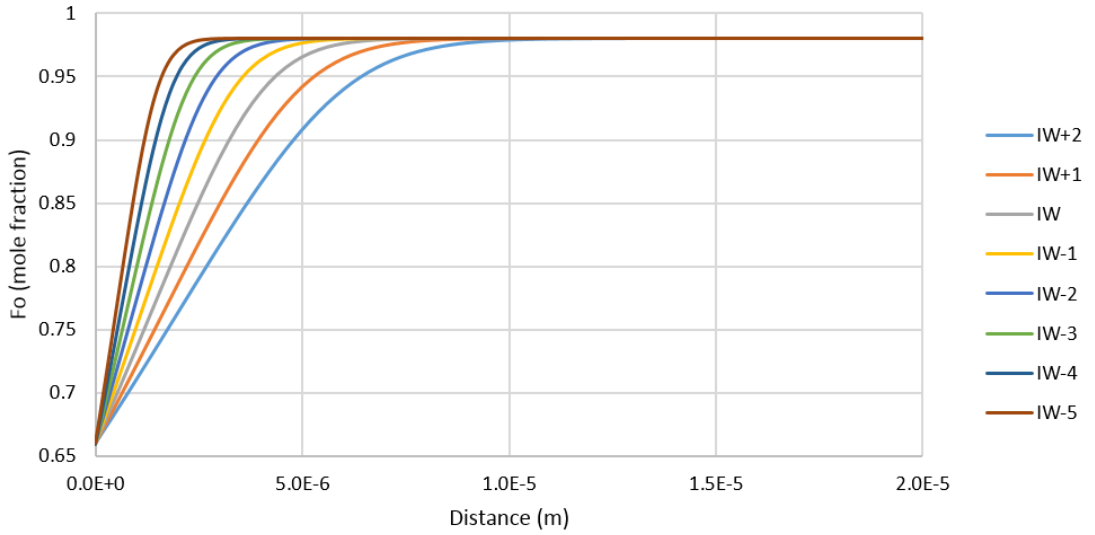

Figure 5.8 – Example model diffusion profiles showing the effect of oxygen fugacity on the model diffusion profile. Apart from oxygen fugacity, the initial conditions are the same as shown in Table 5.4.

Figure 5.7 shows the effect of pressure on the model diffusion profile shape. When examining Equation 5.3, it is clear that increasing pressure works to reduce the diffusion coefficient, slowing diffusion rate, and lowering the width of the model diffusion profile. This only begins to affect the shape of the model diffusion profile at pressures above 10^8 Pa, equivalent to several km depth in the Earth; these pressures are inappropriate to chondrule formation. The pressure of 10^5 Pa used in calculations is much higher than expected for canonical solar nebula pressures. However, as shown by Figure 5.7 this has a negligible effect on Fe-Mg diffusivity and the shape of model diffusion profiles.

The effect of different oxygen fugacity conditions on model diffusion profile shape is shown in Figure 5.8. According to Equation 5.3, more oxidising conditions result in a higher diffusion coefficient, allowing diffusion to occur more rapidly. This is seen in Figure 5.8, where the most oxidising conditions show the widest model diffusion profile and the most reducing conditions show the narrowest diffusion profile. Calculations were undertaken using an oxygen fugacity of 1 log unit beneath the iron-wüstite buffer, based upon the presence of small amounts of Fe,Ni metal in many of the chondrules and the conditions of dynamic crystallisation experiments which reproduced type II chondrule textures at oxygen fugacities of 1 to 0.5 log units beneath the iron-wüstite buffer. Villeneuve et al. (2015) argue that type II chondrules must have formed at more oxidising conditions than these, at a value of 1 log unit above the iron-wüstite buffer. Running diffusion models using these more oxidising conditions results in cooling rates which are only approximately twice as fast as running models at 1 log unit below the iron-wüstite buffer.

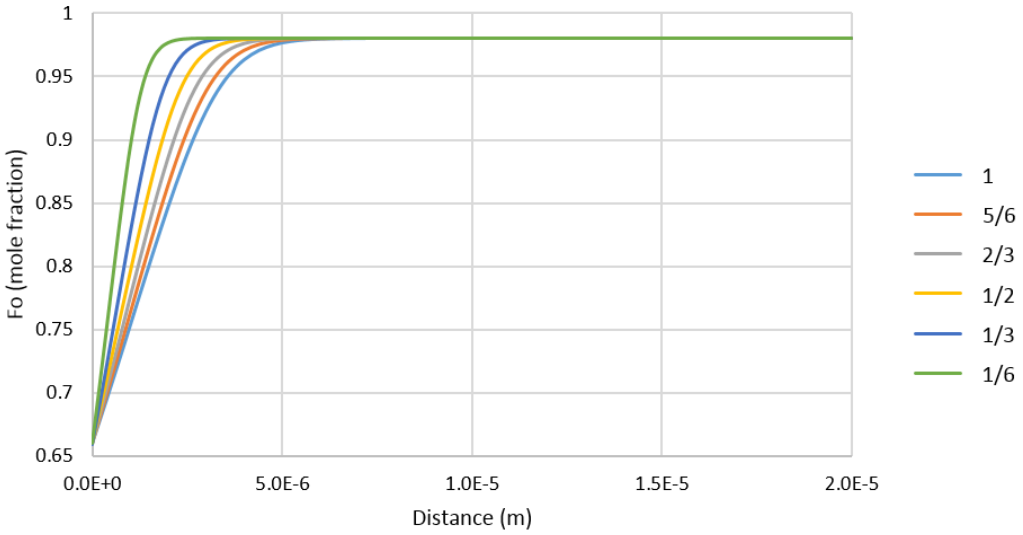

Figure 5.9 – Example model diffusion profiles showing the effects of diffusion anisotropy on model diffusion profile shape. Apart from the anisotropy, the initial conditions are the same as those shown in Table 5.4. Legend is the fraction of c-axis diffusion.

Diffusion anisotropy also influences the resulting model diffusion profile shape and this effect is shown in Figure 5.9. The fastest diffusion occurs along the c-axis, and a factor of 1 refers to the diffusion rate along the c-axis. As diffusion speed is the most rapid, it creates the widest model diffusion profile. Diffusion along the a- or b-axes occurs at 1/6 the rate of diffusion along the c-axis, meaning model diffusion profiles along these axes will be the narrowest. Diffusion anisotropy is therefore set on a scale from 1 for diffusion along the c-

axis, to 1/6 for diffusion along the a- or b-axes. The effect of modifying the anisotropy is seen in Figure 5.9.

Crystal growth has a strong effect on the shape of the model diffusion profile and this is illustrated in Figure 5.10. Crystal growth works to stretch out the model diffusion profile by adding in extra cells to the crystal edge at the boundary with the equilibrium olivine composition at the time of growth. At more rapid growth rates, crystal growth plays a more dominant role than diffusion and creates a distinct growth trend, e.g. the 50 μmh^{-1} growth rate curve in Figure 5.10 which shows a straight line with a more gentle trend towards the grain edge which is not observed in profiles without rapid growth. This shallower trend is observed in compositional profiles which include the overgrowths on the forsteritic-olivine relict grains. This supports the suggestion that there is a diffusion dominated portion within the forsteritic-olivine relict grains which are surrounded by growth dominated zones, i.e. the overgrowth. At 1 μmh^{-1} no growth occurred because not enough time passed to add a new cell.

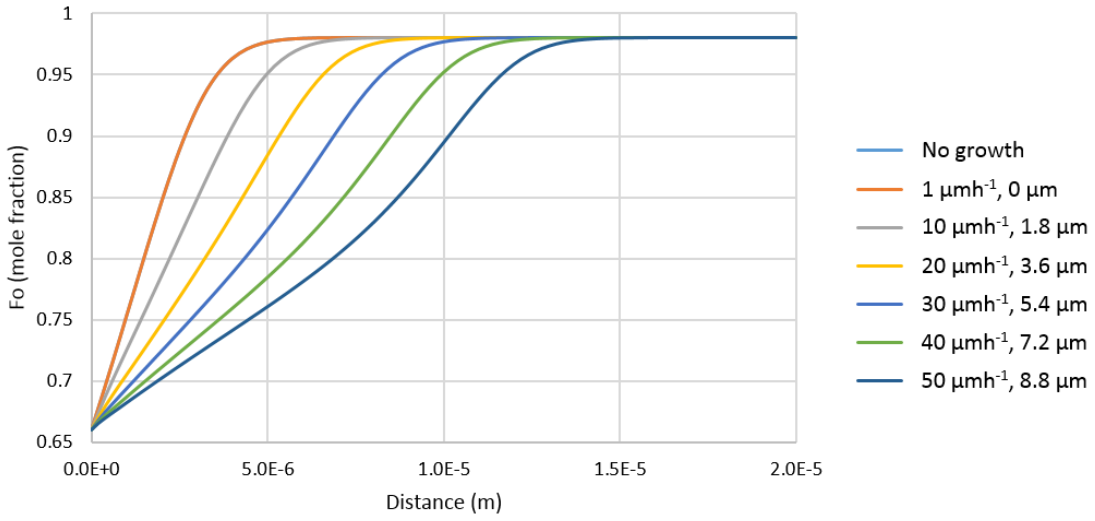

Figure 5.10 – Example model diffusion profiles showing the effect of crystal growth on the model diffusion profile. Apart from growth rate, the initial conditions are the same as shown in Table 5.4. Legend is growth rate and total growth, respectively. The blue no growth curve is behind the orange 1 μmh^{-1} curve. In both these scenarios, no growth occurred, as at a growth rate of 1 μmh^{-1}, not enough time passed to add a new cell.

5.3 Results of diffusion modelling

Overall, 23 compositional profiles present in 13 forsteritic-olivine relict grains across 10 type II, FeO-rich porphyritic olivine chondrules and 2 type II, porphyritic olivine and pyroxene chondrules, were modelled using the 1-D explicit finite difference forward

Table 5.5 – Diffusion model inputs which vary between chondrules and individual compositional profiles for each of the modelled compositional profiles in ALHA 77307, NWA 8276, and NWA 4910.

Profile	Initial temperature (K)	Anisotropy factor	Forsteritic-olivine relict grain composition (Fo mole fraction)	Quadratic equation for the olivine-saturated liquidus curve Fo is Fo mole fraction T is temperature in K	Length scale (m)
Al-1 RG1 A	1906	0.867	0.980	$Fo=-1.39\times10^{-6}T^2+5.86\times10^{-3}T-5.29$	8×10^{-6}
Al-1 RG1 B	1906	0.867	0.977	$Fo=-1.39\times10^{-6}T^2+5.86\times10^{-3}T-5.29$	1.2×10^{-5}
Al-2 RG1 A	1892	0.364	0.978	$Fo=-1.17\times10^{-6}T^2+4.95\times10^{-3}T-4.31$	1.4×10^{-5}
Al-2 RG1 B	1892	0.272	0.977	$Fo=-1.17\times10^{-6}T^2+4.95\times10^{-3}T-4.31$	1×10^{-5}
Al-3 RG1 A	1829	0.331	0.988	$Fo=-1.67\times10^{-6}T^2+6.89\times10^{-3}T-6.23$	1.5×10^{-5}
Al-3 RG1 B	1829	0.954	0.988	$Fo=-1.67\times10^{-6}T^2+6.89\times10^{-3}T-6.23$	1.9×10^{-5}
Al-3 RG1 C	1829	0.962	0.988	$Fo=-1.67\times10^{-6}T^2+6.89\times10^{-3}T-6.23$	1.85×10^{-5}
Al-4 RG1 A	1910	0.483	0.985	$Fo=-1.18\times10^{-6}T^2+5.13\times10^{-3}T-4.62$	5.5×10^{-6}
Al-5 RG1 A	1868	0.168	0.902	$Fo=-1.52\times10^{-6}T^2+6.45\times10^{-3}T-5.92$	4.2×10^{-6}
Al-5 RG1 B	1868	0.837	0.898	$Fo=-1.52\times10^{-6}T^2+6.45\times10^{-3}T-5.92$	3.8×10^{-6}
Al-5 RG2 A	1868	0.933	0.934	$Fo=-1.52\times10^{-6}T^2+6.45\times10^{-3}T-5.92$	3.1×10^{-6}
Al-5 RG2 B	1868	0.952	0.925	$Fo=-1.52\times10^{-6}T^2+6.45\times10^{-3}T-5.92$	2.6×10^{-6}
Al-6 RG1 A	1943	0.418	0.986	$Fo=-1.02\times10^{-6}T^2+4.55\times10^{-3}T-4.10$	7.4×10^{-6}
Al-6 RG1 B	1943	0.858	0.989	$Fo=-1.02\times10^{-6}T^2+4.55\times10^{-3}T-4.10$	6.8×10^{-6}
Al-6 RG1 C	1943	0.869	0.991	$Fo=-1.02\times10^{-6}T^2+4.55\times10^{-3}T-4.10$	1×10^{-5}
Al-6 RG1 D	1943	0.858	0.989	$Fo=-1.02\times10^{-6}T^2+4.55\times10^{-3}T-4.10$	1.12×10^{-5}
N8-1 RG1 A	1883	0.898	0.980	$Fo=-1.15\times10^{-6}T^2+4.70\times10^{-3}T-3.85$	2×10^{-5}
N8-2 RG1 A	1900	0.302	0.966	$Fo=-1.33\times10^{-6}T^2+5.53\times10^{-3}T-4.81$	2.4×10^{-5}
N8-3 RG1 A	1862	0.857	0.951	$Fo=-9.87\times10^{-7}T^2+4.19\times10^{-3}T-3.50$	7×10^{-6}
N4-1 RG1 A	1907	0.726	0.982	$Fo=-8.11\times10^{-7}T^2+3.43\times10^{-3}T-2.66$	1.37×10^{-5}
N4-2 RG1 A	1859	0.196	0.988	$Fo=-1.41\times10^{-6}T^2+5.67\times10^{-3}T-4.79$	1×10^{-5}
N4-2 RG1 B	1859	0.720	0.987	$Fo=-1.41\times10^{-6}T^2+5.67\times10^{-3}T-4.79$	1.2×10^{-5}
N4-3 RG1 A	1936	0.625	0.991	$Fo=-3.92\times10^{-7}T^2+1.74\times10^{-3}T-0.93$	1.5×10^{-5}

modelling program. The compositional profiles show three distinct zones. The innermost zone represents the unmodified core region and the outermost zone is the normal zoning trend caused by fractional crystallisation of the chondrule melt. Between these two zones is the diffusion profile created by the exchange between the forsteritic-olivine relict grain

and the surrounding chondrule melt as it cooled (see Chapter 4 for a more detailed discussion). Diffusion models were only run within the forsteritic-olivine relict grain and overgrowth was not considered. Models were run until the equilibrium olivine composition matched the composition at the boundary between the forsteritic-olivine relict grain and the overgrowth. This is valid as most of the diffusion within the relict grain has already occurred at high temperatures, and when forsteritic-olivine relict grain begins to grow, diffusion is no longer the dominant process.

Some of the model inputs are the same for all chondrules and forsteritic-olivine relict grains. These are pressure, oxygen fugacity with respect to iron-wüstite buffer and growth rate. For pressure, a value of 10^5 Pa was used; for oxygen fugacity, a value of 1 log unit below the iron-wüstite buffer was used; no growth was occurring so models were run with a growth rate of 0 ms^{-1}. Other inputs vary between the individual chondrules e.g. initial temperature and the olivine-saturated liquidus curve. Some inputs are individual to the observed compositional profile, for example, the fraction of c-axis speed because of anisotropy (Anisotropy factor), forsteritic-relict grain composition for the observed compositional profile, and the length-scale of the model profile. Table 5.5 show the inputs that vary between chondrules and individual compositional profiles.

Many previous studies of chondrule cooling rates have usually considered constant (or linear) cooling rates, however, many of the diffusion profiles observed in forsteritic-olivine relict grains display a wide range of shapes. It was impossible to produce model diffusion profiles which matched these using linear cooling rates. However, introducing non-linear cooling, modelled with an instantaneous transition between two cooling rates, produced good fits between the observed and model diffusion profiles. Examples are shown in Figure 5.11. This two-stage history is likely to be an approximation of chondrule formation conditions. Other cooling histories could be considered, for example, thee-stage cooling or exponentially decreasing cooling rates. However, most of the measured compositional profiles were successfully reproduced with a two-stage cooling history, therefore these more complex histories have not been considered.

Figure 5.12 shows the effect of changing transition temperatures in model runs with initial cooling rates of 200 Kh^{-1} transitioning to final cooling rates of 1000 Kh^{-1}. The graphs show that modifying the transition temperature can have profound changes to the shape of the model diffusion profiles. In those with the earliest transition from slower to more rapid

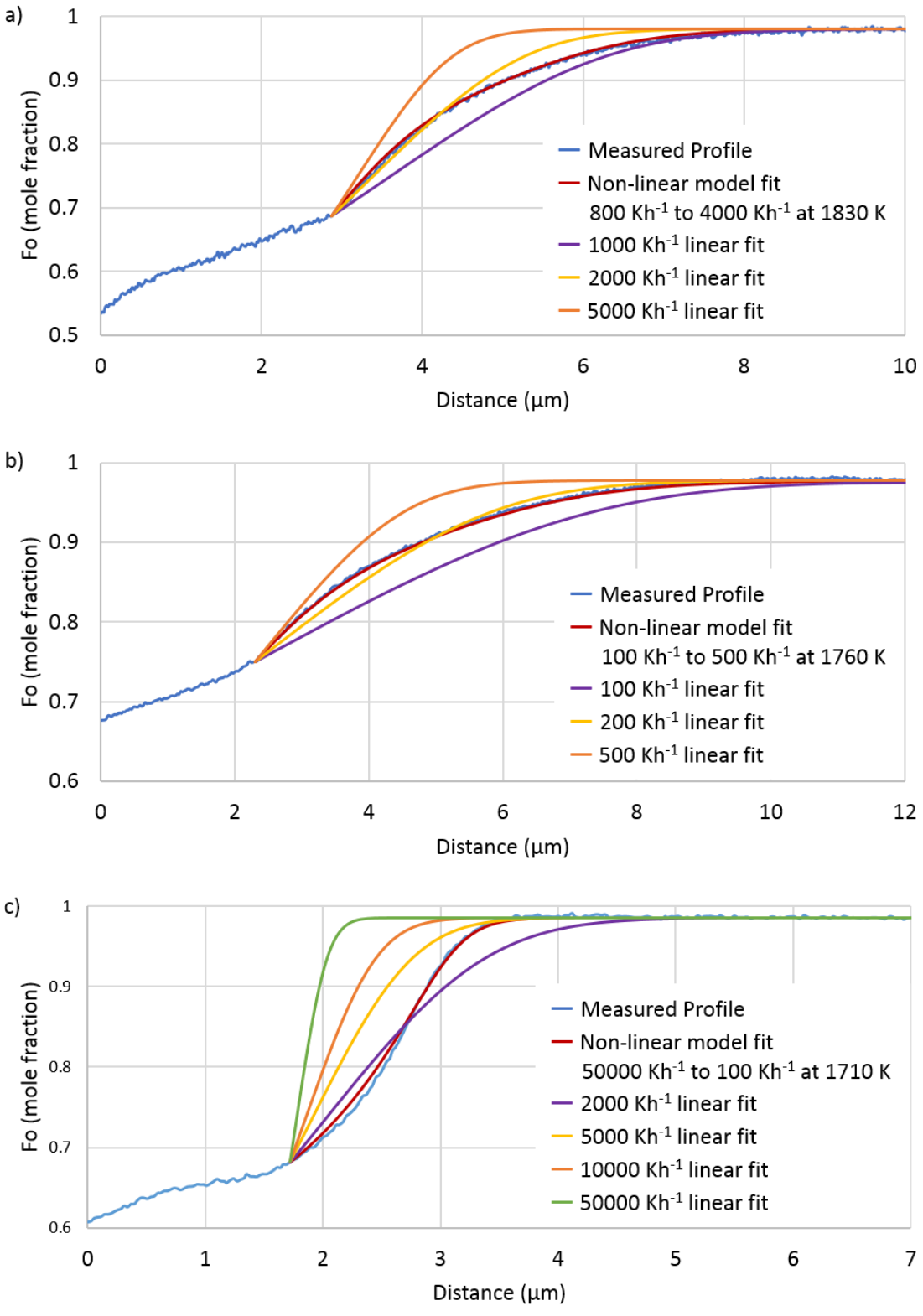

Figure 5.11 – Examples of poor linear cooling rate fits to the observed diffusion profiles that were successfully recreated with non-linear cooling: a) Al-1 RG1 A; b) Al-2 RG1 B; c) Al-4 RG1 A.

cooling rates, there is less overall time for diffusion, so the diffusion profile appears narrowest. In those with later transitions, there is more time for diffusion, so the diffusion profile appears wider. The determined transition temperatures are considered as an accurate estimate (±20K) of the temperature at which the chondrules experienced the fastest change in cooling rate. Outside this range, the model diffusion profile often shows a different shape and displays a poor fit to the observed compositional profile.

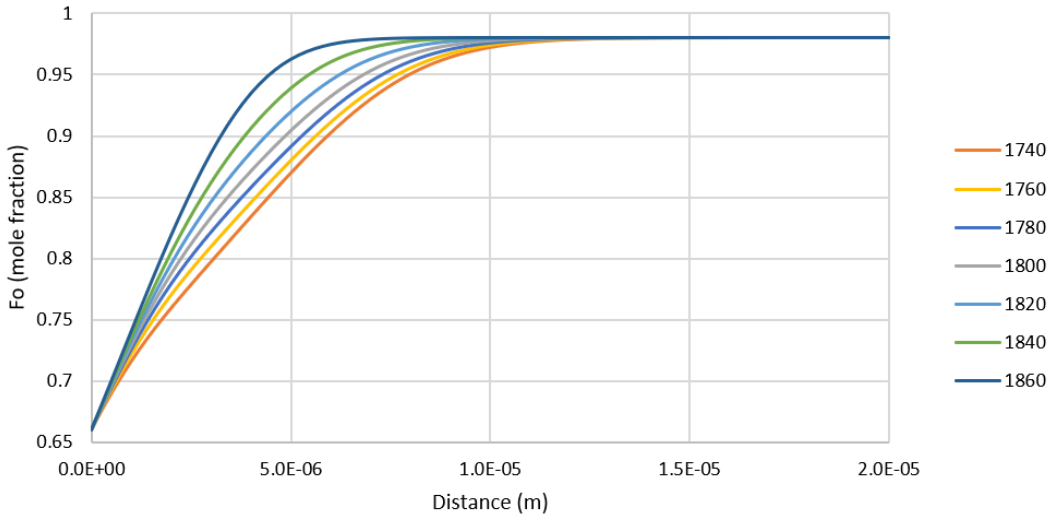

Figure 5.12 – Example model diffusion profiles showing the effect of changing the transition temperature. Initial conditions were the same as in Table 5.4, however, the initial cooling rate was 200 Kh^{-1}, transitioning to 1000 Kh^{-1} at the temperature in the legend in K.

5.3.1 ALHA 77307

Sixteen compositional profiles in 7 forsteritic-olivine relict grains from 6 chondrules in ALHA 77307 have been modelled to determine chondrule cooling rates.

5.3.1.1 Al-1

Chondrule Al-1 contains one forsteritic-olivine relict grain and two compositional profiles were measured. Figure 5.13 shows a BSE image of Al-1 RG1 and the location of compositional profiles A and B. Profile A was successfully reproduced at an initial cooling rate of 800 Kh^{-1} and a final cooling rate of 4000 Kh^{-1} transitioning at 1830 K. Profile B was successfully reproduced at an initial cooling rate of 400 Kh^{-1} and a final cooling rate of 2400 Kh^{-1} transitioning at 1760 K.

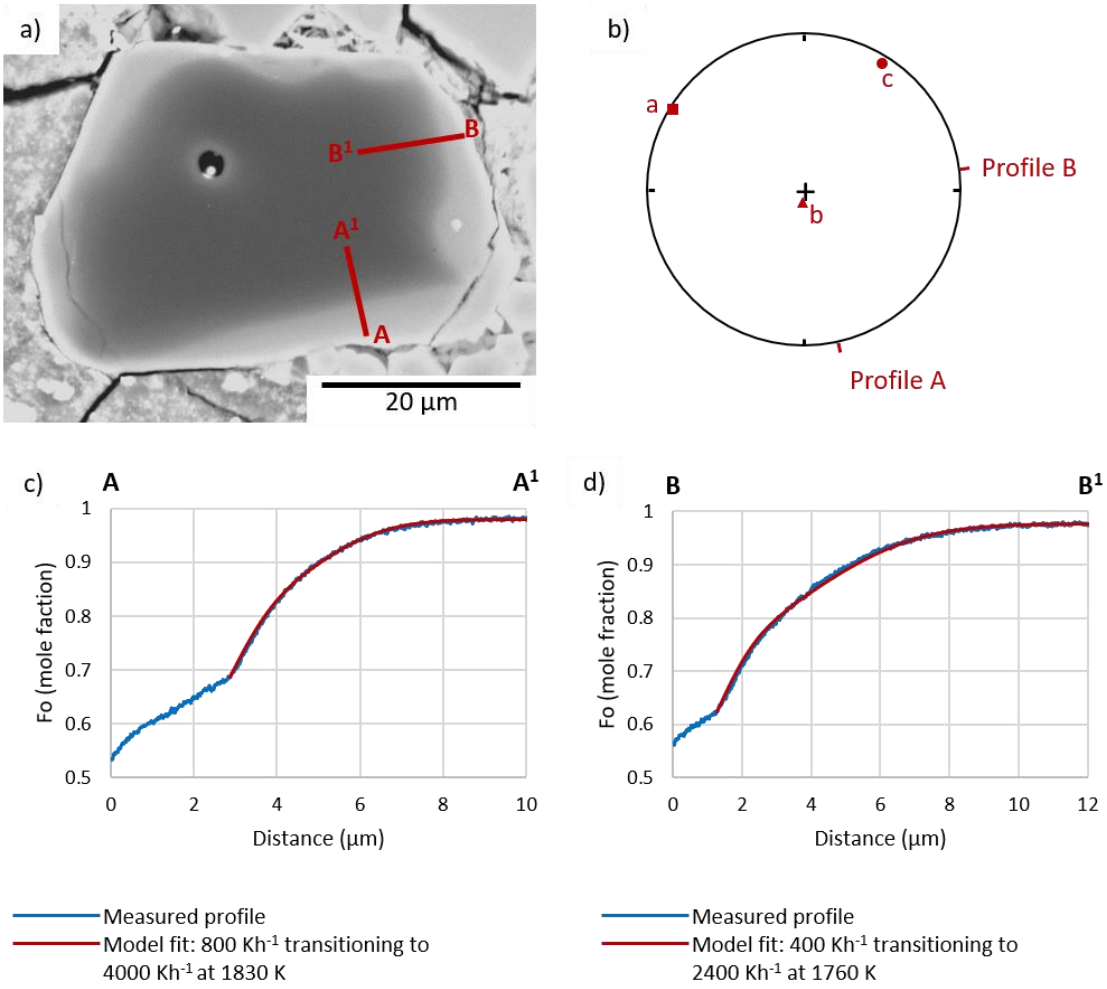

Figure 5.13 – a) BSE image of Al-1 RG1 showing the location of profiles A and B; b) lower hemisphere projection pole figure showing the orientation of the crystallographic axes and measured compositional profiles; c) profile Al-1 RG1 A with model fit; d) profile Al-1 RG1 B with model fit.

5.3.1.2 Al-2

Chondrule Al-2 contains one forsteritic-olivine relict grain and two compositional profiles were measured. Figure 5.14 shows a BSE image of Al-2 RG1 and the location of compositional profiles A and B. Profile A was successfully reproduced at an initial cooling rate of 100 Kh^{-1} and a final cooling rate of 1400 Kh^{-1} transitioning at 1820 K. Profile B was successfully reproduced at an initial cooling rate of 100 Kh^{-1} and a final cooling rate of 500 Kh^{-1} transitioning at 1830 K.

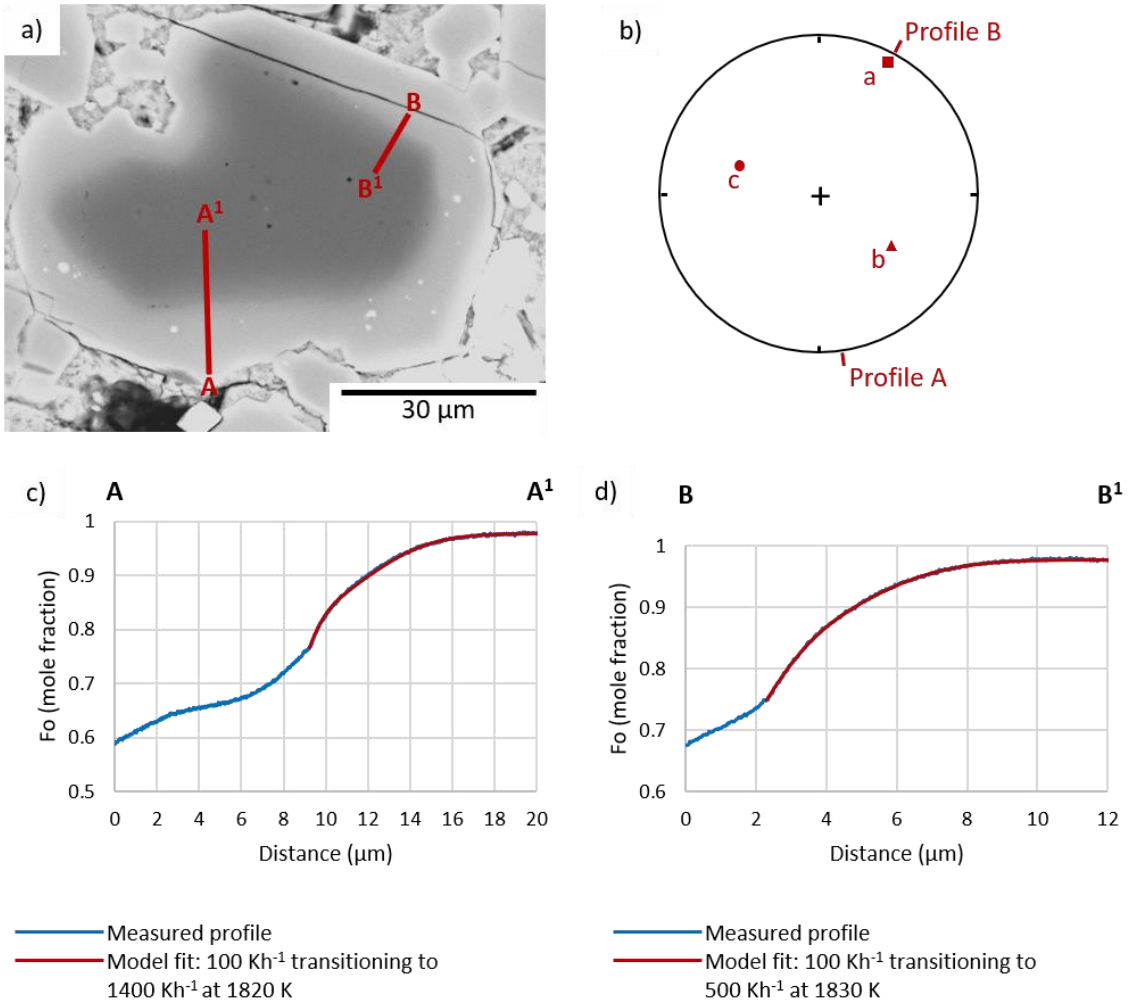

Figure 5.14 – a) BSE image of Al-2 RG1 showing the location of profiles A and B; b) lower hemisphere projection pole figure showing the orientation of the crystallographic axes and measured compositional profiles; c) profile Al-2 RG1 A with model fit; d) profile Al-2 RG1 B with model fit.

5.3.1.3 Al-3

Chondrule Al-3 contains one forsteritic-olivine relict grain and three compositional profiles were measured. Figure 5.15 shows a BSE image of Al-3 RG1 and the location of profiles A, B and C. Profile A was successfully reproduced at an initial cooling rate of 150 Kh^{-1} and final cooling rate of 100 Kh^{-1} transitioning at 1780 K. Profile B was successfully reproduced at an initial cooling rate of 150 Kh^{-1} transitioning to 250 Kh^{-1} at 1780 K. Profile C was successfully reproduced using a linear cooling rate of 200 Kh^{-1}.

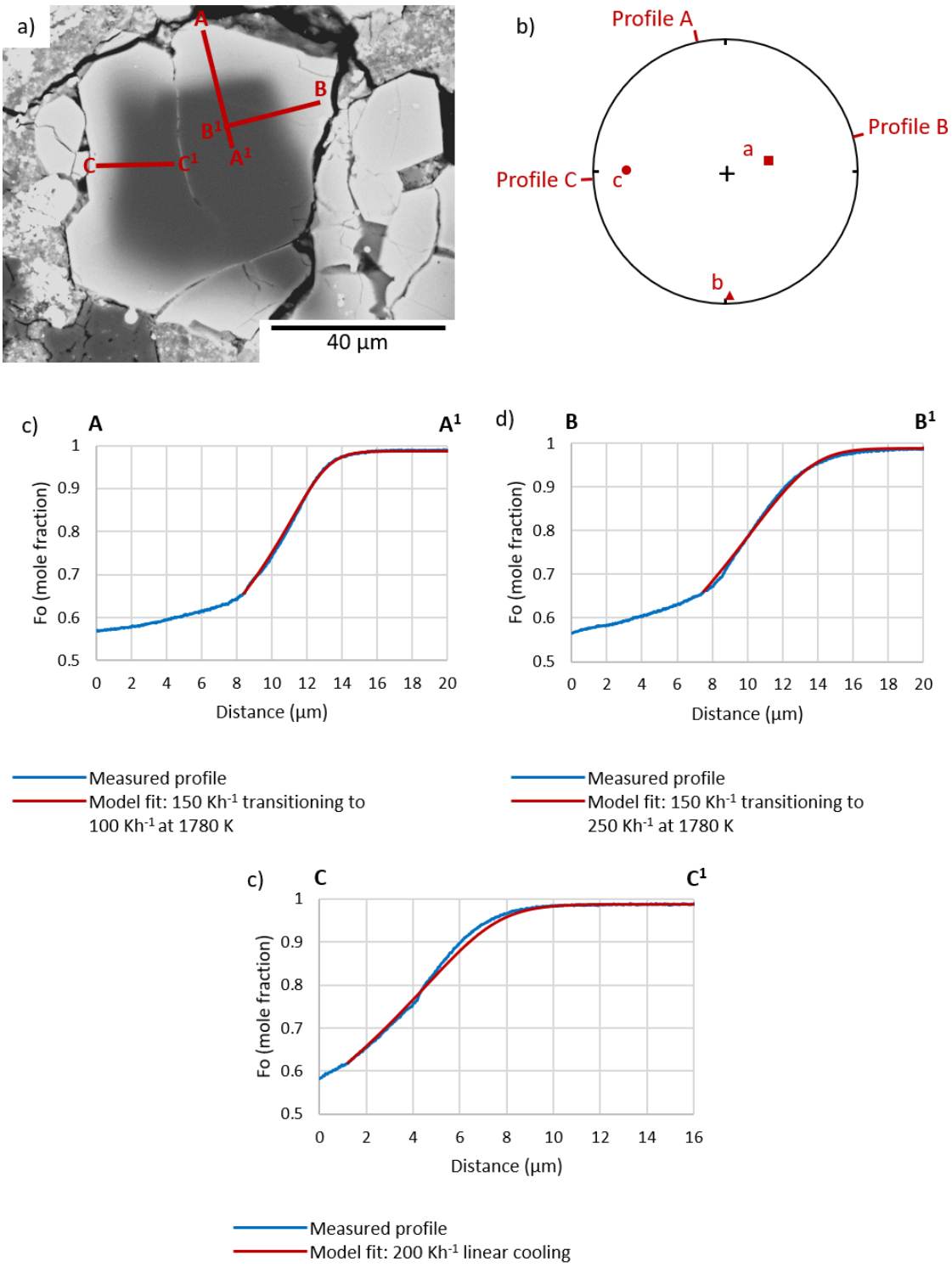

Figure 5.15 – a) BSE image of Al-3 RG1 showing the location of profiles A, B and C; b) low hemisphere projection pole figure showing the orientation of the crystallographic axes and measured compositional profules; c) profile Al-3 RG1 A with model fit; d) profile Al-3 RG1 B with model fit; e) profile Al-3 RG1 C with model fit.

5.3.1.4 Al-4

Chondrule Al-4 contains one forsteritic-olivine relict grain and one compositional profile was measured. Figure 5.16 shows a BSE image of Al-4 RG1 and the location of profile A. This profile was reproduced with an initial cooling rate of 50000 Kh^{-1} and a final cooling rate of 100 Kh^{-1} transitioning at a temperature of 1710 Kh^{-1}. No other boundaries could be tested on this grain. The BSE image of the upper boundary suggests that it is sectioned at a much shallower angle than the lower boundary, and it would be inappropriate to model diffusion on this boundary.

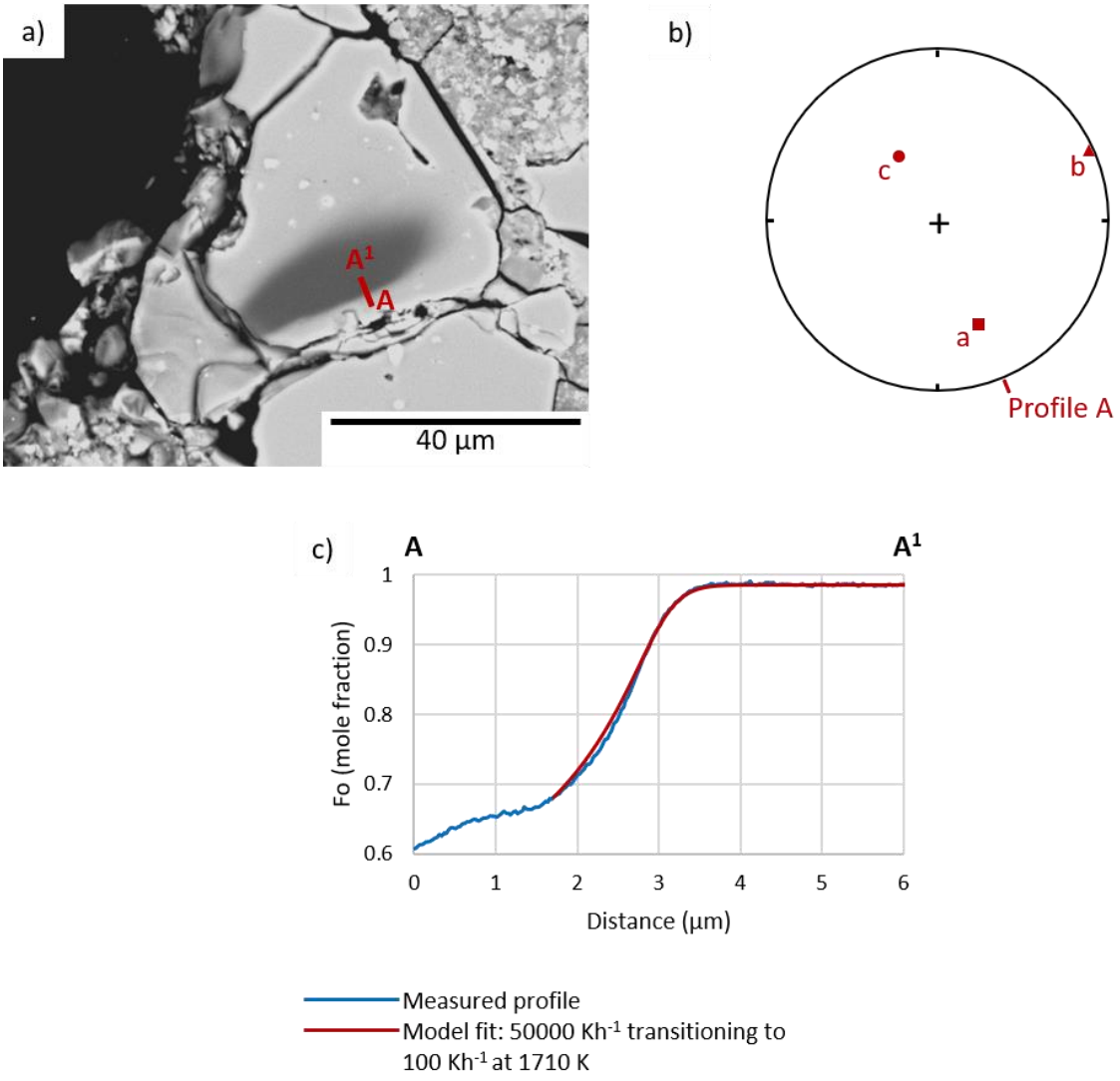

Figure 5.16 – a) BSE image of Al-4 RG1 showing the location of profile A; lower hemisphere projection pole figure showing the orientation of the crystallographic axes and profile A; c) profile Al-4 RG1 A with model fit.

5.3.1.5 Al-5

Chondrule Al-5 contains two forsteritic-olivine relict grains with suitable faces for diffusion modelling, and overall, four compositional profiles were measured. Figure 5.17 shows a BSE image of Al-5 RG1 and the location of profiles A and B. Profile A was successfully reproduced at an initial cooling rate of 250 Kh^{-1} and a final cooling rate of 2000 Kh^{-1} transitioning at a temperature of 1800 K. Profile B was successfully reproduced at an initial cooling rate of 3000 Kh^{-1} and a final cooling rate of 5000 Kh^{-1} transitioning at a temperature of 1750 K.

Figure 5.18 shows a BSE image of Al-5 RG2 and the location of profiles A and B. Profile A was successfully reproduced with an initial cooling rate of 3000 Kh^{-1} and a final cooling rate of 6000 Kh^{-1} transitioning at a temperature of 1780 K. Profile A was successfully reproduced

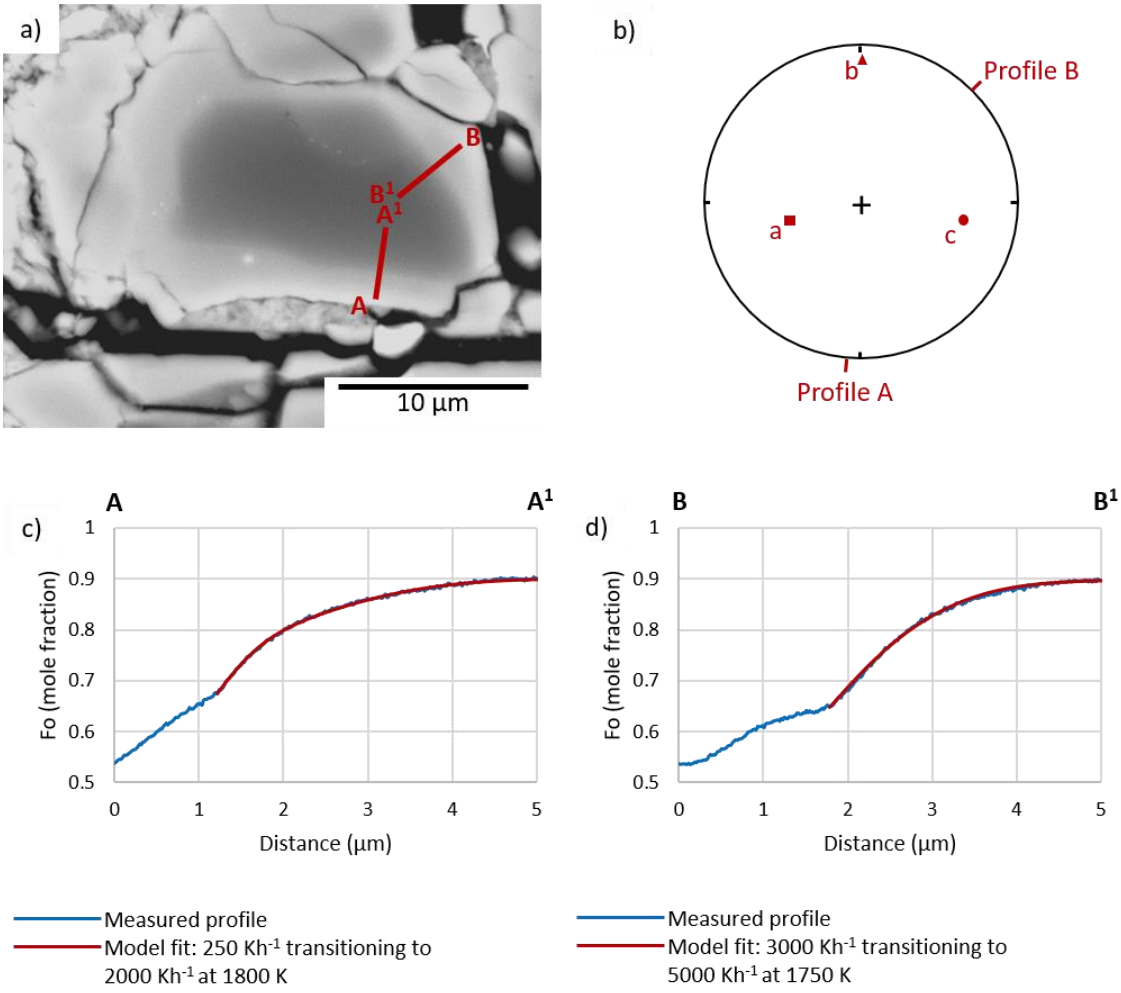

Figure 5.17 – a) BSE image of Al-5 RG1 showing the location of profiles A and B; lower hemisphere projection pole figure showing the orientation of the crystallographic axes and profiles A and B; c) profile Al-5 RG1 A with model fit; d) profile Al-5 RG1 B with model fit.

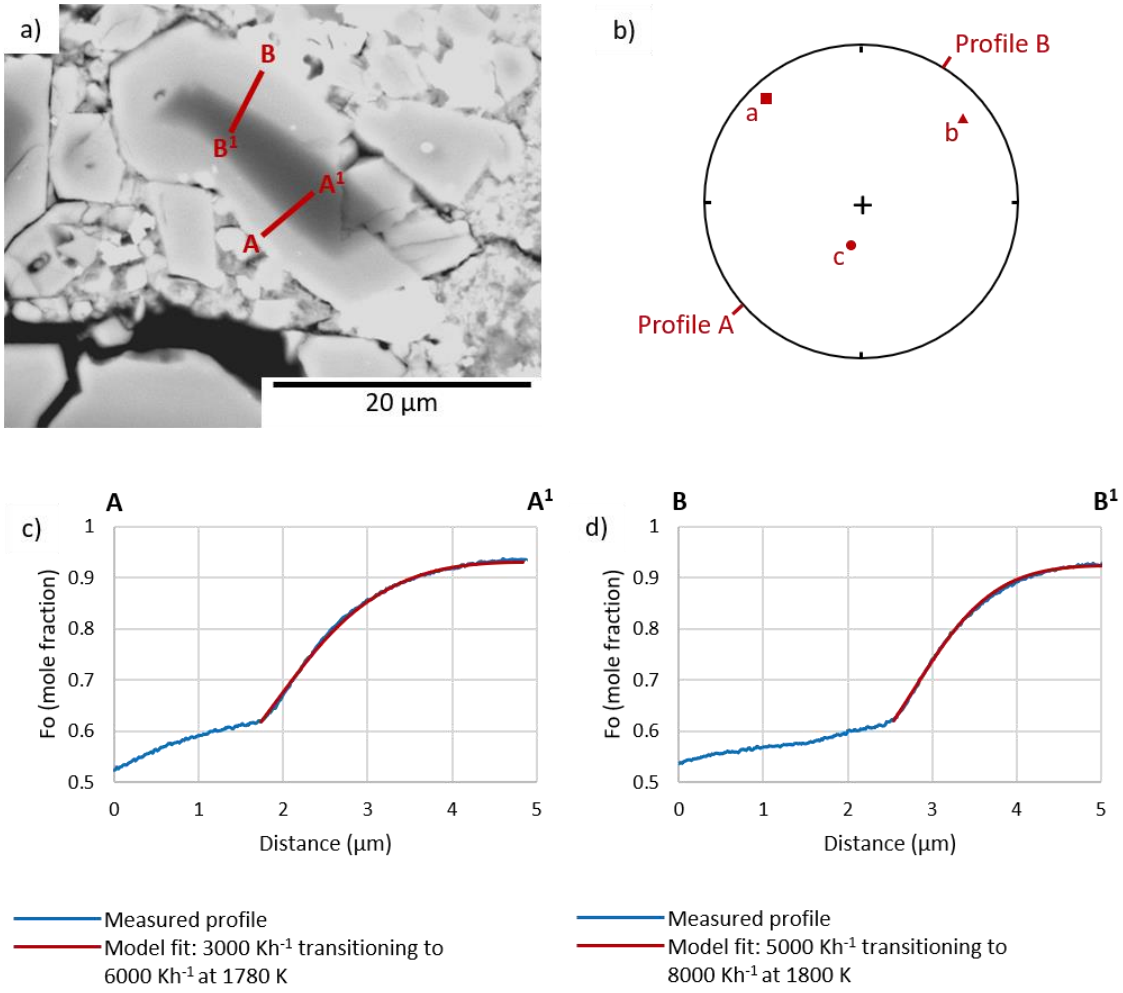

Figure 5.18 – a) BSE image of Al-5 RG2 showing the location of profiles A and B; lower hemisphere projection pole figure showing the orientation of the crystallographic axes and profiles A and B; c) profile Al-5 RG2 A with model fit; d) profile Al-5 RG2 B with model fit.

with an initial cooling rates of 5000 Kh^{-1} and a final cooling rate of 8000 Kh^{-1} transitioning at a temperature of 1800 Kh^{-1}.

5.3.1.6 Al-6

Chondrule Al-6 contains a large forsteritic-olivine relict grain and four compositional profiles were measured. Figure 5.19 shows a BSE image of Al-6 RG1 and the location of profiles A, B, C and D. Profile A was reproduced with a linear cooling rate of 500 Kh^{-1}. Profile B was reproduced with an initial cooling rate of 2000 Kh^{-1} and a final cooling rate of 400 Kh^{-1} with a transition temperature of 1760 K. Profile C was reproduced with a linear cooling rate of 1500 Kh^{-1}. Profile D was reproduced with an initial cooling rate of 1600 Kh^{-1} and a final cooling rate of 800 Kh^{-1} with a transition temperature of 1780 K.

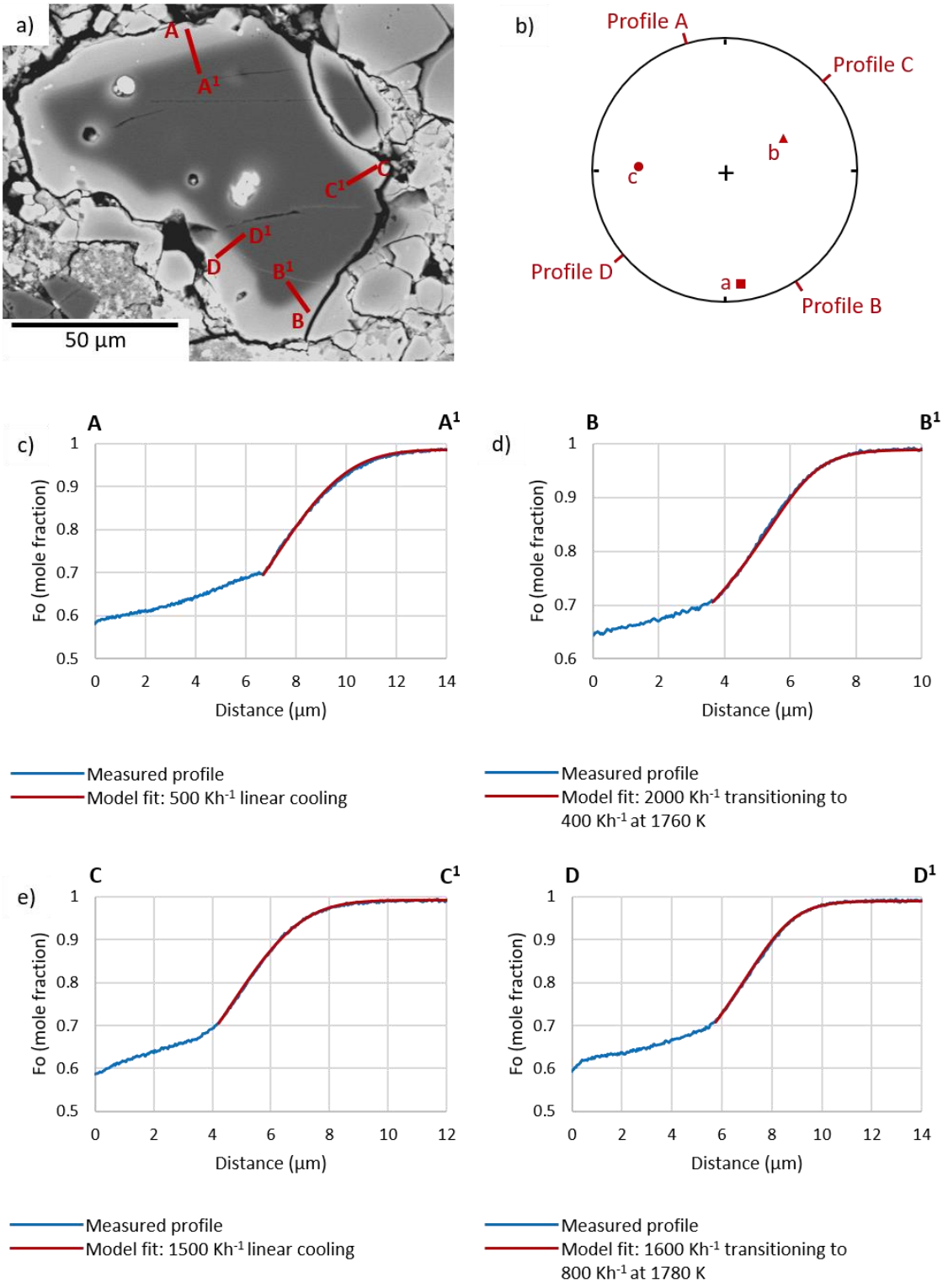

Figure 5.19 – a) BSE image of Al-6 RG1 showing the location of profiles A, B, C and D; b) lower hemisphere projection pole figure showing the orientation of the crystallographic axes and profiles A, B, C and D; c) profile Al-6 RG1 A with model fit; d) profile Al-6 RG1 B with model fit; e) profile Al-6 RG1 C with model fit; f) profile Al-6 RG1 D with model fit.

5.3.1.7 Modelling with reduced liquidus temperatures

In Chapter 3, it was suggested that chondrule liquidus temperatures may have been overestimated because of mesostasis alteration in the chondrules in ALHA 77307. By substituting altered mesostasis compositions for pristine mesostasis compositions from Kainsaz CO3.2 (Berlin et al., 2011), alternative bulk compositions were calculated. Fractional crystallisation calculations using these new bulk compositions show liquidus temperatures which are reduced by 37 to 70 K. Overall, a similar temperature range is modelled, however, as the temperature is lower, the diffusion rate is also reduced. Because of this, more diffusion time is required to produce profiles which match the observed compositional profile. This manifests as a reduction in cooling rate. Diffusion modelling undertaken with these reduced liquidus temperatures suggest cooling rates could be one third to two thirds of their modelled values here with transition temperatures reduced by amounts roughly equivalent to the reduction in liquidus temperature.

5.3.1.8 ALHA 77307 summary

The results of diffusion modelling for the seven forsteritic-olivine relict grains in chondrules from ALHA 77307 generally show cooling rates varying from 100 Kh^{-1} to 8000 Kh^{-1} over the modelled temperature range, ~1950 to ~1660 K, (see Table 5.6 and Figure 5.20) with one

Table 5.6 – Chondrule cooling rates from modelling of diffusion profiles in forsteritic-olivine relict grains in chondrules from ALHA 77307. Initial temperature is the chondrule liquidus temperature. The final temperature is the temperature at which the equilibrium olivine composition matched the composition at the boundary between the forsteritic-olivine relict grain and the overgrowth, which is when models were stopped. Cooling across the considered temperature range was modelled linearly or in 2 stages transitioning instantly at the transition temperature.

Profile	Initial cooling rate (Kh^{-1})	Final cooling rate (Kh^{-1})	Initial temperature (K)	Transition temperature (K)	Final temperature (K)	Modelled temperature range (K)
Al-1 RG1 A	800	4000	1906	1830	1716	190
Al-1 RG1 B	400	2400	1906	1760	1663	243
Al-2 RG1 A	100	1400	1892	1820	1751	141
Al-2 RG1 B	100	500	1892	1830	1731	161
Al-3 RG1 A	150	100	1829	1780	1693	136
Al-3 RG1 B	150	250	1829	1780	1696	133
Al-3 RG1 C	200	200	1829	N/A	1663	166
Al-4 RG1 A	50000	100	1910	1714	1710	229
Al-5 RG1 A	250	2000	1868	1800	1721	147
Al-5 RG1 B	3000	5000	1868	1750	1700	168
Al-5 RG2 A	3000	6000	1868	1750	1677	191
Al-5 RG2 B	5000	8000	1868	1800	1679	189
Al-6 RG1 A	500	500	1943	N/A	1714	219
Al-6 RG1 B	2000	400	1943	1750	1724	220
Al-6 RG1 C	1500	1500	1943	N/A	1723	218
Al-6 RG1 D	1600	800	1943	1780	1725	212

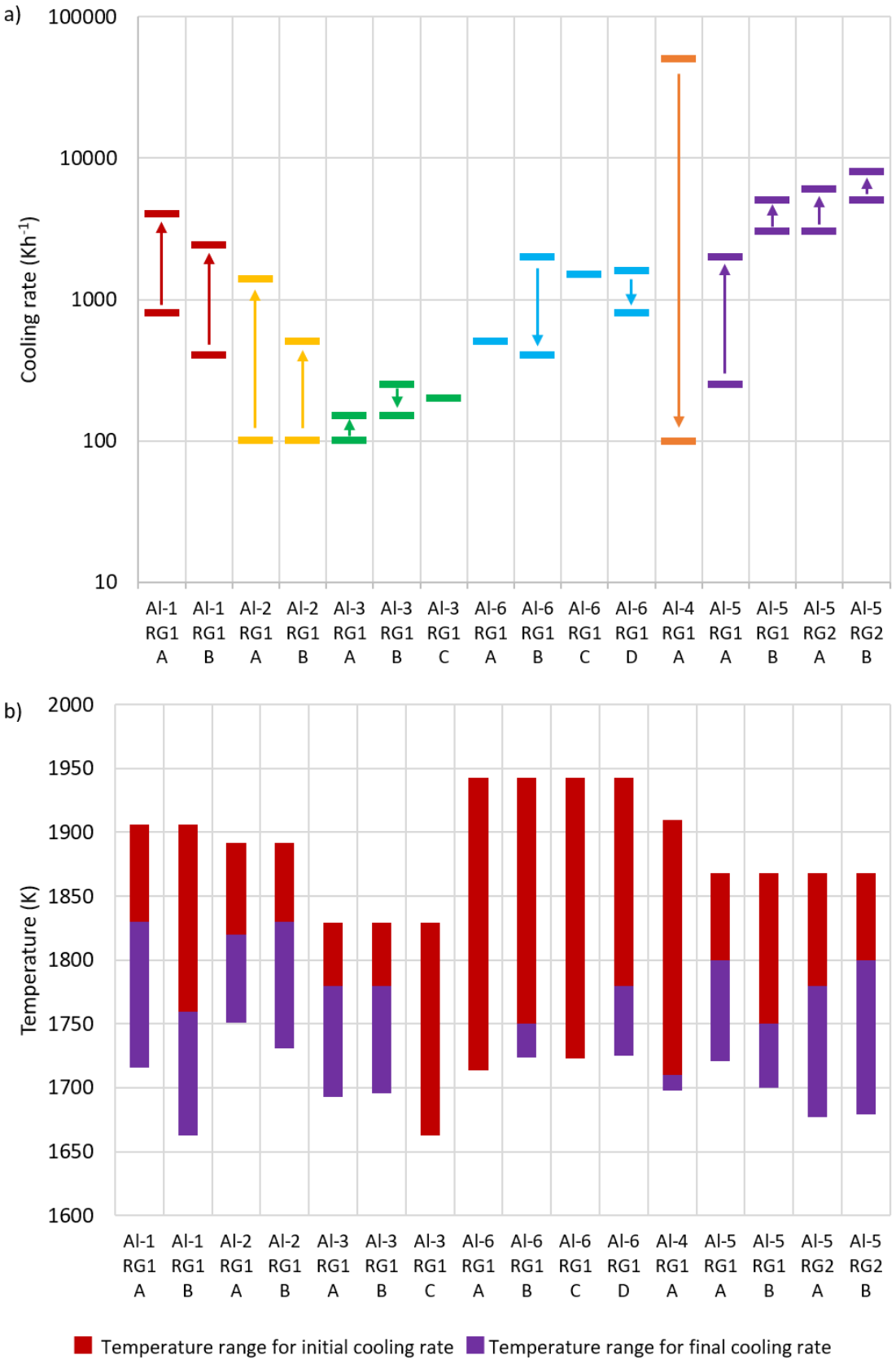

Figure 5.20 – a) summary of cooling rates from profiles in ALHA 77307. Arrow direction indicates whether cooling rates increased or decreased; b) summary of the contribution of initial and final cooling rates across the modelled temperature range for profiles in ALHA 77307.

chondrule experiencing much faster cooling rates. This one exception, Al-4 RG1, has a very narrow diffusion profile, less than 2 µm wide, indicative of cooling very rapidly. Only three of the diffusion profiles could be modelled well assuming linear cooling: Al-3 RG1 C and Al-6 RG1 A and C. The remaining 13 resulted from non-linear cooling, either increasing or decreasing cooling rates, modelled in two stages, transitioning instantly at a transition temperature (see Table 5.6 and Figure 5.20).

5.3.2 NWA 8276 and NWA 4910

5.3.2.1 N8-1

Chondrule N8-1 contains one forsteritic-olivine relict grain and a single compositional profile was measured. Figure 5.21 shows a BSE image of N8-1 RG1 showing the location of

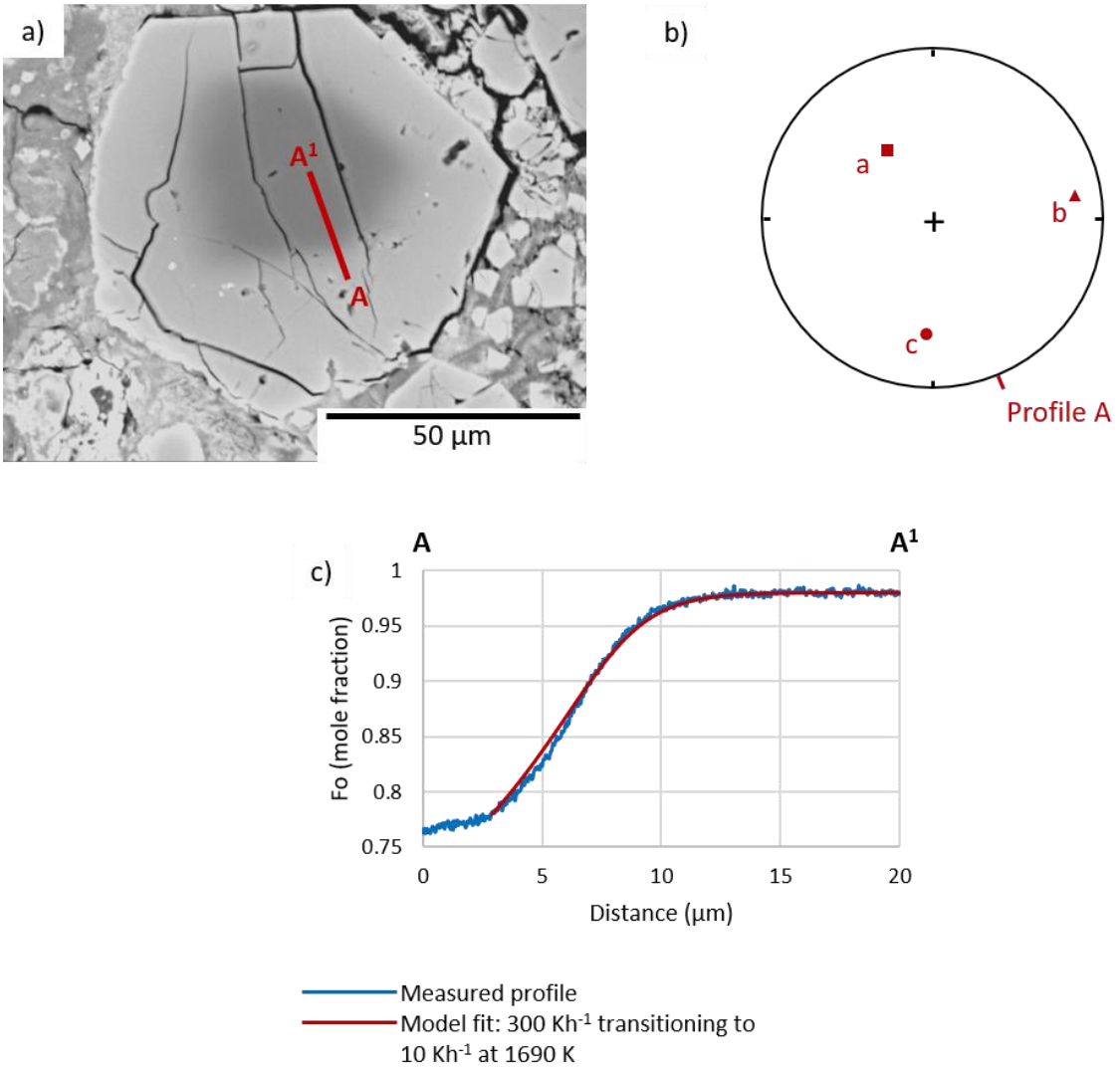

Figure 5.21 – a) BSE image of N8-1 RG1 showing the location of profile A; b) lower hemisphere projection pole figure showing the orientation of the crystallographic axes and profile A; c) profile N8-1 RG1 A with model fit.

profile A. Profile A was reproduced with an initial cooling rate of 300 Kh^{-1} and a final cooling rate of 10 Kh^{-1} transitioning at 1690 K.

5.3.2.2 N8-2

Chondrule N8-2 contains one forsteritic-olivine relict grain and one compositional profile was measured. Figure 5.22 shows a BSE image of N8-2 RG1 showing the location of profile A. Profile A was reproduced with an initial cooling rate of 100 Kh^{-1} and a final cooling rate of 20 Kh^{-1} transitioning at 1800 K.

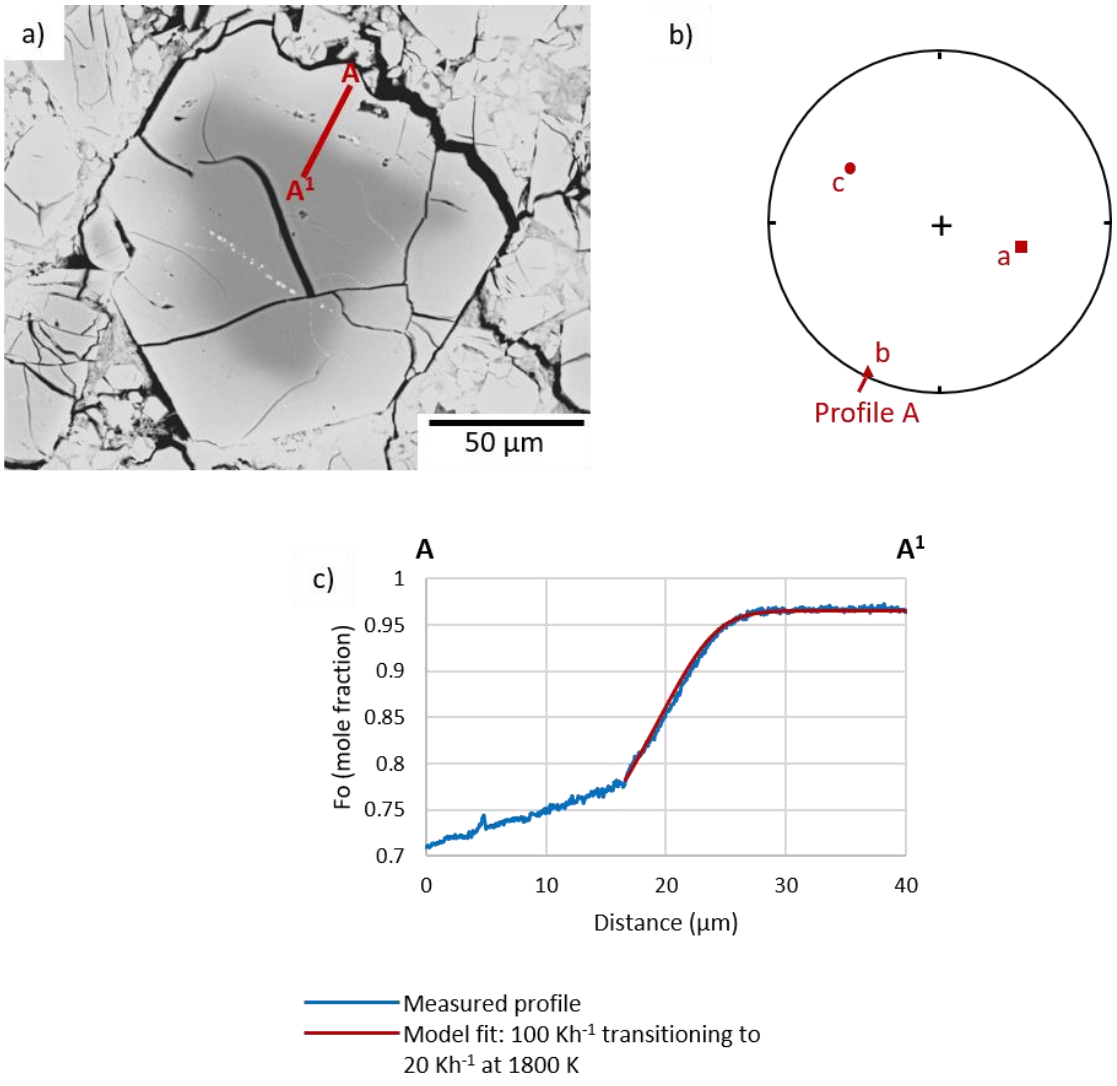

Figure 5.22 – a) BSE image of N8-2 RG1 showing the location of profile A; b) lower hemisphere projection pole figure showing the orientation of the crystallographic axes and profile A; c) profile N8-2 RG1 A with model fit.

5.3.2.3 N8-3

Chondrule N8-3 contains one forsteritic-olivine relict grain with boundaries suitable for diffusion modelling and one compositional profile was measured. Figure 5.23 shows a BSE image of N8-3 RG1 showing the location of profile A. Profile A was reproduced with an initial cooling rate of 2000 Kh^{-1} and a final cooling rate of 50 Kh^{-1} transitioning at 1700 K.

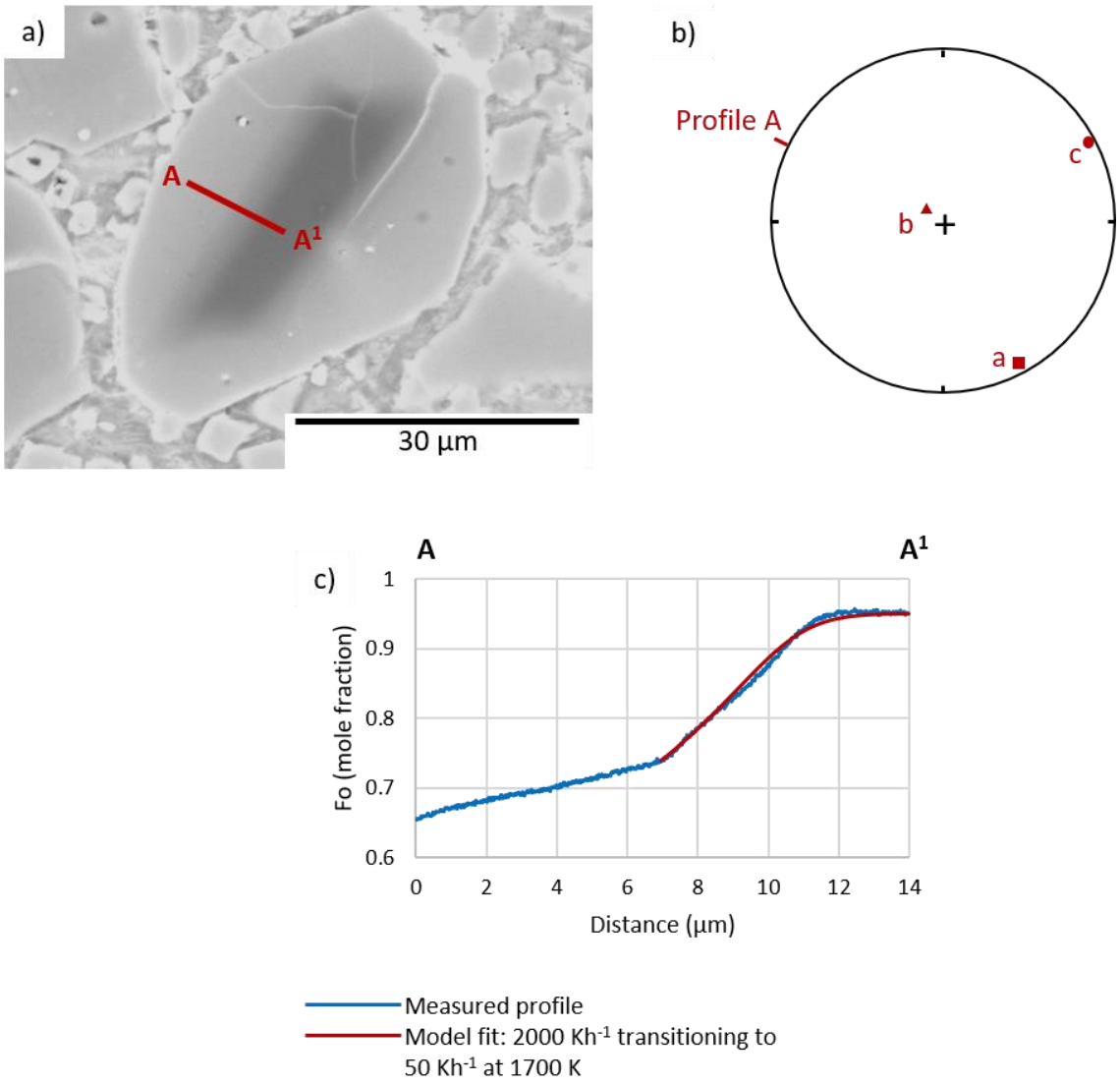

Figure 5.23 – a) BSE image of N8-3 RG1 showing the location of profile A; b) lower hemisphere projection pole figure showing the orientation of the crystallographic axes and profile A; c) profile N8-3 RG1 A with model fit.

5.3.2.4 N4-1

Chondrule N4-1 contains 1 forsteritic-olivine relict grain and 1 compositional profile was measured. Figure 5.24 shows a BSE image of N4-1 RG1 showing the location of profile A. The most successful model fit was produced with an initial cooling rate of 4000 Kh^{-1} and a final cooling rate of 5 Kh^{-1} transitioning at a temperature of 1714 K.

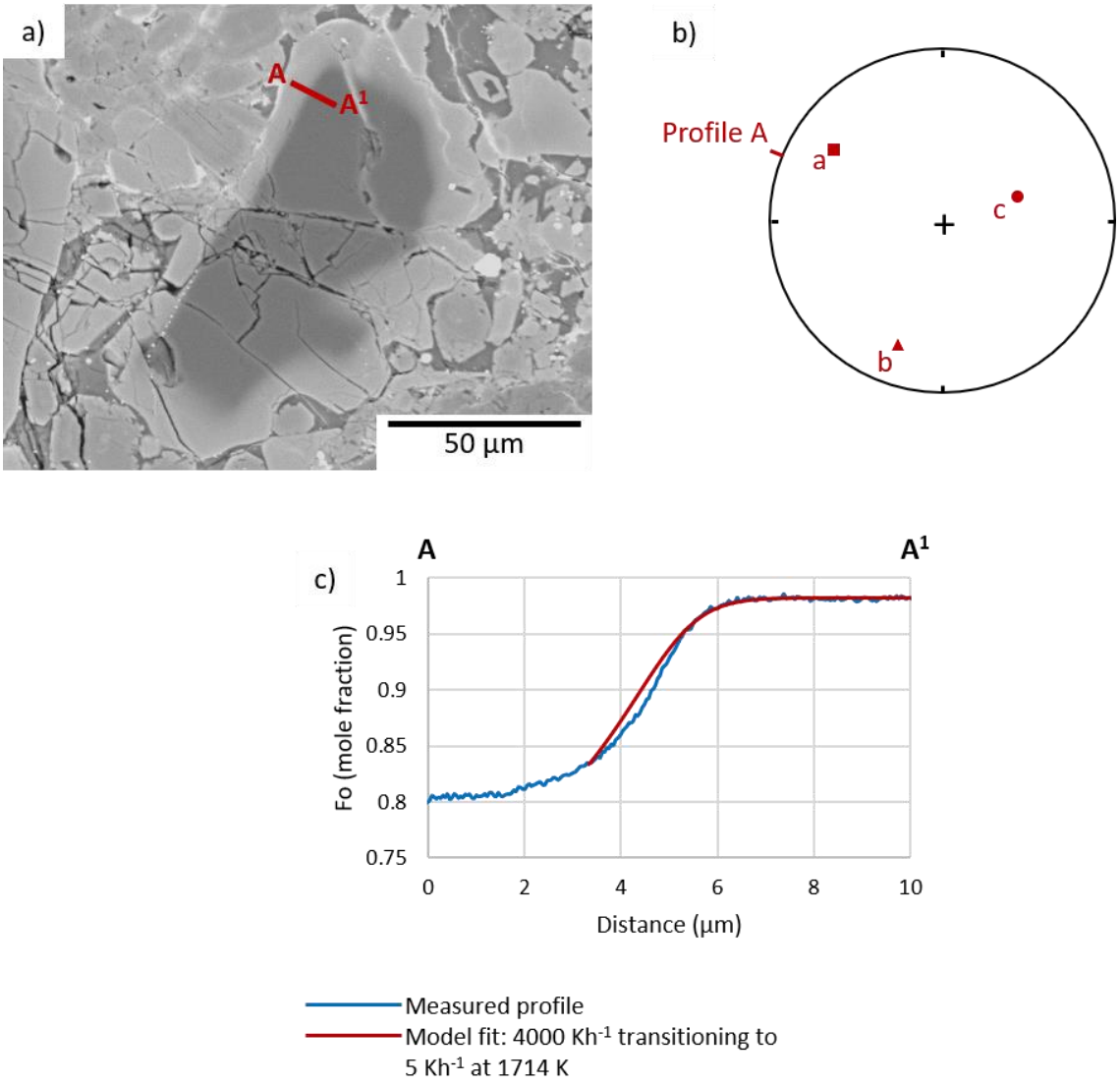

Figure 5.24 – a) BSE image of N4-1 RG1 showing the location of profile A; b) lower hemisphere projection pole figure showing the orientation of the crystallographic axes and profile A; c) profile N4-1 RG1 A with model fit.

5.3.2.5 N4-2

Chondrule N4-2 contains one forsteritic-olivine relict grain and two compositional profiles were measured. Figure 5.25 shows a BSE image of N4-2 RG1 showing the location of profiles A and B. Profile A was successfully modelled with an initial cooling rate of 1000 Kh^{-1} and a final cooling rate of 20 Kh^{-1} transitioning at a temperature of 1725 K. The most successful fit for profile B was created with an initial cooling rate of 5000 Kh^{-1} and a final cooling rate of 5 Kh^{-1} transitioning at a temperature of 1672 K.

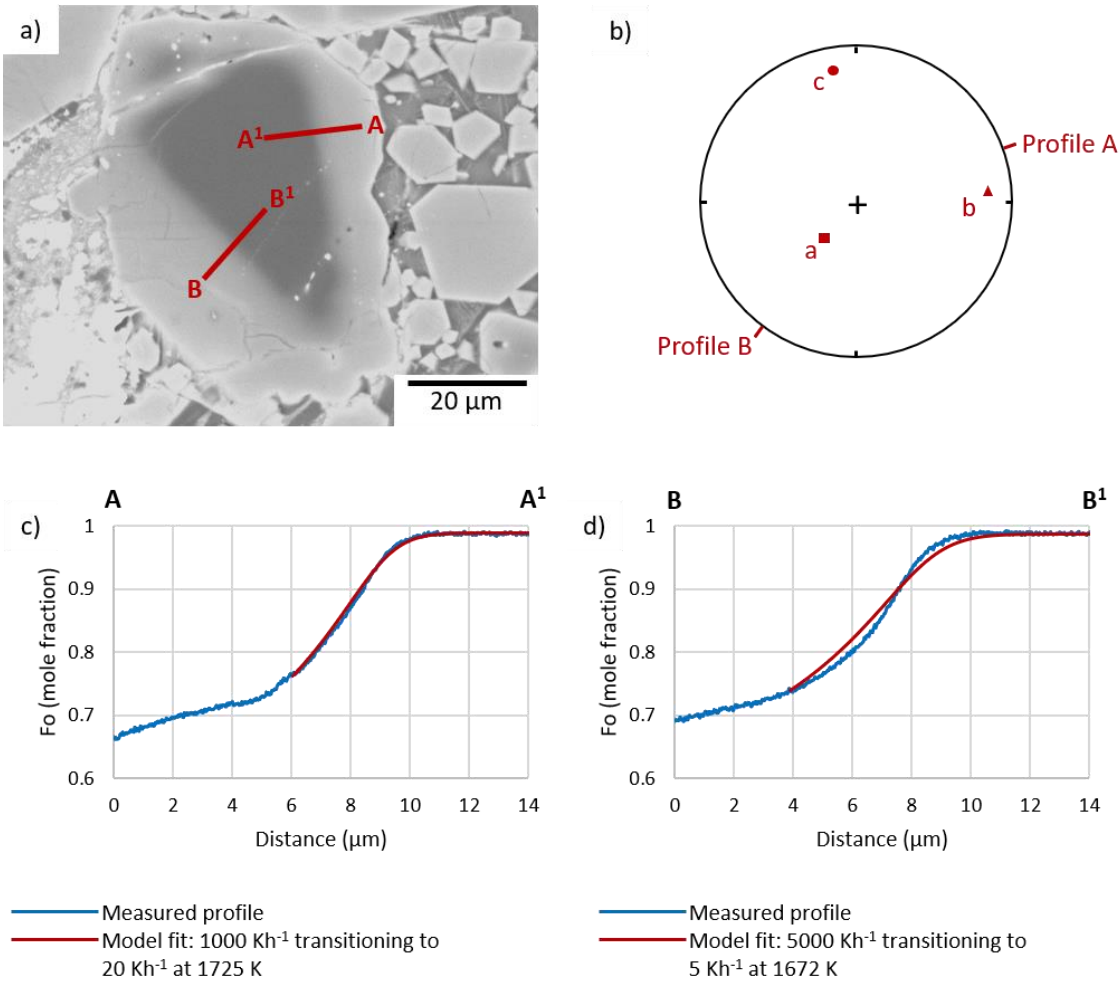

Figure 5.25 – a) BSE image of N4-2 RG1 showing the location of profiles A and B; b) lower hemisphere projection pole figure showing the orientation of the crystallographic axes and profiles A and B; c) profile N4-2 RG1 A with model fit; d) profile N4-2 RG1 B with model fit.

5.3.2.6 N4-3

Chondrule N4-3 contains one forsteritic-olivine relict grain and one compositional profile was measured. Figure 5.26 shows a BSE image of N4-1 RG1 showing the location of profile A. The most successful model fit was produced with an initial cooling rate of 2000 Kh^{-1} and a final cooling rate of 500 Kh^{-1} transitioning at a temperature of 1880 K.

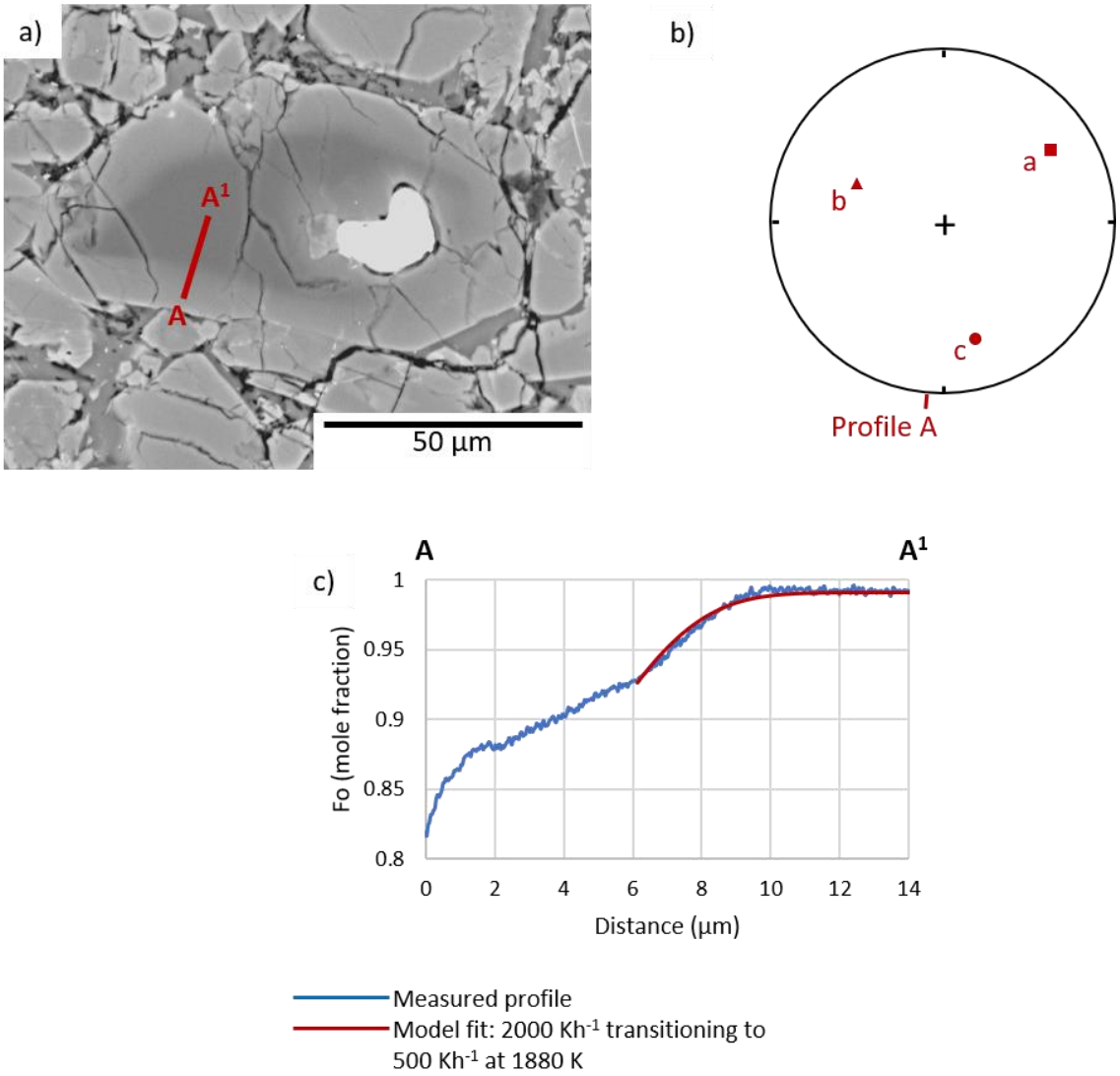

Figure 5.26 – a) BSE image of N4-3 RG1 showing the location of profile A; b) lower hemisphere projection pole figure showing the orientation of the crystallographic axes and profile A; c) profile N4-3 RG1 A with model fit.

5.3.2.7 NWA 8276 and NWA 4910 summary

The results of diffusion modelling for the 6 forsteritic-olivine relict grains present in chondrules from NWA 8276 and NWA 4910 vary from 5 to 5000 Kh^{-1} across the modelled temperature range, ~1940 to ~1660 Kh^{-1} (see Table 5.7 and Figure 5.27). This temperature range is almost identical to the range observed for forsteritic-olivine relict grains in ALHA 77307. However, unlike profiles in ALHA 77307, none of the measured diffusion profiles could be modelled using linear cooling. All require decreasing cooling rates modelled in two stages transitioning instantly at a transition temperature. Diffusion modelling for the observed diffusion profiles was difficult for those from forsteritic-olivine relict grains in NWA 4910 and model fits to the observed profiles are poorer than those achieved for diffusion profiles from grains in ALHA 77307 and NWA 8276. Examples of this are N4-1 RG1 A (Figure 5.24c) and N4-2 RG1 B (Figure 5.25d) where the model profiles do not closely match the observed compositional profile.

Table 5.7 – Chondrule cooling rates from modelling of diffusion profiles in forsteritic-olivine relict grains in chondrules from NWA 8276 and NWA 4910. Initial temperature is the chondrule liquidus temperature. Cooling across the considered temperature range was modelled linearly or in 2 stages transitioning instantly at the transition temperature. Shaded rows indicate that model diffusion profiles had poor fits to the observed compositional profiles.

Profile	Initial cooling rate (Kh^{-1})	Final cooling rate (Kh^{-1})	Initial temperature (K)	Transition temperature (K)	Final temperature (K)	Modelled temperature range (K)
N8-1 RG1 A	300	10	1883	1690	1680	203
N8-2 RG1 A	100	20	1900	1800	1752	148
N8-3 RG1 A	2000	50	1862	1700	1675	187
N4-1 RG1 A	4000	10	1907	1714	1712	195
N4-2 RG1 A	1000	20	1859	1725	1690	169
N4-2 RG1 B	5000	5	1859	1672	1665	194
N4-3 RG1 A	2000	500	1936	1880	1806	130

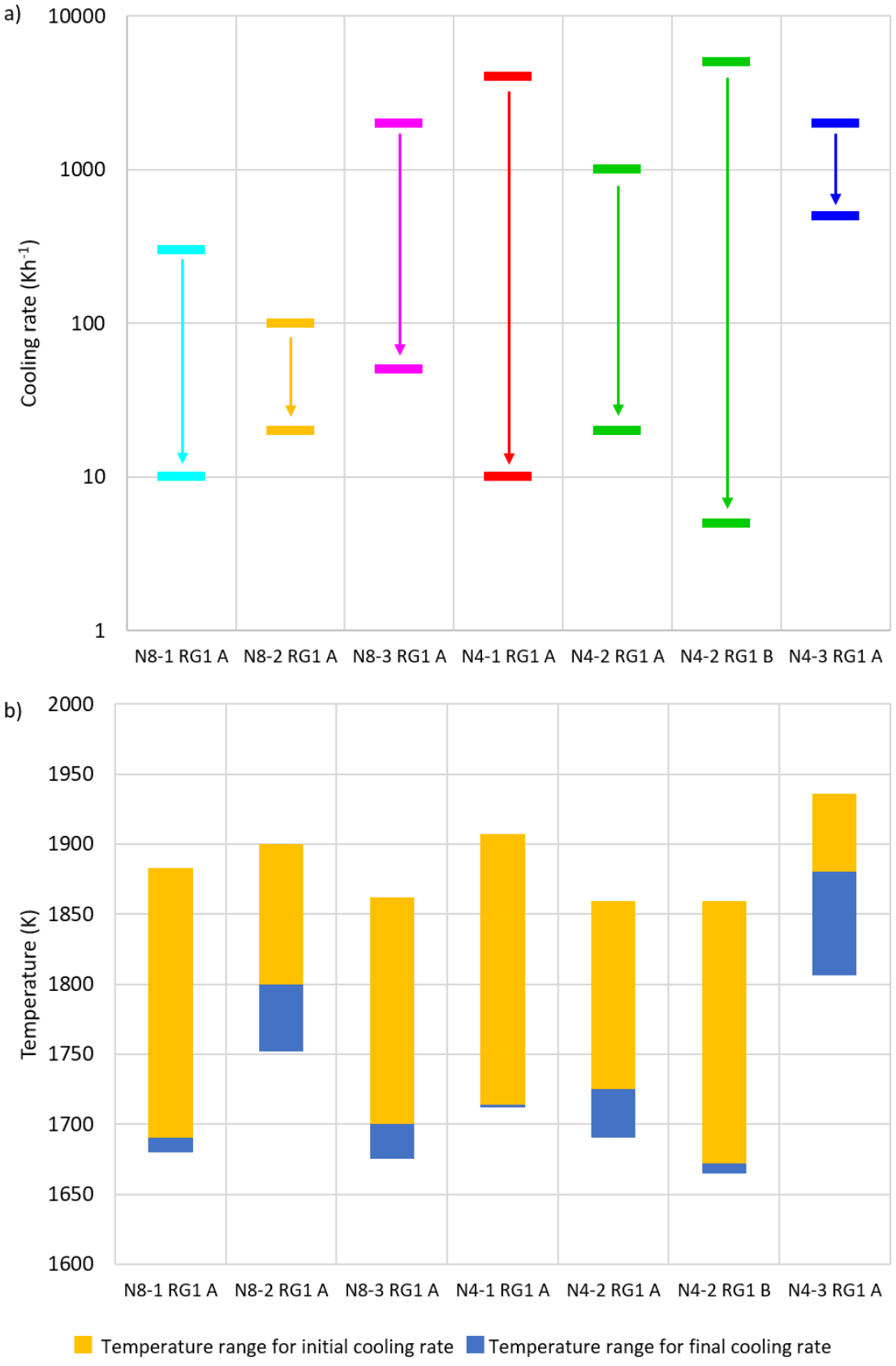

Figure 5.27 – a) summary of cooling rates from profiles in NWA 8276 and NWA 4910; b) summary of the contribution of initial and final cooling rates across the modelled temperature range for profiles in NWA 8276 and NWA 4910.

5.4 Discussion

The range in determined cooling rates across the studied chondrule population generally varies from 5 to 8000 Kh^{-1}, however, only chondrules in ordinary chondrites show cooling rates below 100 Kh^{-1}. Al-4 RG1 is the only grain to fall outside of this range with a very high initial cooling rate of 50000 Kh^{-1}. As previously noted, most of the observed diffusion profiles could not be modelled with linear cooling and required non-linear cooling histories modelled in two stages, with cooling rates changing instantly at a transition temperature. The effect of this on model diffusion profile shape is shown in Figure 5.28. The instantaneous transition between two cooling rates is likely an approximation of chondrule formation conditions, however, it does point to more complex cooling histories than have often been considered.

When compared with grains that experienced linear cooling, many of the observed diffusion profiles display a broad diffusion profile which steepens towards the margins of the forsteritic-olivine relict grain, for example, Al-1 RG1 A and B (Figure 5.13) as well as Al-2 RG1 A and B (Figure 5.14). These must be formed by initial relatively slow cooling. This allows the system to remain at high temperatures when diffusion is fastest allowing the equilibrium boundary composition to propagate far into the grain creating the broad diffusion profile. Increasing cooling rate causes the equilibrium olivine composition to change rapidly to more Fe-rich compositions. Diffusion is strongly dependent on temperature, therefore, reducing temperature significantly reduces the diffusion rate. This

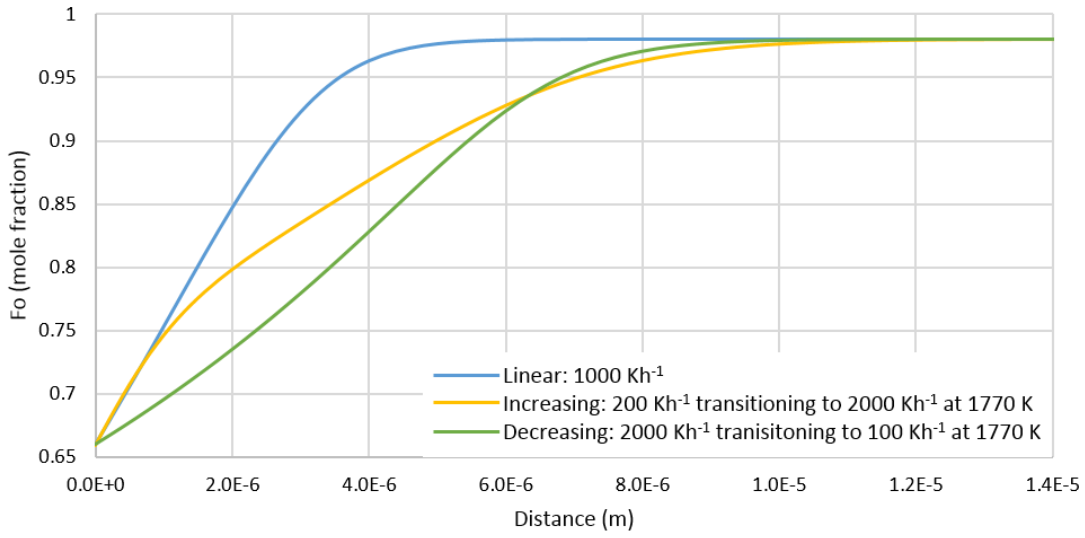

Figure 5.28 – Example model diffusion profiles showing the effect of varying cooling history on the model diffusion profile. Apart from cooling rates, the initial conditions are the same as shown in Table 5.4.

means that exchange with the cooler, more Fe-rich melt is limited to the margins of the grain as cooling progresses. This creates the observed steepened profile compared to profiles modelled with linear cooling. This effect is observed in Figure 5.28 where close to the margins, the yellow line has steepened.

Some diffusion profiles show a degree of shallowing of the observed diffusion profile towards the margins of the forsteritic-olivine relict grain, for example, Al-4 RG1 A (Figure 5.16c) and N4-2 RG1 B (Figure 5.25d). These may result from decreasing cooling rate. Assuming fractional crystallisation takes place, initially relatively rapid cooling changes the equilibrium olivine composition acting as the boundary condition to Fe-rich compositions quickly. As diffusion is strongly temperature-dependent, the reduction in temperature means that overall diffusion is slower. However, exchange with the chondrule melt during this rapid cooling means that the grain edge is now more Fe-rich. Diffusion in olivine also shows strong compositional dependence (Dohmen and Chakraborty, 2007) meaning that as the grain edge becomes more Fe-rich compared to the core region, diffusion becomes faster at the grain edge by up to 16 times. This means that at lower temperatures, diffusive modification occurs much more rapidly at the grain edge creating a shallowing of the diffusion profile at this location.

An alternative explanation for shallowing diffusion profiles at the grain edge would be crystal growth during the final stages of exchange with melt. This would add extra Fe-rich olivine to the edge of the forsteritic-olivine relict grain creating a shallowing profile. For the forsteritic-olivine relict grains in chondrules from ALHA 77307, P compositional profiles, which show a spike, or change, in P abundance at the forsteritic-olivine relict grain boundary suggest that this is not the case (see Chapter 4). Unfortunately, no P data are available for forsteritic-olivine relict grains in chondrules from NWA 8276 and NWA 4910, therefore, it cannot be excluded that growth is playing a role in the shapes of these diffusion profiles.

However, most of the compositional profiles measured in forsteritic-olivine relict grains in chondrules from all three meteorites show a clear transition between the diffusion dominated zone forming the broad diffusion profile and a growth dominated trend, dominated by fractional crystallisation. Notable examples are all those in ALHA 77307, Figure 5.13 to Figure 5.19, except Al-4 RG1 A (Figure 5.16) as well as those in NWA 8276, Figure 5.21, Figure 5.22 and Figure 5.23, although N8-1 RG1 A (Figure 5.21) is less clear. In

these profiles, the transition between the two zones is visible as a distinct kink in the shape of the compositional profile which occurs when rapid crystal growth begins. For three of the compositional profiles in forsteritic-olivine relict grains in NWA 4910, the distinct kink is not visible and instead, the compositional profile curves gently to a straighter growth dominated trend. This may be the result of two different effects which are discussed below.

The first possibility is that the transition from diffusion dominated to growth dominated was more gradual in compositional profiles in NWA 4910, with initially slow growth rates and increasing rates as growth progressed. Another possibility relates to secondary heating on the meteorite parent body. Both ALHA 77307 and NWA 8276 are both classified as petrologic type 3.00 (Grossman and Brearley, 2005; Ruzicka et al., 2017), meaning they experienced minimal secondary heating on their parent bodies. NWA 4910 is classified as petrologic type 3.1 and therefore experienced some significant heating on the parent body. If the compositional profiles present in this meteorite initially displayed a clear transition between the diffusion dominated and growth dominated zones, heating at ~600 K for several Myrs on the meteorite parent body may allow for very slow diffusion, which would blur out this transition creating more gentle curves as are seen in Figure 5.24c and Figure 5.25d. The maximum metamorphic temperature for ALHA 77307 is suggested to be ~470 K (Huss et al., 2006), and Alexander et al. (1989) suggest a metamorphic temperature of ~530 K for Semarkona, which is the same petrographic grade as NWA 8276 (Ruzicka et al., 2017). These are significantly lower than the expected temperature for meteorites with similar petrographic grades to NWA 4910 (3.1), which may have been as high as 620 K (Rambaldi and Wasson, 1981). This may also explain why the model fits to the observed compositional profiles in NWA 4910 were more difficult or impossible to obtain because diffusion is not occurring under the conditions set in the modelling program. However, diffusion length calculations using the relationship $x^2 \sim Dt$ (Jones, 1992) show that diffusion under these metamorphic conditions happens very slowly, with almost no movement of material. Assuming an olivine composition of Fo_{70}, T of 600 K, time of 3 Myrs and D of 6.77×10^{-28} calculated according to Dohmen and Chakraborty (2007), diffusion length is 6.4×10^{-8} µm. This suggests that secondary heating on the parent body is not responsible for blurring the boundary between the forsteritic-olivine relict grains and overgrowths in NWA 4910, or that the temperature of metamorphism has been underestimated for this meteorite.

Chondrule recycling events prior to accretion into the parent body may also play a role in shaping the observed diffusion profile. The forsteritic-olivine relict grains themselves are evidence that chondrule recycling was taking place (e.g. Jones (2012)) and this recycling must have been a common occurrence. Any chondrule recycling events will have influenced the observed diffusion profile. There are three foreseeable categories of chondrule reheating events: 1) low-temperature subsolidus heating; 2) high-temperature heating events with temperatures comparable to chondrule liquidus temperatures; 3) very high-temperature events with superliquidus temperatures.

Low-temperature subsolidus reheating events would not leave any obvious petrographic features but will likely result in diffusion within the forsteritic-olivine relict grain and overgrowth. Because of the composition dependence of diffusion in olivine, any diffusive modification will primarily affect the edge of the forsteritic-olivine relict grain and the overgrowth where diffusion is fastest because of higher FeO contents. This may create a similar effect to the model diffusion profiles where cooling rates decreased. In some of these, a distinct shallowing of the diffusion profile is noted. It may also erase the sharp interface between the forsteritic-olivine relict grain and the overgrowth.

In higher temperature events comparable to chondrule liquidus temperatures, or even higher temperatures, the chondrule will begin to melt, including the overgrowth and possibly the forsteritic-olivine relict grains itself, which either resets the system with a smaller relict grain, or dissolves the relict grain entirely. Therefore, these higher temperature events must not have occurred after the formation of the current forsteritic-olivine relict grains.

Many of the forsteritic-grains show steepening profiles towards the grain rim, e.g. Al-1 RG1 A, Figure 5.13a. These cannot be produced by secondary heating events, as diffusion would occur fastest at the grain rim, where the grain is most FeO-rich, resulting in a shallowing of the diffusion profile towards the grain rim. This means that these grains displaying steepening towards the grain edge must not have experienced significant secondary sub-solidus heating in the form of parent body processing or a secondary heating event.

Three chondrules from ALHA 77307 (Al-1, Al-2, and Al-5, see Figure 5.13, Figure 5.14 Figure 5.18 and Figure 5.17 respectively) consistently show initially slow cooling rates followed by more rapid cooling rates, up to an order of magnitude faster than the initial cooling rate

(see Table 5.6). Within these three chondrules, the results are very reproducible, apart from profile Al-5 RG1 A which required an initial cooling rate significantly slower than recorded by other diffusion profiles present in this chondrule. Other chondrules also show some inconsistent behaviour for example chondrules Al-3 and Al-6 (see Figure 5.15 and Figure 5.19). For Al-3, each of the different profiles records a different thermal history: profile Al-3 RG1 A records slightly increasing cooling rates, profile Al-3 RG1 B records slightly decreasing cooling rates and profile Al-3 RG1 C records a linear cooling history. Despite these inconsistencies, all three record a narrow range of cooling rates from 100 to 250 Kh^{-1}. For Al-6, profiles Al-6 RG1 A and C record linear cooling histories and profiles Al-6 RG1 B and D record decreasing cooling rates. Again, a relatively narrow range of cooling rates is observed (400 to 2000 Kh^{-1}). For those showing decreasing cooling rates, the slow cooling rate occurs at low temperatures towards the end of the model run, and the initial more rapid cooling rate dominates for most of the thermal history. Chondrules Al-1, Al-2, Al-3, Al-5, and Al-6 are the only chondrules where multiple diffusion profiles were modelled successfully. The remaining chondrules (Al-4 and all from NWA 8276 and NWA 4910) either only contain one suitable boundary where diffusion modelling is appropriate or, in the case of N4-1, one of the two profiles could not be successfully modelled. However, if more compositional profiles could be measured and modelled in these chondrules, it is likely that similar inconsistencies would be observed.

One potential cause of these inconsistencies relates to interference from out of plane features. Although compositional profiles and diffusion models are run in 1D, the crystal is a 3D structure and features just above or below the plane of the section, for example, Fe-rich fractures, Fe,Ni metal, troilite or chromite inclusions, may be affecting the observed diffusion profile.

Another, perhaps more likely cause are sectioning effects. Sections through the meteorites will not cut through olivine crystals containing forsteritic-olivine grains in an ideal manner. The sections will likely show randomly oriented, possibly off-centre transects through these crystals. This means that compositional profiles that are measured perfectly perpendicular to the forsteritic-olivine grain boundary visible in the section are likely not perpendicular to the grain boundary in the third dimension which results in artificially extended diffusion profiles. Shea et al. (2015) report that using off-centre, randomly oriented sections through olivine grains results in significant diffusion time overestimates and underestimates ranging

from 50 to ~590 % of the true diffusion time within a single crystal. These profiles across different crystal faces in these cuts often show asymmetrical compositional profiles, which are observed in many of the forsteritic-olivine relict grains. This issue is also compounded by the irregular shapes of many of the forsteritic-olivine relict grains. Also, off-centre transects may not show the original composition of the forsteritic-olivine relict grain, which can result in errors in the diffusion timescales (Shea et al., 2015). If cuts are central but randomly oriented, the original composition of the relict grain is generally preserved, and compositional profiles are generally more symmetrical across the different crystal faces and generally record similar diffusion times which are close to the true time. The results of Shea et al. (2015) are for diffusion resulting from a single heating event at a constant temperature of 1573 K for 144 hours, and while here diffusion timescales were calculated, these sectioning effects may cause similar overestimations, which may be caused by anisotropy overcorrections, and underestimations in determined chondrule cooling rates.

5.4.1 Sectioning effects in the measured compositional profiles

The use of false colour BSE imaging can help determine whether features such as dipping plateaus or merging diffusion fronts are having an impact on the observed compositional profile. Using false colours, it is easier to spot these dipping plateaus or merging diffusion fronts than using standard greyscale BSE images. These images are generated by modifying the greyscale using the 3-3-2 LUT in ImageJ (see Figure 5.29 for comparison between standard BSE greyscale and the false colour scale) (Schneider et al., 2012). The image cycles through colours generating a contour map of forsterite composition in the olivine grains. Crystals cut in a more ideal manner will show a core region with a constant composition with no evidence of dipping plateaus (changing composition from one end of the core to the other). Observed compositional profiles ideally show symmetry on opposite crystal faces and they should be measured away from corners or other areas where there appears

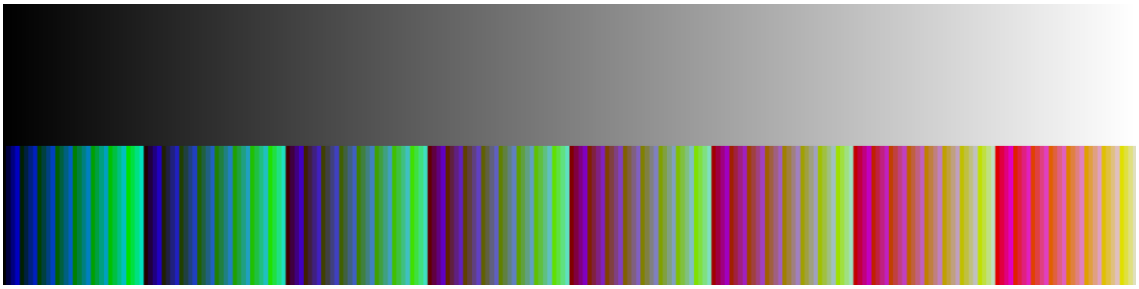

Figure 5.29 – BSE greyscale vs the false colour scale shown in the false colour BSE images

to be a merging diffusion front. These images were examined prior to diffusion modelling to identify clearly anomalous boundaries; however, a more detailed analysis followed modelling of the diffusion profiles to help interpret the effect of these sectioning effects on the modelled diffusion profiles.

5.4.1.1 Al-1

Figure 5.30 shows a false colour BSE image of Al-1 RG1 as well as the locations of profile A and B. The image does not show evidence of any dipping plateaus and there is a core region with a constant composition which represents unmodified forsteritic-olivine relict grain. This makes it likely that it is a relatively central section through the forsteritic-olivine relict grain. Apart from the boundary along the bottom of the grain, the grain boundary is irregular making it difficult to judge the symmetry across opposite crystal faces. EBSD data for this grain shown in Figure 5.30 shows that the section cuts the b- crystallographic axis

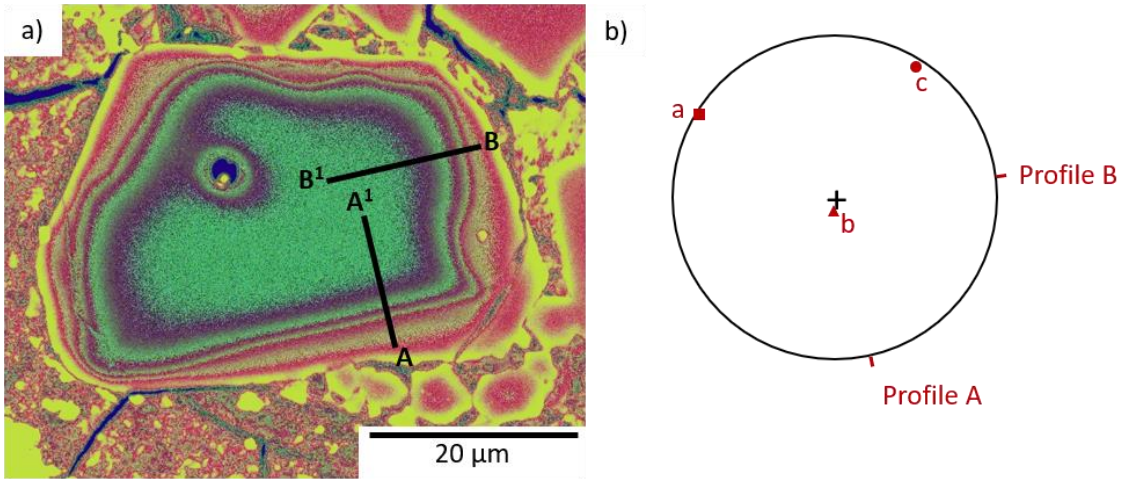

Figure 5.30 – a) False colour BSE image of Al-1 RG1 showing the locations of profile A and B. b) Pole figure showing the orientation of the crystallographic axes.

close to 90° and the a- and c-axes are almost horizontal, suggesting this is a relatively on-axis section. Profile A is measured across a straight boundary; however, it is relatively close to a merging diffusion front. Profile B is measured across a slightly curved area of the grain boundary and therefore may be suffering from the effects of merging diffusion fronts, which possibly explains the discrepancy in cooling rates between profile A and profile B. Neither are measured parallel to any of the crystallographic axes.

5.4.1.2 Al-2

Figure 5.31 shows a false colour BSE image of Al-2 RG1 and the locations of profile A and B. Like Al-1, this image does not show any evidence of any dipping plateaus and the core

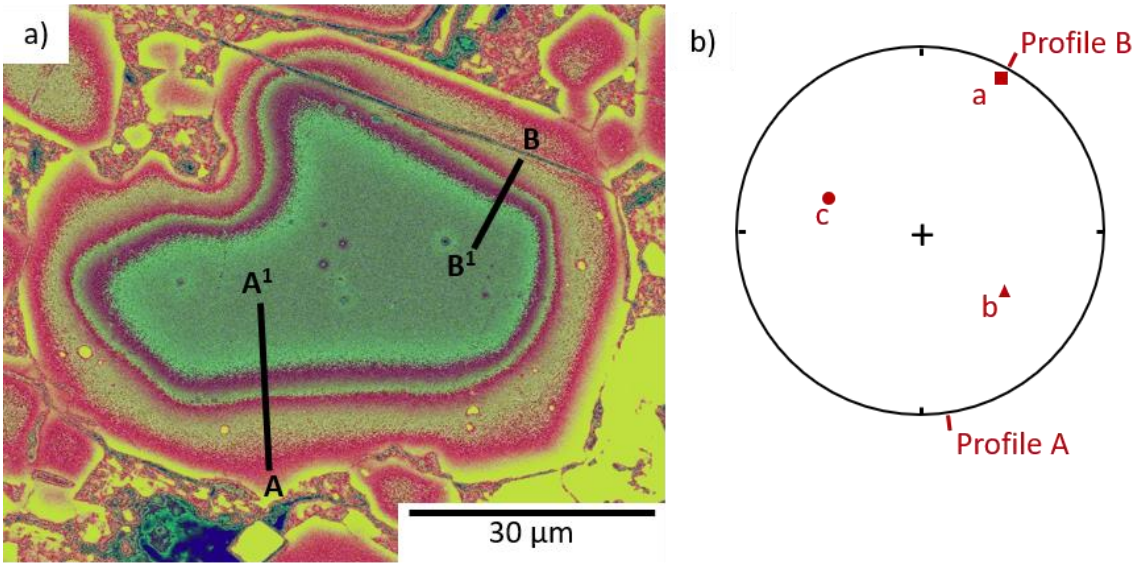

Figure 5.31 – a) False colour BSE image of Al-2 RG1 showing the locations of profile A and B. b) Pole figure showing the orientation of the crystallographic axes.

region shows a constant composition, suggesting that the section is relatively central. There are no opposite crystal faces as the grain has a relatively irregular shape meaning that it is not possible to judge the symmetry. However, EBSD data for this grain (Figure 5.31b) shows that the section cuts across the crystallographic axes randomly, although the a-axis is close to horizontal.

Profile A is measured across a relatively straight boundary and is measured far enough away from the nearby merging diffusion front to avoid any effects of this. Profile B is measured almost along the a-axis; however, it is close to a merging diffusion front.

5.4.1.3 Al-3

Figure 5.32 shows a false colour BSE image of Al-3 RG1 and the locations of profile A, B and C. There is a distinct core region which suggests again that this is a relatively central section through the grain, however, the upper left region shows unusual behaviour in the form of widening of the diffusion profile in this region, and is potentially evidence of a slightly more off-centre cut than for the forsteritic-olivine relict grains in Al-1 and Al-2. The left and right faces of the grain are relatively parallel allowing symmetry to be gauged. In order to achieve this, a compositional traverse was taken across the whole relict grain, shown in Figure 5.33, from the location of profile C to the location of profile B. This shows that there is some asymmetry, which may support a relatively off-centre section through the grain. The EBSD data for this grain (Figure 5.32b) shows that the b-axis is close to horizontal and the c-axis

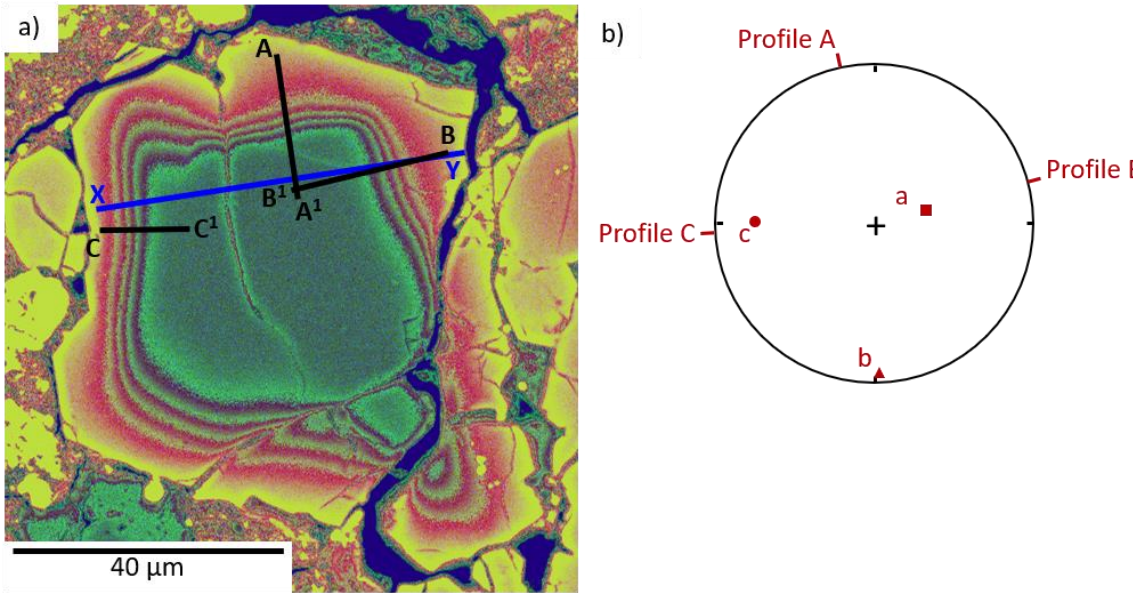

Figure 5.32 – a) False colour BSE image of Al-3 RG1 showing the locations of profiles A, B and C. The blue line, XY, shows the location of the traverse in Figure 5.35. b) Pole figure showing the orientation of the crystallographic axes.

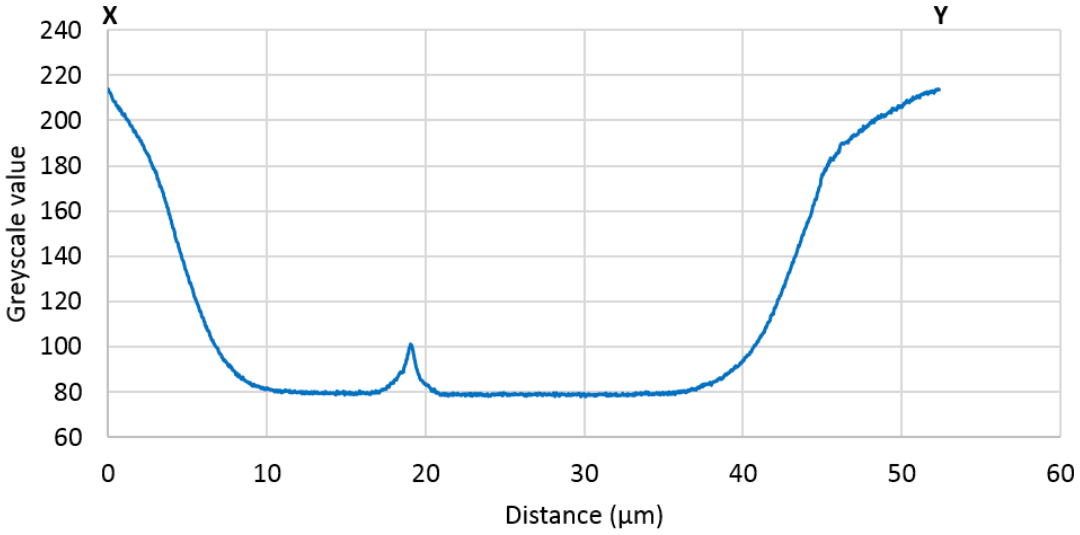

Figure 5.33 – Transect across Al-3 RG1 showing slightly asymmetric profiles. The central spike is caused by the large crack running through the forsteritic-olivine relict grain.

is also relatively close to horizontal. This shows that the section of this grain is relatively on-axis but may be sectioned off-centre.

Profile A is measured across a straight boundary, and although there is a microfracture present in the forsteritic-olivine relict grain at this location, it does not appear to affect the observed compositional profile. According to the EBSD data, this profile is measured in a similar direction to the b-axis. Profile B is measured in the same corner of the grain and therefore crosses the same microfracture but again, this is not visible in the observed

compositional profile. The area around profile B is not wholly straight and there may be some influence of slightly merging diffusion fronts. According to EBSD data, profile B is measured close to the c-axis. Profile C is measured across a relatively straight boundary; however, it is close to the top left corner of the grain which may show evidence of a dipping plateau. This may contribute to the unusual compositional profile which displays a distinct kink (Figure 5.15e), however, preliminary profiles which were measured closer to the bottom of the boundary displayed a more pronounced kink. Measured profiles closer to the top left produced more usual profile shapes, however, there would likely be effects from the potentially dipping plateau. These features may mean the cooling rates determined from profile C should be interpreted with caution.

5.4.1.4 Al-4

Figure 5.34 shows a false colour BSE image of Al-4 RG1 and the location of profile A. This forsteritic-olivine relict grain shows a distinct core region, suggesting a relatively central cut. However, asymmetry is clearly visible, and the compositional profile is much sharper on the lower boundary than the upper boundary, suggesting that the section cuts the lower boundary close to perpendicular, and the upper boundary at a much lower angle. The more diffuse edge towards the right may also represent a dipping plateau, possibly suggesting off-centre sectioning of the grain. Profile A is measured across the sharpest and straightest boundary. As this is the steepest boundary it is closest to perpendicular and is the most

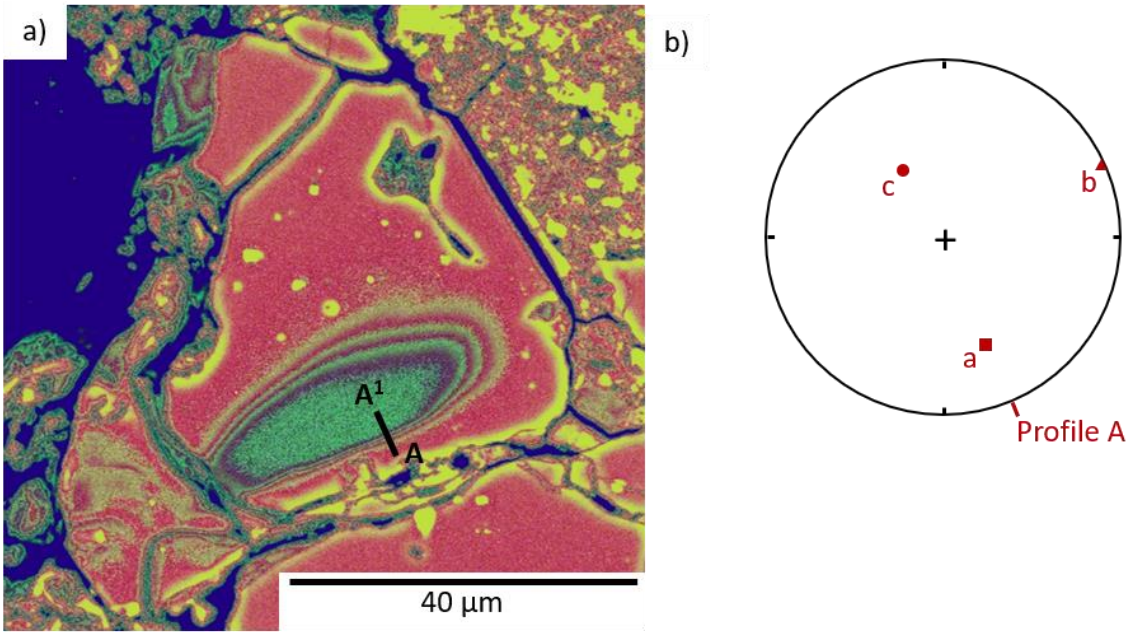

Figure 5.34 – a) False colour BSE image of Al-4 RG1 showing the location of profile A; b) pole figure showing the orientation of the crystallographic axes.

likely to show the true diffusion width. Profiles measured on the opposite edge of the grain may be artificially extended and appear much wider than the actual diffusion profile. Modelling these profiles would result in lower cooling rates, which overestimate the true diffusion time.

5.4.1.5 Al-5

Figure 5.35 shows false colour images of Al-5 RG1 and RG2. These grains do not show constant core compositions and diffusion appears to have modified the original core composition. This is supported by the fact that these are the least forsteritic of the forsteritic-olivine relict grains studied, with values of Fo_{94} and Fo_{91} for RG1 and RG2 respectivelty. As the actual core composition is uncertain, this may introduce errors, with increased diffusion timescales up to 140 % above actual diffusion time-scale (Shea et al., 2015). When considering a cooling rate, this would mean cooling rates are underestimated, which may mean that cooling rates are more rapid than suggested. For Al-5 RG1, there are

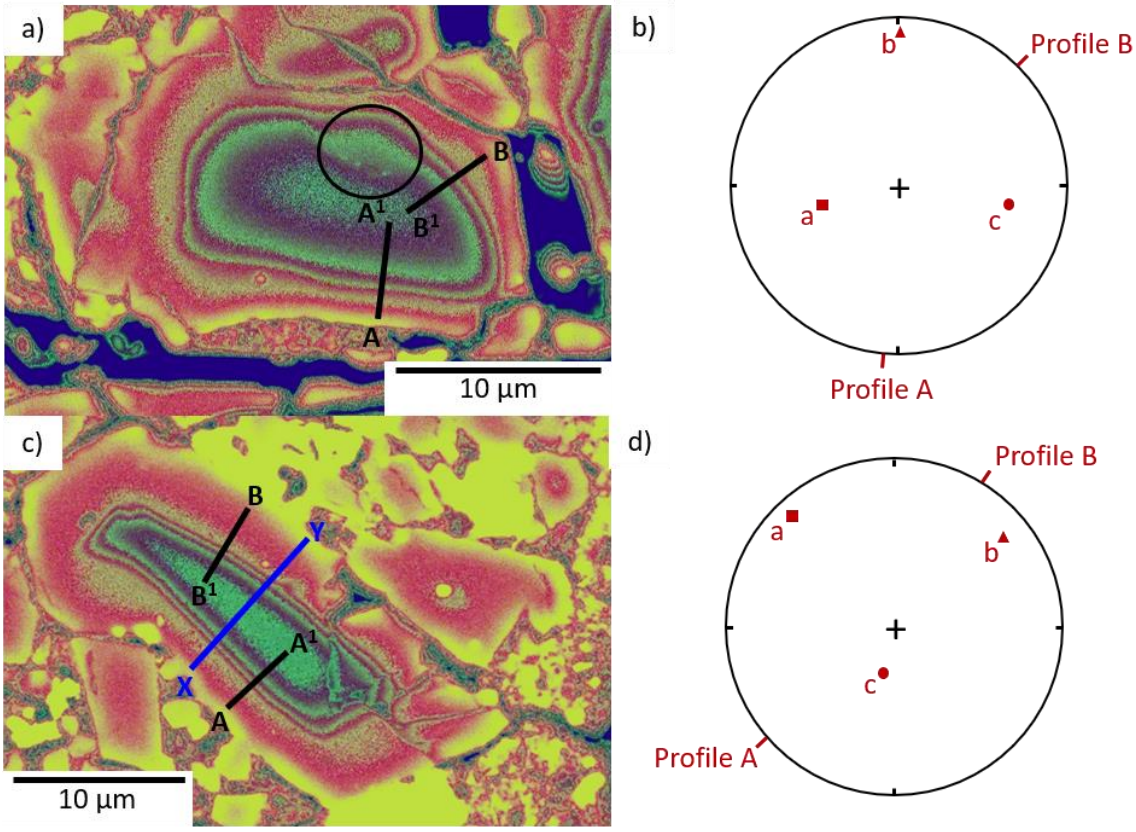

Figure 5.35 – a): false colour BSE image of Al-5 RG1 showing the location of profiles A and B; b) Pole figure showing the orientation of the crystallographic axes of Al-5 RG1 ;c) false colour BSE image of Al-5 RG2 showing the location of profile C and D. The blue line XY shows the location of the traverse in Figure 5.36; d) pole figure showing the orientation of the crystallographic axes of Al-5 RG2

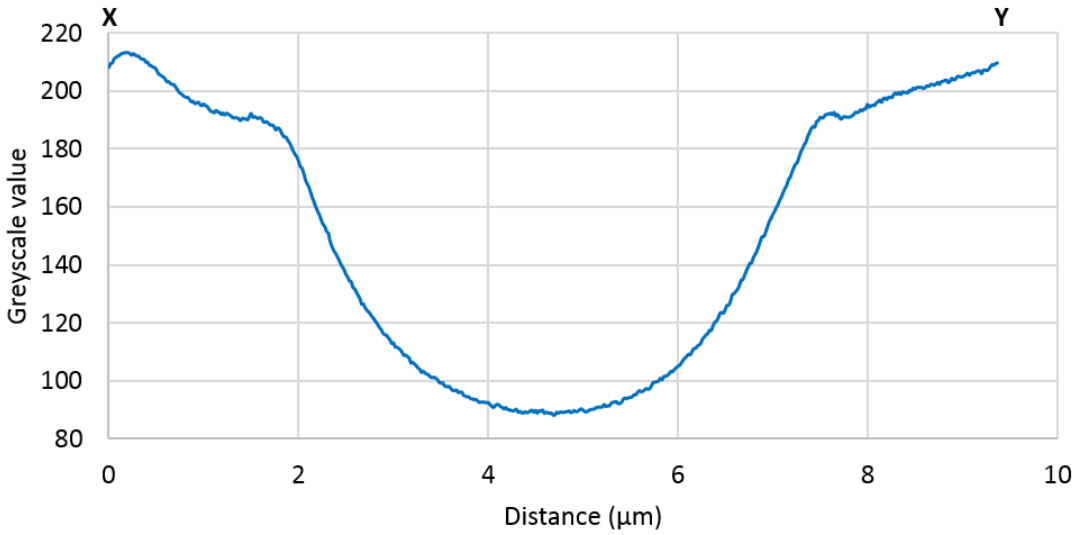

Figure 5.36 - Traverse across Al-5 RG2 showing symmetric compositional profiles.

no good opposite crystal faces with which to judge symmetry. However, for Al-5 RG2, there are a pair of opposite crystal faces which show strong symmetry (see Figure 5.36).

Profile A in Al-5 RG1 is measured across a straight boundary; however, it is close to a merging diffusion front. Profile B in Al-5 RG1 is measured across a relatively straight edge; however, it is close to an unusual feature on the upper grain boundary (circled in Figure 5.35a) and to a merging diffusion front. The proximity of both profiles to merging diffusion fronts and, in the case of profile B, unusual features may be the reason why there is such a discrepancy in cooling rate. Profile A appears wider than profile B which accounts for the slower cooling rates determined for this profile. Determined cooling rates from Profile B, however, show similar cooling rates and thermal histories to the two profiles in Al-5 RG2 despite the proximity to the unusual feature.

Profile A in Al-5 RG2 is measured across a straight boundary and is not close to any merging diffusion fronts, however, the grain does not preserve original unmodified core composition, although this is likely to be the best profile from these two grains. Profile B in Al-5 RG2 is measured across a relatively straight boundary; however, it is relatively close to a merging diffusion front at the top of the crystal. EBSD data for this grain (Figure 5.35d) shows that neither of the profiles are measured parallel to the crystallographic axes.

5.4.1.6 Al-6

Figure 5.37 shows a false colour image of Al-6 RG1 and the locations of profiles A, B, C and D. There is a region of constant core composition and no evidence of dipping plateaus, suggesting this section cuts the grain close to the centre. A compositional profile taken across the forsteritic-olivine relict grain from the location of profile D to the location of profile C (Figure 5.38) shows relatively symmetric diffusion profiles, although the right of the graph shows a slightly steeper profile.

Profile A is measured on a straight boundary and is far away from any merging diffusion fronts. Profile B is measured on a straight boundary; however, it is relatively close to a

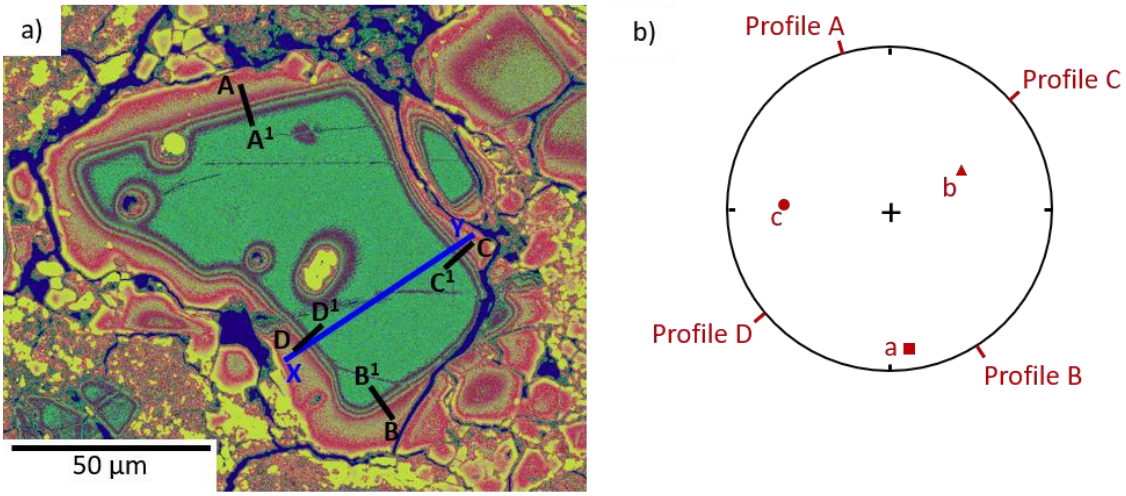

Figure 5.37 – a) False colour BSE image of Al-6 RG1 showing the location of profile A, B, C and D. Profile XY shows the location of traverse in Figure 5.38; b) pole figure showing the orientation of the crystallographic axes.

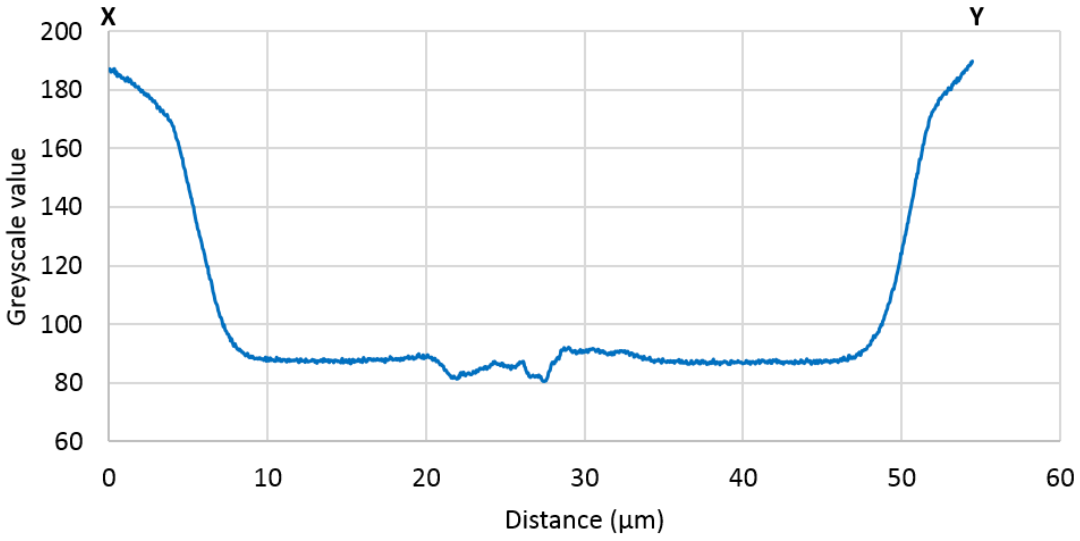

Figure 5.38 – Traverse across Al-6 RG1 showing relatively symmetrical diffusion profiles.

merging diffusion front from the corner to the left of the location of the profile. Profile C and profile D are measured across straight boundaries; however, they are located near to fractures located in the crystal. The boundary at profile A appears much wider than profile B, possibly suggesting this boundary is further from perpendicular than profile B which may account for the significantly slower cooling determined from profile A. None of the profiles are measured parallel to any of the crystallographic axes according to EBSD data (Figure 5.37b).

5.4.1.7 N8-1

Figure 5.39 shows a false colour image of N8-1 RG1 and the location of profile A. There is a region of constant core composition, suggesting this is a relatively central section through the crystal. There are no opposite crystal faces to measure compositional profiles to assess symmetry, however, the image does suggest some asymmetry in the width of compositional profiles which suggests random, possibly off-centre sectioning of the crystal. Profile A is measured across a relatively straight crystal boundary; however, it is close to a merging diffusion front caused by a fracture to the left of the profile. There is another fracture to the right with another merging diffusion front where this meets the grain edge which is also close to the measured profile. These may be influencing the observed diffusion profile. EBSD data shows that the compositional profile is not parallel to any of the crystallographic axes (Figure 5.39b).

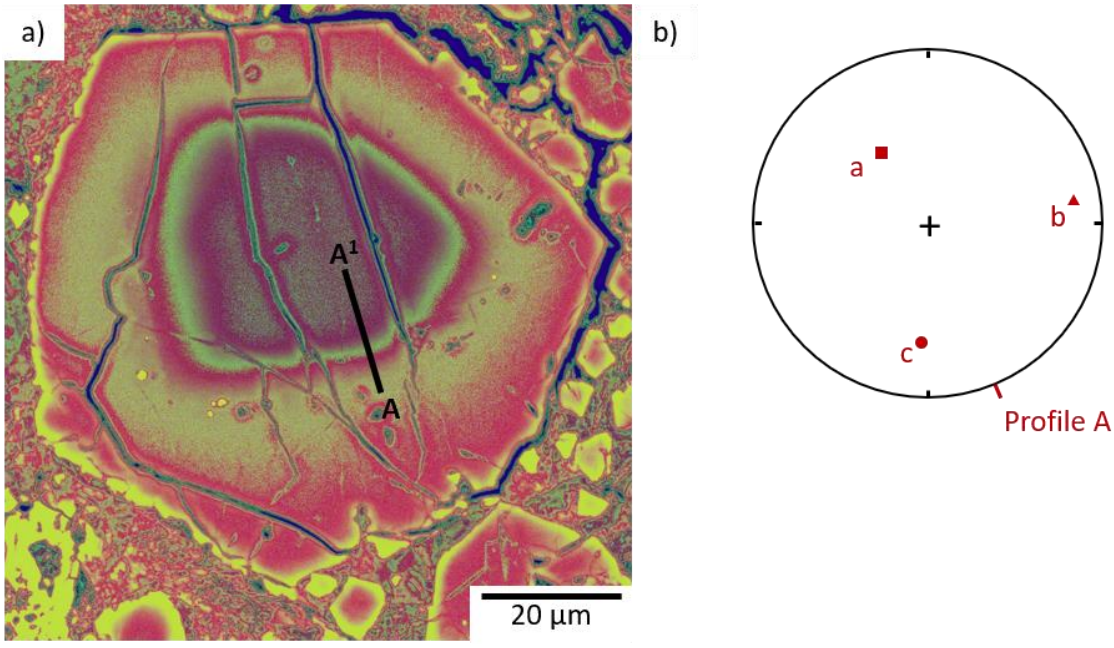

Figure 5.39 – a) False colour BSE image of N8-1 RG1 showing the location of profile A; b) pole figure showing the orientation of the crystallographic axes.

5.4.1.8 N8-2

Figure 5.40 shows a false colour BSE image of N8-2 RG1 and the location of profile A. There is a region of constant composition in the core suggesting this is a relatively central section through the crystal. Profile A is measured across a straight boundary, however, there are numerous Fe-rich inclusions along this boundary. While the compositional profile was measured through a gap between these inclusions, they may still be influencing the observed compositional profile, and there may be inclusions above or below the section which may also influence the composition profile. The profile is measured close to the b-axis according to EBSD data for this grain (Figure 5.40b).

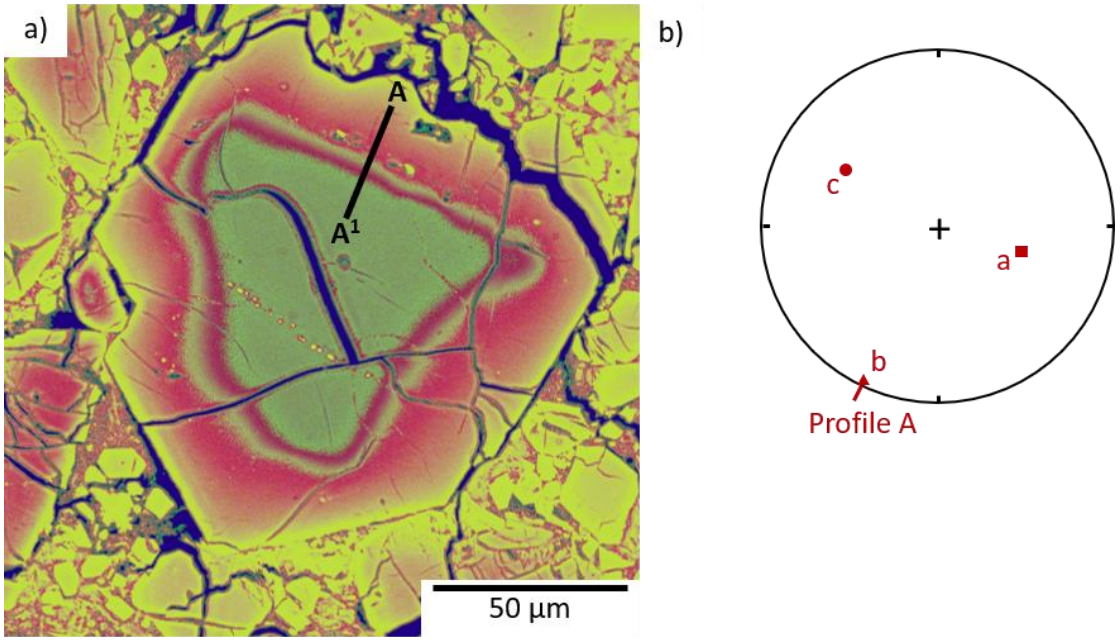

Figure 5.40 – a) false colour BSE image of N8-2 RG1 showing the location of profile A; b) pole figure showing the orientation of the crystallographic axes.

5.4.1.9 N8-3

Figure 5.41 shows a false colour BSE image of N8-3 RG1 and the location of profile A. The crystal shows a region of constant core composition with no immediate evidence of dipping plateaus, suggesting the section cuts the crystal close to the centre. A compositional traverse across the crystal (Figure 5.42) reveals that the compositional profiles are mostly symmetrical, but is slightly wider on the edge profile A is measured on. This is visible in the false colour BSE image and may be suggesting that the boundary is sectioned further from perpendicular, and therefore cooling rates may be underestimated. A profile could not be measured on the opposite side as there are unusual features and a crack visible in the false

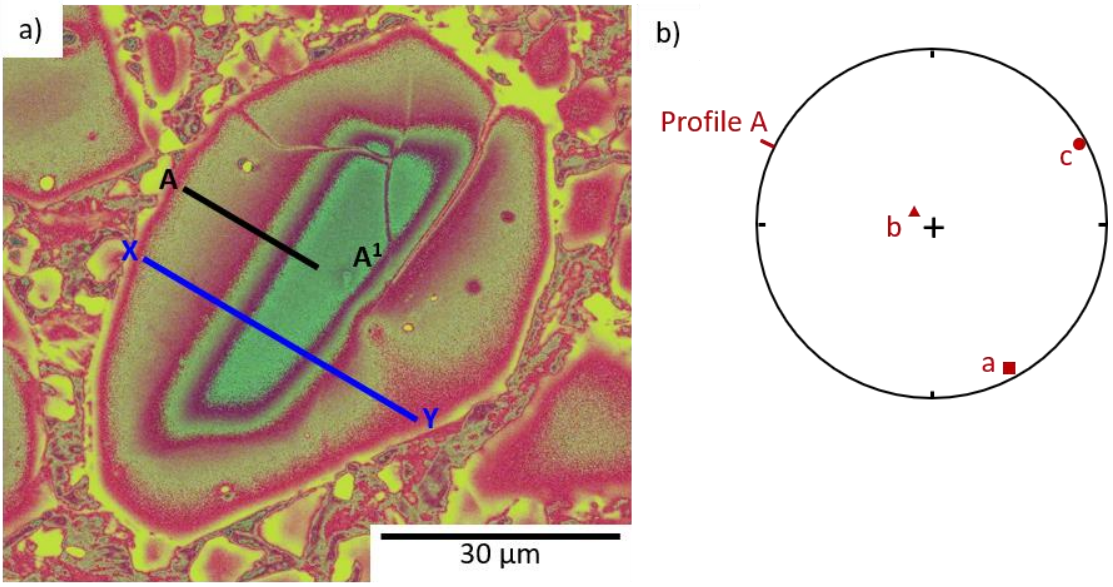

Figure 5.41 – a) false colour BSE image of N8-3 RG1 showing the location of profile A. The blue line XY, shows the location of the compositional traverse in Figure 5.42; b) pole figure showing the orientation of the crystallographic axes.

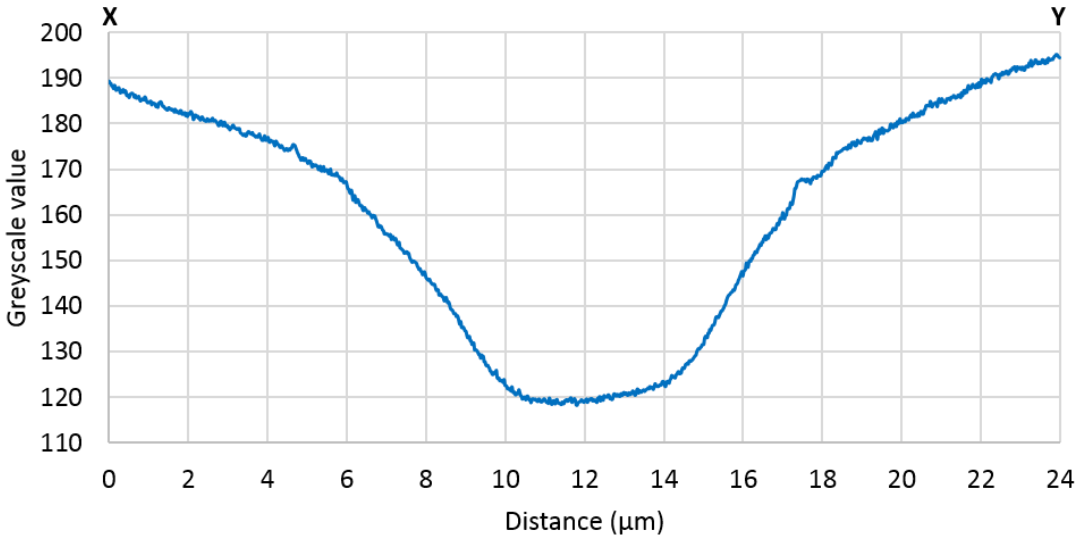

Figure 5.42 – Transect across N8-3 RG1 showing mostly symmetric diffusion profiles.

colour BSE image. The compositional traverse also reveals that, while the core region has a relatively constant composition, diffusive modification has progressed into the grain or the grain shows a slightly dipping plateau. EBSD data for the grain (Figure 5.41b) shows that the section is actually relatively on-axis, with the a- and c-axes almost horizontal and the b-axis almost perpendicular, however profile A is not measured parallel to the a- or c-axes.

5.4.1.10 N4-1

Figure 5.43 shows a false colour BSE image of N4-1 RG1 showing the location of profile A. The grain shows a large area with a constant composition, suggesting the section cuts the crystal close to the centre. A compositional traverse across the crystal shows some asymmetry in the observed compositional profiles (Figure 5.44). This suggests the section cuts the grain off centre. Profile A is measured across the sharpest boundary, which is most

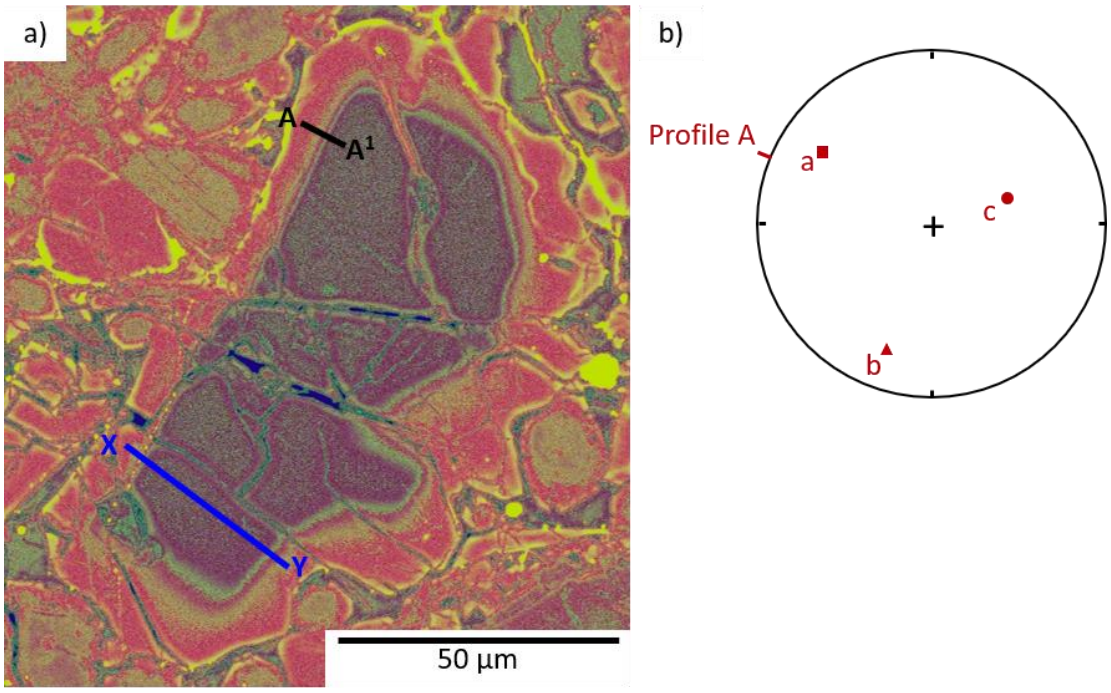

Figure 5.43 – a) False colour BSE image of N4-1 RG1 showing the location of profile A. The blue line XY shows the location of the compositional traverse in Figure 5.44; b) pole figure showing the orientation of the crystallographic axes.

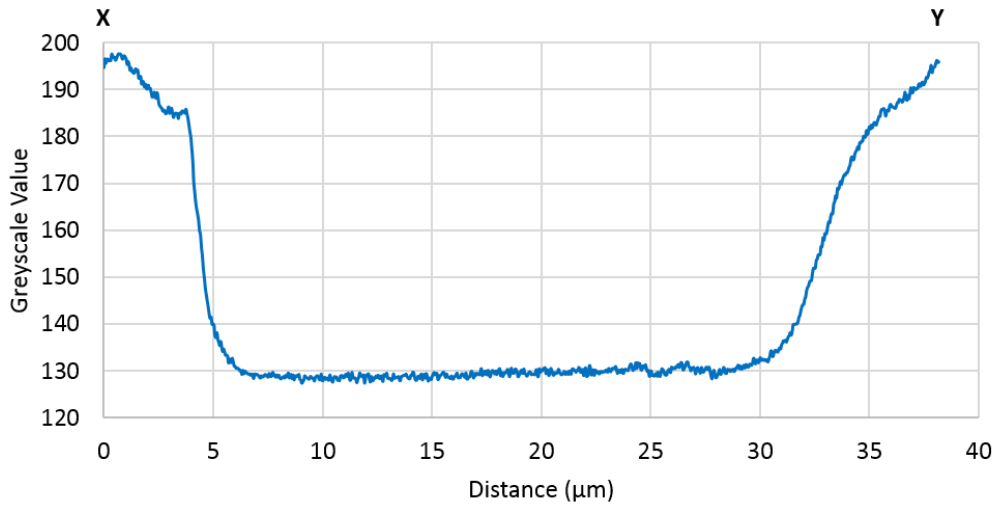

Figure 5.44 – Transect across N4-1 RG1 showing asymmetric diffusion profiles.

likely to be perpendicular and therefore shows the most accurate cooling rates. The profile is measured away from merging diffusion fronts.

5.4.1.11 N4-2

Figure 5.45 shows a false colour BSE image of N4-2 RG1 and the locations of profile A and B. The core region shows an area of constant composition with no evidence of dipping plateaus, again suggesting a relatively central section through the crystal. There are no opposing crystal faces to judge the symmetry, however, the false colour BSE images suggest that the boundaries do show symmetry. This suggests a central section through the grain. Profiles A and B are located on straight boundaries away from any apparent merging diffusion fronts. However, profile B is located close to several small fractures which may influence the observed compositional profile. EBSD data for this grain (Figure 5.45b) shows that neither profile A nor profile B are parallel to any of the crystallographic axes.

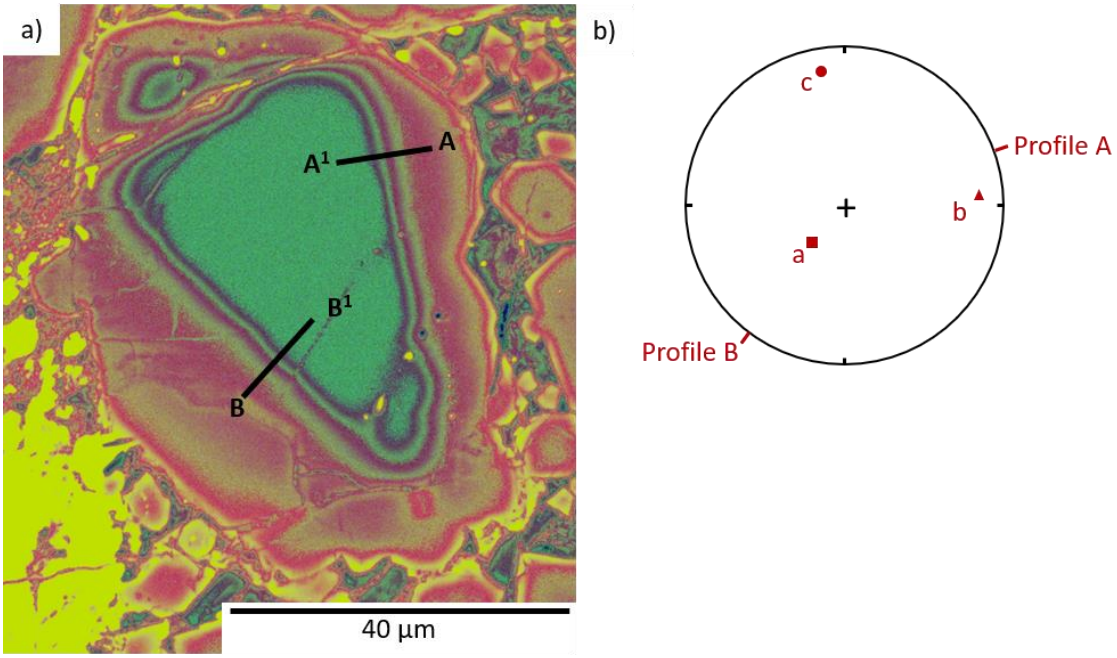

Figure 5.45 – a) false colour BSE image of N4-2 RG1 showing the locations of profile A and B; b) pole figure showing the orientation of the crystallographic axes.

5.4.1.12 N4-3

Figure 5.46 shows a false colour BSE image of N4-3 RG1 and the location of profile A. Like most of the grains, there is a core region with constant composition, even if the grain is highly fractured; there is also no evidence of dipping plateaus. These together suggest that the section cuts through the crystal close to the centre. There are no opposing crystal faces with which to judge symmetry, however, the grain does seem to show relatively

symmetrical grain boundaries suggesting a relatively central section through the grain. Profile A is measured across a straight boundary far from any observed fractures that could potentially affect the profile. There are no discernible merging diffusion fronts, however, the highly fractured nature of this grain may mean that there are fractures above or below the section which may influence the observed diffusion profile. EBSD data (Figure 5.46b) shows that Profile A is not measured parallel to any of the crystallographic axes.

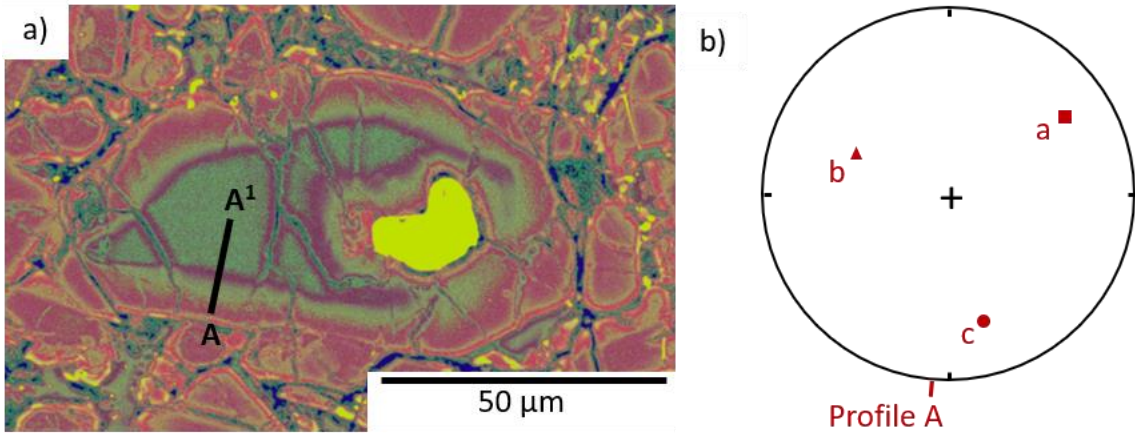

Figure 5.46 – False colour BSE image of N4-3 RG1 showing the location of profile A; b) pole figure showing the orientation of the crystallographic axes.

5.4.1.13 Summary

Most of the forsteritic-olivine relict grains seem to show relatively central sections through the crystal that are randomly oriented: Al-2 RG1, Al-6 RG1, N8-1 RG1, N8-2 RG1, N4-1 RG1, N4-2 RG1 and N4-3 RG1. The unusual behaviour displayed by Al-3 RG1 suggests it is an off-centre section, however, the section cuts through relatively on-axis, making this section an off-centre along axis section. Al-1 RG1 and N8-3 RG1 show that they are on-axis sections with both cut perpendicular to b-axes and parallel to the a- and c-axes. Al-1 shows a constant core composition and no evidence of dipping plateaus suggesting it is an on-centre along axis section. The core region of N8-3 RG1 has either been modified slightly by diffusion or the grain displays a dipping plateau. This suggests that, similar to Al-3, it is an off-centre on-axis section. Al-5 RG1 and RG2 are both small and have core regions that have been modified by diffusion; EBSD data show that the grains are sectioned randomly. Table 5.8 and Table 5.9 summarise the petrographic and sectioning effects which may be acting upon the measured diffusion profiles.

Table 5.8 – Summary of the potential sectioning effects and petrography on the measured diffusion profiles from forsteritic-olivine relict grains in ALHA 77307.

Profile	Cooling rates (Kh^{-1})	Comments on sectioning	Confidence
Al-1 RG1 A	800 to 4000	Measured across the sharpest boundary with no obvious effects from merging diffusion fronts.	Good
Al-1 RG1 B	400 to 2400	Boundary less sharp than for profile A and grain boundary appears curved in false colour BSE image. Possibly affected by merging diffusion front, this may explain why cooling rates lower than profile A.	Moderate
Al-2 RG1 A	100 to 1400	Measured across a straight boundary away from merging diffusion fronts.	Good
Al-2 RG1 B	100 to 500	Measured across a straight boundary with no obvious effects from nearby merging diffusion front. Shows somewhat similar cooling rates to profile A.	Good
Al-3 RG1 A	150 to 100	Measured across a relatively straight boundary. The presence of a small microfracture in the grain does not seem to affect the diffusion profile.	Good
Al-3 RG1 B	150 to 250	Crosses the same microfracture as profile A, with no obvious effects.	Good
Al-3 RG1 C	200	Profile has an unusual shape and resulting model fits are poor, however, determined cooling rates are similar to cooling rates from profiles A and B.	Moderate
Al-4 RG1 A	50000 to 100	Measured across the narrowest grain boundary as this is closest to perpendicular.	Moderate
Al-5 RG1 A	250 to 2000	Lack of constant core composition may introduce errors. Shows considerably slower cooling rates than other profiles in this chondrule.	Poor
Al-5 RG1 B	3000 to 5000	Lack of constant core composition may introduce errors. The profile also is close to a merging diffusion front and an unusual feature. These may introduce errors in determined cooling rates, however, cooling rates are similar to cooling rates from Al-5 RG2 A and B	Moderate
Al-5 RG2 A	3000 to 6000	Lack of constant core composition may introduce errors. This profile is measured on a straight edge away from merging diffusion fronts. Determined cooling rates are similar to those observed in Al-5 RG1 B and Al-5 RG2 B.	Moderate
Al-5 RG2 B	5000 to 8000	Lack of constant core composition may introduce errors. The profile is measured on a straight boundary but may be close to merging diffusion fronts. Determined cooling rates are similar to those observed in Al-5 RG1 B and Al-5 RG2 A.	Moderate
Al-6 RG1 A	500	Measured across a straight boundary away from any merging diffusion fronts. The grain boundary appears wider on this profile than the opposite grain edge, suggesting that the section crosses this boundary at a lower angle, explaining the lower cooling rates.	Poor
Al-6 RG1 B	2000 to 400	This profile is measured on a straight boundary and there is no evidence that it has been affected by nearby merging diffusion fronts. Determined cooling rates are similar to cooling rates determined for profiles C and D.	Good
Al-6 RG1 C	1500	This profile is measured on a straight edge however it is close to a fracture. This profile is roughly opposite profile D and appears symmetrical. This resulted in similar determined cooling rates between profiles C and D, which are also similar to profile B.	Good
Al-6 RG1 D	1600 to 800	This profile is measured on a straight edge however it is close to fractures. This profile is roughly opposite profile C and appears symmetrical. This resulted in similar determined cooling rates between profiles C and D, which are also similar to profile B.	Good

Table 5.9 – Summary of the potential sectioning effects and petrography on the measured diffusion profiles from forsteritic-olivine relict grains in NWA 8276 and NWA 4910.

Profile	Cooling rates (Kh^{-1})	Comments on sectioning	Confidence
N8-1 RG1 A	300 to 10	This profile is measured across a mostly straight boundary; however, it is close to two merging diffusion fronts. This means determined cooling rates may be inaccurate.	Moderate
N8-2 RG1 A	100 to 20	This profile is measured across a straight boundary; however, it is close to numerous Fe-rich inclusions.	Moderate
N8-3 RG1 A	2000 to 50	The core region of this crystal has been slightly modified by diffusion or displays a slightly dipping plateau. The opposite boundaries are mostly symmetrical but are slightly wider on the side where the profile is measured, indicating a shallower sectioning angle. This may mean that cooling rates are slightly underestimated.	Good
N4-1 RG1 A	4000 to 10	The profile is measured across the sharpest straight boundary, away from any merging diffusion fronts. However, model fits to this profile were poor suggesting determined cooling rates may be inaccurate.	Poor
N4-2 RG1 A	1000 to 20	The profile is measured across a straight edge away from merging diffusion fronts and there appears to be symmetry between the two major grain boundaries. Despite this apparent symmetry, determined cooling rates are very different to profile B.	Good
N4-2 RG1 B	5000 to 5	The profile is measured across a straight edge away from merging diffusion fronts and there appears to be symmetry between the two major grain boundaries. However, model fits to this diffusion profile were poor suggesting determined cooling rates may be inaccurate.	Poor
N4-3 RG1 A	2000 to 500	This profile is measured across a straight edge away from merging diffusion fronts.	Good

5.5 Summary and conclusions

Twenty-three Fe-Mg compositional profiles in 13 forsteritic-olivine relict grain across 12 chondrules have been modelled using a 1-D explicit finite difference method. The results of diffusion modelling for the 6 chondrules in ALHA 77307 show cooling rates ranging from 100 to 8000 Kh^{-1} with one chondrule showing evidence of extremely rapid cooling of 50000 Kh^{-1}. The determined cooling rates for chondrules in NWA 8276 and NWA 4910 range from 5 to 5000 Kh^{-1}. While diffusion modelling was undertaken at 1 log unit beneath the iron-wüstite buffer, higher oxygen fugacities, e.g. 1 log unit above the iron-wüstite buffer, as suggested by Villeneuve et al. (2015), result in cooling rates that are approximately twice as fast. The more oxidising conditions result in higher diffusion coefficients, resulting in faster diffusion. Previous studies of chondrule cooling rate have usually considered linear or constant cooling rates, however, to produce good model fits to many of the observed compositional profiles, non-linear cooling histories had to be considered. These were

modelled in two stages with an initial cooling rate changing to a final cooling rate at a transition temperature. To preserve the shapes of the observed compositional profiles, cooling rates at lower temperatures must been rapid (Villeneuve et al., 2015). This would minimise diffusion between the relict grain and the overgrowth, preserving the sharp transition between the two.

Overall, there is a range in behaviour and three different thermal histories were required: increasing cooling rates, decreasing cooling rates and linear cooling rates. Three chondrules in ALHA 77307 (Al-1, Al-2 and Al-5) consistently require increasing cooling rates, chondrule Al-4 shows extremely rapid cooling followed by much slower cooling and the two remaining chondrules (Al-3 and Al-6) show a range of cooling behaviour. All chondrules in NWA 8276 and NWA 4910 require decreasing cooling rates, however, the final slow cooling rate tends to be across a much more restricted temperature range towards the end of the model run than the initial more rapid cooling. When the apparently slow cooling diffusion occurred has not been completely constrained and could be the result of secondary heating, for example, protracted low-temperature parent body metamorphism. The variation in cooling behaviour within a forsteritic-olivine relict grain or a chondrule is most likely caused by sectioning effects where the forsteritic-olivine relict grains are cut off-centre and/or randomly across the crystallographic axes. Examination of the forsteritic-olivine relict grains suggests that many of the grains show relatively centre cut crystals that are randomly oriented. Some grains show evidence that they may not be sectioned through the centre, due to the presence of dipping plateaus (e.g. Al-3 RG1 and Al-4 RG1) and highly asymmetric diffusion profiles (e.g. Al-4 RG1). Two sections are on-axis and are sectioned perpendicular to one of the crystallographic axes and parallel to the others. The best sections, which produce the least error are centre cut on-axis cuts through crystals with compositional profiles measured along one of the crystallographic axes. For randomly oriented off-centre sections, variation in determined diffusion timescales may vary significantly and may result in a significant underestimation of cooling rates. The narrowest boundaries within a relict grain are sectioned closest to perpendicular and are the most likely to show the true diffusion width. Wider profiles are more likely to be sectioned at a shallow angle and show diffusion widths that are artificially extended beyond the true diffusion width. This results in overestimations of diffusion time and underestimations in cooling rate. Therefore, diffusion profiles measured across the narrowest boundaries, resulting in the fastest

cooling rates, are most likely to show the true diffusion time and most accurate cooling rates within a relict grain. The implications of the cooling rates determined from these chondrules are discussed in Chapter 6.

Chapter 6

Discussion

Application of cooling rates to chondrule formation models

Chondrule cooling rate is one of the important constraints on chondrule formation mechanisms and may potentially aid in discriminating between chondrule formation mechanisms that are possible and those which do not match these thermal constraints. This chapter examines how the results of this work compare to other previously determined cooling rates through different techniques, for example, dynamic crystallisation experiments, as well as how they compare to the predictions of different chondrule formation models. The implications of the supported chondrule formation mechanism(s) are also discussed.

6.1 Chondrule cooling rates in carbonaceous and ordinary chondrites

The cooling rates of the chondrules studied here range from 5 to 50000 Kh^{-1} spanning four orders of magnitude (see Figure 6.1). There is some variation in determined cooling rates between chondrules from the ordinary chondrites NWA 8726 and NWA 4910 and the chondrules from the carbonaceous chondrite ALHA 77307. The range in cooling rate for five of the six chondrules from ALHA 77307 is 100 to 8000 Kh^{-1}, with one showing evidence of much more rapid cooling, up to 50000 Kh^{-1}. These cooling rates are generally higher than those recorded in the ordinary chondrites, which range from 10 to 2000 Kh^{-1} (5 to 5000 Kh^{-1} if including the profiles with poorer model fits). There is also a considerable difference in the modelled thermal history (see Figure 6.2). The diffusion profiles in ALHA 77307 reveal a variety of different cooling histories including increasing, decreasing, and linear cooling rates. Three of the six chondrules record consistently increasing cooling rates. One shows significantly decreasing cooling rates, while two show a variety of behaviour. In most cases where decreasing cooling rates are required, it is a minor part of the cooling history occurring at the very end of the model run at the lowest temperatures. The diffusion profiles in NWA 8276 and NWA 4910 all record thermal histories with decreasing cooling rates, often with very slow final cooling rates <100 Kh^{-1}. As with the profiles recording decreasing history in ALHA 77307, this slower cooling often occurs across a restricted temperature range at the end of the model run. This is often accompanied by a distinct shallowing of the diffusion profile towards the grain edge, which to form by diffusion alone, requires decreased cooling rates at lower temperatures, to allow more Fe to diffuse into the crystal. However, as discussed in Chapter 5, there may be other ways to achieve this shape. Firstly, the addition of crystal growth during the final stages of exchange with melt. This would add extra Fe-rich olivine to the edge of the forsteritic-olivine relict grain creating a shallowing profile. The second explanation could be in reheating events or parent body metamorphism, which allow diffusion to occur primarily at the grain edge where diffusion is fastest, creating a shallowing profile. Given this uncertainty, discussion of the cooling rates of the ordinary chondrites is mainly focussed on the initial cooling rates.

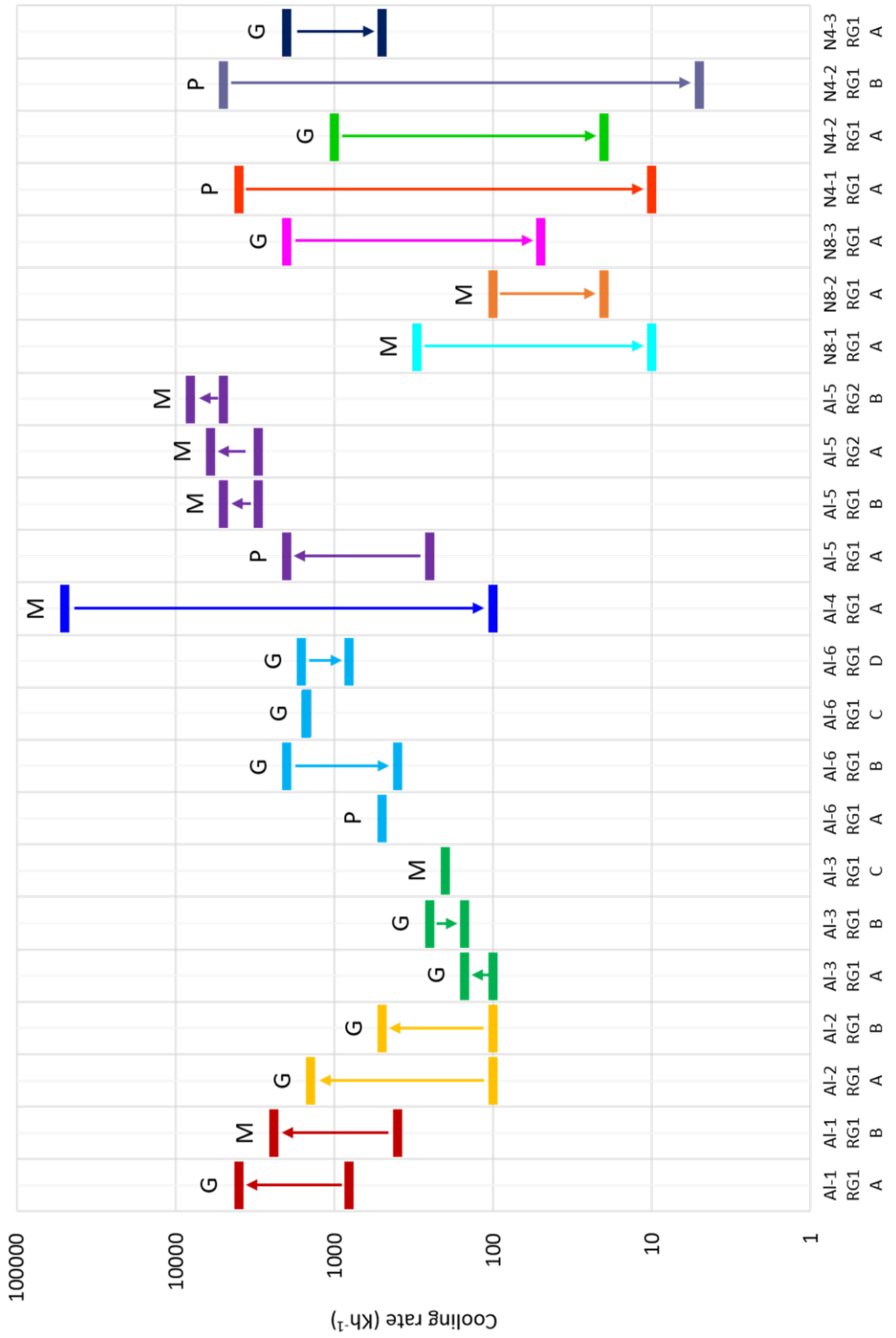

Figure 6.1 – Summary of chondrule cooling rates from profiles in forsteritic-olivine relict grains in chondrules ALHA 77307, NWA 8276 and NWA 4910. The letter indicates the confidence level assigned to the cooling rate: G indicates good, M indicates moderate, while P indicates poor.

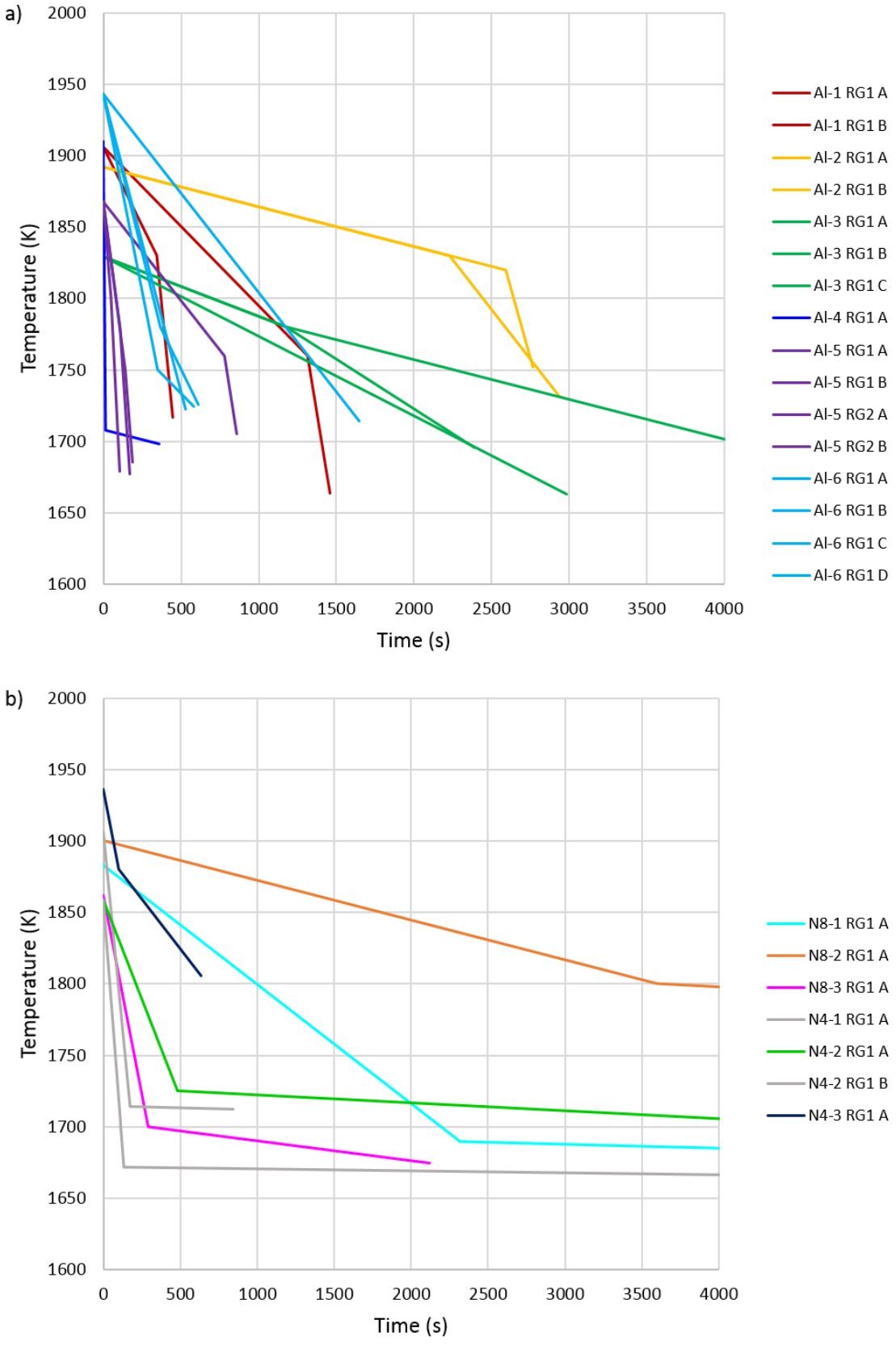

Figure 6.2 – Temperature-time plots from model diffusion profiles in a) ALHA 77307 and b) NWA 8276 and NWA 4910.

6.2 Overview of previously determined cooling rates

This section provides a brief overview of the techniques that have been used previously to determine chondrule cooling rates (see Figure 6.3). For a more detailed discussion, see Chapter 1, section 1.6.

Dynamic crystallisation experiments remain the most widely cited method of determining chondrule cooling rates. These experiments most successfully reproduced porphyritic textures at cooling rates ranging from 10 to 1000 Kh^{-1} (Lofgren and Russell, 1986; Lofgren, 1989; Radomsky and Hewins, 1990; Connolly and Hewins, 1991; Jones and Lofgren, 1993; Kennedy et al., 1993; Connolly and Hewins, 1995; Dehart and Lofgren, 1996; Connolly et al., 1998; Weinbruch et al., 1998; Wick et al., 2010). As discussed in chapter 1, cooling rate and texture are weakly related (e.g. Lofgren, 1996; Hewins et al., 2005; Jones et al., 2018) and require more direct measurements, such as the approach used in this study, to validate and constrain these cooling rates.

Wasson (2004) argue for very rapid chondrule cooling rates, 3.6×10^6 Kh^{-1} based on the widths of overgrowths present on forsteritic-olivine relict grains. These cooling rates were refuted by Connolly Jr and Jones (2005) who suggest these cooling rates are higher than blackbody radiation for a molten chondrule and are impossible.

The microstructure of clinopyroxenes in type I porphyritic olivine and pyroxene chondrules has been used to suggest cooling rates of 0.1 to 50 Kh^{-1} (Weinbruch and Müller, 1995; Weinbruch et al., 2001), however, Cuvillier et al. (2018) suggest that these features could be created at cooling rates of 1000 Kh^{-1} at temperatures of 1620 to 1470 K. The clinoenstatite to orthoenstatite ratio in chondrules also depends upon cooling rate (Smyth, 1974; Brearley and Jones, 1993). A high clinoenstatite to orthoenstatite ratio, often found in porphyritic chondrules, indicates cooling rates were high, up to 10000 Kh^{-1} at ~1270 K (Jones et al., 2018).

Chondrule phenocryst zoning profiles have also been used to infer chondrule cooling rates. Jones and Lofgren (1993) compared zoning profiles in olivine phenocrysts in chondrules in ordinary chondrites to those in experimentally created olivine phenocrysts and found matches at cooling rates of 2, 5 and 100 Kh^{-1}. Miyamoto et al. (2009) modelled the production of zoning profiles and subsequent diffusional modification. Comparing these

models to observed zoning profiles in chondrules from Semarkona yielded chondrule cooling rates of 0.7 to 2400 Kh^{-1}.

Soulié et al. (2017) performed olivine dissolution experiments and found that forsterite dissolution in type IA chondrule melts is very rapid. To preserve forsterite in these chondrules, the time at high temperatures must be low, requiring a short heating event and rapid cooling rates of 1000 to 8000 Kh^{-1}.

Several authors have used diffusional techniques to determine chondrule cooling rates. Greeney and Ruzicka (2004) modelled Mn, Ca and Fe-Mg diffusion profiles between forsteritic-olivine relict grains and the surrounding overgrowth in chondrules from several metamorphosed ordinary chondrites (Sahara 97210 LL3.2, Wells LL3.3 and Chainpur LL3.4). Determined cooling rates varied from ~200 to 6000 Kh^{-1}, however, these meteorites have experienced some degree of metamorphism, which has possibly affected the observed diffusion profiles, and therefore, these cooling rates may not be valid. Béjina et al. (2009) found cooling rates of 700 to 3600 Kh^{-1} for chondrules in the same meteorites. Hewins et al. (2009) reported some preliminary results of modelled Fe-Mg and Cr diffusion profiles in a forsteritic-olivine relict grain in a chondrule in Semarkona. The determined initial cooling rates were 400 Kh^{-1} for Fe-Mg diffusion and 300 Kh^{-1} for Cr diffusion. Modelling of Cu and Ga diffusion profiles across metal grains associated with type I chondrules in the CR2 chondrites Acfer 097 and Renazzo (Humayun, 2012; Chaumard et al., 2018). Possible cooling rates range from 0.5 to 400 Kh^{-1} with the chondrules in Renazzo showing a more restricted range of 21 to 86 Kh^{-1} (Chaumard et al., 2018) at temperatures of ~1470 to 1570 K.

The presence of primary plagioclase in some type I and type II chondrules has also been used to infer very slow cooling rates, ~1 Kh^{-1}, at low temperatures at the end of the crystallisation of the chondrule (Jones, 1997; Rocha and Jones, 2012; Wick and Jones, 2012; Lewis and Jones, 2019).

The cooling rates determined from clinopyroxene microstructures (Weinbruch and Müller, 1995; Weinbruch et al., 2001; Cuvillier et al., 2018; Jones et al., 2018), diffusion modelling in metal grains (Humayun, 2012; Chaumard et al., 2018) and presence of primary plagioclase in chondrules (Jones, 1997; Wick and Jones, 2012; Lewis and Jones, 2019) are valid for cooling rates at lower temperatures than the cooling rates determined from

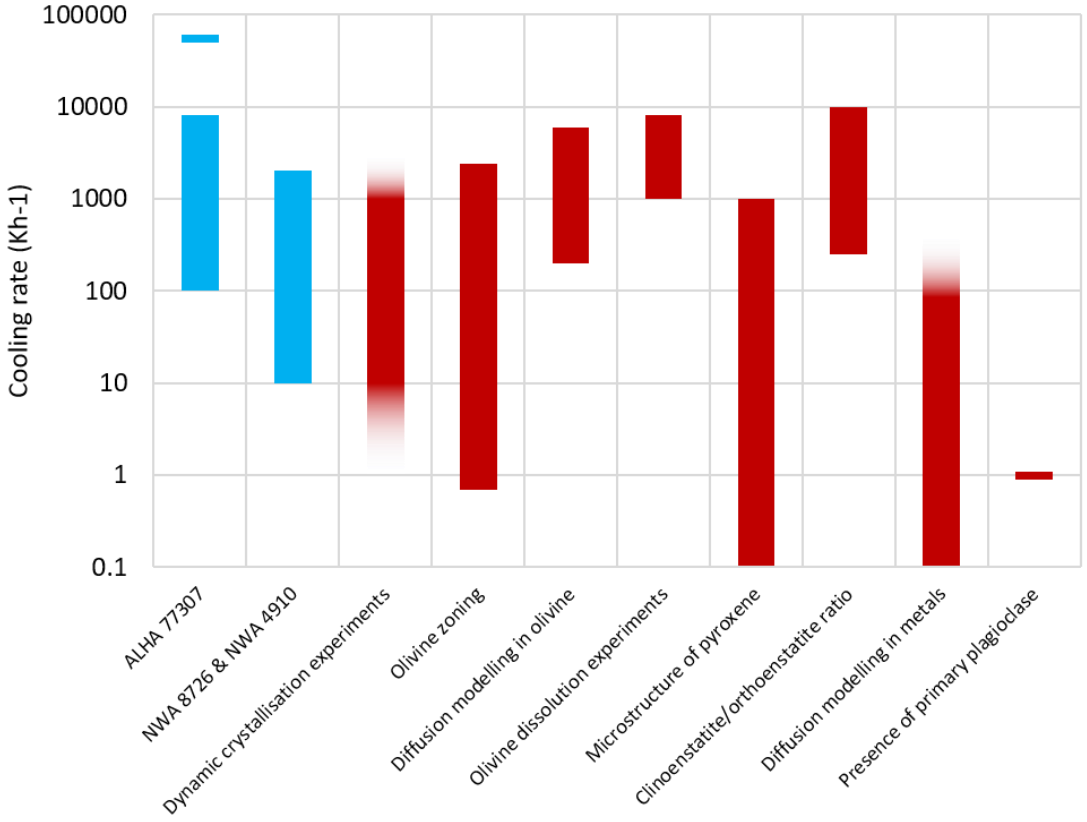

Figure 6.3 – Comparison of chondrule cooling rates determined by modelling diffusion profiles in forsteritic-olivine relict grains in chondrules from ALHA 77307, NWA 8276 and NWA 4910 in comparison to previously determined cooling rates for porphyritic chondrules: dynamic crystallisation experiments (Connolly and Hewins 1991, 1995; Connolly et al. 1998; Dehart and Lofgren 1996; Hewins et al. 1981; Jones and Lofgren 1993; Kennedy et al. 1993; Lofgren 1989; Lofgren and Lanier 1990; Lofgren and Russell 1986; Radomsky and Hewins 1990; Tsuchiyama et al. 2004; Weinbruch et al. 1998; Wick et al. 2010); olivine zoning (Jones and Lofgren 1993; Miyamoto et al. 2009); diffusion modelling in olivine (Béjina et al. 2009; Greeney and Ruzicka 2004; Hewins et al. 2009); olivine dissolution experiments (Soulié et al. 2017); microstructures in clinopyroxenes and plagioclase (Cuvillier et al. 2018; Weinbruch and Müller 1995; Weinbruch et al. 2001); clinoenstatite/orthoenstatite ratio (Jones et al. 2018); diffusion modelling in metals (Chaumard et al. 2018; Humayun 2012); presence of primary plagioclase (Jones 1997; Lewis and Jones 2019; Wick and Jones 2012).

modelling forsteritic-olivine relict grains here. They provide potentially important constraints on chondrule formation; however, they cannot be directly compared to the cooling rates determined here.

Chondrules Al-2, Al-3, Al-6 and profile Al-1 RG1 B show cooling rates that are consistent with cooling rates from crystallisation experiments, although the other profile in Al-1, Al-1 RG1 A indicates more rapid cooling rates for this chondrule. The diffusion profiles from Al-4 and Al-5 indicate cooling rates are more rapid than those suggested by dynamic crystallisation experiments. Cooling rates spanning 3.5 orders of magnitude have been reported from olivine phenocryst zoning profiles and these cooling rates are similar to many of the cooling rates derived from relict grain diffusion profiles here. Chondrule

cooling rates determined by olivine dissolution experiments are generally rather fast and overlap with the faster cooling chondrules reported in this study, namely Al-1, Al-5, and Al-6 as well as one of the profiles from Al-2. For Al-3 and the other profile from Al-2, cooling rates are lower. Cooling rates for chondrule Al-5 are still too rapid to be consistent with these dissolution experiments. Most of the chondrules from ALHA 77307 studied here, i.e. Al-1 to Al-6, are most consistent with cooling rates determined previously from modelling diffusion between forsteritic-olivine relict grains and surrounding overgrowth, although, the cooling rates for Al-4 still falls above the previously reported ranges.

Determined cooling rates from NWA 8276 and NWA 4910 range from 5 to 5000 Kh^{-1}. If removing the profiles that have poor model fits (N4-1 RG1 A and N4-2 RG1 B), this range is reduced to 10 to 2000 Kh^{-1}. Profiles from chondrules N8-1, N8-2, N8-3, and N4-2 show some very low cooling rates of 10 to 50 Kh^{-1}, whereas the profiles from N4-3 shows more rapid rates of 500 to 2000 Kh^{-1}. All these cooling rates are consistent with the results of dynamic crystallisation experiments and cooling rates determined from olivine phenocryst zoning. These chondrules also show some cooling occurring at rates much lower than suggested from olivine dissolution experiments. These cooling rates are also consistent with cooling rates from different diffusion techniques. The faster cooling rates fall within the range of those determined by modelling diffusion between forsteritic-olivine relict grains and the slower cooling rates at lower temperatures are consistent with cooling rates determined by modelling diffusion in metals.

6.2.1 Summary and conclusions

The most widely cited method of determining chondrule cooling rates to date remains dynamic crystallisation experiments. The cooling rates from these (~10 to 1000 Kh^{-1}) have been used to constrain chondrule formation mechanisms. The results from this study show that the cooling rates of the studied chondrules range from ~100 to 8000 Kh^{-1} with one chondrule showing evidence of much more rapid cooling (50000 Kh^{-1}). This range includes much faster cooling rates than indicated by these crystallisation experiments. These cooling rates are similar to constraints provided by olivine dissolution experiments, suggesting that in order to preserve forsterite in chondritic melts, cooling rates must be between 1000 and 8000 Kh^{-1}. They are also broadly similar to results of previous work on diffusion modelling in olivine, however, the data sets were very limited (Hewins et al., 2009), or the results were for meteorites that have experience potentially significant thermal metamorphism

(Greeney and Ruzicka, 2004; Béjina et al., 2009). The cooling rates determined in this study suggest that more rapid cooling rates are applicable to the formation of type II porphyritic chondrules over a temperature range of ~1950 to 1650 K.

6.3 Cooling rates predicted from chondrule formation mechanisms

The most commonly cited chondrule formation mechanisms are nebular shockwaves; either large-scale gravitational instability driven nebular shockwaves (Hood and Horanyi, 1991; Wood, 1996; Ciesla and Hood, 2002; Desch and Connolly, 2002; Boss and Durisen, 2005; Morris and Desch, 2010; Morris et al., 2016; Morris and Boley, 2018) or more local planetesimal or planetary embryo bow shocks (Ciesla et al., 2004; Morris et al., 2012; Boley et al., 2013; Mann et al., 2016; Morris and Boley, 2018). Another group of formation models invoke collisions between planetesimals. Chondrules would either be formed in an impact plume (Hasegawa et al., 2015; Johnson et al., 2015; Wakita et al., 2017; Johnson et al., 2018; Oshino et al., 2019) or as splashes from impacts between molten planetesimals (Asphaug et al., 2011; Sanders and Scott, 2012). Other potential chondrule formation mechanisms include nebular lightning (Desch and Cuzzi, 2000; Johansen and Okuzumi, 2017; Johansen and Okuzumi, 2018); the X-wind (Shu et al., 1996; Shu et al., 1997; Shu et al., 2001; Desch et al., 2010); radiative heating of dust clumps passing molten planetesimals (Herbst and Greenwood, 2016; Herbst and Greenwood, 2019); current sheets close to the sun (McNally et al., 2013); ablation in bipolar outflows (Liffman, 2009); magnetic flares (Levy and Araki, 1989) and X-ray flares (Nakamoto et al., 2005). These formation mechanisms are discussed in more detail in Chapter 1 section 1.8. This section compares the expected cooling rates in these chondrule formation mechanisms to the cooling rates determined for the type II chondrules in this study. This section also considers carefully whether these mechanisms can form these chondrules. Porphyritic olivine chondrules must have been heated to temperatures close to, but not exceeding the liquidus in order to preserve crystalline nuclei (e.g. Hewins et al., 2005). For the studied chondrules, this equates to temperatures in the range of ~1830 to 1940 K.

6.3.1 Large-scale nebular shockwaves

Large-scale nebular shockwaves occur as a result of the formation of spiral arms in the solar nebula, which are formed by gravitational instabilities. These spiral arms can drive strong

shock-fronts into the inner solar nebula (Boss and Durisen, 2005). Chondrule precursors passing through the shockwave are heated by gas-drag frictional heating and can reach peak temperatures of 1720 to >2000 K (in models, chondrule temperatures are capped at 2000 K) for shock speeds ranging from 7 to 10 kms^{-1} (Morris and Desch, 2010). After peak temperatures are reached, initial cooling rates are rapid, several 10^4 Kh^{-1}, however, across the modelled temperature range, cooling rates are expected to be more gentle, several 10s Kh^{-1} (Ciesla and Hood, 2002; Desch and Connolly, 2002; Morris and Desch, 2010), but possibly up to 1000 Kh^{-1} (Morris et al., 2016).

The peak temperatures of up to 2000 K indicate that the formation of these chondrules is achievable in these large-scale nebular shockwaves. Cooling rates from these large-scale nebular shockwaves are generally inconsistent with determined chondrule cooling rates (see Figure 6.4), particularly those from ALHA 77307. For all chondrules in ALHA 77307 except Al-3, cooling rates determined from forsteritic-olivine relict grain diffusion profiles are generally 1 or 2 orders of magnitude higher than those predicted in large scale nebular shockwaves. For Al-3, the determined cooling rates range from 100 to 250 Kh^{-1}, which could be consistent with formation in a large-scale nebular shockwave. For chondrules in NWA 8276 and NWA 4910, cooling rates generally range from 10 to 2000 Kh^{-1}. Chondrules N8-1 and N8-2 show low cooling rates, ranging from 10 to 300 Kh^{-1} that are consistent with formation in large-scale nebular shockwaves. For N8-3 and N4-2, the lower cooling rates at the end of the model runs (50 and 20 Kh^{-1} respectively) are also consistent with formation in a large-scale nebular shockwave, however the higher cooling rates, occurring at higher temperatures are too rapid. The thermal history of chondrules across the modelled temperature range also needs to be considered. For large-scale nebular shockwaves, cooling rates across the olivine crystallisation temperature range are expected to be roughly linear, however, almost all chondrules show evidence of complex, non-linear cooling rates. Three chondrules from ALHA 77307 consistently show increasing cooling rates which is inconsistent with the current understanding of these shocks. All the chondrules from NWA 8276 and NWA 4910 suggest non-linear cooling rates showing decreasing cooling rates, which is again inconsistent with their formation in large scale nebular shockwaves. Interestingly, Al-5, which shows initially very rapid cooling rates of 50000 Kh^{-1} followed by more gentle cooling rates of 100 Kh^{-1}, transitioning at 1714 K, is very similar to the entire thermal history of chondrules formed in large scale nebular

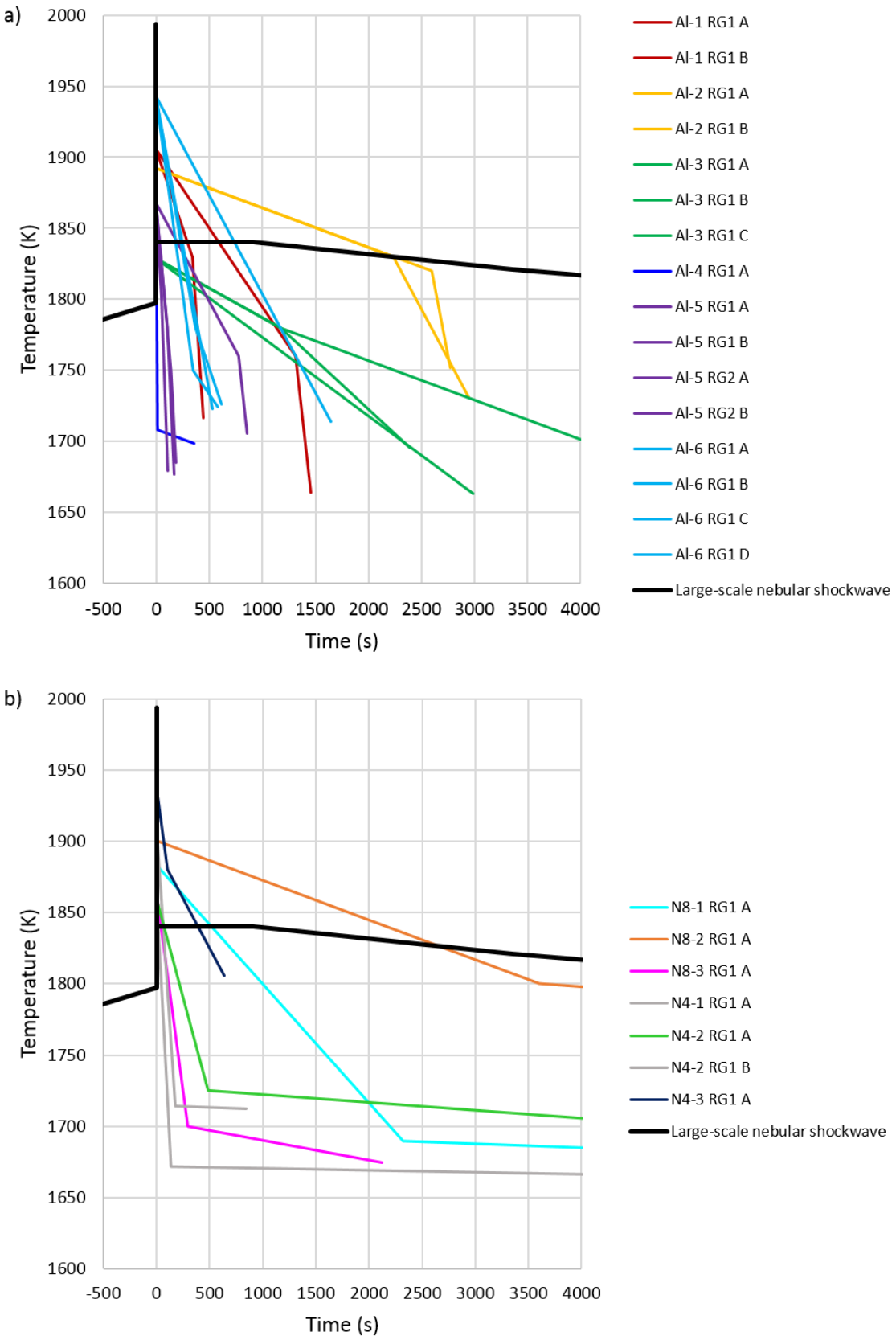

Figure 6.4 - Temperature-time plots from model diffusion profiles in forsteritic-olivine relict grains in a) ALHA 77307 and b) NWA 8276 and NWA 4910, compared to the predicted thermal history of chondrules in a large-scale nebular shock wave. The conditions of the shock are shock speed of 8 kms^{-1} with 10x the concentration of chondrules over canonical conditions (Morris and Desch 2010).

shockwaves (Desch and Connolly, 2002; Morris and Desch, 2010), possibly suggesting that this chondrule formed in a large scale nebular shockwave. However, most chondrules show cooling rates which are too rapid across the modelled temperature range and the observed thermal histories may rule out large-scale nebular shockwaves as a formation mechanism for chondrules in ALHA 77307, NWA 8276 and NWA 4910.

6.3.2 Planetesimals and planetary embryo bow shocks

Planetesimals and planetary embryos moving in eccentric or inclined orbits, travelling supersonically through the solar nebula gas can drive a bow shock in front of them. They will process material in a similar way to large-scale nebular shockwaves but on a much smaller scale. Bow shocks around smaller planetesimals (radius less than 1000 km) are generally inconsistent with thermal constraints on chondrule formation as they provide peak temperatures which are too low to melt chondrule precursors into chondrules and impose very fast cooling rates (up to 10^5 Kh^{-1}) (Ciesla et al., 2004).

The larger size of planetary embryos (radius larger than 1000 km) compared to planetesimals makes them a better candidate for chondrule formation, and there is strong evidence that Mars-sized bodies existed at the same time as chondrule formation (Dauphas and Pourmand, 2011). Cooling rates for chondrules forming in planetary embryo bow shocks are generally rapid. Boley et al. (2013) and Mann et al. (2016) report cooling rates generally ranging from 10^3 to 10^4 Kh^{-1} for bow shocks ranging in speed from 6 to 9 kms^{-1} (e.g. Figure 6.5 and Figure 6.6) around a planetary embryo with a radius of 3000 km. In these figures, the upper black line shows the thermal history of a chondrule passing close to the centre of the bow shock, while the lower black line represents a chondrule passing through the edge of the bow shock. Multiple temperature-time paths exist between the upper and lower boundaries for grains passing through the bow shock between these two extremes. Shocks incorporating radiative cooling as well as cooling caused by adiabatic expansion provide cooling rates closer to 10^4 Kh^{-1} (e.g. Figure 6.5 c, g, h, and i and Figure 6.6 c, g, h, and i). In order to justify cooling caused only by adiabatic expansion, the environment must be very dusty in order to prevent efficient radiation (Boley et al., 2013; Mann et al., 2016). Factors which affect chondrule thermal histories in a bow shock are shock speed, the position of the chondrules as they pass through the bow shock, whether the planetary embryo has an atmosphere, density of chondrules and dust opacity.

More rapid shocks produce higher peak temperatures and experience the fastest cooling rates. For example, Mann et al. (2016) found that for bow shocks with a shock speed of 6 kms^{-1} with adiabatic cooling and a high mass atmosphere (Figure 6.5 and Figure 6.6 f), cooling rates ranged from 200 to 1100 Kh^{-1} with peak temperatures <1800 K, whereas for faster shocks, of 7 kms^{-1}, under the same conditions (Figure 6.5 and Figure 6.6 e), cooling rates are slightly more rapid, ~1000 Kh^{-1}, with much higher peak temperatures between 1900 and 2100 K.

The position of the chondrule as it passes through the shock front also affects its thermal history. Chondrules passing close to the centre of the bow shock experience the highest peak temperatures, while chondrules which pass through the periphery experience much lower peak temperatures. In some models, the position also results in a difference in cooling rate, for example, in Figure 6.5f, chondrules passing close to the centre continue heating slowly after peak heating, before experiencing relatively rapid cooling rates, whereas chondrules close to the edge experience lower cooling rates (Mann et al., 2016). In contrast to this, many other modelled bow shocks show similar cooling rates for chondrules whether they pass through the centre or the edge of the bow shock, e.g. Figure 6.5a and d, however, chondrules passing through the centre experience initially slow cooling before showing parallel cooling rates (Boley et al., 2013; Mann et al., 2016).

The presence of an atmosphere around the planetary embryo also affects the thermal history of chondrules passing through the bow shock. An atmosphere increases the cross-section of the planetary embryo and creates a larger standoff distance. This means it takes longer for chondrules to be transported around the planetary embryo. This results in reduced cooling rates, as the chondrules are kept in contact with hot gas for longer periods of time. This is best illustrated by examining Figure 6.5a, d and e. Cooling rates in 7 kms^{-1} with a high mass atmosphere with cooling as a result of adiabatic expansion are ~1000 Kh^{-1} (Mann et al., 2016). The same shock with a low mass atmosphere results in slightly more rapid cooling rates of ~1500 Kh^{-1} (Mann et al., 2016). A 7 kms^{-1} shock with no atmosphere results in cooling rates of ~4000 Kh^{-1} (Boley et al., 2013), more than twice as rapid as cooling rates in a shock with even a low mass atmosphere. In bow shocks without atmospheres there are noticeable tail shocks which cause secondary heating events (e.g. Figure 6.5a and b) (Boley et al., 2013). These are absent in cases with atmospheres (Mann et al., 2016).

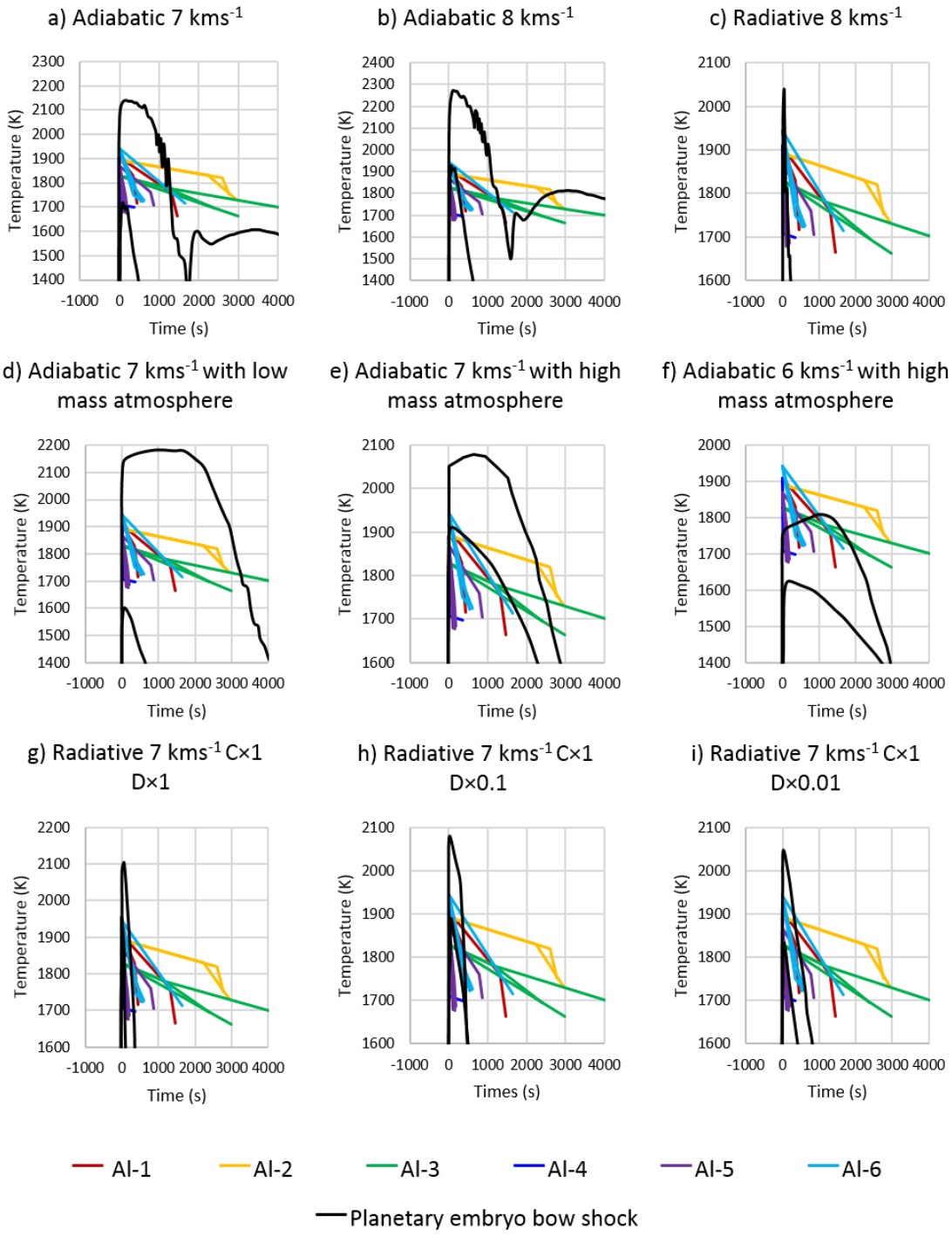

Figure 6.5 – Temperature-time plots from model diffusion profiles in forsteritic-olivine relict grains in chondrules in ALHA 77307 compared to thermal history of chondrules in a planetary embryo bow shock. The upper black line represents a chondrule passing close to the centre of the bow shock whereas the lower black line represents a chondrule passing through the periphery of the bow shock. Coloured lines show the T-t curves for the different relict grains: a) and b) show the effects of cooling adiabatically at different shock speeds; c) adds the effect of radiative cooling; d) adds the effect of a low mass atmosphere; e) and f) add the effects of high mass atmospheres at different shock speeds; g), h) and i) add in the effect of radiative cooling at different chondrule, C, and dust, D, densities relative to canonical conditions. Bow shock curves a) to c) are from Boley et al. (2013), plots d) to i) are from Mann et al. (2016). Graphs are set so that peak heating occurs at 0 s.

In cases where radiative cooling is helping control the thermal history, other important factors which affect cooling rates are chondrule density and dust opacity. Both chondrules and dust contribute to the opacity and are both effective radiators. In shocks with canonical chondrule and dust densities (Figure 6.5g), chondrules and dust are present in quantities which are not high enough to prevent efficient radiation, which results in rapid cooling rates $>10^4$ Kh^{-1}. Reducing dust opacity by a factor of 10 (Figure 6.5h) has two effects: 1) overall opacity is reduced, allowing for more efficient radiation; 2) the number of radiators has reduced meaning energy is transferred more slowly. The net effect of this is to reduce cooling rates to a range of 4000 to 6000 Kh^{-1} for a 7 kms^{-1} shock with a high mass atmosphere. Reducing dust opacity by a factor of 100 reduces cooling rates even further to ~2000 Kh^{-1} (Mann et al., 2016). Boley et al. (2013) report that increasing chondrule density also reduces cooling rates from $>10^4$ Kh^{-1}, for canonical conditions, to 2000 to 4000 Kh^{-1}, however, peak temperatures were reduced to ~1600 K.

The required peak temperatures of up to ~1940 K are achievable in almost all of the bow shocks shown in Figure 6.5 and Figure 6.6. Most bow shocks show peak temperatures of ~1700 to ~2100 K. These temperatures are broadly consistent with the constraints from chondrule liquidus temperatures in this study. The 8 kms^{-1} adiabatic shock in Figure 6.5b shows peak temperatures of ~1900 to 2300 K (Boley et al., 2013), are mostly too high for the formation of the porphyritic chondrules studied here. The high peak temperatures in this shock may result in the destruction of most of the crystalline nuclei within the chondrule melts. Upon crystallising, these chondrules are more likely to produce barred and radial textures (e.g. Jones et al., 2018). The peak temperatures in the 6 kms^{-1} adiabatic shock around a planetary embryo with a high mass atmosphere (Figure 6.5f) show peak temperatures of 1600 to 1800 K. These are lower than the liquidus temperatures of the porphyritic chondrules studied here and suggest that this low speed shock is unable to form these chondrules. However, by increasing shock speeds to 7 kms^{-1}, peak temperatures rise, up to ~2100 Kh^{-1} (e.g. Figure 6.5e).

The expected cooling rates of chondrules in planetary embryo bow shocks are potentially consistent with all chondrules in ALHA 77307, although adiabatic cases produce generally slower cooling rates which are most consistent with the studied chondrules. Chondrules Al-1 and Al-6 show cooling rates that are most consistent with planetary embryo bow shocks with cooling as a result of adiabatic expansion (e.g. Figure 6.5a) (Boley et al., 2013).

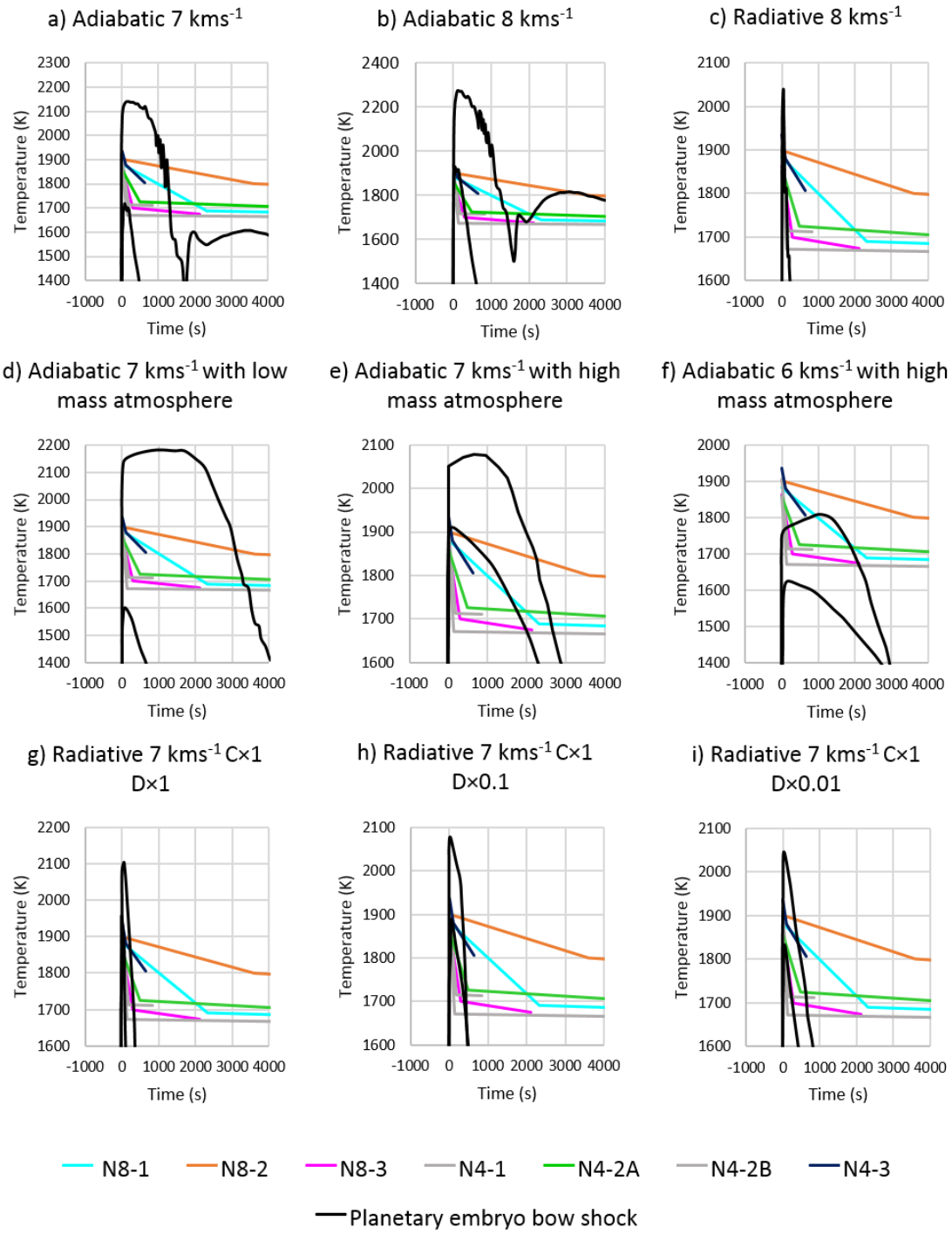

Figure 6.6 – Temperature-time plots from model diffusion profiles in forsteritic-olivine relict grains in chondrules in NWA 8276 and NWA 4910 compared to thermal history of chondrules in a planetary embryo bow shock. The upper black line represents a chondrule passing close to the centre of the bow shock whereas the lower black line represents a chondrule passing through the periphery of the bow shock. Coloured lines show the T-t curves for the different relict grains: a) and b) show the effects of cooling adiabatically at different shock speeds; c) adds the effect of radiative cooling; d) adds the effects of a low mass atmosphere; e) and f) add the effects of high mass atmospheres at different shock speeds; g), h) and i) add in the effect of radiative cooling at different chondrule, C, and dust, D, densities relative to canonical conditions. Bow shock curves a) to c) are from Boley et al. (2013), plots d) to i) are from Mann et al. (2016). Graphs are set so that peak heating occurs at 0 s.

Chondrules Al-2 and Al-3 both show low cooling rates, as low as 100 $Kh^{-1,}$ which may be consistent with the 6 kms^{-1} high mass atmosphere case in Figure 6.5f (Mann et al., 2016). The rapid cooling rates shown by chondrule Al-5 may require a bow shock where cooling is a result of radiation, e.g. Figure 6.5h, where cooling rates range from 4000 to 6000 Kh^{-1} (Mann et al., 2016), which is a similar range to the 3000 to 8000 Kh^{-1} shown by this chondrule. The most difficult chondrule to explain by planetary embryo bow shocks is chondrule Al-4, with its rapid initial cooling rates. These may be possible in radiative bow shocks where cooling rates can be in excess of 10^4 Kh^{-1} e.g Figure 6.5c and g.

Most of the chondrules in ALHA 77307 either show consistently increasing cooling rates (Al-1, Al-2, and Al-5) or cooling rates that are roughly linear (Al-3 and Al-6). These thermal histories are predicted in bow shocks where cooling is a result of adiabatic expansion. In this scenario, immediately after passing through the shock, chondrules experience relatively slow cooling rates, as they are swept around the planetary embryo and kept in contact with hot gas. When behind the planetary embryo, adiabatic expansion of gas allows chondrules to cool more rapidly. This effect is visible in Figure 6.5a, b, d, e, and f for chondrules passing close to the centre of the bow shock. In the same shocks, chondrules passing closer to the edge of the bow shock experience roughly linear cooling rates (Boley et al., 2013; Mann et al., 2016). Overall, cooling rates and thermal histories of chondrules Al-1, Al-2, Al-3, Al-5, and Al-6 are consistent with planetary embryo bow shocks with shock speeds of 6 to 7 kms^{-1} with cooling as a result of adiabatic expansion (except Al-5, which may require some radiation to explain the more rapid cooling rates). Al-4 experienced very rapid cooling which would require a planetary embryo bow shock with cooling as a result of effective radiation (Boley et al., 2013; Mann et al., 2016).

For chondrules in the ordinary chondrites, initial cooling rates range from 100 to 2000 Kh^{-1} (see Figure 6.6), which are potentially consistent with formation in similar bow shocks. Chondrules N8-1 and N8-2 show initial cooling rates of 300 and 100 Kh^{-1}, which are potentially achievable in a 6 kms^{-1} bow shock (see Figure 6.6f). Chondrules N8-3, N4-2 and N4-3 show more rapid initial cooling rates of 1000 to 2000 Kh^{-1}, which is reasonably consistent with bow shocks at 7 kms^{-1} (e.g. Figure 6.6d) (Boley et al., 2013; Mann et al., 2016).

6.3.3 Collisions between planetesimals

The birth of the Solar System was an energetic and chaotic environment, with many collisions between planetesimals, therefore, such events also need to be considered as a potential mechanism for chondrule formation. Asphaug et al. (2011) and Sanders and Scott (2012) invoke low-velocity impacts between molten planetesimals which were melted by the decay of ^{26}Al, a readily available heat source in the early Solar System. In these impacts, a sheet of droplets is created which rains down upon the impacted planetesimal. Cooling rates of chondrules formed in this sheet could be consistent with crystallisation experiments (Desch et al., 2012), however, the models make no detailed predictions on cooling rates. In addition, modelling of impacts between molten planetesimals suggests that metre-scale splashes of material would be produced, which would not resemble chondrules (Johnson et al., 2015).

High-velocity collisions between planetesimals are another possible chondrule formation scenario (Hasegawa et al., 2015; Johnson et al., 2015; Wakita et al., 2017; Johnson et al., 2018; Oshino et al., 2019). During a high-velocity impact, a small amount of material is heated to temperatures consistent with chondrule formation and is ejected in an impact plume. If the impacted planetesimal is undifferentiated or partially differentiated with undifferentiated outer shells (Weiss and Elkins-Tanton, 2013; Fu and Elkins-Tanton, 2014), then melt droplets with primitive, chondrule-like compositions could be produced. Johnson et al. (2015) reported cooling rates of 100 to 2000 Kh^{-1} for impactors between 100 and 1000 km in diameter. Dullemond et al. (2014) modelled the thermal histories of chondrules in an expanding impact cloud. The main factors affecting the cooling rate of the impact cloud are the mass, initial temperature, and expansion rate of the cloud. Reported cooling rates are very wide-ranging depending upon these conditions. Very slow cooling rates of 0.1 Kh^{-1} would be found in a high mass, but slowly expanding impact cloud. At the other extreme, represented by low mass, rapidly expanding clouds, cooling rates could be as high as 10^5 Kh^{-1}. Dullemond et al. (2014) favour cooling rates of 10 to 3000 Kh^{-1} as these match best with crystallisation experiments. However, they have shown that vastly different cooling rates are possible in an impact scenario. Both Johnson et al. (2015) and Dullemond et al. (2014) assume peak temperatures of 2000 K which is broadly consistent with chondrule formation. This is higher than the liquidus temperature of the chondrules

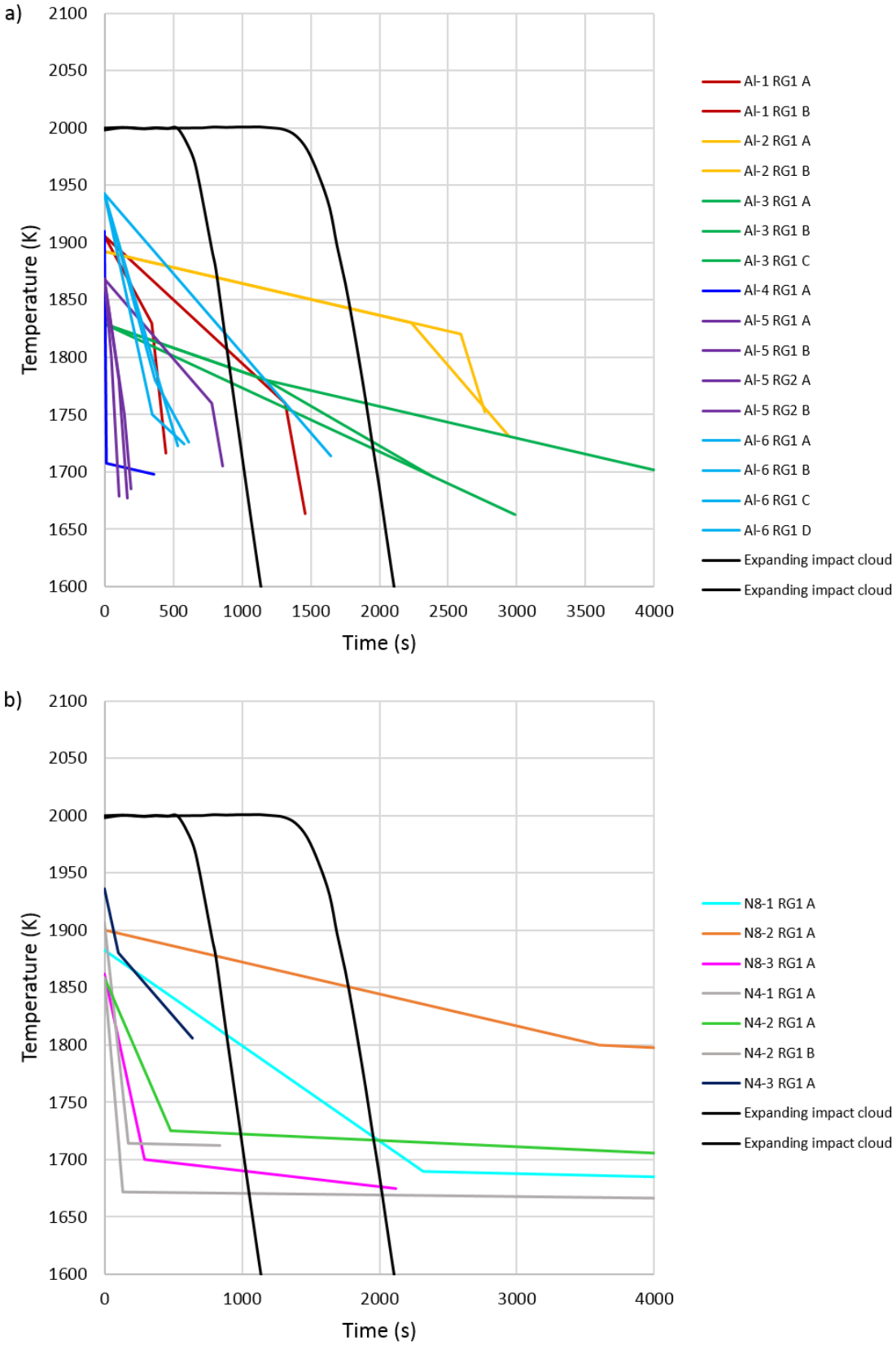

Figure 6.7 – Temperature-time plots from model diffusion profiles for forsteritic-olivine relict grains in chondrules in a) ALHA 77307 and b) NWA 8276 and NWA 4910 compared with the modelled thermal history of particles in an expanding impact cloud. The initial cloud has a radius of 1 km and expands at a rate of 100 ms^{-1}. The black line to the right shows the thermal history of material at the centre of the cloud, while the black line to the left indicates the thermal history of material at 90 % of the radius of the cloud (Dullemond et al. 2014).

studied here, however, the models make no detailed predictions on the peak temperature of material in the impact clouds.

Cooling rates in impact clouds reported in Johnson et al. (2015) of 100 to 2000 Kh^{-1} encompass the cooling rates of many of the studied chondrules in ALHA 77307, including Al-2, Al-3 and Al-6. The more rapid cooling rates shown by Al-1, Al-4 and Al-5 could be a result of a more rapidly expanding cloud as suggested by Dullemond et al. (2014). Similarly, the cooling rates of 100 to 2000 Kh^{-1} are consistent with the initial cooling rates of chondrules in NWA 8276 and NWA 4910 which have the same range.

The predicted thermal histories of the impact clouds are expected to be non-linear. Once peak temperatures are achieved, chondrules remain at a roughly constant temperature before experiencing initially rapid (see Figure 6.7), but exponentially decreasing cooling rates (the exponential decrease is not visible in Figure 6.7, as it is only begins to be noticeable at 1200 K) (Dullemond et al., 2014). If considered as very slow cooling followed by more rapid cooling, this could potentially be consistent with thermal histories for some chondrules in ALHA 77307, for example, Al-1, Al-2, and Al-5. However, overall thermal histories in these impact clouds are inconsistent with most of the studied chondrules.

6.3.4 Nebular lightning

Lightning in the solar nebula is another potential chondrule formation mechanism. Lightning could be generated by triboelectric charging followed by charge separation (Desch and Cuzzi, 2000) or decay of ^{26}Al (Johansen and Okuzumi, 2017; Johansen and Okuzumi, 2018). Lightning causes extremely rapid heating of the zone around the lightning bolt and cooling rates in this zone are expected to be rapid. Johansen and Okuzumi (2018) assume chondrule liquidus temperatures of 2000 K in their models however there are no detailed predictions of peak temperatures. Desch et al. (2012) suggest cooling rates of at least 10^4 Kh^{-1}, however, Johansen and Okuzumi (2018) suggest initial cooling rates of several 10^3 Kh^{-1} which decrease to 100s Kh^{-1} at temperatures close to the solidus. These initial cooling rates are generally more rapid than cooling rates determined for most chondrules in ALHA 77307 and NWA 8276, possibly with the exception of chondrules Al-5, which shows relatively rapid cooling of 3000 to 8000 Kh^{-1}, and Al-4 which requires rapid initial cooling rates of 50000 Kh^{-1}. Thermal histories are expected to show slowly decreasing

cooling rates, which are not observed in any of the chondrules. Together, this seems to suggest lightning is not responsible for the formation of most of the studied chondrules.

6.3.5 X-wind

In the X-wind model, chondrule precursors are lofted from the protoplanetary disk into direct sunlight by a magnetocentrifugal wind where they are heated to peak temperatures of ~1700 K. As chondrules move away from the Sun, they cool linearly at rates of 6 to 10 Kh^{-1} (Shu et al., 1996; Shu et al., 1997; Shu et al., 2001; Desch et al., 2010; Desch et al., 2012). These cooling rates are inconsistent with the determined cooling rates of all chondrules in ALHA 77307 and the initial cooling rates for chondrules in NWA 8276 and NWA 4910. This effectively rules out the X-wind as the formation mechanism for the studied chondrules. In addition, the expected peak temperatures of ~1700 K are too low to explain the formation of the studied chondrules (Desch et al., 2010; Desch et al., 2012).

6.3.6 Radiative heating from molten planetesimals

In the radiative heating model (Herbst and Greenwood, 2016; Herbst and Greenwood, 2019), chondrules and chondrites are formed when pre-existing dust clumps or small primitive planetesimals (1 to 1000 m in diameter) pass close to larger planetesimals (>100 km in diameter) with molten surfaces. The dust clumps or small primitive planetesimals are heated by radiation from exposed magma, driving chondrule and chondrite formation. Peak temperatures and cooling rates are affected by several factors: the size of the large planetesimal, the temperature of exposed magma, degree of melting of the large planetesimal, the closest approach of the small planetesimal and the depth within the small planetesimal. The thermal history in these models is different to many other mechanisms, which invoke flash heating, and instead uses a symmetrical temperature curve produced as the small planetesimal passes close to the larger planetesimal. Cooling rates in these models range from 100s to 1000s Kh^{-1} (e.g. Figure 6.8). These cooling rates are consistent with determined cooling rates in all chondrules in ALHA 77307, except for chondrule Al-4 which experienced much more rapid cooling or 50000 Kh^{-1}. These cooling rates also match the initial cooling rates determined for chondrules in NWA 8276 and NWA 4910. Thermal histories from peak temperatures in the radiative heating model generally show initially slower cooling rates, which increase over time as the heated planetesimal moves away from the heat source. This is consistent with the thermal history in three chondrules in ALHA 77307. Other flyby situations, with different degrees of melting, differently shaped

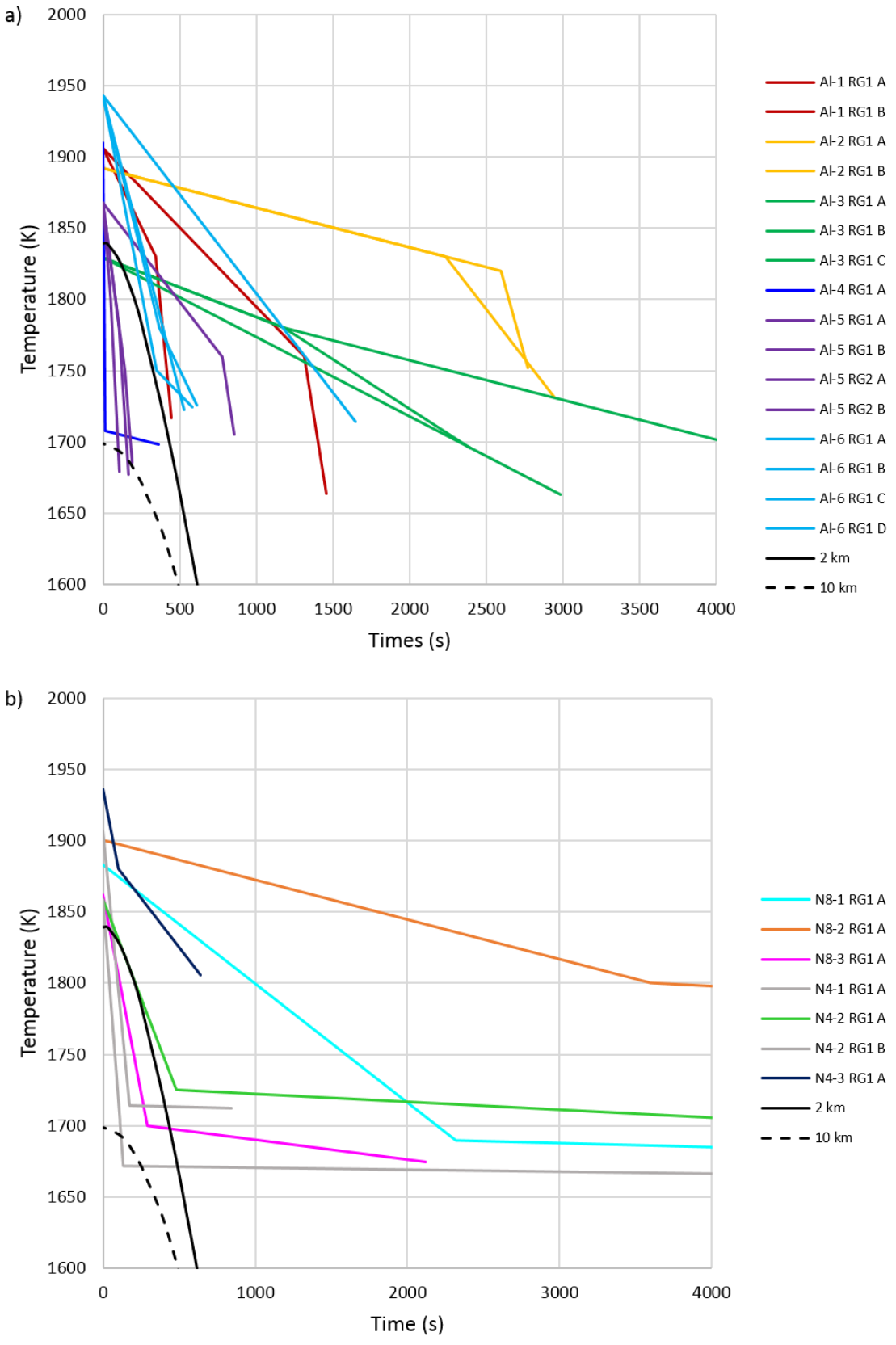

Figure 6.8 – Temperature-time plots from model diffusion profiles for forsteritic-olivine relict grains in a) ALHA 77307 and b) NWA 8276 and NWA 4910 compared to the predicted thermal history of chondrules formed by radiative heating from a 100 km radius planetesimal with a lava ocean at the surface. Solid black line indicates the closest approach to the planetesimal was 2 km whereas the dashed black line indicates that the closest approach to the planetesimal was 10 km (Herbst and Greenwood 2019)

lava oceans on the large planetesimals and different orbits could produce different thermal histories which could potentially match with other chondrules (Herbst and Greenwood, 2019). However, the maximum peak temperatures in this model are ~1850 K, which is lower than the chondrule liquidus of many of the studied chondrules. This may rule this mechanism out as a potential formation mechanism for the studied chondrules.

6.3.7 Summary of observed chondrule cooling rates and implications

Most of the considered chondrule formation mechanisms are inconsistent with the observed cooling rates and thermal histories of chondrules determined from diffusion profiles in forsteritic-olivine relict grains (see Table 6.1 and Figure 6.9). The cooling rates

Table 6.1 – Summary of main features of cooling rates predicted from the main chondrule formation mechanisms compared to cooling rates obtained from diffusion profiles in forsteritic-olivine relict grains in this study. See text for details and references.

Mechanism	Peak temperatures (K)	Cooling rates (Kh^{-1})	Thermal profile	Comments
Large-scale nebular shockwaves	2000	10 to 100s	Linear cooling	Cooling rates are generally too slow
Planetary embryo bow shocks	1600 to 2400	200 to ~20000	Increasing cooling rates or linear	Depending on conditions, can possibly match all chondrules in ALHA 77307 and the initial cooling rates of NWA 8276 and NWA 4910
Impacts	2000	10 to 3000	Chondrules remain at high temperatures then experience rapid cooling	Thermal profiles are not good fits. These cooling rates are preferred by authors, actual range of potential cooling rates is very wide.
Lightning	2000	$>10^3$	Slowly decreasing cooling rates	Generally, too rapid
X-wind	~1700	6 to 10	Linear	Too slow
Radiative heating	~1850	100s to 1000s	Generally increasing, but other thermal profiles could be possible	Peak temperatures may be too low
Cooling rates from diffusion profiles in forsteritic-olivine relict grains	1830 to 1940	100 to 8000 with one chondrule showing rapid cooling of 50000 Kh^{-1}	Increasing cooling rates or roughly linear	Some chondrules show decreasing cooling rates. These could be related to secondary heating events or growth effects.

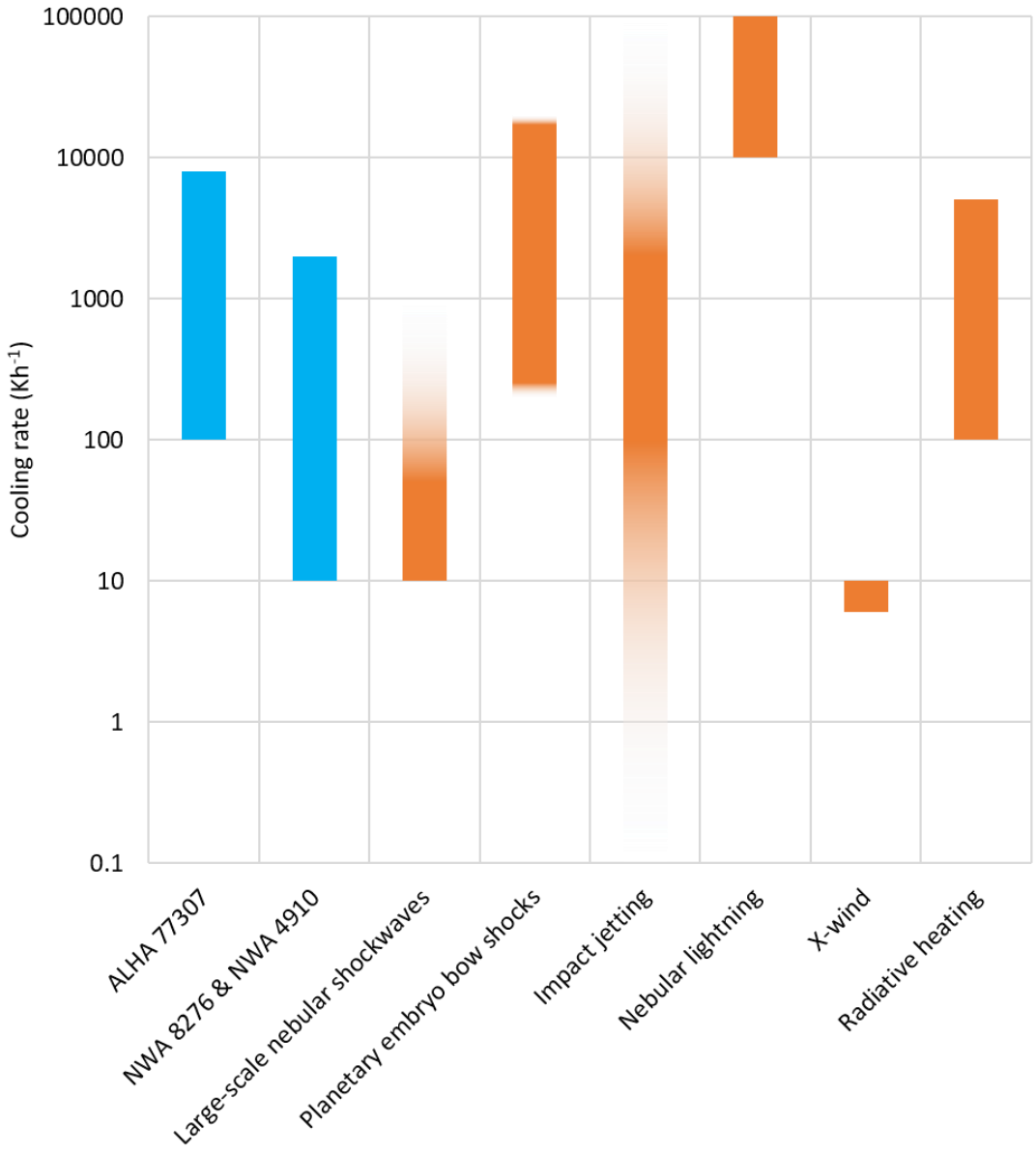

Figure 6.9 – Comparison of chondrule cooling rates determined from modelling diffusion profiles in forsteritic-olivine relict grains in chondrules in ALHA 77307, NWA 8276 and NWA 4910 with predicted cooling rates from different formation mechanisms: large-scale nebular shockwaves (Desch and Connolly 2002; Desch et al. 2010, 2012; Morris et al. 2016); planetary embryo bow shocks (Boley et al. 2013; Mann et al. 2016; Morris et al. 2012); impact jetting (Dullemond et al. 2014; Johnson et al. 2015); nebular lightning (Desch et al. 2012; Johansen and Okuzumi 2018); X-wind (Desch et al. 2010, 2012; Shu et al. 1996, 1997, 2001); Radiative heating (Herbst and Greenwood 2016).

expected for chondrules forming via the X-wind (Shu et al., 1996; Shu et al., 1997; Shu et al., 2001; Desch et al., 2010; Desch et al., 2012) are too low when compared to those derived in this study, and the expected thermal history is linear, which is inconsistent with obtained thermal histories of many chondrules determined by diffusion modelling. Conversely, the expected cooling rates for chondrules formed by nebular lightning are too rapid, except for the initial cooling rate for chondrule Al-4 (Desch et al., 2012) and the

cooling rates of Al-5 may also be consistent with formation by nebular lightning in dense pebble structures (Johansen and Okuzumi, 2018). Determined cooling rates for chondrules are generally inconsistent with cooling rates predicted in large-scale nebular shockwaves (Ciesla and Hood, 2002; Desch and Connolly, 2002; Morris and Desch, 2010; Morris et al., 2016). Many chondrules show cooling rates which are at least an order of magnitude too high, except for chondrules Al-3, N8-1 and N8-2. Large-scale nebular shockwaves also predict linear cooling rates, whereas many chondrules display distinct, non-linear cooling histories. Together, this suggests that large-scale nebular shockwaves were not responsible for the formation of the studied chondrules. Determined cooling rates of many of the chondrules are potentially consistent with formation by planetesimal collisions. As it currently stands, high velocity impacts (Hasegawa et al., 2015; Johnson et al., 2015; Johnson et al., 2017; Wakita et al., 2017; Johnson et al., 2018; Oshino et al., 2019) are more promising candidates than low velocity impacts between molten planetesimals (Asphaug et al., 2011; Sanders and Scott, 2012) because these low velocity collisions may not produce material which resembles chondrules (Johnson et al., 2015). In addition, the high velocity impact models make more detailed predictions on chondrule cooling rates and are easier to compare to the cooling rates determined here. Predicted cooling rates are generally consistent with many of the cooling rates determined from chondrules in this study. The fast cooling rates observed for chondrules Al-4 and Al-5 fall outside the range predicted by Johnson et al. (2015), but may be possible in lower mass or more rapidly expanding impact clouds (Dullemond et al., 2014). The expected thermal history, which shows that chondrules remain at a constant temperature before experiencing rapid cooling rates, may be consistent with chondrules Al-1, Al-2, and Al-5 but is inconsistent with all other chondrules. The most promising fit for the observed thermal histories and cooling rates of the studied chondrules is their formation in planetary embryo bow shocks (Morris et al., 2012; Boley et al., 2013; Mann et al., 2016; Morris and Boley, 2018). Depending upon the shock conditions, environment, and whether radiation can be supressed, cooling rates range from 10^2 to 10^4 Kh^{-1}, which encompasses cooling rates from almost all chondrules from ALHA 77307, NWA 8276 and NWA 4910, the only exception being Al-4 (although, in bow shocks with efficient radiation, these cooling rates may be possible). The predicted thermal histories in planetary embryo bow shocks are diverse and accommodate increasing as well as roughly linear cooling rates, which is consistent with the observed thermal

histories of most chondrules in this study. This makes planetary embryo bow shocks the most likely candidate for the formation of many of the chondrules in this study.

6.4 Other constraints on chondrule formation

In addition to the cooling rates from this study, formation mechanisms must also be able to meet other thermal as well as non-thermal constraints, for example cooling rates at lower temperatures and constraints from evaporative processes. These are overviewed in the following section. For a more in-depth discussion of the non-thermal constraints, see Chapter 1, section 1.7.

6.4.1 Cooling rates at lower temperatures

As well as cooling rates during the initial phases of chondrule cooling as recorded by forsteritic-olivine relict grain diffusion profiles at near-liquidus temperatures, cooling rates at different stages in the cooling history, including those at sub-solidus temperatures may constrain chondrule formation mechanisms. These are summarised in Table 6.2.

Several studies, utilising a number of different approaches have concluded that slow cooling rates are required at near solidus temperatures and sub-solidus temperatures. The microstructure of clinopyroxene and plagioclase crystals in type I chondrules suggests low cooling rates of 0.1 to 50 Kh^{-1} (Weinbruch and Müller, 1995; Weinbruch et al., 2001) at temperatures between 1470 and 1620 K, however Cuvillier et al. (2018) suggest that these clinopyroxenes microstructures may indicate cooling rates up to 1000 Kh^{-1}. Chaumard et al. (2018) and Humayun (2012) determined similar low cooling rates of 0.1 to 100 Kh^{-1} for temperatures of 1470 to 1670 K by modelling diffusion in metal grains associated with type I chondrules in CR chondrites. The presence of primary plagioclase in type I and type II chondrules in both carbonaceous and ordinary chondrites has also been used to suggest cooling rates as low as 1 Kh^{-1} in the final stages of chondrule crystallisation (e.g. Jones, 1997; Wick and Jones, 2012; Lewis and Jones, 2019). The results of crystallisation experiments show plagioclase only crystallises at slow cooling rates of 1 Kh^{-1} across a temperature range of 1070 to 1270 K in type I chondrules (Wick and Jones, 2012). For type II chondrules, similar cooling rates are required to crystallise plagioclase across a similar temperature range (Rocha and Jones, 2012). Together, these pieces of evidence suggest chondrules experienced very slow cooling rates at, or close to, the solidus.

Table 6.2 – Summary of cooling rates at near solidus temperatures

Method	Cooling rates	Chondrule types	Reference(s)
Clinopyroxene and plagioclase microstructure	Generally slow	Type I	Cuvillier et al. (2018); Weinbruch and Müller (1995); Weinbruch et al. (2001)
Diffusion in metal grains	Slow	Type I	Cuvillier et al. (2018); Humayun (2012)
Presence of primary plagioclase	Slow	Type I and II	Jones (1997); Lewis and Jones (2019); Rocha and Jones (2012); Wick and Jones (2012)
Clinoenstatite/orthoenstatite ratio	Fast	Pyroxene bearing type I chondrules	Brearley and Jones (1993); Jones et al. (2018)
Presence of glassy mesostasis	Fast and slow	Type I and II	Wick and Jones (2012); Jones et al. (2018)
Preservation of Fe-Mg diffusion profiles	Fast	Type II	Villeneuve et al. (2015)

The near and post-solidus thermal history of chondrules is far from clear, as a number of other approaches indicate that cooling during this period was relatively rapid. For example, the high ratio of clinoenstatite to orthoenstatite found in low-Ca pyroxene in type I chondrules was used to indicate rapid cooling rates of up to thousands of Kh^{-1} at a temperature of ~1270 K (Brearley and Jones, 1993; Jones et al., 2018). The presence of a glassy mesostasis in many chondrules may also require rapid cooling rates of 10^2 to 10^3 Kh^{-1} through the glass transition temperature (Jones et al., 2018), however, textures containing glass were observed in dynamic crystallisation experiments which cooled at very slowly at rates of 1 to 25 Kh^{-1} (Wick and Jones, 2012). Therefore, cooling rates from glassy textures are ambiguous. Rapid cooling through these lower temperatures is also required for the chondrules studied here, in order to quench the system and prevent further diffusion, which preserves the shape of the observed diffusion profiles. This observation is supported by Villeneuve et al. (2015) who argue that rapid cooling rates are required in order to preserve the shapes of the observed compositional profiles.

In general, the slow cooling rates seem to be mainly restricted to type I chondrules (see Table 6.2). The only constraint which suggests that type II chondrules underwent slow cooling at near-solidus temperatures is the presence of primary plagioclase which suggests cooling rates of ~1 Kh^{-1} (Rocha and Jones, 2012; Wick and Jones, 2012; Lewis and Jones, 2019). Primary plagioclase is present in approximately a fifth of type II chondrules in Semarkona (Lewis and Jones, 2019) but has not been found in the type II chondrules studied here, and therefore these cooling rates may not be applicable to these chondrules.

The requirement of rapid cooling, as shown by the preservation of diffusion profiles in the forsteritic-olivine relict grains (e.g. Villeneuve et al. 2015), is more applicable to the studied chondrules.

As nebular lightning (Desch and Cuzzi, 2000; Johansen and Okuzumi, 2017; Johansen and Okuzumi, 2018) and the X-wind (Shu et al., 1996; Shu et al., 1997; Shu et al., 2001; Desch et al., 2010; Desch et al., 2012) fail to meet most of the thermal constraints on chondrule formation they are not considered further. Large-scale nebular shockwaves (Ciesla and Hood, 2002; Desch and Connolly, 2002; Morris and Desch, 2010; Morris et al., 2016; Morris and Boley, 2018), planetary embryo bow shocks (Morris et al., 2012; Boley et al., 2013; Mann et al., 2016), impact jetting (Hasegawa et al., 2015; Johnson et al., 2015; Johnson et al., 2017; Wakita et al., 2017; Johnson et al., 2018; Oshino et al., 2019) and radiative heating during planetesimal flybys (Herbst and Greenwood, 2016; Herbst and Greenwood, 2019) match some or many of the cooling rates determined in this study and they are discussed further.

Large-scale nebular shockwaves predict low cooling rates, ~10-80 Kh^{-1}, but possibly as low as 1 Kh^{-1}, through temperatures close to the solidus (Desch and Connolly, 2002; Morris and Desch, 2010; Morris et al., 2016), which fits into the constraints provided from plagioclase and pyroxene microstructures (Weinbruch and Müller, 1995; Weinbruch et al., 2001; Cuvillier et al., 2018), diffusion in metal grains (Humayun, 2012; Chaumard et al., 2018) and the presence of primary plagioclase (Rocha and Jones, 2012; Wick and Jones, 2012; Lewis and Jones, 2019). However, these cooling rates are too low to prevent further Fe-Mg diffusion and the shapes of the observed compositional profiles may not preserved (Villeneuve et al., 2015). This argues against the formation of the studied chondrules in large-scale nebular shockwaves.

Planetary embryo bow shocks show initial cooling rates which provide the best matches for the chondrules in this study. At lower temperatures, around 1270 K, chondrule cooling rates in planetary embryo bow shocks are expected to be ~100 to 1000s Kh^{-1} (Boley et al., 2013; Mann et al., 2016). These are mostly consistent with the requirement for rapid cooling rates required to prevent further Fe-Mg diffusion and preserve diffusion profile shapes (Villeneuve et al., 2015). However, these cooling rates are more rapid than indicated by pyroxene and plagioclase microstructures (Weinbruch and Müller, 1995; Weinbruch et al., 2001; Cuvillier et al., 2018), diffusion in metal grains (Humayun, 2012; Chaumard et al.,

2018) and the presence of primary plagioclase in chondrules (Rocha and Jones, 2012; Wick and Jones, 2012; Lewis and Jones, 2019). A further complication for planetary embryo bow shocks is the potential formation of tail shocks behind the planetary embryo. These cause reheating events and keep the zone at relatively high temperatures with low cooling rates (Boley et al., 2013). This again is inconsistent with the need for rapid cooling to prevent further Fe-Mg diffusion, however, could be consistent with the need for slow cooling rates imposed by clinopyroxene and plagioclase microstructures, diffusion in metal grains and the crystallisation of primary plagioclase. However, Mann et al. (2016) report that the addition of atmospheres around the planetary embryo eliminated these tail shocks which may cause more sustained, faster cooling rates.

For impact clouds formed by impact jetting, predicted cooling rates through lower temperatures are rapid, $>10^3$ Kh^{-1} (Dullemond et al., 2014; Johnson et al., 2015; Johnson et al., 2018). These relatively rapid cooling rates may be consistent with the need to quench chondrules rapidly to prevent further Fe-Mg diffusion which would preserve the observed diffusion profiles. They are also in line with rapid cooling rates indicated by the ratio of clinoenstatite to orthoenstatite in low-Ca pyroxenes (Jones et al., 2018). They are, however, at odds with the constraints which suggest much lower cooling rates (Weinbruch and Müller, 1995; Weinbruch et al., 2001; Humayun, 2012; Wick and Jones, 2012; Chaumard et al., 2018).

In the radiative heating model (Herbst and Greenwood, 2016; Herbst and Greenwood, 2019), predicted cooling rates increase with time after peak heating. This naturally leads to more rapid cooling rates at lower temperatures. In many cases, these cooling rates are predicted to be $>10^3$ Kh^{-1} (Herbst and Greenwood, 2019). This is consistent with the required cooling at lower temperatures in order to preserve the observed diffusion profiles (Villeneuve et al., 2015), but is inconsistent with the evidence that cooling was slower at these lower temperatures (Weinbruch and Müller, 1995; Weinbruch et al., 2001; Humayun, 2012; Wick and Jones, 2012; Chaumard et al., 2018).

6.4.2 Volatile elements and open system behaviour

Chondrule formation mechanisms need to be able to account for the lack of volatile and moderately volatile isotope fractionations and high Na content found in chondrules. This is

achieved by chondrule formation in the presence of a gas with high partial pressures of these volatile elements (e.g. Ebel et al. 2018).

In the large-scale nebular shockwave model (Ciesla and Hood, 2002; Desch and Connolly, 2002; Morris and Desch, 2010; Morris et al., 2016; Morris and Boley, 2018), no predictions are made about the retention of volatile elements and the large solid to gas ratios have not been included in models so far, therefore, more modelling needs to be done. However, elevated dust concentrations and high gas pressures are possible in the post-shock region (Morris and Boley, 2018).

Planetary embryos may hold an atmosphere (Morris et al., 2012; Mann et al., 2016). Chondrules entering this atmosphere, post-shock, may experience high partial pressures of Na and K explaining the lack of observed fractionations in K isotopes (Alexander and Grossman, 2005) and retention of Na in chondrule melts (Alexander et al., 2008). Models show that these atmospheres are readily stripped, however, they could be replenished by accreting nebular gas, or from a degassing magma ocean and may persist for several orbits of the planetary embryo (Mann et al., 2016; Morris and Boley, 2018).

The number density of chondrules in jetted material following a planetesimal collision is very high, equivalent to a dust enrichment of 10^6 above canonical nebular conditions (Johnson et al., 2015). This would explain the high volatile content, particularly Na, in chondrules. Dullemond et al. (2016) modelled chondrule formation in an impact cloud and suggested a complex history involving evaporation and condensation of volatile elements during expansion and cooling of the impact cloud. However, as noted previously, there are no, or only very minor fractionations in isotope ratios of volatile elements, e.g. K (Alexander and Grossman, 2005), and concentration of Na remained at roughly constant levels in chondrules throughout crystallisation (Alexander et al., 2008). It is suggested that the number density of chondrules present in the impact cloud, even after expansion, remains high enough to maintain a lack of volatile element fractionations present in chondrules (Johnson et al., 2015; Johnson et al., 2018).

In the radiative heating model (Herbst and Greenwood, 2016; Herbst and Greenwood, 2019), there are two options for suppression of evaporation. Firstly, an atmosphere may be present around the large planetesimal caused by outgassing of the surface lava. However, the small size of the planetesimal results in a low escape velocity which means

the atmosphere is very thin and short-lived. A second option lies in the small primitive planetesimal. If this planetesimal is porous, upon approaching the lava field, evaporation will take place which may become trapped in pore spaces. This may allow high pressures of volatiles to be maintained during chondrule formation preventing evaporation and preserving the lack of volatile element isotope fractionations.

6.4.3 Chondrule matrix complementarity

The presence of chemical and isotopic complementarity between chondrules and matrix may also constrain chondrule formation mechanisms (Hezel and Palme, 2010; Becker et al., 2015; Palme et al., 2015; Budde et al., 2016b).

Although complementarity is not universally accepted as a constraint on chondrule formation (e.g. Zanda et al. 2018), many of the proposed mechanisms are able to satisfy these constraints. For large-scale nebular shockwaves (Ciesla and Hood, 2002; Desch and Connolly, 2002; Morris and Desch, 2010; Morris et al., 2016) and planetary embryo bow shocks (Morris et al., 2012; Boley et al., 2013; Mann et al., 2016), this constraint is easily satisfied as in the models, chondrules and matrix are formed from the same reservoir of dust. Chondrules are dust that has undergone melting, whereas matrix is the dust that has survived the chondrule forming event (Budde et al., 2016b).

For impact jetting during planetesimal collisions (Hasegawa et al., 2015; Johnson et al., 2015; Johnson et al., 2017; Wakita et al., 2017; Johnson et al., 2018; Oshino et al., 2019), the conditions to meet this constraint are more extensive. The first step is to establish a chondritic starting material on the impacted planetesimal. This requirement is difficult to reconcile with the evidence from iron meteorites that planetary differentiation was taking place at the same time as chondrule formation (Kruijer et al., 2014). However, it is possible that even large planetesimals were able to maintain primitive crusts (Weiss and Elkins-Tanton, 2013; Fu and Elkins-Tanton, 2014) allowing for jetted material to come from a chondritic source. In an impact jet, a mix of hot melted droplets and cold protomatrix are ejected (Johnson et al., 2015). Evaporated material may preferentially condense onto cold protomatrix which would lead to a complementary signature in volatile elements, but cannot account for complementarity in more refractory elements e.g. Hf and W (Becker et al., 2015; Budde et al., 2016b; Johnson et al., 2018). Isotopic complementarity could be

created if refractory presolar grains are not melted and are incorporated into the protomatrix material (Budde et al., 2016b; Johnson et al., 2018).

In the radiative heating model (Herbst and Greenwood, 2016; Herbst and Greenwood, 2019), the small primitive planetesimal has a chondritic composition which establishes the correct starting composition. During heating by radiation from the large planetesimal, evaporated material is trapped in pore spaces. On cooling, this will recondense as part of the matrix material creating a complementary relationship. The small primitive planetesimal then undergoes lithification which prevents any mixing between different reservoirs and forms a chondritic body.

6.4.4 Timing of chondrule formation

Chondrules have been dated by three different isotope chronometers, U-Pb, Al-Mg and Hf-W, which show conflicting evidence on the timing of chondrule formation. Pb-Pb ages of chondrules suggest that chondrule formation began contemporaneously with CAIs and continued for ~4 Myrs (Connelly et al., 2012; Bollard et al., 2017; Connelly and Bizzarro, 2018). Al-Mg and Hf-W ages of chondrules suggest that chondrule formation began ~1.5 Myrs after CAI formation and continued for a period of several Myrs (Budde et al., 2016b; Budde et al., 2018; Kleine et al., 2018; Nagashima et al., 2018; Pape et al., 2019). However, Al-Mg dating assumes Al isotope homogeneity throughout the Solar System which may (Villeneuve et al., 2009; Gregory et al., 2020) or may not (Larsen et al., 2011; Luu et al., 2016; Olsen et al., 2016; Van Kooten et al., 2016; Bollard et al., 2019) be valid. Hf-W dating cannot be applied to single chondrules, therefore provides an average age for the 100s to 1000s chondrules analysed in each batch. Also, this technique dates the metal silicate fractionation event, which is assumed to be chondrule formation (Budde et al., 2016b; Budde et al., 2018; Kleine et al., 2018). Chondrule formation mechanisms must be capable of forming chondrules over these timescales.

Large-scale nebular shockwaves are driven by gravitational instabilities and are much more likely to occur during the earliest stages of the protoplanetary disk. For chondrules formed after ~1 Myrs, an alternative mechanism may be required (Connelly and Bizzarro, 2018; Morris and Boley, 2018). This means that large-scale nebular shockwaves may be capable of forming the earliest chondrules according to absolute Pb-Pb ages, however, later formed chondrules may not have formed by large-scale nebular shockwaves (Connelly et al., 2012;

Bollard et al., 2017; Connelly and Bizzarro, 2018). Both Al-Mg and Hf-W ages indicate that chondrules formed significantly after CAIs by ~1.5 Myrs, which is inconsistent with the large-scale nebular shockwave model (Budde et al., 2016b; Budde et al., 2018; Kleine et al., 2018; Nagashima et al., 2018; Pape et al., 2019).

In order to form chondrules by planetary embryo bow shocks (Morris et al., 2012; Boley et al., 2013; Mann et al., 2016; Morris and Boley, 2018), by impact jetting (Hasegawa et al., 2015; Johnson et al., 2015; Wakita et al., 2017; Johnson et al., 2018; Oshino et al., 2019) or by radiative heating from molten planetesimals (Herbst and Greenwood, 2016; Herbst and Greenwood, 2019), significant planet-building must have occurred before the formation of chondrules. The ages of some iron meteorites, using the Hf-W chronometer suggest that planet formation was well underway by 0.1 to 0.3 Myrs after the formation of CAIs (Kruijer et al., 2014), and Hf-W ages of Mars indicate that it reached half its current size within $1.8\pm^{0.9}_{1.0}$ Myrs (Dauphas and Pourmand, 2011), comparable to the bodies considered in the planetary embryo bow shock models (Morris et al., 2012; Boley et al., 2013; Mann et al., 2016). This means that large planetesimals and planetary embryos may predate the formation of most chondrules as shown by Al-Mg and Hf-W dating (Budde et al., 2016b; Budde et al., 2018; Kleine et al., 2018; Nagashima et al., 2018; Pape et al., 2019), however the time gap required to form large planetesimals and planetary embryos may be inconsistent with the ages of the oldest chondrules determined by Pb-Pb dating, which formed concurrently with CAIs (Connelly et al., 2012; Bollard et al., 2017; Connelly and Bizzarro, 2018).

6.5 Constraints applied to chondrule formation mechanisms

Evidence from chondrule ages, evaporative processes, chondrule-matrix complementarity, and thermal history may help constrain chondrule formation mechanisms identified from thermal history alone. However, some of this evidence is contradictory e.g. near-solidus cooling rates and the ages of chondrules. Table 6.3 provides a summary of how large-scale nebular shockwaves, planetary embryo bow shocks, impact jetting and radiative heating compare to these constraints.

There are several lines of evidence that indicate near solidus cooling rates were slow (<100 Kh^{-1}) including microstructure of clinopyroxenes and plagioclase in type I chondrules (Weinbruch and Müller, 1995; Weinbruch et al., 2001; Cuvillier et al., 2018), diffusion in

Table 6.3 – Summary of constraints other than near-liquidus cooling rates. Cooling rates at near-solidus temperatures should be rapid to preserve the observed diffusion profiles in forsteritic-olivine relict grains.

Constraint	Large-scale Nebular Shockwaves	Planetary Embryo Bow Shocks	Impact Jetting	Flyby/Radiative heating
Cooling rates close to the solidus	No	Yes	Yes	Yes
Low degree of isotopic fractionation	Unknown	Yes	Yes	Yes
Chondrule matrix complementarity	Yes	Yes	Maybe	Maybe
Timing of chondrule formation	Yes, for early chondrules, no for late chondrules	Yes for late chondrules, no for early chondrules	Yes for late chondrules, no for early chondrules	Yes for late chondrules, no for early chondrules

metal grains associated with type I chondrules (Humayun, 2012; Chaumard et al., 2018), presence of primary plagioclase in chondrules (Wick and Jones, 2012; Lewis and Jones, 2019). While these are mostly restricted to type I chondrules, the presence of primary plagioclase is noted in 18% of type II chondrules in Semarkona, which require low cooling rates of 1 Kh^{-1} to crystallise (Rocha and Jones, 2012; Wick and Jones, 2012; Lewis and Jones, 2019). There are other lines of evidence indicating cooling rates at near solidus and sub-solidus temperatures were rapid, $>10^3$, including high ratio of clinoenstatite to orthoenstatite in type I pyroxene bearing chondrules (Brearley and Jones, 1993; Jones et al., 2018) and the need to preserve diffusion profiles in forsteritic-olivine relict grains (Villeneuve et al., 2015).

Evidence from evaporative processes and gas-melt exchange are also conflicting. There are no, or only very minor fractionations of volatile and moderately volatile element isotope ratios in chondrules, e.g. K (Alexander and Grossman, 2005), Fe (Alexander and Wang, 2001; Zhu et al., 2001; Kehm et al., 2003; Mullane et al., 2005; Needham et al., 2009; Hezel et al., 2010), Mg (Deng et al., 2017) and Si (Clayton et al., 1991; Hezel et al., 2010). This argues against extensive evaporation, showing only minor amounts of evaporation took place. In addition, the high Na contents of olivine in chondrules from Semarkona argue against significant evaporation (Alexander et al., 2008). However, there is significant evidence for gas-melt exchange in type I chondrules, for example, mineralogically zoned chondrules (Tissandeer et al., 2002; Krot et al., 2004; Libourel et al., 2006; Friend et al., 2016) and evidence of gas-assisted olivine growth (Libourel and Portail, 2018), which imply

condensation from the surrounding gas which directly contradicts the isotopic evidence (Ebel et al., 2018). There is also evidence that type II chondrules may have exchanged with an O-rich vapour (Villeneuve et al., 2015). To suppress evaporation, there needs to be gas with high partial pressures of these volatile and moderately volatile elements, for example, from the evaporation of dust in a region of high solid density.

Chondrule-matrix complementarity is potentially very constraining on chondrule formation mechanisms, and observations of this complementarity have been observed for Mg and Si (Hezel and Palme, 2010), Fe and Mg (Palme et al., 2015) and Hf and W (Becker et al., 2015; Budde et al., 2016b). The implications of this complementarity are that chondrules and matrix must be formed from the same reservoir of material which had an initially CI-like composition. Chondrules and matrix were rapidly assembled into the chondrite after chondrule formation took place to prevent mixing between different reservoirs and preserve this chemical and isotopic complementarity. However, the observation remains controversial, and is not universally accepted. Zanda et al. (2018) suggest that observation of complementarity can be explained by mixing average chondrule compositions with a CI-like matrix and Fe,Ni metal and exposing this assemblage to parent body processing.

Three different isotope systems have been used to date chondrules, Al-Mg (e.g. Nagashima et al. 2018; Pape et al. 2019), Hf-W (Budde et al., 2016b; Budde et al., 2018; Kleine et al., 2018) and Pb-Pb (Connelly et al., 2012; Bollard et al., 2017; Connelly and Bizzarro, 2018). Al-Mg and Hf-W ages of chondrules suggest chondrule formation began ~1.5 Myrs after CAIs and continued for several Myrs. However, Pb-Pb ages of chondrules show chondrule formation began at the same time as CAI formation and continued for ~4 Myrs. Al-Mg and Hf-W ages are generally consistent within a chondrite, suggesting chondrules in that chondrite formed at the same time and were lithified into a chondrite before mixing between different reservoirs took place, consistent with the observation of chemical and isotopic complementarity (Budde et al., 2016b; Budde et al., 2018; Kleine et al., 2018; Nagashima et al., 2018). Pb-Pb ages of chondrules within a chondrite, however, span a wide range of ages, up to 4 Myrs. This suggests that mixing between different reservoirs with different ages did take place, arguing against complementarity. There is evidence that material from different chondrule forming reservoirs did mix together, for example, dusty olivine relict grains have been found in type I chondrules in CM chondrites which have oxygen isotope compositions indicating that they most likely originated from type II

chondrules in LL or, less likely, CR chondrites (Schrader et al., 2020). An alternative explanation could be that chondrules were forming in separate regions over a protracted period and these regions were kept isolated until chondrite formation took place (Connelly and Bizzarro, 2018).

Large scale nebular shockwaves predict low cooling rates at near solidus temperatures, <100 Kh^{-1}, so are able to account for the microstructures present in clinopyroxenes and plagioclase in type I chondrules (Weinbruch and Müller, 1995; Weinbruch et al., 2001; Cuvillier et al., 2018), diffusion in metals (Humayun, 2012; Chaumard et al., 2018) and presence of primary plagioclase in type I and II chondrules (Rocha and Jones, 2012; Wick and Jones, 2012; Lewis and Jones, 2019). These cooling rates, however, are unable to prevent Fe-Mg diffusion, leading to loss of observed diffusion profiles in forsteritic-olivine relict grains in type II chondrules (e.g. Villeneuve et al. 2015). These cooling rates are also inconsistent with the clinopyroxenes to orthopyroxene ratio in pyroxene bearing type I chondrules (Jones et al., 2018). No predictions are currently made on the retention of volatiles, however, gas and dust pressures in the post-shock region could be consistent with the observed lack of isotope fractionations (Morris and Boley, 2018). The model easily complies with the requirement for complementarity as chondrules and matrix form from the same reservoir of dust (Budde et al., 2016b). In terms of chondrule chronology, large-scale nebular shockwaves may be consistent with the earliest formed chondrules as shown by Pb-Pb dating, however, they may not be able to form younger chondrules, as the gravitational instabilities which drive them may not persist after ~1 Myr (Connelly and Bizzarro, 2018; Morris and Boley, 2018).

For planetary embryo bow shocks (Morris et al., 2012; Boley et al., 2013; Mann et al., 2016), cooling rates at near solidus temperatures are relatively high, up to 1000s Kh^{-1}, which is consistent with the ratio of clinoenstatite to orthoenstatite in pyroxene bearing type I chondrules (Jones et al., 2018). These cooling rates may also be rapid enough to preserve the observed diffusion profiles by preventing more Fe-Mg diffusion. These cooling rates are too rapid to account for features suggesting much lower cooling rates close to the solidus (Weinbruch and Müller, 1995; Weinbruch et al., 2001; Humayun, 2012; Rocha and Jones, 2012; Wick and Jones, 2012; Chaumard et al., 2018; Cuvillier et al., 2018; Lewis and Jones, 2019). Planetary embryo bow shocks may also be consistent with the formation of chondrules in a gas with high pressures of volatile and moderately volatile elements as they

may possess an atmosphere (Morris et al., 2012; Mann et al., 2016). Like large-scale nebular shockwaves, they are also able to fulfil the requirement for chondrule-matrix complementarity as chondrules and matrix form from the same reservoir of material. For chondrules to form by planetary embryo bow shocks, planetary embryos must have existed beforehand. This is consistent with Al-Mg and Hf-W ages of chondrules which suggest a time gap of 1.5 Myrs before the formation of chondrules which would allow these large planetary embryos to form, but is inconsistent with the earliest chondrules dated by Pb-Pb dating (Connelly et al., 2012; Budde et al., 2016b; Bollard et al., 2017; Budde et al., 2018; Connelly and Bizzarro, 2018; Kleine et al., 2018; Nagashima et al., 2018; Pape et al., 2019).

The cooling rates of chondrules formed in an impact jet are expected to be $>10^3$ Kh^{-1} (Dullemond et al., 2014; Johnson et al., 2015). This is consistent with the need for rapid cooling in order to preserve the observed diffusion profiles in forsteritic-olivine relict grains (Villeneuve et al., 2015) and the ratio of clinoenstatite to orthoenstatite in type I pyroxene bearing chondrules (Jones et al., 2018). These cooling rates are inconsistent with constraints which require lower cooling rates (Weinbruch and Müller, 1995; Weinbruch et al., 2001; Humayun, 2012; Rocha and Jones, 2012; Wick and Jones, 2012; Cuvillier et al., 2018; Jones et al., 2018; Lewis and Jones, 2019). In the impact jet, the density of material is very high, creating high solid densities which is consistent with the lack of volatile and moderately volatile element isotope fractionations (Johnson et al., 2018). The constraint of chondrule-matrix complementarity can be achieved as a mix of hot melted droplets and cold matrix are produced from the same chondritic source (Johnson et al., 2018). Similar to planetary embryo bow shocks, large planetesimals must already be in existence before chondrules can form by impact jetting. This is consistent with Al-Mg and Hf-W ages of chondrules, however, may not be consistent with the oldest chondrules dated using Pb-Pb (Connelly et al., 2012; Budde et al., 2016b; Bollard et al., 2017; Budde et al., 2018; Connelly and Bizzarro, 2018; Kleine et al., 2018; Nagashima et al., 2018; Pape et al., 2019).

In the radiative heating model (Herbst and Greenwood, 2016; Herbst and Greenwood, 2019), cooling rates are expected to increase over time, with cooling rates close to the solidus of $>10^3$ Kh^{-1}. These may be high enough to preserve the observed diffusion profiles (Villeneuve et al., 2015) and are in agreement with other constraints suggesting rapid cooling at near-solidus temperatures (Jones et al., 2018), but are contrary to evidence that cooling rates were low (Weinbruch and Müller, 1995; Weinbruch et al., 2001; Humayun,

2012; Rocha and Jones, 2012; Wick and Jones, 2012; Chaumard et al., 2018; Cuvillier et al., 2018; Lewis and Jones, 2019). It is possible to suppress evaporation of volatiles by trapping a high pressure of volatiles in pore spaces within the heated planetesimal and a complementary relationship might be formed if this vapour preferentially condenses on the cooler, un-melted material. However, it is not clear how this mechanism can form highly pristine, primitive chondrites such as ALHA 77307 and Acfer 094. These contain both highly heated material in the form of chondrules and CAIs as well as material that has undergone minimal thermal processing, such as a highly unequilibrated matrix, presolar grains and organic material (Brearley, 1993; Greshake, 1997; Huss et al., 2006). It is unclear how part of the small primitive planetesimal can experience heating up to ~1800 K to form chondrules from radiation, while material immediately adjacent is unheated. As with planetary embryo bow shocks and impact jetting, planetesimals must already be formed by the time chondrules could be formed by radiative heating from exposed lava on these planetesimals. This is consistent with Al-Mg and Hf-W ages of chondrules but may not be consistent with the earliest formed chondrules as dated by Pb-Pb (Connelly et al., 2012; Budde et al., 2016b; Bollard et al., 2017; Budde et al., 2018; Connelly and Bizzarro, 2018; Kleine et al., 2018; Nagashima et al., 2018; Pape et al., 2019).

Overall, large-scale nebular shockwaves do not match most of the constraints placed on chondrule formation. Some of the studied chondrules have cooling rates which may match the cooling rates modelled in a large scale nebular shockwave (e.g. Al-3, N8-1 and N8-2), however, fast cooling rates are required through near-solidus temperatures in order to prevent further Fe-Mg diffusion and preserve the observed diffusion profiles present in forsteritic-olivine relict grains in the studied chondrules. They have also not been modelled with the high solid densities required to suppress evaporation and preserve the low degree of isotopic fractionation observed in chondrules. They also may only be able to create chondrules in the first ~1 Myr of the protoplanetary disk which is consistent only with the earliest formed chondrules by Pb-Pb dating. Taken together, this effectively rules out these large-scale nebular shockwaves as a potential mechanism for the formation of the studied chondrules.

Planetary embryo bow shocks, impact jetting and radiative heating are all more promising (see Table 6.3) as they have cooling rates and observed thermal histories that may match the cooling rates and thermal histories in this study, with planetary embryo bow shocks

showing the most promise. For the three mechanisms, cooling rates at near-solidus temperatures are rapid, accounting for the preservation of the observed diffusion profiles in the forsteritic-olivine relict grains. They all have routes for suppressing evaporation: the presence of atmospheres around planetary embryos; high densities of material in the impact jet; and trapping of volatiles in pore spaces of small primitive planetesimals during radiative heating. They all may also be consistent with the constraint for of chondrule-matrix complementarity. And finally, they are also consistent with the timing of chondrule formation from Al-Mg and Hf-W dating, which suggests a time gap, allowing for the formation of large planetesimals and planetary embryos, however, they may not be able to form the oldest chondrules as determined by Pb-Pb dating.

However, as discussed earlier, it is not clear how chondrules and primitive matrix can be formed together in a single chondritic body by radiative heating, which would seem to suggest that these events are not suitable to drive chondrule and chondrite formation. The observed thermal histories and cooling rates from the studied chondrules do not always match the expected cooling rates in an impact jet. Johnson et al. (2015) show cooling rates of 100 to 2000 Kh^{-1} with cooling rates that increase over the modelled temperature range. While these are consistent with some chondrules, e.g. Al-2, it is inconsistent with rapid cooling rates of Al-4 and Al-5. Also, they cannot account for the roughly linear cooling histories shown in chondrules Al-3 and Al-6. Because of this, planetary embryo bow shocks are favoured as the formation mechanism of the studied chondrules over impact jetting.

6.6 Planetary embryo bow shock diversity

Chondrules are diverse showing a wide range of compositions and textures. To explain this diversity chondrules must have experienced a variety of formation conditions, for example, peak temperatures, cooling rates and oxygen fugacities. This means chondrule formation mechanisms must be able to form chondrules with these wide-ranging formation conditions. Bow shocks around planetary embryos are complex 3-D structures and can process material under a wide range of conditions. Even in a single bow shock, a range in peak temperatures and cooling rates are predicted, consistent with the textural diversity shown by chondrules (e.g. Lofgren 1996). When including planetary embryos with different shock speeds as a result of high or lower eccentricities and inclinations, this range in peak temperatures and cooling rates increases. Planetary embryos with more inclined or

eccentric orbits will have higher shock speeds resulting in higher peak temperatures, while embryos moving in more circular orbits or with a lower inclination result in lower shock speeds and cause lower peak temperatures (Morris et al., 2012; Boley et al., 2013; Mann et al., 2016). Planetary embryo size also has a role in peak temperatures and cooling rates. Smaller planetary embryos result in lower peak temperatures and faster cooling rates, while larger planetary embryos result in higher peak temperatures and slower cooling rates (Ciesla et al., 2004).

The capability of these planetary embryos to hold atmospheres could also be important for chondrule formation, not just as a route to suppress volatile evaporation, but also to impose varying oxygen fugacity conditions upon the forming chondrules. If this atmosphere is primarily composed of accreted nebular gas (Morris et al., 2012), primarily H_2, this will impose relatively reducing conditions and may promote the formation of type I FeO-poor chondrules. If this atmosphere contains gases which are outgassed from a degassing magma ocean, it may contain CO_2, H_2O, Na and K which could impose much more oxidising conditions (Holland, 1984; Zahnle et al., 2007; Elkins-Tanton, 2008; Elkins-Tanton, 2012; Morris et al., 2012), promoting the formation of the more oxidised type II FeO-rich chondrules. Modelling of planetary embryo bow shocks shows that these atmospheres would be readily stripped (Morris et al., 2012; Mann et al., 2016). This allows the atmosphere to evolve over time by a combination of processes including stripping, accreting nebular gas, and outgassing from a magma ocean. The atmosphere also has implications for thermal history of chondrules in the bow shock. Firstly, the presence of an atmosphere increases the effective size of the planetary embryo, slightly increasing peak temperatures and reducing cooling rates compared to a planetary embryo with no atmosphere (Boley et al., 2013; Mann et al., 2016). Also, planetary embryos without an atmosphere may produce tail shocks (Boley et al., 2013), which cause reheating, keeping the zone hotter for longer and promoting slower cooling at near solidus temperatures, as suggested by presence of primary plagioclase in both type I and II chondrules (Wick and Jones, 2012; Lewis and Jones, 2019). The presence of an atmosphere, roughly equivalent to the atmosphere of Mars, suppresses these tail shocks and promotes more rapid cooling at near solidus temperatures, as suggested by the presence of a glassy mesostasis in chondrules, and the clinoenstatite to orthoenstatite ratio (Jones et al., 2018).

The cooling rates of chondrules are most consistent with the formation of chondrules in a planetary embryo bow shock where cooling is mainly a result of adiabatic expansion of gas. In a solar nebula with canonical dust density, chondrules and dust would act as effective radiators to cool the heated zone rapidly >10^4 Kh^{-1} (Boley et al., 2013; Mann et al., 2016). In order to suppress this radiation, the environment would have to be very dust rich, increasing the opacity, which reduces the effectiveness of radiation (Mann et al., 2016). This offers another explanation for the observed lack of isotope fractionations in chondrules, as they would be forming in a zone with high dust enrichments (e.g. Ebel et al. 2018).

This suggests that planetary embryo bow shocks may provide a wide range of chondrule formation conditions, including peak temperatures, cooling rates and environments which can evolve over time, even around a single planetary embryo. The presence of multiple planetary embryos moving around the protoplanetary disk with different sizes, eccentricities and atmospheric compositions may be able to explain the observed diversity in chondrules.

For the chondrules in this study, planetary embryo bow shocks with shock speeds between 6 and 7 kms^{-1} with primarily adiabatic cooling are favoured as the chondrule formation mechanism. These shocks provide similar cooling rates and thermal histories to those determined by modelling Fe-Mg diffusion profiles in forsteritic-olivine relict grains in the studied chondrules.

6.7 Implications of a planetary formation mechanism

Although planetary embryo bow shocks are the favoured formation mechanism for the studied chondrules, the observed cooling rates and thermal histories may lend some support to chondrule formation by impact jetting and radiative heating (despite issues with both which are discussed above). All three mechanisms have different heat sources, chondrule precursor materials and environments, but they share some major implications for the formation of chondrules. These have been partly discussed above as to whether the models are realistic but are now considered more explicitly.

Firstly, all three of these mechanisms are “planetary” mechanisms rather than “nebular” mechanisms. Although impact jetting may be the only true “planetary” mechanism, all

three involve interactions with planetesimals and protoplanetary bodies. This means that chondrule formation must be delayed until significant planet-building has progressed and large planetesimals and planetary embryos have formed. This is supported by evidence from Al-Mg and Hf-W radio-isotope chronometers, which indicate that chondrule formation began around 1.5 Myrs after the formation of CAIs and continued for several Myrs (Budde et al., 2016b; Budde et al., 2018; Kleine et al., 2018; Nagashima et al., 2018; Pape et al., 2019). While the Pb-Pb system suggests chondrule formation began at around the same time as CAI formation, it also indicates that it continued for several Myrs (Connelly et al., 2012; Bollard et al., 2017; Connelly and Bizzarro, 2018). To explain this, planet formation must have also started very shortly after CAI formation. Evidence does show that the accretion of planetesimals and planets happened early. Hf-W ages of some iron meteorites suggest their parent bodies accreted to radii of 10 to 100 km within 0.1 to 0.3 Myrs after CAIs (Burkhardt et al., 2008; Kruijer et al., 2012; Kruijer et al., 2014). These parent bodies are unlikely to be of sufficient size to produce chondrule forming bow shocks. Ciesla et al. (2004) show that bow shocks around planetesimals with a radius of <1000 km have low peak temperatures and rapid cooling rates that are inconsistent with chondrule formation. Planetesimals of this size may be able to produce chondrules by planetary collisions (Hasegawa et al., 2015; Johnson et al., 2015; Wakita et al., 2017; Johnson et al., 2018; Oshino et al., 2019) or radiative heating from a lava ocean (Herbst and Greenwood, 2016; Herbst and Greenwood, 2019). The ages of these meteorites suggest that planet building is a rapid process, which may allow large planetary embryos (>1000 km radius) to exist in the protoplanetary disk well before ~2 Myrs after CAIs (Dauphas and Pourmand, 2011). Embryos of this size may be sufficient to drive chondrule formation as they pass through dust rich regions of the protoplanetary disk (Morris et al., 2012; Boley et al., 2013; Mann et al., 2016).

A second important implication of these mechanisms is that while chondrules are abundant in the primitive asteroidal samples that are our meteorite collections, chondrules would not have played a significant role in the accretion of the rocky planets and are actually the by-products of the formation of planets (e.g. Johnson et al. 2015). If this is the case, then they are not representative of the material that accreted to form the terrestrial planets.

6.8 Multiple chondrule formation mechanisms?

There is evidence that there may have been multiple formation mechanisms operating in the protoplanetary disk at different times. The first piece of evidence is the suggestion that chondrules from CB chondrites are formed in an impact plume after the main period of chondrule formation (Krot et al., 2005). Bollard et al. (2017), by using Pb-isotope systematics, suggest that the earliest chondrules, formed within 1 Myr of CAIs, were formed by large-scale nebular shockwaves when material was still accreting onto the protoplanetary disk and gravitational instabilities were likely to be common. This would be the most efficient mechanism of forming chondrules during this time. After this period, material is no longer accreting onto the disk, and the mass of the disk is not high enough to sustain such gravitational instabilities, therefore different formation mechanisms must have been operating. By this time, large planetary embryos may have formed, allowing chondrules to form by planetary embryo bow shocks, or maybe impact jetting or radiative heating.

Many potential chondrule formation mechanisms are known processes, for example, impacts between planetary bodies (e.g. Johnson et al. 2015, 2018) and radiative heating (e.g. Herbst and Greenwood 2016, 2019). These processes would have occurred in some form in the solar nebula, potentially forming chondrules. Many other chondrule formation mechanisms are only theorised, for example, large-scale nebular shockwaves (Ciesla and Hood, 2002; Desch and Connolly, 2002; Morris and Desch, 2010; Morris et al., 2016) and planetary embryo bow shocks (Morris et al., 2012; Boley et al., 2013; Mann et al., 2016). However, Morris and Boley (2018) argue these processes not just may have occurred, but are likely to have occurred. For example, spiral arms have been observed around star Elias 2-27 (Pérez et al., 2016), suggesting that large-scale nebular shockwaves are operating in that system (Morris and Boley, 2018). Also, any planetary embryo moving in an eccentric or inclined orbit with respect to nebular gas will drive a bow shock in front of it (Morris et al., 2012). Planetary embryos could be excited into these orbits by the formation of a proto-Jupiter (Hood and Weidenschilling, 2012).

Given that many different mechanisms may have operated in the protoplanetary disk, it may be that the wide range in cooling rates and thermal histories observed in the studied chondrules is a result of formation by different mechanisms. Although this diversity can be

explained by chondrule formation in a variety of bow shocks, some of the cooling rates are potentially consistent with other formation mechanisms. For example, chondrules Al-3, N8-1 and N8-2 record cooling rates between 10 and 300 Kh^{-1}, which are consistent with formation in large-scale nebular shockwaves (Ciesla and Hood, 2002; Desch and Connolly, 2002; Morris and Desch, 2010; Morris et al., 2016; Morris and Boley, 2018). Although, large-scale nebular shockwaves still cannot allow for fast cooling through near-solidus temperatures to prevent further Fe-Mg diffusion which could erase the observed diffusion profiles in the forsteritic-olivine relict grains. Many other chondrules show cooling rates that are higher, for example, Al-1, with cooling rates of 800 to 4000 Kh^{-1} and Al-5, with cooling rates of 3000 to 8000 Kh^{-1}. These are most consistent with formation in planetary embryo bow shocks (Morris et al., 2012; Boley et al., 2013; Mann et al., 2016; Morris and Boley, 2018). The rapid cooling rates shown by chondrule Al-4 may just be achievable in a bow shock where radiation is effective (Boley et al., 2013; Mann et al., 2016), or it could be suggesting that a mechanism requiring even more rapid cooling rates are necessary, for example, nebular lightning, which may create chondrules with cooling rates of $>10^4$ Kh^{-1} (Desch et al., 2012; Johansen and Okuzumi, 2018). In this scenario, chondrules that were formed by different mechanisms in different regions of the protoplanetary disk would need to be mixed together into the same chondrite. There is some evidence that material was able to mix between the different chondrule formation regions, for example, dusty olivine relict grains found in type I chondrules in CM chondrites which have oxygen isotopic compositions consistent with type II chondrules from unequlilbrated ordinary chondrites (Schrader et al., 2020). However, chondrules from different chondrite groups usually show distinct petrographic properties as well as chemical and isotopic compositions. This implies that each different chondrite group samples a unique reservoir of chondrules, and that mixing between these regions was limited (Jones, 2012), which would preclude chondrules formed by different mechanisms appearing together in the same chondrite.

Determined cooling rates from the ordinary and carbonaceous chondrites show an identical range of initial cooling rates, from 100 to 5000 in both classes, if including the profiles that had less successful model fits. However, there is a major difference in observed thermal histories. For the chondrules in ALHA 77307, three show increasing cooling rates (e.g. Al-1, Al-2 and Al-5), two show roughly linear cooling rates (Al-3 and Al-6), while Al-4 shows rapid initial cooling rates followed by considerably slower cooling. All

chondrules in NWA 8276 and NWA 4910 show final cooling rates that are considerably lower than their initial cooling rates, and only one chondrule (N4-3) shows final cooling rates above 50 Kh^{-1}.

If these final cooling rates are a true reflection of the thermal history of these chondrules, it may suggest that there are significant differences in the formation mechanism or environment of the chondrules formed in carbonaceous chondrites and ordinary chondrites. For example, perhaps chondrules in ALHA 77307 formed in planetary embryo bow shocks in the outer Solar System where there was a greater quantity of volatiles. This means that the planetary embryo was more likely to possess an atmosphere, which allowed the chondrules to experience more rapid final cooling rates. Conversely, chondrules in the ordinary chondrites NWA 8276 and NWA 4910, may have formed in bow shocks in the inner Solar System where there were fewer volatiles. This may result in a planetary embryo with a much smaller, or even no atmosphere. In this scenario, there may be tail shocks behind the planetary embryo which causes secondary heating and prevents rapid cooling, which may account for the slow final cooling rates determined for these chondrules.

Type I and type II chondrules may also require different chondrule formation mechanisms and environments. Type I chondrules formed under relatively reducing conditions while type II chondrules formed under much more oxidising conditions (Jones et al., 2005). These differences may be a result of differences in the chondrule precursor assemblages (e.g. Connolly Jr et al. 1994) or caused by interactions with ambient gas (e.g. Villeneuve et al. 2015). In addition, the cooling rates determined here are valid for type II chondrules, but it is unclear whether they may be valid for type I chondrules. There is evidence to suggest that type I and type II chondrules may have experienced different thermal histories with type II chondrules potentially experiencing more rapid cooling rates than type I chondrules (e.g. Jacquet et al. 2015). This may mean that type I chondrules formed in large scale nebular shockwaves in a relatively reducing environment, accounting for their lower cooling rates. Type II chondrules, which require a more oxidising environment and more rapid cooling rates may have been formed in a more dust rich environment, providing a more oxidising environment, or in an atmosphere around a planetary embryo containing degassed volatiles, which also contributes to a more oxidising environment. Formation of type II chondrules in a planetary embryo bow shock also accounts for their more rapid cooling rates. Reduced type I chondrules may also be able to form in planetary embryo bow

shocks if lacking a planetary atmosphere, or this atmosphere primarily contains accreted nebular gas, which is more reducing than an atmosphere containing outgassed volatiles. If type I and type II chondrules were formed in different regions of the protoplanetary disk, they must have been subsequently mixed to appear together in the same chondrite. This is difficult to reconcile with the distinct petrography and compositions of chondrules within a single chondrite group which suggest there was very little mixing of chondrules between different chondrite groups (Jones, 2012).

While porphyritic chondrules are the dominant textural type found in the meteorite record, other textures do exist, for example, barred and radial chondrules. These may require higher peak temperatures, which exceed the chondrule liquidus, and more rapid cooling rates than porphyritic chondrules (e.g. Jones et al., 2018). The techniques employed by this study cannot be applied to these other textural types and therefore, while beyond the scope of this study, additional direct determinations of cooling histories for all textural types should be sought.

6.9 Summary and conclusions

Cooling rates determined from diffusion profiles in forsteritic-olivine relict grains in type II chondrules generally range from 100 to 8000 Kh^{-1}. Initial cooling rates for chondrules in the carbonaceous chondrite ALHA 77307 and the ordinary chondrites NWA 8276 and NWA 4910 show identical ranges, however, final cooling rates differ between the two groups. In chondrules from ALHA 77307, cooling rates increase or remain roughly linear throughout the observed cooling history, however, chondrules from the ordinary chondrites show very slow final cooling rates, often below 50 Kh^{-1}. This suggests that there may be a difference in the formation mechanism or environment of type II chondrules from ordinary and carbonaceous chondrites. However, the observed slower cooling rates for the ordinary chondrites may be a result of growth effects or secondary heating events.

Dynamic crystallisation experiments remain the most widely cited method of determining chondrule cooling rates and are widely used to constrain chondrule formation mechanisms. The cooling rates determined for the ordinary chondrites NWA 8276 and NWA 4910 are broadly consistent with cooling rates shown by these dynamic crystallisation experiments, however, the cooling rates of chondrules in ALHA 77307 show cooling rates well above this range, suggesting that more rapid cooling rates are acceptable for the formation of

porphyritic olivine chondrules. These more rapid cooling rates are similar to previous determinations of chondrule cooling rates using diffusion in forsteritic-olivine relict grains (e.g. Greeney and Ruzicka 2004). They are also consistent with olivine dissolution experiments which suggest that in order to preserve forsteritic-olivine relict grains in chondrule melts, cooling rates must be up to 8000 Kh^{-1} (Soulié et al., 2017).

The cooling rates of chondrules from ALHA 77307, NWA 8276 and NWA 4910 are generally too rapid for formation in large-scale nebular shockwaves. The observed thermal histories are also inconsistent, as large-scale nebular shockwaves predict roughly linear cooling at slow cooling rates. The rapid cooling rates and more complex thermal histories displayed by chondrules argue for a "planetary" mechanism for the formation of these type II chondrules, for example, planetary embryo bow shocks, impact jetting or radiative heating from molten planetesimals. Of the three mechanisms, planetary embryo bow shocks with shock speeds of 6 to 7 kms^{-1} (e.g. Mann et al. 2016) are favoured based upon cooling rates and observed thermal histories.

Formation of chondrules in planetary embryo bow shocks has major implications for the evolution of the Solar System and formation of the terrestrial planets. Chondrule formation must be delayed until large planetesimals and planetary embryos can form. It also means that chondrules are a by-product of planet formation and not an important building block of planets and are therefore not representative of the material that formed the terrestrial planets.

The textural and compositional diversity of chondrules requires a wide range in chondrule formation conditions. Planetary embryo bow shocks are complex 3-D structures and predict a wide range of cooling rates and peak temperatures, even within a single bow shock. They also may hold an atmosphere which may impose relatively reducing or oxidising conditions depending on the composition. Stripping and replenishing processes may allow this atmosphere to evolve in composition and mass over time leading to different chondrule formation conditions. This means that planetary embryo bow shocks may be able to explain the textural and compositional diversity of chondrules.

Another potential explanation could be that there were multiple mechanisms of chondrule formation working in the protoplanetary disk at different times. For example, large-scale nebular shockwaves are only a potentially efficient source of chondrules during the first

Myr of the Solar System while the protoplanetary disk is still accreting mass. After this period, large-scale nebular shockwaves may not have been able to form chondrules. During this first epoch of chondrule formation, planetesimals and planetary embryos were accreting material, which may have included these early formed chondrules. These planetary embryos would then be able to process and recycle chondrules in bow shocks over the next few Myrs. Type I chondrules require more reducing conditions and may require slower cooling rates which supports their formation in large-scale nebular shockwaves in a relatively reducing nebula environment. Type II chondrules may require faster cooling rates and more oxidising conditions, which supports their formation in planetary embryo bow shocks. The presence of forsteritic-olivine relict grains in type II chondrules, which originated in type I chondrules, suggests that type I chondrules were produced first. This supports the suggestion that type I chondrules formed in large-scale nebular shockwaves before type II chondrules, which were formed later in planetary embryo bow shocks. However, this is an oversimplification; dusty olivine relict grains present in type I chondrules show that some type II chondrules must predate type I chondrules (Rambaldi, 1981; Rambaldi and Wasson, 1981; Kracher et al., 1984; Jones and Danielson, 1997; Leroux et al., 2003; Jones, 2012). In addition to large-scale nebular shockwaves and planetary embryo bow shocks, chondrules in CB chondrites may have formed in an impact plume (Krot et al., 2005). One of the studied chondrules in ALHA 77307 (Al-4) shows evidence of very rapid cooling, which may only be explained by instances of nebular lightning in the protoplanetary disk. This could suggest that at least four different chondrule formation mechanisms were operating over the lifetime of the protoplanetary disk. If chondrules formed by different mechanisms do co-exist within a single chondrite, this implies that chondrules from different regions of the protoplanetary disk were able to mix. There is some evidence that material was transported between different chondrule formation regions (e.g. Schrader et al., 2020). However, chondrules from different chondrite groups usually show distinct compositions and petrography. This implies that each different chondrite group samples a unique reservoir of chondrules, and that mixing between these regions was limited (Jones, 2012) and suggests that chondrules within the same chondrite likely formed by the same mechanism.

Chapter 7
Conclusions and future work

This chapter outlines the main conclusions of this thesis in sections 7.1 and 7.2. Section 7.3 outlines some outstanding questions and future work. Section 7.4 suggests where the future of chondrule research may lead and how this might be achieved.

7.1 Conclusions

Cosmochemical analyses of primitive chondritic meteorites provide detailed records of processes occurring in the protoplanetary disk. Chondrules are one of the primary components of these meteorites and are evidence of widespread transient heating events occurring in the disk. However, details of the actual process remain largely unknown and many different mechanisms for their formation have been proposed and modelled. Chondrule cooling rates and thermal histories are key constraints on the chondrule formation mechanisms and can help identify the environment and mechanism of such event(s), as well as eliminating those that do not meet the constraints. Dynamic crystallisation experiments (Hewins et al., 1981; Lofgren and Russell, 1986; Lofgren, 1989; Lofgren and Lanier, 1990; Radomsky and Hewins, 1990; Connolly and Hewins, 1991; Jones and Lofgren, 1993; Kennedy et al., 1993; Connolly and Hewins, 1995; Dehart and Lofgren, 1996; Connolly et al., 1998; Weinbruch et al., 1998; Tsuchiyama et al., 2004; Wick et al., 2010) provide the most widely cited constraints on cooling rate, however these provide an indirect measure of chondrule cooling rate. The results of these should be validated by or constrained by more direct measurements, of which there remain relatively few.

The aim of this work was to determine chondrule cooling rates using a more direct method than the often cited crystallisation experiments. This was achieved by modelling diffusion profiles present in forsteritic-olivine relict grains present in twelve type II chondrules in three chondrites (ALHA 77307 CO3.00, NWA 8276 L3.00 and NWA 4910 LL3.1). This approach has been explored previously (Greeney and Ruzicka, 2004; Béjina et al., 2009; Hewins et al., 2009) with limited results. Béjina et al. (2009) and Greeney and Ruzicka (2004) studied forsteritic-olivine relict grains in chondrules in metamorphosed meteorites and Hewins et al. (2009) presented results from a single chondrule. In this work, Fe-Mg diffusion profiles were measured using BSE greyscales calibrated to EPMA measurements, an approach that has been used in terrestrial systems (Martin et al., 2008; Hartley et al., 2016). This technique provides a greater spatial resolution than EPMA measurements alone, particularly suited to the narrow diffusion profiles present in the rapidly cooled chondrules. These compositional profiles reveal that the forsteritic-olivine relict grains exchanged extensively with the chondrule melt before experiencing crystal growth. Model diffusion profiles, which were compared to the observed compositional profiles, were

produced using a one-dimensional explicit finite difference forward modelling program coded into Microsoft Excel.

Determined chondrule cooling rates are rapid and the shapes of many of the observed compositional profiles present in the forsteritic-olivine relict grains could not be recreated using linear cooling histories and instead, non-linear histories were considered. Most chondrules show evolving cooling histories with increasing cooling rates (e.g. Al-1, Al-2 and Al-5) or decreasing cooling rates (e.g. Al-4 and all chondrules in NWA 8276 and NWA 4910). Only chondrules Al-3 and Al-6 show cooling rates that are roughly linear. Cooling rates and cooling histories are generally reproducible within a chondrule, for example, diffusion profiles in chondrules Al-1, Al-2 and Al-5 show consistently increasing cooling rates. Where there is some variation in behaviour, for example, Al-3, determined cooling rates from the observed compositional profile are similar and the change in cooling rate is relatively small. The largest sources of error in this work are associated with sectioning effects, where the forsteritic-olivine relict grain boundary is not perpendicular to the section. This artificially extends the observed compositional profile resulting in underestimations in chondrule cooling rates (e.g. Shea et al. 2015).

The results and conclusions of this thesis are summarised below in answer to the research questions posed in Chapter 1.

7.2 Responses to research questions

I. What are the cooling rates of chondrules measured using a direct method?

Model fits to the observed diffusion profiles present in forsteritic-olivine relict grains across the studied chondrule population were produced at cooling rates of 5 to 50000 Kh^{-1}. However, to produce good model fits to many of the observed diffusion profiles, non-linear cooling histories had to be considered. Overall, a range in cooling behaviour was observed across the studied chondrules. For the chondrules in ALHA 77307, the results of diffusion modelling indicate cooling rates ranging from 100 to 8000 Kh^{-1} with one chondrule, Al-5, showing evidence of extremely rapid cooling rates of 50000 Kh^{-1}. Three chondrules in ALHA 77307 (Al-1, Al-2 and Al-5) consistently show cooling rates that increase. Two chondrules, Al-3 and Al-6, show roughly linear cooling, while chondrule Al-5 shows initially very rapid cooling, followed by much slower cooling. For the chondrules in NWA 8276 and NWA 4910, determined cooling rates range from 5 to 5000 Kh^{-1}, however, the more extreme cooling

rates were from relict grains whose diffusion profiles were difficult to model (e.g. N4-1 RG1 A and N4-2 RG1 B), and therefore a more reasonable range for the ordinary chondrite chondrules is 10 to 2000 Kh^{-1}. The chondrules in NWA 8276 and NWA 4910 all show decreasing cooling rates, often with very slow final cooling rates <50 Kh^{-1}, which occurs across a restricted temperature range at the end of the model run. Determined cooling rates are similar to the range in cooling rates determined previously by modelling diffusion profiles in forsteritic-olivine relict grains (Greeney and Ruzicka, 2004; Béjina et al., 2009; Hewins et al., 2009). The cooling rates of some of the studied chondrules are similar to those determined by dynamic crystallisation experiments, however, the range also includes much more rapid cooling rates (e.g. Al-1 and Al-5) and suggests porphyritic chondrules can form at much more rapid cooling rates than suggested by dynamic crystallisation experiments.

II. Do chondrules from carbonaceous chondrites and ordinary chondrites show similar cooling rates and thermal histories?

As discussed above, good model fits to the observed compositional profiles often required non-linear cooling histories. The range in initial cooling rates for chondrules in the carbonaceous chondrite ALHA 77307 range from 100 to 5000 Kh^{-1}. A very similar range of 100 to 2000 Kh^{-1} is reported for chondrules in the ordinary chondrites NWA 8276 and NWA 4910. This suggests a similar process and environment for the formation of these chondrules, however, their subsequent thermal history differs. Three chondrules in ALHA 77307 show consistently increasing cooling rates, two show roughly linear while one shows a very small component of decreasing cooling rate. Chondrules in the ordinary chondrites NWA 8276 and NWA 4910 all show decreasing cooling rates. In all but one of these chondrules, this final cooling rate is <50 Kh^{-1}. This divergence in the thermal history of chondrules in the carbonaceous chondrite ALHA 77307, and the ordinary chondrites NWA 8276 and NWA 4910, suggests that there may be a significant difference in the formation mechanism or environment of these chondrules.

However, the lower cooling rates at lower temperatures shown by chondrules in the ordinary chondrites is often accompanied by a distinct shallowing of the observed diffusion profile towards the grain edge. To form this by diffusion alone, as has been attempted here,

it requires slower cooling rates at lower temperatures allowing more time for the more Fe-rich boundary composition at these lower temperatures to diffuse into the crystal. This profile could also be achieved by a small amount of crystal growth, which adds extra Fe-rich crystal to the grain edge creating a shallowing profile. A second alternative explanation is secondary heating events, potentially at relatively low temperatures, for example, parent body metamorphism.

III. Which chondrule formation mechanism(s) do the cooling rates and thermal histories of chondrules support?

The rapid cooling rates of 100 to 8000 Kh^{-1} accompanied by complex thermal histories are generally inconsistent with formation of the studied chondrules in large-scale nebular shockwaves (Ciesla and Hood, 2002; Desch and Connolly, 2002; Morris and Desch, 2010; Morris et al., 2016). They are much more consistent with "planetary" formation mechanisms, such as planetary embryo bow shocks (Morris et al., 2012; Boley et al., 2013; Mann et al., 2016), impact jetting (Hasegawa et al., 2015; Johnson et al., 2015; Wakita et al., 2017; Johnson et al., 2018; Oshino et al., 2019) or radiative heating from molten planetesimals (Herbst and Greenwood, 2016; Herbst and Greenwood, 2019). However, there are issues with the radiative heating model, such as the requirement to form chondrules which require a high temperature, while simultaneously preserving a primitive, unheated matrix (Brearley, 1993; Greshake, 1997). The peak temperatures from this mechanism also may struggle to reach temperatures approaching the determined chondrule liquidus temperatures. Impact jetting scenarios could be consistent with some chondrules. They can form chondrules with increasing cooling rates, however, they are unable to explain the formation of those with decreasing or roughly linear cooling histories. Overall, planetary embryo bow shocks provide the best fit to the observed thermal histories of the studied chondrules. Planetary embryo bow shocks with shock speeds between 6 and 7 kms^{-1} may be able to explain the cooling rates and thermal histories in the studied chondrules, particularly the increasing cooling rates displayed by Al-1, Al-2 and Al-5 (e.g. Boley et al. 2013; Mann et al. 2016).

However, there may have been multiple chondrule formation mechanisms operating in the protoplanetary disk, simultaneously and at different times. For example, there is good

evidence that the distinctive chondrules from CB chondrites may have formed in an impact plume after the main phase of chondrule formation (Krot et al., 2005). Some chondrules show evidence of relatively slow cooling <300 Kh^{-1} (Al-3, N8-1 and N8-2), which could also be consistent with formation in large scale nebular shockwaves. Chondrule Al-4 shows evidence of very rapid cooling rates of 50000 Kh^{-1}. While this might be achievable in a planetary embryo bow shock with rapid cooling rates as a result of efficient radiation resulting from relatively low chondrule and dust abundance, such rapid cooling rates are usually associated with models of chondrule formation driven by nebular lightning (Desch and Cuzzi, 2000; Desch et al., 2012; Johansen and Okuzumi, 2018). While planetary embryo bow shocks can explain the observed cooling rates and thermal histories of most chondrules studied here, it may be that other mechanisms were also producing chondrules.

IV. What are the implications of the supported chondrule formation mechanism(s) on the evolution of the Solar System?

The formation of chondrules in planetary embryo bow shocks has important implications for the evolution of the early Solar System and the formation of the terrestrial planets. For chondrules to be formed in a planetary embryo bow shock, these planetary embryos must have formed first. This requires that the formation of the studied type II chondrules is delayed until large planetesimals and planetary embryos form. This is consistent with the Al-Mg and Hf-W ages of chondrules which suggest a time gap of ~1.5 Myrs between CAI formation and chondrule formation (Budde et al., 2016b; Budde et al., 2018; Kleine et al., 2018; Nagashima et al., 2018; Pape et al., 2019) as well as the Hf-W age of Mars, indicating large planetary embryos may have formed within ~2 Myrs of CAIs (Dauphas and Pourmand, 2011). It also means that the studied chondrules are a by-product of planet formation, and therefore may not be representative of the material that formed the terrestrial planets.

The textural and compositional diversity of chondrules requires a wide range in chondrule formation conditions, for example, peak temperatures, cooling rates and oxygen fugacity conditions (Lofgren, 1996; Jones et al., 2005; Jones, 2012). Planetary embryo bow shocks are complex 3-D structures and predict a wide range of peak temperatures and cooling rates depending on the size of the planetary embryo, shock speed and presence of atmospheres (Ciesla et al., 2004; Boley et al., 2013; Mann et al., 2016). The composition of

this atmosphere may be able to impose reducing conditions if primarily composed of nebular gas or relatively oxidising conditions if this is composed of volatiles from a degassing magma ocean (Morris et al., 2012). These atmospheres can be stripped and replenished by accreting nebular gas, or a degassing magma ocean which allows them to evolve over time (Mann et al., 2016). Chondrule formation from chemically and isotopically diverse precursors in bow shocks around planetary embryos containing variable atmospheres, sizes and shock speeds may be able to explain the observed diversity in the chondrule population.

7.3 Future work

There are some outstanding questions and some potential avenues for future work. These are outlined in the sections below.

7.3.1 Diffusion profiles in ordinary chondrites

One of the major outstanding questions of this work is whether the final slow cooling rates determined for compositional profiles in forsteritic-olivine relict grains, consistently observed in the ordinary chondrite chondrules, are a product of the initial chondrule formation event or if the shape of the diffusion profile has been altered by another process during or after the formation of the chondrule.

7.3.1.1 Crystal growth

Crystal growth was ruled out for the forsteritic-olivine relict grains in the chondrules from the carbonaceous chondrite ALHA 77307 by phosphorus compositional profiles measured using NanoSIMS. However, no data is available yet for the forsteritic-olivine relict grains in the ordinary chondrites, and therefore crystal growth cannot be completely ruled out in these profiles. The distinct shallowing of the diffusion profiles towards the grain edge may be a result of crystal growth during exchange with the chondrule melt. To investigate this, P and Fe compositional profiles could be measured using NanoSIMS to identify the grain boundary. Alternatively, diffusion models incorporating crystal growth at different stages of the cooling history could be run to test whether the observed compositional profiles can be recreated with crystal growth.

7.3.1.2 Secondary heating

An alternative explanation for the observed shallowing of the diffusion profiles may be secondary heating events. These reheating events, which could be chondrule recycling events or parent body metamorphism, will allow more diffusion to occur along the observed compositional profiles, however, as the grain edge is most Fe-rich, diffusion will happen fastest here, which results in a shallowing profile. Diffusion models could be undertaken to discover whether these profile shapes could be formed either by secondary chondrule recycling events, or parent body metamorphism (e.g. Schwinger et al. 2016).

7.3.2 Trace element diffusion modelling

Another avenue for future work is trace element diffusion modelling. The extensive study of diffusion in olivine has led to determinations of diffusion coefficients for a number of trace and minor elements in olivine crystals which could act as inputs for diffusion modelling. These include Ca (Coogan et al., 2005), Mn (Chakraborty, 2010), Ni (Petry et al., 2004; Holzapfel et al., 2007; Chakraborty, 2010), Cr (Ito and Ganguly, 2006) and Ti (Cherniak and Liang, 2014). EPMA measurements of forsteritic-olivine relict grains show many of these are present in quantities which can be measured. NanoSIMS can be used to measure trace element concentrations down to ppm detection limits, with a very high (<<µm) spatial resolution, and therefore can be used to measure these trace element diffusion profiles. NanoSIMS has been demonstrated as a technique for measuring similar compositional profiles for Ti in quartz by Charlier et al. (2012) and has been used in this thesis to measure P and Fe compositional profiles in forsteritic-olivine relict grains. Using multiple elements and systems is potentially advantageous over one system as they should all provide similar cooling rates and thermal histories. This may support cooling rates determined by Fe-Mg diffusion modelling alone.

7.3.3 O isotopes and Mg isotopes

Oxygen isotope characteristics in chondrules are extremely heterogeneous within and across the different chondrite groups. Phases within a single chondrule in the most primitive and unaltered meteorites, e.g. Acfer 094, show homogeneous O-isotope signatures which indicate that these phases crystallised from the final chondrule melt, which had equilibrated with the ambient gas (Tenner et al., 2015). However, relict grains can show a different isotopic signature, therefore O-isotopes can be used to confirm and identify relict grains (Jones et al., 2000; Ruzicka et al., 2007; Tenner et al., 2018). Chondrules

within a chondrite group generally occupy a similar area in the oxygen-three isotope plot, indicating that they sample localised reservoirs with different O-isotope ratios (Jones, 2012). Forsteritic-olivine relict grains in type II chondrules often show values that are similar to values of olivine in type I chondrules within the same chondrite. This suggests that these forsteritic-olivine relict grains originate from type I chondrules within the same reservoir. However, some show considerable enrichments in ^{16}O, which may indicate these grains originated in CAIs, AOAs or another refractory source (Tenner et al., 2018). Knowing the O-isotope compositions of chondrules and forsteritic-relict grains and how these relate to chondrule cooling histories may be useful for several reasons. If there are differences in thermal history of chondrules containing refractory ^{16}O-enriched forsteritic-olivine relict grains compared to isotopically normal relict grains, it may indicate that different chondrule formation mechanisms were operating at different times and locations within the protoplanetary disk. Other alternative hypotheses could be investigated, for example, are there variations in intrachondrule O-isotopes which could be related to chondrule thermal history? As forsteritic-olivine relict grains are isotopically distinct from their host chondrules, O-isotopic equilibration between the relict grain and the chondrule melt and subsequent overgrowth will have occurred as the chondrule cooled. By measuring O-isotopic compositional profiles using a technique such as NanoSIMS, and modelling these diffusion widths, chondrule cooling rates could be estimated (e.g. Jones et al., 2004). However, this could be challenging as oxygen diffuses very slowly in comparison to cations such as Fe-Mg, with diffusion coefficients that are ~3 orders of magnitude lower (Chakraborty, 2010). This means that O-isotopic diffusion widths over the timescales of chondrule formation would be very small and would create very narrow O-isotopic compositional profiles. To measure these, a technique with very high spatial resolution while retaining analytical precision at the per mil level or better would need to be employed. At the present time such capability is beyond that of current instrumentation.

Mg isotope ratios can be used in order to date chondrules relative to CAIs using the extinct ^{26}Al-^{26}Mg isotope system, however, this depends upon the assumption that ^{26}Al was distributed homogeneously throughout the solar system, which remains controversial (Villeneuve et al., 2009; Larsen et al., 2011; Luu et al., 2016; Olsen et al., 2016; Van Kooten et al., 2016; Nagashima et al., 2018; Bollard et al., 2019; Gregory et al., 2020). If this relative dating is appropriate, it may be used to see whether there are correlations between

chondrule cooling rates and chondrule ages. This might allow us to determine whether different chondrule formation mechanisms were occurring at different times (e.g. Bollard et al. 2017).

Isotopic data can be obtained using Secondary Ion Mass Spectrometry (SIMS) or for small grains NanoSIMS. The highest precision data is likely to be obtained from standard SIMS.

7.3.4 Expansion of dataset

In this study, only twelve type II chondrule have been studied across CO, L and LL chondrites. Increasing the number of chondrules studied would confirm or expand the range of cooling rates determined by modelling diffusion profiles in forsteritic-olivine relict grains. These relict grains have also been found in type II chondrules in CR (Leshin et al., 1998; Connolly and Huss, 2010), CM (Hanowski and Brearley, 2001; Hewins et al., 2014), and CV (Hertwig et al., 2018) chondrites. Expanding the study to include more chondrite groups would also investigate whether type II chondrules in these different groups experienced different cooling rates. If this is the case, then it may indicate that different chondrule formation mechanisms were operating in the different chondrule reservoirs.

7.4 Final comments

Chondrules are fascinating objects which show incredible textural and compositional diversity. They have been studied for over a century, with their igneous textures first recognised by Sorby (1877). Chondrules, along with the other components of chondrites provide important details into the evolution of the early Solar System. Despite decades of study, many aspects of chondrules and chondrule formation remain puzzling and require further study to understand what these objects tell us about the protoplanetary disk. These could include, but are not limited to, further petrographic studies of chondrules, experiments to determine chondrule formation conditions and further, more detailed modelling of astrophysical processes to test whether they are consistent with experimental and petrographic constraints on chondrule formation.

At the time of the submission of this thesis, Hayabusa2 and OSIRIS-Rex are at their target asteroids. They are expected to return samples to Earth by 2020 and 2023. Study of these samples may provide new insights into the link between chondrites and asteroids (e.g.

Nakamura et al. 2011; Tsuchiyama et al. 2011; Yurimoto et al. 2011). This may help lead to a more thorough understanding of chondrule and chondrite formation.

References

Agnor C. B., Canup R. M. and Levison H. F. (1999) On the character and consequences of large impacts in the late stage of terrestrial planet formation. *Icarus* **142**, 219–237.

Alexander C., Barber D. J. and Hutchison R. (1989) The microstructure of Semarkona and Bishunpur. *Geochimica et Cosmochimica Acta* **53**, 3045–3057.

Alexander C. M. O., Grossman J. N., Ebel D. S. and Ciesla F. J. (2008) The Formation Conditions of Chondrules and Chondrites. *Science* **320**, 1617–1619.

Alexander C. M., Taylor S., Delaney J. S., Ma P. and Herzog G. F. (2002) Mass-dependent fractionation of Mg, Si, and Fe isotopes in five stony cosmic spherules. *Geochimica et Cosmochimica Acta* **66**, 173–183.

Alexander C. O. and Grossman J. N. (2005) Alkali elemental and potassium isotopic compositions of Semarkona chondrules. *Meteoritics and Planetary Science* **40**, 541–556.

Alexander C. O. and Wang J. (2001) Iron isotopes in chondrules: Implications for the role of evaporation during chondrule formation. *Meteoritics & Planetary Science* **36**, 419–428.

Asimow P. D. and Ghiorso M. S. (1998) Algorithmic modifications extending MELTS to calculate subsolidus phase relations. *American Mineralogist* **83**, 1127–1132.

Asphaug E., Jutzi M. and Movshovitz N. (2011) Chondrule formation during planetesimal accretion. *Earth and Planetary Science Letters* **308**, 369–379.

Becker M., Hezel D. C., Schulz T., Elfers B.-M. and Münker C. (2015) Formation timescales of CV chondrites from component specific Hf–W systematics. *Earth and Planetary Science Letters* **432**, 472–482.

Béjina F., Sautter V. and Jaoul O. (2009) Cooling rate of chondrules in ordinary chondrites revisited by a new geospeedometer based on the compensation rule. *Physics of the Earth and Planetary Interiors* **172**, 5–12.

Berlin J. (2010) Mineralogy and bulk chemistry of chondrules and matrix in petrologic type 3 chondrites: Implications for early solar system processes.

Berlin J., Jones R. H. and Brearley A. J. (2011) Fe-Mn systematics of type IIA chondrules in unequilibrated CO, CR, and ordinary chondrites. *Meteoritics & Planetary Science* **46**, 513–533.

Berlin J., Jones R. H., Brearley A. J. and Spilde M. N. (2008) Determining bulk chemical compositions of chondrules by electron microprobe: Modal recombination versus defocused beam analyses. *Microscopy and Microanalysis* **14**, 110.

Bizzarro M., Baker J. A. and Haack H. (2004) Mg isotope evidence for contemporaneous formation of chondrules and refractory inclusions. *Nature* **431**, 275.

Bland P. A., Stadermann F. J., Floss C., Rost D., Vicenzi E. P., Kearsley A. T. and Benedix G. K. (2007) A cornucopia of presolar and early solar system materials at the micrometer size range in primitive chondrite matrix. *Meteoritics & Planetary Science* **42**, 1417–1427.

Boley A. C., Morris M. A. and Desch S. J. (2013) High-temperature processing of solids through solar nebular bow shocks: 3D radiation hydrodynamics simulations with particles. *The Astrophysical Journal* **776**, 101.

Bolikhovskaya S. V., Vasil'eva M. O. and Koptev-Dvornikov E. V. (1995) Modelling of low-Ca pyroxene crystallisation in basic systems (New versions of geothermometers). *Geokhimia* **12**, 1710–1727.

Bollard J., Connelly J. N., Whitehouse M. J., Pringle E. A., Bonal L., Jørgensen J. K., Nordlund Å., Moynier F. and Bizzarro M. (2017) Early formation of planetary building blocks inferred from Pb isotopic ages of chondrules. *Science advances* **3**, e1700407.

Bollard J., Kawasaki N., Sakamoto N., Olsen M., Itoh S., Larsen K., Wielandt D., Schiller M., Connelly J. N. and Yurimoto H. (2019) Combined U-corrected Pb-Pb dating and 26Al-26Mg systematics of individual chondrules–evidence for a reduced initial abundance of 26Al amongst inner Solar System chondrules. *Geochimica et Cosmochimica Acta*.

Bonal L., Bourot-Denise M., Quirico E., Montagnac G. and Lewin E. (2007) Organic matter and metamorphic history of CO chondrites. *Geochimica et Cosmochimica Acta* **71**, 1605–1623.

Borisov A., Pack A., Kropf A. and Palme H. (2008) Partitioning of Na between olivine and melt: An experimental study with application to the formation of meteoritic Na2O-rich chondrule glass and refractory forsterite grains. *Geochimica et Cosmochimica Acta* **72**, 5558–5573.

Boss A. P. and Durisen R. H. (2005) Sources of shock waves in the protoplanetary disk. In *Chondrites and the Protoplanetary Disk* p. 821.

Boss A. P. and Goswami J. N. (2006) Presolar cloud collapse and the formation and early evolution of the solar nebula. *Meteorites and the early solar system II*, 171–186.

Bowen N. L. and Schairer J. F. (1935) The system MgO-FeO-SiO 2. *American Journal of Science*, 151–217.

Brearley A. J. (1993) Matrix and fine-grained rims in the unequilibrated CO3 chondrite, ALHA77307: Origins and evidence for diverse, primitive nebular dust components. *Geochimica et Cosmochimica Acta* **57**, 1521–1550.

Brearley A. J. and Jones R. H. (1993) Chondrite thermal histories from low-Ca pyroxene microstructures: Autometamorphism versus prograde metamorphism revisited. In *Lunar and Planetary Science Conference*

Brisett F. (2016) Introduction to EBSD: past and settings, everyday work considerations. In *12th Regional Workshop on Electron Probe Microanalysis Today - Practical Aspects* European Microbeam Analysis Society, CEA Marcoule, France. pp. 25–46.

Budde G., Kleine T., Kruijer T. S., Burkhardt C. and Metzler K. (2016a) Isotopic complementarity of chondrules and matrix and the age and origin of chondrules. In *Lunar Planet. Sci. Conf. XLVII*

Budde G., Kleine T., Kruijer T. S., Burkhardt C. and Metzler K. (2016b) Tungsten isotopic constraints on the age and origin of chondrules. *Proceedings of the National Academy of Sciences*, 201524980.

Budde G., Kruijer T. S. and Kleine T. (2018) Hf-W chronology of CR chondrites: Implications for the timescales of chondrule formation and the distribution of 26Al in the solar nebula. *Geochimica et Cosmochimica Acta* **222**, 284–304.

Burkhardt C., Kleine T., Bourdon B., Palme H., Zipfel J., Friedrich J. M. and Ebel D. S. (2008) Hf–W mineral isochron for Ca, Al-rich inclusions: age of the solar system and the timing of core formation in planetesimals. *Geochimica et Cosmochimica Acta* **72**, 6177–6197.

Chakraborty S. (2010) Diffusion coefficients in olivine, wadsleyite and ringwoodite. *Reviews in mineralogy and geochemistry* **72**, 603–639.

Chakraborty S. (1997) Rates and mechanisms of Fe-Mg interdiffusion in olivine at 980–1300 C. *Journal of Geophysical Research: Solid Earth* **102**, 12317–12331.

Chambers J. E. (2001) Making more terrestrial planets. *Icarus* **152**, 205–224.

Chambers J. E. (2004) Planetary accretion in the inner Solar System. *Earth and Planetary Science Letters* **223**, 241–252.

Charlier B. L., Morgan D. J., Wilson C. J., Franchi I. A. and Starkey N. A. (2012) Timescales recorded in volcanic quartz from Ti and Al diffusion profiles: a NanoSIMS investigation. In *AGU Fall Meeting Abstracts* p. 2800.

Chaumard N., Humayun M., Zanda B. and Hewins R. H. (2018) Cooling rates of type I chondrules from Renazzo: Implications for chondrule formation. *Meteoritics & Planetary Science* **53**, 984–1005.

Cherniak D. J. and Liang Y. (2014) Titanium diffusion in olivine. *Geochimica et Cosmochimica Acta* **147**, 43–57.

Chizmadia L. J., Rubin A. E. and Wasson J. T. (2002) Mineralogy and petrology of amoeboid olivine inclusions in CO3 chondrites: Relationship to parent-body aqueous alteration. *Meteoritics & Planetary Science* **37**, 1781–1796.

Ciesla F. J. and Hood L. L. (2002) The nebular shock wave model for chondrule formation: Shock processing in a particle–gas suspension. *Icarus* **158**, 281–293.

Ciesla F. J., Hood L. L. and Weidenschilling S. J. (2004) Evaluating planetesimal bow shocks as sites for chondrule formation. *Meteoritics and Planetary Science* **39**, 1809–1822.

Clayton R. N. and Mayeda T. K. (1999) Oxygen isotope studies of carbonaceous chondrites. *Geochimica et Cosmochimica Acta* **63**, 2089–2104.

Clayton R. N., Mayeda T. K., Goswami J. N. and Olsen E. J. (1991) Oxygen isotope studies of ordinary chondrites. *Geochimica et Cosmochimica Acta* **55**, 2317–2337.

Connelly J. N. and Bizzarro M. (2018) The Absolute Pb-Pb Isotope Ages of Chondrules: Insights into the Dynamics of the Solar Protoplanetary Disk. In *Chondrules: Records of Protoplanetary Disk Processes* Cambridge Planetary Science. Cambridge University Press. pp. 300–323.

Connelly J. N., Bizzarro M., Krot A. N., Nordlund Å., Wielandt D. and Ivanova M. A. (2012) The absolute chronology and thermal processing of solids in the solar protoplanetary disk. *Science* **338**, 651–655.

Connelly J. N., Bollard J. and Bizzarro M. (2017) Pb–Pb chronometry and the early solar system. *Geochimica et Cosmochimica Acta* **201**, 345–363.

Connolly H. C. and Hewins R. H. (1995) Chondrules as products of dust collisions with totally molten droplets within a dust-rich nebular environment: An experimental investigation. *Geochimica et Cosmochimica Acta* **59**, 3231–3246.

Connolly H. C. and Hewins R. H. (1991) The influence of bulk composition and dynamic melting conditions on olivine chondrule textures. *Geochimica et Cosmochimica Acta* **55**, 2943–2950.

Connolly H. C., Hewins R. H., Ash R. D., Zanda B., Lofgren G. E. and Bourot-Denise M. (1994) Carbon and the formation of reduced chondrules. *Nature* **371**, 136.

Connolly H. C. and Huss G. R. (2010) Compositional evolution of the protoplanetary disk: Oxygen isotopes of type-II chondrules from CR2 chondrites. *Geochimica et Cosmochimica Acta* **74**, 2473–2483.

Connolly H. C. J., Jones B. D. and Hewins R. H. (1998) The flash melting of chondrules: An experimental investigation into the melting history and physical nature of chondrule precursors. *Geochimica et Cosmochimica Acta* **62**, 2725–2735.

Connolly H. C. and Jones R. H. (2005) Understanding the cooling rates experienced by type II porphyritic chondrules. In *36th Annual Lunar and Planetary Science Conference*

Coogan L. A., Hain A., Stahl S. and Chakraborty S. (2005) Experimental determination of the diffusion coefficient for calcium in olivine between 900 C and 1500 C. *Geochimica et Cosmochimica Acta* **69**, 3683–3694.

Costa F., Dohmen R. and Chakraborty S. (2008) Time Scales of Magmatic Processes from Modeling the Zoning Patterns of Crystals. *Reviews in Mineralogy and Geochemistry* **69**, 545–594.

Crank J. (1976) *The mathematics of diffusion*. 2. ed., reprint., Clarendon Press, Oxford.

Cuvillier P., Chaumard N., Leroux H., Zanda B., Hewins R. H., Jacob D. and Devouard B. (2018) A TEM study of exsolution in Ca-rich pyroxenes from the Paris and Renazzo chondrites: Determination of type I chondrule cooling rates. *Meteoritics & Planetary Science* **53**, 482–492.

Cuzzi J. N., Dobrovolskis A. R. and Champney J. M. (1993) Particle-gas dynamics in the midplane of a protoplanetary nebula. *Icarus* **106**, 102–134.

Cuzzi J. N., Hogan R. C., Paque J. M. and Dobrovolskis A. R. (2001) Size-selective concentration of chondrules and other small particles in protoplanetary nebula turbulence. *The Astrophysical Journal* **546**, 496.

Cuzzi J. N. and Weidenschilling S. J. (2006) Particle-gas dynamics and primary accretion. *Meteorites and the early solar system II* **353**.

Dana J. D., Palache C., Berman H. and Frondel C. (1915) *The system of mineralogy*., Wiley.

Danyushevsky L. V. (2001) The effect of small amounts of H2O on crystallisation of mid-ocean ridge and backarc basin magmas. *Journal of Volcanology and Geothermal Research* **110**, 265–280.

Danyushevsky L. V. and Plechov P. (2011) Petrolog3: Integrated software for modeling crystallization processes. *Geochemistry, Geophysics, Geosystems* **12**.

Dauphas N. and Pourmand A. (2011) Hf-W-Th evidence for rapid growth of Mars and its status as a planetary embryo. *Nature* **473**, 489–492.

Davis A. M., Alexander C. M., Nagahara H. and Richter F. M. (2005) Evaporation and condensation during CAI and chondrule formation. In *Chondrites and the protoplanetary disk* p. 432.

Dehart J. M. and Lofgren G. E. (1996) Experimental studies of group A1 chondrules. *Geochimica et cosmochimica acta* **60**, 2233–2242.

Deng Z., Ebel D. S., Gemma M., Moynier F. and Chaussidon M. (2017) Contrasting Mg isotopic signatures in Leoville (CV3r) chondrules. In *80th Annual Meeting of the Meteoritical Society*

Desch S. J. and Connolly H. C. J. (2002) A model of the thermal processing of particles in solar nebula shocks: Application to the cooling rates of chondrules. *Meteoritics & Planetary Science* **37**, 183–207.

Desch S. J. and Cuzzi J. N. (2000) The generation of lightning in the solar nebula. *Icarus* **143**, 87–105.

Desch S. J., Morris M. A., Connolly H. C. and Boss A. P. (2012) The importance of experiments: Constraints on chondrule formation models. *Meteoritics & Planetary Science* **47**, 1139–1156.

Desch S. J., Morris M. A., Connolly Jr H. C. and Boss A. P. (2010) A critical examination of the X-wind model for chondrule and calcium-rich, aluminum-rich inclusion formation and radionuclide production. *The Astrophysical Journal* **725**, 692.

Dijkstra H. (2016) Introduction to EPMA and SEM. In *12th Regional Workshop on Electron Probe Microanalysis Today - Practical Aspects* European Microbeam Analysis Society, CEA Marcoule, France. pp. 47–56.

Dodd R. T. (1969) Metamorphism of the ordinary chondrites: A review. *Geochimica et Cosmochimica Acta* **33**, 161–203.

Dohmen R. and Chakraborty S. (2007) Fe–Mg diffusion in olivine II: point defect chemistry, change of diffusion mechanisms and a model for calculation of diffusion coefficients in natural olivine. *Physics and Chemistry of Minerals* **34**, 409–430.

Dullemond C. P., Harsono D., Stammler S. M. and Johansen A. (2016) FORMING CHONDRULES IN IMPACT SPLASHES. II. VOLATILE RETENTION. *The Astrophysical Journal* **832**, 91.

Dullemond C. P., Stammler S. M. and Johansen A. (2014) Forming chondrules in impact splashes. I. Radiative cooling model. *The Astrophysical Journal* **794**, 91.

Ebel D. S., Alexander C. M. O. and Libourel G. (2018) Vapor-Melt Exchange: Constraints on Chondrite Formation Conditions and Processes. In *Chondrules: Records of Protoplanetary Disk Processes* Cambridge Planetary Science. Cambridge University Press. pp. 151–174.

Elkins-Tanton L. T. (2008) Linked magma ocean solidification and atmospheric growth for Earth and Mars. *Earth and Planetary Science Letters* **271**, 181–191.

Elkins-Tanton L. T. (2012) Magma oceans in the inner solar system. *Annual Review of Earth and Planetary Sciences* **40**, 113–139.

Fedkin A. V. and Grossman L. (2013) Vapor saturation of sodium: Key to unlocking the origin of chondrules. *Geochimica et Cosmochimica Acta* **112**, 226–250.

Florentin L., Faure F., Deloule E., Tissandier L., Gurenko A. and Lequin D. (2017) Origin of Na in glass inclusions hosted in olivine from Allende CV3 and Jbilet Winselwan CM2: Implications for chondrule formation. *Earth and Planetary Science Letters* **474**, 160–171.

Friend P., Hezel D. C. and Mucerschi D. (2016) The conditions of chondrule formation, Part II: Open system. *Geochimica et Cosmochimica Acta* **173**, 198–209.

Fu R. R. and Elkins-Tanton L. T. (2014) The fate of magmas in planetesimals and the retention of primitive chondritic crusts. *Earth and Planetary Science Letters* **390**, 128–137.

Ghiorso M. S. and Sack R. O. (1995) Chemical mass transfer in magmatic processes IV. A revised and internally consistent thermodynamic model for the interpolation and extrapolation of liquid-solid equilibria in magmatic systems at elevated temperatures and pressures. *Contributions to Mineralogy and Petrology* **119**, 197–212.

Gooding J. L. and Keil K. (1981) Relative abundances of chondrule primary textural types in ordinary chondrites and their bearing on conditions of chondrule formation. *Meteoritics* **16**, 17–43.

Greene T. P. (2001) Protostars. *American Scientist* **89**, 316.

Greeney S. and Ruzicka A. (2004) Relict forsterite in chondrules: Implications for cooling rates.

Gregory T., Luu T.-H., Coath C. D., Russell S. S. and Elliott T. (2020) Primordial formation of major silicates in a protoplanetary disc with homogeneous 26Al/27Al. *Science Advances* **6**, eaay9626.

Greshake A. (1997) The primitive matrix components of the unique carbonaceous chondrite Acfer 094: A TEM study. *Geochimica et Cosmochimica Acta* **61**, 437–452.

Greshake A. and Fritz J. (2018) Meteorites. In *Planetary Geology* Springer. pp. 103–121.

Grossman J. N. and Brearley A. J. (2005) The onset of metamorphism in ordinary and carbonaceous chondrites. *Meteoritics & Planetary Science* **40**, 87–122.

Grossman L., Ebel D. S., Simon S. B., Davis A. M., Richter F. M. and Parsad N. M. (2000) Major element chemical and isotopic compositions of refractory inclusions in C3 chondrites: The separate roles of condensation and evaporation. *Geochimica et Cosmochimica Acta* **64**, 2879–2894.

Güttler C., Poppe T., Wasson J. T. and Blum J. (2008) Exposing metal and silicate charges to electrical discharges: Did chondrules form by nebular lightning? *Icarus* **195**, 504–510.

Hanowski N. P. and Brearley A. J. (2001) Aqueous alteration of chondrules in the CM carbonaceous chondrite, Allan Hills 81002: Implications for parent body alteration. *Geochimica et Cosmochimica Acta* **65**, 495–518.

Hartley M. E., Morgan D. J., Maclennan J., Edmonds M. and Thordarson T. (2016) Tracking timescales of short-term precursors to large basaltic fissure eruptions through Fe–Mg diffusion in olivine. *Earth and Planetary Science Letters* **439**, 58–70.

Hasegawa Y., Turner N. J., Masiero J., Wakita S., Matsumoto Y. and Oshino S. (2016) Forming chondrites in a solar nebula with magnetically induced turbulence. *The Astrophysical Journal Letters* **820**, L12.

Hasegawa Y., Wakita S., Matsumoto Y. and Oshino S. (2015) Chondrule Formation via Impact Jetting Triggered by Planetary Accretion. *The Astrophysical Journal* **816**, 8.

Herbst W. and Greenwood J. P. (2016) A new mechanism for chondrule formation: Radiative heating by hot planetesimals. *Icarus* **267**, 364–367.

Herbst W. and Greenwood J. P. (2019) A radiative heating model for chondrule and chondrite formation. *Icarus* **329**, 166–181.

Hertwig A. T., Defouilloy C. and Kita N. T. (2018) Formation of chondrules in a moderately high dust enriched disk: Evidence from oxygen isotopes of chondrules from the Kaba CV3 chondrite. *Geochimica et cosmochimica acta* **224**, 116–131.

Hewins R. H. (1997) Chondrules. *Annual Review of Earth and Planetary Sciences* **25**, 61–83.

Hewins R. H. (1999) RELICT Pyroxene-Constraint on Chondrule Melting?? In *Lunar and Planetary Science Conference*

Hewins R. H., Bourot-Denise M., Zanda B., Leroux H., Barrat J.-A., Humayun M., Göpel C., Greenwood R. C., Franchi I. A. and Pont S. (2014) The Paris meteorite, the least altered CM chondrite so far. *Geochimica et Cosmochimica Acta* **124**, 190–222.

Hewins R. H., Connolly H. C., Lofgren Jr G. E. and Libourel G. (2005) Experimental constraints on chondrule formation. In *Chondrites and the protoplanetary disk* p. 286.

Hewins R. H. and Fox G. E. (2004) Chondrule textures and precursor grain size: an experimental study. *Geochimica et cosmochimica acta* **68**, 917–926.

Hewins R. H., Ganguly J. and Mariani E. (2009) Diffusion modeling of cooling rates of relict olivine in semarkona chondrules. In *Lunar and Planetary Science Conference* p. 1513.

Hewins R. H., Klein L. C. and Fasano B. V. (1981) Conditions of formation of pyroxene excentroradial chondrules. In *Lunar and Planetary Science Conference* pp. 448–450.

Hewins R. H. and Zanda B. (2012) Chondrules: Precursors and interactions with the nebular gas. *Meteoritics & Planetary Science* **47**, 1120–1138.

Hewins R. H., Zanda B. and Bendersky C. (2012) Evaporation and recondensation of sodium in Semarkona Type II chondrules. *Geochimica et Cosmochimica Acta* **78**, 1–17.

Hezel D. C., Bland P. A., Palme H., Jacquet E. and Bigolski J. (2018) Composition of Chondrules and Matrix and Their Complementary Relationship in Chondrites. In *Chondrules: Records of Protoplanetary Disk Processes* Cambridge Planetary Science. Cambridge University Press. pp. 91–121.

Hezel D. C., Needham A. W., Armytage R., Georg B., Abel R. L., Kurahashi E., Coles B. J., Rehkämper M. and Russell S. S. (2010) A nebula setting as the origin for bulk chondrule Fe isotope variations in CV chondrites. *Earth and Planetary Science Letters* **296**, 423–433.

Hezel D. C. and Palme H. (2010) The chemical relationship between chondrules and matrix and the chondrule matrix complementarity. *Earth and Planetary Science Letters* **294**, 85–93.

Holland H. D. (1984) *The Chemical Evolution of the Atmosphere and Oceans*., Princeton University Press.

Holzapfel C., Chakraborty S., Rubie D. C. and Frost D. J. (2007) Effect of pressure on Fe–Mg, Ni and Mn diffusion in (Fe x Mg 1− x) 2 SiO 4 olivine. *Physics of the Earth and Planetary Interiors* **162**, 186–198.

Hood L. L. and Horanyi M. (1991) Gas dynamic heating of chondrule precursor grains in the solar nebula. *Icarus* **93**, 259–269.

Hood L. L. and Weidenschilling S. J. (2012) The planetesimal bow shock model for chondrule formation: A more quantitative assessment of the standard (fixed Jupiter) case. *Meteoritics & Planetary Science* **47**, 1715–1727.

Hoppe P., Cohen S. and Meibom A. (2013) NanoSIMS: technical aspects and applications in cosmochemistry and biological geochemistry. *Geostandards and Geoanalytical Research* **37**, 111–154.

Hubbard A. and Ebel D. S. (2018) Evaluating Non-Shock, Non-Collisional Models for Chondrule Formation. In *Chondrules: Records of Protoplanetary Disk Processes* Cambridge Planetary Science. Cambridge University Press. pp. 400–427.

Humayun M. (2012) Chondrule cooling rates inferred from diffusive profiles in metal lumps from the Acfer 097 CR2 chondrite. *Meteoritics & Planetary Science* **47**, 1191–1208.

Huss G. R., Alexander C. M., Palme H., Bland P. A. and Wasson J. T. (2005) Genetic relationships between chondrules, fine-grained rims, and interchondrule matrix. In *Chondrites and the protoplanetary disk* p. 701.

Huss G. R., Meshik A. P., Smith J. B. and Hohenberg C. M. (2003) Presolar diamond, silicon carbide, and graphite in carbonaceous chondrites: Implications for thermal processing in the solar nebula. *Geochimica et Cosmochimica Acta* **67**, 4823–4848.

Huss G. R., Rubin A. E. and Grossman J. N. (2006) Thermal metamorphism in chondrites. *Meteorites and the early solar system II* **943**, 567–586.

Hutchison R. (2004) *Meteorites: A petrologic, chemical and isotopic synthesis*., Cambridge University Press.

Ikeda Y. (1983) Alteration of chondrules and matrices in the four Antarctic carbonaceous chondrites ALH-77307 (C3), Y-790123 (C2), Y-75293 (C2), and Y-74662 (C2).

Ito M. and Ganguly J. (2006) Diffusion kinetics of Cr in olivine and 53 Mn–53 Cr thermochronology of early solar system objects. *Geochimica et Cosmochimica Acta* **70**, 799–809.

Jacobsen B., Yin Q., Moynier F., Amelin Y., Krot A. N., Nagashima K., Hutcheon I. D. and Palme H. (2008) 26Al–26Mg and 207Pb–206Pb systematics of Allende CAIs: canonical solar initial 26Al/27Al ratio reinstated. *Earth and Planetary Science Letters* **272**, 353–364.

Jacquet E., Alard O. and Gounelle M. (2015) Trace element geochemistry of ordinary chondrite chondrules: The type I/type II chondrule dichotomy. *Geochimica et Cosmochimica Acta* **155**, 47–67.

Johansen A., Oishi J. S., Mac Low M.-M., Klahr H., Henning T. and Youdin A. (2007) Rapid planetesimal formation in turbulent circumstellar disks. *Nature* **448**, 1022–1025.

Johansen A. and Okuzumi S. (2017) Harvesting the Decay Energy of 26-Al to Drive Lightning Discharge and Chondrule Formation. *LPI Contributions* **1963**.

Johansen A. and Okuzumi S. (2018) Harvesting the decay energy of 26Al to drive lightning discharge in protoplanetary discs. *Astronomy & Astrophysics* **609**, A31.

Johnson B. C., Ciesla F. J., Dullemond C. P. and Melosh H. J. (2017) Formation of Chondrules by Planetesimal Collision. *LPI Contributions* **1963**.

Johnson B. C., Ciesla F. J., Dullemond C. P. and Melosh H. J. (2018) Formation of Chondrules by Planetesimal Collisions. In *Chondrules: Records of Protoplanetary Disk Processes* Cambridge Planetary Science. Cambridge University Press. pp. 343–360.

Johnson B. C., Minton D. A., Melosh H. J. and Zuber M. T. (2015) Impact jetting as the origin of chondrules. *Nature* **517**, 339–41.

Jones R. H. (1996) 17: Relict Grains in Chondrules: Evidence for Chondrule Recycling. *Chondrules and the protoplanetary disk*, 163.

Jones R. H. (1992) On the relationship between isolated and chondrule olivine grains in the carbonaceous chondrite ALHA77307. *Geochimica et Cosmochimica Acta* **56**, 467–482.

Jones R. H. (2012) Petrographic constraints on the diversity of chondrule reservoirs in the protoplanetary disk. *Meteoritics & Planetary Science* **47**, 1176–1190.

Jones R. H. (1990) Petrology and mineralogy of Type II, FeO-rich chondrules in Semarkona (LL3.0): Origin by closed-system fractional crystallization, with evidence for supercooling. *Geochimica et Cosmochimica Acta* **54**, 1785–1802.

Jones R. H. (1997) Ubiquitous anorthitic plagioclase in type I chondrules in CO3 chondrites: Implications for chondrule formation and parent body metamorphism. *Meteoritics and Planetary Science Supplement* **32**.

Jones R. H. and Carey E. R. (2006) Identification of relict forsterite grains in forsterite-rich chondrules from the Mokoia CV3 carbonaceous chondrite. *American Mineralogist* **91**, 1664–1674.

Jones R. H. and Danielson L. R. (1997) A chondrule origin for dusty relict olivine in unequilibrated chondrites. *Meteoritics & Planetary Science* **32**, 753–760.

Jones R. H., Grossman J. N. and Rubin A. E. (2005) Chemical, mineralogical and isotopic properties of chondrules: Clues to their origin. In *Chondrites and the protoplanetary disk* p. 251.

Jones R. H., Leshin L. A., Guan Y., Sharp Z. D., Durakiewicz T. and Schilk A. J. (2004) Oxygen isotope heterogeneity in chondrules from the Mokoia CV3 carbonaceous chondrite. *Geochimica et Cosmochimica Acta* **68**, 3423–3438.

Jones R. H. and Lofgren G. E. (1993) A comparison of FeO-rich, porphyritic olivine chondrules in unequilibrated chondrites and experimental analogues. *Meteoritics* **28**, 213–221.

Jones R. H., Saxton J. M., Lyon I. C. and Turner G. (2000) Oxygen isotopes in chondrule olivine and isolated olivine grains from the CO3 chondrite Allan Hills A77307. *Meteoritics & Planetary Science* **35**, 849–857.

Jones R. H. and Scott E. R. D. (1989) Petrology and thermal history of type IA chondrules in the Semarkona (LL3. 0) chondrite. In *Lunar and Planetary Science Conference Proceedings* pp. 523–536.

Jones R. H., Villeneuve J. and Libourel G. (2018) Thermal Histories of Chondrules: Petrologic Observations and Experimental Constraints. In *Chondrules: Records of Protoplanetary Disk Processes* Cambridge Planetary Science. pp. 57–90.

Kataoka A., Tanaka H., Okuzumi S. and Wada K. (2013) Fluffy dust forms icy planetesimals by static compression. *Astronomy & Astrophysics* **557**, L4.

Kehm K., Hauri E. H., Alexander C. O. and Carlson R. W. (2003) High precision iron isotope measurements of meteoritic material by cold plasma ICP-MS. *Geochimica et Cosmochimica Acta* **67**, 2879–2891.

Kennedy A. K., Lofgren G. E. and Wasserburg G. J. (1993) An experimental study of trace element partitioning between olivine, orthopyroxene and melt in chondrules: equilibrium values and kinetic effects. *Earth and Planetary Science Letters* **115**, 177–195.

Kita N. T., Kimura M., Ushikubo T., Valley J. W. and Nyquist L. E. (2008) Oxygen isotope systematics of chondrules from the least equilibrated H chondrite.

Kita N. T., Nagahara H., Tachibana S., Tomomura S., Spicuzza M. J., Fournelle J. H. and Valley J. W. (2010) High precision SIMS oxygen three isotope study of chondrules in LL3 chondrites: Role of ambient gas during chondrule formation. *Geochimica et Cosmochimica Acta* **74**, 6610–6635.

Kleine T., Budde G., Hellman J. L., Kruijer T. S. and Burkhardt C. (2018) Tungsten Isotopes and the Origin of Chondrules and Chondrites. In *Chondrules: Records of Protoplanetary Disk Processes* Cambridge Planetary Science. Cambridge University Press.

Klerner S., Jones R. H., Palme H. and Shearer C. K. (2000) Trace elements and cathodoluminescence in refractory forsterites from Allende and Kaba. In *Lunar and Planetary Science Conference*

Kracher A., Scott E. R. and Keil K. (1984) Relict and other anomalous grains in chondrules: implications for chondrule formation. *Journal of Geophysical Research: Solid Earth* **89**, B559–B566.

Kropf A., Huss G. R., Krot A. N. and Pack A. (2009) Closed System Behavior of Alkalis in Type-1 Chondrules--Understanding Chondrules as Igneous Systems. In *Lunar and Planetary Science Conference*

Kropf A. and Pack A. (2008) Closed System Behavior of Chondrules-New Constraints for the Chondrule Forming Process. In *Lunar and Planetary Science Conference* p. 2222.

Krot A. N., Amelin Y., Cassen P. and Meibom A. (2005) Young chondrules in CB chondrites from a giant impact in the early solar system. *Nature* **436**, 989–992.

Krot A. N., Libourel G., Goodrich C. A. and Petaev M. I. (2004) Silica-rich igneous rims around magnesian chondrules in CR carbonaceous chondrites: Evidence for condensation origin from fractionated nebular gas. *Meteoritics & Planetary Science* **39**, 1931–1955.

Krot A. N., Nagashima K., van Kooten E. M. M. and Bizzarro M. (2017) Calcium–aluminum-rich inclusions recycled during formation of porphyritic chondrules from CH carbonaceous chondrites. *Geochimica et Cosmochimica Acta* **201**, 185–223.

Krot A. N., Nagashima K., Libourel G. and Miller K. E. (2018) Multiple Mechanisms of Transient Heating Events in the Protoplanetary Disk. In *Chondrules: Records of Protoplanetary Disk Processes* Cambridge Planetary Science. Cambridge University Press. pp. 11–56.

Kruijer T. S., Sprung P., Kleine T., Leya I., Burkhardt C. and Wieler R. (2012) Hf–W chronometry of core formation in planetesimals inferred from weakly irradiated iron meteorites. *Geochimica et cosmochimica acta* **99**, 287–304.

Kruijer T. S., Touboul M., Fischer-Gödde M., Bermingham K. R., Walker R. J. and Kleine T. (2014) Protracted core formation and rapid accretion of protoplanets. *Science* **344**, 1150–1154.

Kwon W., Looney L. W. and Mundy L. G. (2011) Resolving the circumstellar disk of HL Tauri at millimeter wavelengths. *The Astrophysical Journal* **741**, 3.

Larsen K. K., Trinquier A., Paton C., Schiller M., Wielandt D., Ivanova M. A., Connelly J. N., Nordlund Å., Krot A. N. and Bizzarro M. (2011) Evidence for magnesium isotope

heterogeneity in the solar protoplanetary disk. *The Astrophysical Journal Letters* **735**, L37.

Lee T., Papanastassiou D. A. and Wasserburg G. J. (1976) Correction [to "Demonstration of 26Mg excess in Allende and evidence for 26Al"]. *Geophysical Research Letters* **3**, 109–112.

Leroux H., Libourel G., Lemelle L. and Guyot F. (2003) Experimental study and TEM characterization of dusty olivines in chondrites: Evidence for formation by in situ reduction. *Meteoritics & Planetary Science* **38**, 81–94.

Leshin L. A., McKeegan K. D., Engrand C., Zanda B., Bourot-Denise M. and Hewins R. H. (1998) Oxygen isotopic studies of isolated and chondrule olivine from Renazzo and Allende. *Meteoritics and Planetary Science Supplement* **33**, A93.

Levy E. H. and Araki S. (1989) Magnetic reconnection flares in the photoplanetary nebula and the possible origin of meteorite chondrules. *Icarus* **81**, 74–91.

Lewis J. A. and Jones R. H. (2019) Primary feldspar in the Semarkona LL 3.00 chondrite: Constraints on chondrule formation and secondary alteration. *Meteoritics & Planetary Science* **54**, 72–89.

Li K., Liu J., Grovenor C. R. and Moore K. L. (2020) NanoSIMS Imaging and Analysis in Materials Science. *Annual Review of Analytical Chemistry* **13**.

Libourel G., Krot A. N. and Tissandier L. (2006) Role of gas-melt interaction during chondrule formation. *Earth and Planetary Science Letters* **251**, 232–240.

Libourel G. and Portail M. (2018) Chondrules as direct thermochemical sensors of solar protoplanetary disk gas. *Science advances* **4**, eaar3321.

Liffman K. (2009) A shocking solar nebula? *The Astrophysical Journal Letters* **694**, L41.

Lodders K. (2019) The Chemical Composition of the Solar System. In *Nuclei in the Cosmos XV* Springer. pp. 165–170.

Lofgren G. (1989) Dynamic cyrstallization of chondrule melts of porphyritic olivine composition: Textures experimental and natural. *Geochimica et Cosmochimica Acta* **53**, 461–470.

Lofgren G. E. (1996) *A dynamic crystallization model for chondrule melts. Pp. 187-196 in: Chondrules and the Protoplanetary Disk (R.H. Hewins, R.H. Jones, and E. R. D. Scott, editors)*., Cambridge University Press, Cambridge, UK.

Lofgren G. E. and Le L. (2000) Experimental evidence for a partial melting origin for most porphyritic chondrules. In *Lunar and Planetary Science Conference*

Lofgren G. and Lanier A. B. (1990) Dynamic crystallization study of barred olivine chondrules. *Geochimica et Cosmochimica Acta* **54**, 3537–3551.

Lofgren G. and Russell W. J. (1986) Dynamic crystallization of chondrule melts of porphyritic and radial pyroxene composition. *Geochimica et Cosmochimica Acta* **50**, 1715–1726.

Luu T.-H., Hin R. C., Coath C. D. and Elliott T. (2016) High Precision Mg-Isotope Measurements of Bulk Chondrites and the Homogeneity of 26Al in the Solar Nebula. In *79th Annual Meeting of the Meteoritical Society*

Mann C. R., Boley A. C. and Morris M. A. (2016) Planetary embryo bow shocks as a mechanism for chondrule formation. *The Astrophysical Journal* **818**, 103.

Mariani E., Prior D. J., McNamara D., Pearce M. A., Seaton N., Seward G., Tatham D. and Wheeler J. (2008) Electron backscatter diffraction (EBSD) in the SEM: applications to microstructures in minerals and rocks and recent technological advancements. *Seminarios de la Sociedad Espanola de Mineralogıa* **5**, 7–19.

Martin V. M., Morgan D. J., Jerram D. A., Caddick M. J., Prior D. J. and Davidson J. P. (2008) Bang! Month-scale eruption triggering at Santorini volcano. *Science* **321**, 1178–1178.

Matthews M. B. (2016) Performance Characteristics of WDS and EDS detectors. In *12th Regional Workshop on Electron Probe Microanalysis Today - Practical Aspects* European Microbeam Analysis Society, CEA Marcoule, France. pp. 83–114.

McCanta M. C., Beckett J. R. and Stolper E. M. (2016) Correlations and zoning patterns of phosphorus and chromium in olivine from H chondrites and the LL chondrite Semarkona. *Meteoritics & Planetary Science* **51**, 520–546.

McCanta M. C., Beckett J. R. and Stolper E. M. (2008) Zonation of phosphorus in olivine: Dynamic crystallization experiments and a study of chondrule olivine in unequilibrated ordinary chondrites. *LPI*, 1807.

McNally C. P., Hubbard A., Mac Low M.-M., Ebel D. S. and D'Alessio P. (2013) Mineral processing by short circuits in protoplanetary disks. *The Astrophysical Journal Letters* **767**, L2.

McSween H. Y. (1977) Carbonaceous chondrites of the Ornans type: A metamorphic sequence. *Geochimica et Cosmochimica Acta* **41**, 477–491.

Merlet C. (1994) An accurate computer correction program for quantitative electron probe microanalysis. *Microchimica Acta* **114**, 363–376.

Milman-Barris M. S., Beckett J. R., Baker M. B., Hofmann A. E., Morgan Z., Crowley M. R., Vielzeuf D. and Stolper E. (2008) Zoning of phosphorus in igneous olivine. *Contributions to Mineralogy and Petrology* **155**, 739–765.

Miyamoto M., Mikouchi T. and Jones R. H. (2009) Cooling rates of porphyritic olivine chondrules in the Semarkona (LL3. 00) ordinary chondrite: A model for diffusional equilibration of olivine during fractional crystallization. *Meteoritics & Planetary Science Archives* **44**, 521–530.

Morbidelli A. and Raymond S. N. (2016) Challenges in planet formation. *Journal of Geophysical Research: Planets* **121**, 1962–1980.

Morris M. A. and Boley A. C. (2018) Formation of Chondrules by Shockwaves. In *Chondrules: Records of Protoplanetary Disk Processes* Cambridge Planetary Science. Cambridge University Press. pp. 375–399.

Morris M. A., Boley A. C., Desch S. J. and Athanassiadou T. (2012) Chondrule formation in bow shocks around eccentric planetary embryos. *The Astrophysical Journal* **752**, 27.

Morris M. A. and Desch S. J. (2011) Thermal histories of chondrules: An assessment of the effect of a size distribution of precursor particles. *Meteoritics and Planetary Science Supplement* **74**.

Morris M. A. and Desch S. J. (2010) Thermal histories of chondrules in solar nebula shocks. *The Astrophysical Journal* **722**, 1474.

Morris M. A., Weidenschilling S. J. and Desch S. J. (2016) The effect of multiple particle sizes on cooling rates of chondrules produced in large-scale shocks in the solar nebula. *Meteoritics & Planetary Science* **51**, 870–883.

Mullane E., Russell S. S. and Gounelle M. (2005) Nebular and asteroidal modification of the iron isotope composition of chondritic components. *Earth and Planetary Science Letters* **239**, 203–218.

Myers J. t and Eugster H. P. (1983) The system Fe-Si-O: Oxygen buffer calibrations to 1,500 K. *Contributions to Mineralogy and Petrology* **82**, 75–90.

Nagashima K., Kita N. T. and Luu T. (2018) 26Al-26Mg Sysematics of Chondrules. In *Chondrules: Records of Protoplanetary Disk Processes* Cambridge Planetary Science. Cambridge University Press. pp. 247–275.

Nagashima K., Park C. and Krot A. N. (2015) An amoeboid olivine aggregate surrounded by an igneous ferroan olivine-rich rim from CO3. 0 chondrite DOM 08006.

Nakamoto T., Hayashi M. R., Kita N. T. and Tachibana S. (2005) Chondrule-forming shock waves in the solar nebula by X-ray flares. In *Chondrites and the protoplanetary disk* p. 883.

Nakamura T., Noguchi T., Tanaka M., Zolensky M. E., Kimura M., Tsuchiyama A., Nakato A., Ogami T., Ishida H. and Uesugi M. (2011) Itokawa dust particles: a direct link between S-type asteroids and ordinary chondrites. *Science* **333**, 1113–1116.

Natta A., Testi L., Calvet N., Henning T., Waters R. and Wilner D. (2006) Dust in proto-planetary disks: properties and evolution. *arXiv preprint astro-ph/0602041*.

Needham A. W., Porcelli D. and Russell S. S. (2009) An Fe isotope study of ordinary chondrites. *Geochimica et Cosmochimica Acta* **73**, 7399–7413.

Nielsen R. L. (1985) EQUIL: a program for the modeling of low-pressure differentiation processes in natural mafic magma bodies. *Computers & Geosciences* **11**, 531–546.

Norris T. L., Gancarz A. J., Rokop D. J. and Thomas K. W. (1983) Half-life of 26Al. *Journal of Geophysical Research: Solid Earth* **88**, B331–B333.

Olsen M. B., Wielandt D., Schiller M., Van Kooten E. M. and Bizzarro M. (2016) Magnesium and 54Cr isotope compositions of carbonaceous chondrite chondrules–Insights into early disk processes. *Geochimica et cosmochimica acta* **191**, 118–138.

Oshino S., Hasegawa Y., Wakita S. and Matsumoto Y. (2019) The Properties of Planetesimal Collisions under Jupiter's Perturbation and the Application to Chondrule Formation via Impact Jetting. *arXiv preprint arXiv:1909.03655*.

Palme H., Hezel D. C. and Ebel D. S. (2015) The origin of chondrules: Constraints from matrix composition and matrix-chondrule complementarity. *Earth and Planetary Science Letters* **411**, 11–19.

Pape J., Mezger K., Bouvier A.-S. and Baumgartner L. P. (2019) Time and duration of chondrule formation: Constraints from 26Al-26Mg ages of individual chondrules. *Geochimica et cosmochimica acta* **244**, 416–436.

Perez A. M. (2018) Can Porphyritic Chondrules Form in Planetary Embryo Bow Shocks? Arizona State University.

Pérez L. M., Carpenter J. M., Andrews S. M., Ricci L., Isella A., Linz H., Sargent A. I., Wilner D. J., Henning T. and Deller A. T. (2016) Spiral density waves in a young protoplanetary disk. *Science* **353**, 1519–1521.

Petry C., Chakraborty S. and Palme H. (2004) Experimental determination of Ni diffusion coefficients in olivine and their dependence on temperature, composition, oxygen fugacity, and crystallographic orientation. *Geochimica et Cosmochimica Acta* **68**, 4179–4188.

Pouchou J. L. and Pichoir F. (1987) Basic expression of "PAP" computation for quantitative EPMA. *Proceedings of ICXOM* **11**, 249–253.

Radomsky P. M. and Hewins R. H. (1990) Formation conditions of pyroxene-olivine and magnesian olivine chondrules. *Geochimica et Cosmochimica Acta* **54**, 3475–3490.

Rambaldi E. R. (1981) Relict grains in chondrules. *Nature* **293**, 558.

Rambaldi E. R. and Wasson J. T. (1981) Metal and associated phases in Bishunpur, a highly unequilibrated ordinary chondrite. *Geochimica et Cosmochimica Acta* **45**, 1001–1015.

Raymond S. N. (2007) Terrestrial planet formation in extra-solar planetary systems. *Proceedings of the International Astronomical Union* **3**, 233–250.

Reed S. J. B. (2005) *Electron microprobe analysis and scanning electron microscopy in geology*., Cambridge University Press.

Richardson S. M. (1981) Alteration of mesostasis in chondrules and aggregates from three C2 carbonaceous chondrites. *Earth and Planetary Science Letters* **52**, 67–75.

Roberts W. L., Campbell T. J. and Rapp G. R. (1990) *Encyclopedia of minerals*., Van Nostrand Reinhold.

Rocha S. E. and Jones R. H. (2012) An experimental study of the conditions of type II chondrule formation in ordinary chondrites. In *Lunar and Planetary Science Conference*

Rubin A. E. (1984) Coarse-grained chondrule rims in type 3 chondrites. *Geochimica et Cosmochimica Acta* **48**, 1779–1789.

Rubin A. E. (2010) Physical properties of chondrules in different chondrite groups: Implications for multiple melting events in dusty environments. *Geochimica et Cosmochimica Acta* **74**, 4807–4828.

Rubin A. E., Sailer A. L. and Wasson J. T. (1999) Troilite in the chondrules of type-3 ordinary chondrites: Implications for chondrule formation. *Geochimica et Cosmochimica Acta* **63**, 2281–2298.

Rubin A. E. and Wasson J. T. (2005) Non-spherical lobate chondrules in CO3. 0 Y-81020: General implications for the formation of low-FeO porphyritic chondrules in CO chondrites. *Geochimica et cosmochimica acta* **69**, 211–220.

Ruzicka A., Floss C. and Hutson M. (2008) Relict olivine grains, chondrule recycling, and implications for the chemical, thermal, and mechanical processing of nebular materials. *Geochimica et Cosmochimica Acta* **72**, 5530–5557.

Ruzicka A., Grossman J., Bouvier A. and Agee C. B. (2017) The Meteoritical Bulletin, No. 103. *Meteorit. Planet. Sci* **52**, 1014.

Ruzicka A., Hiyagon H., Hutson M. and Floss C. (2007) Relict olivine, chondrule recycling, and the evolution of nebular oxygen reservoirs. *Earth and Planetary Science Letters* **257**, 274–289.

Sanders I. S. and Scott E. R. (2012) The origin of chondrules and chondrites: Debris from low-velocity impacts between molten planetesimals? *Meteoritics & Planetary Science* **47**, 2170–2192.

Schneider C. A., Rasband W. S. and Eliceiri K. W. (2012) NIH Image to ImageJ: 25 years of image analysis. *Nature methods* **9**, 671.

Schrader D. L., Nagashima K., Davidson J., McCoy T. J., Ogliore R. C. and Fu R. R. (2020) Relict Grains with a Non-Local Origin: Evidence for UOC Chondrule Migration into the CM Chondrite Chondrule Forming Region. *LPI*, 1643.

Schwinger S., Dohmen R. and Schertl H.-P. (2016) A combined diffusion and thermal modeling approach to determine peak temperatures of thermal metamorphism experienced by meteorites. *Geochimica et Cosmochimica Acta* **191**, 255–276.

Scott E. R. D. (2007) Chondrites and the Protoplanetary Disk. *Annual Review of Earth and Planetary Sciences* **35**, 577–620.

Scott E. R. D. and Krot A. N. (2003) Chondrites and their components. *Treatise on geochemistry* **1**, 711.

Scott E. R. and Jones R. H. (1990) Disentangling nebular and asteroidal features of C03 carbonaceous chondrite meteorites. *Geochimica et Cosmochimica Acta* **54**, 2485–2502.

Scott E. R. and Krot A. N. (2005) Chondritic meteorites and the high-temperature nebular origins of their components. In *Chondrites and the protoplanetary disk* p. 15.

Scott E. R. and Taylor G. J. (1983) Chondrules and other components in C, O, and E chondrites: Similarities in their properties and origins. *Journal of Geophysical Research: Solid Earth* **88**.

Sears D. W., Grossman J. N., Melcher C. L., Ross L. M. and Mills A. A. (1980) Measuring metamorphic history of unequilibrated ordinary chondrites. *Nature* **287**, 791–795.

Shea T., Costa F., Krimer D. and Hammer J. E. (2015) Accuracy of timescales retrieved from diffusion modeling in olivine: A 3D perspective. *American Mineralogist* **100**, 2026–2042.

Shu F. H., Shang H., Glassgold A. E. and Lee T. (1997) X-rays and fluctuating X-winds from protostars. *Science* **277**, 1475–1479.

Shu F. H., Shang H., Gounelle M., Glassgold A. E. and Lee T. (2001) The origin of chondrules and refractory inclusions in chondritic meteorites. *The Astrophysical Journal* **548**, 1029.

Shu F. H., Shang H. and Lee T. (1996) Toward an astrophysical theory of chondrites. *SCIENCE-NEW YORK THEN WASHINGTON-*, 1545–1551.

Smyth J. R. (1974) Experimental study on the polymorphism of enstatite. *American Mineralogist: Journal of Earth and Planetary Materials* **59**, 345–352.

Sorby H. C. (1877) On the structure and origin of meteorites. *Nature* **15**, 495–498.

Soulié C., Libourel G. and Tissandier L. (2017) Olivine dissolution in molten silicates: An experimental study with application to chondrule formation. *Meteoritics & Planetary Science* **52**, 225–250.

Sparks R. S. J., Meyer P. and Sigurdsson H. (1980) Density variation amongst mid-ocean ridge basalts: implications for magma mixing and the scarcity of primitive lavas. *Earth and Planetary Science Letters* **46**, 419–430.

Stammler S. M. and Dullemond C. P. (2014) A critical analysis of shock models for chondrule formation. *Icarus* **242**, 1–10.

Steele I. M. (1986) Compositions and textures of relic forsterite in carbonaceous and unequilibrated ordinary chondrites. *Geochimica et Cosmochimica Acta* **50**, 1379–1395.

Steele I. M., Smith J. V. and Skirius C. (1985) Cathodoluminescence zoning and minor elements in forsterites from the Murchison (C2) and Allende (C3V) carbonaceous chondrites. *Nature* **313**, 294.

Sutton S. R., Bajt S. and Jones R. (1996) In situ determination of chromium oxidation state in olivine from chondrules. In *Lunar and Planetary Science Conference*

Tachibana S., Tamada S., Kawasaki H., Ozawa K. and Nagahara H. (2013) Interdiffusion of Mg–Fe in olivine at 1,400–1,600° C and 1 atm total pressure. *Physics and Chemistry of Minerals* **40**, 511–519.

Tanga P., Babiano A., Dubrulle B. and Provenzale A. (1996) Forming planetesimals in vortices. *Icarus* **121**, 158–170.

Taylor S., Delaney J., Ma P., Herzog G. F. and Engrand C. (2005) Isotopic fractionation of iron, potassium, and oxygen in stony cosmic spherules: Implications for heating histories and sources. *Geochimica et Cosmochimica Acta* **69**, 2647–2662.

Tenner T. J., Nakashima D., Ushikubo T., Kita N. T. and Weisberg M. K. (2015) Oxygen isotope ratios of FeO-poor chondrules in CR3 chondrites: Influence of dust enrichment and H2O during chondrule formation. *Geochimica et Cosmochimica Acta* **148**, 228–250.

Tenner T. J., Ushikubo T., Nakashima D., Schrader D. L., Weisberg M. K., Kimura M. and Kita N. T. (2018) Oxygen Isotope Characteristics of Chondrules. In *Chondrules: Records of Protoplanetary DIsk Processes* Cambridge Planetary Science. Cambridge University Press. pp. 196–246.

Throop H. B. and Bally J. (2005) Can photoevaporation trigger planetesimal formation? *The Astrophysical Journal Letters* **623**, L149.

Tissandeer L., Libourel G. and Robert F. (2002) Gas-melt interactions and their bearing on chondrule formation. *Meteoritics & Planetary Science* **37**, 1377–1389.

Tsuchiyama A., Osada Y., Nakano T. and Uesugi K. (2004) Experimental reproduction of classic barred olivine chondrules: Open-system behavior of chondrule formation. *Geochimica et cosmochimica acta* **68**, 653–672.

Tsuchiyama A., Uesugi M., Matsushima T., Michikami T., Kadono T., Nakamura T., Uesugi K., Nakano T., Sandford S. A. and Noguchi R. (2011) Three-dimensional structure of Hayabusa samples: origin and evolution of Itokawa regolith. *Science* **333**, 1125–1128.

Urey H. C. and Craig H. (1953) The composition of the stone meteorites and the origin of the meteorites. *Geochimica et Cosmochimica Acta* **4**, 36–82.

Ushikubo T., Kimura M., Kita N. T. and Valley J. W. (2012) Primordial oxygen isotope reservoirs of the solar nebula recorded in chondrules in Acfer 094 carbonaceous chondrite. *Geochimica et Cosmochimica Acta* **90**, 242–264.

Van Kooten E. M., Wielandt D., Schiller M., Nagashima K., Thomen A., Larsen K. K., Olsen M. B., Nordlund Å., Krot A. N. and Bizzarro M. (2016) Isotopic evidence for primordial molecular cloud material in metal-rich carbonaceous chondrites. *Proceedings of the National Academy of Sciences* **113**, 2011–2016.

Van Schmus W. R. and Wood J. A. (1967) A chemical-petrologic classification for the chondritic meteorites. *Geochimica et Cosmochimica Acta* **31**, 747–765.

Villeneuve J., Chaussidon M. and Libourel G. (2009) Homogeneous distribution of 26Al in the solar system from the Mg isotopic composition of chondrules. *Science* **325**, 985–988.

Villeneuve J., Libourel G. and Soulié C. (2015) Relationships between type I and type II chondrules: Implications on chondrule formation processes. *Geochimica et Cosmochimica Acta* **160**, 277–305.

Wakaki S., Itoh S., Tanaka T. and Yurimoto H. (2013) Petrology, trace element abundances and oxygen isotopic compositions of a compound CAI–chondrule object from Allende. *Geochimica et Cosmochimica Acta* **102**, 261–279.

Wakita S., Matsumoto Y., Oshino S. and Hasegawa Y. (2017) Planetesimal collisions as a chondrule forming event. *The Astrophysical Journal* **834**, 125.

Ward W. R. (1996) Planetary accretion. In *Completing the Inventory of the solar system* pp. 337–361.

Wasson J. T. (2004) Petrographic evidence for rapid heating and cooling during chondrule formation. In *Workshop on Chondrites and the Protoplanetary Disk* p. 9113.

Wasson J. T. and Rubin A. E. (2003) Ubiquitous low-FeO relict grains in type II chondrules and limited overgrowths on phenocrysts following the final melting event. *Geochimica et Cosmochimica Acta* **67**, 2239–2250.

Watson E. B. (2004) A conceptual model for near-surface kinetic controls on the trace-element and stable isotope composition of abiogenic calcite crystals1. *Geochimica et Cosmochimica Acta* **68**, 1473–1488.

Watson E. B., Cherniak D. J. and Holycross M. E. (2015) Diffusion of phosphorus in olivine and molten basalt. *American Mineralogist* **100**, 2053–2065.

Watson E. B. and Liang Y. (1995) A simple model for sector zoning in slowly grown crystals: Implications for growth rate and lattice diffusion, with emphasis on accessory minerals in crustal rocks. *American Mineralogist* **80**, 1179–1187.

Weidenschilling S. J. and Cuzzi J. N. (2006) Accretion dynamics and timescales: Relation to chondrites. *Meteorites and the early solar system II* **1**, 473–485.

Weinbruch S., Buettner H., Holzheid A., Rosenhauer M. and Hewins R. H. (1998) On the lower limit of chondrule cooling rates: The significance of iron loss in dynamic crystallization experiments. *Meteoritics & Planetary Science* **33**, 65–74.

Weinbruch S. and Müller W. F. (1995) Constraints on the cooling rates of chondrules from the microstructure of clinopyroxene and plagioclase. *Geochimica et Cosmochimica Acta* **59**, 3221–3230.

Weinbruch S., Müller W. F. and Hewins R. H. (2001) A transmission electron microscope study of exsolution and coarsening in iron-bearing clinopyroxene from synthetic analogues of chondrules. *Meteoritics & Planetary Science* **36**, 1237–1248.

Weisberg M. K., Smith C., Benedix G., Herd C. D., Righter K., Haack H., Yamaguchi A., Aoudjehane H. C. and Grossman J. N. (2009) The Meteoritical Bulletin, No. 96, September 2009. *Meteoritics & Planetary Science* **44**, 1355–1397.

Weiss B. P. and Elkins-Tanton L. T. (2013) Differentiated planetesimals and the parent bodies of chondrites. *Annual Review of Earth and Planetary Sciences* **41**, 529–560.

Wick M. J. and Jones R. H. (2012) Formation conditions of plagioclase-bearing type I chondrules in CO chondrites: A study of natural samples and experimental analogs. *Geochimica et Cosmochimica Acta* **98**, 140–159.

Wick M. J., Jones R. H., Morris M. and Desch S. J. (2010) Formation conditions of type I chondrules: Comparison of experimentally determined cooling rates with the shock wave model for chondrule formation. *Meteoritics and Planetary Science Supplement* **73**, 5278.

Wood J. A. (1996) Processing of chondritic and planetary material in spiral density waves in the nebula. *Meteoritics & Planetary Science* **31**, 641–645.

Yoneda S. and Grossman L. (1995) Condensation of CaOMgOAl2O3SiO2 liquids from cosmic gases. *Geochimica et Cosmochimica Acta* **59**, 3413–3444.

Youdin A. N. and Chiang E. I. (2004) Particle pileups and planetesimal formation. *The Astrophysical Journal* **601**, 1109.

Youdin A. N. and Goodman J. (2005) Streaming instabilities in protoplanetary disks. *The Astrophysical Journal* **620**, 459.

Yu Y. and Hewins R. H. (1998) Transient heating and chondrule formation: Evidence from sodium loss in flash heating simulation experiments. *Geochimica et Cosmochimica Acta* **62**, 159–172.

Yurimoto H., Abe K., Abe M., Ebihara M., Fujimura A., Hashiguchi M., Hashizume K., Ireland T. R., Itoh S. and Katayama J. (2011) Oxygen isotopic compositions of asteroidal materials returned from Itokawa by the Hayabusa mission. *Science* **333**, 1116–1119.

Zahnle K., Arndt N., Cockell C., Halliday A., Nisbet E., Selsis F. and Sleep N. H. (2007) Emergence of a habitable planet. *Space Science Reviews* **129**, 35–78.

Zanda B., Lewin E. and Humayun M. (2018) The Chondritic Assemblage: Complementarity Is Not a Required Hypothesis. In *Chondrules: Records of Protoplanetary Disk Processes* Cambridge Planetary Science. Cambridge University Press. pp. 122–150.

Zhu X. K., Guo Y., O'Nions R. K., Young E. D. and Ash R. D. (2001) Isotopic homogeneity of iron in the early solar nebula. *Nature* **412**, 311.

Appendix A
Diffusion model instructions

This appendix describes the diffusion model used in this thesis and provides instructions for its use. The final section is a worked example, which guides the reader through the steps required to run the diffusion model. The diffusion model can be found on the supplementary materials CD along with a completed copy of the worked example.

A1. Opening a new file

On opening the diffusion model excel file (Contained in the supplementary materials: *F. Diffusion model/FiniteModel_ShiftBoundary_morecorrect*) you will be presented with the screen shown in Figure A1. The spreadsheet is divided into three sections: the uppermost sections above the solid green line is the initial parameters section; the middle section between the solid green line and the upper solid blue line is where calculations take place; the lower area below the two solid blue lines are where resulting model diffusion profiles are shown after each time step.

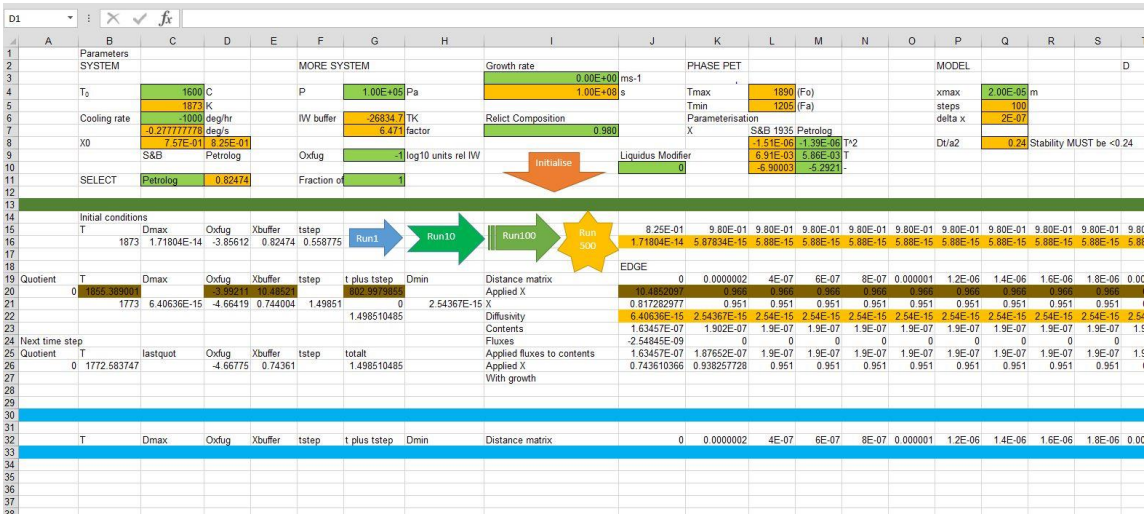

Figure A1 – The initial diffusion model excel file.

A2. Setting up initial parameters

The first step in using the diffusion mode is to set the initial conditions in the uppermost section. Only values in green cells should be modified as yellow cells show parameters which should not be modified, with some possible exceptions which are mentioned.

- The first initial condition to set is T_0 (Cell C4, Figure A2), or the initial temperature in °C. This is converted to K in the cell below (Cell C5, Figure A2). For diffusion models run in this work, this is the chondrule liquidus temperature calculated from the chondrule bulk composition using Petrolog3 (Danyushevsky and Plechov, 2011).
- The second parameter is the initial cooling rates in Kh^{-1}, which is entered into cell C6, Figure A2.
- The third input is to choose how equilibrium olivine composition is calculated. The first option is to use the pure olivine binary loop from Bowen and Schairer (1935).

This is achieved by entering "S&B" into cell C11, Figure A2. The second option is to calculate the equilibrium olivine from an olivine-saturated liquidus curve calculated from the chondrule bulk composition, for example, by using modelling software Petrolog3 (Danyushevsky and Plechov, 2011). To select the externally calculated option, enter "Petrolog" into cell C7, Figure A2 (even if Petrolog3 was not used to calculate the olivine-saturated liquidus curve). Cell D11 will show the value of the crystal edge buffer composition at the initial temperature in mole fraction of forsterite.

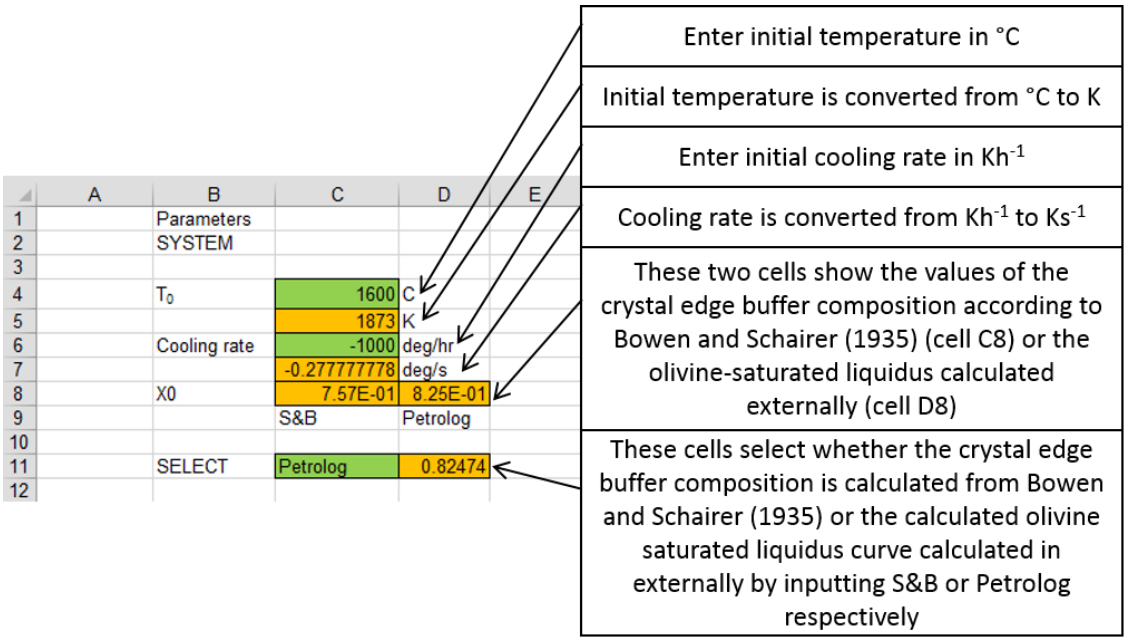

Figure A2 – Cells where initial temperature (T0) and cooling rates are entered as well as which crystal edge buffer composition is used.

- If using an externally calculated olivine-saturated liquidus curve, values for A, B and C in Equation A1 should be entered into cells M8, M9 and M10 respectively (see Figure A3).

$$Fo = AT^2 + BT + C$$

Equation A1 – General quadratic equation for the olivine-saturated liquidus, where Fo is the forsterite mole fraction of the olivine saturated liquidus in and T is temperature in K.

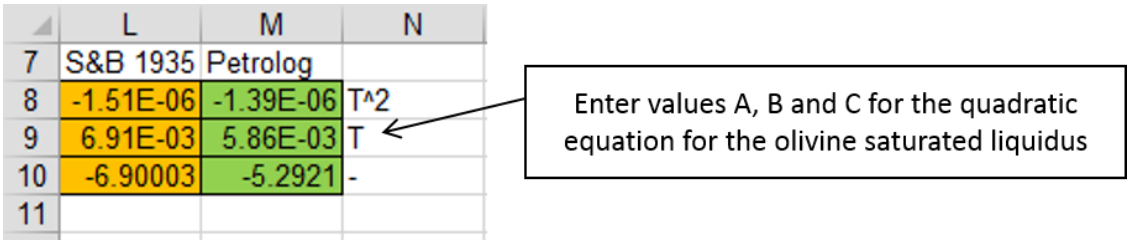

Figure A3 – Cells where A, B and C for the quadratic equation for the olivine saturated liquidus (Equation A1) should be entered. A, B and C should be entered into cells M8, M9 and M10 respectively. Column L shows these values for Bowen and Schairer (1935).

- The next parameter to input is pressure in Pa into cell G4, Figure A4. As pressure only begins to affect Fe-Mg diffusivity at relatively high pressures comparable to several km depth in the Earth, this can usually be left at 10^5 Pa (See Chapter 5).
- Oxygen fugacity in log units relative to the iron-wüstite buffer (Myers and Eugster, 1983) is entered into cell G9, Figure A4.
- The fraction of c-axis diffusion speed caused by diffusion anisotropy along the diffusion profile is entered into cell G11, Figure A4. This should be a value between 1 (diffusion along the c-axis) and $\frac{1}{6}$ (diffusion along the a- or b-axis). This must be calculated externally (e.g. Costa et al. 2008).

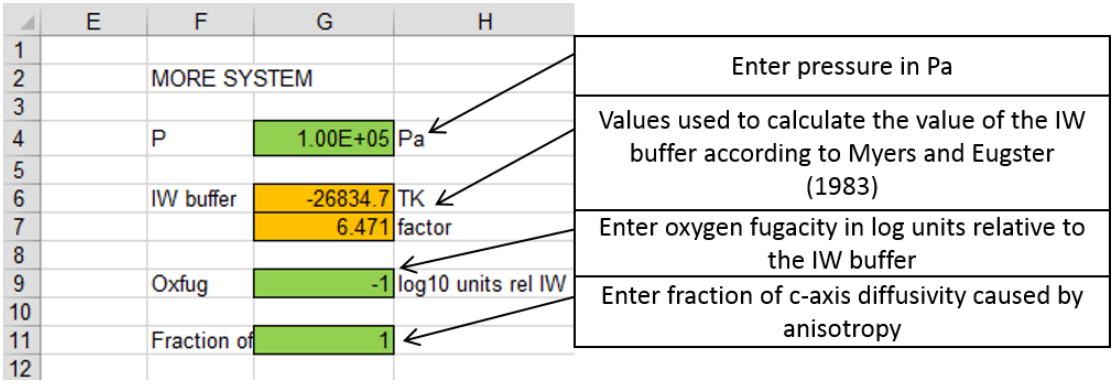

Figure A4 – Cells where pressure, oxygen fugacity relative to the iron-wüstite buffer and fraction of c-axis diffusivity along the profile caused by diffusion anisotropy.

- Crystal growth rate in ms^{-1} is entered into Cell I3, Figure A5. This is converted into length of time required to grow a new cell onto the edge of the crystal which is related to the length scale of the model in m, which is entered into cell Q4, Figure A6.
- Core composition in forsterite mole fraction is entered into cell I7, Figure A6.

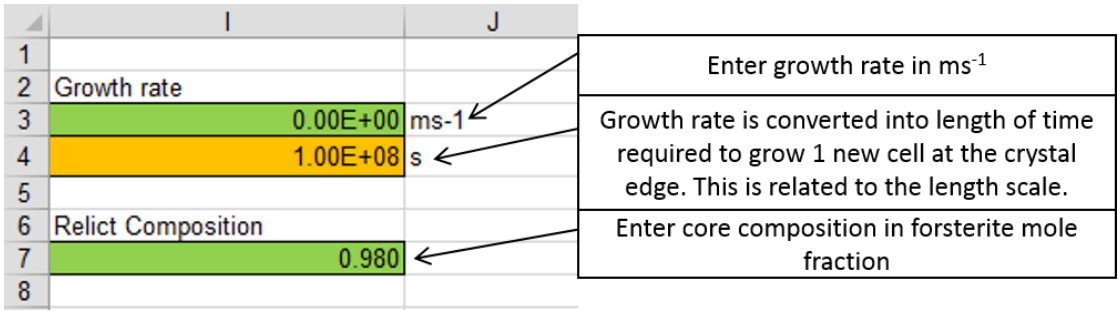

Figure A5 – Cells where growth rate and core composition are entered.

- Cell Q8, Figure A6, which appears yellow, is a stability factor which is involved in the calculation of length of a time step. Larger numbers allow for longer time steps which move more material allowing models to run faster, however, if this cell is larger than 0.24, the model becomes numerically unstable. In some circumstances, for example, using very rapid cooling rates, it may be useful to reduce this value to decrease time step length.

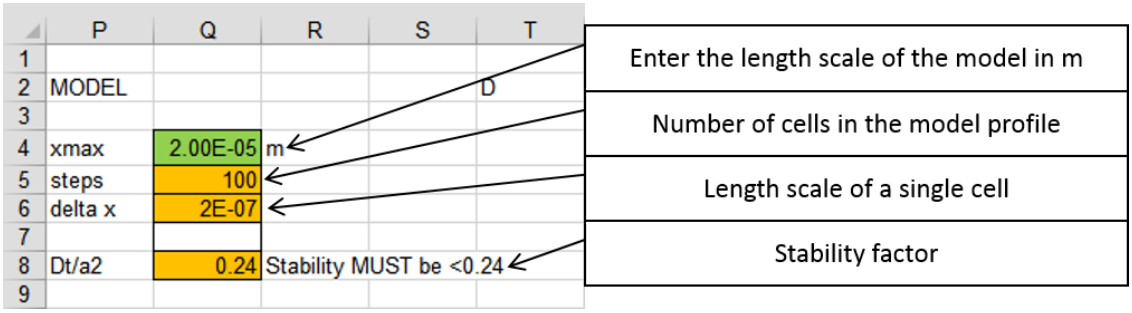

Figure A6 – Cells where the length scale of the model diffusion profile is entered

- The cells shown in Figure A7 show the values used to calculate the Fe-Mg diffusion coefficients in olivine according to (Dohmen and Chakraborty, 2007). Column V shows the values used to calculate the diffusion coefficient in the Transition Metal Extrinsic Domain (TaMED) at oxygen fugacity above 10^{-10} Pa. Column Y shows the values used to calculate diffusivity in the Purely Extrinsic Domain (PED) at oxygen fugacity below 10^{-10} Pa. The value in cell AA4 shows the oxygen fugacity that the switch between TaMED and PED occurs.

	T	U	V	W	X	Y	Z	AA	AB
1									
2	D	TaMED				PED		SWITCH	
3									
4		logD0	-9.21	m2s-1		-8.91	m2s-1	-10	log Pa
5		DH	201000	J Mol-1		220000	J Mol-1		
6		Pterm	7.00E-06	factor		7.00E-06	factor		
7		Pnorm	1.00E+05	Pa		1.00E+05	Pa		
8	24	Oterm	0.166667	factor					
9		Onorm	-7.00E+00	logPa					
10		X factor	3	Factor		3	Factor		
11		log units across rangefrom Fo to Fa							
12									

Figure A7 – Cells which contain values to calculate the Fe-Mg diffusion coefficient along the mode diffusion profiles. Column V is used to calculate diffusivity in the Transition Metal Extrinsic Domain (TaMED) ot oxygen fugacity above 10-10 Pa, while column Y is used to calculate diffusivity in the Purely Extrinsic Domain at oxygen fugacity below 10-10. Column AA shows the value at which the transition occurs between TaMED and PED (Dohmen and Chakraborty 2007).

Once the initial parameters set up correctly, the next stage is to initialise the model by clicking the initialise arrow in column I shown in Figure A8. This runs a macro which transfers the initial conditions to the calculations section and resets the calculations to the start of a new run.

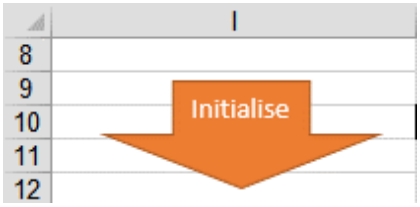

Figure A8 – The initialise arrow. Clicking on this transfers the initial parameters to the calculation area.

A3. The calculations section and running time steps

Once the model has been initialised, many cells should match values in the initial conditions. The initial temperature should be shown in cells C5, B16 and B21 (red in Figure A9). The crystal edge buffer composition should be shown in cells D11, E16, E21, J15 and J21 (light blue in Figure A9). The core composition should be shown in cell I7 and arrays K15:DF15 and K21:DF21 (dark blue in Figure A9). The distance between cells, in m, shown in cell Q6 should also appear in K19 (pink in Figure A9). The value of cells to the right should also increase in multiples of this value until cell DF19, which should match the length scale of the model in cell Q4.

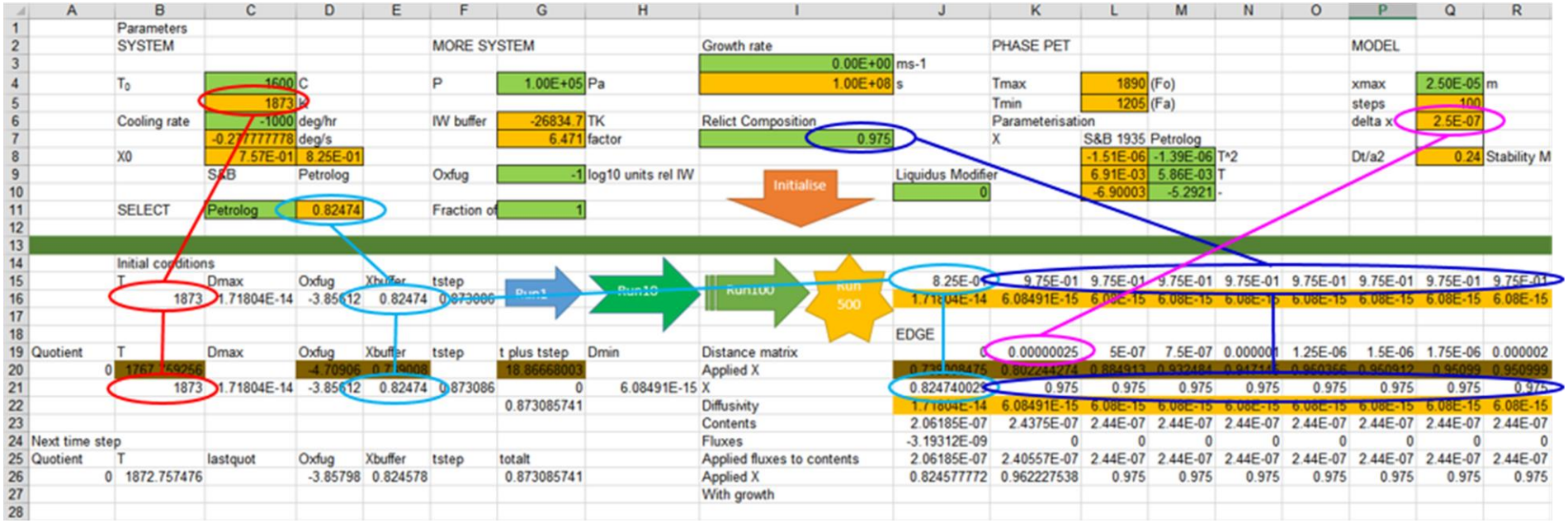

Figure A9 – Initial conditions and calculations sections annotated to show which cells should show identical values. In red is the initial temperature in cells C5, B16 and B21. Light blue shows the crystal edge buffer composition in cells D11, E16, E21, J15 and J21. Dark blue shows the crystal core composition in cells I7, K7:DF7 and K21:DF21. Pink shows the length between cells, cell Q6 should match cell K19.

If the model has correctly initialised, the next stage is to run time steps. This is achieved by clicking one of four run time shapes shown in Figure A10. Clicking on these runs a macro performing a series of calculations to run a time step which is then repeated 10, 100 or 500 times depending upon which shape is clicked.

Figure A10 – Shapes which when clicked will run the corresponding number of time steps.

Running a time step starts a series of calculations, which are fully described in Chapter 5, are outlined here. One of the first calculations involved in a time step is to calculate the length of the time step. As this is an explicit finite difference forward modelling program, it relies upon relatively simple approximations to diffusion behaviour which are extrapolated over large datasets. This is only valid when flux of material is low, which is only achieved with small time steps. The length of time steps in the model is related to the stability factor (see Equation A2) in cell Q8, Figure A6, and is calculated using Equation A3.

$$Stability\ Factor = \frac{Dt}{a^2}$$

Equation A2 - Equation to calculate the stability factor. To keep the model numerically stable, this must be ≤ 0.24. D is diffusion coefficient, t is time step length in s, and a is the length scale of diffusion for a single cell in m.

$$Time\ step\ length = \frac{stability\ factor \times x^2}{D}$$

Equation A3 - Equation showing how the time step length is calculated in the model. Stability factor must be ≤ 0.24, x is the length scale of diffusion for a single cell in m and D is the maximum diffusion coefficient in the current time step along the model diffusion profile.

Another calculation involved in a time step is to calculate the crystal edge buffer composition. This is calculated using the values in cells M8, M9 and M10 (see Figure A3) in Equation A1 using the temperature during the time step.

The next step calculates the fluxes between the cells along the model diffusion profile. This is achieved by using a small variation of Fick's first law.

$$\frac{\partial C_t}{\partial t} = -D\frac{\partial C_x}{\partial x}$$

Equation A4 – Small variation of Fick's first law, where ∂Ct is change in abundance of material with respect to time in forsterite mole fraction, ∂t is time step length in s, D is the diffusion coefficient in m2s-1, ∂Cx is the difference in composition between the two cells in forsterite mole fraction, and ∂x is the distance between the two cells in m.

$$\partial C_t = -D\frac{\partial C_x}{\partial x} \times \partial t$$

Equation A5 – Equation used to calculate the amount of material moved in a time step due to diffusion where ∂Ct is change in abundance of material with respect to time in forsterite mole fraction, D is the diffusion coefficient in m2s-1, ∂x is the distance between the two cells in m and ∂t is time step length in s.

The next stage during the calculations are to determine whether enough time has passed to add a growth increment. This is determined from the growth rate in cell I3 (Figure A5) as shown in Equation A6. The time passed in the model is compared to this value to determine if a new cell is required. If a growth increment is required, all the cells are moved one cell to the right and a new cell is created with the current edge buffer composition.

$$time\ for\ growth\ of\ a\ cell = \frac{length\ scale\ of\ cell}{growth\ rate}$$

Equation A6 – Equation used to calculate time required to grow one new cell.

The final stage in the calculation is to change the temperature due to cooling during the time step.

A4. Changing parameters during a model run

Some of the initial parameters can be changed between time steps including cooling rate, pressure, oxygen fugacity with respect to the iron-wüstite buffer and growth rate. To achieve this, modify the appropriate cell (cooling rate, C6; pressure, G4; oxygen fugacity relative to the iron-wüstite buffer, G9; growth rate, I3). The conditions in the current time step are already set, therefore modification to these parameters only occur in the following time step. This means that changes must be made in the time step before the necessary change.

When modifying cooling rate in cell C5, there should be a corresponding change in cell B26 reflecting a different temperature change because of the modified cooling rate. Modifying pressure in cell G4 causes a corresponding change in diffusivity and provided the pressure change is high enough, this alters the diffusion coefficients and an effect should be noted in many places throughout the calculations sections to reflect this. The easiest cells to check

whether this has occurred are cells C21 and H21. Changing oxygen fugacity also results in changes to the diffusion coefficients causing similar changes throughout the calculations section, most notably cells D16, D21 and D26 as well as C21 and H21. Modifying growth rate may cause a change in cell A26 which would cause the spreadsheet to add a growth increment in the next time step. Figure A11 shows where changes to these parameters take effect. Overrunning the temperature, time, or composition where a modification of the initial conditions is required will mean that the model must be repeated from the start.

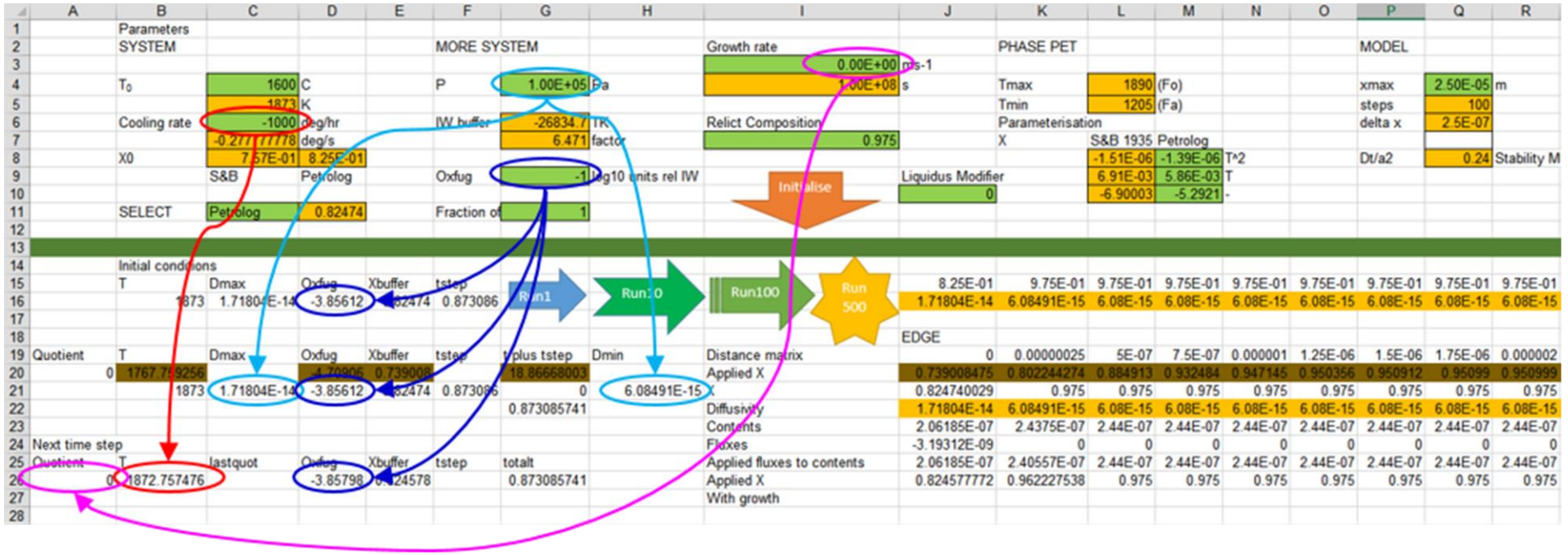

Figure A11 – Initial conditions which can be changed between time steps. Arrows indicate cells where significant changes may occur to indicate that modification of the conditions was successful. Red shows cooling rate in cell C6 and the corresponding change in temperature in cell B26. Light blue shows pressure in cell G4 and corresponding changes in maximum and minimum diffusion coefficients in cells C21 and H21 respectively. Dark blue shows oxygen fugacity in cell G9 and corresponding changes in oxygen fugacity in cells D16, D21 and D26. Pink shows growth rate in cell I4 and a possible corresponding change in cell A26.

A5. Results

The results of each time step are stored in the results section below the two blue lines in Figure A1. After each time step the resulting diffusion profile is displayed in reverse order, along with the temperature, oxygen fugacity, crystal edge buffer composition, minimum and maximum diffusion coefficients along the diffusion profile, length of the time step and total time. Examples of uses for this data are tracking model diffusion profiles over time (e.g. Figure A12) and temperature-time plots (e.g. Figure A13).

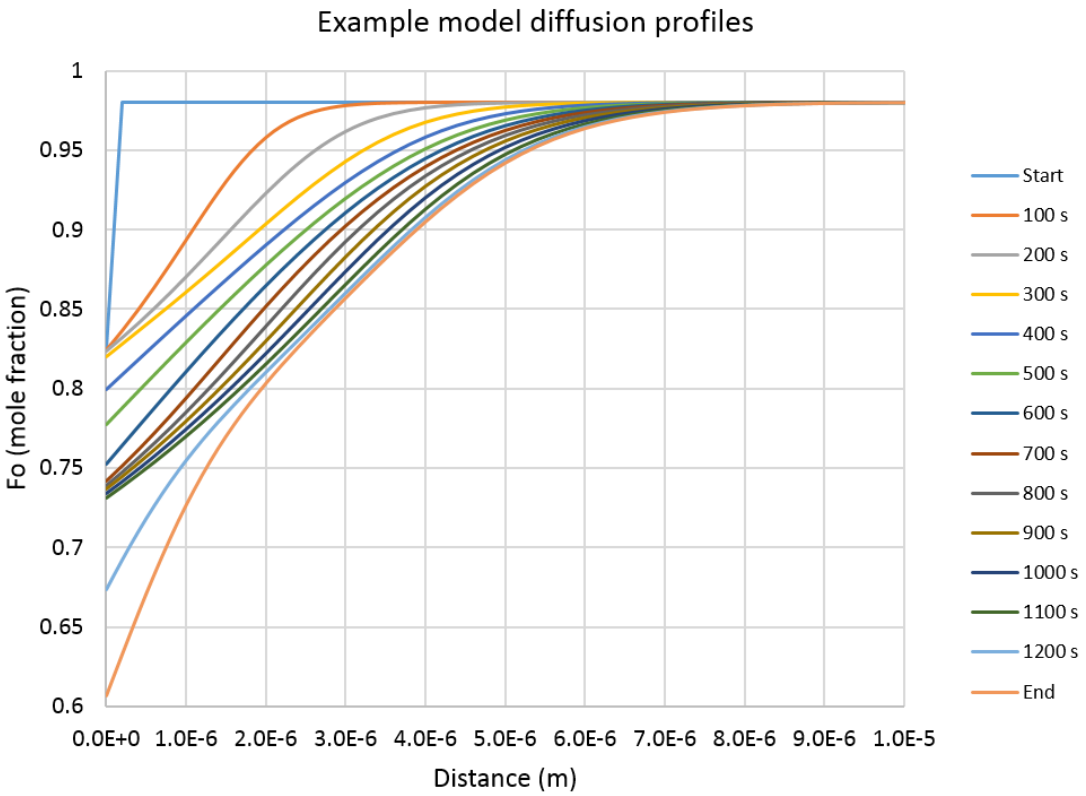

Figure A12 – Example model diffusion profiles created using the temperature time history shown in Figure A13

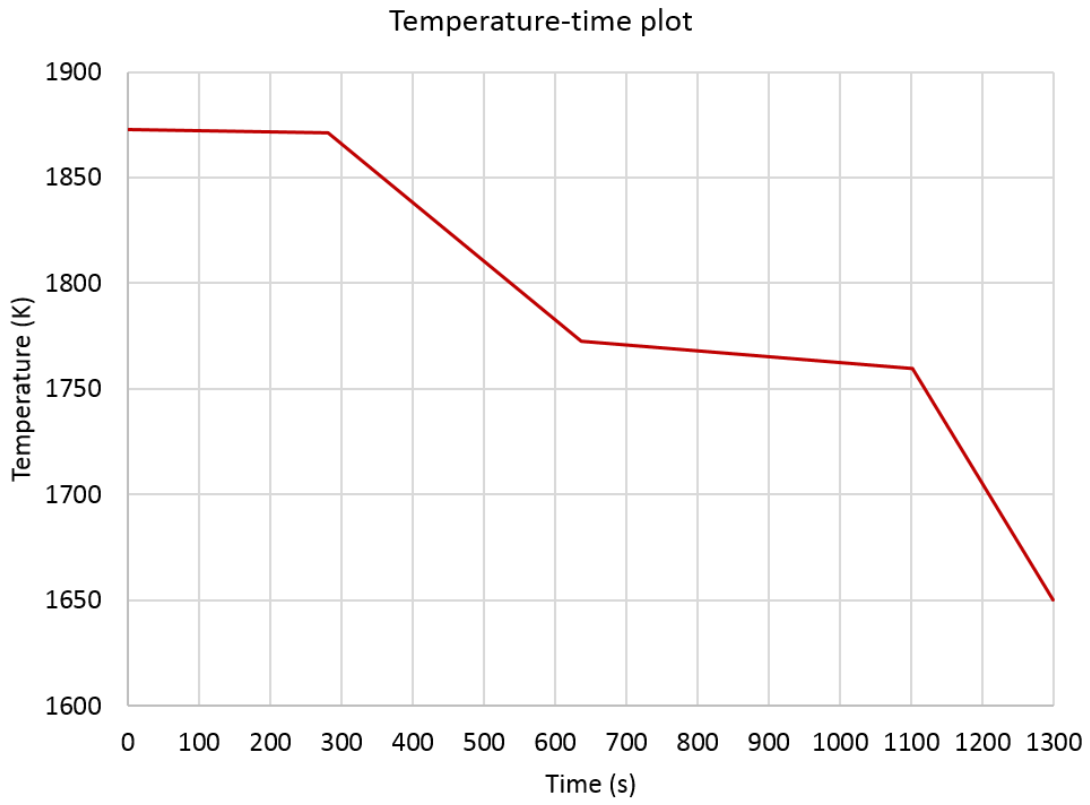

Figure A13 - Temperature time plot for the model run for the diffusion profiles in Figure A12

A6. Worked example

This section will guide the reader through a worked example with a relatively simple 2 stage thermal history.

The first stage is to input the initial conditions into the initial parameters section from Table A1, then press the initialise arrow. The initial parameters section should appear as in Figure A14.

Table A1 - Initial conditions to input into the worked example diffusion model

Initial condition	Cell	Value
Initial temperate, T_0 (°C)	C4	1650
Cooling rate (Kh^{-1})	C6	-800
Pressure, P (Pa)	G4	100000
Oxygen fugacity	G9	0
Fraction of c-axis speed	G11	1
Growth rate	I3	0
Relict composition	I7	0.990
Values for the olivine saturated liquidus	M8, M9, M10	-1.2E-6, 5.1E-3, -4.6
Length scale of model diffusion profile	Q4	2.5E-5

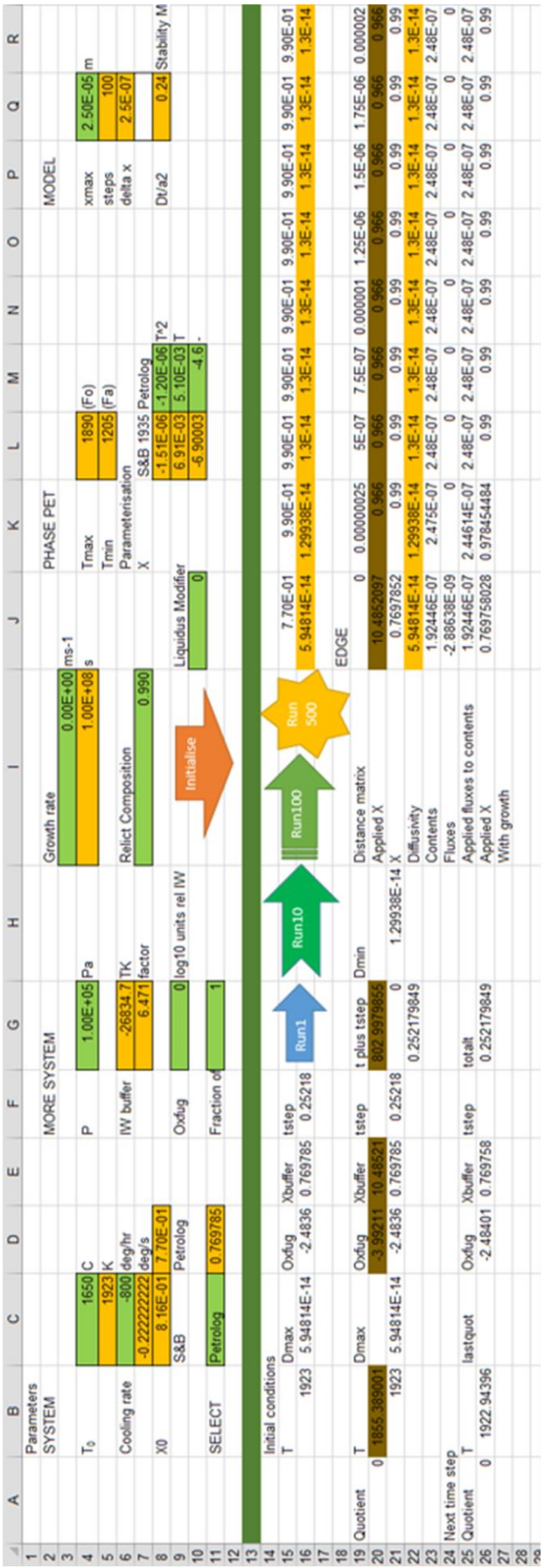

Figure A14 - The worked example spreadsheet after entering the initial conditions and clicking the initialise arrow

The next stage is to run to a temperature of 1850 K by running time steps until the spreadsheet appears like Figure A15, where the temperature of the current time step is as close to 1850 K as possible (cell B21). This is achieved by clicking the 500 time steps shape twice, allowing the first set of time steps to complete before clicking for the second. Once these are complete, run single time steps until the appropriate temperature is achieved (~60 times). Overrunning will mean that the model needs to be run again from the beginning (this is achieved by pressing the initialise arrow).

The next stage is to change the cooling rate in cell C6 from -800 to -4000 and run time steps until a temperature of 1700 K is reached. There is no need to click the initialise arrow, in fact, clicking the initialise arrow will reset the model and it will need to be run again from the beginning. As this is the final stage, overrunning is not a problem as diffusion profiles from the correct temperature and time can be extracted from the results section. Approximately 250 time steps are required at this cooling rate. At this point, the spreadsheet should appear like Figure A16. Temperature is related to the melt composition, and therefore the crystal edge composition. The final temperature is selected based upon the crystal edge composition based upon the olivine-saturated liquidus for the chondrule.

By extracting temperature and time, temperature time plots, for example Figure A17. Diffusion profiles from every time step are stored for extraction and can be plotted in graphs like Figure A18. To plot a temperature-time graph, extract the temperature column (column B) from the start temperature (at the bottom of the results section) until the end temperature of 1700 K. If overrun slightly, the final few time steps below 1700 K should be ignored. For time data, extract “t plus tstep” in the corresponding cells in column G. To plot model diffusion profiles, first extract the distance matrix in array J32:DF32. Diffusion profiles during in each time step are stored in reverse order in rows under this distance matrix from row 36 down (blue ellipse in Figure A15). Extract the row from column J to column DF for the correct temperature (column B), time (column G) or crystal edge composition (column J) and plot with the previously extracted distance matrix.

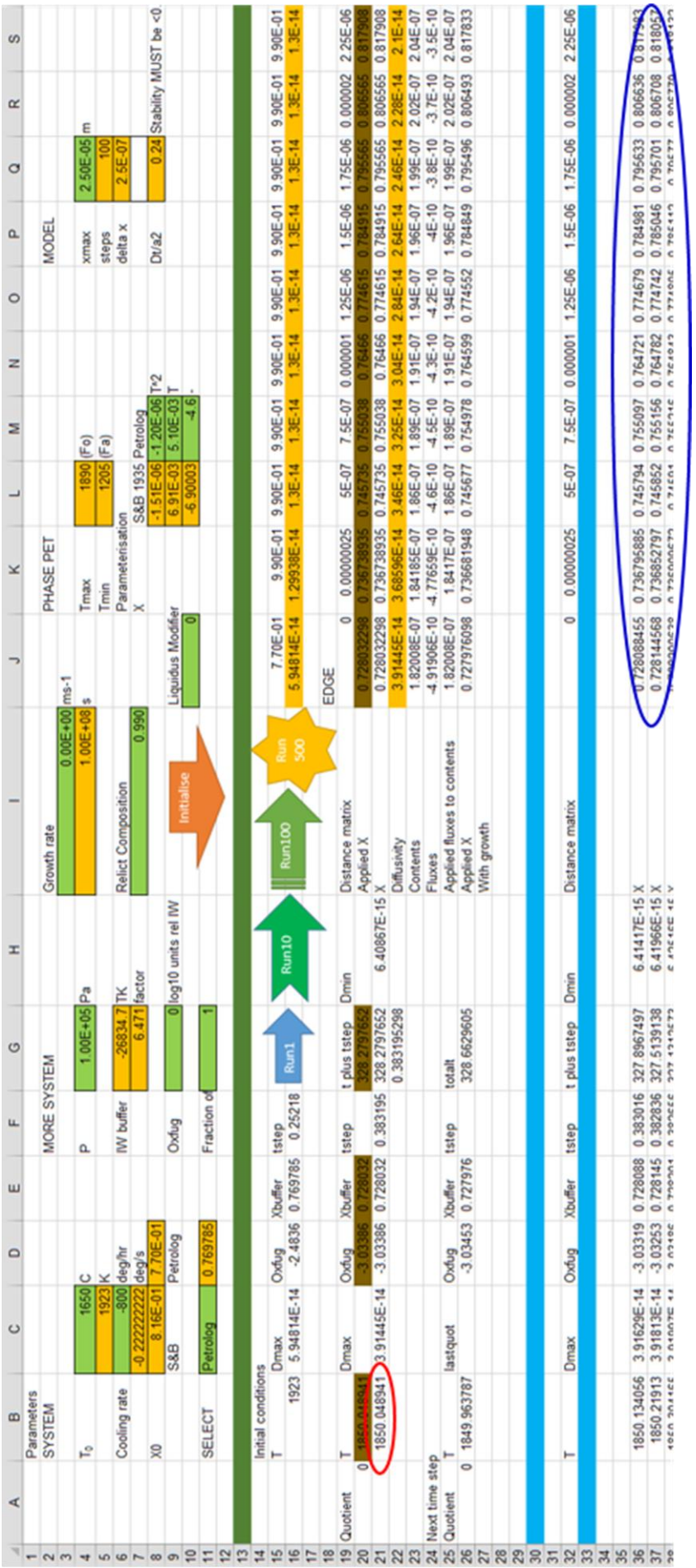

Figure A15 – The worked example spreadsheet after running time steps until the temperature is 1850 K. The temperature of the current time step (red ellipse) is as close to 1850 K as possible. The blue ellipse shows where diffusion profiles are stored in reverse order.

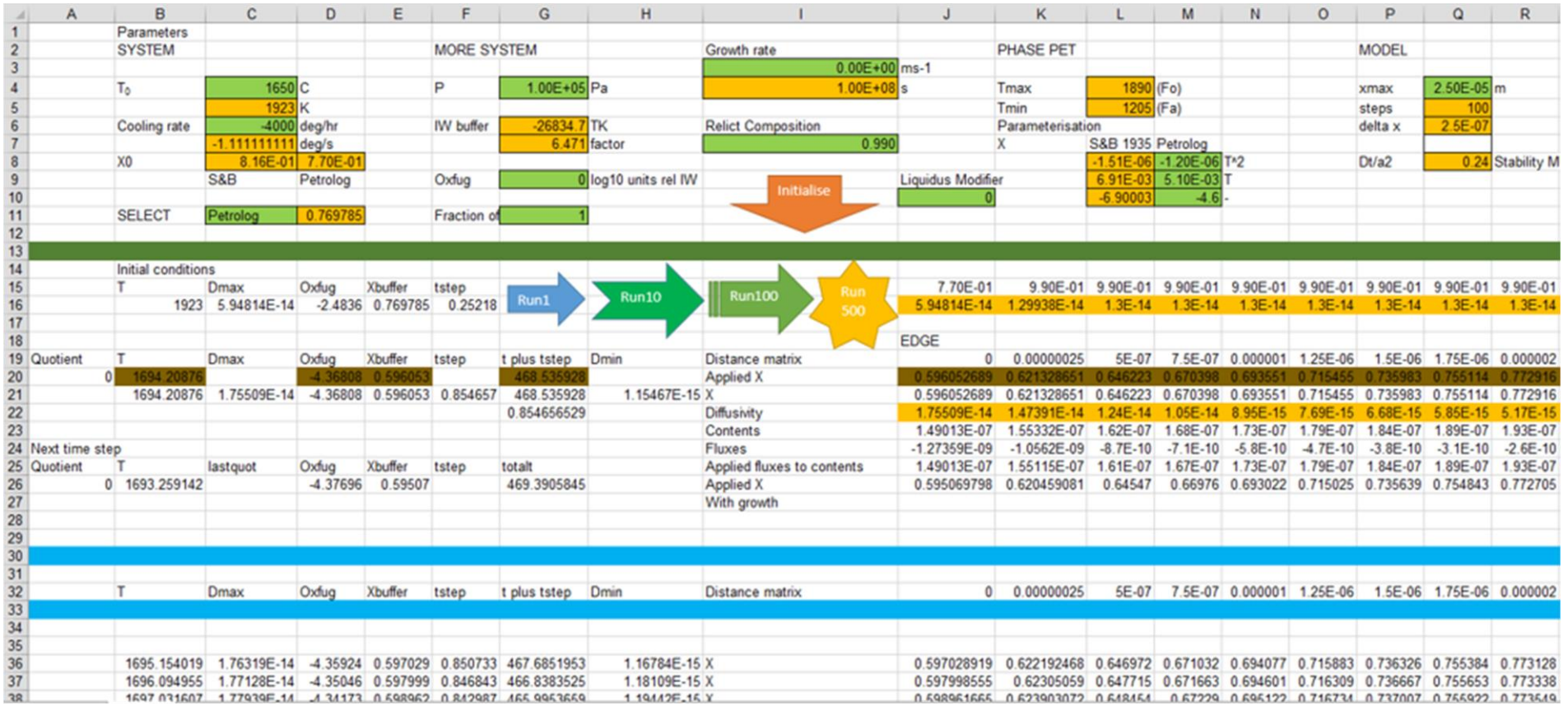

	A	B	C	D	E	F	G	H	I	J	K	L	M	N	O	P	Q	R
1		Parameters																
2		SYSTEM				MORE SYSTEM			Growth rate		PHASE PET					MODEL		
3									0.00E+00	ms-1								
4		T_0	1650	C		P	1.00E+05	Pa	1.00E+08	s	Tmax	1890	(Fo)			xmax	2.50E-05	m
5			1923	K							Tmin	1205	(Fa)			steps	100	
6		Cooling rate	-4000	deg/hr		IW buffer	-26834.7	TK	Relict Composition		Parameterisation					delta x	2.5E-07	
7			-1.111111111	deg/s			6.471	factor	0.990		X	S&B 1935	Petrolog					
8		X0	8.16E-01	7.70E-01								-1.51E-06	-1.20E-06	T^2		Dt/a2	0.24	Stability M
9			S&B	Petrolog		Oxfug	0	log10 units rel IW		Liquidus Modifier		6.91E-03	5.10E-03	T				
10										0		-6.90003	-4.6	-				
11		SELECT	Petrolog	0.769785		Fraction of	1											
12																		
13																		
14		Initial conditions																
15		T	Dmax	Oxfug	Xbuffer	tstep				7.70E-01	9.90E-01	9.90E-01	9.90E-01	9.90E-01	9.90E-01	9.90E-01	9.90E-01	9.90E-01
16		1923	5.94814E-14	-2.4836	0.769785	0.25218				5.94814E-14	1.29938E-14	1.3E-14	1.3E-14	1.3E-14	1.3E-14	1.3E-14	1.3E-14	1.3E-14
17																		
18										EDGE								
19	Quotient	T	Dmax	Oxfug	Xbuffer	tstep	t plus tstep	Dmin	Distance matrix	0	0.00000025	5E-07	7.5E-07	0.000001	1.25E-06	1.5E-06	1.75E-06	0.000002
20	0	1694.20876		-4.36808	0.596053		468.535928		Applied X	0.596052689	0.621328651	0.646223	0.670398	0.693551	0.715455	0.735983	0.755114	0.772916
21		1694.20876	1.75509E-14	-4.36808	0.596053	0.854657	468.535928	1.15467E-15	X	0.596052689	0.621328651	0.646223	0.670398	0.693551	0.715455	0.735983	0.755114	0.772916
22							0.854656529		Diffusivity	1.75509E-14	1.47391E-14	1.24E-14	1.05E-14	8.95E-15	7.69E-15	6.68E-15	5.85E-15	5.17E-15
23									Contents	1.49013E-07	1.55332E-07	1.62E-07	1.68E-07	1.73E-07	1.79E-07	1.84E-07	1.89E-07	1.93E-07
24	Next time step								Fluxes	-1.27359E-09	-1.0562E-09	-8.7E-10	-7.1E-10	-5.8E-10	-4.7E-10	-3.8E-10	-3.1E-10	-2.6E-10
25	Quotient	T	lastquot	Oxfug	Xbuffer	tstep	totalt		Applied fluxes to contents	1.49013E-07	1.55115E-07	1.61E-07	1.67E-07	1.73E-07	1.79E-07	1.84E-07	1.89E-07	1.93E-07
26	0	1693.259142		-4.37696	0.59507		469.3905845		Applied X	0.595069798	0.620459081	0.64547	0.66976	0.693022	0.715025	0.735639	0.754843	0.772705
27									With growth									
28																		
29																		
30																		
31																		
32		T	Dmax	Oxfug	Xbuffer	tstep	t plus tstep	Dmin	Distance matrix	0	0.00000025	5E-07	7.5E-07	0.000001	1.25E-06	1.5E-06	1.75E-06	0.000002
33																		
34																		
35																		
36		1695.154019	1.76319E-14	-4.35924	0.597029	0.850733	467.6851953	1.16784E-15	X	0.597028919	0.622192468	0.646972	0.671032	0.694077	0.715883	0.736326	0.755384	0.773128
37		1696.094955	1.77128E-14	-4.35046	0.597999	0.846843	466.8383525	1.18109E-15	X	0.597998555	0.62305059	0.647715	0.671663	0.694601	0.716309	0.736667	0.755653	0.773338
38		1697.031607	1.77939E-14	-4.34173	0.598962	0.842987	465.9953659	1.19442E-15	X	0.598961665	0.623903072	0.648454	0.67229	0.695122	0.716734	0.737007	0.755922	0.773549

Figure A16 - The worked example spreadsheet after running time steps until a temperature of at least 1700 K. In this spreadsheet, the model has overrun to a temperature of 1695 K, however diffusion profiles from the correct temperature and time can be extracted from further down the spreadsheet.

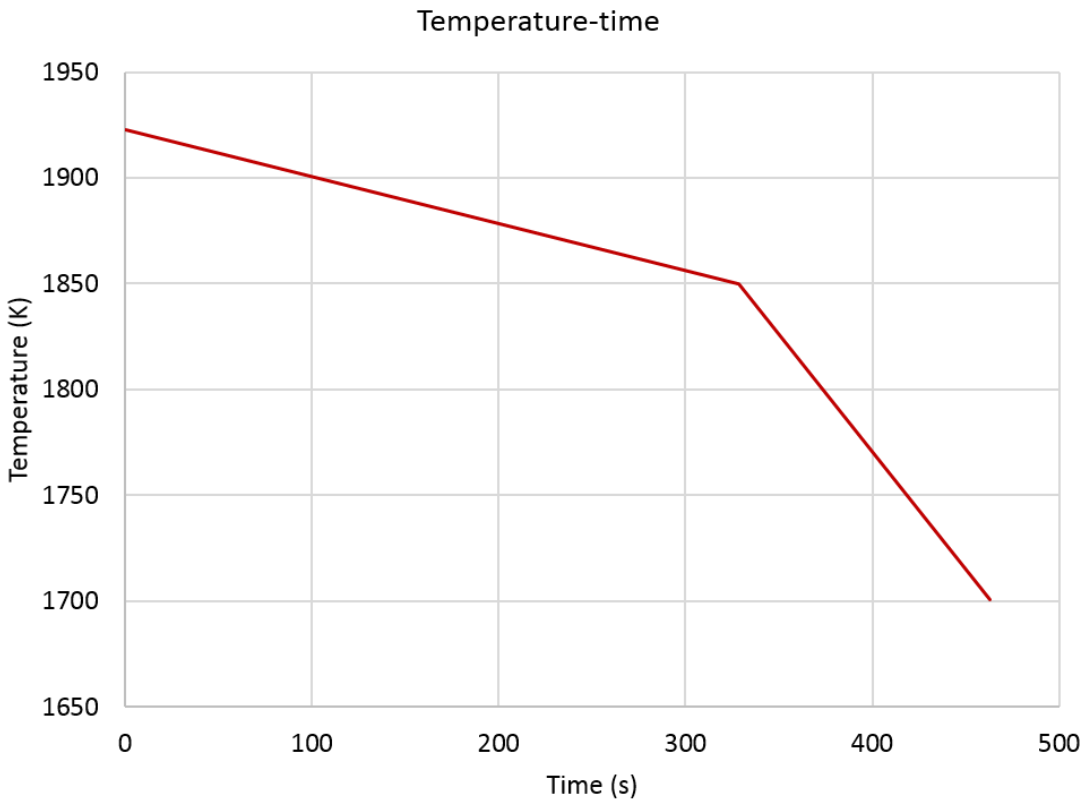

Figure A17 – Worked example temperature-time plot

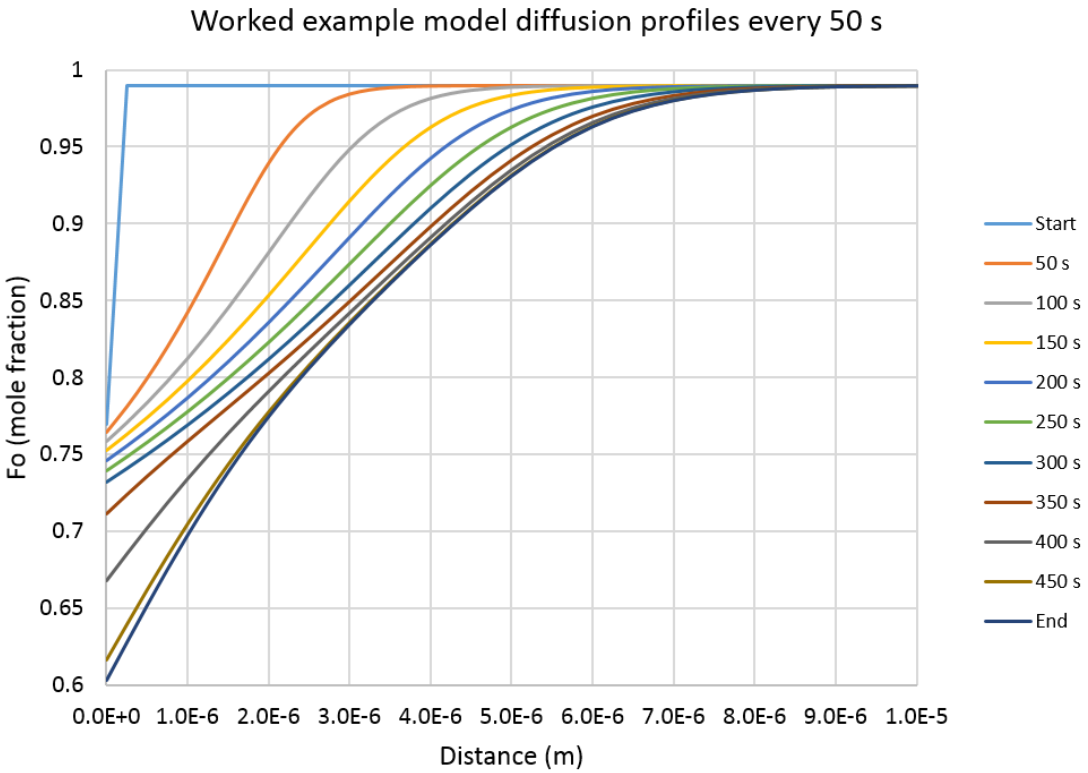

Figure A18 – Worked example diffusion profiles extracted every 50 s from the start and the ending diffusion profile at 1700 K and 462 s.

Appendix B
Electron microprobe analyses

This appendix contains all the electron microprobe analyses used in this work that are not already contained in another chapter.

B1. Olivine

Table B1 – Olivine EPMA analyses for chondrule Al-1

Analysis	Na_2O	MgO	Al_2O_3	SiO_2	P_2O_5	K_2O	CaO	TiO_2	Cr_2O_3	MnO	FeO	NiO	Total
1	<0.05	33.2	<0.05	37.4	<0.09	<0.02	0.32	<0.04	0.25	0.31	29.2	0.09	100.8
2	<0.05	32.9	<0.05	37.4	<0.09	<0.02	0.38	<0.04	0.25	0.28	29.9	<0.06	101.3
3	<0.05	36.0	0.07	37.9	<0.09	<0.02	0.28	<0.04	0.31	0.25	26.6	0.07	101.5
4	<0.05	35.0	<0.05	37.4	<0.09	<0.02	0.26	<0.04	0.33	0.27	27.6	0.28	101.2
5	<0.05	34.8	<0.05	37.6	0.09	<0.02	0.32	<0.04	0.34	0.27	27.7	0.07	101.3
6	0.07	33.3	0.25	37.4	0.15	<0.02	0.51	0.04	0.91	0.25	28.7	0.08	101.6
7	<0.05	35.8	<0.05	37.9	<0.09	<0.02	0.26	<0.04	0.37	0.29	26.5	0.10	101.3
8	0.33	28.8	0.76	37.0	0.09	<0.02	0.61	<0.04	0.25	0.34	32.8	<0.06	101.0
9	<0.05	30.5	<0.05	36.6	<0.09	<0.02	0.51	<0.04	0.21	0.36	32.7	0.07	101.0
10	<0.05	32.8	<0.05	37.1	<0.09	<0.02	0.35	<0.04	0.28	0.27	30.8	<0.06	101.7
11	<0.05	39.2	<0.05	38.9	<0.09	<0.02	0.22	<0.04	0.31	0.30	22.2	0.08	101.2
12	<0.05	31.4	<0.05	36.9	<0.09	<0.02	0.45	<0.04	0.30	0.35	32.2	0.09	101.8
13	0.06	33.8	<0.05	37.4	<0.09	<0.02	0.25	<0.04	0.26	0.25	29.0	<0.06	101.0
14	<0.05	29.3	<0.05	36.5	0.11	<0.02	0.65	<0.04	0.21	0.35	33.6	<0.06	100.8
15	<0.05	29.8	0.16	36.4	0.11	<0.02	0.44	<0.04	0.42	0.33	32.8	0.07	100.6
16	<0.05	29.4	<0.05	36.4	0.11	<0.02	0.44	<0.04	0.17	0.31	33.6	<0.06	100.5
17	0.07	30.5	0.05	36.5	0.13	<0.02	0.53	<0.04	0.23	0.35	32.8	0.06	101.2
18	<0.05	30.5	<0.05	36.7	<0.09	<0.02	0.39	<0.04	0.23	0.31	33.0	0.06	101.2
19	0.05	29.5	0.06	36.1	0.26	<0.02	0.57	<0.04	0.20	0.33	33.5	0.11	100.7

Table B2 – Olivine EPMA analyses for chondrule Al-2

Analysis	Na_2O	MgO	Al_2O_3	SiO_2	P_2O_5	K_2O	CaO	TiO_2	Cr_2O_3	MnO	FeO	NiO	Total
1	<0.05	36.1	<0.05	38.0	0.13	<0.02	0.29	<0.04	0.44	0.26	25.9	<0.06	101.2
2	<0.05	37.3	<0.05	38.2	<0.09	<0.02	0.25	<0.04	0.36	0.35	24.7	0.07	101.3
3	<0.05	35.5	<0.05	37.7	<0.09	<0.02	0.29	<0.04	0.30	0.32	26.9	<0.06	101.0
4	<0.05	35.5	<0.05	37.6	0.11	<0.02	0.32	<0.04	0.44	0.23	26.3	<0.06	100.6
5	<0.05	34.2	0.05	36.9	0.14	<0.02	0.38	<0.04	0.51	0.30	27.6	0.19	100.3
6	<0.05	34.4	<0.05	37.2	<0.09	<0.02	0.35	<0.04	0.43	0.29	27.4	0.06	100.2
7	<0.05	34.5	0.09	36.9	0.19	<0.02	0.29	0.07	0.66	0.30	27.6	0.06	100.7
8	<0.05	35.1	<0.05	37.7	<0.09	<0.02	0.26	<0.04	0.41	0.28	27.3	0.06	101.1
9	<0.05	32.5	<0.05	36.6	0.16	<0.02	0.37	<0.04	0.29	0.32	28.8	0.16	99.2
10	<0.05	32.7	<0.05	36.8	0.22	<0.02	0.47	<0.04	0.36	0.30	29.4	0.10	100.4
11	<0.05	31.7	<0.05	36.7	0.18	<0.02	0.44	<0.04	0.34	0.32	30.8	0.09	100.6
12	<0.05	35.1	<0.05	37.5	<0.09	<0.02	0.31	0.05	0.50	0.29	26.9	0.07	100.8
13	<0.05	33.9	<0.05	37.1	<0.09	<0.02	0.37	<0.04	0.34	0.32	28.4	0.08	100.6
14	<0.05	33.6	<0.05	36.7	0.25	<0.02	0.39	<0.04	0.36	0.25	28.8	0.07	100.4
15	<0.05	36.9	<0.05	37.5	<0.09	<0.02	0.27	<0.04	0.35	0.24	23.5	0.06	98.8
16	<0.05	34.2	<0.05	37.3	0.14	<0.02	0.38	0.04	0.31	0.28	28.2	0.07	101.0
17	<0.05	35.5	<0.05	37.3	<0.09	<0.02	0.27	<0.04	0.42	0.32	26.6	0.07	100.4
18	<0.05	37.0	<0.05	38.2	<0.09	<0.02	0.31	<0.04	0.49	0.28	25.2	<0.06	101.6
19	<0.05	37.3	0.06	38.1	0.10	<0.02	0.39	<0.04	0.37	0.24	23.5	<0.06	100.1
20	<0.05	31.2	<0.05	36.7	<0.09	<0.02	0.41	<0.04	0.35	0.32	32.6	0.09	101.8
21	<0.05	34.9	<0.05	37.5	<0.09	<0.02	0.30	<0.04	0.51	0.28	27.0	0.07	100.7
22	<0.05	33.3	0.10	37.0	<0.09	<0.02	0.26	<0.04	0.67	0.30	28.4	<0.06	100.2
23	<0.05	36.5	0.07	36.7	0.20	<0.02	0.45	<0.04	0.38	0.33	25.5	0.36	100.4
24	<0.05	33.8	<0.05	37.4	0.10	<0.02	0.42	<0.04	0.36	0.28	28.4	0.09	100.8

Table B3 – Olivine EPMA analyses for chondrule Al-3

Analysis	Na_2O	MgO	Al_2O_3	SiO_2	P_2O_5	K_2O	CaO	TiO_2	Cr_2O_3	MnO	FeO	NiO	Total
1	<0.05	21.4	<0.05	33.6	<0.09	<0.02	0.23	<0.04	0.32	0.35	43.6	0.16	99.7
2	<0.05	25.7	<0.05	34.1	0.15	<0.02	0.29	<0.04	0.37	0.31	38.5	0.44	99.9
3	<0.05	24.8	<0.05	34.6	0.12	<0.02	0.34	<0.04	0.41	0.33	39.2	0.12	100.0
4	<0.05	28.1	<0.05	35.5	<0.09	<0.02	0.28	<0.04	0.42	0.33	34.1	0.10	98.9
5	<0.05	41.1	<0.05	38.2	<0.09	<0.02	0.19	<0.04	0.30	0.16	20.5	0.09	100.6
6	<0.05	25.8	<0.05	34.6	<0.09	<0.02	0.25	<0.04	0.34	0.31	38.9	0.11	100.5
7	0.05	22.0	<0.05	33.8	<0.09	<0.02	0.30	<0.04	0.26	0.35	43.9	0.14	100.8
8	<0.05	27.9	<0.05	34.9	<0.09	<0.02	0.27	<0.04	0.30	0.30	36.2	0.08	100.0
9	<0.05	38.3	<0.05	37.7	<0.09	<0.02	0.21	<0.04	0.33	0.19	22.7	0.07	99.5
10	<0.05	25.0	<0.05	34.2	0.30	<0.02	0.38	<0.04	0.45	0.33	37.6	0.10	98.4
11	<0.05	24.4	<0.05	33.9	<0.09	<0.02	0.24	<0.04	0.32	0.34	40.1	0.17	99.5
12	<0.05	31.3	<0.05	35.3	<0.09	<0.02	0.18	0.04	0.27	0.25	31.7	0.08	99.2
13	<0.05	20.3	<0.05	33.2	<0.09	<0.02	0.31	<0.04	0.25	0.37	43.6	0.36	98.4
14	<0.05	20.6	<0.05	33.1	<0.09	<0.02	0.30	<0.04	0.24	0.41	44.5	0.13	99.2
15	0.05	18.8	<0.05	31.8	<0.09	<0.02	0.51	<0.04	0.18	0.47	46.4	0.12	98.4
16	<0.05	21.2	<0.05	33.5	<0.09	<0.02	0.27	<0.04	0.28	0.37	44.0	0.16	99.8
17	<0.05	25.1	<0.05	33.7	<0.09	<0.02	0.26	<0.04	0.22	0.35	40.0	0.09	99.8
18	<0.05	25.7	<0.05	33.3	<0.09	<0.02	0.22	<0.04	0.33	0.33	39.3	0.16	99.3

Table B4 – Olivine EPMA analyses for chondrule Al-4

Analysis	Na_2O	MgO	Al_2O_3	SiO_2	P_2O_5	K_2O	CaO	TiO_2	Cr_2O_3	MnO	FeO	NiO	Total
1	<0.05	31.2	<0.05	36.8	<0.09	<0.02	0.45	<0.04	0.27	0.29	32.3	0.07	101.5
2	<0.05	36.3	<0.05	38.1	<0.09	<0.02	0.19	<0.04	0.25	0.22	24.5	<0.06	99.6
3	<0.05	45.7	<0.05	40.5	<0.09	<0.02	0.18	<0.04	0.38	0.12	14.7	0.08	101.7
4	<0.05	31.7	<0.05	37.1	<0.09	<0.02	0.25	<0.04	0.26	0.28	31.0	0.06	100.7
5	0.05	36.2	<0.05	38.1	<0.09	<0.02	0.25	<0.04	0.25	0.24	25.5	0.15	100.7
6	<0.05	31.1	<0.05	36.6	<0.09	<0.02	0.41	<0.04	0.22	0.27	31.1	0.11	99.8
7	<0.05	30.9	<0.05	36.7	<0.09	<0.02	0.43	<0.04	0.19	0.27	31.8	0.08	100.4
8	<0.05	33.9	<0.05	37.5	0.09	<0.02	0.42	<0.04	0.29	0.25	27.6	<0.06	100.1
9	<0.05	32.7	<0.05	37.2	<0.09	<0.02	0.44	<0.04	0.26	0.25	30.4	<0.06	101.4
10	<0.05	30.3	<0.05	36.7	0.14	<0.02	0.49	0.05	0.18	0.28	32.5	0.08	100.9
11	<0.05	30.3	<0.05	37.0	<0.09	<0.02	0.52	<0.04	0.23	0.29	32.5	0.10	101.0
12	<0.05	31.0	0.05	36.7	0.09	<0.02	0.47	<0.04	0.35	0.28	31.2	<0.06	100.2
13	<0.05	30.0	0.12	37.0	<0.09	<0.02	0.46	<0.04	0.18	0.27	32.7	0.20	101.0
14	<0.05	30.4	<0.05	36.8	0.09	<0.02	0.45	<0.04	0.25	0.29	33.2	0.06	101.5
15	<0.05	31.7	0.18	37.0	0.13	<0.02	0.40	<0.04	0.69	0.28	31.5	0.12	102.0

Table B5 – Olivine EPMA analyses for chondrule Al-5

Analysis	Na_2O	MgO	Al_2O_3	SiO_2	P_2O_5	K_2O	CaO	TiO_2	Cr_2O_3	MnO	FeO	NiO	Total
1	<0.05	38.3	<0.05	38.4	<0.09	<0.02	0.21	<0.04	0.05	0.24	23.0	0.06	100.4
2	0.14	26.2	0.56	34.7	0.38	<0.02	0.78	<0.04	0.09	0.35	37.5	0.28	100.9
3	0.12	24.3	0.32	34.8	0.45	<0.02	1.26	<0.04	0.20	0.39	38.9	0.22	101.0
4	0.17	24.5	0.87	34.2	0.25	<0.02	1.05	0.09	0.19	0.37	38.8	0.31	100.8

Table B6 – Olivine EPMA analyses for chondrule Al-6

Analysis	Na_2O	MgO	Al_2O_3	SiO_2	P_2O_5	K_2O	CaO	TiO_2	Cr_2O_3	MnO	FeO	NiO	Total
1	<0.05	37.2	<0.05	38.6	<0.09	<0.02	0.24	0.06	0.85	0.23	24.2	<0.06	101.5
2	<0.05	38.3	0.08	38.3	0.15	<0.02	0.28	<0.04	0.30	0.26	23.0	<0.06	100.7
3	<0.05	40.9	<0.05	38.9	<0.09	<0.02	0.25	<0.04	0.44	0.20	19.6	<0.06	100.4
4	<0.05	32.7	<0.05	37.4	<0.09	<0.02	0.35	<0.04	0.32	0.30	30.1	0.06	101.3
5	<0.05	28.5	<0.05	36.4	0.15	<0.02	0.55	0.04	0.33	0.34	34.5	<0.06	100.9
6	<0.05	28.0	0.17	36.4	0.18	<0.02	0.61	<0.04	0.28	0.36	34.7	0.13	100.9
7	<0.05	30.2	<0.05	36.7	0.18	<0.02	0.51	<0.04	<0.04	0.31	32.9	<0.06	101.0
8	<0.05	40.4	0.05	39.0	0.13	<0.02	0.25	<0.04	0.49	0.21	19.8	<0.06	100.3
9	<0.05	34.4	0.09	37.2	<0.09	<0.02	0.35	<0.04	0.91	0.24	27.6	0.16	101.1

Table B7 – Olivine EPMA analyses for chondrule N8-1

Analysis	Na_2O	MgO	Al_2O_3	SiO_2	P_2O_5	K_2O	CaO	TiO_2	Cr_2O_3	MnO	FeO	NiO	Total
1	<0.05	39.9	<0.05	38.9	<0.09	<0.02	0.20	<0.04	0.54	0.37	21.1	<0.06	101.1
2	<0.05	38.8	<0.05	37.3	<0.09	<0.02	0.21	<0.04	0.56	0.37	21.8	<0.06	99.2
3	0.06	37.8	<0.05	36.7	<0.09	<0.02	0.29	<0.04	0.57	0.37	22.9	<0.06	98.8
4	<0.05	37.3	<0.05	36.1	0.24	<0.02	0.27	<0.04	0.51	0.39	23.5	<0.06	98.4
5	<0.05	37.7	<0.05	36.5	0.17	<0.02	0.25	<0.04	0.49	0.39	24.3	0.30	100.2
6	<0.05	36.3	<0.05	35.0	0.21	<0.02	0.29	<0.04	0.44	0.43	25.2	0.06	98.1
7	<0.05	40.6	<0.05	36.4	<0.09	<0.02	0.18	<0.04	0.56	0.35	20.4	<0.06	98.6
8	<0.05	40.7	<0.05	36.5	<0.09	<0.02	0.18	<0.04	0.59	0.36	19.8	<0.06	98.2
9	<0.05	35.6	<0.05	36.7	<0.09	<0.02	0.24	<0.04	0.52	0.40	24.6	<0.06	98.1
10	<0.05	36.8	<0.05	37.2	<0.09	<0.02	0.25	<0.04	0.60	0.40	24.1	<0.06	99.3
11	<0.05	38.1	<0.05	38.0	0.12	<0.02	0.23	<0.04	0.57	0.43	23.2	<0.06	100.6
12	0.07	35.8	<0.05	36.6	0.17	<0.02	0.30	<0.04	0.48	0.43	25.3	0.06	99.2

Table B8 – Olivine EPMA analyses for chondrule N8-2

Analysis	Na_2O	MgO	Al_2O_3	SiO_2	P_2O_5	K_2O	CaO	TiO_2	Cr_2O_3	MnO	FeO	NiO	Total
1	<0.05	38.6	<0.05	37.7	<0.09	<0.02	0.17	<0.04	0.37	0.43	22.7	0.06	100.2
2	<0.05	34.8	<0.05	36.5	0.38	<0.02	0.26	<0.04	0.47	0.49	26.6	<0.06	99.6
3	<0.05	35.1	<0.05	36.3	0.23	<0.02	0.26	<0.04	0.56	0.49	26.7	<0.06	99.7
4	<0.05	34.7	<0.05	36.1	<0.09	<0.02	0.20	<0.04	0.30	0.50	27.0	0.06	98.9
5	<0.05	37.4	<0.05	38.1	<0.09	<0.02	0.13	<0.04	0.54	0.45	23.4	0.06	100.0
6	<0.05	36.1	<0.05	37.6	0.09	<0.02	0.22	<0.04	0.49	0.47	24.8	0.06	99.8
7	0.05	38.3	<0.05	37.6	<0.09	<0.02	0.18	<0.04	0.44	0.38	22.2	<0.06	99.2
8	<0.05	38.0	<0.05	37.5	0.10	<0.02	0.17	<0.04	0.59	0.38	22.5	<0.06	99.3
9	<0.05	36.2	<0.05	37.6	<0.09	<0.02	0.23	<0.04	0.26	0.47	25.7	<0.06	100.6
10	<0.05	41.2	<0.05	38.5	<0.09	<0.02	0.19	<0.04	0.43	0.33	18.6	<0.06	99.4
11	<0.05	37.5	<0.05	37.5	0.30	<0.02	0.20	<0.04	0.54	0.41	23.6	<0.06	100.0
12	0.05	36.0	<0.05	37.3	<0.09	<0.02	0.23	<0.04	0.41	0.47	25.8	<0.06	100.4
13	<0.05	34.9	<0.05	37.4	0.12	<0.02	0.23	<0.04	0.47	0.51	26.8	0.06	100.5
14	<0.05	35.7	<0.05	37.5	0.16	<0.02	0.21	<0.04	0.47	0.49	25.9	<0.06	100.4
15	0.07	35.8	<0.05	37.2	0.20	<0.02	0.25	<0.04	0.39	0.50	26.2	0.09	100.7
16	<0.05	40.0	<0.05	38.7	0.14	<0.02	0.20	<0.04	0.58	0.39	21.1	<0.06	101.2
17	<0.05	36.2	<0.05	37.9	<0.09	<0.02	0.20	<0.04	0.40	0.49	24.9	<0.06	100.2
18	<0.05	36.5	<0.05	37.9	<0.09	<0.02	0.20	<0.04	0.46	0.46	25.0	<0.06	100.7

Table B9 – Olivine EPMA analyses for chondrule N8-3

Analysis	Na_2O	MgO	Al_2O_3	SiO_2	P_2O_5	K_2O	CaO	TiO_2	Cr_2O_3	MnO	FeO	NiO	Total
1	<0.05	34.3	<0.05	37.0	0.29	<0.02	0.31	<0.04	0.51	0.39	26.6	<0.06	99.4
2	<0.05	34.7	<0.05	37.6	0.21	<0.02	0.33	<0.04	0.44	0.40	26.6	<0.06	100.3
3	0.05	35.7	<0.05	37.6	<0.09	<0.02	0.30	<0.04	0.25	0.39	26.3	0.06	100.7
4	<0.05	33.3	0.09	37.2	0.25	<0.02	0.40	<0.04	0.44	0.42	26.9	<0.06	99.1
5	<0.05	40.6	<0.05	38.5	0.14	<0.02	0.22	<0.04	0.56	0.33	21.0	<0.06	100.9
6	<0.05	39.2	<0.05	38.1	<0.09	<0.02	0.19	<0.04	0.56	0.35	21.7	<0.06	100.2
7	<0.05	36.2	<0.05	37.7	<0.09	<0.02	0.28	<0.04	0.33	0.37	25.3	<0.06	100.3
8	<0.05	37.9	<0.05	37.3	0.12	<0.02	0.25	<0.04	0.36	0.40	23.7	<0.06	100.0
9	<0.05	34.1	<0.05	36.8	0.17	<0.02	0.29	<0.04	0.32	0.43	27.6	<0.06	99.7
10	<0.05	35.5	<0.05	37.3	0.09	<0.02	0.22	<0.04	0.32	0.39	25.2	<0.06	99.0
11	<0.05	36.8	<0.05	37.5	0.15	<0.02	0.25	<0.04	0.42	0.37	23.3	0.07	98.9
12	<0.05	35.9	<0.05	37.4	0.17	<0.02	0.25	<0.04	0.42	0.37	25.1	<0.06	99.6
13	<0.05	36.9	<0.05	37.9	0.15	<0.02	0.22	<0.04	0.46	0.41	24.6	<0.06	100.7
14	<0.05	33.8	0.06	37.1	0.09	<0.02	0.35	<0.04	0.37	0.45	28.4	<0.06	100.7
15	<0.05	34.6	<0.05	36.9	0.12	<0.02	0.32	<0.04	0.29	0.44	28.1	<0.06	100.9
16	<0.05	34.4	0.11	37.1	<0.09	<0.02	0.31	<0.04	0.40	0.39	27.5	0.11	100.5
17	<0.05	35.1	0.05	37.3	0.20	<0.02	0.24	0.04	0.79	0.38	26.0	0.07	100.2
18	<0.05	33.4	<0.05	37.2	<0.09	<0.02	0.31	<0.04	0.23	0.40	28.3	<0.06	100.0
19	<0.05	36.1	<0.05	37.3	<0.09	<0.02	0.21	<0.04	0.29	0.42	25.9	<0.06	100.3

Table B10 – Olivine analyses for chondrule N4-1

Analysis	Na_2O	MgO	Al_2O_3	SiO_2	P_2O_5	K_2O	CaO	TiO_2	Cr_2O_3	MnO	FeO	NiO	Total
1	<0.05	45.1	<0.05	40.0	<0.09	<0.02	0.11	<0.04	0.47	0.40	13.9	<0.06	100.1
2	<0.05	42.1	0.13	39.0	<0.09	<0.02	0.16	<0.04	0.49	0.46	17.2	0.06	99.6
3	<0.05	45.2	<0.05	39.9	<0.09	<0.02	0.11	<0.04	0.51	0.40	14.6	0.06	100.8
4	<0.05	49.1	<0.05	41.1	<0.09	<0.02	0.09	<0.04	0.34	0.29	9.66	<0.06	100.6
5	<0.05	45.4	<0.05	40.2	<0.09	<0.02	0.09	<0.04	0.47	0.38	13.3	<0.06	100.0
6	<0.05	40.8	<0.05	39.1	<0.09	<0.02	0.25	<0.04	0.60	0.56	18.3	0.06	99.7
7	<0.05	39.9	0.08	38.9	0.09	<0.02	0.34	<0.04	0.67	0.58	19.5	0.16	100.2
8	<0.05	40.5	<0.05	38.9	<0.09	<0.02	0.32	0.04	0.62	0.63	19.1	0.08	100.2
9	<0.05	38.1	0.30	38.4	<0.09	<0.02	0.40	0.04	0.55	0.63	20.8	0.85	100.2
10	<0.05	41.3	<0.05	39.2	<0.09	<0.02	0.17	<0.04	0.56	0.55	18.5	0.07	100.5
11	<0.05	42.5	<0.05	39.3	<0.09	<0.02	0.15	<0.04	0.48	0.51	17.2	0.07	100.2
12	<0.05	41.4	<0.05	39.2	<0.09	<0.02	0.20	<0.04	0.47	0.54	18.5	0.07	100.4
13	<0.05	38.9	0.13	38.5	<0.09	<0.02	0.36	0.06	0.45	0.66	20.7	0.20	100.1
14	<0.05	41.5	<0.05	39.4	<0.09	<0.02	0.18	0.03	0.51	0.55	18.2	<0.06	100.5
15	0.07	39.4	0.06	38.5	0.17	<0.02	0.37	<0.04	0.37	0.70	20.0	0.26	99.9
16	<0.05	40.1	<0.05	39.0	<0.09	<0.02	0.27	<0.04	0.56	0.56	18.9	<0.06	99.5
17	0.10	38.5	0.13	40.4	0.12	<0.02	0.82	0.05	0.45	0.69	18.8	<0.06	100.0
18	<0.05	41.6	<0.05	39.5	<0.09	<0.02	0.23	<0.04	0.50	0.53	17.3	<0.06	99.7
19	<0.05	41.4	<0.05	38.7	<0.09	<0.02	0.20	<0.04	0.49	0.53	19.5	0.25	101.1
20	0.13	40.7	0.21	39.0	<0.09	<0.02	0.28	<0.04	0.52	0.57	18.3	0.41	100.2
21	0.07	40.2	0.32	38.4	<0.09	<0.02	0.33	<0.04	0.60	0.49	18.3	0.52	99.3
22	<0.05	41.0	<0.05	39.1	<0.09	<0.02	0.28	<0.04	0.52	0.54	19.0	<0.06	100.5

Table B11 – Olivine EPMA analyses for chondrule N4-2

Analysis	Na_2O	MgO	Al_2O_3	SiO_2	P_2O_5	K_2O	CaO	TiO_2	Cr_2O_3	MnO	FeO	NiO	Total
1	<0.05	35.5	<0.05	37.8	0.19	<0.02	0.21	<0.04	0.46	0.40	24.2	0.06	98.9
2	0.05	33.5	<0.05	37.6	0.09	<0.02	0.32	<0.04	0.40	0.46	27.6	0.18	100.2
3	<0.05	31.1	0.13	36.4	0.17	<0.02	0.38	<0.04	0.32	0.52	29.4	0.92	99.3
4	<0.05	34.1	<0.05	37.0	0.09	<0.02	0.33	<0.04	0.35	0.48	28.8	0.08	101.2
5	<0.05	32.2	0.15	37.5	0.13	<0.02	0.45	0.05	0.35	0.50	28.7	0.11	100.1
6	<0.05	33.7	0.22	37.6	0.13	<0.02	0.22	<0.04	0.36	0.42	25.0	0.55	98.2
7	<0.05	41.4	0.08	39.1	<0.09	<0.02	0.16	<0.04	0.44	0.29	18.7	0.30	100.5
8	0.14	36.2	0.30	38.7	0.13	<0.02	0.36	<0.04	0.38	0.43	24.7	<0.06	101.5
9	<0.05	42.3	<0.05	40.0	<0.09	<0.02	0.19	<0.04	0.43	0.32	16.7	<0.06	100.0
10	<0.05	39.0	<0.05	38.3	<0.09	<0.02	0.15	<0.04	0.45	0.32	20.8	0.11	99.2
11	<0.05	31.7	0.07	37.1	0.13	<0.02	0.38	<0.04	0.33	0.52	29.2	0.26	99.7
12	<0.05	32.4	<0.05	37.0	<0.09	<0.02	0.35	<0.04	0.32	0.47	28.2	0.35	99.3
13	0.07	31.8	0.53	37.7	0.25	<0.02	0.42	0.04	0.45	0.48	28.7	0.62	101.1
14	0.05	34.7	<0.05	37.3	<0.09	<0.02	0.30	<0.04	0.38	0.45	26.5	0.19	99.9
15	<0.05	35.5	<0.05	37.6	0.30	<0.02	0.26	<0.04	0.39	0.45	25.4	<0.06	100.0
16	<0.05	40.3	<0.05	38.9	<0.09	<0.02	0.18	<0.04	0.51	0.32	19.7	0.08	100.1
17	<0.05	40.2	<0.05	39.0	0.10	<0.02	0.19	<0.04	0.49	0.33	19.8	<0.06	100.1
18	<0.05	39.7	<0.05	39.2	<0.09	<0.02	0.17	<0.04	0.49	0.32	19.9	<0.06	99.9
19	0.06	39.5	<0.05	39.2	0.10	<0.02	0.16	<0.04	0.44	0.33	19.6	0.06	99.4
20	<0.05	38.6	0.05	38.4	0.35	<0.02	0.19	<0.04	0.50	0.31	19.8	0.18	98.4
21	<0.05	40.2	<0.05	38.8	0.17	<0.02	0.19	<0.04	0.46	0.37	20.6	0.32	101.1
22	0.05	32.2	<0.05	36.7	0.19	<0.02	0.38	<0.04	0.34	0.49	28.3	0.16	98.9
23	<0.05	35.1	<0.05	37.7	0.18	<0.02	0.24	<0.04	0.49	0.41	25.0	0.06	99.2
24	<0.05	30.4	<0.05	36.8	0.41	<0.02	0.39	<0.04	0.32	0.57	31.7	<0.06	100.7
25	<0.05	38.3	<0.05	38.9	0.20	<0.02	0.17	<0.04	0.48	0.37	23.0	0.17	101.7
26	<0.05	37.0	<0.05	38.4	0.09	<0.02	0.19	<0.04	0.44	0.42	24.9	0.06	101.6
27	0.05	35.2	<0.05	38.2	0.09	<0.02	0.25	<0.04	0.44	0.44	26.3	<0.06	101.1
28	<0.05	38.3	<0.05	38.7	<0.09	<0.02	0.25	<0.04	0.31	0.32	22.6	0.06	100.6
29	<0.05	32.3	0.07	37.2	0.19	<0.02	0.35	<0.04	0.35	0.48	28.2	0.30	99.5
30	<0.05	36.3	<0.05	38.3	0.19	<0.02	0.28	<0.04	0.42	0.42	25.2	0.13	101.2
31	<0.05	31.8	<0.05	37.4	0.22	<0.02	0.38	<0.04	0.30	0.53	30.9	0.26	101.7
32	<0.05	26.3	<0.05	35.4	0.40	<0.02	0.36	<0.04	0.23	0.63	36.9	0.12	100.3
33	<0.05	37.5	<0.05	38.9	<0.09	<0.02	0.16	<0.04	0.44	0.39	23.9	<0.06	101.4
34	<0.05	32.1	<0.05	37.3	0.13	<0.02	0.37	<0.04	0.43	0.51	30.1	0.09	101.1
35	0.05	32.2	<0.05	37.3	0.13	<0.02	0.33	<0.04	0.37	0.50	29.0	0.44	100.4
36	0.05	26.8	<0.05	36.4	0.20	<0.02	0.48	<0.04	0.35	0.64	36.5	0.06	101.4
37	0.05	32.6	0.14	36.8	0.25	<0.02	0.38	<0.04	0.35	0.52	29.6	0.29	101.1
38	0.08	31.6	0.17	36.6	0.22	<0.02	0.37	<0.04	0.33	0.50	29.1	0.85	99.9

Table B12 – Olivine EPMA analyses for chondrule N4-3

Analysis	Na_2O	MgO	Al_2O_3	SiO_2	P_2O_5	K_2O	CaO	TiO_2	Cr_2O_3	MnO	FeO	NiO	Total
1	<0.05	47.7	<0.05	40.2	<0.09	<0.02	0.18	<0.04	0.60	0.45	11.6	<0.06	100.9
2	<0.05	48.2	<0.05	40.5	<0.09	<0.02	0.16	<0.04	0.57	0.44	11.0	<0.06	100.8
3	<0.05	48.8	<0.05	40.5	<0.09	<0.02	0.15	<0.04	0.55	0.43	11.1	<0.06	101.6
4	<0.05	48.1	<0.05	40.1	<0.09	<0.02	0.18	<0.04	0.55	0.45	11.5	0.06	101.0
5	<0.05	47.7	<0.05	40.3	<0.09	<0.02	0.16	<0.04	0.58	0.49	11.8	<0.06	101.1
6	<0.05	48.3	<0.05	40.3	<0.09	<0.02	0.14	<0.04	0.62	0.47	11.5	<0.06	101.4
7	<0.05	50.0	<0.05	40.5	<0.09	<0.02	0.11	<0.04	0.28	0.36	8.96	<0.06	100.2
8	<0.05	48.7	0.08	40.6	<0.09	<0.02	0.15	<0.04	0.51	0.43	10.4	<0.06	100.9
9	<0.05	50.8	<0.05	40.9	<0.09	<0.02	0.10	<0.04	0.38	0.28	8.21	0.17	100.9
10	<0.05	50.9	<0.05	41.1	<0.09	<0.02	0.10	<0.04	0.43	0.29	8.31	<0.06	101.1
11	<0.05	48.8	0.17	39.9	<0.09	<0.02	0.26	0.09	0.61	0.34	10.8	0.27	101.3
12	<0.05	50.9	<0.05	40.3	<0.09	<0.02	0.12	<0.04	0.38	0.29	8.08	0.08	100.2
13	<0.05	47.9	<0.05	40.2	<0.09	<0.02	0.16	<0.04	0.49	0.38	10.6	0.11	100.0
14	<0.05	46.4	<0.05	40.1	<0.09	<0.02	0.20	<0.04	0.61	0.48	12.2	<0.06	100.0
15	<0.05	47.2	<0.05	39.6	<0.09	<0.02	0.28	<0.04	0.64	0.49	12.4	0.07	100.7
16	<0.05	47.3	<0.05	40.0	<0.09	<0.02	0.16	<0.04	0.55	0.48	13.0	0.08	101.5

B2. Mesostasis

Table B13 – Mesostasis EPMA analyses for chondrule Al-1

Analysis	Na_2O	MgO	Al_2O_3	SiO_2	P_2O_5	K_2O	CaO	TiO_2	Cr_2O_3	MnO	FeO	NiO	Total
1	1.08	7.45	8.00	35.1	1.39	0.03	17.9	1.28	0.13	0.14	22.2	0.69	95.4
2	1.33	4.02	9.11	25.3	2.81	0.10	9.34	1.14	<0.04	0.19	32.5	4.49	90.3
3	1.77	5.26	10.1	27.8	1.22	0.10	6.35	0.44	0.07	0.11	36.1	2.30	91.6

Table B14 – Mesostasis EPMA analyses for chondrule Al-2

Analysis	Na_2O	MgO	Al_2O_3	SiO_2	P_2O_5	K_2O	CaO	TiO_2	Cr_2O_3	MnO	FeO	NiO	Total
1	0.94	7.25	9.68	32.2	0.51	0.07	8.08	0.38	0.12	0.23	29.9	3.46	92.7
2	0.76	5.22	9.25	32.7	2.37	0.11	14.8	0.79	0.08	0.15	24.5	2.66	93.4
3	0.82	4.88	3.49	20.0	0.60	<0.02	5.98	0.31	0.13	0.11	53.4	2.52	92.3
4	0.78	10.2	5.15	32.8	0.87	0.04	7.23	0.54	0.49	0.34	30.8	3.15	92.4
5	1.40	6.36	6.24	35.1	0.97	0.10	11.9	0.99	<0.04	0.23	28.0	2.88	94.2
6	0.67	5.40	9.01	34.5	1.04	0.04	14.5	0.98	0.18	0.18	26.7	2.20	95.4

Table B15 – Mesostasis EPMA analyses for chondrule Al-3

Analysis	Na_2O	MgO	Al_2O_3	SiO_2	P_2O_5	K_2O	CaO	TiO_2	Cr_2O_3	MnO	FeO	NiO	Total
1	1.84	4.47	7.78	23.6	7.75	0.16	11.0	0.62	0.15	0.22	28.7	4.41	90.8
2	1.48	4.68	8.81	28.2	5.39	0.20	10.8	0.79	0.09	0.19	29.7	2.37	92.6

Table B16 – Mesostasis EPMA analyses for chondrule Al-4

Analysis	Na_2O	MgO	Al_2O_3	SiO_2	P_2O_5	K_2O	CaO	TiO_2	Cr_2O_3	MnO	FeO	NiO	Total
1	0.30	21.9	3.12	35.7	0.29	0.14	0.55	0.05	0.30	0.25	31.0	2.61	96.2
2	0.48	12.2	3.34	27.1	0.48	0.12	2.22	0.23	0.19	0.21	38.7	2.75	88.0
3	0.51	15.8	2.10	39.2	1.03	<0.02	14.0	1.25	0.44	0.18	21.5	1.89	97.9
4	0.74	6.58	3.53	30.7	4.49	0.04	15.4	1.43	0.48	0.60	18.7	5.62	88.3

Table B17 – Mesostasis EPMA analyses for chondrule Al-5

Analysis	Na_2O	MgO	Al_2O_3	SiO_2	P_2O_5	K_2O	CaO	TiO_2	Cr_2O_3	MnO	FeO	NiO	Total
1	1.02	12.3	5.68	29.4	0.42	0.29	1.12	0.05	0.14	0.19	38.8	2.59	92.0
2	1.12	9.76	4.66	29.9	5.14	0.10	9.75	0.50	0.33	0.16	30.7	1.45	93.6
3	0.95	13.2	5.24	29.4	0.34	0.26	0.78	0.06	0.42	0.15	38.2	3.36	92.4

Table B18 – Mesostasis EPMA analyses for chondrule Al-6

Analysis	Na_2O	MgO	Al_2O_3	SiO_2	P_2O_5	K_2O	CaO	TiO_2	Cr_2O_3	MnO	FeO	NiO	Total
1	0.30	21.2	1.31	33.9	0.36	<0.02	1.23	0.12	0.38	0.33	37.3	0.39	96.8
2	1.02	6.28	5.44	36.8	6.21	0.02	21.3	1.64	0.32	0.14	13.5	0.23	92.9
3	0.08	28.3	0.18	35.8	0.27	<0.02	1.15	0.04	0.29	0.30	32.4	0.08	98.9
4	0.06	23.1	2.01	30.8	0.15	<0.02	0.66	0.04	0.08	0.34	33.3	0.16	90.6
5	0.88	11.7	3.33	30.6	7.65	0.04	16.0	0.80	0.16	0.18	22.0	0.98	94.3

Table B19 – Mesostasis EPMA analyses for chondrule N8-1

Analysis	Na_2O	MgO	Al_2O_3	SiO_2	P_2O_5	K_2O	CaO	TiO_2	Cr_2O_3	MnO	FeO	NiO	Total
1	7.31	2.35	11.1	58.0	1.00	0.02	7.03	0.49	0.09	0.20	11.9	0.31	99.8
2	4.35	6.28	8.71	55.6	0.80	0.03	11.6	0.50	0.36	0.16	9.64	0.12	98.1

Table B20 – Mesostasis EPMA analyses for chondrule N8-2

Analysis	Na_2O	MgO	Al_2O_3	SiO_2	P_2O_5	K_2O	CaO	TiO_2	Cr_2O_3	MnO	FeO	NiO	Total
1	1.48	6.12	5.59	40.7	0.88	0.30	8.95	0.52	0.15	0.17	26.5	2.88	94.2
2	3.63	3.92	7.68	47.0	0.81	0.18	6.02	0.42	0.12	0.17	22.1	2.68	94.7
3	1.55	7.58	5.44	41.6	0.94	0.26	7.90	0.80	0.23	0.23	26.0	2.07	94.8

Table B21 – Mesostasis EPMA analyses for chondrule N8-3

Analysis	Na_2O	MgO	Al_2O_3	SiO_2	P_2O_5	K_2O	CaO	TiO_2	Cr_2O_3	MnO	FeO	NiO	Total
1	1.46	11.2	3.85	41.7	0.49	0.30	3.26	0.31	0.21	0.20	30.0	0.75	93.7
2	1.36	11.2	3.32	44.6	2.10	0.24	14.3	0.98	0.36	0.15	17.5	0.55	96.6
3	0.60	11.8	2.66	43.0	1.14	0.34	11.4	0.40	0.68	0.21	21.0	0.37	93.6

Table B22 – Mesostasis EPMA analyses for chondrule N4-1

Analysis	Na_2O	MgO	Al_2O_3	SiO_2	P_2O_5	K_2O	CaO	TiO_2	Cr_2O_3	MnO	FeO	NiO	Total
1	9.77	3.11	15.4	61.3	0.34	1.00	0.43	0.49	0.10	0.15	6.80	0.38	99.3
2	9.46	2.17	15.1	62.6	0.26	1.27	1.13	0.51	0.10	0.14	5.85	0.33	99.0
3	7.52	4.60	13.5	62.6	0.31	0.97	4.94	0.57	0.48	0.19	4.12	<0.06	99.8
4	8.81	6.63	13.5	56.7	0.30	0.98	1.11	0.35	0.15	0.22	9.35	1.24	99.3
5	7.74	6.12	12.5	60.3	0.30	0.91	4.90	0.43	0.57	0.22	4.90	0.12	99.0

Table B23 – Mesostasis EPMA analyses for chondrule N4-2

Analysis	Na_2O	MgO	Al_2O_3	SiO_2	P_2O_5	K_2O	CaO	TiO_2	Cr_2O_3	MnO	FeO	NiO	Total
1	6.86	5.77	11.0	53.7	1.45	0.10	4.54	0.27	0.16	0.23	12.4	1.00	97.6
2	3.03	9.08	8.54	50.2	1.37	0.48	3.34	0.28	0.16	0.27	16.8	2.30	95.9
3	5.97	8.44	10.8	50.9	2.43	0.14	5.66	0.26	0.13	0.29	16.6	0.44	102.0

Table B24 – Mesostasis EPMA analyses for chondrule N4-3

Analysis	Na_2O	MgO	Al_2O_3	SiO_2	P_2O_5	K_2O	CaO	TiO_2	Cr_2O_3	MnO	FeO	NiO	Total
1	5.96	1.44	16.5	67.3	<0.09	0.92	2.40	0.61	0.10	0.19	3.57	<0.06	99.0
2	6.49	1.62	14.8	69.0	0.12	1.02	1.73	0.53	0.08	0.21	4.32	<0.06	99.9
3	5.72	2.26	15.6	67.2	0.11	0.85	4.06	0.62	0.08	0.21	4.65	0.11	101.4
4	6.13	1.32	16.1	64.2	0.12	0.97	1.64	0.53	0.03	0.18	8.67	0.42	100.3
5	7.00	3.61	14.0	60.9	0.15	0.67	6.90	0.51	0.74	0.27	4.32	0.08	99.2

B3. Pyroxene

Table B25 – Pyroxene EPMA analyses for chondrule N4-1

Analysis	Na_2O	MgO	Al_2O_3	SiO_2	P_2O_5	K_2O	CaO	TiO_2	Cr_2O_3	MnO	FeO	NiO	Total
1	0.09	27.5	0.49	55.2	<0.09	<0.02	2.14	<0.04	1.19	0.60	11.5	0.23	99.0
2	0.05	29.3	0.25	55.6	<0.09	<0.02	1.49	<0.04	0.99	0.54	11.3	0.28	99.8
3	0.13	27.6	0.43	55.1	<0.09	<0.02	2.78	0.13	1.02	0.59	11.9	0.15	99.8
4	0.38	23.6	1.40	53.7	<0.09	0.08	5.85	0.30	0.98	0.51	12.8	0.41	100.0
5	0.10	29.1	0.27	55.7	<0.09	<0.02	2.07	0.06	1.15	0.56	11.8	<0.06	100.8
6	0.13	27.9	0.36	55.8	<0.09	<0.02	2.48	0.08	1.13	0.62	12.5	<0.06	101.1
7	0.25	27.9	0.48	56.4	<0.09	<0.02	2.78	0.04	1.08	0.58	11.3	<0.06	100.8
8	0.09	29.9	0.28	56.8	<0.09	<0.02	1.20	0.05	1.04	0.56	10.9	<0.06	100.8
9	0.09	28.0	0.47	54.2	<0.09	<0.02	1.60	0.05	1.05	0.58	12.7	0.57	99.3
10	0.27	24.9	0.69	52.6	<0.09	<0.02	6.17	0.16	1.17	0.59	11.8	0.39	98.8

Table B26 – Pyroxene EPMA analyses for chondrule N4-3

Analysis	Na_2O	MgO	Al_2O_3	SiO_2	P_2O_5	K_2O	CaO	TiO_2	Cr_2O_3	MnO	FeO	NiO	Total
1	<0.05	33.5	0.16	58.0	<0.09	<0.02	1.13	<0.04	0.85	0.46	7.66	<0.06	101.9
2	<0.05	33.0	0.16	58.3	<0.09	<0.02	1.24	0.06	0.86	0.52	7.71	<0.06	101.8
3	0.07	33.7	0.24	56.6	<0.09	<0.02	1.35	0.05	0.88	0.46	7.91	<0.06	101.3
4	0.06	33.0	0.38	55.6	<0.09	<0.02	1.19	0.07	0.95	0.43	7.02	0.07	98.2
5	<0.05	34.4	0.24	56.6	<0.09	<0.02	0.97	0.04	0.89	0.44	7.39	<0.06	101.0
6	0.26	28.2	0.95	54.5	<0.09	0.05	4.72	0.11	1.00	0.51	7.56	0.18	98.1
7	<0.05	32.7	0.17	56.1	<0.09	<0.02	1.14	<0.04	0.85	0.48	8.22	0.26	100.0
8	0.10	31.2	0.49	55.6	<0.09	<0.02	2.33	0.06	1.00	0.49	8.20	0.11	99.9

B4. Chromite

Table B27 – Chromite EPMA analyses

Analysis	Na_2O	MgO	Al_2O_3	SiO_2	P_2O_5	K_2O	CaO	TiO_2	Cr_2O_3	MnO	FeO	NiO	Total
Al-1 Cr 1	0.08	6.83	17.9	1.02	<0.09	<0.02	0.18	0.86	42.3	0.24	26.6	0.17	96.1
Al-1 Cr 2	<0.05	6.09	16.2	1.26	<0.09	<0.02	0.08	1.47	42.5	0.28	29.1	0.09	97.1
Al-2 Cr 1	<0.05	7.29	13.9	0.34	<0.09	<0.02	0.19	1.50	46.6	0.31	26.2	0.07	96.4
Al-2 Cr 2	<0.05	7.89	15.2	0.31	<0.09	<0.02	0.18	0.93	46.1	0.25	24.8	<0.06	95.7
Al-4 Cr 1	<0.05	7.27	20.6	0.93	<0.09	<0.02	0.19	1.11	40.3	0.34	27.5	0.40	98.6
N8-1 Cr 1	<0.05	9.37	5.66	6.78	0.09	<0.02	0.14	1.61	44.9	0.55	28.0	0.06	97.2
N8-2 Cr 2	<0.05	6.55	8.76	0.49	<0.09	<0.02	0.21	1.44	53.7	0.48	25.2	0.09	96.9
N8-3 Cr 1	<0.05	5.24	5.37	0.53	<0.09	<0.02	0.08	2.08	54.0	0.44	28.6	0.13	96.4
N8-3 Cr 2	<0.05	6.73	9.44	0.41	<0.09	<0.02	0.14	0.87	53.7	0.43	24.8	<0.06	96.6

Appendix C
List of supplementary material

A. Microprobe data and bulk composition calculations

This folder contains Microsoft Excel spreadsheets with EPMA measurements of phases present in the twelve studied chondrules and the bulk compositions of the studied chondrules determined by modal recombination analysis.

B. Calibrated BSE compositional profiles

This folder contains a Microsoft Excel spreadsheet containing the calibrated BSE compositional profiles measured in the studied forsteritic-olivine relict grains.

C. Measured compositional profiles with model fits

This folder contains a Microsoft Excel spreadsheet containing the studied compositional profiles and model fits to the observed compositional profiles. These model fits were created using the explicit finite difference forward modelling program contained in F.

D. Diffusion model runs

This folder contains a set of folders, which house the successful diffusion model runs for each of the measured compositional profiles.

E. NanoSIMS profiles

This folder contains a spreadsheet of the FeO and P compositional profiles measured using NanoSIMS.

F. Diffusion model

This folder contains an unused copy of the explicit finite difference forward modelling program titled "*FiniteModel_ShiftBoundary_morecorrect*" and the worked example described in Chapter 5 and Appendix A.

G. Electronic copy of thesis

This folder contains an electronic copy of the thesis.